

THE UNIVERSITY of ADELAIDE

IMT Atlantique
Bretagne-Pays de la Loire
École Mines-Télécom

Quantum information processing with geometric phases, cavity magnonics, and semiconductor nanostructures

by Alan GARDIN

Principal supervisors:
Giuseppe Tettamanzi, senior lecturer, The University of Adelaide
Christian Person, professor, IMT Atlantique

Co-supervisors:
Christophe Fumeaux, professor, The University of Queensland
Vincent Castel, senior lecturer, IMT Atlantique

Examining commitee:
Andrew White, professor, The University of Queensland
Joseph Salfi, assistant professor, The University of British Columbia
Marianne Le Dantec, PhD, Thales

External advisers:
Ian Fuss, professor, The University of Adelaide
Gilles Coppin, professor, IMT Atlantique
Peter Veitch, professor, The University of Adelaide

Submitted March 2024
Defended on 19th July 2024 at the University of Adelaide

A thesis submitted in fulfilment of the requirements for

- *the degree of Doctor of Philosophy in the School of Physics of the University of Adelaide and,*
- *the degree of Doctor of Philosophy in the SPIN Doctoral School (specialty telecomunications) of IMT-Atlantique,*

under a joint cotutelle PhD program between the University of Adelaide and IMT-Atlantique.

To my mother.

Abstracts

English version

The broad objective of this thesis is to contribute to the practical realisation of quantum information processing, and more generally quantum technologies. Therefore, we first identify various physical resources and behaviours of interest. Among these, we focus in this thesis on coherent control (the ability to manipulate quantum information), quantum information transduction (the conversion of quantum information), non-reciprocal behaviours, and the creation of non-classical states.

Concerning coherent control, we examine the use of semiconductor-based nanostructures, notably electrostatically defined quantum dots in silicon-germanium heterostructures for quantum computing. By considering such a structure in the presence of a slightly tilted silicon-germanium interface, we theoretically demonstrate the control of a quantum bit based on the valley degrees of freedom, originating from the degenerate conduction band minima of silicon.

We also study the ultrastrong coupling of light and matter, which can occur in various physical systems such as cavity magnonics and semiconductor nanostructures. Notably, the ultrastrong coupling regime allows for faster quantum information transduction and the creation of non-classical states.

Cavity magnonics is shown to be a versatile platform with applications in quantum information transduction, the creation of non-classical states, and the engineering of non-reciprocal effects. Concerning the latter, we show that it can be created using synthetic gauge fields, themselves induced by combining various Zeeman interactions by a process reminiscent of geometric phases.

Keywords: phase, silicon, magnonics, cavity, quantum information transduction, non-reciprocity.

French version

L'objectif est de contribuer à la réalisation du traitement de l'information quantique et plus généralement des technologies quantiques. Nous commençons par identifier plusieurs ressources physiques et comportements d'intérêt. Parmi ces derniers, nous nous concentrons sur le contrôle cohérent (la capacité à manipuler l'information quantique), la transduction de l'information quantique, les comportements non-réciproques, et la création d'états non-classiques.

Nous examinons l'utilisation de nano-structures à base de semi-conducteurs, notamment des points quantiques définis électro-statiquement dans des hétéro-structures de silicium-germanium, pour le calcul quantique. En considérant une telle structure en présence d'une inclinaison de l'interface silicium-germanium, nous montrons théoriquement le contrôle d'un bit quantique utilisant les degrés de liberté des vallées, provenant de minimums dégénérés de la bande de conduction du silicium.

Nous étudions le couplage ultra-fort, qui intervient dans divers systèmes physiques comme la magnonique en cavité et les nano-structures semiconductrices. En particulier, le couplage ultra-fort permet une transduction de l'information quantique plus rapide, ainsi que la création d'états non-classiques.

Nous montrons que la magnonique en cavité est polyvalente avec des applications en transduction de l'information quantique, la création d'états non-classiques, et l'ingénierie de comportements non-réciproques. Concernant ces derniers, nous montrons qu'ils peuvent être obtenus en créant un champ de jauge synthétique, lequel peut être induit en combinant plusieurs interactions de Zeeman par un processus similaire à celui des phases géométriques.

Mots clés: phase, silicium, magnonique, cavité, transduction, non-réciprocité.

Declaration

I certify that this work contains no material which has been accepted for the award of any other degree or diploma in my name, in any university or other tertiary institution and, to the best of my knowledge and belief, contains no material previously published or written by another person, except where due reference has been made in the text. In addition, I certify that no part of this work will, in the future, be used in a submission in my name, for any other degree or diploma in any university or other tertiary institution without the prior approval of the University of Adelaide and where applicable, any partner institution responsible for the joint award of this degree.

The author acknowledge that copyright of published works contained within the thesis resides with the copyright holder(s) of those works.

I give permission for the digital version of my thesis to be made available on the web, via the University's digital research repository, the Library Search and also through web search engines, unless permission has been granted by the University to restrict access for a period of time.

I acknowledge the support I have received for my research through the provision of an Australian Government Research Training Program Scholarship.

Alan Gardin, 20/03/2024

Acknowledgments

First of all, I would like to thank my supervisors, Dr. Giuseppe Carlo Tettamanzi[1], Dr. Vincent Castel, professor Christophe Fumeaux, and professor Christian Person. Aside from their guidance and support on technical and research-related problems, they have taught me how much of a human experience a PhD can be. I would also like to thank my fellow students, Ross[2], Tyler[3], Thomas[4], Jonathan and Guillaume[5] for various physics and frustration-related conversations. Furthermore, I would like to acknowledge Dr. Jeremy Bourhill, Dr. Vincent Vlaminck, Dr. Isabella Boventer, and associate professor Rajib Rahman[6], with whom I had the pleasure to collaborate during this thesis.

I would also like to acknowledge all the people who made this co-tutelle PhD possible, namely Dr. Giuseppe Tettamanzi, professor Gilles Coppin, Dr. Paolo Bortolotti, Dr. John Best, Dr. Damien Leclercq, Marine Le Corre and Lisa Staines to name a few. Similarly, I would also like to thank professor Gilles Coppin and Dr. Ian Fuss for their advice throughout the PhD. Additionally, I would like to thank professor Pablo Arrighi and professor Giuseppe Di Molfetta[7], who sparked my interest in quantum physics in the first place.

Importantly, I would like to thank my family for letting me embark on this journey. Indeed, I recognise that having the freedom to follow one's interest, however diverse they may be, is a chance that not everyone has. I know that regardless of whether you thought I would succeed or not, you would have supported me just the same, so thank you for this peace of mind.

Finally, I would like to acknowledge financial support from Thales Australia and Thalès Research & Technology. This work was supported with supercomputing resources provided by the Phoenix HPC service at the University of Adelaide. This work is also part of the research program supported by the European Union through the European Regional Development Fund (ERDF), by the Ministry of Higher Education and Research, and Brittany region, through the CPER SpaceTech DroneTech, and the ANR projects ICARUS and MagFunc.

[1]Notably for the regular jokes about France and Italy, and telling me about the best restaurant in Adelaide.

[2]In particular, thank you for taking an incredible amount of time to listen to my questions about basic physics, because in the end "I'm just an engineer".

[3]For not shooting me with his Nerf gun.

[4]AKA the bulldozer.

[5]For going to the gym without fault, and sharing my interest in cheese and wine.

[6]Even though he left afraid students alone at their first international conference dinner in Sydney.

[7]I distinctly remember how, over coffee on the top of the building I interned in at the time, he explained in layman's terms the principles of gauge theories and the relation with the standard model. This conversation of merely five minutes decided me to attempt a PhD in quantum physics despite my differing engineering background.

Contents

Abstracts . . . 1
Declaration . . . 2
Acknowledgments . . . 3

Contents **5**

I. Introduction **11**

II. An overview of quantum information processing **14**
1) Introduction . . . 15
2) Quantum information . . . 15
2.1 Discrete variables . . . 15
2.2 Continuous variables . . . 18
2.2.1 Quantum harmonic oscillator and number states . . . 18
2.2.2 Bosonic modes . . . 19
2.2.3 Coherent states . . . 20
2.2.4 (Schrödinger) Cat states . . . 22
2.2.5 Squeezed states . . . 22
2.3 Non-classical measures . . . 23
2.3.1 Entanglement, quantum steering and Bell non-locality . . . 23
2.3.2 Entanglement measures for Gaussian continuous variables . . . 24
2.3.3 Non-classical statistics . . . 26
3) An overview of quantum technologies . . . 27
3.1 Quantum sensing and metrology . . . 27
3.2 Quantum (secure) communication . . . 28
3.2.1 Quantum networks . . . 28
3.2.2 Quantum cryptography . . . 29
4) Circuit-model of universal quantum computation . . . 30
4.1 The various forms of quantum computation . . . 30
4.2 Di-Vicenzo criteria . . . 31
4.3 Characterising the lifetime of quantum information . . . 32
4.4 Quantum gates . . . 32
4.4.1 Single-qubit rotations . . . 32
4.4.2 Universal quantum computation . . . 33
4.5 Quantum error correction . . . 34
5) Some physical platforms . . . 34
5.1 Photons . . . 35
5.2 Cavity and circuit quantum electrodynamics . . . 35
5.3 Trapped ions . . . 36
5.4 Cavity optomechanics . . . 36
6) Conclusion . . . 37

III. Introduction to light/matter interactions **39**
1) Introduction . . . 40
2) Quantum description of the electromagnetic field . . . 40
2.1 Introduction . . . 40

2.2 Classical electrodynamics . . . 41
2.2.1 Maxwell's equations . . . 41
2.2.2 Gauge degree of freedom . . . 42
2.2.3 Dynamics and solutions . . . 43
2.3 Canonical quantisation in the Coulomb gauge . . . 44
3) Some models of light/matter interactions . . . 45
3.1 Interaction with the electromagnetic field . . . 46
3.2 The electric dipole interaction . . . 47
3.3 The quantum Rabi model . . . 48
3.4 Multi-dipole extension: Dicke model . . . 50
3.5 The rotating wave approximation and the Jaynes-Cummings model . . . 51
4) Closed-system analysis . . . 52
4.1 Diagonalisation: spectrum and polaritons . . . 52
4.2 Perturbation theory using Schrieffer-Wolff transformations . . . 55
4.2.1 Principle . . . 55
4.2.2 Dispersive regimes . . . 56
4.2.3 Indirect coupling . . . 58
5) Open quantum systems . . . 59
5.1 Quantum Langevin equations . . . 60
5.1.1 Coherent drive . . . 63
5.2 Input-output formalism . . . 65
5.2.1 Input-output relations . . . 65
5.2.2 Application: coupled bosonic modes . . . 66
6) Conclusion . . . 69

IV. Coherent microwave cavity magnonics 70
1) Introduction . . . 71
1.1 Magnonics . . . 71
1.2 Cavity magnonics . . . 72
2) Fundamentals of magnetism . . . 73
2.1 Magnetic order . . . 73
2.2 Zeeman interaction . . . 74
3) Spin waves . . . 75
3.1 Angular momenta in quantum mechanics . . . 75
3.2 Quantum model of ferrimagnets . . . 77
3.3 Quantum model of spin-waves . . . 78
4) Microwave photon/magnon interaction . . . 79
4.1 Interaction Hamiltonian . . . 79
4.2 Further comments on the microwave photon/magnon interaction . . . 81
4.3 Relevance of the coupling phase . . . 83
4.4 Classical electrodynamics model . . . 84
4.4.1 Landau-Lifschitz-Gilbert equation . . . 84
4.4.2 Linearisation . . . 85
4.4.3 Linearisation with demagnetising factors . . . 86
5) Experimental aspects and cavity engineering . . . 88
5.1 COMSOL Multiphysics® for microwave cavity magnonics . . . 88
5.2 Coupling phase engineering . . . 88
6) Conclusion . . . 89

V. Geometric phases and gauge fields 90
1) Introduction . . . 91
2) Non-adiabatic physics . . . 91
2.1 Introduction on the harmonic oscillator . . . 91
2.2 Quantum adiabatic theorem and adiabatic approximation . . . 92
2.3 Application: massive particle in an harmonic potential . . . 94
2.4 Landau-Zener transitions . . . 95

3) Continuous geometric phases and their applications . . . 95
3.1 Adiabatic abelian case: the Berry phase . . . 96
3.2 Non-abelian case: holonomies . . . 98
3.3 Non-adiabatic generalisations . . . 99
3.4 Application to quantum computation . . . 101
4) Gauge theories . . . 103
4.1 Gauge symmetry in particle physics . . . 104
4.2 Gauge structure of geometric phases . . . 104
4.3 Further remarks and applications . . . 106
5) Discrete gauge-invariant phases . . . 107
5.1 Connection to a particle in a magnetic field on a lattice . . . 107
5.2 Connection with geometric phases . . . 108
6) Conclusion . . . 108

VI. Dissipative couplings and non-reciprocal behaviours 109
1) Introduction . . . 109
2) Theory of dissipative coupling and level attraction . . . 110
2.1 Common coupling to a strongly dissipative mode . . . 111
2.2 Common coupling to a bath . . . 113
2.3 Analysis of the dissipative coupling Hamiltonian . . . 114
3) Observations of level attraction . . . 116
3.1 Level attraction due to dissipative coupling . . . 116
3.2 Level attraction in other physical systems . . . 117
3.3 Anti-resonances in three-dimensional cavities . . . 117
3.4 Two-tone driving in cavity magnonics . . . 119
4) Engineering non-reciprocal behaviour . . . 119
4.1 Ring of three bosonic modes . . . 120
4.2 Engineering non-reciprocal interactions in a ring of four bosonic modes . 121
4.3 Controlling $U(1)$ gauge fields in loop-coupled systems . . . 121
5) Conclusion . . . 122

VII. Physics of the ultrastrong coupling regime and beyond 124
1) Introduction . . . 124
2) Hopfield-Bogoliubov diagonalisation . . . 126
2.1 Principles . . . 126
2.2 Applications . . . 127
2.2.1 Diagonalisation of squeezing terms . . . 127
2.2.2 Diagonalisation of the Hopfield model . . . 128
3) Input-output formalism . . . 129
3.1 Differences with the standard input-output theory . . . 129
3.2 Example: Hopfield model . . . 130
4) Phenomenology of the USC regime . . . 131
4.1 Virtual excitations and squeezing . . . 131
4.2 Sum rules . . . 132
4.3 Diamagnetic term and its consequences . . . 135
4.4 Gauge invariance . . . 136
5) Cavity magnonics in the USC . . . 136
6) Cavity-mediated ultrastrong magnon-magnon coupling . . . 136
7) Conclusion and outlook . . . 137

VIII. Engineering non-classical states using non-linear bosonic interactions 138
1) Introduction . . . 138
2) General principles . . . 139
2.1 Method and example . . . 139
2.2 Linearisation and strong driving . . . 141
3) Some non-linear bosonic interactions . . . 141

3.1 Optomechanical interaction . . . 141
3.2 Kerr interactions . . . 143
3.3 Wave mixing . . . 143
3.3.1 Three-wave mixing . . . 143
3.3.2 Parametric and squeezed driving . . . 144
4) Hybrid schemes . . . 144
5) Enhancing entanglement . . . 147
6) Conclusion . . . 148

IX. Silicon-based quantum computing 149
1) Introduction . . . 149
2) Nanostructures and quantum confinement . . . 150
3) Valley physics in silicon . . . 151
3.1 Introduction to valley physics . . . 153
3.2 Tight-binding approach . . . 154
3.3 Effective mass approach . . . 156
3.3.1 General case . . . 157
3.3.2 Flat quantum well . . . 158
4) Charge qubits . . . 159
4.1 Standard charge qubits . . . 159
4.2 Valley qubits . . . 160
5) Conclusion . . . 161

X. Conclusion and perspectives 163
1) Summary of contributions . . . 163
2) Outstanding work . . . 164
3) Future directions . . . 165

A. Theoretical reminders 168
A.1) Operator identities . . . 168
A.2) Unitary transformations . . . 170
A.2.1 Displacement transformation . . . 170
A.2.2 Squeezing transformation . . . 171
A.3) Fourier transforms . . . 171

B. Supplemental calculations 173
B.1) Commutation relations of the input fields . . . 173
B.2) Coherent drives and displacement transformations . . . 173
B.2.1 Cavity driven by a coherent drive . . . 173
B.2.1.1 Empty cavity . . . 173
B.2.1.2 Cavity with linear coupling to a bosonic mode . . . 174
B.2.1.3 Empty cavity with complex coupling to the drive . . . 175
B.3) Indirect coupling in a ring of three bosonic modes . . . 175
B.4) Normalisation of the mode functions of the electromagnetic field . . . 177
B.5) Derivation of the Zeeman interaction . . . 178
B.5.1 Orbital angular momentum . . . 178
B.5.2 Spin orbital angular momentum . . . 179
B.6) Derivation of the magnon Hamiltonian . . . 180
B.7) Derivation of the Polder susceptibility tensor . . . 183
B.7.1 Without demagnetisation fields . . . 184
B.7.2 Including demagnetising factors . . . 184
B.7.3 Pertubation along the equilibrium direction . . . 185
B.8) Equation for the magnetic field in a medium . . . 187
B.9) Input-output theory for two bosonic modes coupling to a common waveguide . 188
B.10) Simplification of the effective Hamiltonian for two bosonics modes coupled to a common waveguide . . . 190

B.11) Additional examples of Hopfield–Bogoliubov transformation . . . 191
B.11.1 Hopfield model with several cavity modes . . . 191
B.11.2 Multimode Hopfield model . . . 192
B.11.3 Another multimode Hopfield model . . . 193
B.12) Heisenberg equation of motions of the averages of the harmonic oscillator . . . 194
B.13) Input-output for two cavity modes . . . 195
B.14) Input-output theory of the Hopfield model in the USC . . . 196
B.14.1 Quantum Langevin equations in the time domain . . . 197
B.14.2 Quantum Langevin equations in the frequency domain . . . 199
B.14.3 Input-output relations and frequency domain Langevin forces and memory kernels . . . 200
B.14.4 Relation between the output and input fields in frequency space . . . 201
B.14.5 Reflection and transmission coefficients . . . 201
B.15) Bloch-Siegert corrections to the Dicke model . . . 202
B.16) Proof of the standard sum rule . . . 203
B.17) A shortcut to computing the equation of motion of quadratures . . . 204
B.18) Proof of the sum rule for interacting photons . . . 205

C. Original works **206**
C.1) Manifestation of the coupling phase in microwave cavity magnonics . . . 207
C.2) Using COMSOL Multiphysics® to model hybrid magnon-photon systems . . . 224
C.3) Engineering synthetic gauge fields through the coupling phases in cavity magnonics . . . 238
C.4) Discrete (geometric) phases in loop-coupled bosonic systems . . . 254
C.5) Level attraction from interferences in two-tone driving . . . 260
C.6) Engineering non-reciprocal behaviour in a ring of four bosonic modes . . . 281
C.7) Effective Hamiltonian for the ultrastrong magnon-photon Zeeman coupling . . . 289
C.8) Cavity-mediated ultrastrong magnon-magnon coupling . . . 299
C.9) Study of the optomechanical coupling between a cavity photon and a magnon . . . 304
C.10) Nonadiabatic quantum control of valley states in silicon . . . 312

Bibliography **327**

Included publications

1. Alan Gardin et al. “Manifestation of the Coupling Phase in Microwave Cavity Magnonics”. In: *Physical Review Applied* 19.5 (May 2023), p. 054069. DOI: 10.1103/physrevapplied.19.054069. arXiv: 2212.05389 [quant-ph]

2. Alan Gardin et al. “Engineering synthetic gauge fields through the coupling phases in cavity magnonics”. In: *Physical Review Applied* 21.6 (June 13, 2024), p. 064033. DOI: 10.1103/PhysRevApplied.21.064033. arXiv: 2312.04915 [quant-ph]. URL: https://link.aps.org/doi/10.1103/PhysRevApplied.21.064033 (visited on 06/18/2024)

3. Alan Gardin et al. *Level attraction from interference in two-tone driving*. arXiv:2404.17108. type: article. arXiv, Apr. 25, 2024. arXiv: 2404.17108. URL: http://arxiv.org/abs/2404.17108 (visited on 04/29/2024)

4. Alan Gardin et al. “Nonadiabatic quantum control of valley states in silicon”. In: *Physical Review B* 105.7 (Feb. 2022), p. 075406. DOI: 10.1103/physrevb.105.075406

Related publications

1. Guillaume Bourcin et al. “Level attraction in a quasi-closed cavity”. In: arXiv:2402.06258 (Feb. 9, 2024). type: article. arXiv: 2402.06258[quant-ph]. URL: http://arxiv.org/abs/2402.06258 (visited on 02/12/2024)

Chapter I

Introduction

Motivation and context. In recent years, quantum technologies have attracted more and more interest thanks to their potential to revolutionise information processing and technologies. For instance, quantum computation and quantum simulation are expected to improve the performance of big data, finance, communications security, drug discovery, sensors, fundamental physics and so on. While many of these "quantum-enhanced" proposals have been around for quite some time, so far only a reduced subset, such as boson sampling or quantum key distribution, have led to a practical "quantum advantage" over classical technologies. One reason is that the physical implementations of many quantum technologies are facing challenges due to somewhat oxymoronic requirements: the need to preserve quantum information, while also interacting with it. Indeed, the best way to protect quantum information from many sources of noise is to isolate it from its external environment. At the same time, one needs the ability to manipulate quantum information (say to perform quantum computation) and read it out using measurements. This inevitably involves coupling the quantum system to its external environment, which introduces additional sources of loss. Therefore, moving forward it seems essential to simultaneously understand the high-level "quantum software" requirements while paying attention to the low-level "quantum hardware" constraints.

In this thesis, we attempt to take this approach, albeit with more focus on the physical side of quantum information processing. We particularly explore the potential of two promising physical systems, cavity magnonics and semiconductor nanostructures, for various quantum technologies. The following outline, pictured in figure I.1, summarises the contents of the thesis and the contributions.

Outline and contributions. *Chapter II: An overview of quantum information processing.* In this chapter, we begin by defining the concept of quantum information and we highlight some of its non-classical properties. Then, we give an overview of quantum technologies and different physical platforms, with the purpose of identifying the physical resources and some behaviours of interest for quantum information processing. The concepts identified are developed in the next chapters, and hence chapter II can be thought of as a technical justification of the contents of this thesis.

Chapter III: Introduction to light/matter interactions. One of the highlights of chapter II is the importance of light in quantum information processing. In particular, its interaction with matter allows to overcome some of its intrinsic limitations. Thus, in this chapter, we develop the formalism to describe light quantum-mechanically, and discuss some basic models of light-matter interaction. The tools introduced here are used in chapters IV and VI to VIII.

Chapter IV: Coherent microwave cavity magnonics. Among the many elementary building blocks of quantum technologies identified in chapter II, *quantum information transduction*, the conversion and exchange of information between different physical systems, is a task particularly suited to cavity magnonics systems. In this chapter, cavity magnonics is introduced from first-principles, and in so doing we notice the presence of a *coupling phase* which had not been discussed before in the literature. In Gardin et al. (2023) [1] published in *Physical Review Applied*, we theoretically discuss the physical relevance of these coupling phases, based on (at the time) unpublished experimental results. Then, in Gardin et al. (2024) [2], submit-

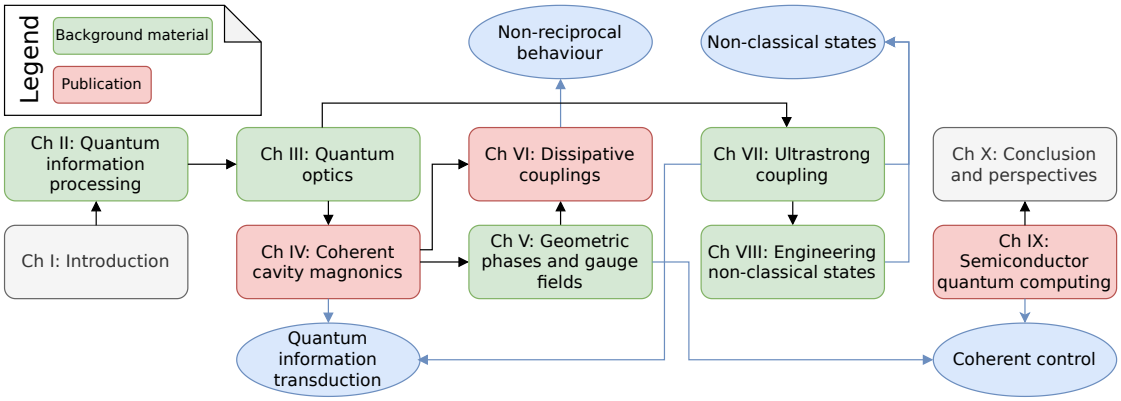


Figure I.1: Outline of the thesis, linking each chapter with the concepts (in blue) identified in chapter II. The chapters containing publications, published or submitted, are shown in red. Additionally, the notion of geometric phase (not shown) intervenes in chapters IV to VI.

ted to *Physical Review Applied*, we provide experimental evidence of the relevance of these coupling phases, and explain how they can be engineered. Both publications [1, 2] contribute to fundamental aspects of cavity magnonics, and the practical use of cavity magnonics system for *quantum information transduction* and *quantum memories*.

Chapter V: Geometric phases and gauge fields. In chapter IV, the coupling phases only lead to physical consequences in the presence of a coupling loop. This phenomenon is akin to the physics of *geometric phases*. Thus, in chapter V, we review (conitnuous) geometric phases with the objective of better understanding the physicality and applications of the coupling phases. In this chapter, an unpublished comparison between the coupling phases and geometric phases is carried out. During the review of geometric phases, we shall notice they have applications to *coherent control*, i.e. the manipulation of quantum information, which is useful for quantum computing. Such an application seems, however, not applicable to the coupling phases of chapter IV due to their discrete nature.

Chapter VI: Dissipative couplings and non-reciprocal behaviours. Instead, in this chapter we shall see that a combination of the coupling phases and an engineering of the losses can lead to *non-reciprocal behaviours*, which is another important primitive capability identified in chapter II. Additionally, during our study of the engineering of dissipation, we will consider the experimental response of a system in the presence of excitations provided by the environment. We shall see that the observation of the spectral signature of some physics does not guarantee that this physics is indeed taking place, as shown by the original work [3] of appendix C.5. This work is under review by *Physical Review Letters*, and contributes to the fundamental understanding of the experimental signatures of coherent and dissipative couplings.

Chapter VII: Physics of the ultrastrong coupling regime and beyond. In this chapter, we consider the ultrastrong coupling regime of light/matter interactions. This peculiar regime in which many standard approximations fail can be seen as a resource for faster *quantum information transduction*, and the creation of *non-classical states*, which once again are two concepts identified in chapter II. The assumptions of chapter III will be relaxed, which will require us to introduce additional theoretical methods for the treatment of this regime. Concerning the contributions, we investigate the theoretical model of a cavity magnonics system in the ultrastrong coupling regime, which constitutes unpublished work. Furthermore, we examine a cavity magnonics system similar to that studied in chapter IV in the ultrastrong coupling regime, and comment on its potential for *quantum information transduction*. This latter work remains currently also unpublished.

Chapter VIII: Engineering non-classical states using non-linear bosonic interactions. Non-classical states are essential resources for many quantum information processing schemes, as discussed in chapter II. Thus in this chapter we investigate several methods to create such quantum states. We will see that cavity magnonics, due to its many non-linearities, is a good platform to create non-classical states. Inspired by a non-linear interaction naturally arising in cavity optomechanics, we will investigate whether a formally identical interaction in cavity

magnonics can be used to create non-classical states, a work that is also still unpublished.

Chapter IX: Silicon-based quantum computing. The use of semiconductor nanostructures, especially based on silicon, is discussed under the lens of quantum computing. After a review of silicon physics and silicon-based quantum computing, we propose in Gardin et al. (2022) [4] a new way of potentially carrying out quantum computation based on the valley degrees of freedom. In this contribution, we take advantage of non-adiabatic physics, first introduced in chapter V, to manipulate quantum states. Therefore, in this work published in *Physical Review B*, we achieve *coherent control* of quantum states, which is identified in chapter II as being another elementary building block of many quantum technologies. Gardin et al. (2022) [4] also contributes to the fundamental understanding of valley physics in silicon nanostructures, a topic relevant for other silicon-based implementations of quantum information systems.

Finally, in chapter X: Conclusion and perspectives, we conclude on our work, and identify several future work and topic of interest. Notably, we comment on what remains to be performed on the many unpublished works in this thesis. A reflection on the different concepts studied in this thesis, and their application to cavity magnonics and semiconductor nanostructures is also undertaken.

Structure and conventions. Throughout this manuscript, a basic knowledge of quantum mechanics and electrical engineering is assumed. Nevertheless, *Appendix A: Theoretical reminders* gives some theoretical reminders, and will be referred to as needed. Having strongly benefited from reading other Masters' and PhD theses, we have adopted a pedagogical style, and hopefully provided enough details[1] on calculations to be useful for students. Thus, for the sake of completeness, most calculations are included, with a significant amount in *Appendix B: Supplemental calculations* so that they do not obscure the flow of the discussion. To clearly distinguish between a review of the literature from original works, the latter are embedded in the form of papers in *Appendix C: Original works*. Some of the works included have been published, others have been submitted, while others are not ready for submission yet.

Footnotes indicate more details on a given topic, and since they do not contain any critical information impeding the understanding of the rest of the thesis, they can be skipped. Each chapter, except for this introduction and the conclusion, are preceded by a summary of the content and contributions present in the chapter. In particular, the summary aims at placing each chapter in the context of the whole thesis. Bold letters, such as $\boldsymbol{v}$ denote three-dimensional vectors. In the case of unit vectors, a hat is used, e.g $\hat{\mathbf{x}}$. The Fourier transform has several definitions depending on the field it is applied in. The definition in use throughout this thesis is defined in appendix A.3. Finally, we simply write $\omega/2\pi$ instead of the formal $\omega/(2\pi)$ to denote the frequency associated with the angular frequency ω.

[1] Which unfortunately I have found to be too limited in many so-called "pedagogical" texts.

Chapter II

An overview of quantum information processing

Summary

Quantum mechanics allows to improve many classical information processing tasks by using quantum information and quantum-mechanical principles. Understanding quantum information is hence a prerequisite to study quantum technologies. Therefore, we introduce the appropriate formalism to describe both discrete and continuous variables, highlighting several non-classical states of interest. Next, we attempt to identify elementary capabilities required for quantum information processing. Thus, we give an overview of several quantum technologies, including quantum computation, quantum sensing and quantum communication. Finally, we review several physical platforms for implementing some of identified building blocks. The goal of this discussion is to offer a basis of comparison with the systems at the core of this thesis, i.e. cavity magnonics and semiconductor nanostructures.

Contents

1) Introduction . . . **15**
2) Quantum information . . . **15**
2.1 Discrete variables . . . 15
2.2 Continuous variables . . . 18
2.2.1 Quantum harmonic oscillator and number states . . . 18
2.2.2 Bosonic modes . . . 19
2.2.3 Coherent states . . . 20
2.2.4 (Schrödinger) Cat states . . . 22
2.2.5 Squeezed states . . . 22
2.3 Non-classical measures . . . 23
2.3.1 Entanglement, quantum steering and Bell non-locality . . . 23
2.3.2 Entanglement measures for Gaussian continuous variables . . . 24
2.3.3 Non-classical statistics . . . 26
3) An overview of quantum technologies . . . **27**
3.1 Quantum sensing and metrology . . . 27
3.2 Quantum (secure) communication . . . 28
3.2.1 Quantum networks . . . 28
3.2.2 Quantum cryptography . . . 29
4) Circuit-model of universal quantum computation . . . **30**
4.1 The various forms of quantum computation . . . 30
4.2 Di-Vicenzo criteria . . . 31
4.3 Characterising the lifetime of quantum information . . . 32
4.4 Quantum gates . . . 32
4.4.1 Single-qubit rotations . . . 32

4.4.2 Universal quantum computation . . . 33
4.5 Quantum error correction . . . 34
5) Some physical platforms . . . **34**
5.1 Photons . . . 35
5.2 Cavity and circuit quantum electrodynamics . . . 35
5.3 Trapped ions . . . 36
5.4 Cavity optomechanics . . . 36
6) Conclusion . . . **37**

1) Introduction

In this chapter, we attempt to justify the research interests proposed in thesis, which include quantum information transduction, non-reciprocal behaviours, coherent control, and the creation of non-classical states. This justification proceeds by reviewing various quantum technologies, and identifying some phenomena that are particularly suited for cavity magnonics and semiconductors platforms.

The axioms of quantum mechanics allow the existence of states with no classical equivalent. These non-classical states are useful resources for various quantum technologies. The first step towards this goal is to understand how to define and characterise quantum information, which is the purpose of section 2. The language provided by section 2 allows us to discuss some modern applications of quantum mechanics to technology in section 3. The goal is to describe these technologies, and identify on which quantum resources or elementary principles they are based on, and thus our review is not exhaustive. A notable exception in section 3 is quantum computing, to which we dedicate section 4. Next, we discuss in more details quantum computation in section 4, with an emphasis on the circuit model. The measures of coherence of the system are introduced, along with universal single-qubit gates. Finally, in section 5 we shall turn our attention to some of the physical platforms being studied for quantum technologies, and their strengths and weaknesses with respect to the elementary capabilities identified in sections 3 and 4. In light of all these results, we conclude in section 6 by recalling the relevance of the next chapters.

2) Quantum information

Quantum information can be hosted by two types of variables: discrete variables (DV) and continuous variables (CV). Discrete variables are closer to the classical unit of information, the bits, so we begin our discussion with them.

2.1) Discrete variables

Quantum bits: the quantum unit of information. Classical computing[1] uses bits as the unit of information, with only two possibles values (0 and 1). In quantum information, the analogue of a bit is simply referred to as a quantum bit, which we will abbreviate as *qubit*. Contrary to classical bits, qubits encode information as a linear combination of 0s and 1s, thanks to the superposition principle of quantum mechanics [5]. Hence, a qubit is a quantum system with two possible states, which using Dirac's braket notation are written $|0\rangle$ and $|1\rangle$. There are many physical systems that can implement a qubit, e.g. electron spins, electronic orbitals of atoms, or the polarisation of photons. For the moment, it is sufficient to think in terms of the abstract states $|0\rangle$ and $|1\rangle$ without considering the underlying physical implementation, which we leave for section 5.

[1] Other forms of classical computation exists, for instance neuromorphic computing. Furthermore, we use the word "bit" here in an abstract way, without referring to a specific physical implementation. Indeed, one can perform classical computation using a billboard, but it is so unconvenient that we do not, see [5].

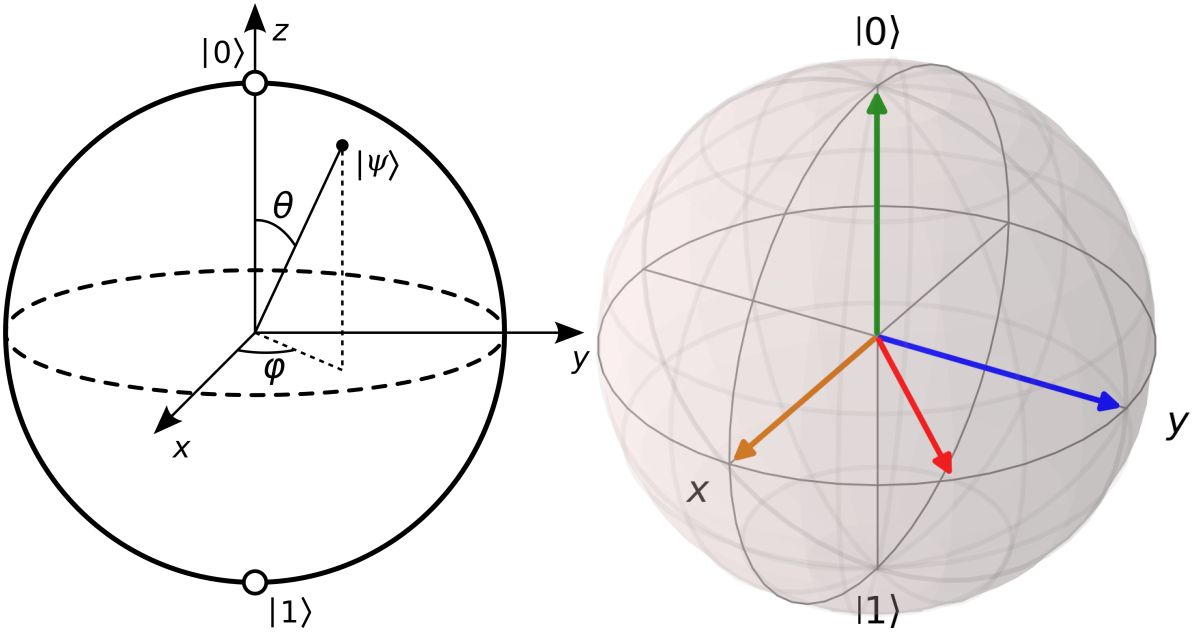


Figure II.1: Left: illustration of an arbitrary state described by equation (II.2) on the Bloch sphere. Image taken from [6] licensed under CC BY-SA 3.0 Deed [7]. Right: illustration on the Bloch sphere of the states $|0\rangle$ (green), $\frac{|0\rangle+|1\rangle}{\sqrt{2}}$ (orange), $\frac{|0\rangle+i|1\rangle}{\sqrt{2}}$ (blue), and $\frac{|0\rangle+e^{i\pi/4}|1\rangle}{\sqrt{2}}$ (red) generated using QuTiP [8, 9].

Formally, qubits live in a two-dimensional Hilbert space $\mathcal{H}$. The set $\{|0\rangle, |1\rangle\}$ is referred to as the computational basis[1], and hence any state $|\phi\rangle \in \mathcal{H}$ can be decomposed in terms of $|0\rangle$ and $|1\rangle$, i.e.

$$|\psi\rangle = \alpha\,|0\rangle + \beta\,|1\rangle\,, \tag{II.1}$$

where $\alpha, \beta \in \mathbb{C}$. The coefficients α and β satisfy $|\alpha|^2 + |\beta|^2 = 1$, which is a *normalisation condition* imposed by quantum mechanics. Physically, as per the axioms of quantum mechanics, $|\alpha|^2$ ($|\beta|^2$) gives the probability of measuring $|\psi\rangle$ in the state $|0\rangle$ ($|1\rangle$).

The Bloch sphere. The normalisation of the state $|\psi\rangle$ allows to rewrite it as

$$|\psi\rangle = \cos\frac{\theta}{2}\,|0\rangle + e^{i\varphi}\sin\frac{\theta}{2}\,|1\rangle\,, \tag{II.2}$$

in terms of a pair of angles $(\theta, \varphi) \in [0, \pi] \times [0, 2\pi]$. These two angles allow to visually represent states on the *Bloch sphere*, as pictured in figure II.1. The Bloch sphere is particularly convenient to observe the evolution of quantum states, especially for single-qubit operations for quantum computing (see section 4 below).

Describing two-level systems. As we mentioned, qubits are linear combinations of the two basis states $|0\rangle$ and $|1\rangle$. Physically, this describes a two-level system (TLS), where each state has its own energy level (assumed to be non-degenerate). Let us assume that $|0\rangle$ is the ground state of some physical system (e.g. spin, atomic orbitals...), with energy[2] $\hbar\Omega_0$, and $|1\rangle$ is the excited state with energy $\hbar\Omega_1 > \hbar\Omega_0$. We can write the Hamiltonian of this system in matrix form as

$$H = \hbar\begin{pmatrix} \Omega_1 & 0 \\ 0 & \Omega_0 \end{pmatrix} \tag{II.3}$$

[1]The basis is not unique, and some are more useful than others. We will see later that choosing alternative bases is a key element of some quantum information processing schemes, such as the quantum key distribution protocol BB84.

[2]Here, $\hbar$ is the reduced Planck constant with unit of angular momentum. Multiplied with a frequency Ω_0, this gives the dimension of energy. Thus, we follow the common practice of assimilating frequency with energy in the rest of this thesis.

after assimilating states to vectors as $|0\rangle \mapsto (0\,1)^t$ and $|1\rangle \mapsto (1\,0)^t$. However, it is more convenient to describe a TLS in terms of the difference in energy $\Delta = \Omega_1 - \Omega_0$ between the two states. We can separate the Hamiltonian above in two terms as

$$H = \frac{\hbar}{2}\begin{pmatrix} \Omega_0 + \Omega_1 & 0 \\ 0 & \Omega_0 + \Omega_1 \end{pmatrix} + \frac{\hbar}{2}\begin{pmatrix} \Omega_1 - \Omega_0 & 0 \\ 0 & \Omega_0 - \Omega_1 \end{pmatrix} \tag{II.4}$$

$$= \hbar\frac{\Omega_0 + \Omega_1}{2} I_2 + \frac{1}{2}\hbar\Delta\sigma_z \tag{II.5}$$

where I_2 is the 2×2 identity matrix and σ_z is one of the three Pauli matrices

$$\sigma_x = \begin{pmatrix} 0 & 1 \\ 1 & 0 \end{pmatrix}, \quad \sigma_y = \begin{pmatrix} 0 & -i \\ i & 0 \end{pmatrix}, \quad \sigma_z = \begin{pmatrix} 1 & 0 \\ 0 & -1 \end{pmatrix}. \tag{II.6}$$

In equation (II.5), the first term corresponds to a constant energy shift, which has no observable consequence. Hence, neglecting this term, the Hamiltonian becomes

$$H = \hbar\frac{\Delta}{2}\sigma_z. \tag{II.7}$$

Additionally, we can introduce operators which transform $|0\rangle$ into $|1\rangle$ and conversely. Formally, they read

$$\sigma^{\pm} = \frac{1}{2}(\sigma_x \pm i\sigma_y) \tag{II.8}$$

which in matrix form look like

$$\sigma^+ = \begin{pmatrix} 0 & 1 \\ 0 & 0 \end{pmatrix}, \quad \sigma^- = \begin{pmatrix} 0 & 0 \\ 1 & 0 \end{pmatrix}, \tag{II.9}$$

Using this definition, we have the relations $\sigma^+ |0\rangle = |1\rangle$, $\sigma^- |0\rangle = 0$, $\sigma^+ |1\rangle = 0$, $\sigma^- |1\rangle = |0\rangle$. We thus see that σ^+ (σ^-) adds (remove) a quantum of energy $\hbar\Delta$ to the TLS. For this reason, these operators are called *the raising and lowering operators*, or equivalently the *creation and annihilation operators* since they create and destroy a quantum of energy $\hbar\Delta$.

Multiple qubits. In quantum mechanics, the combined state of two systems is given by the *tensor product*, indicated by the symbol $\otimes$. The tensor product of two Hilbert spaces $\mathcal{H}_A$ and $\mathcal{H}_B$ is $\mathcal{H} = \mathcal{H}_A \otimes \mathcal{H}_B$. A basis for $\mathcal{H}$ is given by all the tensor products of the bases of each Hilbert space.

As an example, let us take the example of two qubits, so that their Hilbert spaces have dimension two. If we write $\{|0\rangle_A, |1\rangle_A\}$ the basis of $\mathcal{H}_A$ and $\{|0\rangle_B, |1\rangle_B\}$ the basis of $\mathcal{H}_B$, then the basis of $\mathcal{H} = \mathcal{H}_A \otimes \mathcal{H}_B$ is

$$\{|0\rangle_A \otimes |0\rangle_B, |0\rangle_A \otimes |1\rangle_B, |1\rangle_A \otimes |0\rangle_B, |1\rangle_A \otimes |1\rangle_B\} \tag{II.10}$$

To simplify the notations, one often omits the $\otimes$ symbol, so we equivalently rewrite equation (II.10) as

$$\{|0\rangle_A |0\rangle_B, |0\rangle_A |1\rangle_B, |1\rangle_A |0\rangle_B, |1\rangle_A |1\rangle_B\} \equiv \{|00\rangle, |01\rangle, |10\rangle, |11\rangle\}. \tag{II.11}$$

Qutrits, qudits, and discrete variables. So far we have taken a two-level system, or qubit, as our unit of information. However, we can generalise to higher-dimensional systems. For instance, a three-level system, known as a *qutrit*, lives in a Hilbert space of dimension three, and noting its basis as $|0\rangle, |1\rangle$ and $|2\rangle$, a general qutrit can be written as

$$|\psi\rangle = \alpha |0\rangle + \beta |1\rangle + \gamma |2\rangle, \tag{II.12}$$

where $\alpha, \beta, \gamma \in \mathbb{C}$. More generally, we can define *qudits*, which refer to a d dimensional state. Qudits are of interest because they higher dimension is beneficial to several quantum information processing tasks. Qubits, qutrits and qudits are part of a single class of called *discrete variables* (DV), which refer to the finite dimension of their Hilbert space. This is to be contrasted with *continuous variables*, where the Hilbert space is infinite.

2.2) Continuous variables

A case in point of a continuous variable is the quantum harmonic oscillator. Hence, we begin by reviewing the standard properties of the quantum harmonic oscillator, which can then be applied to every continuous variable.

2.2.1) Quantum harmonic oscillator and number states

The quantum harmonic oscillator. The study and quantisation of the harmonic oscillator is covered in countless textbook on quantum mechanics, see e.g. [10]. Accordingly, we shall not discuss this example in depth, and we content ourselves with the concepts of use later in this thesis.

The classical Hamiltonian of a particle of mass m in a one-dimensional harmonic potential (along $\hat{\mathbf{x}}$) reads

$$H = \frac{p^2}{2m} + \frac{1}{2}m\omega^2 x^2, \tag{II.13}$$

where p is the momentum operator and x the position operator. The first term is the kinetic energy of the particle[1], while the second is that of the harmonic potential[2], with "strength" ω (with dimension of angular frequency).

The quantum version of this Hamiltonian can be obtained through the principle of *quantisation*, where observables (e.g. position x) are replaced by operators, and a commutation relation is imposed on observables. For simplicity, we use the same notation for the classical momentum p and its "quantum" operator, while for the classical position x we note q its operator. The canonical commutation relation[3] between position and momentum is $[x, p] = i\hbar$. Thus, the Hamiltonian for the quantum harmonic oscillator can be written

$$H = \frac{p^2}{2m} + \frac{1}{2}m\omega^2 q^2, \tag{II.14}$$

We now rewrite equation (II.14) in terms of dimensionless operators P and Q such that

$$q = \sqrt{\frac{\hbar}{m\omega}}Q, \quad p = \sqrt{\hbar\omega m}P, \tag{II.15}$$

which gives

$$H = \frac{\hbar\omega}{2}\left(Q^2 + P^2\right). \tag{II.16}$$

With a bit of algebra, these operators can be expressed in terms of annihilation (creation) operators a ($a^\dagger$) to diagonalise the Hamiltonian. Indeed, we have

$$Q = \frac{a + a^\dagger}{\sqrt{2}}, \quad P = i\frac{a^\dagger - a}{\sqrt{2}}, \tag{II.17}$$

and replacing in equation (II.16) the Hamiltonian becomes diagonal[4],

$$H = \hbar\omega\left(a^\dagger a + \frac{1}{2}\right), \tag{II.18}$$

after using the bosonic commutation relation[5] $\left[a, a^\dagger\right] = 1$. Often, one neglects the energy offset $\frac{\hbar\omega}{2}$ (like we did for the two-level system in equation (II.5)), and simply write $H = \hbar\omega a^\dagger a$. Furthermore, the commutation relation corresponds to that of bosons, so that $a^\dagger, a$ are called bosonic creation/annihilation operators.

[1] If this is unclear, recall that for a classical uncharged particle, $p = mv$ with v the speed of the particle. Then $\frac{p^2}{2m} = \frac{1}{2}mv^2$, which is the standard expression of the kinetic energy.

[2] For instance, the potential felt by a mass attached to a spring of constant k is $\frac{1}{2}kx^2$, and we see that we can identify the natural oscillation angular frequency $\omega = \sqrt{\frac{k}{m}}$, which we can also derive by considering the equation of movement (Newton's second law).

[3] The commutator $[A, B]$ between two operators A and B is defined as $[A, B] = AB - BA$.

[4] After introducing an appropriate basis, see the following paragraphs.

[5] This can be derived from the commutation relation $[q, p] = i\hbar$.

Number states. The creation and annihilation operators work similarly to the raising and lowering operators $\sigma^{\pm}$ for a two-level system: a removes a quantum of energy $\hbar\omega$ from the oscillator, while $a^\dagger$ creates a quantum. The critical difference is that for the harmonic oscillator, one can add an infinite number of quantum to the system, i.e. there is an infinity of possible states. This is why two level systems are discrete variable (there is a finite number of state), while a harmonic oscillator represents a continuous variable: the energy spans an infinite number of values (even though the values are only accessible in discrete "jumps"). The quanta can be viewed as quasi-particles called bosons, and thus a state with n excitations corresponds to a state made up of n bosonic particles.

The ground state of the quantum harmonic oscillator is written $|0\rangle$, and $|1\rangle$ is the first excited state, which has an additional energy of $\hbar\omega$ compared to $|0\rangle$. More generally, the *number states* $|n\rangle$ with $n \in \mathbb{N}$ correspond to the addition of n quanta of energy $\hbar\omega$ to the ground state. We have the relations [11]

$$a\,|n\rangle = \sqrt{n}\,|n-1\rangle\,, \quad n \geqslant 1 \tag{II.19}$$

$$a^\dagger\,|n\rangle = \sqrt{n+1}\,|n+1\rangle\,, \quad n \geqslant 0 \tag{II.20}$$

$$a^\dagger a\,|n\rangle = n\,|n\rangle\,, \quad n \geqslant 0. \tag{II.21}$$

In particular, note that the last equation tells us that the number states are eigenstates (with eigenvalue n) of the *number operator*[1] $a^\dagger a$. Thus, the Hamiltonian equation (II.18) is indeed diagonal: the term in parenthesis essentially counts the number of excitations, adds $\frac{1}{2}$, and multiplies the result by the energy of a single quantum. Note that $a\,|0\rangle = 0$, and $H\,|0\rangle = \frac{\hbar\omega}{2}$, i.e. the ground state has a non-zero energy.

2.2.2) Bosonic modes

Definition of a bosonic mode. The harmonic oscillator is ubiquitous in physics and engineering, and thus it is not surprising that the Hamiltonian of many quantum systems reduce to a quantum harmonic oscillator. We define a *bosonic mode* to be any physical system whose Hamiltonian can be written as equation (II.18). By analogy with the harmonic oscillator, we can attribute a *quasi-particle* to these systems. For instance, the collective mechanical motion of ions in a crystal results takes the form of a sum of harmonic oscillators, and corresponds to quasi-particles called *phonons*. In the next chapter, we shall see another example of a bosonic quasi-particle, the photon, which corresponds to the quanta of the electromagnetic field. We conclude this paragraph with some terminology: the ground state $|0\rangle$ of a bosonic mode is also called the vacuum, and we remind the reader that it has a non-vanishing energy (called the zero-point energy). Finally, the number states are also routinely called *Fock states* in the literature, and we shall use this terminology from now on.

Quadratures. For a general bosonic mode with creation/annihilation operators $a^\dagger, a$, we can define the (hermitian[2]) *quadrature operators*

$$X = \frac{a + a^\dagger}{\sqrt{2}}, \quad Y = i\frac{a^\dagger - a}{\sqrt{2}}, \tag{II.22}$$

and we can verify that $\left[a, a^\dagger\right] = 1$ implies the commutation relation $[X, Y] = i$ for the quadratures.

Statistics. To conclude, we introduce some definitions that will be useful to characterise the "non-classicality" of some states. For an operator A and some state $|\psi\rangle$, we define the

[1] The name comes from the fact that its eigenvalues corresponds to the number n of quantum, i.e. $a^\dagger a$ "counts" the number of excitation in the system.

[2] An operator is hermitian if $A^\dagger = A$, where † indicates the conjugate transposition. This guarantees that the operator is diagonalisable and it has real eigenvalues.

average, or expectation value of A as $\langle A\rangle = \langle\psi|A|\psi\rangle$. The variance $(\Delta A)^2$ is defined as

$$(\Delta A)^2 = \left\langle (A - \langle A\rangle)^2 \right\rangle = \langle\psi|(A - \langle\psi|A|\psi\rangle)^2|\psi\rangle \tag{II.23}$$
$$= \langle\psi|A^2 + (\langle\psi|A|\psi\rangle)^2 - 2A\langle\psi|A|\psi\rangle|\psi\rangle = \langle\psi|A^2 + \langle A\rangle^2 - 2A\langle A\rangle|\psi\rangle \tag{II.24}$$
$$= \langle\psi|A^2|\psi\rangle + \langle A\rangle^2 - 2\langle\psi|A|\psi\rangle\langle A\rangle \tag{II.25}$$
$$= \left\langle A^2\right\rangle - \langle A\rangle^2, \tag{II.26}$$

and ΔA is called the standard deviation.

As an example, consider the variance $(\Delta N)^2$ of the number operator $N = a^\dagger a$ for a Fock state $|n\rangle$. Using $a^\dagger a = aa^\dagger - 1$ (from $[a, a^\dagger] = 1$), we find

$$(\Delta N)^2 = \left\langle (a^\dagger a)^2 \right\rangle - \left\langle a^\dagger a \right\rangle^2 = \left\langle \left(aa^\dagger - 1\right)\left(aa^\dagger - 1\right)\right\rangle - n^2 \tag{II.27}$$
$$= \left\langle aa^\dagger aa^\dagger \right\rangle - 2\left\langle aa^\dagger \right\rangle + 1 - n^2 \tag{II.28}$$
$$= \sqrt{n+1}\,\langle n|aa^\dagger a|n+1\rangle - 2\sqrt{n+1}\,\langle n|a|n+1\rangle + 1 - n^2 \tag{II.29}$$
$$= (n+1)\langle n|aa^\dagger|n\rangle - 2(n+1)\langle n|n\rangle + 1 - n^2 \tag{II.30}$$
$$= (n+1)^2 - 2(n+1) + 1 - n^2 \tag{II.31}$$
$$= 0. \tag{II.32}$$

This result will be useful when looking at non-classical measures in section 2.3.

Finally, one can show that for any two hermitian operators A, B with standard deviation ΔA and ΔB, we have the uncertainty relation $(\Delta A)(\Delta B) \geqslant \frac{1}{2}|\langle[A, B]\rangle|$ [12]. For general quadratures X and Y of a bosonic mode, we thus have $(\Delta X)(\Delta Y) \geqslant \frac{1}{2}$. For the momentum and position operators of the harmonic oscillator, for which $[x, p] = i\hbar$, this gives the Heisenberg uncertainty relation $(\Delta x)(\Delta p) \geqslant \frac{\hbar}{2}$. So far we have only considered isolated energy eigenstates, the Fock states. We now consider different superpositions of Fock states.

2.2.3) Coherent states

Problematic. Quantum mechanics should be able to reproduce the classically observed averaged dynamics. The eigenstates of the quantum harmonic oscillator are number states, but these do not behave "classically", it is actually quite the opposite. To see this, we first note that

$$x(t) = x_0\cos(\omega t) + \frac{p_0}{m\omega}\sin(\omega t), \tag{II.33}$$

is a general solution[1] of the classical harmonic oscillator with initial conditions $x(t = 0) = x_0$ and $p(t = 0) = m\dot{x}(t = 0) = p_0$.

To compare with the quantum-mechanical case, notice that the classical result describes the time evolution of the position. Thus, we first need to introduce time evolution in quantum mechanics. In the Schrödinger picture[2]of quantum mechanics, the time-evolution of a state $|\psi(t)\rangle$ is given by the Schrödinger equation

$$i\hbar\frac{\partial|\psi\rangle}{\partial t} = H|\psi(t)\rangle, \tag{II.34}$$

where H is the Hamiltonian of the system. If the Hamiltonian is time-independent, then the solution is $|\psi(t)\rangle = e^{-iHt/\hbar}|\psi(t = 0)\rangle$. Naturally, we see that if $|\psi\rangle$ is expanded in energy eigenstates, and H is diagonal, then the expression of $|\psi(t)\rangle$ is simple to obtain since it amounts to multiplying each eigenstate by the exponential of its eigenvalue. For instance, if $|\psi(t = 0)\rangle = |n\rangle$ is an energy eigenstate, then

$$|\psi(t)\rangle = e^{-iHt/\hbar}|n\rangle = e^{-i[\hbar\omega(a^\dagger a + \frac{1}{2})]t/\hbar}|n\rangle = e^{-i\omega(n+\frac{1}{2})t}|n\rangle. \tag{II.35}$$

[1] To convince yourself, simply insert this expression in the differential equation fo x, which we recall reads $\frac{\mathrm{d}^2x}{\mathrm{d}t^2} + \omega^2 x = 0$.

[2] In the Schrödinger picture of quantum mechanics, states carry the time-dependence, instead of the operators in the Heisenberg picture.

We now consider the quantum-mechanical expectation value of the X quadrature (which from equation (II.15) we can assimilate to the position operator of an harmonic oscillator): we find for any number state $|n\rangle$ that

$$\forall n \in \mathbb{N}, \quad x(t) \propto \langle n|X|n\rangle\,(t) = \langle n|e^{i\omega(n+\frac{1}{2})t}\frac{a+a^\dagger}{\sqrt{2}}e^{-i\omega(n+\frac{1}{2})t}|n\rangle = \frac{\langle n|a+a^\dagger|n\rangle}{\sqrt{2}} = 0. \quad \text{(II.36)}$$

In other words, it seems that the position of any energy eigenstate $|n\rangle$ vanishes at all times, which contrasts with the classical result. Furthermore, we also find $\langle n|Y|n\rangle = 0$, which again we expect should be non-vanishing for a classical harmonic oscillator since Y is akin to the momentum. In the following paragraphs, we introduce a superposition of Fock states that reproduces the classical dynamics and we discuss its statistics.

Definition of a coherent state. The answer to this classical/quantum correspondence are *coherent states*. They are superposition of number states, and successfully reproduce the classical dynamics. Formally, a coherent state $|\alpha\rangle$ is characterised by a complex number α, and is defined as

$$|\alpha\rangle = e^{-|\alpha|^2/2}\sum_{n=0}^{\infty}\frac{\alpha^n}{\sqrt{n!}}|n\rangle \quad \text{(II.37)}$$

in terms of the number state $|n\rangle$. Such states can be created by acting on the vacuum using the displacement operator[1] $D(\alpha) = \exp\big(\alpha a^\dagger - \alpha^* a\big)$, i.e. $|\alpha\rangle = D(\alpha)\,|0\rangle$.

Dynamics of a coherent state. To find the time-evolution of a coherent state, we take $|\psi(t=0)\rangle = |\alpha\rangle$ and using equations (II.34) and (II.37),

$$|\psi(t)\rangle = e^{-iHt/\hbar}\,|\alpha\rangle = e^{-|\alpha|^2/2}\sum_{n=0}^{\infty}\frac{\alpha^n}{\sqrt{n!}}e^{-iHt/\hbar}\,|n\rangle \quad \text{(II.38)}$$

$$= e^{-|\alpha|^2/2}\sum_{n=0}^{\infty}\frac{\alpha^n}{\sqrt{n!}}e^{-in\omega t}e^{-i\omega t/2}\,|n\rangle = e^{-i\omega t/2}e^{-|\alpha|^2/2}\sum_{n=0}^{\infty}\frac{\left(\alpha e^{-i\omega t}\right)^n}{\sqrt{n!}}\,|n\rangle \quad \text{(II.39)}$$

$$= e^{-i\omega t/2}\left|\alpha e^{-i\omega t}\right\rangle. \quad \text{(II.40)}$$

One interesting property of coherent states is that they are eigenstates of the annihilation operator a, with eigenvalue α [5]. As a consequence, we have

$$\langle\psi(t)|X|\psi(t)\rangle = \frac{\langle\psi(t)|a|\psi(t)\rangle + \langle\psi(t)|a^\dagger|\psi(t)\rangle}{\sqrt{2}} = \frac{\alpha e^{-i\omega t} + \alpha^* e^{i\omega t}}{\sqrt{2}} \quad \text{(II.41)}$$

$$= \frac{2\,\mathrm{Re}\big\{\alpha e^{-i\omega t}\big\}}{\sqrt{2}} \neq 0. \quad \text{(II.42)}$$

In particular, noting $\alpha = re^{i\phi}$ and using equation (II.40),

$$\langle\psi(t)|X|\psi(t)\rangle = r\sqrt{2}\cos(\omega t - \phi). \quad \text{(II.43)}$$

Similarly, we can compute

$$\langle\psi(t)|Y|\psi(t)\rangle = i\frac{\alpha^* e^{i\omega t} - \alpha e^{-i\omega t}}{\sqrt{2}} = \sqrt{2}\,\mathrm{Im}\big\{\alpha e^{-i\omega t}\big\} = r\sqrt{2}\sin(\omega t - \phi). \quad \text{(II.44)}$$

With $\phi = \frac{\pi}{2}$, equations (II.43) and (II.44) recover the classical results (see equation (II.33)) with $x_0 = 0$.

[1] Some standard properties of the displacement operator are derived in appendix A.2.1.

Statistics of coherent states. On the other hand, a notable difference is that the probabilistic nature of quantum mechanics manifests in non-vanishing fluctuations for position and momentum, contrary to the classical result (where there is no uncertainty). The variance of the quadratures are

$$(\Delta X)^2 = \frac{1}{2}\left\langle (a+a^\dagger)^2 \right\rangle - \frac{1}{2}\left\langle a+a^\dagger \right\rangle^2 = \frac{1}{2}\left\langle a^2 + aa^\dagger + a^\dagger a + a^{\dagger 2} \right\rangle - \frac{1}{2}(\alpha+\alpha^*)^2 \tag{II.45}$$

$$= \frac{1}{2}\left(\alpha^2 + 1 + 2|\alpha|^2 + \alpha^{*2}\right) - \frac{1}{2}(\alpha^2 + \alpha^{*2} + |\alpha|^2) = \frac{1}{2}. \tag{II.46}$$

Similarly,

$$(\Delta Y)^2 = -\frac{1}{2}\left\langle (a^\dagger - a)^2 \right\rangle - \frac{i^2}{2}\left\langle a^\dagger - a \right\rangle^2 = -\frac{1}{2}\left\langle a^2 - aa^\dagger - a^\dagger a + a^{\dagger 2} \right\rangle + \frac{1}{2}(\alpha+\alpha^*)^2 \tag{II.47}$$

$$= -\frac{1}{2}\left(\alpha^2 - 1 - 2|\alpha|^2 + \alpha^{*2}\right) + \frac{1}{2}(\alpha^2 + \alpha^{*2} + |\alpha|^2) = \frac{1}{2}. \tag{II.48}$$

We thus have $(\Delta X)(\Delta Y) = \frac{1}{2}$, which achieves the minimal bound on the uncertainty.

Furthermore, the expectation value the number operator for a coherent state is $\left\langle a^\dagger a \right\rangle = |\alpha|^2$, and its variance is

$$V(a^\dagger a) = \langle\alpha|(a^\dagger a)^2|\alpha\rangle - (|\alpha|^2)^2 = \alpha^*\alpha \langle\alpha|aa^\dagger|\alpha\rangle - |\alpha|^4 = |\alpha|^2 \langle\alpha|1 + a^\dagger a|\alpha\rangle - |\alpha|^4 \tag{II.49}$$

$$= |\alpha|^2 + |\alpha|^2 \langle\alpha|a^\dagger a|\alpha\rangle - |\alpha|^4 = |\alpha|^2 + |\alpha|^2\alpha^*\alpha - |\alpha|^4 \tag{II.50}$$

$$= |\alpha|^2 = \left\langle a^\dagger a \right\rangle. \tag{II.51}$$

Finally, using the expansion of equation (II.37) the probability to measure a coherent state is an eigenstate $|m\rangle$ is given by

$$|\langle m|\alpha\rangle|^2 = \left| e^{-|\alpha|^2/2} \sum_{n=0}^{\infty} \frac{\alpha^n}{\sqrt{n!}} \langle m|n\rangle \right|^2 = \left| e^{-|\alpha|^2/2} \frac{\alpha^m}{\sqrt{m!}} \right|^2 = e^{-|\alpha|^2} \frac{\alpha^{2m}}{m!} \tag{II.52}$$

$$= e^{-\langle a^\dagger a\rangle} \frac{\left\langle a^\dagger a \right\rangle^m}{m!} \tag{II.53}$$

which describes a Poissonian distribution parametrised by the mean number of particle $\left\langle a^\dagger a \right\rangle$.

2.2.4) (Schrödinger) Cat states

If one thinks of the coherent states as classical states, then a superposition of such classical states is a Schrödinger cat state. Formally, a cat state can be written as

$$|\psi\rangle = \frac{|\alpha\rangle + \exp\{i\phi\}\,|-\alpha\rangle}{\sqrt{2 + 2\cos(\phi)\exp\left(-2|\alpha|^2\right)}}, \tag{II.54}$$

where $|\alpha\rangle$ are coherent states. For $\phi = 0$ ($\phi = \pi$), we have an even (odd) cat state. These states are useful for various quantum information processing tasks, and notably quantum error correction [13, 14]. Alternatively, being superposition of macroscopic states, they are of fundamental interest to study the quantum to classical transition, in particular with respect to decoherence [15].

2.2.5) Squeezed states

We saw in section 2.2.2 that the quadratures X and Y of a bosonic mode satisfy the uncertainty relation $(\Delta X)(\Delta Y) \geqslant \frac{1}{2}$. We saw that the coherent states are such that $(\Delta X)(\Delta Y) = \frac{1}{2}$, but there exists another class of states for which the uncertainty relation reaches its minimum. Notably, ΔX can be as high as one wants provided $\Delta Y = \frac{1}{\Delta X}$, and then the minimum of uncertainty is still reached.

Squeezed states are a class of states for which the uncertainties of the quadratures satisfy $\Delta Y = \frac{1}{\Delta X}$ (or the other way around). Formally, they can be generated by a combination of the displacement operator $D(\alpha)$ introduced above and the squeeze operator

$$S(\eta) = \exp\left\{\frac{1}{2}\left(\eta^* a^2 - \eta a^{\dagger 2}\right)\right\}. \tag{II.55}$$

As we will see below, squeezed states have applications in quantum computing, quantum sensing and quantum communications. Thus, their creation and manipulation is of interest. Having introduced various states associated with continuous variables, we now discuss some metrics characterising their non-classical behaviour.

2.3) Non-classical measures

As we will see in the next section, quantum information offers additional properties to process information, compared to the classical case. Thus, we are naturally brought to assume that non-classical behaviour is specifically what allows to obtain a quantum "advantage" to process information. In this section, we give some directions toward quantifying these non-classical features. We begin by developing some terminology (and hopefully intuition) by taking the example of qubits, and then we discuss a method to quantify entanglement for continuous variables. We finish another way to detect non-classical behaviour, through particle statistics. Good references for this section are section IV.C of [16], and section 2.2 of [17].

2.3.1) Entanglement, quantum steering and Bell non-locality

Entanglement is a purely quantum-mechanical effect that can be traced back to the tensor product structure of composite quantum quantum systems. Some related concepts are quantum steering and Bell (non-)locality, which also have applications for quantum technologies. A formal and intuitive understanding of these concepts is beyond the scope of this thesis, so here we merely attempt to define and distinguish them using qubits as an example, and provide references for further details.

Non-separability. To introduce the concept of entanglement, we begin by examining the simplest case of qubits. Consider that two parties, say Alice (A) and Bob (B), each possess a qubit. Alice's qubit lives in the Hilbert space $\mathcal{H}_A$, while that of Bob lives in $\mathcal{H}_B$. As per section 2.1, the state $|\phi\rangle$ of the composite system made up of Alice and Bob lives in the Hilbert space $\mathcal{H} = \mathcal{H}_A \otimes \mathcal{H}_B$, with $\otimes$ indicating the tensor product.

A state $|\phi\rangle \in \mathcal{H}$ is separable if it can be written $|\phi\rangle = |\psi\rangle \otimes |\varphi\rangle$ with $|\psi\rangle \in \mathcal{H}_A$ and $|\varphi\rangle \in \mathcal{H}_B$. Else, $|\phi\rangle$ is entangled. As an example, the states

$$|00\rangle\,, \quad |01\rangle\,, \quad \frac{|00\rangle + |01\rangle}{\sqrt{2}} = |0\rangle_A \left(\frac{|0\rangle_B + |1\rangle_B}{\sqrt{2}}\right), \tag{II.56}$$

$$\frac{1}{2}\left(|00\rangle + |01\rangle - e^{i\phi}|10\rangle - e^{i\phi}|11\rangle\right) = \left(\frac{|0\rangle_A - e^{i\phi}|1\rangle_A}{\sqrt{2}}\right)\left(\frac{|0\rangle_B + |1\rangle_B}{\sqrt{2}}\right) \tag{II.57}$$

are separable, since they can always be factored as the tensor product of a state in $\mathcal{H}_A$, and a state in $\mathcal{H}_B$. On the other hand, the famous Bell states

$$\frac{|00\rangle \pm |11\rangle}{\sqrt{2}}, \quad \frac{|01\rangle \pm |10\rangle}{\sqrt{2}} \tag{II.58}$$

are entangled states, since they cannot be decomposed as a tensor product. We thus see that non-separability is a manifestation of entangled states.

Quantum steering and Bell non-locality. Formally, the Bell states describe a correlation between the qubit of Alice and that of Bob. For instance, for $\frac{|00\rangle \pm |11\rangle}{\sqrt{2}}$, we see that necessarily, if one party measures a certain value for his qubit, then it completely determines the state of the other qubit. If Alice and Bob are spatially separated, this suggests the possibility of Alice

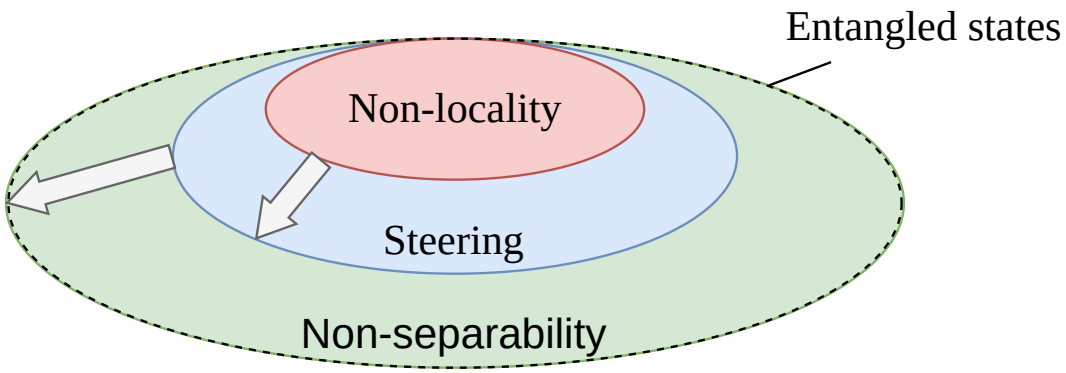


Figure II.2: Hierarchy of entanglement [18–20]: Bell non-locality implies quantum steering, which itself implies non-separable (entangled) states. However, the converse is, in general, not true [21]. This figure is inspired by fig 13 of [16].

to act on Bob's particle by performing (local) measurements on her qubit. This fact hints at the concept of *quantum steering* (also called EPR steering, where EPR refers to Einstein Podolsky and Rosen who first discussed this in a 1935 paper [22]). Notably, quantum steering can be asymmetric, so that it is possible that Alice can steer Bob's state, but not the other way around: this is referred to as *one-way quantum steering*. We refer the reader to the reviews Reid et al. (2009) [23] and Uola et al. (2020) [24] for more technical details on quantum steering and its applications, some of which will be discussed in section 3.

The example of Alice and Bob sharing a Bell state can also be used to understand the principle of Bell non-locality. Classically, it is widely assumed that nature is local, that is a state can only be affected by the objects around it. However, in principle, Alice and Bob can be sufficiently spatially distant (spacelike separation in the language of special relativity) such that Alice's measurement of her qubit cannot affect Bob's qubit: this is the essence of the Einstein Podolsky and Rosen paradox [22]. The underlying assumption in this argument is nature is local. Under the join assumptions of realism and locality, Bell showed that in a hidden variable theory of quantum mechanics, some of these variables had to verify an inequality, now called the *Bell inequalities*. However, it has since be shown that appropriately designed quantum mechanical experiments break those inequalities, which was recognised by the 2022 Nobel prize in physics attributed to Aspect, Clauser and Zeilinger. For further detail on Bell nonlocality, we refer the reader to the review of Brunner et al. (2014) [25].

Multipartite entanglement. To conclude this introduction to entanglement, we would like to mention the possibility of multipartite entanglement, where more than two particles are entangled. For bipartite entanglement, the definition corresponds to the non-separability of a state in two Hilbert spaces. For n entangled particles, the same definition is naturally extended to n Hilbert spaces. However, the phenomenology of multipartite entangled states is much more complicated that for bipartite entangled state (already for tripartite entanglement). For a pedagogical introduction to multipartite entanglement, we refer the reader to [26].

2.3.2) Entanglement measures for Gaussian continuous variables

Gaussian states. Gaussian states are a particularly convenient class of continuous variables. They are made up of bosonic modes with some specific properties. For the sake of generality, consider N bosonic modes a_i with quadratures X_i, Y_i. We organise these quadratures in a column vector u as $u = (X_1, Y_1, X_2, Y_2, \ldots, X_N, Y_N)^t$. In practical physical systems, the Heisenberg equation of motion gives the time-dependence of the quadratures X_i and Y_i for each mode. We assume that the dynamics of the system can be linearised and written in the form

$$\dot{u}(t) = A(t)u(t) + n(t), \tag{II.59}$$

where A is called the drift matrix and n is a column vector representing a noise input. The noise vector is $n = (\sqrt{\kappa_1}X_1^{\text{in}}, \sqrt{\kappa_1}Y_1^{\text{in}}, \ldots, \sqrt{\kappa_1}X_N^{\text{in}}, \sqrt{\kappa_N}Y_N^{\text{in}})^t$ where $X_i^{\text{in}}, Y_i^{\text{in}}$ are input noise operators for the bosonic mode a_i, and $\kappa_i/2\pi$ its damping rate (unit of frequency).

If the noises are Gaussian-distributed, then u describes a N-mode continuous variable Gaussian state. For Gaussian systems, the first and second-order moments completely determine the observables of the system, see [16, 27] and references therein. Furthermore, the first moments $\langle u_k \rangle$ can be chosen such that $\langle u_k \rangle = 0$: this is allowed because one can perform a displacement transformation to adjust the value of $\langle u_k \rangle$, and this does not affect the entanglement [27]. Thus, the gaussian state is completely determined by its covariance matrix $V = (V_{ij})$ with

$$V_{ij} = \frac{1}{2}\left\langle u_i(t)u_j(t') + u_j(t')u_i(t)\right\rangle. \tag{II.60}$$

The covariance matrix characterises the correlations between the bosonic modes a_i. Further defining the diffusion matrix $D = (D_{ij})$ where

$$\delta(t-t')D_{ij} = \frac{1}{2}\left\langle n_i(t)n_j(t') + n_j(t')n_i(t)\right\rangle, \tag{II.61}$$

it can be shown that in the steady-state[1], solving the *Lyapunov equation*

$$AV + VA^t = -D \tag{II.62}$$

gives the steady-state covariance matrix V. From this covariance matrix, we can for instance quantify both bipartite and tripartite entanglement and quantum steering, which we now discuss.

Bipartite entanglement for Gaussian states: logarithmic negativity. In the context of continuous variables, bipartite entanglement characterises how much two bosonic modes are entangled. The first step to quantify this entanglement is to find a covariance matrix between the two modes, which can be extracted from the full covariance matrix V by selecting the appropriate 2×2 block. Formally, the 4×4 reduced covariance matrix of the modes i and j reads

$$V = \begin{pmatrix} V_i & V_{i,j} \\ V_{j,i} & V_j \end{pmatrix} \tag{II.63}$$

where $V_{i,j}^t = V_{j,i}$.

Then, a useful metric to quantify the bipartite entanglement between two bosonic modes is the logarithmic negativity [28] defined as

$$E = \max\left\{0, -\ln\left(2\eta^-\right)\right\} \tag{II.64}$$

where η^- is the smallest symplectic eigenvalue [27] of the steady-state covariance matrix V. To find η^-, we first compute the partial transposition of V, which reads

$$\widetilde{V} = \Omega_2 P_{12} V P_{12}. \tag{II.65}$$

where $\Omega_2 = -\oplus_{j=1}^2 \sigma_y$ and $P_{12} = \text{diag}\{1, 1, -1, 1\}$. For the sake of clarity, Ω_2 is a block diagonal matrix, where each block is $-\sigma_y$. As for P_{12}, some authors place the minus sign in the first upper block instead, but it doesn't change the final results for η^-. The minimum symplectic value is then given by

$$\eta^- = \min\left\{\left|\text{eig}\left(\widetilde{V}\right)\right|\right\}. \tag{II.66}$$

where eig corresponds to the set of eigenvalues of $\widetilde{V}$. Note the presence of the absolute value, which is necessary to obtain a positive number for η^- hence making equation (II.64) well-defined.

[1] Formally, this consists of replacing the annihilation operator a by their expectation value $\langle a \rangle$, and neglecting time-derivatives. Without referring to a specific physical system, we cannot justify the validity of such a replacement, but we shall do so in the next chapters.

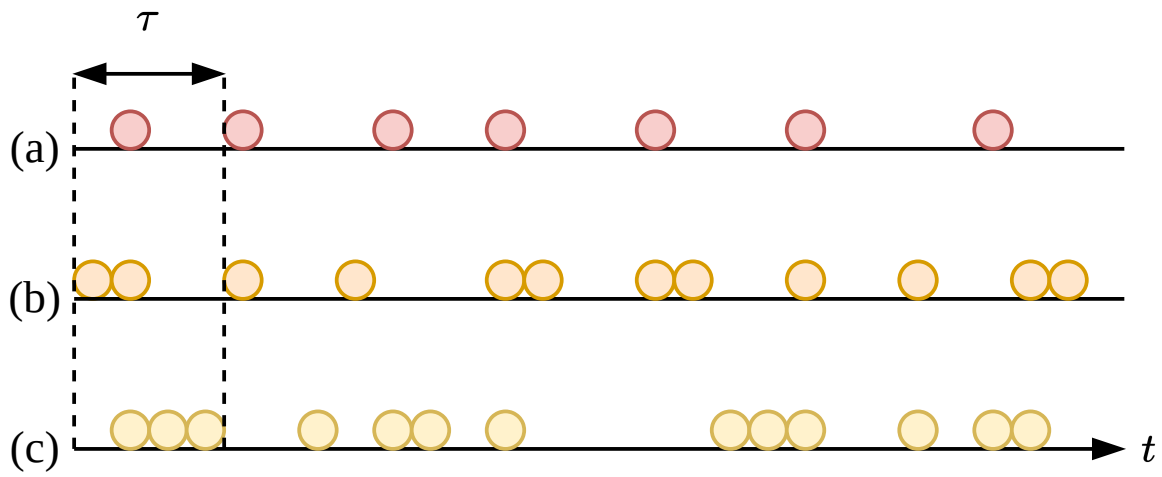


Figure II.3: Illustration of different photon (circles) emission depending on the value of $g^{(2)}$. (a) Anti-bunched light with $g^{(2)} < 1$. (b) Coherent light with $g^{(2)} = 1$. (c) Bunched light with $g^{(2)} > 1$. Reproduction of [35] licensed under a CC BY-SA 4.0 Deed [36].

Quantum steering and tripartite entanglement. The formalism provided by the covariance matrices can also be used to compute other non-classical measures, for instance bipartite quantum steering [29]. For tripartite entanglement, the concept of logarithmic negativity can be generalised to define the minimum residual cotangle [27, 30], which measures tripartite entanglement in a three mode Gaussian system. Similarly, quantum steering can be generalised [31, 32], and we refer the reader to [16] for more details on computing these metrics. The important point is that all of these metrics use covariance matrices for their calculations.

2.3.3) Non-classical statistics

Second-order correlation functions. Another tool to characterise non-classical states is their statistical distribution, which can be classified using the second-order[1] correlation function $g^{(2)}$. In general, the second-order correlation function depends on some time delay τ, but it is sufficient for our discussion to consider $\tau = 0$. Then, its expression is [17]

$$g^{(2)}(0) = \frac{\langle a^\dagger a^\dagger a a \rangle}{\langle a^\dagger a \rangle^2} = 1 + \frac{(\Delta n)^2 - \langle n \rangle}{\langle n \rangle^2} \tag{II.67}$$

where we defined the number operator $n = a^\dagger a$ for the bosonic mode a and used the definition of the variance $(\Delta n)^2 = \langle n^2 \rangle - \langle n \rangle^2$ in the second equality.

Sub-Poissonian, Poissonian, and super-Poissonian statistics. Depending on the value of $g^{(2)}$, one can distinguish between non-classical and classical statistics. First, let us take the example of a coherent state $|\alpha\rangle$ representative of classical dynamics. In section 2.2.2, we calculated that $(\Delta n)^2 = \langle n \rangle = |\alpha|^2$ (see equation (II.51)), which leads to $g^{(2)} = 1$. Alternatively, an example of a non-classical state[2] is given by the Fock state $|k\rangle$ containing k particles. Equation (II.32) shows that for such a state, $(\Delta n)^2 = 0$, which gives $g^{(2)} = 1 - \frac{1}{k} < 1$. In particular, the state with a single particle $|1\rangle$ gives $g^{(2)} = 0$. Furthermore, it can be shown that for a bosonic mode in thermal equilibrium, which follows the Bose-Einstein distribution, we have $g^{(2)} = 2$.

[1] This name suggests that there exists a first-order correlation function, $g^{(1)}$. This is indeed the case, but we do not use it in this thesis. For more details, we refer the reader to textbooks on quantum optics, such as [33, 34].

[2] The argument is that such a state does not reproduce the classically expected dynamics, as we showed at he beginning of our discussion of coherent states.

Accordingly, we define[1] $g^{(2)} \geq 1$ as describing classical statistics, while $g^{(2)} < 1$ describes non-classical statistics. Since a coherent state, which has Poissonian statistics (see equation (II.53)), corresponds to $g^{(2)} = 1$, then $g^{(2)} < 1$ corresponds to sub-Poissonian statistics where $(\Delta n)^2 < \langle n \rangle$ (see equation (II.67)). Conversely, $g^{(2)} > 1$ is identified with super-Poissonian statistics, for which $(\Delta n)^2 > \langle n \rangle$.

Bunching and anti-bunching. Super-Poissonian and sub-Poissonian statistics manifest in the bunching and anti-bunching of particles. To understand it, let us assume that our bosonic particles are photons[2], and consider the stream of photon emitted by a source at a function of time, as pictured in figure II.3. In the first case, the photons have $g^{(2)} < 1$, and the photons are being emitted at relatively stable time intervals. In the second case, corresponding to coherent light with $g^{(2)} = 1$, the photons follow a Poisson distribution, and hence the time interval between different photons is randomly distributed. In the final case, the photons are bunched together and lead to $g^{(2)} > 1$. In other words, if a photon is emitted, it is more likely that another photon is going to be emitted sooner rather than later.

3) An overview of quantum technologies

It has been shown on various occasions that quantum-mechanical properties can be used to improve classical information processing tasks. In the previous section, we identified several non-classical states (Fock state, squeezed states and Schrödinger cat states) and behaviour (entanglement, quantum steering, sub-Poissonian statistics) resulting from these quantum-mechanical properties. In this section, we now examine how these quantum features can be leveraged to create various quantum technologies. A notable omission is quantum computing, to which we dedicate section 4.

3.1) Quantum sensing and metrology

In the previous section, we saw that both coherent states and squeezed states reached the minimal uncertainty[3] allowed by quantum mechanics. The quadratures of the coherent states have equal uncertainty, while for squeezed states one quadrature can be made smaller (at the expense of making the uncertainty in the other quadrature bigger). Thus, we can legitimately expect that the reduced uncertainty in one of the quadratures of squeezed states could be used to improve the accuracy of measurements. This falls within the fields of quantum sensing and quantum metrology[4] [38], which aim at going beyond the classical limits[5] of measurements by using quantum-mechanical effects.

Sensors based on quantum mechanical effects have already been around for quite some time. For instance, superconducting quantum interference devices (SQUIDs) and nuclear magnetic resonance (NMR) are now routinely used in medicine [39] as non-invasive diagnostic tools. Modern uses consist of measuring various physical quantities such as gravity [40], gravitational waves[6] [41], time [42], of magnetic fields [43]. In all of these latter applications (and others), squeezed states were used to improve the performance of measurements [44, 45].

Alternatively, entanglement is a precious resource for quantum sensing, as illustrated by the quantum illumination protocols [47, 48], pictured in figure II.4. The idea behind quantum illumination is that even if entanglement is lost (due to noise), strong (quantum) correlations

[1] For light, it can be shown that any classical treatment leads to $g^{(2)} \geq 1$, see section 6.3 of [33].

[2] The fact that photons, the quanta of light, are bosons will be justified in the next chapter.

[3] Recall that we had $\Delta X \Delta Y = \frac{1}{2}$ with X and Y the two quadratures.

[4] What is the difference between quantum sensing and quantum metrology? It seems that there is no consensus on their definitions [37], and hence researchers use them interchangeably. However, by definition, metrology refers to the theory of measurement, in which one assigns a value to a physical quantity, while sensing corresponds to "being aware" of the presence of some physical phenomenon. Thus, metrology assigns a value to a physical quantity, while sensing simply detect the occurrence of some event.

[5] Note that there remains a fundamental limit imposed by quantum mechanics (the Heisenberg limit), which originates from the uncertainty principle.

[6] For instance the Laser Interferometer Gravitational-Wave Observatory (LIGO) and Virgo interferometer programs use squeezed states of light for their functioning.

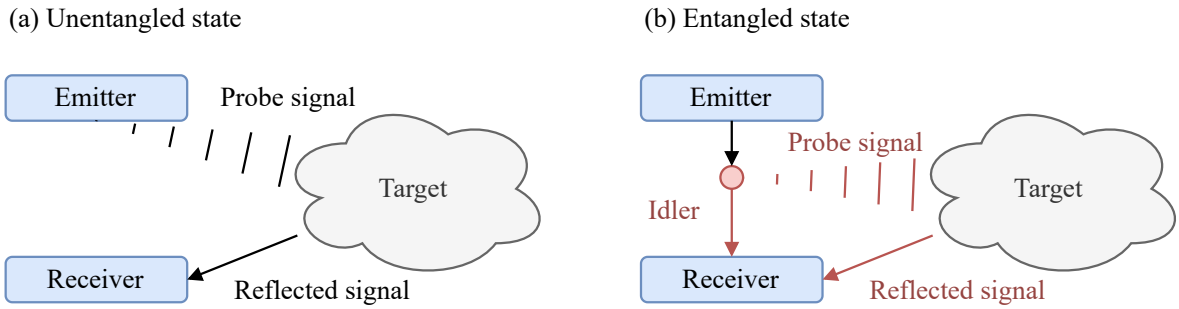


Figure II.4: (a) Illustration of the classical protocol to detect a target. (b) The quantum illumination protocol, where the emitter create two entangled signals, the idler and probe, and then perform a joint measurement on the idler and reflected signals. Inspired from [46].

remain, and can still lead to performance improvement over classical correlations. The emitter creates a pair of entangled signals, the idler, and the probe. The probe is sent, and its reflection is compared with the idler signal. While the original proposals for discrete [47] and continuous [48] variables focused on optical wavelengths, the scheme was later extended to microwaves by Barzanjeh et al. (2015) [49], which would make this protocol useful to create a quantum radar [50, 51]. Without going into details, we can distinguish two capabilities for such a protocol. First, one need the ability to create entangled signals, and then detect the reflected signal. This requires adapted sources and detectors, with sufficient efficiencies. Second, a quantum memory is required to preserve the idler signal for the time needed for the probe to be reflected [46]. Finally, in the microwave version of quantum illumination [49], one could create entangled signals at optical frequencies, and then convert the probe to microwaves wavelengths, and then back, to compare it with the idler. Therefore, the conversion of quantum states between microwave and optical frequencies is of interest.

3.2) Quantum (secure) communication

3.2.1) Quantum networks

Just like for classical computing, the ability to exchange quantum information over spatially distant nodes offers new opportunities, both for classical and quantum information processing. For instance, the exchange of quantum information[1], and more generally a quantum internet [52], allows for distributed quantum computation, and thus represents another way to scale up quantum computation. However, the concepts underlying quantum networks are very different from their classical counterpart.

No-cloning theorem. The most natural idea to transmit quantum information is to send the associated quantum state. However, losses prevent such an idea to be realised in practice, as the quantum state would loose its information too rapidly. Losses also exist in classical networks, but unfortunately, the associated techniques (e.g. amplification, or simply re-sending the state if it lost like in the UDP protocol) are not permitted by quantum mechanics. Indeed, the *no-cloning theorem* states that unknown quantum information cannot be copied [53, 54].

Quantum teleportation. Instead of transporting the physical state, one can use entanglement to teleport a quantum state over space [55]. Quantum teleportation works by first sharing a maximally entangled two-qubit state, for instance the Bell states of equation (II.58), between two spatial locations A and B. Then, if A wants to teleport a state $|\psi\rangle$ to B, A performs local operations and a measurement and sends the measured value to B. Depending on the value received, B performs some manipulation on its half of the Bell state to transform it to $|\psi\rangle$.

[1] When qubits are the unit of information travelling through the network, they are called flying qubits in the literature.

The protocol thus allows to transmit quantum information without the need of a quantum communication channel. The price to pay is the ability to share an entangled qubit pair in the first place, and a classical communication channel to exchange the result of the measurement performed at A. Aside from its use in quantum networks, quantum teleportation can be useful for quantum computation to create long-range interactions [56].

Entanglement swapping and quantum repeaters. The requirements of the quantum teleportation protocol tell us that to send a quantum state over two spatially separated nodes, we first need to be able to create entanglement between them. For long distances between A and B, this is a challenging requirement. *Entanglement swapping* is a protocol that uses quantum teleportation with an intermediary node C, to which both A and B share an entangled state, to create an entangled state between A and B.

The entanglement swapping protocol allows to build a *quantum repeater* [56, 57], which is a device that can be use to extend the range of the links in a quantum network. In the presence of losses entanglement swapping only succeeds with a non-unity probability. Hence, it may be necessary to repeat the entanglement swapping until it succeeds, which require the other party to preserve their entanglement with the intermediary node. This necessitates the use of *quantum memories* in quantum repeaters [58], which is a major obstacle to their real-world implementation [57].

Converting and routing quantum information. As we will see in section 5, the nodes of quantum networks will most likely be based on solid state systems, while the links will use optical photons at telecom wavelengths to use existing optical fibres infrastructures [57]. However, just like classical computers, the nodes are envisioned to operate at microwave frequencies. Thus, similarly to the quantum illumination protocol, there is a need for the *bi-directional conversion of light between microwaves and optical frequencies* [57, 59].

Furthermore, the nodes storing quantum information can be composed of various physical platforms (for instance entanglement swapping could be done by one physical system, while the quantum memories could be made from another). Therefore, another requirement for quantum networks to operate is *quantum information transduction* [59], most likely from a solid state platform to light at telecom wavelengths.

Finally, *quantum routers* are required to perform entanglement swapping between selected nodes [60]. Such a capability calls for the engineering of non-reciprocal interactions to switch on specific links and turn off the others.

3.2.2) Quantum cryptography

The possibilities of offered by quantum networks raise the question of the security of the exchanged quantum information, which is the affair of *quantum cryptography* [61]. Generally speaking, quantum cryptography [1] aims at using the principles of quantum mechanics to guarantee the security of classical or quantum information. The two main topics we shall discuss here are quantum random number generators (useful for classical cryptography), and quantum key distribution, one of the most mature quantum technologies. However, it is worth mentioning that quantum cryptography is not limited to these two applications (for an overview see the reviews [64, 65]).

Quantum random number generators (QRNGs). The security of many cryptographic schemes rely on a source of random numbers. Standard random number generator usually rely on the observed statistical randomness of some physical phenomena (electric noise for instance). Classically, such randomness is fake, since classical physics is deterministic: in principle, with a precise knowledge of physical parameters and enough computing power, one should be able to completely determine any seemingly random phenomena. On the other hand, quantum mechanics, due to its intrinsic probabilistic nature, represents a perfect source

[1] Not to be confused with post-quantum cryptography [62, 63], which is essentially classical cryptography relying on mathematics that are resistant to the "quantum advantage" provided by quantum computers.

of randomness. Thus, much effort has been put into developing quantum random number generators (QRNG), which is a source of random number relying on quantum physics for the generation of randomness.

Several phenomena can be used as a source of quantum randomness. One of them is noise, but its origin must genuinely be quantum. For instance, shot noise can be used for random number generation, but it is often accompanied by thermal noise. Thus, schemes based on extracting noise must have the ability to properly characterise and isolate different sources of noise, and use that of quantum-mechanical origin. An alternative method consists of creating a superposition of states, and then measuring. For instance, if one can reliably put a qubit in a superposition of its basis states, for instance

$$|\psi\rangle = \frac{|0\rangle + |1\rangle}{\sqrt{2}}, \tag{II.68}$$

then by measuring the qubit, one randomly obtains $|0\rangle$ or $|1\rangle$ (with probability 1/2 in the example above). Finally, one can use the statistics of bosonic modes[1] to generate random numbers. By creating states with these statistics, and measuring them, we can then create a sequence of random numbers after some post-processing.

Quantum key distribution (QKD). Several classical cryptographic schemes, such as AES, are provably secure, provided both parties share a secret key. This raises the question of securely sharing such a key in the first place. The purpose of Quantum Key Distribution (QKD) is to enable the exchange of such a secret information by using the principles of quantum mechanics [66]. More specifically, QKD takes advantage of two principles: that measurements perturb the quantum states, and the no-cloning theorem previously introduced. Indeed, imagine that A and B want to exchange a secret key by sending quantum states to each other. If an eavesdropper C intercepts a quantum state, he has to measure it to gain information. But since he cannot make a copy of that state, he cannot re-inject it in the communication channel to gain information without perturbing the exchange of A and B.

This idea was first proposed by Bennet and Brassard in 1984, in what is now know as the BB84 protocol [67]. It requires a uni-directional quantum channel, and a bi-directional classical channel. While the establishment of a shared key is not guaranteed, if such a key is established it is provably secure (from an information-theoretic point of view) since we can detect the presence of an eavesdropper. Since this protocol is theoretically secure, the only attack surface concerns the real-world implementation of this and other protocols.

The possible targets for these side-channel attacks are the source, the link, and the receiver. QKD schemes often use indistinguishable single photons, and thus many attacks rely on perturbing this single-photon physics by injecting light into the system [68–75]. To prevent these attacks, the ability to prevent external photons from entering the system is required. This calls for *uni-directional* transmission of light, or in other words non-reciprocal devices such as isolators and circulators.

4) Circuit-model of universal quantum computation

In this section, we introduce the basics of the circuit-model of quantum computation. The concepts in this section will be useful for chapters V and IX, when discussing respectively holonomic and silicon quantum computations.

4.1) The various forms of quantum computation

Quantum simulation. One of the most promising quantum technologies is quantum computation, or more specifically universal quantum computation. However, the first proposal which started this research was actually one for *quantum simulation*, proposed by Feynman in a 1982 speech [76]. Feynman remarked that classical computers required exponential resources

[1] For instance, we saw in section 2.2.3 that coherent states have Poissonian statistics, while number states have sub-Poissonian statistics.

to simulate quantum systems, whereas a quantum computer would be naturally suited to simulate quantum physics. Since Feynman's original proposal, the field of quantum simulation has significantly matured with applications in quantum chemistry, condensed matter, high-energy physics, cosmology, nuclear and atomic physics [77–81]. Note that quantum simulation aims at using quantum systems, not necessarily quantum computers, to simulate classical of quantum systems.

Universal quantum computation. More generally, a universal quantum computer is a device with the ability to perform an arbitrary unitary evolution of a quantum system. Just like for classical computing[1], several models exists for performing universal quantum computation. One such model is adiabatic quantum computing [82, 83], which consists of encoding the solution of a problem in the ground state of some Hamiltonian. Alternatively, measurement-based quantum computation [84, 85] uses a large scale entangled state (a cluster state) and perform a sequence of measurements. Nevertheless, the most common model of quantum computation is the quantum circuit model, which we discuss in more details in section 4 below. Regardless of the underlying model and physical platform, a universal quantum computer has promising applications in many different fields, such as optimisation problems [86], quantum simulations [78], cryptanalysis and algebraic problems [87, 88], finance [80, 89] or machine learning [80, 90]. The requirements for quantum simulation and quantum computation are similar and will be detailed in section 4.2.

4.2) Di-Vicenzo criteria

As we will examine in section 5, a variety of physical platform can implement qubits. However, for such two-level systems to be suitable for quantum computation, there are several additional requirements, which were first put forward by DiVincenzo (2000) [91]. The first five Di-Vicenzo criteria are

1. *a scalable physical system with well characterised qubits,*
2. *the ability to initialise the state of the qubits to a simple fiducial state,*
3. *long relevant decoherence times, much longer than the gate operation time,*
4. *a universal set of quantum gates,*
5. *a qubit-specific measurement capability.*

and all depend on the underlying physical system implementing the qubit. We shall review several examples in section 5 and in chapter IX. The first and second criteria are self-explanatory (we refer the reader to the original paper [91] for more details), while the third and fourth criteria are discussed below. Concerning the 5th criteria, we would like to stress that the "qubit-specific" measurement means the measurement of a selected individual qubit (among an array or grid of qubits).

Additionally, there are two other criteria if the quantum computer is to be connected to a quantum network [91]:

6. *the ability to interconvert stationary and flying qubits,*
7. *the ability to faithfully transmit flying qubits between specified locations.*

We recall that flying qubits, introduced in section 3.2, refer to qubits used for quantum communication purposes. Thus, the sixth requirement describes the connection of the elementary unit for quantum computation (qubits) with the elementary unit for quantum communication (flying qubits), or in other words the connection of the quantum computer to a quantum network. Finally, the seventh requirement is synonymous with a properly operating quantum network: that quantum information can be transmitted over spatially distant locations.

[1]There is of course the circuit model on which everyday computers are based. But alternatives include cellular automata, Turing machines, or even billiards [5].

4.3) Characterising the lifetime of quantum information

Decoherence times. The third Di-Vicenzo requirement refers to the *decoherence time* of the qubit. Roughly speaking, the decoherence time is the time for which the qubit can hold its quantum information. The third criteria thus says that the decoherence time must be smaller than the time required to perform an operation on the qubit.

In physical implementations of qubits, there are often several sources of decoherence. One possibility is the decay of the excited state to the ground state. This energy decay is characterised by the *relaxation time*[1] T_1 [5].

More generally, the lifetime of a qubit, or how long a qubit can preserve quantum information, is characterised by another quantity, the *dephasing time*[2], noted T_2 [5]. The dephasing time tells us how long a superposition state

$$|\psi\rangle = \frac{|0\rangle + e^{i\phi}|1\rangle}{\sqrt{2}} \tag{II.69}$$

retains its relative phase ϕ. It is thus a better figure or merit for qubits than T_1, since it considers the lifetime of a general superposition state (while T_1 only considers the transition from the excited state e.g. $|1\rangle$, to the ground state). The dephasing time takes into account the relaxation time and potentially other sources of decoherence. For instance, if energy relaxation is the only source of decoherence, then $T_2 = 2T_1$. More generally, if other decoherence processes can be characterised by a time scale T', then [92]

$$\frac{1}{T_2} = \frac{1}{2T_1} + \frac{1}{T'}, \tag{II.70}$$

so that in general $T_2 < 2T_1$. Note that in general we also have $T_2 < T_1$, but this is not necessarily always the case.

A similar metric, although it is not distinguished from T_2 by some authors [93], is T_2^*, which contrary to T_2, is obtained by averaging several measurements of T_2 and includes instrumental imperfections. Hence it is smaller than T_2.

Cooperativity. Another relevant metric is the cooperativity between two systems A and B, defined as [94]

$$C = \frac{4g^2}{\kappa_A \kappa_B} \tag{II.71}$$

where $g/2\pi$ is the coupling strength (with dimension of frequency) between the two systems, $\kappa_A/2\pi$ the dissipation rate of system A (dimension of frequency) and $\kappa_B/2\pi$ the dissipation rate of system B. The cooperativity is useful to characterise the coherent information exchange between the two systems, where $g/2\pi$ describes how fast this information is transferred, and $\kappa_{A,B}/2\pi$ how fast this information is lost by each system. If A and B are different physical systems, the cooperativity allows to quantify the quality of the hybrid system for quantum information transduction. Experimentally, the dissipation rate $\kappa/2\pi$ is obtained by measuring the linewidths of the resonances of the individual (uncoupled) systems, and it can be linked to the dephasing time T_2^* by $\kappa = \frac{2}{T_2^*}$.

4.4) Quantum gates

4.4.1) Single-qubit rotations

According to quantum mechanics, the most general transformation on a qubit is described by a 2×2 unitary matrix U which maps an initial state $|\psi_i\rangle = \alpha_i|0\rangle + \beta_i|1\rangle$ to

$$U|\psi_i\rangle \equiv |\psi_f\rangle = \alpha_f|0\rangle + \beta_f|1\rangle . \tag{II.72}$$

[1] This is also called the longitudinal or decay time.

[2] Also called the transverse relaxation time.

As we explained in section 2.1, the initial ($|\psi_i\rangle$) and final ($|\psi_f\rangle$) states can be pictured on the Bloch sphere. Thus, we can guess that any unitary transformation U can be written in terms of rotations around the $\hat{\mathbf{x}}, \hat{\mathbf{y}}$ and $\hat{\mathbf{z}}$ axes on the Bloch sphere.

Formally, the rotations R_u of an angle ϕ about the unit vector $\hat{\mathbf{u}}$ are given by [5]

$$\forall u \in \{x, y, z\}, \quad R_u(\phi) = \exp\left(-i\phi\frac{\sigma_u}{2}\right). \tag{II.73}$$

where σ_x, σ_y and σ_z are the Pauli matrices. More generally, the transformation [5]

$$R_{\hat{\mathbf{n}}}(\phi) = \exp\left(-i\phi\frac{\hat{\mathbf{n}}\cdot\boldsymbol{\sigma}}{2}\right) \tag{II.74}$$

where $\boldsymbol{\sigma} = (\sigma_x, \sigma_y, \sigma_z)$ corresponds to a rotation by ϕ about the $\hat{\mathbf{n}}$ axis. Then, it can be shown that any unitary transformation acting on a qubit can be decomposed in terms of two rotations about non-collinear axes. Formally, if $\hat{\mathbf{n}}$ and $\hat{\mathbf{m}}$ are two non-collinear unit vectors, then for any unitary transformation U [5]

$$\exists \varphi, \phi_1, \phi_2, \phi_3 \in \mathbb{R}, \quad U = e^{i\varphi} R_{\hat{\mathbf{n}}}(\phi_3) R_{\hat{\mathbf{m}}}(\phi_2) R_{\hat{\mathbf{n}}}(\phi_1). \tag{II.75}$$

This shows that to implement arbitrary single-qubit operations U, it is sufficient to be able to perform two rotations $R_{\hat{\mathbf{n}}}, R_{\hat{\mathbf{m}}}$ about different axes $\hat{\mathbf{n}}$ and $\hat{\mathbf{m}}$.

Depending on the physical implementation, it may be very hard to have the ability to perform two independent rotations. Instead, the ability to approximate a single-qubit rotation to an arbitrary precision is sufficient [95]. Nevertheless, the present discussion shows that *coherent control* of quantum states is required for quantum computing.

4.4.2) Universal quantum computation

In classical computing, any logic gate can be made up from NAND (Not AND) gates only. Thus, the singleton {NAND} is a universal gate set for classical computation: this means that any computation can be performed by wiring NAND gates together. This set of gates is not unique, for instance the singleton made of a NOR gate is also universal.

A similar principle applies in quantum computing: it is sufficient to be able to implement a universal set of gates to perform any quantum computation [95]. Depending on the physical system implementing the qubit, some gates may be easier to implement than others. Luckily, there are many different universal gate sets.

A simple universal set of gates is the *standard circuit model* [95]. It comprises all single-qubit rotations, and the CNOT gate, which is quantum "conditional XOR" operation on two qubits. Formally, the CNOT gate is such that

$$\mathrm{CNOT}\,|x\rangle\,|y\rangle = |x\rangle\,|x \oplus y\rangle\,, \tag{II.76}$$

where $\oplus$ corresponds to the XOR logical operator, and therefore the CNOT gate acts on the basis states as

$$|00\rangle \mapsto |00\rangle\,, \tag{II.77}$$
$$|01\rangle \mapsto |01\rangle\,, \tag{II.78}$$
$$|10\rangle \mapsto |11\rangle\,, \tag{II.79}$$
$$|11\rangle \mapsto |10\rangle\,. \tag{II.80}$$

In other words, it conditionally flips the second qubit if the first qubit is $|1\rangle$. While in principle a CNOT gate is sufficient, the ability to couple two remote qubits together is also useful to reduce the number of swap operations in quantum algorithms. This entails an additional level of difficulty for coherent control.

4.5) Quantum error correction

A closer look at errors. During a computation, errors of different origins can occur. One possibility is the loss of quantum information stored on the qubits, which we saw in section 4.3 are characterised by decoherence times. As per the third Di-Vicenzo criteria [91], it is thus desirable to apply the quantum gates as fast as possible[1], but this requires fast control pulses. Depending one the physical system, this may be hard to realise perfectly[2], which thus lead to *control errors*.

Alternatively, it may be that only an approximative unitary gate is realised, which introduces gate errors [97]. For instance the underlying physical system may not support exact single-qubit rotations, but they are instead approximated by other non-unitary transformations. Such imperfections can also affect the initialisation and measurement steps (corresponding to the second and fifth Di-Vincenzo criteria [91]). Finally, it is worth remembering that in practice a quantum computer should have many qubits, often spatially close to each other. This can lead to crosstalk errors [97], where an operation on one qubit affects another[3].

Quantum error correction (QEC). One solution against error is, just like for classical computing, error correction. A simple example of classical error correction is the three bit repetition code [97], which consists of duplicating the bit three times. Assuming a single bit flip error is the most probable error, then by the majority rule we can detect and correct this error successfully. Thus, this simple error correcting code uses three *physical bits* to encode a single *logical bit*. However, *by the no-cloning theorem*, we deduce that this simple scheme is not applicable to qubits.

Therefore, we need to use an alternative strategy, first proposed by Shor (1995) [98]. The idea consists of encoding a logical qubit on several entangled qubits [99]. In practice, however, these scheme face several challenges. One of them is related to the connectivity of qubits to other qubits. For instance, in some promising quantum error correcting codes such as toric and surface codes, qubits must be connected to each other in a lattice, which can be hard to scale up [97]. Furthermore, the introduction of additional qubits to encode logical qubits require far too many physical qubits than what is currently available when scaling up the system.

Instead, we could take advantage of the infinitely large Hilbert space offered by bosonic modes. The first such proposal for bosonic codes appeared in 1997 [100], and in the following years several promising extensions were put forward [14, 101]. These include cat codes [13, 102] which use cat states to encode quantum information, the Gottesman-Kitaev-Preskill (GKP) code [103] which uses squeezed states, or binomial codes [104] which use particle number states. Of course, the correction process requires the ability to control the bosonic modes, so that *coherent control* is another requirement for quantum error correction, whether it is based on continuous or discrete variables. Finally, note that since QEC allows to preserve quantum information, it is also of interest to any quantum technology limited by decoherence effects. For instance, quantum error correction was shown to help achieve the Heisenberg limit in quantum metrology [105].

5) Some physical platforms

So far, our review of several quantum technologies allowed us to identify several desirable capabilities for quantum information processing. We now give an overview of some promising physical platforms to realise such operations.

[1] In other words, *non-adiabatic* gates are desirable. Here, non-adiabatic characterises a "fast" operation, a concept which we can be formally defined [96], as we do in chapter V. We will also revisit this concept in chapter IX in the context of the original work appendix C.10.

[2] An example discussed in chapter IX is that of silicon charge qubit, where fast control pulses are required to limit decoherence.

[3] For instance, we will see in chapter IX that localised magnetic fields are used to control silicon spin qubits, but in practice such magnetic fields often also affect neighbouring qubits.

5.1) Photons

Photons, the bosonic particles associated to the electromagnetic field, take a particular place among the many physical platforms susceptible to be used for quantum information processing, a fact owing to its versatility. First of all, photons exists for a wide frequency range, from radio frequencies (wavelengths of 10^3 meters) to gamma rays (wavelengths of 10^{-12} meters, the atomic nuclei scale). In particular, photons at optical frequencies have a great decoherence time and can be faithfully transmitted over long distances (hundreds of kilometres) using optical fibres. Thus, photons with appropriate wavelengths[1] can take advantage of the existing telecommunication infrastructure for quantum communication.

Furthermore, their integration on silicon chips [106, 107] is promising for quantum networks [108–110] and quantum computing [110, 111]. Furthermore, (entangled) single-photons are useful for (secure) quantum communication [112–114], quantum computing [113, 114] and quantum sensing [114, 115]. Sources of single photons and entangled photons based on semiconductor quantum dots[2] can be integrated on silicon chips [116–121] for general-purpose quantum computing [122]. On the detection side, superconducting nanowires can be used to detect single photons at optical frequencies [123–131], but detectors for microwave frequencies are harder to create. Nevertheless, proposals for single-photon detection in the microwave regime using Josephson functions and superconducting transmon qubits exist [132].

Additionally, photons offer several degrees of freedom on which quantum information can be encoded [133], which has several advantages for quantum information processing and *quantum information transduction*. As an example of the omnipresence of light in quantum information processing, we shall see in the rest of this section that light is an essential element of many other physical platforms, such as circuit QED or trapped ions to name a few.

The biggest shortcoming of photons is that it is hard to make them interact with each other, because only weak non-linearities exist. A solution to this problem is to couple light with matter degrees of freedom. For instance, non-reciprocal behaviours – which we saw in section 3 are desired to prevent side-channels attacks in QKD – can be obtained using magneto-optical effects, but these are hard to integrate with silicon photonics [134–136]. Nevertheless, this idea of using *hybrid systems* (for instance coupling light and matter) is important as demonstrated by the following physical platforms.

5.2) Cavity and circuit quantum electrodynamics

Cavity quantum electrodynamics. Light can interact with some atoms when an electric or magnetic moment are present, and the associated theory is given by quantum electrodynamics (QED). To enhance the coupling of the light with matter, a cavity resonator is used. It confines light and thus allows it to interact several times with the atoms. Such a setup is the basis of cavity QED [5, 137], which can be used for quantum computing by using single photons as qubits [138]. More generally, cavity QED is concerned with the interaction of light confined to a cavity with matter.

Circuit QED. An attractive replacement for atoms are superconducting qubits, due to their ease of fabrication and design. This leads to the field of circuit QED, which can be seen as a subset of cavity QED. Superconducting qubits are based on Josephson junctions appropriately placed in circuits (along with other components such as capacitors and inductances), hence the name circuit QED. The integration of superconducting qubits on chips is shown in figure II.5.

A strength of superconducting qubits is their versatility. Their quantum state can be encoded on different degrees of freedom, such as charge, flux or phase [92, 139, 141–144]. These degrees of freedom can be controlled and result in discrete energy levels, and thus superconducting quits are also called *artificial atoms*. Their design flexibility make them one of the leading platforms for creating a quantum computer [145–149], with decoherence times

[1] Several *communication windows* exist, and the C band, corresponding to wavelength between 1530 and 1565 nm, is the most used window for communication over optical fibres. Therefore, photons in the C band can be used in standard optical fibres for long distance quantum communication.

[2] Quantum dots will be described in more details in chapter IX.

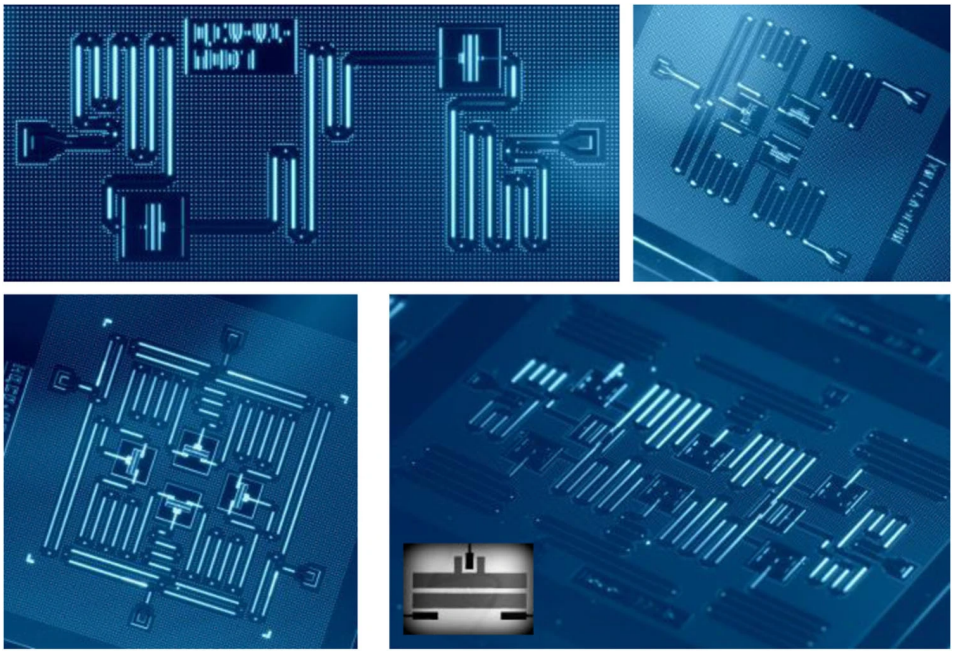


Figure II.5: Examples of superconducting qubits with buses and readout resonators from IBM. Image originally from fig 4 of [139] and licensed under a CC BY 4.0 Deed license [140].

reaching the microseconds [150]. Outside of quantum computing, Josephson junctions and superconducting qubits can be used to detect single photons at microwave frequencies [132], and have been used to create non-reciprocal devices [151–153].

5.3) Trapped ions

Another promising platform are trapped ions[1], which are useful for quantum computing [154–156] and quantum networks [157]. The system comprises two elements: ions, whose electronic states are used as qubits, and phonons, the quanta of collective motion of the ions in one dimension. The movement of ions in the other two dimensions are reduced (ideally removed) by using an electrostatic trap illustrated in figure II.6. The remaining mechanical motion is frozen by cooling down the system, and takes the form of a harmonic oscillator (frequency $\omega/2\pi \simeq 1$ MHz). The phonons, which can be manipulated by lasers, are used to couple ions, and thus qubits, together.

Two types of qubits can be built using trapped ions: optical qubits and hyperfine qubits. Optical qubits use electronic ground and excited states with an energy gap corresponding to hundreds of THz, hence their name. Alternatively, hyperfine qubits use two hyperfine ground states instead, with an energy gap in the microwave range. Trapped ions benefit from impressive decoherence times, of the order of a second for optical qubits, and ten minutes for hyperfine qubits. While quantum computing [158, 159] and quantum error correction [160] have been demonstrated, the biggest limitation of this platform is scalability, due to the amount of control wires that need to be integrated [161].

5.4) Cavity optomechanics

Optmechanical system are concerned with the interaction of light with mechanical resonators, such as cantilevers or mirrors [162, 163]. In optomechanics, the quanta of light, the photons, interact with the quanta of mechanical motion, the phonons. Both photons and phonons are bosonic modes (say with annihilation operators c, m and frequencies $\omega_c/2\pi, \omega_m/2\pi$), and they can interact for instance due to radiation pressure of the photons impact a mirror. If a movable mirror constitutes one end of a cavity resonator, its movement changes the resonance

[1] We recall that an ion is originally a neutral atom, where one electron has been added (cation) or removed (anion). After the removal/addition of the electron, the atom is not neutral anymore.

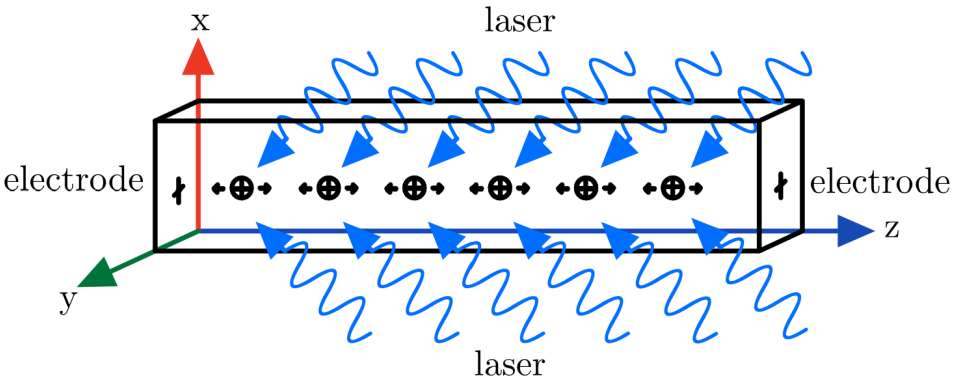


Figure II.6: Schematic of trapped ions, where (optical or hyperfine) qubits are encoded on individual ions, and phonons (movement of ions) are controlled by lasers to couple the qubits together. Image originally from fig 1 of [156] licensed under a CC BY 4.0 Deed license [140].

frequency of the cavity, which can be described by the Hamiltonian [162]

$$H = \hbar\omega_c c^\dagger c + \hbar\omega_m m^\dagger m + \hbar g c^\dagger c(m + m^\dagger), \tag{II.81}$$

where $g/2\pi$ is the coupling strength, with dimension of frequency. This Hamiltonian is the basis of *cavity optomechanics*, a particularly useful playground for quantum information transduction and the generation of non-classical states [164, 165].

Indeed, in the presence of a coherent drive of the cavity (represented by a time-dependent coherent state, see equation (II.40)) at frequency $\omega_d/2\pi$, this Hamiltonian can be linearised and the quantum fluctuations, represented by the annihilation operators $\delta c, \delta m$, have Hamiltonian [163]

$$H = \hbar\Delta\delta c^\dagger\delta c + \hbar\omega_m\delta m^\dagger\delta m - \hbar G(\delta c + \delta c^\dagger)(\delta m + \delta m^\dagger) \tag{II.82}$$

where $\Delta \simeq \omega_c - \omega_d$ is the detuning and $G/2\pi$ an effective coupling strength in the presence of the drive. In particular, in the red-detuned regime where $\Delta = \omega_m$, the interaction Hamiltonian $H_{\text{int}} = -\hbar G(\delta c + \delta c^\dagger)(\delta m + \delta m^\dagger)$ becomes [162, 163]

$$H_{\text{int}} = -\hbar G(\delta c\delta m^\dagger + \delta c^\dagger\delta m), \tag{II.83}$$

which describes linearly coupled bosonic modes. This interaction, often called a *beam splitter interaction*, describes the coherent exchange of quanta of energy between the two bosonic modes, or in other words the conversion of phonons into photons and back. In light of this result, it is not surprising that cavity optomechanics can be used for microwave to optical conversion [166, 167], and the creation of non-reciprocal devices [167–174].

Another interesting case is when the drive is blue-detuned, corresponding to $\Delta = -\omega_m$. The interaction Hamiltonian is

$$H_{\text{int}} = -\hbar G(\delta c\delta m + \delta c^\dagger\delta m^\dagger), \tag{II.84}$$

and corresponds to a parametric (and non-linear) interaction. Such non-linear interactions are essential to create entanglement, and indeed it is possible to create phonon cat states [175], squeezing [176–178], entanglement [179–182], quantum steering [183], and perform quantum teleportation [182] using cavity optomechanical systems.

6) Conclusion

Over the course of this chapter, we have identified several resources which can be useful for quantum information processing. Entanglement and non-classical bosonic states (such as squeezed states, cat states and Fock states) are useful for quantum sensing, quantum computing and quantum communications. For quantum networks, quantum information transduction, for instance the conversion of light from optical to microwave frequencies or the coupling of light with solid state systems, is an important primitive. Non-reciprocal behaviours are relevant to route quantum information in quantum networks, protect quantum key distribution

devices against side-channel attacks, or to create asymmetric quantum behaviour such as quantum steering, useful for quantum cryptography. The coherent control of quantum information is also an elementary building block of quantum computing and quantum communication protocols.

The succinct panorama of physical platforms presented above shows that each of them has intrinsic advantages and disadvantages. For instance, while microwave photons seem promising for quantum information processors based on superconducting qubits, they require very low temperatures to overcome thermal noise, and cannot be useful for long distance quantum communication using existing optical fibres. This suggests that quantum technologies would benefit from hybrid systems, where association of two different physical platforms allows to overcome their individual limitations. Naturally, the study of systems that can couple to light at optical or microwave frequencies is desirable, since light is so present in various physical platforms. More generally, any platform that can act as a bridge between different systems is of interest, especially if non-reciprocal interactions can be create.

We will see that similar to cavity optomechanics, cavity magnonics, introduced in chapter IV, has many desirable qualities for quantum information processing. Using magnons, the quanta of spin waves, cavity magnonics platforms can interact with both microwave and optical photons, and also couple to phonons, making it interesting for quantum information transduction. By appropriately engineering dissipation, non-reciprocal behaviours can also be obtained, as will be discussed in chapter VI. Cavity magnonics can also reach the ultrastrong coupling regime (discussed in chapter VII), which induces non-linearities that are useful for fast quantum information transduction and the creation of non-classical states. Since cavity magnonics involves light confined in cavity resonators, we shall first introduce their description in the next chapter.

Chapter III

Introduction to light/matter interactions

Summary

We introduce the quantum-mechanical description of the electromagnetic field using the canonical quantisation in the Coulomb gauge. The starting point is classical electrodynamics, described by Maxwell's equations in vacuum, which is then quantised. Next, we discuss the classical coupling between matter and light. A classical Hamiltonian describing the electric dipole interaction of atoms with the electromagnetic field is given, and then quantised. This allows us to introduce the two most common light/matter interaction models used in quantum optics, namely the Jaynes-Cummings model and the Dicke model. We then introduce theoretical methods for the study of light/matter interactions, such as diagonalisation, quantum Langevin equations, and input-output theories. The semi-classical approximation is discussed and applied to coherent drives. Aside from introducing these theoretical methods, we derive some results of interest for the next chapters.

Contents

1) Introduction . . . **40**
2) Quantum description of the electromagnetic field . . . **40**
2.1 Introduction . . . 40
2.2 Classical electrodynamics . . . 41
2.2.1 Maxwell's equations . . . 41
2.2.2 Gauge degree of freedom . . . 42
2.2.3 Dynamics and solutions . . . 43
2.3 Canonical quantisation in the Coulomb gauge . . . 44
3) Some models of light/matter interactions . . . **45**
3.1 Interaction with the electromagnetic field . . . 46
3.2 The electric dipole interaction . . . 47
3.3 The quantum Rabi model . . . 48
3.4 Multi-dipole extension: Dicke model . . . 50
3.5 The rotating wave approximation and the Jaynes-Cummings model . . . 51
4) Closed-system analysis . . . **52**
4.1 Diagonalisation: spectrum and polaritons . . . 52
4.2 Perturbation theory using Schrieffer-Wolff transformations . . . 55
4.2.1 Principle . . . 55
4.2.2 Dispersive regimes . . . 56
4.2.3 Indirect coupling . . . 58
5) Open quantum systems . . . **59**
5.1 Quantum Langevin equations . . . 60
5.1.1 Coherent drive . . . 63
5.2 Input-output formalism . . . 65

5.2.1 Input-output relations 65
5.2.2 Application: coupled bosonic modes 66
6) Conclusion **69**

1) Introduction

Why study light? Light occupies a special place for quantum information processing schemes due to its versatility. Indeed, photons, the quanta of an electromagnetic wave, can exist in a wide range of frequencies, from microwaves to X-rays. This property allows light to couple to various physical systems. Additionally, by simultaneously coupling to several objects, photons can act as a bridge, and mediate an interaction between fundamentally different systems. Furthermore, light offer several degrees of freedom on which quantum information can be encoded.

For all of these reasons, light has been studied extensively, both for fundamental physics and quantum technologies. Surprisingly, a classical description of the electromagnetic field suffices for describing several light/matter interaction physical effects, where only the matter degrees of freedom are quantised[1]. Still, a quantum theory of light is required to describe many important phenomena such as spontaneous emission, the Lamb shift[2], resonance fluorescence and the anomalous gyromagnetic moment of the electron. Most notably, non-classical states of light, which are omnipresent in many quantum information processing schemes, do require a quantum-mechanical formalism for light.

Outline. We begin by quantising the electromagnetic field in section 2. We adopt the Coulomb gauge, which is the standard gauge to use for quantisation. Having quantised the electromagnetic field, we then discuss the interaction between light and matter in section 3, where we focus on the electric dipole interaction. We derive two standard models of quantum optics, the Jaynes-Cummings model and its multiple dipole generalisation, the Dicke model. In the next two sections, we introduce different methods for the study of light/matter interactions. Section 4 focuses on a closed system analysis, and we notably explain how to diagonalise Hamiltonians to find the spectrum and the associated quasi-particles, the *polaritons*. On the other hand, section 5 considers an open-system analysis, where both light and matter are coupled to the environment.

Notations. We write c_k and $\omega_k/2\pi$ with $k \geqslant 1$ for the annihilation operator and frequency of the mode k of the electromagnetic field. In the special case of a single mode, we will use c and ω_c instead[3]. Similarly, we denote by m and $\omega_m/2\pi$ the matter annihilation operator and the matter frequency. Some properties related to commutators are recalled in appendix A.1. In the rest of this document, the Fourier transform of a time-dependent operator a is $\mathcal{F}[a](\omega) = \tilde{a}(\omega) = \tilde{a}$. Often, the frequency dependence will be dropped for conciseness. Some useful properties of Fourier transforms are recalled in appendix A.3.

2) Quantum description of the electromagnetic field

2.1) Introduction

The goal of this section is to describe the quantisation of the electromagnetic field. Unfortunately, the rigorous quantisation of the electromagnetic field is not as easy as it may appear. One problem is related to the gauge degree of freedom of the electromagnetic field. Part of this problem is only present if one wants to do relativistic calculations, where a covariant

[1] This is called the *semi-classical* approximation, where the matter degrees of freedom are quantised, and the light is classical. For instance, the first twelve chapters (out of twenty) of the textbook by Meystre and Sargent (2007) [184] make use of the semi-classical approximation.

[2] The Lamb shift corresponds to the renormalisation of the energy levels due to vacuum fluctuations.

[3] The notation c refers to a cavity mode. It should not be confused with the speed of light!

description of electromagnetism is required. In the context of this thesis, we only consider non-relativistic physics, so this problem can be bypassed. Still, a common approach for quantisation is to choose a gauge (most commonly the Coulomb gauge), and then quantise the associated classical field theory. Thus, one obtains a quantum theory of light that is gauge-dependent, and changing the gauge afterwards is not trivial[1]. This is problematic since a straightforward derivation of the electric dipole interaction of atoms with light is obtained by using another gauge.

Another issue is related to the generality of the methods encountered in the literature. For instance, a common approach, presented in several textbooks of quantum optics [33, 184–186], considers the classical expression of a single-mode electric field confined between two mirrors. The resulting Hamiltonian is formally equivalent to that of a classical harmonic oscillator. Using the standard quantisation of the harmonic oscillator, we can similarly quantise the electric field. This single-mode quantisation is then generalised to several modes. Such a generalisation if enticing, but it is hard to justify for diversely-shaped microwave cavities, as will be considered in the next chapters. Alternatively, often the electromagnetic field is quantised in vacuum, without the presence of magnetic materials.

Here, we take a pragmatic approach to quantisation, following [34, 187]. What we shall do is consider an empty cubic space of volume $L \times L \times L$. In other words, there will be no charges, no current, and we assume that the medium is vacuum, even though [187] proposes a generalisation to an arbitrary space-dependent relative permittivity. We shall impose the Coulomb gauge, and write a classical expression for the vector potential suggestive of a mode decomposition. We can then apply the canonical quantisation procedure to obtain a quantised formulation of light. Note that taking $L \to \infty$ we obtain the continuum limit, describing light as plane waves in free space.

Before delving into technicalities, we mention several useful references for this section. The covariant quantisation of light can be found in [11, 188]. In particular, Maggiore (2005) [188] discusses the aforementioned difficulties related to retaining covariance when quantising gauge field theories. A rigorous treatment of the quantisation of light for quantum optics is given in the lecture notes of Keeling [189]. Two more accessible lecture notes are Genes (2019) [190] and Navarrete-Benlloch (2022) [191], and the previously mentioned textbooks [33, 184–186]. Finally, the quantisation of the electromagnetic field in dielectrics can be found in [192, 193].

2.2) Classical electrodynamics

2.2.1) Maxwell's equations

Maxwell's equations can be written differently depending on the authors, and the choice of units (SI or Gaussian units). Notably, we can distinguish between Maxwell's equations in vacuum, and Maxwell's equations in a medium. The former is the most well known formulation, where the presence of a material is accounted for through the (total) charges and currents. Here, we adopt the formulation in a medium[2] with SI units, so that Maxwell's equations are written as [187]

$$\boldsymbol{\nabla} \cdot \mathbf{D} = \rho, \quad \boldsymbol{\nabla} \times \mathbf{E} = -\frac{\partial \mathbf{B}}{\partial t}, \tag{III.1}$$

$$\boldsymbol{\nabla} \cdot \mathbf{B} = 0, \quad \boldsymbol{\nabla} \times \mathbf{H} = \mathbf{J} + \frac{\partial \mathbf{D}}{\partial t}, \tag{III.2}$$

with ρ the free electric charge volume density in $\mathrm{C/m^3}$, $\mathbf{J}$ the free electric volume current density in $\mathrm{A/m^2}$, $\mathbf{D}$ the electric displacement (also called electric induction and electric flux density) in $\mathrm{C/m^2}$, $\mathbf{E}$ the electric field in V/m, $\mathbf{H}$ is the magnetic field (intensity) in A/m and $\mathbf{B}$ the magnetic flux density – the magnetic analogue of $\mathbf{D}$ – in Tesla. Note that some authors adopt different names for these fields, distinguishing between intensity and flux. For instance, Stancil and Prabhakar (2009) [194] call $\mathbf{D}$ the electric flux density, and $\mathbf{E}$ the electric field intensity.

[1] Some of these problems will be discussed in chapter VII.

[2] Note that both formulations are equivalent, as long as one correctly interpret the fields.

As can be intuitively expected from the names of these quantities, the field intensities are related to the field flux densities. In general, it is possible to write:

$$\mathbf{D} = \epsilon_0 \mathbf{E} + \mathbf{P}, \tag{III.3}$$

$$\mathbf{B} = \mu_0 (\mathbf{H} + \mathbf{M}), \tag{III.4}$$

with $\epsilon_0 \simeq \frac{1}{36\pi} \times 10^{-9}$ F/m the electric permittivity[1] of the vacuum[2], $\mu_0 = 4\pi \times 10^{-7}$ H/m the magnetic permeability of vacuum, $\mathbf{P}$ the electric polarisation field, and $\mathbf{M}$ the magnetisation. The field $\mathbf{P}$ ($\mathbf{M}$) has unit of an electric (magnetic) dipole moment per volume, and describes the response of a material to an applied electric (magnetic) field[3]. Note that some authors identify $\mathbf{M}' = \mu_0 \mathbf{M}$, which has the same unit as $\mathbf{B}$, with $\mathbf{M}$.

Often, the response of a material to an applied field is linear, and we can write

$$\mathbf{D} = \underline{\epsilon}\mathbf{E}, \quad \mathbf{B} = \underline{\mu}\mathbf{H} \tag{III.5}$$

where $\underline{\epsilon}, \underline{\mu}$ are the material's (absolute) electric permittivity and magnetic permeability tensors, which in general are matrices of dimension three. That $\underline{\epsilon}$ and $\underline{\mu}$ are matrices allows to describe the anisotropic nature of materials, but if the material is electrically (magnetically) isotropic, then $\underline{\epsilon}$ ($\underline{\mu}$) reduces to a constant times the identity matrix, which we simply note ϵ (μ). We further define the relative permittivity/permeability as the ratio of the permittivity/permeability of the material over that of the vacuum:

$$\underline{\epsilon}_r = \frac{\underline{\epsilon}}{\epsilon_0}, \quad \underline{\mu}_r = \frac{\underline{\mu}}{\mu_0}, \tag{III.6}$$

where $\underline{\epsilon}_r$ ($\underline{\mu}_r$) can also be written ϵ_r (μ_r) if the material is isotropic. Finally, recalling that the speed of light in vacuum is $c^2 = \frac{1}{\mu_0 \epsilon_0}$, provided the material is isotropic, we can define its refractive index $n = \sqrt{\mu_r \epsilon_r}$.

2.2.2) Gauge degree of freedom

We recall that the electromagnetic field has a gauge degree of freedom, which can be intuited from the form of Maxwell's equations. Using this formulation, $\mathbf{B}$ being divergence-less[4], we can express it as the curl of a vector potential $\mathbf{A}$. Indeed, writing $\mathbf{B} = \boldsymbol{\nabla} \times \mathbf{A}$, we immediately recover $\boldsymbol{\nabla} \cdot \mathbf{B} = 0$. Furthermore, inserting $\mathbf{B} = \boldsymbol{\nabla} \times \mathbf{A}$ into $\boldsymbol{\nabla} \times \mathbf{E} = -\frac{\partial \mathbf{B}}{\partial t}$, we see that $\boldsymbol{\nabla} \times \left(\mathbf{E} + \frac{\partial \mathbf{A}}{\partial t}\right) = 0$, so that we can write $\mathbf{E} = -\boldsymbol{\nabla}\phi - \frac{\partial \mathbf{A}}{\partial t}$, with ϕ an arbitrary scalar potential. Overall, we have the relations

$$\mathbf{B} = \boldsymbol{\nabla} \times \mathbf{A}, \quad \mathbf{E} = -\boldsymbol{\nabla}\phi - \frac{\partial \mathbf{A}}{\partial t}, \tag{III.7}$$

between $\mathbf{A}, \mathbf{B}$ and $\mathbf{E}$, which is valid for any vector potential $\mathbf{A}$ and scalar potential ϕ. This ambiguity in the choice of $\mathbf{A}$ and ϕ is what we refer to as the gauge degree of freedom.

Indeed, if we consider a transformation of the vector potential $\mathbf{A} \mapsto \mathbf{A}' = \mathbf{A} + \boldsymbol{\nabla}\varphi$, we see that the observable $\mathbf{B} \mapsto \mathbf{B}' = \boldsymbol{\nabla} \times \mathbf{A}' = \boldsymbol{\nabla} \times \mathbf{A} = \mathbf{B}$ is unchanged. On the other hand, we have

$$\mathbf{E} \mapsto \mathbf{E}' = -\boldsymbol{\nabla}\phi - \frac{\partial \mathbf{A}'}{\partial t} = -\boldsymbol{\nabla}\left(\phi - \frac{\partial \varphi}{\partial t}\right) - \frac{\partial \mathbf{A}}{\partial t} \neq \mathbf{E}. \tag{III.8}$$

To compensate this change in $\mathbf{E}$, we see that we also need to transform $\phi \mapsto \phi' = \phi - \frac{\partial \varphi}{\partial t}$, and Maxwell's equations are unchanged. More specifically, the *observable* fields $\mathbf{E}$ and $\mathbf{B}$ are invariant under a gauge transformation. We will return to the notion of gauge invariance in chapter V.

[1] This used to be called the dielectric constant, but according to the 1997 IEEE standard [195] its usage is deprecated. On the other hand, the 2018 standard [196] does not mention it is.

[2] For some authors, "free space" refers to the vacuum, while for others it refers to air, which is close to vacuum but not exactly the same. Here, I will not use the term "free space" for vacuum.

[3] The electric displacement field $\mathbf{D}$ accounts for both free and bound charges, while $\mathbf{H}$ accounts for both free and bound currents. In other words, we distinguish between permanent and induced dipoles.

[4] Note that $\mathbf{B}$ is divergence-less, but not $\mathbf{H}$. If $\mathbf{M} = 0$, then $\mathbf{H}$ becomes divergence-less too, but in general this is not the case. Accordingly, the vector potential $\mathbf{A}$ is defined from $\mathbf{B}$, and not $\mathbf{H}$.

2.2.3) Dynamics and solutions

From now on, we assume for simplicity that $\underline{\epsilon}_r = \epsilon_r$ and $\underline{\mu}_r = \mu_r$ are scalars, and we follow the approach of [34]. We use the Coulomb gauge by imposing $\boldsymbol{\nabla} \cdot \mathbf{A} = 0$. Using equation (III.7), we can show that the vector potential satisfies the wave equation

$$\left(\boldsymbol{\nabla}^2 - \frac{n^2}{c^2}\frac{\partial^2}{\partial t^2}\right)\mathbf{A}(\mathbf{r}, t) = 0, \tag{III.9}$$

with the refractive index $n = \sqrt{\epsilon_r \mu_r}$. This equation can be solved by separation of variables, distinguishing between the spatial and time-dependence. For instance, the solutions can be written[1]

$$\mathbf{A}(\mathbf{r}, t) = \sum_k \left(c_k e^{-i\omega_k t} + c_k^* e^{i\omega_k t}\right)\mathbf{u}_k(\mathbf{r}), \tag{III.10}$$

where c_k are complex constants[2], and $\mathbf{u}_k$ are real-valued spatial eigenmodes[3]. Equation (III.10) shows that the vector potential is a linear combinations of modes (index k), with frequency $\omega_k/2\pi$ and field distribution $\mathbf{u}_k$.

Here the intrinsic polarisation of the electromagnetic field due to the gauge degree of freedom is "hidden" in the wave number k. Some authors make it explicit by distinguishing between k and a polarisation ϵ that takes two values. Since *we do not make use of polarisation* in this thesis, it is sufficient to embed it into k.

Preparing the stage for quantisation, we can expand the vector potential in two terms with positive ($\mathbf{A}^+$) and negative ($\mathbf{A}^-$) frequencies as

$$\mathbf{A}(\mathbf{r}, t) = \mathbf{A}^+(\mathbf{r}, t) + \mathbf{A}^-(\mathbf{r}, t), \tag{III.11}$$

where $\mathbf{A}^+ = (\mathbf{A}^-)^*$. The positive frequency component varies in time as $e^{-i\omega t}$ with $\omega > 0$, and hence the negative frequency varies as $e^{i\omega t}$. Using this formulation, we can verify that $\mathbf{A}^* = \mathbf{A}$ and hence the vector potential is real-valued. En passant, this holds even if the spatial eigenmode functions $\mathbf{u}_k$ are complex-valued, as considered in [34].

More on the spatial eigenmodes. The spatial eigenmodes are solutions of the Helmholtz equation

$$\left(\boldsymbol{\nabla}^2 + k^2\right)\mathbf{u}_k(\mathbf{r}) = 0, \tag{III.12}$$

with wave-vector $k^2 = n^2\frac{\omega_k^2}{c^2}$. This can be seen by inserting equation (III.10) into the Helmholtz equation (III.9) for $\mathbf{A}$. Formally, equation (III.12) can be interpreted as an eigenvalue problem, where $\mathbf{u}_k$ is the eigenvector of the operator $\boldsymbol{\nabla}^2$ with eigenvalue $-k^2$. It is easy to move from complex-valued spatial eigenmodes to real-valued eigenmodes, since

$$\mathbf{u}'_k(\mathbf{r}) = \frac{\mathbf{u}_k(\mathbf{r}) + \mathbf{u}_k^*(\mathbf{r})}{2} \in \mathbb{R} \tag{III.13}$$

is still an eigenmode with the same eigenvalue (or equivalently a solution of the eigenvalue equation (III.12)).

A basic result of linear algebra is that eigenmodes are orthogonal. Formally, this reads

$$\int_{V_c} \mathrm{d}^3 r\, \mathbf{u}_k(\mathbf{r})\mathbf{u}_{k'}(\mathbf{r}) = \delta_{k,k'} V_c, \tag{III.14}$$

with V_c the volume of the cavity. Note that alternative normalisation of the mode functions exist, but we shall discuss them after quantising the EM field. Furthermore, due to the Coulomb gauge condition $\boldsymbol{\nabla} \cdot \mathbf{A} = 0$, the eigenmodes satisfy $\boldsymbol{\nabla} \cdot \mathbf{u}_k = 0$, which is called the transversality condition by some authors [34].

[1] This is just one way of writing the solutions.

[2] They are constants in the classical description of the electromagnetic field, but will be promoted to annihilation operators after quantisation.

[3] More precisely, they can be *chosen* real-valued without loss of generality, as we show below.

Finally, we note that the spatial eigenmode functions $\mathbf{u}_k$, as determined by the Helmholtz equation (III.12), depend only on the geometry of the cavity. For instance, for a cubic cavity, the spatial eigenmodes can be written [34]

$$\mathbf{u}_k(\mathbf{r}) = \frac{e^{i\mathbf{k}\cdot\mathbf{r}}}{L^{3/2}} \tag{III.15}$$

where the wave numbers are $k_{x,y,z} = \frac{2\pi n}{L}$ with $n \in \mathbb{N}$. Note also that one can recover the free-space solutions, by taking $L \to \infty$. The solutions can then be expressed as plane waves, leading to the common expression

$$\mathbf{A}^+(\mathbf{r},t) = \sum_k c_k e^{i(\mathbf{k}\cdot\mathbf{r} - i\omega_k t)}, \tag{III.16}$$

for the vector potential. Using a plane wave basis for the mode functions, one can write $\boldsymbol{\nabla} = i\mathbf{k}$, which is sometimes used to find the expression of the magnetic field from $\mathbf{B} = \boldsymbol{\nabla} \times \mathbf{A}$.

Identification with the harmonic oscillator. In this last paragraph, we would like to give an intuitive view on the relation between the electromagnetic field and the harmonic oscillator. As previously mentioned, the wave equation (III.9) satisfied by the vector potential $\mathbf{A}$ can be solved by separation of variables, by writing $\mathbf{A}$ as the product of a space-dependent function, and a time-dependent function. The spatial functions correspond to the spatial eigenmode functions $\mathbf{u}_k$, as it can be shown that they satisfy the Helmholtz equation (III.12). We can similarly derive an equation for the time-dependent function too, which we shall call $q_k(t)$. Following [187] the vector potential can be written

$$\mathbf{A}(\mathbf{r},t) = \sum_k \frac{q_k(t)}{\sqrt{\epsilon_0 \epsilon_r}} \mathbf{u}_k(\mathbf{r}) \tag{III.17}$$

and then one can show that the Hamiltonian comes out as

$$H = \sum_k \left(\frac{1}{2}\dot{q}_k^2(t) + \frac{1}{2}\omega_k^2 q_k(t)^2 \right). \tag{III.18}$$

Defining $p_k(t) = \dot{q}_k(t)$, we have a suggestive identification with a sum of harmonic oscillators. We conclude that classically, the modes of the electromagnetic field are formally equivalent to harmonic oscillators.

2.3) Canonical quantisation in the Coulomb gauge

Following the canonical quantisation procedure [11, 188], we now promote the amplitudes c_k to operators $\hat{c}_k$, and replace complex conjugation by hermitian conjugation. The operators $\hat{c}_k$ are chosen[1] to be bosons, and hence we enforce the bosonic commutation relations $\left[\hat{c}_k, \hat{c}_{k'}^\dagger\right] = \delta_{k,k'}$. For simplicity, we keep the same notations for the operators and simply write $\hat{c}_k = c_k$. The quantised version of equation (III.10) is written as

$$\mathbf{A}(\mathbf{r},t) = \sum_k \sqrt{\frac{\hbar}{2V_c\epsilon_0\omega_k}} \left(c_k e^{-i\omega_k t} + c_k^\dagger e^{i\omega_k t} \right) \mathbf{u}_k(\mathbf{r}), \tag{III.19}$$

where the Heisenberg picture is assumed, and we recall that V_c is the volume of the cavity. The normalisation constant is chosen such that the operators c_k are dimensionless, and depends on the choice of normalisation of the mode functions $\mathbf{u}_k$.

From the expression of the vector potential we can deduce

$$\mathbf{B}(\mathbf{r},t) = \boldsymbol{\nabla} \times \mathbf{A} = \sum_k \sqrt{\frac{\hbar}{2V_c\epsilon_0\omega_k}} \left(c_k e^{-i\omega_k t} + c_k^\dagger e^{i\omega_k t} \right) \boldsymbol{\nabla} \times \mathbf{u}_k(\mathbf{r}). \tag{III.20}$$

Similarly, the relation between $\mathbf{E}$ and $\mathbf{A}$ in the Coulomb gauge gives

$$\mathbf{E}(\mathbf{r},t) = -\frac{\partial \mathbf{A}(\mathbf{r},t)}{\partial t} = i \sum_k \sqrt{\frac{\hbar\omega_k}{2V_c\epsilon_0}} \left(c_k e^{-i\omega_k t} - c_k^\dagger e^{i\omega_k t} \right) \mathbf{u}_k(\mathbf{r}). \tag{III.21}$$

[1] Note that we could have tried fermions instead, but experimentally the photons behave as bosons, hence our "choice".

Hamiltonian. The classical expression of the energy of the electromagnetic field is

$$H = \int_{V_c} \left(\frac{1}{2}\epsilon_0 \mathbf{E}^2 + \frac{1}{2}\mu_0 \mathbf{H}^2 \right) \mathrm{d}^3\mathbf{r} = \int_{V_c} \left(\frac{1}{2}\epsilon_0 \mathbf{E}^2 + \frac{1}{2\mu_0}\mathbf{B}^2 \right) \mathrm{d}^3\mathbf{r}\,. \tag{III.22}$$

Inserting the quantised expressions for $\mathbf{E}$ and $\mathbf{B}$, one can show[1] that the Hamiltonian reduces to

$$H = \sum_k \hbar\omega_k \left(c_k^\dagger c_k + \frac{1}{2} \right), \tag{III.23}$$

and hence the electromagnetic field can be interpreted as an infinite[2] collection of harmonic oscillators.

It is common to neglect the zero point energies $\frac{\hbar\omega_k}{2}$, but this can affect some calculations [94]. For instance, this vacuum energy is responsible for spontaneous emission phenomena, and hence neglecting it can affect the physics. In the calculations of this thesis, it will be sufficient to neglect it, and we shall do so from now on.

It is good at this stage to summarise our approximations. The expression of the quantised vector potential is valid in electrically and magnetically isotropic materials. Furthermore, these expressions are only valid in the Coulomb gauge, but we are still free to perform gauge transformations on them. While we assumed $\underline{\epsilon}_r$ to be a scalar, recall that [187] generalises these results for an arbitrary $\underline{\epsilon}_r$.

Normalisation. There exist two main normalisation choice for the mode functions, and we chose to normalise to the cavity volume V_c so that the condition

$$\int_{V_c} \mathbf{u}_k \cdot \mathbf{u}_{k'}\, \mathrm{d}^3\mathbf{r} = \delta_{k,k'} V_c, \tag{III.24}$$

is fulfilled. Another common choice is

$$\int_{V_c} \mathbf{u}_k \cdot \mathbf{u}_{k'}\, \mathrm{d}^3\mathbf{r} = \delta_{k,k'}, \tag{III.25}$$

but then the expressions for the fields differ from a factor of $\frac{1}{\sqrt{V_c}}$, so that equations (III.19) to (III.21) become

$$\mathbf{A}(\mathbf{r},t) = \sum_k \sqrt{\frac{\hbar}{2\epsilon_0\omega_k}} \left(c_k e^{-i\omega_k t} + c_k^\dagger e^{i\omega_k t} \right) \mathbf{u}_k(\mathbf{r}), \tag{III.26}$$

$$\mathbf{B}(\mathbf{r},t) = \sum_k \sqrt{\frac{\hbar}{2\epsilon_0\omega_k}} \left(c_k e^{-i\omega_k t} + c_k^\dagger e^{i\omega_k t} \right) \boldsymbol{\nabla} \times \mathbf{u}_k(\mathbf{r}), \tag{III.27}$$

$$\mathbf{E}(\mathbf{r},t) = i \sum_k \sqrt{\frac{\hbar\omega_k}{2\epsilon_0}} \left(c_k e^{-i\omega_k t} - c_k^\dagger e^{i\omega_k t} \right) \mathbf{u}_k(\mathbf{r}). \tag{III.28}$$

3) Some models of light/matter interactions

Now that the formalism for describing light has been introduced in section 2, we focus on the matter part. Historically, the description of the matter part in cavity quantum electrodynamics (QED) was limited to single atoms or an atomic ensemble. A common approximation is that of a two-level system (TLS) describing atomic levels. The formulation of the EM field as a harmonic oscillator and the matter as a TLS is the foundation of most light-matter interaction models.

[1] This may sound trivial, but it is not so easy. One needs to use the properties of Fourier transforms, the orthogonality of the spatial eigenmodes, the transversality condition and some vector calculus identities.

[2] The infinite sum over modes breaks down for very high frequencies. Intuitively, for such high frequencies, the spatial variations of the spatial modes approach the Planck length scale (10^{-33} m), where it is unknown whether quantum electrodynamics (and the standard model) even holds true.

In this section, we will consider a single cavity mode. We decompose the Hamiltonian of the system in three terms

$$H = H_p + H_m + H_I \tag{III.29}$$

where H_p describe the electromagnetic field, H_m describe the matter part, and H_I the light-matter interaction. The Hamiltonian H_p of a single cavity mode is obtained by truncating the sum of the equation (III.23), which reads[1]

$$H_p = \hbar\omega_c c^\dagger c. \tag{III.30}$$

3.1) Interaction with the electromagnetic field

According to quantum electrodynamics (QED), light couples to charged particles. The only charged particle of interest in this thesis is the electron, which possesses orbital and spin degrees of freedom, best described using a spinorial representation. In turn, the presence of charges, and more specifically their spatial distribution, can lead to the appearance of dipoles, which can be of two nature: electric or magnetic. In this chapter, we shall focus on the electric dipole, leaving the magnetic dipole for chapter IV.

A non-relativistic particle of mass m and momentum $\mathbf{p}$ is described by the Hamiltonian

$$H_m = \frac{\mathbf{p}^2}{2m} + V(\mathbf{r}), \tag{III.31}$$

with V the potential. Classically, a particle of charge q interacts with an electromagnetic field by the Lorentz force $q(\mathbf{E} + \mathbf{v} \times \mathbf{B})$ with $\mathbf{v}$ the speed of the particle. From this classical force, we can derive how the Hamiltonian of a particle needs to be changed to include the coupling to the electromagnetic field: this is the so-called *minimal coupling replacement* [197], which formally corresponds to replacing $\mathbf{p} \mapsto \mathbf{p} - q\mathbf{A}$, with $\mathbf{A}$ the vector potential. Additionally, a scalar potential ϕ leads to an additional term $q\phi$. Hence, the Hamiltonian of equation (III.31) becomes

$$H_m = \frac{(\mathbf{p} - q\mathbf{A})^2}{2m} + V(\mathbf{r}) + q\phi. \tag{III.32}$$

Expanding $(\mathbf{p} - q\mathbf{A})^2$, the Hamiltonian becomes

$$H_m = \frac{\mathbf{p}^2}{2m} + V(\mathbf{r}) + \frac{q}{m}\mathbf{p}\cdot\mathbf{A} + \frac{q^2}{2m}\mathbf{A}^2 \tag{III.33}$$

after assuming that $\mathbf{p}$ and $\mathbf{A}$ commute[2]. Comparing this Hamiltonian with equation (III.31), we see that the interaction with the electromagnetic term manifests by the additional two terms

$$\frac{q}{m}\mathbf{p}\cdot\mathbf{A} + \frac{q^2}{2m}\mathbf{A}^2. \tag{III.34}$$

The last term is the diamagnetic term, and is second-order in the magnetic field. Hence, it can be neglected for weak electromagnetic fields.

Alternatively, after quantisation, the diamagnetic term A^2 is identified to describe a self-interaction[3], or in other words multi-photon processes [34]. If we are not interested in these processes, we can also neglect this term. The diamagnetic term plays an important in certain regime light/matter interactions (see chapter VII), and for completeness we shall keep this term in what follows.

[1] We define $\omega_k = \omega_c$ and $c_k = c$ to simplify notations.

[2] It seems natural that these operators commute: they act on different objects. However, in section 2.2.2 of [198], it seems that the vector potential acts on the atomic Hilbert space. Since it is unclear to me, I will assume that $\mathbf{p}$ and $\mathbf{A}$ commute, similar to [197].

[3] Formally, write $A = A_0(c + c^\dagger)$, and hence A^2 has products of c and $c^\dagger$ describing interaction of the mode with itself.

3.2) The electric dipole interaction

Dipole approximation. Before discussing the electric dipole interaction, we must introduce the dipole approximation. The idea is to neglect the spatial dependence of the electromagnetic field by considering its value at the average location of the dipole. This is a good approximation, since for instance for electric dipoles in atoms, the spatial variations of the electromagnetic field over atomic distances (around 10^{-10} m) is negligible.

Of course, this approximation breaks down for high-frequency modes, when the wavelength[1] $\lambda = \frac{v_c}{f}$ becomes comparable to atomic distances. This becomes the case for $f \simeq 3\times10^9$ GHz, which is far beyond microwave and optical frequencies. Thus, this approximation is very reasonable for the microwave frequencies we are limiting ourselves to in this thesis.

Electric dipole and interaction Hamiltonian. Usually, an electric dipole moment $\boldsymbol{\mu}$ exists whenever we have two spatially separated charges of different value. Formally, if the point charges have charge q and $-q$, and are separated by $\mathbf{r}$, then $\boldsymbol{\mu} = q\mathbf{r}$. The resulting energy gives the interaction Hamiltonian, which is

$$H_I = -\boldsymbol{\mu}\cdot\mathbf{E}. \tag{III.35}$$

However, this Hamiltonian seems a bit *ad-hoc*, and it is possible to derive it by using the results of the preceding sections.

Derivation of the electric dipole interaction with a gauge transformation. One way to derive equation (III.35) is to perform a gauge transformation on the Hamiltonian of a charged particle minimally coupled to the electromagnetic field (see equation (III.32)) [186, 197]. As previously mentioned (equation (III.7)), we have the relation

$$\mathbf{E} = -\frac{\partial\mathbf{A}}{\partial t}, \tag{III.36}$$

in the radiation gauge (the Coulomb gauge with $\phi = 0$). Performing the gauge transformation

$$\mathbf{A}' = \mathbf{A} + \boldsymbol{\nabla}\varphi, \tag{III.37}$$

$$\phi' = \phi - \frac{\partial\varphi}{\partial t}, \tag{III.38}$$

with $\varphi = -\mathbf{r}\cdot\mathbf{A}$, we obtain

$$\mathbf{A}' = \mathbf{A} - \mathbf{A} = 0, \tag{III.39}$$

$$\phi' = -\mathbf{r}\cdot\frac{\partial A}{\partial t} = -\mathbf{r}\cdot\mathbf{E}. \tag{III.40}$$

Hence the Hamiltonian equation (III.32) is transformed to

$$H_m = \frac{(\mathbf{p} - q\mathbf{A}')^2}{2m} + V(\mathbf{r}) + q\phi' \tag{III.41}$$

$$= \frac{\mathbf{p}^2}{2m} + V(\mathbf{r}) - q\mathbf{r}\cdot\mathbf{E} \tag{III.42}$$

$$= \frac{\mathbf{p}^2}{2m} + V(\mathbf{r}) - \boldsymbol{\mu}\cdot\mathbf{E}, \tag{III.43}$$

where we defined the electric dipole moment $\boldsymbol{\mu} = q\mathbf{r}$. One may worry that due to the gauge transformation we performed, the electromagnetic field is not strictly in the Coulomb gauge anymore. This means that we cannot employ the quantised expression of the electric field we derived in section 2.

[1] In vacuum, we have the dispersion relation $\omega = kv_c$ with k the wave number (see the previous section) and v_c the speed of light. Using $k = \frac{2\pi}{\lambda}$ gives the formula in the main text.

Derivation of the electric dipole interaction in the Coulomb gauge. Instead, let use consider the full Hamiltonian of a charged particle and the electromagnetic field in the Coulomb gauge

$$H = \hbar\omega_c c^\dagger c + \frac{(\mathbf{p} - q\mathbf{A})^2}{2m} + V(\mathbf{r}) \tag{III.44}$$

$$= \underbrace{\hbar\omega_c c^\dagger c}_{H_p} + \underbrace{\frac{\mathbf{p}^2}{2m} + V(\mathbf{r})}_{H_m} + \underbrace{\frac{q}{m}\mathbf{p}\cdot\mathbf{A} + \frac{q^2}{2m}\mathbf{A}^2}_{H_I}. \tag{III.45}$$

We can write the Hamiltonian for the particle in diagonal form as

$$H_m = \sum_k \Omega_k \left|\psi_k\right\rangle \left\langle\psi_k\right|, \tag{III.46}$$

with $|\psi_k\rangle$ the k-th energy level and $\hbar\Omega_k$ its eigen-energy. We further write $|\mathbf{A}| = A_0(c+c^\dagger)$ with $A_0 = \sqrt{\frac{\hbar}{2V_c\epsilon_0\omega_c}}$ (see equation (III.19)). Then, using the commutation relation $\left[\mathbf{r}, \mathbf{p}^2\right] = 2i\hbar\mathbf{p}$ (see appendix A.1) and the resolution of the identity $1 = \sum_k |\psi_k\rangle\langle\psi_k|$ twice, we have [198]

$$\frac{q}{m}\mathbf{p}\cdot\mathbf{A} = \frac{A_0 q}{m}\sum_{k,k'} \left|\psi_k\right\rangle \left\langle\psi_k|p|\psi_{k'}\right\rangle \left\langle\psi_{k'}\right| \left(c + c^\dagger\right) \tag{III.47}$$

$$= \frac{A_0 q}{2i\hbar m}\sum_{k,k'} \left\langle\psi_k\right|\left[\mathbf{r}, p^2\right]\left|\psi_{k'}\right\rangle \left|\psi_k\right\rangle \left\langle\psi_{k'}\right| \left(c + c^\dagger\right) \tag{III.48}$$

$$= \frac{A_0 q}{i\hbar}\sum_{k,k'} \left\langle\psi_k\right|[\mathbf{r}, H_m]\left|\psi_{k'}\right\rangle \left|\psi_k\right\rangle \left\langle\psi_{k'}\right| \left(c + c^\dagger\right) \tag{III.49}$$

$$= \frac{A_0 q}{i\hbar}\sum_{k,k'} \left(\hbar\Omega_{k'} \left\langle\psi_k|\mathbf{r}|\psi_{k'}\right\rangle - \hbar\Omega_k \left\langle\psi_k|\mathbf{r}|\psi_{k'}\right\rangle\right) \left|\psi_k\right\rangle \left\langle\psi_{k'}\right| \left(c + c^\dagger\right) \tag{III.50}$$

$$= iA_0 q\sum_{k,k'} \left(\Omega_k - \Omega_{k'}\right) \left\langle\psi_k|\mathbf{r}|\psi_{k'}\right\rangle \left|\psi_k\right\rangle \left\langle\psi_{k'}\right| \left(c + c^\dagger\right) \tag{III.51}$$

where we assumed that $[\mathbf{r}, V(\mathbf{r})] = 0$ for the third line. Since we are still in the radiation gauge, $\mathbf{E} = -\frac{\partial\mathbf{A}}{\partial t} = i\omega_c A_0\big(c - c^\dagger\big)$ and then applying the unitary transformation $U = \exp\big\{i\frac{\pi}{2}c^\dagger c\big\}$, $\mathbf{E} = i\omega_c A_0\big(-ic - ic^\dagger\big) = \omega_c A_0\big(c + c^\dagger\big)$. Hence, we find that

$$\frac{q}{m}\mathbf{p}\cdot\mathbf{A} = i\left[\sum_{k,k'} \frac{\Omega_k - \Omega_{k'}}{\omega_c} \left\langle\psi_k|\boldsymbol{\mu}|\psi_{k'}\right\rangle \left|\psi_k\right\rangle \left\langle\psi_{k'}\right|\right] \cdot \mathbf{E}, \tag{III.52}$$

and we recover an expression suggestive of an electric dipole interaction, but involving several energy levels as degree of freedom for the matter.

3.3) The quantum Rabi model

Summarising the results, the Hamiltonian of a charged particle coupled to a single cavity mode reads

$$H = \underbrace{\hbar\omega_c c^\dagger c}_{H_p} + \underbrace{\sum_k \Omega_k \left|\psi_k\right\rangle \left\langle\psi_k\right|}_{H_m} + \underbrace{\frac{q}{m}\mathbf{p}\cdot\mathbf{A} + \hbar D\Big(c + c^\dagger\Big)^2}_{H_I}. \tag{III.53}$$

where $\frac{q}{m}\mathbf{p}\cdot\mathbf{A}$ is an electric dipole interaction given by equation (III.51), and $D = \frac{1}{\hbar}\frac{A_0^2 q^2}{2m}$.

Description of the matter part. Having discussed the electric dipole interaction, we now perform a two-level system approximation for the matter degree of freedom. Formally, we only consider two neighbouring states in equation (III.46), e.g. the index i, which gives

$$H_m = \sum_k \Omega_k \left|\psi_k\right\rangle \left\langle\psi_k\right| = \hbar\Omega_i \left|\psi_i\right\rangle \left\langle\psi_i\right| + \hbar\Omega_{i+1} \left|\psi_{i+1}\right\rangle \left\langle\psi_{i+1}\right|. \tag{III.54}$$

These two states could represent the ground state $|\psi_i\rangle \equiv |g\rangle$ and excited state $|\psi_{i+1}\rangle \equiv |e\rangle$ of an atom, with energies $\Omega_g \equiv \Omega_i$ and $\Omega_e \equiv \Omega_{i+1}$. Since this represents a two-level system, we can use the formalism we introduced for the description of qubits in section 2.1. In particular, the Hamiltonian for the matter part can be written

$$H_m = \hbar\frac{\omega_m}{2}\sigma_z. \tag{III.55}$$

where $\omega_m = \Omega_e - \Omega_g$ is the energy difference between the two atomic levels.

Interaction term and coupling strength. We now focus on the interaction term $\frac{q}{m}\mathbf{p}\cdot\mathbf{A}$. Under the two-level system, the interaction term of equation (III.51) simplifies to

$$\frac{q}{m}\mathbf{p}\cdot\mathbf{A} = iA_0(\omega_m \langle e|\boldsymbol{\mu}|g\rangle |e\rangle\langle g| + \omega_m \langle g|\boldsymbol{\mu}|e\rangle |g\rangle\langle e|)\Big(c + c^\dagger\Big) \tag{III.56}$$

$$= iA_0\omega_m(\langle e|\boldsymbol{\mu}|g\rangle |e\rangle\langle g| - \langle e|\boldsymbol{\mu}|g\rangle^* |g\rangle\langle e|)\Big(c + c^\dagger\Big). \tag{III.57}$$

The operators $|e\rangle\langle g|$ and $|g\rangle\langle e|$ corresponds to the raising and lowering operators $\sigma^\pm = \frac{1}{2}(\sigma_x \pm i\sigma_y)$ we introduced in section 2.1. This allows us to rewrite equation (III.57) as

$$\frac{q}{m}\mathbf{p}\cdot\mathbf{A} = i\omega_m A_0\big[\langle e|\boldsymbol{\mu}|g\rangle\sigma^- - \langle e|\boldsymbol{\mu}|g\rangle^*\sigma^+\big]\Big(c + c^\dagger\Big) \tag{III.58}$$

Defining $\mu = i\langle e|\boldsymbol{\mu}|g\rangle$,

$$\frac{q}{m}\mathbf{p}\cdot\mathbf{A} = \omega_m A_0\big(\mu\sigma^- + \mu^*\sigma^+\big)\Big(c + c^\dagger\Big). \tag{III.59}$$

To simplify the final expression, we now assume[1] that $\mu \in \mathbb{R}$, and obtain

$$\frac{q}{m}\mathbf{p}\cdot\mathbf{A} = \hbar g\big(\sigma^- + \sigma^+\big)\Big(c + c^\dagger\Big) \tag{III.60}$$

with $g = \omega_m A_0\mu/\hbar$ the *coupling strength*.

The quantum Rabi Hamiltonian. Collecting all the terms derived above, we obtain the Rabi Hamiltonian

$$H = H_p + H_m + H_I \tag{III.61}$$

$$= \hbar\omega_c c^\dagger c + \frac{1}{2}\hbar\omega_m\sigma_z + \hbar g\Big(c + c^\dagger\Big)\big(\sigma^+ + \sigma^-\big) + \hbar D\Big(c + c^\dagger\Big)^2 \tag{III.62}$$

$$= \hbar\omega_c c^\dagger c + \frac{1}{2}\hbar\omega_m\sigma_z + \hbar g\Big(c + c^\dagger\Big)\sigma_x + \hbar D\Big(c + c^\dagger\Big)^2. \tag{III.63}$$

The Rabi model is sometimes referred to as a spin-boson model. Indeed, a spin is an exact two-level system, so that we can think of the matter degrees of freedom as a spin degree of freedom. Furthermore, note that we derived the Rabi model by considering the coupling of a charged particle to the electromagnetic field. However, such a spin-boson model can appear in various physical systems. In particular, the bosonic mode could represent different quasi-particles, and similarly the two-level system could be a spin, a superconducting qubit or an exciton. Hence, the study of equation (III.62) can be useful in many different physical scenarios.

We note that it is common to see the Rabi model written without the diamagnetic term. It turns out that the first and last term can be diagonalised using a *Bogoliubov transformation*, which we introduce in chapter VII. For the moment, it is sufficient to consider that the Rabi model can be recast as

$$H = \hbar\widetilde{\omega}_p\widetilde{p}^\dagger\widetilde{p} + \frac{1}{2}\hbar\omega_m\sigma_z + \hbar g\Big(\widetilde{p} + \widetilde{p}^\dagger\Big)\big(\sigma^+ + \sigma^-\big), \tag{III.64}$$

where a new bosonic mode p for the cavity field has been introduced, along with a renormalised frequency $\omega_p/2\pi$. As a final remark, it is interesting to mention that the Rabi model is not gauge-invariant. The issue can be traced back to the two-level approximation, and has been addressed by several works discussed in chapter VII.

[1] It may be possible to find a unitary transformation to do that without making an assumption.

3.4) Multi-dipole extension: Dicke model

The Dicke model is a generalisation of the Rabi model to many dipoles, or equivalently, many spins. The Dicke model is often analysed in terms of spin and angular momentum. Thus, we shall follow this approach, and consider the matter degrees of freedom to be composed of N spins, each having an energy gap Ω. For simplicity, we shall also neglect the diamagnetic term, but we shall go back to it in chapter VII. The extension of equation (III.63) to N spins thus reads

$$H = \hbar\omega_c c^\dagger c + \frac{1}{2}\hbar\omega_m \sum_{j=1}^{N} \sigma_z^{(j)} + \frac{\hbar\lambda}{\sqrt{N}}\left(c + c^\dagger\right)\sum_{j=1}^{N}\sigma_x^{(j)} \tag{III.65}$$

and we introduced $\lambda = g\sqrt{N}$ so that the final expressions below agree with the common formulations used in the literature.

The commutation relations for the Pauli matrices are

$$\left[\sigma_x^{(j)}, \sigma_y^{(k)}\right] = 2i\delta_{j,k}\sigma_z^j, \tag{III.66}$$

but the commutation relations for angular momentum operators, including spins, are

$$\left[s_x^{(j)}, s_y^{(k)}\right] = i\hbar\delta_{j,k}s_z^j. \tag{III.67}$$

Thus, we see that it is convenient to introduce the spin operators

$$s_x^{(j)} = \frac{\hbar}{2}\sigma_x^{(j)} \tag{III.68}$$

with a similar definition for $s_y^{(j)}$ and $s_z^{(j)}$. Using these operators, the Dicke Hamiltonian reads

$$H = \hbar\omega_c c^\dagger c + \omega_m \sum_{j=1}^{N} s_z^{(j)} + \frac{2\lambda}{\sqrt{N}}\left(c + c^\dagger\right)\sum_{j=1}^{N} s_x^{(j)}, \tag{III.69}$$

which is a form often encountered in the literature [199–201]. Note that in some works, e.g. [202, 203], the authors use an alternative coupling strength $\lambda' = 2\lambda$ instead. It is also worth noting that some authors do not absorb the factor $\hbar$ into the definitions of $s_{x,y,z}^{(i)}$. If one does so, then the operators do not have the appropriate dimension of angular momentum.

The macrospin operators. The description of the N spins is associated with an Hilbert space of dimension 2^N. Instead, it is convenient to work in a reduced Hilbert space, by considering the macrospin operators

$$S_x = \sum_{j=1}^{N} s_x^{(j)} \tag{III.70}$$

with S_y and S_z defined in a similar fashion. Then, the Dicke Hamiltonian is written

$$H = \hbar\omega_c c^\dagger c + \omega_m S_z + \frac{2\lambda}{\sqrt{N}}\left(c + c^\dagger\right)S_x, \tag{III.71}$$

which is another formulation commonly encountered in the literature. From the commutation relations of $s_{x,y,z}^{(i)}$, we immediately deduce that

$$[S_x, S_y] = i\hbar S_z, \tag{III.72}$$

so the macrospin does behave like angular momentum. Notice how now, we have a single spin[1] which can take values in the range $\left[-\frac{N}{2}, \frac{N}{2}\right]$.

[1] Strictly speaking this is not a spin anymore, since it does not take the two values $\pm\frac{1}{2}$. Still, it is common to continue to refer to it as a spin in the literature.

Holstein-Primakoff transformation. The Holstein-Primakoff transformation establishes a relation between fermionic and bosonic operators [204]. In our case, we will use Holstein-Primakoff transformation to write the raising and lowering macrospin operators $S^{\pm} = S_x \pm iS_y$ in terms of dimensionless bosonic operators $m, m^\dagger$ describing excitations of the matter degree of freedom. We consider the mappings [200]

$$S_z \mapsto -\hbar\frac{N}{2} + \hbar m^\dagger m, \quad S^+ \mapsto \hbar m^\dagger \sqrt{N - m^\dagger m}, \tag{III.73}$$

which at this stage should be understood as a convenient ansatz[1]. In particular, if $\langle m^\dagger m\rangle \ll N$, i.e. there is a weak number of matter excitations, then we can simplify S^+ since

$$S^+ = \hbar m^\dagger\sqrt{N}\left(1 - \frac{m^\dagger m}{N}\right)^{1/2} \simeq \hbar\sqrt{N}m^\dagger. \tag{III.74}$$

Consequently, we have

$$S_x = S^+ + S^- = \hbar\sqrt{N}\left(m + m^\dagger\right). \tag{III.75}$$

Note that this transformation assumes that the total spin is conserved [200], and that it has the proper dimensions.

The Dicke model in terms of bosonic operators. Returning to the Dicke Hamiltonian of equation (III.71) and using the Holstein-Primakoff transformation above,

$$H = \hbar\omega_c c^\dagger c + \hbar\omega_m\left(-\frac{N}{2} + m^\dagger m\right) + \frac{2\lambda}{\sqrt{N}}\left(c + c^\dagger\right)\hbar\sqrt{N}\left(m + m^\dagger\right) \tag{III.76}$$

$$= \hbar\omega_c c^\dagger c + \hbar\omega_m m^\dagger m + \hbar 2\lambda\left(c + c^\dagger\right)\left(m + m^\dagger\right) - N\hbar\omega_m. \tag{III.77}$$

Defining the coupling strength $g = 2\lambda$, and dropping the constant energy shift $-\frac{N}{2}\omega_m$, we finally obtain the Hamiltonian:

$$H = \hbar\omega_c c^\dagger c + \hbar\omega_m m^\dagger m + \hbar g\left(c + c^\dagger\right)\left(m + m^\dagger\right). \tag{III.78}$$

This is also sometimes referred to as the Hopfield Hamiltonian. However, historically, the Hopfield modelled the interaction between photons and excitons, and included the diamagnetic term [205, 206].

3.5) The rotating wave approximation and the Jaynes-Cummings model

Let us return to the quantum Rabi model Hamiltonian of equation (III.62) and focus in the interaction term, neglecting the diamagnetic term. It reads

$$H_I = \hbar g\left(c + c^\dagger\right)\left(\sigma^+ + \sigma^-\right). \tag{III.79}$$

We can identify two types of terms: co-rotating and counter-rotating terms. This can be seen by switching to the interaction picture, in which the operators evolve as

$$c(t) = c(0)e^{-i\omega_c t}, \quad c^\dagger(t) = c^\dagger(0)e^{i\omega_c t}, \quad \sigma^\pm(t) = \sigma^\pm(0)e^{\pm i\omega_m t/2} \tag{III.80}$$

Then the interaction Hamiltonian becomes

$$H_I(t) = \hbar g\left(c\sigma^+ + c\sigma^- + c^\dagger\sigma^+ + c^\dagger\sigma^-\right) \tag{III.81}$$

$$= \hbar g\left(c\sigma^+ e^{-i(\omega_c-\omega_m)t/2} + c\sigma^- e^{-i(\omega_c+\omega_m)t/2} + c^\dagger\sigma^+ e^{i(\omega_c+\omega_m)t/2} + c^\dagger\sigma^- e^{i(\omega_c-\omega_m)t/2}\right). \tag{III.82}$$

[1]The specific form of the mapping can be understood when the operators $S^\pm$ can be linked to angular momentum. In the next chapter, we will discuss the properties of angular momentum, and we shall see how this mapping can be formally justified. For the moment, it is sufficient to think of the Holstein-Primakoff transformation as a good transformation to represent many two-level systems as a bosonic mode.

The counter-rotating terms $c\sigma^-$ and $c^\dagger\sigma^+$ oscillate with frequency $\omega_c+\omega_m/2$, which is usually much faster than the co-rotating terms $c\sigma^+$ and $c^\dagger\sigma^-$ oscillating as $\omega_c-\omega_m/2$. The rotating wave approximation then prescribes to drop the counter-rotating terms, since their effect is negligible[1]. The rotating wave approximation is valid when the coupling strength g is much smaller than the bare frequencies of both the light and matter degrees of freedom: $g \ll \omega_c, \omega_m/2$ [207, 208]. Note that if $|\omega_c - \omega_m/2| \gg 1$, then the RWA implies that the co-rotating terms also have a negligible effect. When the cavity mode and the TLS are significantly detuned, satisfying $|\omega_c - \omega_m/2| \gg 1$, we are in the dispersive regime, and the effect of the coupling can be treated using perturbation theory (see section 4.2).

The Jaynes-Cummings model. The Jaynes-Cummings Hamiltonian corresponds to the Rabi Hamiltonian after performing the RWA. This corresponds to dropping the terms $\sigma^- c$ and $\sigma^+ c^\dagger$ in equation (III.62), which reads

$$H_{\mathrm{JC}} = \hbar\omega_c c^\dagger c + \frac{1}{2}\hbar\omega_m\sigma_z + \hbar g\Big(c^\dagger\sigma^- + c\sigma^+\Big). \tag{III.83}$$

Contrary to the Rabi model, the Jaynes-Cummings model conserves the number of quanta in the system and is exactly solvable[2]. Interestingly, we can view the conservation of the number of particles as a $U(1)$ symmetry (it is the conserved quantity of this symmetry), which means that the quantum Rabi model breaks this $U(1)$ symmetry [209].

This model is of paramount importance in many quantum-optical scenarios, since it describes for instance transmon qubits [210].

The Tavis-Cummings model. The Tavis-Cummings model is simply the result of applying the RWA to the Dicke Hamiltonian. Equivalently, it is the generalization of the Jaynes-Cummings model to multiple two-level atoms. Like the Jaynes-Cummings model, it does not include counter-rotating terms and exhibits a $U(1)$ symmetry, and hence conserves the number of quanta in the system. If we consider the Dicke Hamiltonian after the Holstein-Primakoff transformation, i.e. the Hopfield model without a diamagnetic term of equation (III.78), the Tavis-Cummings model reads

$$H = \hbar\omega_c c^\dagger c + \hbar\omega_m m^\dagger m + \hbar g\Big(cm^\dagger + c^\dagger m\Big). \tag{III.84}$$

4) Closed-system analysis

4.1) Diagonalisation: spectrum and polaritons

In the previous sections, we introduced several models of light/matter interactions. We now turn our attention to the physics described by some of these models. The models introduced are expressed in terms of the cavity's bare operators: the creation/annihilation operators for the electromagnetic $(c^\dagger, c)$ and the matter $(m^\dagger, m)$ degrees of freedom. However, the interaction between these two subsystems leads to hybridisation of the original operators, and is best described in terms of a new basis[3]. Such a basis can be obtained in some simple cases, such as for bosonic Hamiltonian quadratic in creation/annihilation operators. In the following, we shall illustrate diagonalisation on the Tavis-Cummings model introduced in the previous section.

Polaritons. As can be expected from a non-zero coupling between light and matter, the eigenstates of the system will be mixed light-matter states. The quasi-particle due to the hybridisation of a photon with another particles is known as a *polariton*. Depending on which particle hybridises with the photon, different type of polaritons can emerge. In the particular

[1] More precisely, they don't contribute much if we are interested in effects observable due to the co-rotating terms, which is usually the case unless we consider the ultrastrong coupling regime, discussed in chapter VII.

[2] See Chapter 10, section 2 of [34]

[3] This is also referred to as the "dressed" basis. Such dressing is due to the interaction.

case of cavity magnonics, the hybridisation of the light and magnon degree of freedoms gives the cavity magnon polariton.

Dicke model in the RWA. As a first example, we consider the Dicke model in the RWA, i.e. the Tavis-Cummings model of equation (III.84) reproduced below:

$$H = \hbar\omega_c c^\dagger c + \hbar\omega_m m^\dagger m + \hbar g(cm^\dagger + c^\dagger m). \tag{III.85}$$

The polaritons are expected to be linear combinations of c and m, so that we want to express the Hamiltonian in terms of a column vector $\boldsymbol{v} = (c\ m)^t$.

Using the bosonic commutation relations[1] for c and m, we rewrite the Hamiltonian as

$$H = \hbar\omega_c c^\dagger c + \hbar\omega_m m^\dagger m + \hbar g(cm^\dagger + c^\dagger m) \tag{III.86}$$

$$= \hbar\begin{pmatrix} c^\dagger & m^\dagger \end{pmatrix}\begin{pmatrix} \omega_c & g \\ g & \omega_m \end{pmatrix}\begin{pmatrix} c \\ m \end{pmatrix} \tag{III.87}$$

$$= \hbar \boldsymbol{v}^\dagger M \boldsymbol{v}. \tag{III.88}$$

The polaritonic operators $p_\pm$ and their associated energies $\hbar\omega_\pm$ are given by the eigenvectors and eigenvalues of M. The eigenvalues are found to be

$$\omega_\pm = \frac{\omega_c + \omega_m}{2} \pm \frac{\sqrt{(\omega_c - \omega_m)^2 + 4g^2}}{2}, \tag{III.89}$$

with polaritons[2]

$$p_- = \frac{\omega_- - \omega_m}{\sqrt{(\omega_- - \omega_m)^2 + g^2}}c + \frac{g}{\sqrt{(\omega_- - \omega_m)^2 + g^2}}m \tag{III.90}$$

$$= \frac{\omega_c - \omega_+}{\sqrt{(\omega_c - \omega_+)^2 + g^2}}c + \frac{g}{\sqrt{(\omega_c - \omega_+)^2 + g^2}}m, \tag{III.91}$$

$$p_+ = \frac{\omega_+ - \omega_m}{\sqrt{(\omega_+ - \omega_m)^2 + g^2}}c + \frac{g}{\sqrt{(\omega_+ - \omega_m)^2 + g^2}}m \tag{III.92}$$

$$= \frac{\omega_c - \omega_-}{\sqrt{(\omega_c - \omega_-)^2 + g^2}}c + \frac{g}{\sqrt{(\omega_c - \omega_-)^2 + g^2}}m. \tag{III.93}$$

We can verify that in general, as long as the matrix M is real and symmetric, the resulting polaritonic operators are bosonic. Indeed, assume that $p_\mu = \sum_k v_{\mu k} c_k$ with c_k the cavity operators (including both photonic and matter degrees of freedom). Then

$$\left[p_\mu, p_\nu^\dagger\right] = \sum_{k,k'} v_{\mu k} v^*_{\nu k'} \left[c_k, c_{k'}^\dagger\right] = \sum_{k,k'} v_{\mu k} v^*_{\nu k'} \delta_{k,k'} = \sum_k v_{\mu k} v^*_{\nu k} \tag{III.94}$$

$$= \delta_{\mu\nu}, \tag{III.95}$$

where we used the fact that real symmetric matrices have real and orthogonal eigenvectors[3].

The use of the RWA make the diagonalisation of the Hopfield Hamiltonian rather easy. To diagonalise the system without performing the RWA (for instance in the ultrastrong coupling regime), one needs to resort to the Hopfield-Bogoliubov method, introduced in chapter VII.

[1] Reminder: $\left[c, c^\dagger\right] = \left[m, m^\dagger\right] = 1$, and $\left[c, m\right] = \left[c, m^\dagger\right] = 0$.

[2] This can also be expressed in terms of cosines and sines, see [211].

[3] The quantity $\sum_k v_{\mu k} v_{\nu k}$ is the scalar product of each eigenvector.

Energy Level repulsion. The spectrum described by equation (III.89) leads to an anti-crossing in the spectrum, or equivalently an avoided crossing of the energy levels. Such an anti-crossing is a characteristics of coupled systems, which we could also obtain classically by calculating the eigenfrequencies of two coupled harmonic oscillators. Each frequency $\omega_\pm/2\pi$ corresponds to a polariton, and we see that the angular frequency gap between them is

$$\delta\omega = \omega_+ - \omega_- = \sqrt{(\omega_c - \omega_m)^2 + 4g^2}, \tag{III.96}$$

and we remark that we always have $\omega_+ > \omega_m -$. Clearly, the frequency gap $\delta\omega/2\pi$ is minimum when $\omega_c = \omega_m$, i.e. both modes are "on resonance" with each other. On resonance, the angular frequency gap is $2g$.

We can also infer that when $|\omega_c - \omega_m| \gg g$,

$$\omega_\pm = \frac{\omega_c + \omega_m}{2} \pm \frac{|\omega_c - \omega_m|}{2} \tag{III.97}$$

and thus

$$\begin{cases} \omega_+(\omega_m \ll \omega_) = \omega_c \\ \omega_+(\omega_m \gg \omega_) = \omega_m \\ \omega_-(\omega_m \ll \omega_) = \omega_m \\ \omega_-(\omega_m \gg \omega_) = \omega_c \end{cases}. \tag{III.98}$$

Let us now examine the properties of the polaritons in these two limits.

Light and matter hybridisation. Let us first examine the case of perfect resonance, when $\omega_m = \omega_c$. Using equations (III.90) and (III.92), we find[1]

$$p_+(\omega_m = \omega_c) = \frac{c+m}{\sqrt{2}}, \quad p_-(\omega_m = \omega_c) = \frac{c-m}{\sqrt{2}}, \tag{III.99}$$

and hence we see that the polaritons are equally made up of half light and half matter, precessing in-phase (p_+) for the upper polaritonic branch and out-of-phase (p_-) for the lower polaritonic branch. Equivalently, we can view p_+ as a constructive interference between light and matter, and p_- as a destructive interference between light and matter. The associated energies are $\hbar\omega_\pm(\omega_m = \omega_c) = \hbar\big(\frac{\omega_c+\omega_m}{2} \pm 2g\big)$, with the constructive interference being higher in energy.

On the other hand, far from resonance,

$$\begin{cases} p_+(\omega_m \ll \omega) = c \\ p_+(\omega_m \gg \omega) = m \\ p_-(\omega_m \ll \omega) = m \\ p_-(\omega_m \gg \omega) = c \end{cases}. \tag{III.100}$$

Note that this agrees with the results we found for the polaritonic frequencies: close to resonance, the polaritons are completely hybridised, and far from resonance they look like the uncoupled light and matter states.

These conclusions are supported by a numerical diagonalisation of equation (III.88), and plotted in figure III.1. We first notice the avoided crossing when $\omega_m = \omega_c$, as theoretically predicted. We also notice that far from the resonance, the two polaritonic branches follows the frequencies of the uncoupled light and matter degrees of freedom ($\omega_c/2\pi$ and $\omega_m/2\pi$, respectively) as described by equation (III.98). Additionally, we plotted the proportion of light (left column) and matter (right column) in the polaritons. Once again, the results agree with equations (III.99) and (III.100), where we observe perfect hybridisation at the anti-crossing, and uncoupled light and matter states far from resonance.

[1] Remember that eigenvectors are defined up to a multiplicative constant. Here, we multiplied p_- by -1 so that the factor before c is always positive. In other words, we equivalently have $p_-(\omega_m = \omega_c) = -\frac{c-m}{\sqrt{2}}$.

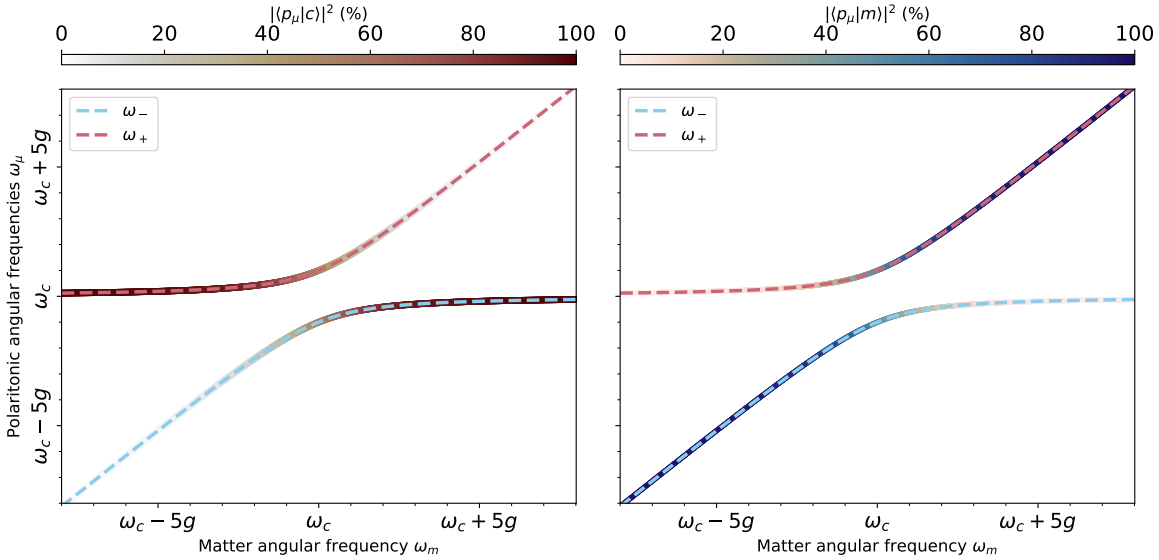


Figure III.1: Spectra of the Dicke model in the RWA as a function of the matter frequency $\omega_m/2\pi$, with the cavity mode frequency set to $\omega_c/2\pi = 10$ GHz and the coupling strength $g/2\pi = 100$ MHz . On the left side, the proportion of light $|\langle p_\mu|c\rangle|^2$ is plotted on top of the spectrum, while on the right side the proportion of matter $|\langle p_\mu|m\rangle|^2$ is plotted.

4.2) Perturbation theory using Schrieffer-Wolff transformations

The Schrieffer-Wolff transformation consists of applying a proper unitary transformation, so that higher-order terms of the Baker–Campbell–Hausdorff formula vanish. It was first used by Schrieffer and Wolff in a 1966 paper [212] dedicated to the Anderson and Kondo Hamiltonians. Among its many applications, it is used to derive the dispersive form of the Jaynes-Cumming Hamiltonian used to readout qubits in circuit QED [145], make apparent some indirect coupling by virtual photons [1, 213–215], and perform perturbation theory.

Here, we shall give the general principle and then apply it on a few examples of interest for the remaining chapters. For a detailed mathematical discussion, see Bravyi, DiVincenzo, and Loss (2011) [216].

4.2.1) Principle

Consider $H = H_0 + V$, with H_0 an unperturbed Hamiltonian, V a perturbation, and $U = e^\Lambda$. The Baker-Campbell-Hausdorff formula (equation (A.17)) gives the transformed Hamiltonian

$$H' = e^\Lambda H e^{-\Lambda} = \sum_{n=0}^{\infty} \frac{\left[\Lambda^{(n)}, H\right]}{n!}. \tag{III.101}$$

By choosing a transformation such that $V + [\Lambda, H_0] = 0$, we can compute H' using only the n-th iterated commutator $\left[\Lambda^{(n)}, V\right]$ instead of $\left[\Lambda^{(n)}, H\right]$.

Indeed, we can rewrite the condition $V + [\Lambda, H_0] = 0$ as $\left[\Lambda^{(1)}, H_0\right] = -\left[\Lambda^{(0)}, V\right]$, from which we easily deduce that $\forall n \geqslant 1$, $\left[\Lambda^{(n)}, H_0\right] = -\left[\Lambda^{(n-1)}, V\right]$. Hence in general,

$$H' = \sum_{n=0}^{\infty} \frac{\left[\Lambda^{(n)}, H\right]}{n!} = H_0 + V + \sum_{n=1}^{\infty} \frac{-\left[\Lambda^{(n-1)}, V\right] + \left[\Lambda^{(n)}, V\right]}{n!} \tag{III.102}$$

$$= H_0 + \sum_{n=1}^{\infty} \frac{\left[\Lambda^{(n)}, V\right]}{n!} - \sum_{n=2}^{\infty} \frac{\left[\Lambda^{(n-1)}, V\right]}{n!} = H_0 + \sum_{n=1}^{\infty} \frac{\left[\Lambda^{(n)}, V\right]}{n!} - \sum_{n=1}^{\infty} \frac{\left[\Lambda^{(n)}, V\right]}{(n+1)!} \tag{III.103}$$

$$= H_0 + \sum_{n=1}^{\infty} \frac{1}{n!}\left(1 - \frac{1}{n+1}\right)\left[\Lambda^{(n)}, V\right] = H_0 + \sum_{n=1}^{\infty} \frac{n}{(n+1)!}\left[\Lambda^{(n)}, V\right] \tag{III.104}$$

and we see that only the n-th order commutators $\left[\Lambda^{(n)}, V\right]$ are needed.

Often, one defines Λ such that $\left[\Lambda^{(n)}, V\right]$ becomes smaller and smaller as n increases. The goal is then to find Λ such that H' is simpler than H, as we illustrate in the following examples.

4.2.2) Dispersive regimes

A common use of the Schrieffer-Wolff transformations is to find effective Hamiltonians under the dispersive regime. This regime can be defined as the limit in which the light and matter frequencies are strongly detuned with respect to their coupling. Formally, the limit reads $|\omega_m - \omega_c| \gg g$ with $g/2\pi$ the coupling strength. In this limit, the dimension-less quantity $\lambda = \frac{g}{\omega_m - \omega_c}$ is small, and we can perform perturbation theory in λ.

We shall first illustrate this principle on the Jaynes-Cummings model, since it will allow us to introduce the so-called dispersive measurement of superconducting qubits. Next, we consider the dispersive regime of the Dicke model in the RWA, which will be of interest for the next chapter.

Jaynes-Cummings model. We consider the Jaynes-Cumming model

$$H = \underbrace{\hbar\omega_c c^\dagger c + \frac{\hbar\Omega}{2}\sigma^z}_{=H_0} + \underbrace{\hbar g(c^\dagger\sigma^- + \sigma^+ c)}_{=V}, \tag{III.105}$$

describing the interaction between a qubit (two-level system) and a cavity mode. We treat the interaction term V as a perturbation to the free Hamiltonian H_0. We consider the transformation

$$U = \exp\Big(\lambda\Big(c\sigma^+ - c^\dagger\sigma^-\Big)\Big), \tag{III.106}$$

with $\lambda = \frac{g}{\Delta}$ where $\Delta = \Omega - \omega_c$ is the detuning between the qubit and the cavity's frequency. In the following, we assume that $|\Delta| \gg g$ such that $\lambda \ll 1$.

Recalling $[c, c^\dagger c] = c$, $[\sigma^+, \sigma_z] = -2\sigma_+$ and $[\sigma^-, \sigma_z] = 2\sigma_-$, the Schrieffer-Wolff condition is satisfied since

$$\begin{aligned}
V + [\Lambda, H_0] &= \hbar g(c^\dagger\sigma^- + \sigma^+ c) + \lambda\hbar\omega_c\Big[c\sigma^+ - c^\dagger\sigma^-, c^\dagger c\Big] + \lambda\frac{\hbar\Omega}{2}\Big[c\sigma^+ - c^\dagger\sigma^-, \sigma^z\Big] && \text{(III.107)}\\
&= \hbar g(c^\dagger\sigma^- + \sigma^+ c) + \lambda\hbar\omega_c\Big(c\sigma^+ + c^\dagger\sigma^-\Big) + \lambda\hbar\Omega\Big(-c\sigma^+ - c^\dagger\sigma^-\Big) && \text{(III.108)}\\
&= \hbar g(c^\dagger\sigma^- + \sigma^+ c) - \hbar\lambda(\Omega - \omega_c)\Big(c\sigma^+ + c^\dagger\sigma^-\Big) = 0 && \text{(III.109)}
\end{aligned}$$

by definition of λ and Δ.

Hence, using $[\sigma^+, \sigma^-] = \sigma_z$ and $[AB, CD] = A[B, C]D + [A, C]BD + CA[B, D] + C[A, D]B$, we have

$$\begin{aligned}
[\Lambda, V] &= \hbar g\lambda\left[c\sigma^+ - c^\dagger\sigma^-, c^\dagger\sigma^- + \sigma^+ c\right] && \text{(III.110)}\\
&= \hbar g\lambda\left(\left[c\sigma^+, c^\dagger\sigma^-\right] - \left[c^\dagger\sigma^-, \sigma^+ c\right]\right) && \text{(III.111)}\\
&= \hbar g\lambda\left(\left(\sigma^+\sigma^- + c^\dagger c\sigma_z\right) - \left(-\sigma^-\sigma^+ - cc^\dagger\sigma_z\right)\right) && \text{(III.112)}\\
&= \hbar g\lambda\left(\sigma^+\sigma^- + \sigma^-\sigma^+ + \left(c^\dagger c + cc^\dagger\right)\sigma_z\right) && \text{(III.113)}\\
&= \hbar g\lambda\left(\frac{1}{2}(1 + \sigma_z) + \frac{1}{2}(1 - \sigma_z) + \left(2c^\dagger c + 1\right)\sigma_z\right) && \text{(III.114)}\\
&= \hbar g\lambda\left(1 + \left(2c^\dagger c + 1\right)\sigma_z\right), && \text{(III.115)}
\end{aligned}$$

from which we deduce the transformed Hamiltonian

$$\begin{aligned}
H' &= \hbar\omega_c c^\dagger c + \frac{\hbar\Omega}{2}\sigma^z + \frac{1}{2}\hbar g\lambda\left(1 + \left(2c^\dagger c + 1\right)\sigma_z\right) && \text{(III.116)}\\
&= \hbar\left(\omega_c + \frac{g^2}{\Delta}\sigma_z\right)c^\dagger c + \frac{\hbar}{2}\left(\Omega + \frac{g^2}{\Delta}\right)\sigma_z + \frac{1}{2}\hbar g\lambda, && \text{(III.117)}
\end{aligned}$$

which we recall is valid when $\lambda \ll 1$, i.e. $|\Delta| \gg g$. We note that the last term is a constant, so it can be ignored.

We observe that in this regime, the interaction manifests as a shift of qubit frequency, and a shift of the cavity resonance depending on the state of the qubit. In particular, we see that the shift of the cavity frequency depends on the state of the qubit through the operator σ_z. Thus, for a fixed detuning Δ, the cavity resonance is shifted either by $+\frac{g^2}{\Delta}/2\pi$ if the qubit is in the ground state, and $-\frac{g^2}{\Delta}/2\pi$ if the qubit is excited. Hence by monitoring the resonance of the cavity, we can read the state of the qubit. This method corresponds to the dispersive readout of qubit [145].

Dicke model in the RWA. We now consider the Dicke model in the RWA, which we recall reads

$$H = \underbrace{\hbar\omega_c c^\dagger c + \hbar\omega_m m^\dagger m}_{H_0} + \underbrace{\hbar g(cm^\dagger + c^\dagger m)}_{V}. \tag{III.118}$$

We consider the transformation e^Λ with

$$\Lambda = \lambda(cm^\dagger - c^\dagger m), \quad \lambda = \frac{g}{\omega_m - \omega_c}, \tag{III.119}$$

and we note that we have $\Lambda^\dagger = -\Lambda$ so e^Λ is unitary. Using $[AB, CD] = A[B, C]D + [A, C]BD + CA[B, D] + C[A, D]B$ (see appendix A.1), we have

$$\begin{aligned}
[\Lambda, H_0] &= \hbar\Big[cm^\dagger - c^\dagger m, \omega_c c^\dagger c + \omega_m m^\dagger m\Big] && \text{(III.120)}\\
&= \hbar\lambda\omega_c\Big(cm^\dagger + c^\dagger m\Big) + \hbar\lambda_1\omega_m\Big(-cm^\dagger - c^\dagger m\Big) && \text{(III.121)}\\
&= \hbar\lambda(\omega_c - \omega_m)\Big(cm^\dagger + c^\dagger m\Big) && \text{(III.122)}\\
&= -V && \text{(III.123)}
\end{aligned}$$

and also

$$\begin{aligned}
[\Lambda, V] &= \lambda g\Big[cm^\dagger - c^\dagger m, cm^\dagger + c^\dagger m\Big] && \text{(III.124)}\\
&= \lambda g\Big[cm^\dagger, c^\dagger m\Big] - \lambda g\Big[c^\dagger m, cm^\dagger\Big] = 2\lambda g\Big[cm^\dagger, c^\dagger m\Big] && \text{(III.125)}\\
&= 2\lambda g\Big(m^\dagger m - cc^\dagger\Big) && \text{(III.126)}\\
&= 2\lambda g\Big(m^\dagger m - c^\dagger c\Big) - 2\lambda g. && \text{(III.127)}
\end{aligned}$$

Thus, the Schrieffer-Wolff condition $V + [\Lambda, H_0] = 0$ is satisfied. We observe that $[\Lambda, V] = \mathcal{O}(\lambda)$, and we easily deduce that $\big[\Lambda^{(2)}, V\big] = [\Lambda, [\Lambda, V]] = \mathcal{O}(\lambda^2)$. Hence, in the dispersive regime where $|\lambda| \ll 1$, we can truncate the expansion of equation (III.101). To first order equation (III.104) simplifies to $H' = H_0 + \frac{1}{2}[\Lambda, V] + \mathcal{O}(\lambda^2)$, which gives

$$\begin{aligned}
H' &= \hbar\omega_c c^\dagger c + \hbar\omega_m m^\dagger m + \frac{1}{2}2\lambda g\Big(m^\dagger m - c^\dagger c\Big) && \text{(III.128)}\\
&= \hbar\omega_c' c^\dagger c + \hbar\omega_m' m^\dagger m && \text{(III.129)}
\end{aligned}$$

with the new angular frequencies

$$\begin{aligned}
\omega_c' &= \omega - \frac{g^2}{\omega_m - \omega_c}, && \text{(III.130)}\\
\omega_m' &= \omega_m + \frac{g^2}{\omega_m - \omega_c}. && \text{(III.131)}
\end{aligned}$$

We see that the resulting system described by equation (III.129) is diagonal, i.e. there are no interactions remaining. This is in contrast with the results of the Jaynes-Cummings model above. On the other hand, we do observe a shift of the resonances.



Figure III.2: Indirect coupling G (given by equation (III.150) below) between the cavity modes c_0 and c_1 mediated by the matter mode m.

4.2.3) Indirect coupling

Another application of the Schrieffer-Wolff transformations is the derivation of an indirect coupling between two modes, mediated by another mode. As an example, we shall consider a system in which two cavity modes c_0, c_1 couple to a matter mode m with couplings g_0, g_1, as pictured in figure III.2. Here, the matter mode m mediates an indirect coupling between c_0 and c_1.

Formally, we adopt the Hamiltonian $H = H_0 + H_I$ with

$$H_0 = \hbar\omega_0 c_0 c_0^\dagger + \hbar\omega_1 c_1^\dagger c_1 + \hbar\omega_m m^\dagger m, \tag{III.132}$$

$$H_I = \hbar g_0\Big(c_0 m^\dagger + c_0^\dagger m\Big) + \hbar g_1\Big(c_1 m^\dagger + c_1^\dagger m\Big), \tag{III.133}$$

and we treat the interaction Hamiltonian as the perturbation $V = H_I$.

The right transformation to eliminate the couplings between the cavity modes and the matter mode is

$$\Lambda = \lambda_0\Big(c_0 m^\dagger - c_0^\dagger m\Big) + \lambda_1\Big(c_1 m^\dagger - c_1^\dagger m\Big), \tag{III.134}$$

with λ_0, λ_1 constants to determine. Note that for e^Λ to be a unitary transformation, we need Λ to be anti-hermitian, which is satisfied only if λ_0, λ_1 are real. This is fine as long as the couplings g_0, g_1 are also real, which we now assume[1].

Recalling that for a bosonic operator a we have $\big[a, a^\dagger a\big] = a$ and $\big[a^\dagger, a^\dagger a\big] = -a^\dagger$ (see appendix A.1), we have

$$[\Lambda, H_0] = \Big[\lambda_0\Big(c_0 m^\dagger - c_0^\dagger m\Big) + \lambda_1\Big(c_1 m^\dagger - c_1^\dagger m\Big), \hbar\omega_0 c_0 c_0^\dagger + \hbar\omega_1 c_1^\dagger c_1 + \hbar\omega_m m^\dagger m\Big] \tag{III.135}$$

$$= \hbar\omega_0\lambda_0\Big(c_0 m^\dagger + c_0^\dagger m\Big) + \hbar\omega_1\lambda_1\Big(c_1 m^\dagger + c_1^\dagger m\Big) \tag{III.136}$$

$$- \hbar\omega_m\lambda_0\Big(c_0 m^\dagger + c_0^\dagger m\Big) - \hbar\omega_m\lambda_1\Big(c_1 m^\dagger + c_1^\dagger m\Big)$$

$$= \hbar(\omega_0 - \omega_m)\lambda_0\Big(c_0 m^\dagger + c_0^\dagger m\Big) + \hbar(\omega_1 - \omega_m)\lambda_1\Big(c_1 m^\dagger + c_1^\dagger m\Big). \tag{III.137}$$

We deduce

$$\begin{aligned} V + [\Lambda, H_0] = {} & \hbar g_0\Big(c_0 m^\dagger + c_0^\dagger m\Big) + \hbar g_1\Big(c_1 m^\dagger + c_1^\dagger m\Big) \\ & + \hbar(\omega_0 - \omega_m)\lambda_0\Big(c_0 m^\dagger + c_0^\dagger m\Big) + \hbar(\omega_1 - \omega_m)\lambda_1\Big(c_1 m^\dagger + c_1^\dagger m\Big). \end{aligned} \tag{III.138}$$

Imposing the Schrieffer-Wolff condition $V + [\Lambda, H_0] = 0$, we need

$$\begin{cases} g_0 + \lambda_0(\omega_0 - \omega_m) = 0 \\ g_1 + \lambda_1(\omega_1 - \omega_m) = 0 \end{cases}, \tag{III.139}$$

i.e. $\lambda_0 = \frac{g_0}{\omega_m - \omega_0}$ and $\lambda_1 = \frac{g_1}{\omega_m - \omega_1}$.

As previously explained, we only need to compute the transformed Hamiltonian only depends on the n-th iterated commutator $\big[\Lambda^{(n)}, V\big]$. From appendix A.1, we have $[AB, CD] = A[B, C]D + [A, C]BD + CA[B, D] + C[A, D]B$ so that

$$\Big[c_0 m^\dagger - c_0^\dagger m, c_0 m^\dagger + c_0^\dagger m\Big] = \Big[c_0 m^\dagger, c_0^\dagger m\Big] - \Big[c_0^\dagger m, c_0 m^\dagger\Big] = 2\Big[c_0 m^\dagger, c_0^\dagger m\Big] \tag{III.140}$$

$$= 2m^\dagger m + 2c_0^\dagger c_0. \tag{III.141}$$

[1] If we want the couplings g_0, g_1 to be complex, then we need to promote λ_0, λ_1 to complex numbers as well. In order to have Λ anti-hermitian, we can write it as $\Lambda = \Big(\lambda_0 c_0 m^\dagger - \lambda_0^* c_0^\dagger m\Big) + \Big(\lambda_1 c_1 m^\dagger - \lambda_1^* c_1^\dagger m\Big)$.

Hence the first iterated commutator is

$$[\Lambda, V] = \hbar\Big[\lambda_0\Big(c_0 m^\dagger - c_0^\dagger m\Big) + \lambda_1\Big(c_1 m^\dagger - c_1^\dagger m\Big), g_0\Big(c_0 m^\dagger + c_0^\dagger m\Big) + g_1\Big(c_1 m^\dagger + c_1^\dagger m\Big)\Big] \tag{III.142}$$

$$= 2\hbar\lambda_0 g_0\Big(c_0^\dagger c_0 + m^\dagger m\Big) + 2\hbar\lambda_1 g_1\Big(c_1^\dagger c_1 + m^\dagger m\Big) \tag{III.143}$$
$$+ \hbar\lambda_0 g_1\Big[c_0 m^\dagger - c_0^\dagger m, c_1 m^\dagger + c_1^\dagger m\Big] + \hbar\lambda_1 g_0\Big[c_1 m^\dagger - c_1^\dagger m, c_0 m^\dagger + c_0^\dagger m\Big]$$

$$= 2\hbar\lambda_0 g_0\Big(c_0^\dagger c_0 + m^\dagger m\Big) + 2\hbar\lambda_1 g_1\Big(c_1^\dagger c_1 + m^\dagger m\Big) \tag{III.144}$$
$$+ \hbar\lambda_0 g_1\Big(-c_0 c_1^\dagger - c_0^\dagger c_1\Big) + \hbar\lambda_1 g_0\Big(-c_1 c_0^\dagger - c_1^\dagger c_0\Big)$$

$$= 2\hbar\lambda_0 g_0\Big(c_0^\dagger c_0 + m^\dagger m\Big) + 2\hbar\lambda_1 g_1\Big(c_1^\dagger c_1 + m^\dagger m\Big) - \hbar(\lambda_0 g_1 + \lambda_1 g_0)\Big(c_0 c_1^\dagger + c_0^\dagger c_1\Big). \tag{III.145}$$

We observe that $[\Lambda, V] = \mathcal{O}(\lambda_0, \lambda_1)$, and we easily deduce that $\big[\Lambda^{(2)}, V\big] = [\Lambda, [\Lambda, V]] = \mathcal{O}(\lambda_0^2, \lambda_1^2)$. Hence, we can truncate the expansion of equation (III.101), provided that $|\lambda_0| \ll 1$ and $|\lambda_1| \ll 1$, which corresponds to the *dispersive regime*. Hence, assuming that the matter mode is significantly detuned from the cavity modes, to first order equation (III.104) reduces to $H' = H_0 + \frac{1}{2}[\Lambda, V] + \mathcal{O}(\lambda_0^2, \lambda_1^2)$, which gives

$$H' = \hbar\omega_0' c_0 c_0^\dagger + \hbar\omega_1' c_1^\dagger c_1 + \hbar\omega_m' m^\dagger m - \hbar G(c_0 c_1^\dagger + c_0^\dagger c_1), \tag{III.146}$$

with the new angular frequencies

$$\omega_0' = \omega_0 + \frac{g_0^2}{\omega_m - \omega_0}, \tag{III.147}$$

$$\omega_1' = \omega_1 + \frac{g_1^2}{\omega_m - \omega_1}, \tag{III.148}$$

$$\omega_m' = \omega_m + \frac{g_0^2}{\omega_m - \omega_0} + \frac{g_1^2}{\omega_m - \omega_1} \tag{III.149}$$

and the indirect coupling

$$G = \frac{g_0 g_1}{2}\left(\frac{1}{\omega_m - \omega_0} + \frac{1}{\omega_m - \omega_1}\right) = \frac{g_0 g_1}{2}\frac{\Delta_0 + \Delta_1}{\Delta_0 \Delta_1} = \frac{\Delta_0 + \Delta_1}{2}\frac{g_0 g_1}{\Delta_0 \Delta_1} \tag{III.150}$$

where we defined the detunings $\Delta_0 = \omega_m - \omega_0$ and $\Delta_1 = \omega_m - \omega_1$. We conclude that to first order, the couplings "pulls" the frequencies of each mode, by an amount determined by the detuning and the coupling. As for the indirect coupling, recall that $\lambda_0, \lambda_0 \ll 1$ and $\lambda_0 = \frac{g_0}{\Delta_0}, \lambda_1 = \frac{g_1}{\Delta_1}$. Finally, note that this indirect coupling, although weaker than the bare couplings g_0 and g_1 can still allow to reach the strong coupling regime. Furthermore, notice how the matter mode has become non-interacting.

5) Open quantum systems

Until now, we have only introduced the formalism for the description of the physics inside the cavity. We considered the cavity system isolated from its environment, and neglected dissipation. Inevitably, a useful application to quantum information processing will require some coupling to the environment, for instance to control or measure the system. In this case, the cavity cannot be considered isolated anymore: the system becomes "open", and dissipation/decoherence can occur.

There are several approaches to model open quantum systems. A very common method is to use a master equation, but one disadvantage is that it rapidly becomes computationally expensive to simulate. Another approach is to make use of Floquet theory [217], to describe periodically driven systems.

A simpler formalism, which we introduce first, is based on the quantum Langevin equations (QLEs). These equations allow to model many experimental scenarios, such as thermal noise,

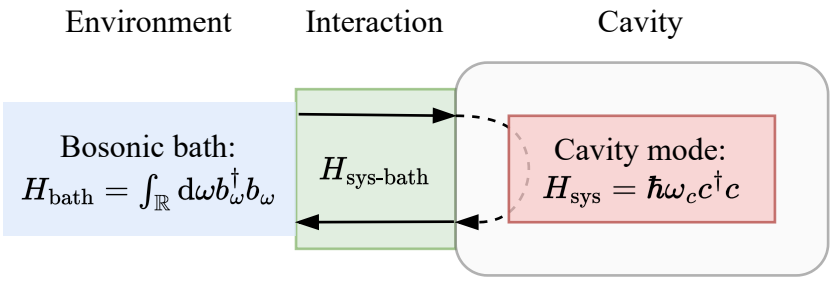


Figure III.3: Illustration of the principle behind quantum Langevin equation (QLE) to model dissipation. The environment is modelled as a bath of harmonic oscillators to which the cavity system couples.

coherent driving of a cavity, or transmission/reflection experiments using the input-output formalism [218]. Note that the input-output formalism is very general: it can complement the master equation mentioned above [219], as well as model photon transport in waveguides [220]. We should mention that to compute transmission, one can also use a Green's function approach [221]. This approach allows to compute the transmission spectra without considering coupling to the environment. Finally, we note that similar results about scattering can be obtained using the Keldysh path-integral formalism [222].

5.1) Quantum Langevin equations

The idea behind the quantum Langevin equations (QLEs) is to consider the Hamiltonian $H = H_{\text{sys}} + H_{\text{bath}} + H_{\text{sys–bath}}$, where H_{sys} is the Hamiltonian of the cavity system (often including a cavity mode coupling with a matter mode), H_{bath} the Hamiltonian of a "heat" bath, and $H_{\text{sys–bath}}$ the interaction between the cavity and the bath. This is summarised in figure III.3 above. The coupling of the cavity system to the bath then introduces damping from the cavity's point of view. This approach can model different sources of dissipation, depending on the statistics one imposes on the heat bath. Our discussion follows the seminal paper by Gardiner and Collett (1985) [218].

Modelling of the environment. The environment is modelled as a "bosonic bath", i.e. an ensemble of harmonic oscillators of every possible frequency[1,2]. We adopt a continuous formulation, following [218]. The Hamiltonian for the environment then reads

$$H_{\text{bath}} = \int_{\mathbb{R}} \mathrm{d}\omega\, \hbar\omega b_\omega^\dagger b_\omega, \tag{III.151}$$

with $b_\omega^\dagger, b_\omega$ being the independent bosonic creation/annihilation operators, satisfying $\left[b_\omega, b_{\omega'}^\dagger\right] = \delta(\omega - \omega')$. The degrees of freedom of the environment can also be formulated using a discrete set of modes, replacing the integral with a sum[3]. Note the peculiar dimension of the operator b_ω, which is $1/\sqrt{\omega}$, so that equation (III.151) is dimensionally correct.

System-bath coupling. The simplest coupling we can think of is bilinear in the cavity and bath operators,

$$H_{\text{sys–bath}} = \int_{\mathbb{R}} \mathrm{d}\omega\, \hbar\kappa(\omega)(c + c^\dagger)(b_\omega + b_\omega^\dagger), \tag{III.152}$$

[1] In the ultrastrong coupling regime (see chapter VII), we will see that considering negative frequencies gives erroneous results. We chose to stick with negative frequencies here for several reasons. First, considering integrals over the entire real numbers makes the derivations simpler, thanks to Fourier analysis. Furthermore, it is usually sufficient to consider that these integrals only have a significant contribution around a certain frequency range, so that extending the bounds to $\pm\infty$ does not change its value very much.

[2] The interpretation depends on the nature of the system we are modelling. In the case of the electromagnetic field, such a bosonic bath represents the continuous background of electromagnetic radiation existing outside of the cavity.

[3] This is the approach taken in [223] for instance, on which several other works are based.

and $\kappa(\omega)$ a real[1] coupling constant, with dimension $\sqrt{\omega}$, which in general is frequency-dependent. This coupling can be thought of as phenomenological, but it turns out that a first-principle derivation confirms this expression for the electromagnetic field[2]. Applying the rotating wave approximation (RWA), this interaction reduces to

$$H_{\text{sys–bath}} = \int_{\mathbb{R}} \mathrm{d}\omega\, \hbar\kappa(\omega)(cb_\omega^\dagger + c^\dagger b_\omega). \tag{III.153}$$

The RWA is usually well justified here, since the coupling κ is often weak[3].

The false ambiguity of the system-environment coupling. It is worth mentioning that one can find in the literature descriptions of $H_{\text{sys–bath}}$ with different conventions. Another common expression for $H_{\text{sys–bath}}$ is that used in Gardiner and Collett (1985) [218],

$$H_{\text{sys–bath}} = \int_{\mathbb{R}} \mathrm{d}\omega\, i\hbar\kappa(\omega)(cb_\omega^\dagger - c^\dagger b_\omega), \tag{III.154}$$

where the couplings are still real, and $H_{\text{sys–bath}}$ still hermitian. However, we could have also used

$$H_{\text{sys–bath}} = \int_{\mathbb{R}} \mathrm{d}\omega\, \hbar(\kappa(\omega)cb_\omega^\dagger + \kappa(\omega)^* c^\dagger b_\omega), \tag{III.155}$$

where the couplings are now complex-valued. It turns out that the exact form of the coupling (real or complex) does not really matter for input-output theories, and is just a question of choice. For our purposes, it will be sufficient to use equation (III.154) for our discussion of QLEs. Alternative formulations can be found in the appendices.

Heisenberg equations of motion. The coupling between the cavity operator c and the bath operators b_ω can give two relations between them, by writing the Heisenberg equation of motion for each. The Heisenberg equation of motion for b_ω reads

$$\dot{b}_\omega = \frac{1}{i\hbar}[b_\omega, H] = \frac{1}{i\hbar}[b_\omega, H_{\text{bath}}] + \frac{1}{i\hbar}\left[b_\omega, H_{\text{sys–bath}}\right] \tag{III.156}$$

$$= \frac{1}{i\hbar}\hbar\omega + \frac{1}{i\hbar} i\hbar \int_{\mathbb{R}} \mathrm{d}\omega'\, \kappa(\omega') c \left[b_\omega, b_{\omega'}^\dagger\right] \tag{III.157}$$

$$= -i\omega + \kappa(\omega)c, \tag{III.158}$$

which has a formal solution[4] for $t_0 < t$

$$b_\omega(t) = e^{-i\omega(t-t_0)} b_\omega(t_0) + \kappa(\omega) \int_{t_0}^{t} \mathrm{d}t'\, c(t') e^{-i\omega(t-t')}. \tag{III.159}$$

Inserting the expression for b_ω into the Heisenberg equation for c, we find

$$\dot{c} = \frac{1}{i\hbar}[c, H_{\text{sys}}] + \frac{1}{i\hbar}\left[c, H_{\text{sys–bath}}\right] \tag{III.160}$$

$$= \frac{1}{i\hbar}[c, H_{\text{sys}}] - \frac{1}{i\hbar} i\hbar \int_{\mathbb{R}} \mathrm{d}\omega\, \kappa(\omega) b_\omega \tag{III.161}$$

$$= \frac{1}{i\hbar}[c, H_{\text{sys}}] - \int_{\mathbb{R}} \mathrm{d}\omega\, \kappa(\omega) e^{-i\omega(t-t_0)} b_\omega(t_0) - \int_{\mathbb{R}} \mathrm{d}\omega \int_{t_0}^{t} \mathrm{d}t'\, \kappa(\omega)^2 e^{-i\omega(t-t')} c(t'). \tag{III.162}$$

[1] It is *chosen* real to guarantee the hermitian character of $H_{\text{sys–bath}}$, more on this seemingly arbitrary choice in the next paragraphs.

[2] See section 5 of [224]

[3] The coupling is often weak because we experimentally set the conditions so that it is weak. In this case, the environment has negligible effects on the system.

[4] The easiest way to check this is simply to verify that this indeed solve the equation with the proper initial condition.

Markov approximation. We now use the first Markov approximation[1], which consists in assuming that the coupling to the bath is frequency-independent. We write

$$\kappa(\omega) = \sqrt{\frac{\gamma}{2\pi}}, \tag{III.163}$$

where the factor $1/\sqrt{2\pi}$ is chosen to simplify forthcoming notations[2]. As a result of this approximation, the coupling between the system and the environment is memory-less, i.e. Markovian.

Quantum Langevin equation. We rewrite equation (III.162) as

$$\dot{c} = \frac{1}{i\hbar}[c, H_{\text{sys}}] - \sqrt{\gamma}\frac{1}{\sqrt{2\pi}}\int_{\mathbb{R}} \mathrm{d}\omega\, e^{-i\omega(t-t_0)} b_\omega(t_0) - \frac{\gamma}{2\pi}\int_{t_0}^{t} \mathrm{d}t'\, c(t') \int_{\mathbb{R}} \mathrm{d}\omega\, e^{-i\omega(t-t')} \tag{III.164}$$

$$= \frac{1}{i\hbar}[c, H_{\text{sys}}] - \sqrt{\gamma} c^{\text{in}}(t) - \gamma \int_{-\infty}^{t} \mathrm{d}t'\, c(t')\delta(t-t'), \tag{III.165}$$

where we defined the *input field* c_{in} as

$$c^{\text{in}}(t) = \lim_{t_0 \to -\infty} \frac{1}{\sqrt{2\pi}} \int_{\mathbb{R}} \mathrm{d}\omega\, e^{-i\omega(t-t_0)} b_\omega(t_0) \tag{III.166}$$

and thus took $t_0 \to -\infty$ in equation (III.165). The input field can be interpreted as the free time evolution of a wave-packet, whose explicit form depends on the state of the bath operators at t_0, described by the term $b_\omega(t_0)$. Note that using the commutation relations $\left[b_\omega, b_{\omega'}^\dagger\right] = \delta(\omega - \omega')$, we can prove that $\left[c^{\text{in}}(t), c^{\text{in}\,\dagger}(t')\right] = \delta(t-t')$, see appendix B.1 for details of the calculation.

We now use the fact [218, 223] that for a function going smoothly to zero in $\pm\infty$, we have[3]

$$\int_{-\infty}^{t} \mathrm{d}t'\, c(t')\delta(t-t') = \frac{1}{2}c(t), \tag{III.167}$$

and we finally obtain the QLE for c as

$$\dot{c} = \frac{1}{i\hbar}[c, H_{\text{sys}}] - \frac{\gamma}{2}c(t) - \sqrt{\gamma}c^{\text{in}}(t). \tag{III.168}$$

As we mentioned earlier, the definition of the Hamiltonian used for the interaction between the bath and the system is arbitrary. For instance, if we consider $-H_{\text{sys–bath}}$ instead, we obtain the equivalent QLE

$$\dot{c} = \frac{1}{i\hbar}[c, H_{\text{sys}}] - \frac{\gamma}{2}c(t) + \sqrt{\gamma}c^{\text{in}}(t), \tag{III.169}$$

where the sign of the input field has been flipped.

Noise input. The second term on the right-hand side of the equation is interpreted as a damping term, because it introduces an imaginary part to the frequency of the operator c, leading to a finite lifetime. To exemplify this, consider that $H_{\text{sys}} = \hbar\omega_c c^\dagger c$, i.e. the system is an empty cavity. The QLE then reads

$$\dot{c} = -i\omega_c c(t) - \frac{\gamma}{2}c(t) - \sqrt{\gamma}c^{\text{in}}(t) \tag{III.170}$$

$$= -i\Big(\omega_c - i\frac{\gamma}{2}\Big)c(t) - \sqrt{\gamma}c^{\text{in}}(t) \tag{III.171}$$

$$= -i\widetilde{\omega}_c c(t) - \sqrt{\gamma}c^{\text{in}}(t), \tag{III.172}$$

[1] This can be linked to the Fermi Golden rule [223, 225, 226].

[2] This choice will lead to a damping rate $\frac{\gamma}{2}$ of the operator c, and a coupling $\sqrt{\gamma}$ to the noise input.

[3] An intuitive understanding of this formula can be obtained by remembering that usually t_0 is taken in the far past, i.e. $t_0 \to -\infty$. Hence, for t close to 0, this integral is effectively half of the integral over $\mathbb{R}$.

with $\widetilde{\omega}_c = \omega_c - i\frac{\gamma}{2}$ is the effective angular frequency of the operator c. It will be shown below how the imaginary part in $\widetilde{\omega}_c$ leads to a finite linewidth in reflection/transmission experiments.

The last term is a noise term, which could model e.g. a field driving the cavity (see section 5.1.1 below) or thermal noise. This is implemented by specifying the state that the bath is in, or imposing some statistics on c^{in} by specifying correlation functions of the noise operator. For instance, to model thermal noise one assumes that the oscillators in H_{bath} are at thermal equilibrium at a finite temperature T, and then we have $\left\langle c^{\text{in}} \right\rangle = 0$ and

$$\left\langle c^{\text{in}}(t) c^{\text{in}\dagger}(t') \right\rangle = (N(\omega_c, T) + 1)\delta(t - t'), \quad \left\langle c^{\text{in}\dagger}(t) c^{\text{in}}(t') \right\rangle = N(\omega_c, T)\delta(t - t'), \tag{III.173}$$

where

$$N(\omega, T) = \frac{1}{e^{\frac{\hbar\omega}{k_b T}} - 1} \tag{III.174}$$

is the Bose-Einstein[1] distribution and $k_B = 86.17 \times 10^{-3}$ meV/K is the Boltzmann constant. The QLE for the cavity mode then models the thermal noise.

If the noise input has zero mean, then the steady-state value of c vanishes, since taking the expectation value of equation (III.172) gives

$$\dot{\langle c \rangle} = -i\widetilde{\omega}_c \langle c \rangle , \tag{III.175}$$

with solution $\langle c(t) \rangle = \langle c(t=0) \rangle e^{-i\widetilde{\omega}_c t} = \langle c(t=0) \rangle e^{-i\omega_c t} e^{-\gamma t}$ which exponentially decays.

Effective non-hermitian Hamiltonians. We saw above that the QLE for an uncoupled bosonic mode c is

$$\dot{c} = -i\omega_c c(t) - \frac{\gamma}{2} c(t) - \sqrt{\gamma} c^{\text{in}}(t). \tag{III.176}$$

Defining $\widetilde{\omega}_c = \omega - i\frac{\gamma}{2}$, we can see that the Hamiltonian

$$H = \hbar\widetilde{\omega}_c c^\dagger c + i\hbar\sqrt{\gamma}\Big(c c^{\text{in}\dagger} - c^\dagger c^{\text{in}} \Big) \tag{III.177}$$

recovers equation (III.176) by writing the Heisenberg equation of motion for c. Importantly, while this Hamiltonian is non-hermitian, due to the imaginary part in $\widetilde{\omega}_c$, it can still be considered a valid effective model to describe the physics.

In particular, if the noise input is semi-classical, we can replace $c^{\text{in}} \mapsto \langle c_{\text{in}} \rangle$, and the Hamiltonian becomes equivalent to

$$H = \hbar\widetilde{\omega}_c c^\dagger c \tag{III.178}$$

after performing an appropriate unitary transformation (see appendix B.2).

Units. The QLE for c when the system is simply a single harmonic oscillator, equation (III.170), reads

$$\dot{c} = -i\omega_c c(t) - \frac{\gamma}{2} c(t) - \sqrt{\gamma} c^{\text{in}}(t), \tag{III.179}$$

from which we see that γ has units of angular frequency. Consequently, c^{in} has unit of the square root of an angular frequency.

5.1.1) Coherent drive

Calculation of the expectation value. We now assume that the input field is a coherent drive at frequency $\omega_d/2\pi$. This is described by a coherent state $\lim_{t_0 \to -\infty} \left| \alpha e^{-i\omega_d t_0} \right\rangle$ (the presence of the exponential factor is a choice to simplify the calculations below), but only for the mode of frequency $\omega_d/2\pi$. Formally, the state of the bath is a product of the state of each oscillator,

$$|\text{in}\rangle = \prod_{\omega=-\infty}^{+\infty} |\psi\rangle_\omega . \tag{III.180}$$

[1] This is also called the Planck distribution by some authors.

Our assumption of a coherent state for mode ω_d corresponds to $|\psi\rangle_\omega = |0\rangle$ for $\omega \neq \omega_d$, and $|\psi\rangle_{\omega_d} = \lim_{t_0\to-\infty} \left|\alpha e^{-i\omega_d t_0}\right\rangle$, i.e. all the other modes are in their vacuum state. Hence, performing a semi-classical approximation, we replace p_1 by its expectation value

$$\left\langle c^{\text{in}}(t)\right\rangle = \langle \text{in}|c^{\text{in}}(t)|\text{in}\rangle \tag{III.181}$$

$$= \lim_{t_0\to-\infty} \frac{1}{\sqrt{2\pi}} \int_{\mathbb{R}} \mathrm{d}\omega\ \langle \text{in}|e^{-i\omega(t-t_0)} b_\omega(t_0)|\text{in}\rangle \tag{III.182}$$

$$= \lim_{t_0\to-\infty} \frac{\alpha e^{-i\omega_d t_0}}{\sqrt{2\pi}} e^{-i\omega_d(t-t_0)} \tag{III.183}$$

$$= \frac{\alpha}{\sqrt{2\pi}} e^{-i\omega_d t} \tag{III.184}$$

In the frequency domain, we readily obtain

$$\left\langle c^{\text{in}}(\omega)\right\rangle = \frac{\alpha}{2\pi} \int_{\mathbb{R}} \mathrm{d}t\, e^{-i(\omega_d-\omega)t} = \alpha\delta(\omega-\omega_d). \tag{III.185}$$

Unit and relation with power. There is a slight ambiguity concerning the dimensions of α, which we now clarify. Usually, bosonic operators are dimensionless, and in this context a coherent state $|\beta\rangle$ is also dimensionless. In particular, since β is dimensionless, the average number of particles in $|\beta\rangle$ is given by $|\beta|^2$.

Recall, however, that c^{in} has dimension of $\sqrt{\omega} = 1/\sqrt{t}$. Hence, when c^{in} is a single-mode coherent state as described by equation (III.184), then $\left|\left\langle c^{\text{in}}\right\rangle\right|$ is a number of particles per second. In other words, we can view $|\alpha|^2$ as being the average number of particles per unit time. This can be linked to the drive power P, since $\frac{P}{\hbar\omega_d}$ is also the number of particles per unit time, with $\omega_d/2\pi$ the frequency of the coherent drive. Hence, neglecting the phase of α, we can write

$$\alpha = \sqrt{\frac{P}{\hbar\omega}}. \tag{III.186}$$

Note that authors often write $\epsilon = \sqrt{\frac{P}{\hbar\omega}}$ the amplitude of the drive, but this is not quite correct due to the peculiar dimensions of c^{in}.

Effective Hamiltonian. If we consider the QLE for an uncoupled bosonic mode c described by equation (III.179), we find the effective non-hermitian Hamiltonian equation (III.177). Using equation (III.184) in the latter, we obtain

$$H = \hbar\widetilde{\omega}_c c^\dagger c + i\hbar\sqrt{\frac{\gamma}{2\pi}}\left(c\alpha^* e^{i\omega_d t} - c^\dagger \alpha e^{-i\omega_d t}\right) \tag{III.187}$$

where $\widetilde{\omega}_c = \omega_c - i\frac{\gamma}{2}$.

Resulting physics. What is the effect of the coherent drive? In a rotating frame at the frequency of the drive[1], equation (III.187) becomes

$$H = \hbar\widetilde{\Delta}_c c^\dagger c + i\hbar\sqrt{\frac{\gamma}{2\pi}}\left(c\alpha^* - c^\dagger\alpha\right). \tag{III.188}$$

with $\widetilde{\Delta}_c = \widetilde{\omega}_c - \omega_d$. An additional displacement transformation (see appendix A.2.1 for the properties of the displacement operator) $D(\beta) = \exp\left(\beta c^\dagger - \beta^* c\right)$ leads to

$$H' = \hbar\widetilde{\Delta}_c\left(c^\dagger c + \beta^* c + \beta c^\dagger + |\beta|^2\right) + i\hbar\sqrt{\frac{\gamma}{2\pi}}\left(c\alpha^* - c^\dagger\alpha\right) + i\hbar\sqrt{\frac{\gamma}{2\pi}}(\beta\alpha^* - \beta^*\alpha) \tag{III.189}$$

$$= \hbar\widetilde{\Delta}_c c^\dagger c + \hbar\widetilde{\Delta}_c\left(\beta^* c + \beta c^\dagger\right) + i\hbar\sqrt{\frac{\gamma}{2\pi}}\left(c\alpha^* - c^\dagger\alpha\right). \tag{III.190}$$

[1] Formally, we consider the unitary transformation $U = e^{i\omega_d t c^\dagger c}$.

Strictly speaking, $\widetilde{\Delta}_c$ is complex-valued due to the small imaginary par $\frac{\gamma}{2}$ damping the cavity mode. However, assuming that $\frac{\gamma}{2} \ll \omega_c - \omega_d$, $\widetilde{\Delta}_c$ becomes real, and then choosing $\beta = -i\sqrt{\frac{\gamma}{2\pi}}\frac{\alpha}{\widetilde{\Delta}_c}$, the Hamiltonian simplifies to

$$H' = \hbar\widetilde{\Delta}_c c^\dagger c, \tag{III.191}$$

i.e. the Hamiltonian of an uncoupled cavity mode. We immediately deduce that the spectrum is unchanged by the coherent drive, at least in the limit of small coupling $\gamma/2\pi$ to the environment. Interestingly, when the drive is on resonance, $\omega_d = \omega_c$, and $\widetilde{\Delta}_c$ is purely imaginary. Then the same choice of β applies, and we recover the same Hamiltonian.

The previous displacement transformation showed that the coherent drive effectively puts the cavity mode in a coherent state. To see this, recall that the transformed Hamiltonian is $H' = D(\alpha)^\dagger H D(\alpha) = \hbar\widetilde{\Delta}_c c^\dagger c$, and accordingly the state vectors transforms to $|\psi'\rangle = D(\beta)\,|\psi\rangle$. Assuming the cavity mode was initially in the vacuum state, we see that the state of the transformed Hamiltonian is $|\psi'\rangle = |\beta\rangle$, i.e. a coherent state. Finally, returning to the frame of the cavity, the state becomes $|\psi''\rangle = e^{-i\omega_d t}\,|\beta\rangle$ as found in chapter II.

5.2) Input-output formalism

Some properties of the system inside the cavity can be probed by measuring the transmission or reflection through the cavity (S parameter). This is where the input-output formalism, also called input-output theory, comes in. The goal is to express the intra-cavity modes in terms of the bath operators only.

The principle of the derivation is the same as that for the QLEs: we consider that the modes of interest couple to a memory-less (first Markov approximation) bosonic bath. Additionally, the *input-output relations* allow to relate the fields inside the cavity with the input and output field at each port.

5.2.1) Input-output relations

The input-output relations are derived for each bath considered. Often, one has one bath per port. As per the previous subsection, using the formal solution for the bath operator b_ω at $t < t_0$

$$b_\omega(t) = e^{-i\omega(t-t_0)}b_\omega(t_0) + \sqrt{\frac{\gamma}{2\pi}}\int_{t_0}^{t} \mathrm{d}t'\, c(t')e^{-i\omega(t-t')}, \tag{III.192}$$

and the input field

$$c^{\mathrm{in}}(t) = \lim_{t_0\to-\infty} \frac{1}{\sqrt{2\pi}}\int_{\mathbb{R}} \mathrm{d}\omega\, e^{-i\omega(t-t_0)}b_\omega(t_0), \tag{III.193}$$

we can derive[1]

$$\frac{1}{\sqrt{2\pi}}\int_{\mathbb{R}} \mathrm{d}\omega\, b_\omega(t) = \sqrt{2\pi}c^{\mathrm{in}}(t) + \frac{\sqrt{\gamma}}{2}c(t). \tag{III.194}$$

Similarly, one can write the formal solution for $t < t_1$ as

$$b_\omega(t) = e^{-i\omega(t-t_1)}b_\omega(t_1) - \sqrt{\frac{\gamma}{2\pi}}\int_{t}^{t_1} \mathrm{d}t'\, c(t')e^{-i\omega(t-t')}, \tag{III.195}$$

and define the output field

$$c^{\mathrm{out}}(t) = \lim_{t_1\to\infty} \frac{1}{\sqrt{2\pi}}\int_{\mathbb{R}} \mathrm{d}\omega\, e^{-i\omega(t-t_1)}b_\omega(t_1). \tag{III.196}$$

This leads to

$$\frac{1}{\sqrt{2\pi}}\int_{\mathbb{R}} \mathrm{d}\omega\, b_\omega(t) = \sqrt{2\pi}c^{\mathrm{out}}(t) - \frac{\sqrt{\gamma}}{2}c(t). \tag{III.197}$$

[1] This is the same calculus that leads to the QLE for c.

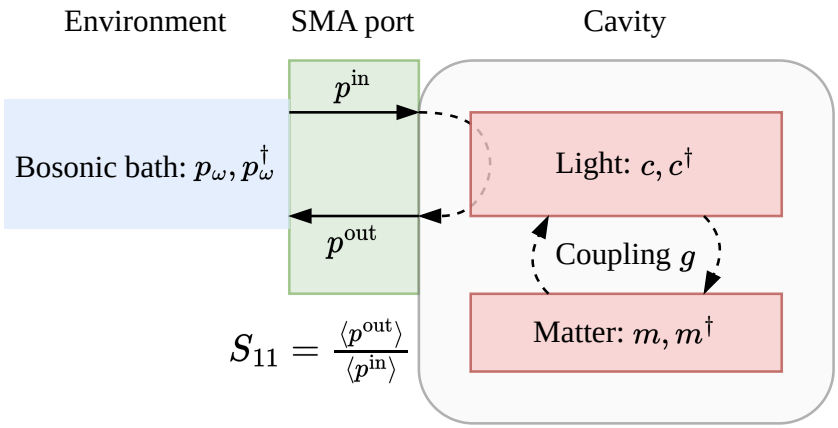


Figure III.4: Schematic of using the input-output formalism to find the reflection coefficient of the cavity.

which we can use to find the time-reversed QLE for c, see Gardiner and Collett (1985) [218] for more details. Combining equations (III.194) and (III.197), we can derive the *input-output relation*

$$c^{\text{out}}(t) = c^{\text{in}}(t) + \sqrt{\gamma} c(t). \tag{III.198}$$

It is worth mentioning that depending on the convention used for the coupling between c and the bath, the input-output relation may take different signs.

5.2.2) Application: coupled bosonic modes

To illustrate the method, we will consider a cavity system composed of two bosonic modes c (cavity mode) and m (matter mode), where only c couples to the environment through a port, described by input and output fields $p_1^{\text{in}}, p_1^{\text{out}}$, with coupling rate $\gamma_1/2\pi$. We take the Hamiltonian for the cavity system to be the Dicke Hamiltonian in the RWA, which reads

$$H_{\text{cav}} = \hbar\omega_c c^\dagger c + \hbar\omega_m m^\dagger m + \hbar g(cm^\dagger + c^\dagger m), \tag{III.199}$$

where we consider the coupling strength g to be real. As per the previous subsection, we replace $(\omega_c, \omega_m) \mapsto \widetilde{\omega}_c = \omega_c - i\frac{\gamma_c}{2}, \widetilde{\omega}_m = \omega_m - i\frac{\gamma_m}{2}$, where γ_c, γ_m are the intrinsic dissipation rates of each mode. Using the general QLE equation (III.168),

$$\dot{c} = \frac{1}{i\hbar}[c, H_{\text{sys}}] - \frac{\gamma_1}{2}c - \sqrt{\gamma_1}p_1^{\text{in}} \tag{III.200}$$

$$= -i\widetilde{\omega}_c - igm - \frac{\gamma_1}{2}c - \sqrt{\gamma_1}p_1^{\text{in}}. \tag{III.201}$$

while the Heisenberg equation of motion for b is

$$\dot{m} = -i\widetilde{\omega}_m m - igc. \tag{III.202}$$

In frequency space, this gives[1]

$$-i\omega\widetilde{m} = -i\widetilde{\omega}_m\widetilde{m} - ig\widetilde{c}, \tag{III.203}$$

$$\widetilde{m} = \frac{g}{\omega - \widetilde{\omega}_m}\widetilde{c} = \frac{g}{\widetilde{\Delta}_m}\widetilde{c}, \tag{III.204}$$

where $\widetilde{\Delta}_m = \omega - \omega_m + i\frac{\gamma_m}{2}$. Inserting into the frequency-space QLE for c, we obtain

$$-i\omega\widetilde{c} = -i\Big(\widetilde{\omega}_c - i\frac{\gamma_1}{2}\Big)\widetilde{c} - ig\widetilde{m} - \sqrt{\gamma_1}\widetilde{p}_1^{\text{in}}, \tag{III.205}$$

$$\Big(\omega - \widetilde{\omega}_c + i\frac{\gamma_1}{2}\Big)\widetilde{c} - g\widetilde{m} = -i\sqrt{\gamma_1}\widetilde{p}_1^{\text{in}}, \tag{III.206}$$

$$\left(\omega - \widetilde{\omega}_c + i\frac{\gamma_1}{2} - \frac{g^2}{\widetilde{\Delta}_m}\right)\widetilde{c} = -i\sqrt{\gamma_1}\widetilde{p}_1^{\text{in}}, \tag{III.207}$$

[1] Note that if we had neglected the dissipation rate γ_m, we would have had a singularity in $\omega = \omega_m$.

and defining $\widetilde{\Delta}_c = \omega - \omega_c + i\frac{\gamma_c+\gamma_1}{2}$,

$$\widetilde{c}(\omega) = -i\frac{\sqrt{\gamma_1}}{\widetilde{\Delta}_c - \frac{g^2}{\widetilde{\Delta}_m}}\widetilde{p}_1^{\text{in}} \tag{III.208}$$

$$= -i\frac{\sqrt{\gamma_1}\widetilde{\Delta}_m}{\widetilde{\Delta}_c\widetilde{\Delta}_m - g^2}\widetilde{p}_1^{\text{in}}. \tag{III.209}$$

Reflection coefficient. We now perform a semi-classical approximation and assume that p_1 in a coherent state of frequency $\omega/2\pi$. Then the reflection coefficient can be defined as

$$S_{11}(\omega) = \frac{\left\langle \widetilde{p}_1^{\text{out}}(\omega)\right\rangle}{\left\langle \widetilde{p}_1^{\text{in}}(\omega)\right\rangle}. \tag{III.210}$$

The input-output relation is

$$p_1^{\text{out}}(t) = p_1^{\text{in}}(t) + \sqrt{\gamma_1}c(t), \tag{III.211}$$

which allows to rewrite the reflection coefficient as

$$S_{11}(\omega) = \frac{\left\langle \widetilde{p}_1^{\text{in}}\right\rangle + \sqrt{\gamma_1}\left\langle \widetilde{c}\right\rangle}{\left\langle \widetilde{p}_1^{\text{in}}\right\rangle} \tag{III.212}$$

$$= 1 - i\frac{\gamma_1\widetilde{\Delta}_m}{\widetilde{\Delta}_c\widetilde{\Delta}_m - g^2} = 1 - i\frac{\gamma_1(\omega - \widetilde{\omega}_m)}{(\omega - \widetilde{\omega}_c)(\omega - \widetilde{\omega}_m) - g^2}. \tag{III.213}$$

In a measurement using a vector network analyser, the measured phase is $\arg S_{11}$ while the amplitude is $|S_{11}|$.

Analysis of the reflection coefficient. Let us examine what information the reflection coefficient can provide about the system. One can see that there is a singularity when the denominator of the second term vanishes. This corresponds to the condition

$$(\omega - \widetilde{\omega}_c)(\omega - \widetilde{\omega}_m) - g^2 = 0, \tag{III.214}$$

and solving for the resulting complex-valued quadratic equation for ω, one finds

$$\widetilde{\omega}_\pm = \frac{\widetilde{\omega}_c + \widetilde{\omega}_m}{2} \pm \frac{\sqrt{(\widetilde{\omega}_c - \widetilde{\omega}_m)^2 + 4g^2}}{2}. \tag{III.215}$$

If the dissipation rates are small with respect to the frequencies $\omega_c/2\pi$ and $\omega_m/2\pi$, then we can approximate $\widetilde{\omega}_c = \omega_c$ and $\widetilde{\omega}_m = \omega_m$, and we obtain

$$\omega_\pm = \frac{\omega_c + \omega_m}{2} \pm \frac{\sqrt{(\omega_c - \omega_m)^2 + 4g^2}}{2}, \tag{III.216}$$

which we identify as being the polaritonic frequencies of the Dicke model in the RWA. Hence, we expect a singularity at frequencies close to the spectrum of the system[1]. This is indeed what is observed, as figure III.6 shows. We observe that the reflection has a dip at frequencies close to the theoretical spectrum. Note that the dissipations are responsible for the finite linewidths of the reflection: without them, the denominator of S_{11} vanishes, leading to a singularity.

Transmission coefficients. The input-output formalism can also model the transmission through a cavity system. To model this situation, we need to consider an additional bosonic bath, to which the cavity mode operator c couples. This additional bath, describing a second port attached the cavity, is modelled by input/output fields $p_2^{\text{in}}, p_2^{\text{out}}$ with coupling γ_2. The QLE for m is unchanged, and still reads $\widetilde{m} = \frac{g}{\widetilde{\Delta}_m}\widetilde{c}$ in frequency space. Conversely, the QLE for c, equation (III.201), is modified to

$$\dot{c} = -i\widetilde{\omega}_c - igm - \frac{\gamma_1}{2}c - \sqrt{\gamma_1}p_1^{\text{in}} - \frac{\gamma_2}{2}c - \sqrt{\gamma_2}p_2^{\text{in}}. \tag{III.217}$$

[1]Note that due to the non-vanishing imaginary parts, the reflection is not singular, but does exhibit a resonance behaviour.

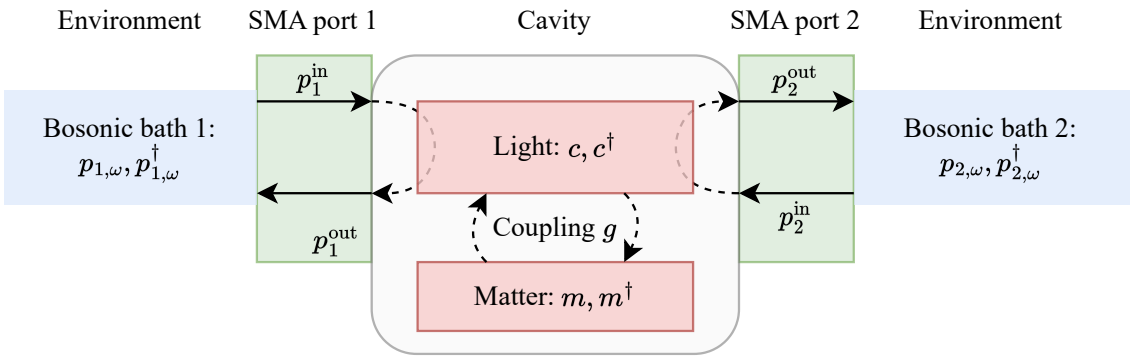


Figure III.5: Schematic of using the input-output formalism to find the reflection and transmission coefficients of the cavity. Compared with the calculation of only the reflection, one simply needs to add another bosonic bath to model the other port (compare with figure III.4).

By following the same steps as before, we obtain

$$\widetilde{c}(\omega) = -i\widetilde{\Delta}_m \frac{\sqrt{\gamma_1}\widetilde{p}_1^{\text{in}} + \sqrt{\gamma_2}\widetilde{p}_2^{\text{in}}}{\widetilde{\Delta}_c\widetilde{\Delta}_m - g^2}. \tag{III.218}$$

where this time $\widetilde{\Delta}_c = \omega - \omega_c + i\frac{\gamma_c+\gamma_1+\gamma_2}{2}$.

The S-parameter of the cavity can be defined as

$$S_{11} = \left.\frac{\langle \widetilde{p}_1^{\text{out}}\rangle}{\langle \widetilde{p}_1^{\text{in}}\rangle}\right|_{\langle \widetilde{p}_2^{\text{in}}\rangle=0}, \quad S_{22} = \left.\frac{\langle \widetilde{p}_2^{\text{out}}\rangle}{\langle \widetilde{p}_2^{\text{in}}\rangle}\right|_{\langle \widetilde{p}_1^{\text{in}}\rangle=0}, \tag{III.219}$$

$$S_{21} = \left.\frac{\langle \widetilde{p}_2^{\text{out}}\rangle}{\langle \widetilde{p}_1^{\text{in}}\rangle}\right|_{\langle \widetilde{p}_1^{\text{in}}\rangle=0}, \quad S_{12} = \left.\frac{\langle \widetilde{p}_1^{\text{out}}\rangle}{\langle \widetilde{p}_2^{\text{in}}\rangle}\right|_{\langle \widetilde{p}_1^{\text{in}}\rangle=0}. \tag{III.220}$$

As before, the input-output relations,

$$p_1^{\text{out}}(t) = p_1^{\text{in}}(t) + \sqrt{\gamma_1}c(t), \tag{III.221}$$

$$p_2^{\text{out}}(t) = p_2^{\text{in}}(t) + \sqrt{\gamma_2}c(t), \tag{III.222}$$

allow to express S parameters analytically. In particular, S_{11} has the same expression as before (equation (III.213)), and S_{22} can be obtained by replacing $\gamma_1 \mapsto \gamma_2$ in equation (III.213). The transmission from port 1 to port 2 reads

$$S_{21}(\omega) = \left.\frac{\langle \widetilde{p}_2^{\text{in}}\rangle + \sqrt{\gamma_2}\langle \widetilde{c}\rangle}{\langle \widetilde{p}_1^{\text{in}}\rangle}\right|_{\langle \widetilde{p}_2^{\text{in}}\rangle=0} = \sqrt{\gamma_2}\frac{\langle \widetilde{c}\rangle}{\langle \widetilde{p}_1^{\text{in}}\rangle} \tag{III.223}$$

$$= -i\frac{\sqrt{\gamma_1\gamma_2}\widetilde{\Delta}_m}{\widetilde{\Delta}_c\widetilde{\Delta}_m - g^2} = -i\frac{\sqrt{\gamma_1\gamma_2}(\omega - \widetilde{\omega}_m)}{(\omega-\widetilde{\omega}_c)(\omega-\widetilde{\omega}_m) - g^2}, \tag{III.224}$$

and one can check that we have $S_{12} = S_{21}$.

As before, we expect the transmission to have a maximum when the denominator vanishes, i.e. for frequencies close to the polaritonic frequencies. This is again confirmed by figure III.6, exhibiting an anti-crossing in both reflection and transmission. However, contrary to the reflection coefficient, we obtain an anti-resonance behaviour for the transmission: there is significant dip for frequencies $\omega \simeq \omega_m$, corresponding to the diagonal black line. This can be explained by the nominator, since when $\omega = \omega_m$ it vanishes and hence $S_{21}(\omega_m) = 0$ (in the limit of weak damping, i.e. neglecting the imaginary part).

Finally, we can notice that the expression of the transmission shows that the coupling takes the form of a self energy[1], reminiscent of Green functions: the real parts shifts the frequency, while the imaginary part accounts for damping.

[1] See [94] and also SM note 4 of [227] for more details.

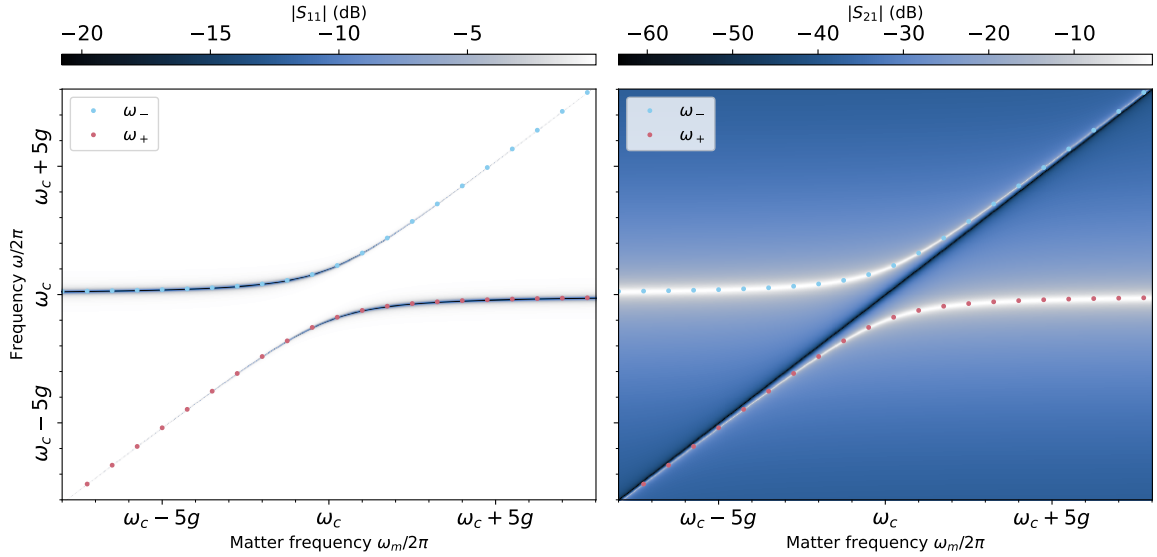


Figure III.6: Plot of the reflection (left) and transmission (right) coefficient for the Dicke model in the RWA, with the typical parameters for cavity magnonics $\gamma_c/2\pi = 2$ MHz, $\gamma_m/2\pi = 1$ MHz, $\gamma_1/2\pi = \gamma_2/2\pi = 10$ MHz, and other parameters as in figure III.1. The theoretical spectra is shown in dots.

6) Conclusion

In this chapter, we have introduced various methods to analyse the interaction with light and matter, using a formalism compatible with the discussion of quantum-mechanical effects. We have made several common approximations, such as neglecting the diamagnetic term $\mathbf{A}^2$, and using the rotating wave approximation (RWA). We will revisit the validity of some of these approximations in chapter VII. In the next chapter, we will apply the methods developed here to the magnetic dipole interaction, and discuss the field of cavity magnonics.

Chapter IV

Coherent microwave cavity magnonics

Summary

We develop the theoretical background specific to the coherent coupling between light and ferromagnets in a cavity at microwave frequencies. Notably, we derive a second-quantised Hamiltonian for spin waves, which are the normal modes of the magnetic order. Combined with the previously introduced quantum description of the magnetic field, the interaction Hamiltonian of light with spin waves is obtained at microwave frequencies. Importantly, as shown in the original published work Gardin et al. (2023) [1] available in appendix C.1, a theoretical investigation of this interaction reveals the existence of a coupling phase, which albeit often rightfully neglected, can have physical consequences in multimode systems. In the other original unpublished work of appendix C.2, we show how COMSOL Multiphysics® can be used to model and engineer cavity magnonics systems. This finally allows us, in the submitted original work Gardin et al. (2024) [2] (available in appendix C.3), to provide an experimental proof of the existence and consequences of the coupling phases introduced in Gardin et al. (2023) [1].

Contents

1) Introduction . . . **71**
- 1.1 Magnonics . . . 71
- 1.2 Cavity magnonics . . . 72

2) Fundamentals of magnetism . . . **73**
- 2.1 Magnetic order . . . 73
- 2.2 Zeeman interaction . . . 74

3) Spin waves . . . **75**
- 3.1 Angular momenta in quantum mechanics . . . 75
- 3.2 Quantum model of ferrimagnets . . . 77
- 3.3 Quantum model of spin-waves . . . 78

4) Microwave photon/magnon interaction . . . **79**
- 4.1 Interaction Hamiltonian . . . 79
- 4.2 Further comments on the microwave photon/magnon interaction . . . 81
- 4.3 Relevance of the coupling phase . . . 83
- 4.4 Classical electrodynamics model . . . 84
  - 4.4.1 Landau-Lifschitz-Gilbert equation . . . 84
  - 4.4.2 Linearisation . . . 85
  - 4.4.3 Linearisation with demagnetising factors . . . 86

5) Experimental aspects and cavity engineering . . . **88**
- 5.1 COMSOL Multiphysics® for microwave cavity magnonics . . . 88
- 5.2 Coupling phase engineering . . . 88

6) Conclusion . . . **89**

1) Introduction

1.1) Magnonics

In the previous chapter, we discussed the interaction of light with matter due to the electric dipole interaction. Here, we shall discuss the magnetic dipole interaction instead, leading to the field of cavity magnonics, where light will interact with *magnons*. Thus, we first need to define what magnons are.

Definition. In some materials, local magnetic moments $\boldsymbol{\mu}$ can exist[1], and their collective behaviour can lead to the emergence of a macroscopic magnetisation $\mathbf{M}$. The microscopic details of the material[2] and the presence of an applied static magnetic field, determine the equilibrium magnetisation, defining the magnetic ground state of the system. The excited states are standing waves of the magnetisation, and form the different "modes" of the system. The quantisation of these waves leads to bosonic quasi-particles known as magnons.

The origin of magnetic moments is linked to angular momentum, which stems from orbital and spin angular momenta, or even a combination thereof. Often, spin will be the source of angular momentum. Hence, the modes are often referred to as *spin waves*. Magnons are thus the quanta associated with spin waves, just like photons are the quanta of electromagnetic waves. Magnonics can then be defined as the study of spin waves in magnetic materials, which is interesting for several reasons.

Applications. A major application of magnonics resides in the possibility to create more efficient classical computing and memory architectures [228–237]. Indeed, the semiconductor-based integration of computing devices resides in the transport of electrons, which carry charges hence leading to thermal dissipation, which creates challenges for integration. Spin waves, on the other hand, do not transport charges, so there is no thermal Joule effect associated to their use. The study of the spin degree of freedom for new technologies such as logic and sensing devices is known as *spintronics*, by analogy with conventional *electronics* based on transport of electrons. Notably, it seems that hybrid complementary metal-oxide-semiconductor (CMOS)/magnonics devices are the most promising [234, 238], which motivates extensive research on spin-to-charge conversion, spin-wave transducers [239], and the electrical detection of magnetisation dynamics [240] to name a few. A notable success of spintronics has been the development of magnetic random access memories (MRAMs), which are reviewed in [241].

Furthermore, despite the success of Moore's law for the development of CMOS-based computing power, the miniaturisation is approaching a scale close to atomic distances, making further size reductions harder and harder[3]. To overcome this hurdle, alternative computing architectures have been developed, for instance the co-existence of performance cores and energy-efficient cores, notably by Intel. Alternatively, different computing paradigms can be used, such as wave-based, neuromorphic and reservoir computing [242–244] which take advantage of non-linear effects in magnonics. While most of these applications rely on ferromagnetic materials, anti-ferromagnetic spintronics is an emerging research direction [245–247]. Additionally, using the ability of superconductors to electrically control spintronics without heating is an exciting direction.

Aside from advancements in classical computing and data storage, magnonics is also of fundamental interest, e.g. for the study of hermitian [248] and non-hermitian [249] topological phases, the Casimir effect [250], magnonic black holes with antimagnons [251], altermagnetism [252] and Bose-Einstein condensation [253].

[1] By analogy with the electric dipole interaction $\boldsymbol{\mu}' \cdot \mathbf{E}$ studied in the previous chapter, the magnetic dipoles interact with a static magnetic field as $-\boldsymbol{\mu} \cdot \mathbf{B}$.

[2] More specifically, the crystal structure, the electronic structures of the atoms involved, the spatial distribution of magnetic moments, and their possibly different magnitudes. We shall return to this in the next section.

[3] This is mainly due to the appearance of quantum effects at such a small scale. These effects are called short channel effects.

1.2) Cavity magnonics

In this thesis, we shall limit ourselves to the interaction of magnons with light confined to a cavity, which is referred to as cavity magnonics. In a sense, cavity magnonics is a subset of the field of magnonics, and when magnons are based on spins, we can call this field cavity spintronics. Cavity magnonics naturally falls within the definition of quantum optics, since it is based on the study of light/matter interactions, with the matter being a magnetic material.

Physics and applications. Cavity magnonics has potential applications in both applied and fundamental physics, spanning both classical and quantum information processing. On the classical applied side, cavity magnonics find applications in switches and memories, leveraging the bistable behaviour of the magnon Kerr effect [254–256]. The quantum applications are much more varied, and include quantum information transducers[1], quantum memories, non-reciprocal behaviours, and sensing. Additionally, as we will see in chapter VIII, cavity magnonics is also a versatile platform for the generation of non-classical states.

On the fundamental side, similar to magnonics, cavity magnonics is an interesting platform for the study of non-hermitian physics, exceptional points and PT-symmetry (we define these concepts further in chapter VI). A more exotic application concerns dark matter searches. Indeed, the axion, a dark matter candidate, can couple to the electron and act as an oscillating magnetic field [258, 259], potentially detectable using cavity magnonics devices.

Outline of the chapter. The first step consists of understanding the origin of magnetism. Classically, much of magnetism can be modelled by considering a macroscopic magnetisation $\mathbf{M}$, whose dynamics is given by the Landau-Lifschitz-Gilbert equation. However, classical physics cannot explain why a net magnetisation exists in the first place[2]. Indeed, permanent magnetic moments are due to a non-vanishing angular momentum of the material. We thus begin in section 2 by discussing the origin of the magnetic moments, and how their spatial distribution leads to ferromagnetic, anti-ferromagnetic, and ferrimagnetic materials. Importantly, we introduce Yttrium–Iron–Garnet, which is the only magnetic material that will be considered in this thesis. We also explain the physical origin of the coupling between magnetic moments and a magnetic field, a magnetic dipole interaction known as the Zeeman interaction.

The next section is dedicated to the detailed description of spin waves, which as already discussed can be thought of as the elementary excitations of the magnetic ground state of the material. Using a second-quantised formalism, we demonstrate that the resulting spin wave modes take the form of a sum of harmonic oscillators, which are naturally described in terms of bosonic quasi-particles, the magnons.

The following section, the core of the chapter, details the interaction of light with the lowest-order magnon mode. The derivation of the interaction Hamiltonian boils down to quantising the Zeeman interaction. We note that the resulting quantum model is necessary for many applications of interest, such as the coupling of magnons with qubits, the few-magnon/photon regime, cooperative magnon dynamics [260] or bistability [254–256]. However, we find that the physics of light/magnon coupling is essentially that of two coupled harmonic oscillators [94, 221, 226, 261], which can be dominated by either coherent coupling, leading to energy level repulsion, or dissipative coupling, leading to level attraction[3]. In particular, at room temperature, the physic is purely classical, and a description of the physics as two coupled springs [221, 226] or pendulums [94, 261] is sufficient. While this simplistic model allows to capture the signature of the photon-magnon hybridisation it will be insufficient to describe quantum information processing applications based on magnons.

[1] Remarkably, magnons can couple to a variety of systems, offering a wealth of hybrid quantum systems [257]. For instance, magnons can couple to light at both microwave and optical frequencies, but also to mechanical modes. These three coupling paths then allow to couple magnons with other systems, for instance superconducting qubits through by indirect coupling.

[2] This was proven independently by Bohr and van Leeuwen in their respective doctoral theses.

[3] The latter regime will be studied in chapter VI.

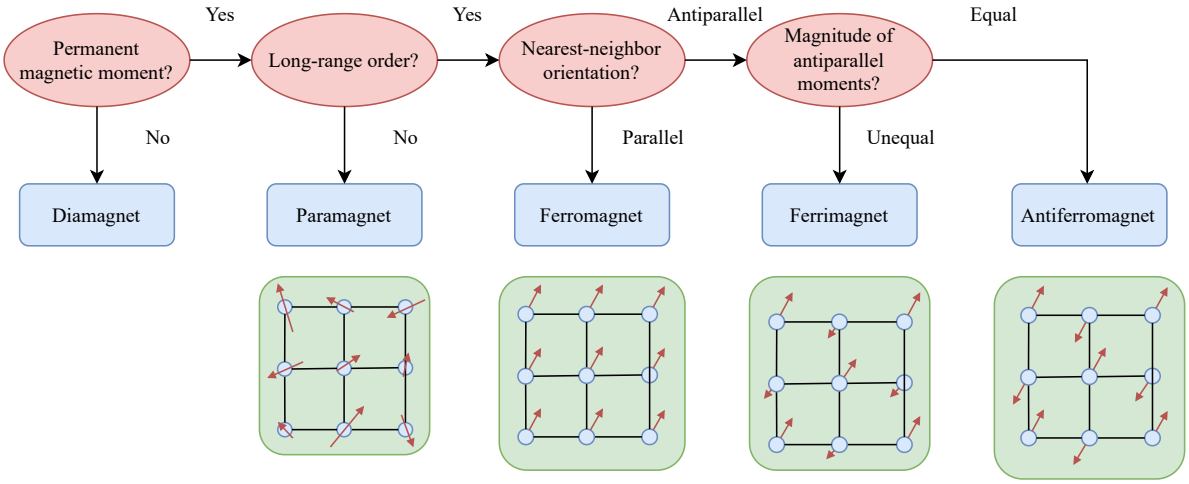


Figure IV.1: Overview of the different types of magnets. Inspired from figure 1.1 of [194], and figures 20.1 and 20.3 of [262].

2) Fundamentals of magnetism

As we will see in this section, magnetic behaviour can be traced to the angular momenta of atoms. Thus, we begin by recalling how one can predict the angular momenta of the electrons of atoms and ions. Once the source of magnetic moments is identified, we can then discuss the distribution of these magnetic moments in the crystal, which allows to distinguish between ferromagnets, anti-ferromagnets and ferrimagnets. We then tackle the Zeeman interaction, to understand how matter with magnetic moments responds to an external applied magnetic field. Useful references for this section are the textbook on spin waves by Stancil and Prabhakar (2009) [194], and the solid-state textbook by Simon (2013) [262].

2.1) Magnetic order

Ferromagnets, anti-ferromagnets and ferrimagnets. Magnetic properties emerge due to the presence of microscopic magnetic moments. There are several types of magnets, depending on the type of magnetic moment present in the material, as summarised in figure IV.1. In diamagnets, there is no permanent magnetic moment, but the application of a static applied magnetic field can temporarily induce a magnetic moment. In other words, diamagnets exhibit a magnetic moment only in the presence of an applied magnetic field. Here, we will mostly be interested in ferromagnets, where permanent magnetic moments exist. Depending on the alignment of neighbouring moments, and their magnitudes, one can have a ferromagnet, an anti-ferromagnet, or a ferrimagnet, as sketched in figure IV.1. Let us now quickly look into the origin of these magnetic moments.

Magnetic moments. Recall that the electronic orbitals of an isolated atom is described by four quantum numbers as $|n, l, m, s\rangle$, where $n \in \mathbb{N}$ is the orbital number, $0 \leqslant l \leqslant n-1$ the norm of the angular momentum, $-l \leqslant m \leqslant l$ a component (often $\hat{\mathbf{z}}$ component) of the angular momentum, and $s = \pm\frac{1}{2}$ the spin angular momentum. Each value of l corresponds to a "shell", which is filled in an order described by the Aufbau principle [262]. The energy ordering of orbitals and shells is described by the Madelung-Klechkovsky rule [262]. Often, an isolated atom will have a certain number shells completely filled, and one shell partially filled. The *Hund's rules* dictate how the angular momenta are distributed.

A material of particular interest in this thesis is Yttrium–Iron–Garnet (YIG) with chemical formula $Y_3Fe_5O_{12}$. Technically, YIG is a ferrimagnet with two sublattices, and only the iron ions Fe_3^+ contribute to the magnetic properties. Of the five Fe ions, two are located on one sublattice, and the remaining three on the second lattice, so that the net moment is that of a single iron ion (see page 4 of [194]). The ion Fe_3^+ has a half-filled 3d shell. In the ground state, the Russell-Saunders coupling scheme indicates that these ions do not have orbital

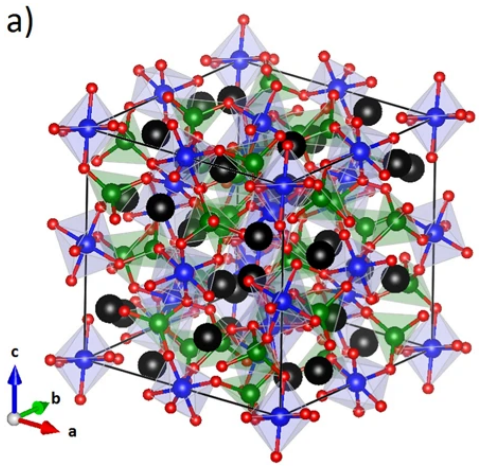


Figure IV.2: Crystal structure of Yttrium-Iron Garnet (fig 1a of [263] licensed under CC BY 4.0 [140]). Black spheres are Yttrium atoms, while red spheres are oxygen atoms. The blue (green) spheres are Fe_3^+ ions on the tetrahedral (octahedral) lattices.

angular momentum. Thus, the ion contributes a spin $s = \frac{5}{2}$ [194, p. 84]. Hence, to a good approximation one can model YIG as a ferromagnet.

2.2) Zeeman interaction

An external static electromagnetic field can shift the energy levels of atoms in two ways. For an electric field, this lead to the Stark effect[1], while for a magnetic field one obtains the Zeeman effect. Both these effects stem from a dipolar interaction between a moment, and an external electric/magnetic field. In the magnetic case, the magnetic moment exists due to a non-vanishing angular momentum [10]. The different sources of angular momentum, orbital and spin, induce slightly different Zeeman effects[2].

Regardless of the source of angular momentum – orbital or spin – a particle of charge q always has some sort of Zeeman interaction, resulting from the minimal coupling replacement $\mathbf{p} \mapsto \mathbf{p} - q\mathbf{A}$, where $\mathbf{p}$ is the momentum of the particle. For instance, for orbital angular momentum it is sufficient to consider the Schrödinger equation in the Coulomb gauge (see appendix B.5.1), and we obtain a Zeeman interaction [194]

$$H_{\text{Zeeman,orbital}} = -\boldsymbol{\mu}_L \cdot \mathbf{B}, \tag{IV.1}$$

with $\boldsymbol{\mu}_L = \frac{q}{2m}\mathbf{L}$ the magnetic dipole moment operator, $\mathbf{L} = \mathbf{r} \times \mathbf{p}$ the orbital angular momentum operator. Note that for an electron, $q = -e$ and the magnetic moment is opposed to the orbital angular momentum. Additionally, for electrons it is convenient to define the Bohr magneton [194] $\mu_B = \frac{e\hbar}{2m_e}$, where e is the elementary charge and m_e the mass of the electron. The orbital magnetic moment of the electron can then be written as $\boldsymbol{\mu} = -\mu_B \frac{\mathbf{L}}{\hbar}$.

For the spin angular momentum, it is slightly more complicated, since the Schrödinger equation does not include the spin degrees of freedom. The right equation to start from is the Dirac equation, which in the non-relativistic limit becomes the Pauli equation. The Zeeman interaction due to spin is found to be [262] (see appendix B.5.2 for the derivation)

$$H_{\text{Zeeman,spin}} = -\boldsymbol{\mu} \cdot \mathbf{B}, \tag{IV.2}$$

but this time $\boldsymbol{\mu} = -g_L \mu_B \frac{\mathbf{S}}{\hbar}$ is the magnetic moment for spin with $g_L \simeq 2$ the electron's Landé g_L-factor, $\mathbf{S} = \hbar\boldsymbol{\sigma}$ is the spin angular momentum operator, and $\boldsymbol{\sigma} = (\sigma_x, \sigma_y, \sigma_z)$. Equations (IV.1) and (IV.2) can be readily added to a Hamiltonian when both a charged particle and a static magnetic field are present.

[1] We refer the reader to "Complément E_{XII}" of reference [264] for more details.

[2] Historically, the "Zeeman effect" discovered in 1896 by Zeeman was strictly due to orbital angular momentum. Conversely, the "anomalous Zeeman effect", first observed in 1897, is due to both orbital and spin angular momentum, and takes its name from the fact that the spin degree of freedom had not yet been discovered.

Convention for the sign of the Zeeman interaction. Expressing the Zeeman interaction with the spin operator, we find

$$H_{\text{Zeeman,spin}} = g_L \mu_B \frac{\mathbf{S}}{\hbar} \cdot \mathbf{B}, \tag{IV.3}$$

and therefore having the spin anti-align with the magnetic field minimises the energy [262]. However, it is common to have the opposite convention in cavity magnonics, where the spin aligns with the magnetic field [94]. Therefore, in the following we will often write $H_{\text{Zeeman,spin}} = -g_L \mu_B \frac{\mathbf{S}}{\hbar} \cdot \mathbf{B}$ instead, and assume the magnetic moment is aligned with the spin, i.e. $\boldsymbol{\mu} = g_L \mu_B \frac{\mathbf{S}}{\hbar}$.

Macroscopic view. Interestingly, the Zeeman interaction is somewhat naturally included in Maxwell's equations. Indeed, consider the Hamiltonian $\int_{V_c} \mathrm{d}^3 r\, \mathcal{H}$ for the electromagnetic field, where the Hamiltonian density[1] is

$$\mathcal{H} = \left(\frac{1}{2} \epsilon_0 \mathbf{E}^2 + \frac{1}{2\mu_0} \mathbf{B}^2 \right). \tag{IV.4}$$

Then, using the relation of equation (III.4), which reads $\mathbf{B} = \mu_0(\mathbf{H} + \mathbf{M})$, we obtain[2]

$$\mathcal{H} = \frac{1}{2} \epsilon_0 |\mathbf{E}|^2 + \frac{1}{2} \mu_0 |\mathbf{H}|^2 + \mathbf{M} \cdot \mu_0 \mathbf{H} + \frac{1}{2} \mu_0 |\mathbf{M}|^2, \tag{IV.5}$$

and the Zeeman interaction appears in the third term. Indeed, recall from section 2.2 that $\mathbf{M}$ is the magnetic dipole moment per volume, and hence it can be assimilated to the magnetic dipole moments $\boldsymbol{\mu}$. Notably, if all the microscopic constituents have identical magnetic moments $\boldsymbol{\mu}$ over a volume V_m, then $\mathbf{M} = \boldsymbol{\mu}/V_m$.

3) Spin waves

In the previous section, we explained the existence of magnetic moments, and we understood how they interact with the magnetic field. In this section, we consider a YIG sample and model it as a ferromagnet. We shall describe the elementary spin excitations of the magnetic order.

3.1) Angular momenta in quantum mechanics

To simplify the forthcoming discussion, we need to recall some elementary results on angular momentum. The results presented are covered in any reasonable textbook on quantum mechanics, and we refer the reader to e.g. sections 1.4.3, 1.4.4 and 2.7.1 of [194] for the details of the proofs.

Definition of angular momentum. In quantum mechanics, any operator $\mathbf{J} = (J_x, J_y, J_z)$ satisfying

$$\mathbf{J} \times \mathbf{J} = i\hbar \mathbf{J} \tag{IV.6}$$

is by definition an angular momentum, where the symbol $\times$ indicates the cross product. Equation (IV.6) fixes the commutation relations between the components of angular momentum, which explicitly read

$$[J_x, J_y] = i\hbar J_z, \tag{IV.7}$$
$$[J_y, J_z] = i\hbar J_x \tag{IV.8}$$
$$[J_z, J_x] = i\hbar J_y. \tag{IV.9}$$

[1] We use the Hamiltonian density to avoid using the symbol H for the Hamiltonian, and $\mathbf{H}$ for the magnetic flux, and thus avoid any confusion.

[2] Note that using $\mathcal{H} = \left(\frac{1}{2}\epsilon_0 \mathbf{E}^2 + \frac{1}{2}\mu_0 \mathbf{H}^2\right)$ instead yields $\mathcal{H} = \frac{1}{2}\epsilon_0 |\mathbf{E}|^2 + \frac{1}{2\mu_0} |\mathbf{B}|^2 + \mu_0 \mathbf{H} \cdot \mathbf{M} + \frac{1}{2}\mu_0 |\mathbf{M}|^2$, and the sign of the Zeeman interaction is switched.

Properties of angular momentum. Since different components do not commute, we deduce than we cannot measure different components simultaneously. However, defining $J^2 = \mathbf{J} \cdot \mathbf{J} = J_x^2 + J_y^2 + J_z^2$, one can show that

$$\left[J^2, J_x\right] = \left[J^2, J_y\right] = \left[J^2, J_z\right] = 0, \tag{IV.10}$$

so that the angular momentum is fully characterised by measuring $\mathbf{J}^2$ and one of the component of $\mathbf{J}$, often taken to be J_z.

Contrary to the continuous values taken by classical angular momenta, in quantum mechanics angular momentum is quantised, and described by two quantum numbers. Formally, an angular momentum eigenstate $|m, l\rangle$ is such that

$$J_z |m, l\rangle = \hbar m |m, l\rangle, \quad J^2 |m, l\rangle = \hbar^2 l(l+1) |m, l\rangle, \tag{IV.11}$$

$$-l \leqslant m \leqslant l, \quad 2l \in \mathbb{N}. \tag{IV.12}$$

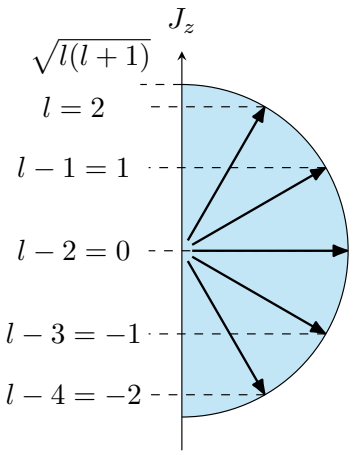


Figure IV.3: Schematic of the distribution of the angular momentum states for fixed $l = 6$.

Hence, the maximum value of the magnitude of the angular momentum is $\sqrt{l(l+1)}$, while the maximum value of the z component is simply l. Classically, $l \to \infty$ so that $\sqrt{l(l+1)} \simeq l$ and the measure of J and J_z agree. Schematically, one can imagine the situation pictured in figure IV.3. The magnitude of J is constant and equal to $\sqrt{l(l+1)}$, while the measure of the z component can take all values between $-l$ and l.

Spin and orbital angular momentum. There are two possible sources of angular momentum for particles: the orbital angular momentum $\mathbf{L} = \mathbf{r} \times \mathbf{p}$, due to the movement of the particle, and the intrinsic spin angular momentum $\mathbf{S}$. The orbital angular momentum has a classical analogue ($\mathbf{L} = \mathbf{r} \times \mathbf{p}$ is the classical expression of angular momentum), while the spin angular momentum does not. In particular, one can show using spherical coordinates that the eigenvalue equation for the orbital angular momentum component J_z imposes $l \in \mathbb{N}$, and consequently m takes $2l + 1$ different values.

Conversely, the spin angular momentum of some particles, such as electrons, protons or neutrons, $m = \pm\frac{1}{2}$ so that $l = \frac{1}{2}$.

Angular momentum raising and lowering operators. We define the angular momentum raising (J_+) and lowering (J_-) operators as

$$J_\pm = J_x \pm i J_y. \tag{IV.13}$$

Let us consider an angular momentum eigenstate $|m, l\rangle$, i.e $J_z |m, l\rangle = \hbar m |m, l\rangle$ and $J^2 |m, l\rangle = \hbar^2 l(l+1) |m, l\rangle$. We fix the value l of J^2, and write an angular momentum eigenstate $|m, l\rangle$ simply as $|m\rangle$. One can show that

$$J_+ |m\rangle = \hbar\sqrt{l(l+1) - m(m+1)}\, |m+1\rangle, \tag{IV.14}$$

$$J_- |m\rangle = \hbar\sqrt{l(l+1) - m(m-1)}\, |m-1\rangle. \tag{IV.15}$$

Bosonic representation. Instead of using the quantum number m, we can consider another[1] integer number n such that $m = l - n$. Since l is the maximum value of m (which represent a measure of the z component), we can interpret n as the number of spin deviation from its maximum value l, as pictured in figure IV.3. Since $-l \leqslant m \leqslant l$, the number of spin deviation satisfies $0 \leqslant n \leqslant n_{\max} = 2l$. We can introduce a new basis $|n\rangle_d = |m\rangle = |l-n\rangle$ where the d indicates that we consider the number of spin deviation instead of the eigenvalue of J_z. Using this new basis[2],

$$J_+ |m\rangle = \hbar\sqrt{l(l+1) - (l-n)(l-n+1)}\,|m+1\rangle \tag{IV.16}$$

$$= \hbar\sqrt{l^2 + l - (l^2 - 2nl + n^2 + l - n)}\,|l-n+1\rangle \tag{IV.17}$$

$$= \hbar\sqrt{2nl + n - n^2}\,|n-1\rangle_d = \hbar\sqrt{2l}\sqrt{1 + \frac{1-n}{2l}}\sqrt{n}\,|n-1\rangle_d \tag{IV.18}$$

$$= \hbar\sqrt{2l}\sqrt{1 - \frac{n-1}{2l}}\sqrt{n}\,|n-1\rangle_d\,, \tag{IV.19}$$

and we deduce that

$$J_+ |n\rangle_d = \hbar\sqrt{2l}\sqrt{1 - \frac{n-1}{2l}}\sqrt{n}\,|n-1\rangle_d\,. \tag{IV.20}$$

Recalling the properties $a|n_a\rangle = \sqrt{n_a}\,|n_a - 1\rangle$ and $a^\dagger a\,|n_a\rangle = n_a\,|n_a\rangle$ of a bosonic annihilation operator a, we can expect that

$$\sqrt{1 - \frac{a^\dagger a}{2l}}\sqrt{a}\,|n_a\rangle = \sqrt{1 - \frac{a^\dagger a}{2l}}\sqrt{n_a}\,|n_a - 1\rangle = \sqrt{1 - \frac{n_a - 1}{2l}}\sqrt{n_a}\,|n_a - 1\rangle\,, \tag{IV.21}$$

which suggests that

$$J_+ = \hbar\sqrt{2l}\sqrt{1 - \frac{a^\dagger a}{2l}}a, \tag{IV.22}$$

with hermitian conjugate

$$J_- = \hbar\sqrt{2l}a^\dagger\sqrt{1 - \frac{a^\dagger a}{2l}}. \tag{IV.23}$$

Additionally, $S_z\,|m\rangle = \hbar m\,|m\rangle$ gives $S_z\,|n\rangle_d = \hbar(l-n)\,|n\rangle_d$ so that $S_z = \hbar(l - a^\dagger a)$. These results give a pseudo-justification of the Holstein-Primakoff transformation: an angular momentum operator can be described by a bosonic operator counting the number of spin deviation from the maximal value. We will see below that in the context of ferrimagnets, the maximum value of the angular momentum corresponds to the equilibrium state, so that a effectively counts the number of angular momentum excitation. Note that we can consider $-l$ to be the equilibrium state instead, we only need to redefine the bosonic operators to count the excitations in the other direction.

3.2) Quantum model of ferrimagnets

Ferromagnets, anti-ferromagnets and ferrimagnets can all be described using the Heisenberg exchange Hamiltonian

$$H_m = -\frac{1}{2}\frac{J}{\hbar^2}\sum_{\langle i,j\rangle}\mathbf{S}_i \cdot \mathbf{S}_j \tag{IV.24}$$

where $\mathbf{S}_i$ is the spin operator (with dimension of angular momentum) at position i, J is the exchange energy[3], and $\langle i,j\rangle$ restricts the sum to neighbouring lattice sites.

The origin of this interaction is rather complicated, but it is essentially due to the Coulomb interactions between electrons. This competes with other Coulomb interactions, notably the attractive Coulomb interaction between an electron and the nucleus. Of course, one needs

[1] Note that this is not the orbital number we discussed in section 2.1.

[2] Doing the same calculation for $J_-|m\rangle$ gives something inconsistent for $n = 0$.

[3] For historical reasons (see note 5 of chapter 20 of Simon [262].), the value of the exchange factor varies in the literature, another common choice being $2J$, e.g. used in [194].

to remember that most materials are not made up of a single atom: one also needs to consider screening effects, and the presence of other atoms, with a potentially different electronic structure. For further details, we refer to the reader to [194, 262].

For all of these reasons, the exchange energy can be positive or negative, and sometimes also position dependent. When $J > 0$, energy is lowered when the spins are aligned, so this describes a ferromagnetic behaviour. Conversely, $J < 0$ describes an anti-ferromagnetic behaviour. Here, we limit ourselves to ferromagnetic behaviour and so we assume $J > 0$ unless stated otherwise.

Before moving to the description of spin waves, we note that additional effects can be added to the exchange Hamiltonian, for instance long-range dipole-dipole interactions, or the dipolar interaction, which dominate for long wavelengths. These effects can be included [94, 221] by writing

$$H_m = -\frac{1}{2}\frac{1}{\hbar^2}\sum_{\langle i,j\rangle}\sum_{\alpha,\beta}\left[J\delta^{\alpha\beta} + D_{ij}^{\alpha\beta}\right]S_i^\alpha S_j^\beta \tag{IV.25}$$

where $D_{ij}^{\alpha\beta}$ is the dipolar tensor. In what follows, we neglect the dipolar tensor, and only consider the neighbouring spin/spin interaction, i.e. the simple Heisenberg Hamiltonian of equation (IV.24).

3.3) Quantum model of spin-waves

Spin waves are excitations of the magnetic order, and their quantisation leads to the magnon, the quasi-particle associated with a spin wave. The Heisenberg exchange Hamiltonian of equation (IV.24) can already successfully describe spin waves by considering a one-dimensional spin chain as shown in section 2.5 of [194]. The idea is to consider an elementary excitation of a ferromagnetic ground state, composed of all the spins oriented in the same direction. The resulting dispersion relation correctly describe the expected quadratic behaviour with the wave vector, but it lacks the energy offset due to the Zeeman term.

To find the appropriate dispersion relation, we can extend the Heisenberg Hamiltonian by considering a Zeeman interaction with an external magnetic field $\mathbf{B}_0$. The Hamiltonian becomes [194, 214, 257].

$$H_m = -\frac{1}{2}\frac{J}{\hbar^2}\sum_{\langle i,j\rangle}\mathbf{S}_i\cdot\mathbf{S}_j - \frac{g_L\mu_B}{\hbar}\sum_i^N\mathbf{B}_0(\mathbf{r}_i)\cdot\mathbf{S}_i. \tag{IV.26}$$

We further assume that the static applied magnetic field is constant over the magnetic sample, which is amounts to a *dipole approximation* that we discussed in the previous chapter. In the rest of this thesis, we consider the static magnetic field to be applied along z, so that $\mathbf{B}_0 = \mathbf{B}_0(\mathbf{r}_i)\hat{\mathbf{z}} = \mathbf{B}_0\hat{\mathbf{z}}$, and the Hamiltonian becomes

$$H_m = -\frac{1}{2}\frac{J}{\hbar^2}\sum_{\langle i,j\rangle}\mathbf{S}_i\cdot\mathbf{S}_j - \frac{g_L\mu_B B_0}{\hbar}\sum_i^N S_i^z. \tag{IV.27}$$

The rest of the derivation is rather cumbersome, so that we only discuss the main steps involved here, and leave the details of the full derivation for appendix B.6. The first step is to introduce local spin raising and lowering operators $S_i^\pm$, similar to equation (IV.13). We can then use a Holstein-Primakoff transformation to introduce bosonic operators m_i counting the spin excitation at the i-th lattice site. This is valid provided that the local number of spin excitations, given by $m_i^\dagger m_i$, is small[1].

Expanding the Hamiltonian to second order in the bosonic operators m_i, we obtain a Hamiltonian suggestive of a tight-binding model[2]. Tight-binding models are naturally diagonalised in reciprocal space, which corresponds to considering collective excitations. In

[1] It is sufficient to be at low enough temperature so that thermal excitations of magnons are negligible. For YIG, room temperature suffices.

[2] We discuss the impact of higher-order terms below.

the context of magnons, we effectively consider collective spin excitations by introducing the bosonic operators $m_{\mathbf{k}}, m_{\mathbf{k}^\dagger}$ with wave vector $\mathbf{k}$ defined as

$$m_{\mathbf{k}} = \frac{1}{\sqrt{N}} \sum_{j}^{N} e^{-i\mathbf{k}\cdot\mathbf{r}_j} m_j, \tag{IV.28}$$

where $\mathbf{r}_i$ the position of the i-th site of the crystal.

After some algebra, and up to a constant energy offset, we obtain

$$H_m = \sum_{\mathbf{k}} \hbar\omega_{\mathbf{k}} m_{\mathbf{k}}^\dagger m_{\mathbf{k}}. \tag{IV.29}$$

In the particular case of a cubic lattice (as for YIG), the centre of symmetry allows to simplify the dispersion relation $\omega_{\mathbf{k}}$, which in the long wavelength limit[1] reads

$$\hbar\omega_{\mathbf{k}} = \hbar\omega_0 + 2Jsa^2k^2 \tag{IV.30}$$

with $\hbar\omega_0 = g_L\mu_B B_0$ and s the value of the spin contributed by each lattice site.

In this thesis, we will only work with the so-called *Kittel mode*, where all the spins precess in phase, corresponding to $\mathbf{k} = 0$ [265]. The Hamiltonian for the matter degrees of freedom is then

$$H_m = \hbar\omega_m m^\dagger m \tag{IV.31}$$

with $\hbar\omega_m = \hbar\omega_{\mathbf{k}=0} = g_L\mu_B B_0$ and $m = m_{\mathbf{k}=0}$.

Higher-order terms in the Holstein-Primakoff transformation. There is a subtlety concerning the validity of the first-order approximation the Holstein-Primakoff transformation. If the local bosonic operator on site i is m_i, then we can expand of the Holstein-Primakoff to first order when $m_i^\dagger m_i \ll 2s$, with s the maximal value of the spin contributed by this lattice site. It is often said that s is big and the temperature is small, so that $m_i^\dagger m_i \ll 2s$ is verified. However, at a single lattice site, s is not big, e.g. for YIG $s = \frac{5}{2}$. Still, the approximation is still valid. Indeed, the operators $m_i, m_i^\dagger$ correspond to spin excitations in position space, which costs an energy on the order of the critical temperature, above which ferromagnetic behaviour vanishes (see section 2.5.2 of [266] for a discussion). This is in contrast with the operators in reciprocal space, where the energy of thermal excitation is given by $\omega_{\mathbf{k}}$ instead. For YIG, the critical temperature is $T_c = 580$ K, far above room temperature. We thus conclude that it is a good approximation to neglect higher-order terms, which lead to magnon-magnon interactions (see section 2.7.2 of [194], or [16]).

4) Microwave photon/magnon interaction

So far, we have explained how, in some materials such as YIG, the spins are arranged, and what are the elementary excitations of such a magnetic order. In this section, we shall examine the coupling of magnons with light at microwave frequencies. Intuitively, this coupling originates from another Zeeman interaction, but this time with a time-dependent magnetic field, that of a cavity mode. This coupling will therefore be able to excite the lowest order magnon mode: the Kittel mode.

4.1) Interaction Hamiltonian

We now derive the interaction Hamiltonian, following the supplementary material of Flower et al. [267]. The general idea of the derivation is as follows. Starting from the Zeeman interaction, one assimilate the magnetisation to a macrospin operator, describing the in-phase precession of all the spins, i.e. the Kittel mode. Then, invoking the Holstein-Primakoff transformation, one writes the relation between the macrospin operator $\mathbf{S}$ and a bosonic operator m representing the uniform magnon mode. Inserting the expression for the quantised magnetic field, we obtain the photon-magnon interaction Hamiltonian.

[1] This limit corresponds to $ak \ll 1$, with a the lattice constant and k the norm of $\mathbf{k}$.

Interaction term for photon-magnon coupling. As is often done in the literature [214, 267–269], we start from a macroscopic description and quantise it. Thus the starting point is interaction Hamiltonian

$$H_I = -\mu_0 \int_{V_m} \mathbf{M} \cdot \mathbf{h} \, \mathrm{d}V \tag{IV.32}$$

where $\mathbf{M}$ is the magnetisation, $\mathbf{h}$ the magnetic field of the cavity's mode, μ_0 the permeability of free space, and V_m the volume of the magnetic sample. The integration over the volume of the magnetic sample reminds us that the Zeeman term only exists in the region of space where there is a magnetisation $\mathbf{M}$.

The next step consists of expressing the interaction Hamiltonian in terms of a macrospin operator $\mathbf{S} = \sum_i \mathbf{s}_i$. For a homogeneous system, the macrospin[1] corresponds to the total magnetisation vector [94]. By definition of the magnetisation $\mathbf{M} = \boldsymbol{\mu}/V_m$, we have [94, 267, 269–271]

$$\mathbf{M} = -\frac{\gamma}{V_m}\mathbf{S} \tag{IV.33}$$

where $\gamma = \frac{g_e \mu_B}{\hbar} = 2\pi \times 28.04$ GHz/T is the gyromagnetic ratio and $g_L = 2$ is the Landé factor for pure spin[2]. Hence, we can write

$$H_I = -\int_{V_m} \mu_0 \frac{\gamma}{V_m} \mathbf{S} \cdot \mathbf{h} \, \mathrm{d}^3 r = \int_{V_m} \mathcal{H}_I \, \mathrm{d}^3 r \, . \tag{IV.34}$$

where we defined the Hamiltonian density $\mathcal{H}_I = -\mu_0 \frac{\gamma}{V_m} \mathbf{S} \cdot \mathbf{h}$.

Quantisation. We now express $\mathbf{S}$ and $\mathbf{h}$ using creation/annihilation operators. For $\mathbf{h}$, we simplify equation (III.20) by considering a single cavity mode of frequency $\omega_c/2\pi$ and in the interaction picture we write

$$\mathbf{h} = \frac{1}{\mu_0}\mathbf{b}(\mathbf{r}, t) = \frac{1}{\mu_0}\sqrt{\frac{\hbar}{2V_c \epsilon_0 \omega_c}}\left(c + c^\dagger\right) \nabla \times \mathbf{u}(\mathbf{r}) \tag{IV.35}$$

$$= \left(c + c^\dagger\right)(h_x \hat{\mathbf{x}} + h_y \hat{\mathbf{y}} + h_z \hat{\mathbf{z}}), \tag{IV.36}$$

where we defined $h_v = \frac{1}{\mu_0}\sqrt{\frac{\hbar}{2V_c \epsilon_0 \omega_c}} \nabla \times \mathbf{u}(\mathbf{r}) \cdot \hat{\mathbf{v}}$ for $v \in \{\hat{\mathbf{x}}, \hat{\mathbf{y}}, \hat{\mathbf{z}}\}$. Writing the macrospin $\mathbf{S} = S^x \hat{\mathbf{x}} + S^y \hat{\mathbf{y}} + S^z \hat{\mathbf{z}}$, the interaction Hamiltonian density is

$$\mathcal{H}_I = -\frac{\mu_0 \gamma}{V_m}\left(c + c^\dagger\right)(S^x h_x + S^y h_y + S^z h_z) \tag{IV.37}$$

We take $\hat{\mathbf{z}}$ to be the equilibrium direction of the macrospin $\mathbf{S}$ due to the static applied magnetic field $\mathbf{H}_0 = H_0 \hat{\mathbf{z}}$. Using the macrospin raising and lowering operators $S^\pm = S^x \pm i S^y$, we can then write

$$\mathcal{H}_I = -\frac{\mu_0 \gamma}{V_m}\left(c + c^\dagger\right)\left(\frac{h_x}{2}\left(S^+ + S^-\right) + \frac{h_y}{2i}\left(S^+ - S^-\right) + h_z S^z\right). \tag{IV.38}$$

Holstein-Primakoff transformation. We now use the Holstein-Primakoff transformation on the macrospin operators[3]. To first order, the transformations read[4]

$$S^+ = \hbar\sqrt{2S - m^\dagger m}\, m \simeq \hbar\sqrt{2S} m \tag{IV.39}$$

$$S^- = \hbar m^\dagger \sqrt{2S - m^\dagger m} \simeq \hbar\sqrt{2S} m^\dagger \tag{IV.40}$$

$$S^z = S - m^\dagger m \tag{IV.41}$$

[1] The macrospin formulation constitutes an approximation, see [199, 200] for instance.

[2] Recall that for YIG, the magnetic properties are exclusively due to spin, see section 2.1.

[3] Note that in the derivation of the magnon Hamiltonian, we used the Holstein-Primakoff transformation on spatially local spin operators, i.e. operators that depended on the spatial location instead.

[4] How are the bosonic operators m related to those of equation (B.119)? The answer is $m_{\mathbf{k}} = m$ for $\mathbf{k} = 0$. Indeed, the macrospin approximation assumes all spins precess in phase, i.e. it is the Kittel mode.

where S is the total spin [267]. The interaction Hamiltonian density comes out as

$$\mathcal{H}_I = -\frac{\mu_0\gamma}{V_m}\left(c+c^\dagger\right)\left(\frac{\hbar\sqrt{2S}}{2}h_x\left(m+m^\dagger\right) - \frac{i\hbar\sqrt{2S}}{2}h_y\left(m-m^\dagger\right) + h_z\left(S-m^\dagger m\right)\right). \quad \text{(IV.42)}$$

Integrating the Hamiltonian density over the magnetic sample volume[1], we finally obtain the interaction Hamiltonian

$$H_I/\hbar = -g_x\left(c+c^\dagger\right)\left(m+m^\dagger\right) + ig_y\left(c+c^\dagger\right)\left(m-m^\dagger\right) + g_z\left(c+c^\dagger\right)\left(m^\dagger m - S\right) \quad \text{(IV.43)}$$

where the interaction strengths are defined as [267]

$$g_x = \frac{\gamma\sqrt{2S}}{2V_m}\int_{V_m}\mu_0 h_x\,\mathrm{d}^3\mathbf{r} = \frac{\gamma}{2V_m}\sqrt{\frac{\hbar S}{V_c\epsilon_0\omega_c}}\int_{V_m}(\nabla\times\mathbf{u})\cdot\hat{\mathbf{x}}\,\mathrm{d}^3\mathbf{r} \quad \text{(IV.44)}$$

$$g_y = \frac{\gamma\sqrt{2S}}{2V_m}\int_{V_m}\mu_0 h_y\,\mathrm{d}^3\mathbf{r} = \frac{\gamma}{2V_m}\sqrt{\frac{\hbar S}{V_c\epsilon_0\omega_c}}\int_{V_m}(\nabla\times\mathbf{u})\cdot\hat{\mathbf{y}}\,\mathrm{d}^3\mathbf{r} \quad \text{(IV.45)}$$

$$g_z = \frac{\gamma}{V_m}\int_{V_m}\mu_0 h_z\,\mathrm{d}^3\mathbf{r} = \frac{\gamma}{V_m}\sqrt{\frac{\hbar}{2V_c\epsilon_0\omega_c}}\int_{V_m}(\nabla\times\mathbf{u})\cdot\hat{\mathbf{z}}\,\mathrm{d}^3\mathbf{r}\,. \quad \text{(IV.46)}$$

Note that in the presence of multiple YIG samples, these formulas remain valid by linearity: one just needs to be careful about integrating over the volume of the correct magnetic sample, and then it suffices to introduce additional lowering/raising operators $m', m'^\dagger$ for the Kittel mode of the second magnetic sample.

4.2) Further comments on the microwave photon/magnon interaction

Approximations. Note that if the magnetic sample is small compared to the cavity, one can consider the cavity magnetic field to be uniform over the sample [269]. Zhang, Scully, and Agarwal (2019) [272] justified why it's fine to consider that only the Kittel mode couples to the photons. It is also mentioned how the magnetic dipolar coupling between two magnets can be neglected over macroscopic distances of around 1 mm. Additionally, the magnetostrictive effect, i.e radiation pressure can be neglected if the length of the YIG spheres is much smaller than the microwave wavelengths [273].

Normalisation of the spatial eigenmodes. A useful normalisation of the mode function is that used in Flower et al. [267]. In the supplemental material of their work, they consider

$$\mathbf{h} = \frac{1}{\mu_0}\sqrt{\frac{\hbar}{2\omega_c\epsilon_0}}(c+c^\dagger)\nabla\times\mathbf{u} \quad \text{(IV.47)}$$

for the magnetic field[2]. They indicate that the relations

$$\mathbf{u} = \frac{\mathbf{E}}{\sqrt{\int_{V_c}|\mathbf{E}|^2\,\mathrm{d}^3r}} \quad \text{(IV.48)}$$

$$\nabla\times\mathbf{u} = \frac{\omega_c}{c}\frac{\mathbf{h}}{\sqrt{\int_{V_c}|\mathbf{h}|^2\,\mathrm{d}^3r}}, \quad \text{(IV.49)}$$

are normalised to cavity energy. What this means is that these expressions ensure that the classical electromagnetic energy density correspond to the zero point energy of the quantised electromagnetic field. These formula are checked in appendix B.4.

[1] Remember that the magnetisation $\mathbf{M}$, and hence $\mathbf{S}$, only exists within the YIG, so the Zeeman interaction vanishes outside of the magnetic sample volume V_m.

[2] The absence of the time-dependent exponentials can be understood by considering the Schrodinger picture.

Note that we have chosen to normalise the cavity modes with respect to the cavity volume V_c, and therefore the expressions of Flower et al. become

$$\mathbf{u} = \sqrt{V_c}\frac{\mathbf{E}}{\sqrt{\int_{V_c}|\mathbf{E}|^2\,\mathrm{d}^3r}}, \tag{IV.50}$$

$$\nabla\times\mathbf{u} = \sqrt{V_c}\frac{\omega_c}{c}\frac{\mathbf{h}}{\sqrt{\int_{V_c}|\mathbf{h}|^2\,\mathrm{d}^3r}} = \omega_c\sqrt{\epsilon_0\mu_0 V_c}\frac{\mathbf{h}}{\sqrt{\int_{V_c}|\mathbf{h}|^2\,\mathrm{d}^3r}}, \tag{IV.51}$$

Using the latter into equation (IV.44) we obtain

$$g_x = \frac{\gamma}{2V_m}\sqrt{\frac{\hbar S}{V_c\epsilon_0\omega_c}}\int_{V_m}(\nabla\times\mathbf{u})\cdot\hat{\mathbf{x}}\,\mathrm{d}^3\mathbf{r} \tag{IV.52}$$

$$= \frac{\gamma}{2V_m}\sqrt{\frac{\hbar S}{V_c\epsilon_0\omega_c}}\int_{V_m}\left(\omega_c\sqrt{\epsilon_0\mu_0 V_c}\frac{\mathbf{h}}{\sqrt{\int_{V_c}|\mathbf{h}|^2\,\mathrm{d}^3r}}\right)\cdot\hat{\mathbf{x}}\,\mathrm{d}^3\mathbf{r} \tag{IV.53}$$

$$= \frac{\gamma}{2V_m}\sqrt{\hbar\omega_c S\mu_0}\frac{\int_{V_m}h_x\,\mathrm{d}^3\mathbf{r}}{\sqrt{\int_{V_c}|\mathbf{h}|^2\,\mathrm{d}^3r}}, \tag{IV.54}$$

and similarly

$$g_y = \frac{\gamma}{2V_m}\sqrt{\hbar\omega_c S\mu_0}\frac{\int_{V_m}h_y\,\mathrm{d}^3\mathbf{r}}{\sqrt{\int_{V_c}|\mathbf{h}|^2\,\mathrm{d}^3r}}, \tag{IV.55}$$

$$g_z = \frac{\gamma}{V_m}\sqrt{\frac{\hbar\omega_c}{2}}\frac{\int_{V_m}h_z\,\mathrm{d}^3\mathbf{r}}{\sqrt{\int_{V_c}|\mathbf{h}|^2\,\mathrm{d}^3r}}. \tag{IV.56}$$

Coherent coupling strength. Both g_x and g_y above depend on S which is becomes a sizeable value due to the number of spin in the sample. On the other hand, g_z does not have such a scaling, and therefore we can drop this last term[1]. Then the interaction Hamiltonian of equation (IV.43) becomes

$$H_I = -\hbar g_x\left(c+c^\dagger\right)\left(m+m^\dagger\right) + i\hbar g_y\left(c+c^\dagger\right)\left(m-m^\dagger\right) \tag{IV.57}$$

$$= \hbar(c+c^\dagger)([-g_x+ig_y]m + [-g_x-ig_y]m^\dagger) \tag{IV.58}$$

$$= bar g_y\left(c+c^\dagger\right)\left(m-m^\dagger\right) \tag{IV.59}$$

$$= \hbar(c+c^\dagger)(gm+g^*m^\dagger), \tag{IV.60}$$

where we defined the complex-valued coupling strength $g = -g_x + ig_y$ describing the coherent coupling between photon and magnons.

Using the expressions of g_x and g_y above, the magnitude of the coupling strength can be written

$$|g|/2\pi = \frac{\sqrt{g_x^2+g_y^2}}{2\pi} = \frac{\gamma}{4\pi V_m}\sqrt{\hbar\omega_c S\mu_0}\frac{\sqrt{\left(\int_{V_m}\mu_0 h_x\,\mathrm{d}^3\mathbf{r}\right)^2+\left(\int_{V_m}\mu_0 h_y\,\mathrm{d}^3\mathbf{r}\right)^2}}{\sqrt{\int_{V_c}|\mathbf{h}|^2\,\mathrm{d}^3r}} \tag{IV.61}$$

$$= \sqrt{\frac{\left(\int_{V_m}\mu_0 h_x\,\mathrm{d}^3\mathbf{r}\right)^2+\left(\int_{V_m}\mu_0 h_y\,\mathrm{d}^3\mathbf{r}\right)^2}{V_m\int_{V_c}|\mathbf{h}|^2\,\mathrm{d}^3r}}\sqrt{\omega_c}\frac{\gamma}{4\pi}\sqrt{\frac{\hbar S\mu_0}{V_m}} \tag{IV.62}$$

Defining the form-factor [267]

$$\eta = \sqrt{\frac{\left(\int_{V_m}\mu_0 h_x\,\mathrm{d}^3\mathbf{r}\right)^2+\left(\int_{V_m}\mu_0 h_y\,\mathrm{d}^3\mathbf{r}\right)^2}{V_m\int_{V_c}|\mathbf{h}|^2\,\mathrm{d}^3r}}, \tag{IV.63}$$

[1] We shall return to this interaction in chapter VIII and in appendix C.9.

we obtain

$$|g|/2\pi = \eta\sqrt{\omega_c}\frac{\gamma}{4\pi}\sqrt{\frac{\hbar S}{V_m\mu_0}} = \eta\sqrt{\omega_c}A, \tag{IV.64}$$

with $A = \frac{\gamma}{4\pi}\sqrt{\frac{\hbar S}{V_m\mu_0}}$ a constant. At first sight the constant depends on the geometry of the magnetic sample though V_m and S. However, as shown by Bourhill et al. (2020) [274], the form-factor contains all the geometric information. Indeed, the total spin can be written $S = \frac{\mu}{g_L\mu_B}N_s$ with $g_L = 2$ the Landé $g-$factor of an electron spin, μ_B is the Bohr magneton, μ the magnetic moment of the material and N_s the number of spin it contains. Further introducing the spin density n_s, we have $N_s = n_s V_m$ and obtain [274]

$$|g/2\pi| = \eta\sqrt{\omega_c}\frac{\gamma}{4\pi}\sqrt{\frac{\mu}{g_L\mu_B}\mu_0\hbar n_s}, \tag{IV.65}$$

where now the constant A in equation (IV.64) only depends on the properties of the material, not its geometry. For instance, for Yttirum-Iron-Garnet we have $\mu = 5\mu_B$ and $n_s = 4.22 \times 10^{27}\,\mathrm{m}^{-3}$ which gives[1]

$$A = \frac{\gamma}{4\pi}\sqrt{\frac{\mu}{g_L\mu_B}\mu_0\hbar n_s} = 16568\sqrt{\mathrm{Hz}} \tag{IV.66}$$

with $\omega_c/2\pi$ and $g/2\pi$ expressed in Hertz. This suggests that increasing the coupling strength can be done by working at higher frequencies, or focusing the magnetic field better inside the magnetic sample to increase η. Intuitively, working at higher frequency can be done rather simply by simply scaling the dimensions down. However, we will see in section 5 that microwave cavities can be very sensitive to small geometric defects, so that miniaturisation ends up being more complicated than optimising the form-factor.

Expectation of a Dicke model. In section 3 of chapter III, we introduced the Dicke model, which described the interaction of many two-level systems with a single light mode. Since spins are two-level systems, it was rather natural to expect that the light-magnon Hamiltonian could be written in the form of a Dicke model. While it turns out to be the true, the derivation boils down to the quantisation of a magnetic dipole interaction, while the Dicke Hamiltonian rested on an electric dipole interaction instead.

4.3) Relevance of the coupling phase

The coherent coupling between a photon and a magnon described by equation (IV.60) depends on a complex-valued coupling strength $g/2\pi$. Such a complex number can be written $g = |g|e^{i\varphi}$, with $|g|$ its magnitude and φ its phase. In the literature, the phase φ has been ignored and therefore only the Hamiltonian

$$H_I = \hbar(c + c^\dagger)(gm + g^* m^\dagger) = \hbar|g|(c + c^\dagger)(m + m^\dagger), \tag{IV.67}$$

has been considered, instead of

$$H_I = \hbar|g|(c + c^\dagger)(e^{\varphi}m + e^{-\varphi}m^\dagger). \tag{IV.68}$$

Therefore, in the work of appendix C.1, published in *Physical Review Applied* [1], we investigate the physical relevance of these coupling phases. We find that ignoring these phases can lead to an incorrect description of multimode cavity magnonics systems, i.e. systems containing several cavity or magnon modes. Most notably, two applications of cavity magnonics systems are impacted: cavity-mediated coupling (useful for quantum information transduction) and dark mode physics (which can be used to create quantum memories [227]).

While this work was inspired by existing (unpublished) experimental data, the publication is only made up of theory. Naturally, the next step is to provide experimental evidence of these coupling phases, a topic we consider in section 5 below.

[1] Recall that $\gamma = 2\pi \times 28.024$ GHz/T is the gyromagnetic ratio for spins, and $\hbar = 1.05457 \times 10^{-34}$ J/s.

4.4) Classical electrodynamics model

Despite the quantum origin of magnetism, the physics of spin waves at room temperature can be described classically. The cavity-magnon polariton results from the interplay between photon and magnon dynamics, respectively described by Maxwell's equations and the Landau-Lifschitz-Gilbert equation. It is hence necessary to solve both these equations simultaneously, so that the "back action" of the magnetisation on the electromagnetic field is taken into account.

4.4.1) Landau-Lifschitz-Gilbert equation

The Landau-Lifschitz equation. The Landau-Lifschitz equation describes the response of the magnetisation $\mathbf{M}$ to an applied magnetic field $\mathbf{H}_0$. It reads [94]

$$\frac{\mathrm{d}\mathbf{M}}{\mathrm{d}t} = -\gamma \mathbf{M} \times \mathbf{H}_0, \tag{IV.69}$$

with $\gamma = \frac{g_L \mu_B}{\hbar}$ is the gyromagnetic ratio, g_L the Landé factor, and μ_B the Bohr magneton. It can be derived from classical mechanics and quantum mechanics [94]. This implies that the quantum average satisfy this equation too. Recalling the macrospin $\mathbf{S} = -V_m \frac{\mathbf{M}}{\gamma}$ we introduced in section 4.1, the Landau-Lifschitz equation shows that $\mathbf{S}$ precesses around $\mathbf{H}$.

In general, there are additional effective magnetic fields felt by the magnetisation, for instance due to exchange ($\mathbf{H}_{\mathrm{ex}}$), anisotropy ($\mathbf{H}_{\mathrm{an}}$), or a time-dependent electromagnetic field $\mathbf{h}_c$ due to a cavity mode. The Landau-Lifschitz equation keeps the same form,

$$\frac{\mathrm{d}\mathbf{M}}{\mathrm{d}t} = -\gamma \mathbf{M} \times \mathbf{H}, \tag{IV.70}$$

with $\mathbf{H} = \mathbf{H}_0 + \mathbf{H}_{\mathrm{ex}} + \mathbf{H}_{\mathrm{an}} + \mathbf{h}_c(t)$. At equilibrium, $\frac{\mathrm{d}\mathbf{M}_{\mathrm{eq}}}{\mathrm{d}t} = 0$ so that $\mathbf{M}_{\mathrm{eq}} \times \mathbf{H} = 0$ and hence $\mathbf{M}_{\mathrm{eq}}$ is collinear with $\mathbf{H}$. If the only magnetic field present is the static applied field $\mathbf{H} = \mathbf{H}_0 = H_0 \hat{\mathbf{z}}$, we find $\mathbf{M}_{\mathrm{eq}} \propto \mathbf{H}_0$ and the equilibrium magnetisation is aligned with the applied magnetic field. The presence of other magnetic fields, usually weak, leads to a deviation from this equilibrium state.

The Landau-Lifschitz-Gilbert equation. The Landau-Lifschitz equation represents an ideal, in which dissipation is neglected. This can be accounted for using the phenomenological Landau-Lifschitz-Gilbert equation [94, 226],

$$\frac{\mathrm{d}\mathbf{M}}{\mathrm{d}t} = -\gamma \mu_0 \mathbf{M} \times \mathbf{H} + \frac{\alpha}{M_s}\left(\mathbf{M} \times \frac{\mathrm{d}\mathbf{M}}{\mathrm{d}t}\right) \tag{IV.71}$$

where $\gamma = \frac{g_L \mu_B}{\hbar}$ is the gyromagnetic ratio for spins, g_L the Landé factor, μ_B the Bohr magneton, and α a phenomenological Gilbert damping constant. Solving this equation, we now obtain an exponentially decaying precession, thanks to the additional viscosity term. The Gilbert damping constant α takes values between 10^{-4} and 10^{-5} for YIG [94].

We note that while the LL equation can be derived, the inclusion of damping here is phenomenological[1]. Other possibilities to describe damping exist, for instance, Landau-Lifschiz originally introduced a damping term of the form [194]

$$\frac{\lambda \gamma \mu_0}{M_S} \mathbf{M} \times (\mathbf{M} \times \mathbf{H}_{\mathrm{eff}}). \tag{IV.72}$$

When the damping is small, this is equivalent to the LLG equation, but the latter is more convenient to work with mathematically[2].

[1] The LLG equation can still be derived quantum-mechanically, see page 9 of [17]. The idea is to consider the QLE for the magnon, and further assume it is in a coherent state. Then the equation of movement for the macrospin components should lead to the LLG equation. If the coupling to the bath is κ_m, we have $\kappa_m = \alpha \omega_m$, with $\omega_m/2\pi$ the FMR of the magnons

[2] See section 3.8 of Stancil and Prabhakar (2009) [194] for an example.

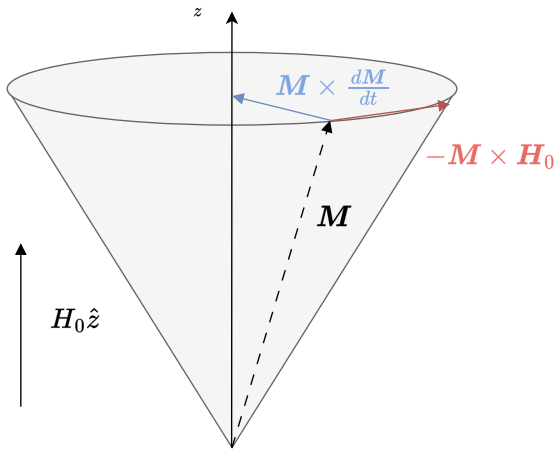


Figure IV.4: Precession of the magnetisation $\mathbf{M}$ around the static applied magnetic field $\mathbf{H}_0$, as described by equation (IV.71). Inspired from figure 3.14 of [194].

4.4.2) Linearisation

By expanding the Landau-Lifschitz-Gilbert equation, it is easy to see that it corresponds to three non-linear coupled differential equations, whose solution(s) is non-trivial. Without further approximations, one often has to resort to (computationally expensive) micromagnetic simulations to obtain the dynamics. Luckily, if we are only interested in the response of the magnetisation to a small RF perturbation, the Landau-Lifschitz-Gilbert equation can be linearised to give analytical solutions[1].

The method consists of splitting the magnetisation $\mathbf{M}$ and the magnetic field $\mathbf{H}$ into two contributions, one being time-independent equilibrium configuration (we adopt uppercase letters for these quantities), and the other time-dependent (lowercase letters). We consider the time-independent contribution to be a macroscopic magnetisation $\mathbf{M}_S = M_S\hat{\mathbf{z}}$ due to a static applied magnetic field $\mathbf{H}_0 = H_0\hat{\mathbf{z}}$. Formally, we write

$$\mathbf{M}(\mathbf{r},t) = \mathbf{M}_S + \mathbf{m}(\mathbf{r},t), \tag{IV.73}$$

$$\mathbf{H}(\mathbf{r},t) = \mathbf{H}_0 + \mathbf{h}(\mathbf{r},t). \tag{IV.74}$$

where $\mathbf{h}(\mathbf{r},t) = h_x(\mathbf{r},t)\hat{\mathbf{x}} + h_y(\mathbf{r},t)\hat{\mathbf{y}}$ is a small time-dependent magnetic field and $\mathbf{m}(\mathbf{r},t)$ a small time-dependent magnetisation. Physically, $\mathbf{h}$ perturbs the equilibrium magnetisation $\mathbf{M}_S$, which responds with a small magnetisation $\mathbf{m}$. For simplicity, we neglected the contribution of anisotropic and exchange interactions, we direct the reader to section 3.7.3 of [194] for such a treatment.

The leading order in small quantities corresponds to terms linear in lowercase letters, so that the LLG equation equation (IV.71) becomes

$$\dot{\mathbf{m}} = -\gamma\mu_0(\mathbf{M}_S + \mathbf{m}) \times (\mathbf{H}_0 + \mathbf{h}) + \frac{\alpha}{M_s}\left([\mathbf{M}_S + \mathbf{m}] \times \frac{\mathrm{d}\mathbf{M}_S + \mathbf{m}}{\mathrm{d}t}\right) \tag{IV.75}$$

$$= -\gamma\mu_0(\mathbf{M}_S \times \mathbf{h} + \mathbf{m} \times \mathbf{H}_0) + \frac{\alpha}{M_s}\mathbf{M}_S \times \dot{\mathbf{m}} + \mathcal{O}(\mathbf{h},\mathbf{m}), \tag{IV.76}$$

where we used $\mathbf{M}_S \times \mathbf{H}_0 = \mathbf{0}$. Following [94, 194, 226] this linearised equation can be solved for $\mathbf{h}$ as a function of $\mathbf{m}$ in frequency space, by writing $\mathbf{m}(\mathbf{r},t) = \mathbf{m}(\mathbf{r})e^{-i\omega t}$ and $\mathbf{h}(\mathbf{r},t) = \mathbf{h}(\mathbf{r})e^{-i\omega t}$.

As shown in appendix B.7.1, we find a relation $\mathbf{m} = \chi\mathbf{h}$ with the Polder susceptibility tensor

$$\chi = \begin{pmatrix} u & -iv & 0 \\ iv & u & 0 \\ 0 & 0 & 0 \end{pmatrix} \tag{IV.77}$$

[1] The solution given by the linearised LLG equation can also be obtained quantum-mechanically, see page 8 of [17].

with

$$u = \frac{\omega_M(\omega_0 - i\alpha\omega)}{(\omega_0 - i\alpha\omega)^2 - \omega^2} \simeq \frac{\omega_M(\omega_0 - i\alpha\omega)}{\omega_0^2 - \omega^2 - 2i\alpha\omega\omega_0}, \tag{IV.78}$$

$$v = \frac{\omega_M\omega}{(\omega_0 - i\alpha\omega)^2 - \omega^2} \simeq \frac{\omega_M\omega}{\omega_0^2 - \omega^2 - 2i\alpha\omega\omega_0}, \tag{IV.79}$$

where $\omega_M = \gamma\mu_0 M_S$ and $\omega_0 = \gamma\mu_0 H_0$ and the second equation is valid for small dampings[1]. The coefficients u and v describe a resonant response of the magnetisation when $\omega = \omega_0$: we deduce that the ferromagnetic resonance frequency $\omega_m/2\pi$ is given by $\omega_m = \omega_0$, similar to that obtained quantum-mechanically. This can also be interpreted by considering the torque: the torque acting on the spin precession must have the correct frequency, so that the torque is always acting "constructively" on the spin.

4.4.3) Linearisation with demagnetising factors

So far, we have neglected the impact of the geometry of the sample. The finite geometry of the sample modifies the FMR frequency due to demagnetising fields. A simple way to take it into account is to perform the replacements [226, 275]

$$h_x \mapsto h_x - N_x m_x, \tag{IV.80}$$

$$h_y \mapsto h_y - N_y m_y, \tag{IV.81}$$

$$H_0 \mapsto H_0 - N_z M_s \tag{IV.82}$$

where it is still assumed that $\mathbf{H}_0$ is along $\hat{\mathbf{z}}$. After some calculations detailed in appendix B.7.2, and neglecting terms of order α^2, we again find

$$\chi = \begin{pmatrix} u_y & -iv & 0 \\ iv & u_x & 0 \\ 0 & 0 & 0 \end{pmatrix} \tag{IV.83}$$

but where, for $j \in x, y$

$$u_j = \frac{\omega_M(\omega_0 + (N_j - N_z)\omega_M - i\alpha\omega)}{\omega_m^2 - \omega^2 - i\alpha\omega(2(\omega_0 - N_z\omega_M) + (N_x + N_y)\omega_M)}, \tag{IV.84}$$

$$v = \frac{\omega_M\omega}{\omega_m^2 - \omega^2 - i\alpha\omega(2(\omega_0 - N_z\omega_M) + (N_x + N_y)\omega_M)}, \tag{IV.85}$$

with

$$\omega_m^2 = (\omega_0 + (N_x - N_z)\omega_M)(\omega_0 + (N_y - N_z)\omega_M). \tag{IV.86}$$

Ferromagnetic resonance. We see that the expression of the ferromagnetic resonance frequency $\omega_m/2\pi$ is modified by the inclusion of the demagnetisation factors. Recalling that $\omega_M = \gamma\mu_0 M_S$ and $\omega_0 = \gamma\mu_0 H_0$, the FMR can be rewritten as

$$\omega_m = \gamma\mu_0\sqrt{(H_0 + (N_x - N_z)M_s)(H_0 + (N_y - N_z)M_s)}. \tag{IV.87}$$

For a spherical shape uniformly magnetised, it can be shown that $N_x = N_y = N_z = \frac{1}{3}$, in which case the FMR reduces to $\omega_m = \gamma\mu_0 H_0$. On the other hand, for a thin film [276],

$$\omega_m = \gamma\mu_0\sqrt{H_0(H_0 + M_S)}. \tag{IV.88}$$

As we mentioned before, the Kittel mode corresponds to a uniform precession of spins with a homogeneous magnetisation. This is the mode expected when a YIG sphere is homogeneously traversed by a magnetic field [269]. The Kittel formula for a YIG sphere reads

$$\omega_m = \gamma\mu_0(H_0 + H_A), \tag{IV.89}$$

[1] This is fine for small Gilbert damping α. Remember that for YIG, $10^{-4} \geqslant \alpha \geqslant 10^{-5}$ [94].

where we added a contribution from anisotropy, which is expected to be small for YIG[1].

Returning to equation (IV.86), we can write

$$\omega_m = \sqrt{(\omega_0 + (N_x - N_z)\omega_M)(\omega_0 + (N_y - N_z)\omega_M)} \tag{IV.90}$$

$$= \sqrt{\omega_0^2 + \omega_0\omega_M(N_x + N_y - 2N_z) + \omega_M^2(N_x - N_z)(N_y - N_z)} \tag{IV.91}$$

$$= \omega_0\sqrt{1 + \frac{\omega_M}{\omega_0}\omega_M(N_x + N_y - 2N_z) + \left(\frac{\omega_M}{\omega_0}\right)^2(N_x - N_z)(N_y - N_z)}. \tag{IV.92}$$

Since $\frac{\omega_M}{\omega_0} = \frac{M_S}{H_0}$, and usually $M_S < 200$ mT, we can assume $\frac{\omega_M}{\omega_0} \ll 1$ and expand the square root to find

$$\omega_m = \omega_0 + \frac{1}{2}\omega_M(N_x + N_y - 2N_z) + \mathcal{O}\left(\left(\frac{\omega_M}{\omega_0}\right)^2\right). \tag{IV.93}$$

Recalling that $\gamma = 28$ GHz/T, note that $H_0 < 200$ mT corresponds to frequencies below 5.6 GHz.

Analytical response for small dampings. The solutions are elliptically polarised modes [226]

$$m^+ = Dm_x + im_y, \quad h^+ = h_x + iDh_y, \tag{IV.94}$$

with ellipticity

$$D = \sqrt{\frac{\omega_0 + (N_x - N_z)\omega_M - i\alpha\omega}{\omega_0 + (N_y - N_z)\omega_M - i\alpha\omega}}. \tag{IV.95}$$

Note that for spherical sample, $N_x = N_y = N_z = \frac{1}{3}$, so that $D = 1$ and the magnetisation is circularly polarised[2]. Further assuming that $\omega_m \simeq \omega_0 + \frac{1}{2}\omega_M(N_x + N_y - 2N_z)$, we obtain [226]

$$m^+ = \frac{-\omega_M}{\omega - \omega_m + i\alpha\omega}h^+. \tag{IV.96}$$

Numerical solution. Depending on the cavity design, the form of the electromagnetic mode $\mathbf{h}$ can have a very complicated spatial dependence, and solving for the magnetisation using $\mathbf{m} = \chi\mathbf{h}$ is not analytically possible in general[3]. However, using Maxwell's equations in the absence of sources, and assuming the linear relationships

$$\mathbf{D} = \underline{\epsilon}\mathbf{E}, \quad \mathbf{B} = \underline{\mu}\mathbf{h}, \tag{IV.97}$$

with $\underline{\epsilon}$ and $\underline{\mu}$ the electric permittivity and magnetic permeability tensors, we can derive[4]

$$\boldsymbol{\nabla} \times \left[\underline{\epsilon}_r^{-1} \cdot \left(\boldsymbol{\nabla} \times \left(\underline{\mu}_r^{-1} \cdot \mathbf{B}\right)\right)\right] + k^2\mathbf{B} = 0 \tag{IV.98}$$

with $k^2 = \frac{\omega^2}{c^2}$, c the speed of light. The magnetic permeability tensor $\underline{\mu} = \mu_0(\mathbf{1} + \chi)$, and using the boundary condition [94]

$$\mathbf{n} \cdot (\mathbf{B}_{\text{out}} - \mathbf{B}_{\text{in}}) = 0, \tag{IV.99}$$

one can numerically solve for $\mathbf{B}$, for instance using COMSOL Multiphysics®. From there, one can deduce $\mathbf{H}$, and then $\mathbf{m}$.

[1] Actually, it should be exactly zero in YIG, because anisotropy is due to spin-orbit coupling. Indeed, the magnetic properties of YIG are contributed by orbitals with no orbital angular momentum. The origin of the small anisotropy can be understood by going beyond the usual Saunder-Russel coupling scheme to determine the orbital momentum of electronic states. See section 3.6 of [194] for more details.

[2] Small deviations from this are due to anisotropy, which we recall is small for YIG.

[3] There are two cases in which this can be possible. First, when the symmetry of the problem is such that a "good basis" simplifies the problem (e.g. using spherical harmonics for a spherical magnet in a spherical cavity [277]). The second case consists of performing perturbation theory, which is only valid for magnetic sample that only weakly perturb the electromagnetic modes.

[4] See appendix B.8 for the details of the calculation.

5) Experimental aspects and cavity engineering

Microwave cavities are an essential ingredient of cavity magnonics systems. For instance, the measurement of such hybrid platforms are mostly performed through the measurement of the reflection and transmission coefficients of the cavity. Thus, understanding how to model, characterise and engineer cavities, both from a theoretical and experimental standpoint, naturally complements our discussion of cavity magnonics.

In section 5.1, we discuss the usage of COMSOL Multiphysics®[278], a finite element method (FEM) software, for modelling cavity magnonics systems. Finally, with the knowledge acquired in section 5.1, we conclude this chapter in section 5.2, by engineering cavities to experimentally verify the existence of the coupling phase described in the previous section.

5.1) COMSOL Multiphysics® for microwave cavity magnonics

Cavity magnonics systems are composed of two elements: the cavity photons, and the magnons. Concerning the former, we note that while the electromagnetic modes of certain cavities can be calculated simply, it is not the case for arbitrary geometry. Furthermore, while we discussed the theoretical calculation of the S parameters in chapter III, note that we did so under the Markov approximation, assuming a frequency-independent coupling of the cavity mode to the environment. Therefore, the results of the input-output formalism can only approximate the real response of cavities to external drives [279]. The RF module [280] of COMSOL Multiphysics® allows to precisely model and numerically compute several quantities of interest for cavities, notable the resonance frequencies of the cavity modes, the spatial dependence of their fields $\mathbf{E}, \mathbf{B}$, and the S parameters. Additionally, we saw above that the magnon-photon coupling strength depends on the form-factor η (see equation (IV.63)), which describes how much of the magnetic field is focused into the ferromagnetic sample. The optimisation of this quantity is best performed using numerical simulations. Finally, the electrodynamical approach of section 4.4 allows to define a magnetic permeability $\underline{\mu}$ which can be used by a finite element modelling software to compute the electromagnetic field in the presence of a ferromagnet. In other words, this allows to obtain the reflection and transmission spectrum of a cavity magnonics system, by examining the S parameters of the cavity.

Therefore, in the unpublished original work of appendix C.2, we investigate the usage of COMSOL Multiphysics® to model cavity magnonics systems. Because the results of COMSOL Multiphysics® accurately reproduces experimental data, we also discuss the experimental aspect of cavity magnonics in this work. This unpublished paper is written in a tutorial manner, giving a pedagogical introduction to cavity magnonics supported by the input-output formalism and the numerical results obtained from COMSOL Multiphysics®. In this work, the limitations of COMSOL Multiphysics® are also investigated, notably is accuracy. Additionally, we show how the coupling strength $g/2\pi$ between photons and magnons can be predicted through the numerical evaluation of the form-factor η derived in the previous section.

5.2) Coupling phase engineering

In the previous section, we showed in Gardin et al. (2023) [1] that the coupling phase depended on the relative orientation of the magnetic field through different magnetic samples in a multimode system. While we studied the physical consequences of the coupling phases, we only did so theoretically, and therefore our results lacked experimental verification. Therefore, in the original work of appendix C.3, submitted to *Physical Review Applied*, we engineer cavities such that different phases parametrise the physics. This serves to confirm the theoretical predictions [1], and experimentally exemplify the relevance of the coupling phases. In this paper, we framed our results in the language of synthetic gauge fields, which is the topic of the chapter. Therefore, we recommend reading the next chapter before reading the work of appendix C.3.

6) Conclusion

In summary, we introduced the field of coherent cavity magnonics at microwave frequencies, where spins couple to photons through a magnetic dipole interaction. The resulting Hamiltonian corresponds to the Dicke model, describing the linear coupling of two harmonic oscillators, one for the cavity mode, and the other for the magnon mode. The resulting physics was already analysed in section 4.1 of the preceding chapter, and in particular we found that the spectrum is characterised by an anti-crossing of energy levels.

The first-principle derivation of the magnon/photon coupling strength at microwave frequencies highlighted its dependence on the cavity geometry through the form-factor η and the resonance frequency $\omega_c/2\pi$, both of which can be predicted and engineered using COMSOL Multiphysics®. Additionally, we found that a coupling phase factor existed, and we verified its impact experimentally by engineering appropriate microwave resonators. The process by which the coupling phases can become relevant in some settings is reminiscent of those involved in Berry phases and the Aharonov–Bohm effect. Hence, we are naturally brought to examine the geometric phases and the associated physics in the next chapter.

Chapter V

Geometric phases and gauge fields

Summary

The contributions in chapter IV [1, 2] showed that a gauge-invariant phase existed in any loop-coupling of bosonic modes. In the case of magnon-photon coupling due to a Zeeman interaction, the coupling phases can make this gauge-invariant phase non-trivial. The goal of the present chapter is to understand better the occurrence of such gauge-invariant phases in general loop-coupled bosonic systems. We shall do so by studying geometric phases, which arise due to varying some physical parameter over a loop. To properly discuss geometric phases, we first need to introduce the notions of adiabatic and non-adiabatic evolutions, where the former will be revisited in chapter IX. Next, we review the different types of geometric phases, which can be abelian (non-degenerate energy levels) or non-abelian (degenerate energy levels), but also result from adiabatic or non-adiabatic evolutions. The applications of geometric phases to the circuit model of universal quantum computation are briefly discussed. Both adiabatic evolutions and geometric phases can be described using the formalism of gauge theories, thus we succinctly go over this formalism and apply it to geometric phases. This allows us to properly interpret gauge-invariant phases as $U(1)$ synthetic gauge fields mentioned in chapter IV. Finally, we speculate on the connections between the discrete gauge-invariant phases discovered in the previous chapter, and the standard (continuous) geometric phases.

Contents

1) Introduction . . . **91**
2) Non-adiabatic physics . . . **91**
2.1 Introduction on the harmonic oscillator . . . 91
2.2 Quantum adiabatic theorem and adiabatic approximation . . . 92
2.3 Application: massive particle in an harmonic potential . . . 94
2.4 Landau-Zener transitions . . . 95
3) Continuous geometric phases and their applications . . . **95**
3.1 Adiabatic abelian case: the Berry phase . . . 96
3.2 Non-abelian case: holonomies . . . 98
3.3 Non-adiabatic generalisations . . . 99
3.4 Application to quantum computation . . . 101
4) Gauge theories . . . **103**
4.1 Gauge symmetry in particle physics . . . 104
4.2 Gauge structure of geometric phases . . . 104
4.3 Further remarks and applications . . . 106
5) Discrete gauge-invariant phases . . . **107**
5.1 Connection to a particle in a magnetic field on a lattice . . . 107
5.2 Connection with geometric phases . . . 108
6) Conclusion . . . **108**

1) Introduction

In the previous chapter, we saw the appearance of an observable quantity when the system was loop-coupled. This phenomenon is reminiscent of the Berry phase [281] and the Aharonov–Bohm effect [282], where a phase factor appears due to slowly varying some physical parameter around a loop. Importantly, these factors only depend on geometrical properties of the set of parameters being varied, hence they are named geometric phases. Since the paper of Berry, the concept of a geometric phase has been linked to the closely related concept of conical intersections, which can be used to unify many different physical phenomena[1] under the same formalism.

The first formal description of geometrical phases given by Berry (1984) [281] assumed the slow variation of a set of parameters. Here, "slow" is a notion that refers to the concept of adiabaticity, which we formally define in section 2. When the *adiabatic condition* is broken, non-adiabatic physics comes into play, and some consequences will be discussed. Next, we begin our introduction to geometric phases and their application(s) in section 3. Two important types of geometric phases can be distinguished: the abelian case, leading to the well-known Berry phase, and the non-abelian case, leading to the concept of holonomies. For each of these types, one can further generalise them to the case of non-adiabatic evolutions. An interesting application of these geometrical phases is quantum computation, were different schemes were developed for different phases. A unifying formalism for the discussion of adiabatic physics and geometric phases are gauge theories, succinctly introduced in section 4. In light of these results, we return to the discrete gauge-invariant phases in section 5 and interpret them as synthetic gauge fields.

2) Non-adiabatic physics

2.1) Introduction on the harmonic oscillator

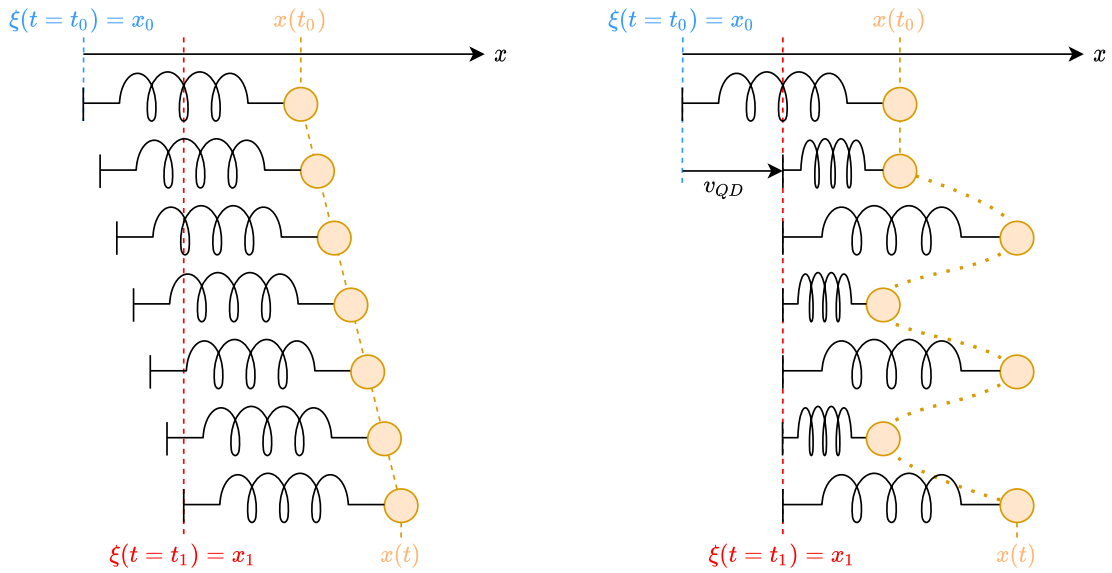
Terminology. In physics, a process is considered adiabatic[2] if it happens "slowly enough‘" that the system can be considered to remain at equilibrium at all times. In other words, if a perturbation is applied to a system "slowly" compared to other timescales, we can consider that the system adapts to that perturbation as it happens, remaining at equilibrium. This rather intuitive definition can be illustrated on the standard example in physics: the harmonic oscillator.

Classical example. Consider a one-dimensional harmonic oscillator made up of a mass attached to a spring as depicted in figure V.1. Assuming the system is at equilibrium at $t = 0$, if one pushes the spring over a fixed distance Δx with constant speed, we can observe two different behaviours depending on the time Δt over which this perturbation happened. If Δt is rather large (figure V.1a), we can expect the mass to continuously follow the displacement of the spring, and then the system "looks" like it remains at equilibrium at all times: this is an adiabatic process. However, if the spring were to be pushed faster over the same distance (i.e. smaller Δt for a fixed Δx, see figure V.1b), the spring would contract, and at the end of the perturbation the mass would continue oscillating due to the accumulated potential energy in the contracted spring. The resulting oscillations distinguish this non-adiabatic regime, from the adiabatic one.

The quantum analogy. The example of figure V.1 is purely classical, so what happens for a quantum harmonic oscillator? For this simple example, as shown in appendix B.12, the averages of the quantum model satisfy the classical equations of motion, so the classical model is a good approximation to understand non-adiabatic physics.

[1] Without being exhaustive, this covers spin-orbit couplings in cold-atom physics and condensed matter physics, the Jahn-Teller effect, the molecular Aharonov-Bohm effect, Bose-Einstein condensates, and band theories to describe e.g. superconductors, graphene and Weyl semimetals [96].

[2] This should not be confused with the notion of adiabaticity in thermodynamics, see the Wikipedia articles [283, 284] for a comparison.



(a) Adiabatic evolution

(b) Non-adiabatic evolution

Figure V.1: Example of adiabatic versus non-adiabatic physics using a mass-spring system. In both cases, the spring is pushed over a fixed distance Δx with constant speed over two different time scales Δt.

We can then conclude that the transition from the adiabatic to non-adiabatic regime is smooth, and hence rather arbitrary. Indeed, in this example, the observable allowing us to "see" the non-adiabatic regime is the amplitude of the oscillations of the mass at the end of the perturbation. But formally, any small deviation from the initial equilibirum position will lead to oscillations. Hence it is unclear at which value of the oscillation amplitude one can say that the non-adiabatic regime is reached. Luckily, this system being analytically solvable, one can decide which amplitude leads to the non-adiabatic regime, which of course shall depend on the application for which the system is being considered[1].

2.2) Quantum adiabatic theorem and adiabatic approximation

Adiabatic theorem. The intuition developed on the harmonic oscillator can be formalised by the *adiabatic theorem*, and we follow the approach of Larson, Sjöqvist, and Öhberg (2020) [96]. Consider a Hamiltonian H that depends on a set of time-dependent parameters described by the real-valued vector $\mathbf{R}$. We shall assume that the parameters are evolved in time over a runtime T, and thus it is convenient to introduce $s = \frac{t}{T} \in [0,1]$ to parametrise the evolution, where initially $t = 0$ and at the end $t = T$. The speed at which the evolution takes place can be controlled by adjusting T, and an infinitely slow process corresponds to the limit $T \to \infty$.

We expand the Hamiltonian in terms of the eigenstates $|\psi_{n,k}(s)\rangle$ where n indexes the degenerate energy level $E_n(s)$ with degeneracy g_n, so that and $1 \leqslant k \leqslant g_n$. Formally,

$$H(\mathbf{R}(s)) = \sum_{n=1}^{N} E_n(s) \left(\sum_{k=1}^{g_n} |\psi_{n,k}(s)\rangle \langle \psi_{n,k}(s)| \right) = \sum_{n=1}^{N} E_n(s) P_n(s), \tag{V.1}$$

where N is the number of energy levels and P_n the projector on the n-th eigenspace. We also introduce the time-evolution operator $U(s,0)$ which evolves a state from $s = 0$ to s, and formally reads [96]

$$U(s,0) = \mathcal{T}\left\{ \exp\left\{ -iT \int_0^s \mathrm{d}s' \, H(\mathbf{R}(s')) \right\} \right\} \tag{V.2}$$

[1] Another example discussed in chapter IX is that of a qubit based on a harmonic oscillator. Since we need a two-level system to have a qubit, we do not want the energy levels above the first excited states to be populated. The probability that the systems remains in the first two energy levels can be estimated, and made as small as required.

where $\mathcal{T}$ denotes time-ordering. Under the condition that the energy levels do not cross over $s \in [0,1]$, and that the functions E_n are sufficiently smooth functions[1] of s, then the adiabatic theorem reads [96]

$$\forall n \in \{1,\dots,N\}, \quad U(s,0)P_n(0) - P_n(s)U(s,0) = \mathcal{O}\left(\frac{1}{T}\right). \tag{V.3}$$

What the equation above tells us is that if the system is initially ($s = 0$) in some eigenstate $|\varphi\rangle = |\psi_n(\mathbf{R}(0))\rangle$, then in the limit of $T \to \infty$ this state becomes $|\varphi'\rangle = e^{i\gamma_n(s)} |\psi_n(\mathbf{R}(s))\rangle$ where $\gamma_n(s)$ is a (geometric) phase factor, which we shall discuss in the next section. In other words, up to a phase factor, the eigenstate is smoothly evolving from $|\psi_n(\mathbf{R}(0))\rangle$ to $|\psi_n(\mathbf{R}(1))\rangle$

Adiabatic approximation. Formally, the adiabatic theorem is only valid in the limit $T \to \infty$, which is never satisfied in practice. Instead, one can use the adiabatic approximation for a finite T. Consider an arbitrary solution $|\varphi(s)\rangle$ of the Schrödinger equation expanded in terms of the eigenstates $|\psi_{n,k}\rangle$ introduced above. One can write[2] $|\varphi(s)\rangle$ as [96]

$$|\varphi(s)\rangle = \sum_{n=1}^{N} e^{-iT\int_0^s \mathrm{d}s' E_n(s')} \sum_{k=1}^{g_n} c_{n,k}(s) \, |\psi_{n,k}(\mathbf{R}(s))\rangle \,, \tag{V.4}$$

where the $c_{n,k}$ are complex coefficients describing the probability of each eigenstates. One can show that these coefficients satisfy a system of differential equations which can be formally integrated to give [96]

$$\begin{aligned} c_{n,k}(s) = c_{n,k}(0) &- \sum_{l=1}^{g_n} \int_0^s \mathrm{d}s' \left\langle \psi_{n,k}(\mathbf{R}(s')) \middle| \tfrac{\partial \psi_{n,l}(\mathbf{R}(s'))}{\partial s} \right\rangle c_{n,l}(s') \\ &- \sum_{m=1,m\neq n}^{N} \sum_{l=1}^{g_n} \int_0^s \mathrm{d}s' \, e^{iT\int_0^{s'} \mathrm{d}s''(E_n(\mathbf{R}(s'')) - E_m(\mathbf{R}(s'')))} \left\langle \psi_{n,k}(\mathbf{R}(s')) \middle| \tfrac{\partial \psi_{m,l}(\mathbf{R}(s'))}{\partial s} \right\rangle c_{m,l}(s'). \end{aligned} \tag{V.5}$$

The first two terms characterise the adiabatic evolution of the system: they only involve the coefficients of index n, i.e. transition between eigenspaces of the same energy level E_n. On the other hand, the last term is responsible for non-adiabatic transitions between different energy ($m \neq n$) eigenspaces. In the non-adiabatic term, the transition rates between different energy eigenspaces are given by the brakets [96]. However, the adiabatic limit corresponds to the phase factors oscillating very fast compared to the transition rate between the different energy eigenspaces, so much so that this non-adiabatic term vanishes (this argument is similar to the rotating wave approximation). Formally, the adiabatic condition reads [96]

$$\forall m \in \{1,\dots,N\}, \quad T \gg \left| \frac{\left\langle \psi_{n,k}(\mathbf{R}(s)) \middle| \frac{\partial \psi_{m,l}(\mathbf{R}(s))}{\partial s} \right\rangle}{E_n(\mathbf{R}(s)) - E_m(\mathbf{R}(s)} \right|, \tag{V.6}$$

but using the Schrödinger equation it can also be written [96]

$$T \gg \left| \frac{\langle \psi_{n,k}(\mathbf{R}(s)) | \frac{\partial H(\mathbf{R}(s))}{\partial s} | \psi_{m,l}(\mathbf{R}(s)) \rangle}{\left(E_n(\mathbf{R}(s)) - E_m(\mathbf{R}(s))\right)^2} \right|. \tag{V.7}$$

To summarise, the adiabatic theorem holds in the limit of $T \to \infty$, but this result can be approximated by the adiabatic condition for a finite T. If the adiabatic condition is not met, then transitions to higher energy eigenstates becomes possible. This indicates that non-adiabatic physics can be seen as a resource to induce transitions from the ground state to other eigenstates, with a transition probability determined by the energy level spacing. This idea will be revisited in chapter IX.

[1] These conditions can be mathematically formalised, see [96].

[2] To convince yourself that this is valid, simply insert this expression in the Schrödinger equation $i\frac{\partial|\varphi(s)\rangle}{\partial s} = TH(\mathbf{R}(s))\,|\varphi(s)\rangle$ to see that it is indeed a solution.

2.3) Application: massive particle in an harmonic potential

As an application of these concepts, let us revisit the case of a one-dimensional harmonic oscillator which has been moved non-adiabatically, but this time quantum-mechanically. We shall assume that in the far past $t \to t_0 = -\infty$, the harmonic potential was at x_0 as in figure V.1. Then, the oscillator was non-adiabatically moved from x_0 to x_1 during $T = t_1 - t_0$ and from t_1 onward the oscillator remains at x_1. Choosing $x_1 = 0$ and $t_1 = 0$, the Hamiltonian for $t > t_1$ is time-independent and reads

$$H = \frac{p^2}{2m} + \frac{1}{2}m\omega^2 x^2, \tag{V.8}$$

where m is the mass of the particle, p its momentum and x its position operator.

For simplicity, let us assume that T is chosen such that the adiabatic condition is broken, but so that the final state of the system is confined to the two lowest energy levels $E_0 = \frac{\hbar\omega}{2}$ and $E_1 = E_0 + \hbar\omega = \frac{3}{2}\hbar\omega$, with eigenstates $|\varphi_0\rangle$ and $|\varphi_1\rangle$. The Hamiltonian can then be written in the $\{|\varphi_0\rangle, |\varphi_1\rangle\}$ basis as

$$H = \begin{pmatrix} E_0 & 0 \\ 0 & E_1 \end{pmatrix}, \tag{V.9}$$

while the initial state can be written

$$|\psi(t=0)\rangle = \sqrt{1-p}\,|\varphi_0\rangle + \sqrt{p}\,|\varphi_1\rangle = \begin{pmatrix} \sqrt{1-p} \\ \sqrt{p} \end{pmatrix}. \tag{V.10}$$

Here, the probability p will depend on how much the adiabatic condition has been broken. We will see below that in the case of perfect two-level systems, this probability can be calculated using the Landau-Zener formula, which we introduce in section 2.4 below.

Rabi oscillations. Let us turn our attention to the time evolution. The Schrödinger equation can be written $i\hbar\frac{\mathrm{d}|\psi\rangle}{\mathrm{d}t} = H|\psi\rangle$ or equivalently $\frac{\mathrm{d}|\psi\rangle}{\mathrm{d}t} + \frac{iH}{\hbar}|\psi\rangle = 0$. For a time-independent Hamiltonian, the solution is $|\psi(t)\rangle = e^{-\frac{i}{\hbar}Ht}|\psi(t=0)\rangle$. We can then write the time-evolution operator as

$$U(t) = e^{-\frac{i}{\hbar}Ht} = \begin{pmatrix} e^{-\frac{i}{\hbar}E_0 t} & 0 \\ 0 & e^{-\frac{i}{\hbar}E_1 t} \end{pmatrix} = \begin{pmatrix} 1 & 0 \\ 0 & e^{-\frac{i}{\hbar}\hbar\omega t} \end{pmatrix} e^{-i\frac{\omega t}{2}}. \tag{V.11}$$

Thus for $t > t_1$, this state becomes

$$|\psi(t)\rangle = U(t)\,|\psi(t=0)\rangle = \begin{pmatrix} 1 & 0 \\ 0 & e^{-i\omega t} \end{pmatrix} \begin{pmatrix} \sqrt{1-p} \\ \sqrt{p} \end{pmatrix} e^{-i\frac{\omega t}{2}} \tag{V.12}$$

$$= \left(\sqrt{1-p}\,|\varphi_0\rangle + e^{-i\omega t}\sqrt{p}\,|\varphi_1\rangle\right) e^{-i\frac{\omega t}{2}}, \tag{V.13}$$

and we see that the state of the system describes Rabi oscillations between the two eigenstates, induced by non-adiabatic transitions.

Evolution of the average position. Classically, we saw that at the end of the movement of the oscillator, the mass oscillates. For $t > t_1$, this behaviour can be obtained quantum-mechanically by computing the position expectation value of the time-evolved state of equation (V.13). Indeed,

$$\langle\hat{x}\rangle = \langle\psi(t)|\hat{x}|\psi(t)\rangle \tag{V.14}$$

$$= (1-p)\langle\varphi_0|x|\varphi_0\rangle + p\langle\varphi_1|x|\varphi_1\rangle + \sqrt{p(1-p)}\left[e^{-i\omega t}\langle\varphi_0|\hat{x}|\varphi_1\rangle + e^{i\omega t}\langle\varphi_1|\hat{x}|\varphi_0\rangle\right] \tag{V.15}$$

$$= (1-p)\langle\varphi_0|x|\varphi_0\rangle + p\langle\varphi_1|x|\varphi_1\rangle + 2\sqrt{p(1-p)}\cos(\omega t)\langle\varphi_0|\hat{x}|\varphi_1\rangle, \tag{V.16}$$

where we used the fact that the wave functions of the harmonic oscillator are real-valued in the last line. Thus, we see that because the system is in a superposition of eigenstates, the average position oscillates with period $\frac{2\pi}{\omega}$, as expected classically. In practice, these spatial oscillations can be used to detect non-adiabatic dynamics, for instance that of an electron in a single-electron pump at high frequencies [285]. Finally, note that while we studied the dynamics assuming the non-adiabatic transitions, a fully quantum-mechanical analysis of a forced quantum harmonic oscillator can be found in Husimi (1953) [286].

2.4) Landau-Zener transitions

In the problem above, we considered the physics of a system that was put in a superposition of eigenstates due to non-adiabatic transitions. In a case of two-level systems, the calculations of the non-adiabatic transitions can be performed within the Landau-Zener-Stückelberg-Majorana formalism, and this has found numerous applications in quantum information science [287, 288].

Formally, the problem can be described by the Hamiltonian

$$H(t) = -\frac{\Delta}{2}\sigma_x - \frac{\epsilon(t)}{2}\sigma_z = -\frac{1}{2}\begin{pmatrix} \epsilon & \Delta \\ \Delta & -\epsilon \end{pmatrix}, \tag{V.17}$$

where Δ can be interpreted as the coupling between the two states, and ϵ is a function allowing to sweep over the energy spectrum of the system. To understand this, note that the system can be diagonalised, and we find the eigen-energies [288]

$$E_\pm(t) = \pm\frac{1}{2}\sqrt{\Delta^2 + \epsilon(t)^2}, \tag{V.18}$$

which describes energy level repulsion when $E_\pm$ is plotted as a function of ϵ. Assuming that ϵ is a linear function time by writing $\epsilon(t) = vt$, then the probability p of the ground state at $t = -\infty$ transitioning to the excited state at $t = +\infty$ is given by the LZSM formula [288]

$$p = \exp(-2\pi\delta) = \exp\left(-\frac{\pi\Delta^2}{2\hbar v}\right), \tag{V.19}$$

where $\delta = \frac{\Delta^2}{4\hbar v}$. This latter parameter can be interpreted as a measure of the "adiabaticity" of the system (compare with the adiabatic condition given in equation (V.7)). The phase of the final state can also be calculated, but we shall not make use of it here.

The formula above gives the probability of non-adiabatic transitions assuming a linear sweep over ϵ, but another common use of the LZSM formalism is when the system is continuously swept back and forth over the anti-crossing. The harmonic modulation of the two-level system can be used for spectroscopy and interferometry, and for quantum state preparation [289, 290]. Notably, these techniques are used in various superconducting and semiconductor qubits, and for the latter more shall be said in chapter IX.

3) Continuous geometric phases and their applications

In the preceding section, we saw that according to the adiabatic theorem, if one starts in an eigenstate $|\psi_n(0)\rangle$ of some parameter-dependent Hamiltonian $H(\mathbf{R})$ at $t = 0$, then the system remains in the eigenstate $|\psi_n(t)\rangle$ at all times (provided the change in the parameters $\mathbf{R}$ is slow enough). However, the final state picks up two phase factors: a dynamical one, and a geometrical one. The dynamical phase factor is simply due to the time-evolution, and does not lead to any experimental observation. On the other hand, it an be shown that the geometrical phase factor is time-independent, and instead it depends on the path taken to vary the Hamiltonian's parameters $\mathbf{R}$.

In this section, we shall precise these observations, and examine how they can be leveraged for performing quantum computation. Our discussion will focus on states[1] (kets in a Hilbert

[1] A second-quantisation approach has been developed in [291], but requires the use of the Feynman's path integral.

space $\mathcal{H}$), which is the main approach used in the literature. The Hamiltonian is assumed to be parametrised by a real vector $\mathbf{R} \in \mathcal{M}$ of parameters, and thus we note $\mathcal{M}$ the parameter space. We note $\mathcal{V}_n$ the eigenspace of energy E_n of the Hamiltonian.

3.1) Adiabatic abelian case: the Berry phase

Derivation. We begin by considering the most simple case, where the Hamiltonian $H(\mathbf{R})$ only has non-degenerate energy levels E_n, and the evolution is adiabatic. We write a general solution $|\psi(t)\rangle$ of the Schrodinger equation in terms of the instantaneous eigenstates $|\psi_n(\mathbf{R}(t))\rangle$ as

$$|\psi(t)\rangle = \sum_{n=1}^{N} c_n(t)\,|\psi_n(\mathbf{R}(t))\rangle\,. \tag{V.20}$$

Inserting this expression into the Schrödinger equation, we obtain

$$i\hbar\frac{\partial\,|\psi(t)\rangle}{\partial t} = H(\mathbf{R}(t))\,|\psi(t)\rangle\,, \tag{V.21}$$

$$i\hbar\sum_{n=1}^{N}\left(\dot{c}_n\,|\psi_n(\mathbf{R}(t))\rangle + c_n\frac{\partial\,|\psi_n(\mathbf{R}(t))\rangle}{\partial t}\right) = \sum_{n=1}^{N} c_n E_n(\mathbf{R}(t))\,|\psi_n(\mathbf{R}(t))\rangle\,, \tag{V.22}$$

and multiplying by $\langle\psi_k(\mathbf{R}(t))|$ on both sides,

$$i\hbar\sum_{n=1}^{N}\left(\dot{c}_n\delta_{n,k} + c_n\left\langle\psi_k(\mathbf{R}(t))\middle|\frac{\partial}{\partial t}\psi_n(\mathbf{R}(t))\right\rangle\right) = \sum_{n=1}^{N} c_n E_n(\mathbf{R}(t))\delta_{n,k}, \tag{V.23}$$

$$\dot{c}_k + \sum_{n=1}^{N} c_n\left\langle\psi_k(\mathbf{R}(t))\middle|\frac{\partial}{\partial t}\psi_n(\mathbf{R}(t))\right\rangle = -\frac{i}{\hbar}E_k(\mathbf{R}(t))c_k. \tag{V.24}$$

In the adiabatic limit[1], this simplifies to

$$\dot{c}_k + c_k\left\langle\psi_k(\mathbf{R}(t))\middle|\frac{\partial}{\partial t}\psi_k(\mathbf{R})\right\rangle = -\frac{i}{\hbar}E_k(\mathbf{R}(t))c_k, \tag{V.25}$$

$$\dot{c}_k = -\frac{i}{\hbar}E_k(\mathbf{R}(t))c_k + i\left(i\left\langle\psi_k(\mathbf{R}(t))\middle|\frac{\partial}{\partial t}\psi_k(\mathbf{R}(t))\right\rangle\right)c_k. \tag{V.26}$$

Thus, after integrating, the coefficients c_k take the form of two phase factors

$$c_k(t) = e^{-\frac{i}{\hbar}\int_0^t \mathrm{d}t' E_k(\mathbf{R}(t'))}e^{i\gamma_k(t)}, \tag{V.27}$$

where the first is the usual dynamical phase factor due to time evolution, and the second is the geometrical phase

$$\gamma_k(t) = \int_0^t \mathrm{d}t'\,i\left\langle\psi_k(\mathbf{R}(t'))\middle|\frac{\partial}{\partial t'}\psi_k(\mathbf{R}(t'))\right\rangle \tag{V.28}$$

$$= \int_0^t \mathrm{d}t'\,i\left\langle\psi_k(\mathbf{R}(t'))\middle|\frac{\partial\mathbf{R}(t')}{\partial t'}\cdot\frac{\partial}{\partial\mathbf{R}(t')}\psi_k(\mathbf{R}(t'))\right\rangle \tag{V.29}$$

$$= \int_0^t \mathrm{d}t'\,\frac{\partial\mathbf{R}(t')}{\partial t'}\cdot i\left\langle\psi_k(\mathbf{R}(t'))\middle|\frac{\partial}{\partial\mathbf{R}(t')}\psi_k(\mathbf{R}(t'))\right\rangle \tag{V.30}$$

$$= \int_{\mathbf{R}(0),\mathcal{C}}^{\mathbf{R}(t)} \mathrm{d}\mathbf{R}\cdot i\,\langle\psi_k(\mathbf{R})|\boldsymbol{\nabla}\psi_k(\mathbf{R})\rangle\,, \tag{V.31}$$

where we defined the gradient operator $\boldsymbol{\nabla} = \frac{\partial}{\partial\mathbf{R}}$ acting on the parameter variables, and $\mathcal{C}$ is the path taken by the parameters $\mathbf{R}$ in $\mathcal{M}$.

[1] Recall that in the adiabatic limit, we cannot have transitions between eigenstates of different energy levels. Thus, the sum over $n \in \{1,\dots,N\}$ reduces to the single term $n = k$.

Characteristics of the geometric phase. Having changed the integration from the time variable to the parameters $\mathbf{R}$, we now see that the geometrical phase only depends on the path $\mathcal{C}$ taken by $\mathbf{R}$. Notably, any path can be taken – as long as their endpoints are identical – and it does not matter how fast this path is traversed. In other words, the phase γ_n is geometrical in the sense that it depends only the shape of the path taken. This interesting fact was first discussed in the seminal paper of Berry (1984) [281], and thus such an adiabatic geometrical phase is often called a *Berry phase*.

Note that $\langle\psi_k(\mathbf{R})|\boldsymbol{\nabla}\psi_k(\mathbf{R})\rangle$ is vector-valued because of the gradient, and is purely imaginary[1]. Assuming the path $\mathcal{C}$ is a loop, i.e. $\mathbf{R}(0) = \mathbf{R}(T)$, then, using Stoke's theorem, we can transform the integral over the path $\mathcal{C}$ to an integral over a surface in the parameter space $\mathcal{M}$, delimited by the path $\mathcal{C}$. Indeed, let us write $\mathbf{A}_k(\mathbf{R}) = i\langle\psi_k(\mathbf{R})|\boldsymbol{\nabla}\psi_k(\mathbf{R})\rangle$ and assume that $\mathbf{R} \in \mathbb{R}^3$, then by Stoke's theorem [292],

$$\oint_{\mathcal{C}} \mathrm{d}\mathbf{R}\cdot\mathbf{A}_k = -\iint_{\Sigma(\mathcal{C})} \mathrm{d}\sigma\,(\boldsymbol{\nabla}\times\mathbf{A}_k)\cdot\mathbf{n} \tag{V.32}$$

where $\Sigma(\mathcal{C})$ is the surface in parameter space determined by the contour $\mathcal{C}$, and $\mathbf{n}$ is the vector normal to thus surface. This alternative expression involves the *Berry curvature* tensor $F_{\mu\nu} = \partial_\mu(A_k)_\nu - \partial_\nu(A_k)_\mu$ which for three-dimensional vectors reduces to $\boldsymbol{\nabla}\times\mathbf{A}_k$, and describes the curvature of the parameter space [281, 292, 293]. Thus, expressed with the Berry curvature, the Berry phase clearly depends on the geometry of the parameter space, which further accounts for its geometric interpretation.

Cyclic evolution. Note also that up to a unitary transformation, states can pickup an arbitrary phase factor too. Thus, by a process similar to that we uncovered on the coupling phases in cavity magnonics (see chapter IV), the geometrical phases cannot be observable unless the parameters are varied cyclically. However, the Berry phases are eigenstate-dependent, i.e. they are indexed by n, which labels the eigenstates of different energies. Thus, in principle if we have an adiabatic evolution of a superposition of eigenstates, each of them would pickup a different phase factor after some time. Such dephasing may be measurable, and partly due to the Berry phase (different eigenstates imply different energy levels, and hence different dynamical phase factors) without the need of a cyclic evolution.

Connection to fiber bundles in differential geometry. The first formalisation of the geometric phase by Berry (1984) [281] was quickly[2] followed by a paper by Simon [294], in which the mathematical structure associated with Berry's phase was laid out. Indeed, the parameter space, which we shall note $\mathcal{M}$ from now on, has the mathematical structure of a manifold [295]. Thus, at each instant the Hamiltonian of the system can be described by a point $\mathbf{R} \in \mathcal{M}$. Recalling that $\mathbf{R}$ is a vector of scalars parameterised by time, $\mathbf{R}(t)$ is nothing but a curve in $\mathcal{M}$. In particular, if the evolution is cyclic with runtime T, then $\mathbf{R}(0) = \mathbf{R}(T)$ and $\mathbf{R}$ is a loop over the manifold $\mathcal{M}$. The loops over a manifold form a group, which for the Berry phase is simply the abelian[3] group $U(1)$. Thus, any abelian geometrical phase, obtained by adiabatic evolution, is often called a Berry phase.

One can show that if a state is to satisfy the Schrodinger equation, and that the adiabatic theorem holds, then this amounts to imposing that infinitesimally close states (in time) must be in phase [294]. Formally, this condition is [293, 294]

$$\left\langle \psi(t)\middle|\frac{\mathrm{d}}{\mathrm{d}t}\psi(t)\right\rangle = 0, \tag{V.33}$$

[1] To see this, apply the gradient operator to the normalisation condition $\langle\psi_n(\mathbf{R})|\psi_n(\mathbf{R})\rangle = 1$, and by the product rule we find $2\,\mathrm{Re}\{\langle\psi_n(\mathbf{R})|\boldsymbol{\nabla}\psi_n(\mathbf{R})\rangle\} = \mathbf{0}$ ($\mathbf{0}$ is the null vector), and hence all the components of the vector $\langle\psi_n(\mathbf{R})|\boldsymbol{\nabla}\psi_n(\mathbf{R})\rangle$ are purely imaginary. Note that this implies that the associated Berry phase γ_n is real.

[2] So quick in fact, that he published his analysis in 1983, while Berry's paper was only published in 1984.

[3] This means that two loops over $\mathcal{M}$ commute. Indeed, we trivially have $e^a e^b = e^b e^a$ for a and b two phases associated to different curves over $\mathcal{M}$.

which corresponds to the mathematical condition of *parallel transport* of vectors over manifolds. Thus, in the adiabatic limit, the evolution of states consists of a parallel transport between two points in $\mathcal{M}$. In differential geometry, this is usually done using a one-form called *connection* [295], which here is $i\langle\psi_k(\mathbf{R})|\boldsymbol{\nabla}\psi_k(\mathbf{R})\rangle$, and hence it is often called the Berry connection. Note also that the curvature $\boldsymbol{\nabla}\times\mathbf{A}$ of the space is usually a two-form (an antisymmetric second rank tensor field [295]), which in the simple case considered here reduces to the curl of some vector $\mathbf{A}$.

Finally, we see that in a sense each point $\mathbf{R}\in\mathcal{M}$ corresponds to a Hilbert space $\mathcal{H}$. Formally, $\mathcal{M}$ and $\mathcal{H}$ define a *vector bundle* [296], and after combining it with a group structure, we obtain a fibre bundle [297]. It is only natural that fibre bundles are the appropriate formalism to describe geometric phases. Indeed, they are adapted to the description of gauge theories [297], and we will see below (in section 4) that geometric phases arise from a gauge structure.

3.2) Non-abelian case: holonomies

Derivation. For our discussion of the Berry phase, we assumed that the energy levels were non-degenerate, so that the eigenspaces $\mathcal{V}_n$ were all of dimension one. We now return to the general case, which was first discussed by Wilczek and Zee (1984) [298], where the energy levels can be degenerate, with a degree of degeneracy g_n. The eigenstates of energy E_n are $|\psi_{n,k}\rangle$, where $1\leqslant k\leqslant g_n$, and form a basis of the eigenspace $\mathcal{V}_n$. We proceed as in the non-degenerate case above, and expand a general solution of the Schrodinger equation as

$$|\psi(t)\rangle=\sum_{n=1}^{N}e^{-\frac{i}{\hbar}\int_0^t\mathrm{d}t'E_n(t)}\sum_{k=1}^{g_n}c_{n,k}(t)\,|\psi_{n,k}(\mathbf{R}(t))\rangle\,, \tag{V.34}$$

where we see that we factored the dynamical phase factor out of the definition of the coefficients $c_{n,k}$. Inserting this expression into the Schrödinger equation $i\hbar\frac{\partial|\psi\rangle}{\partial t}=H(\mathbf{R})\,|\psi\rangle$ leads to

$$\begin{aligned}\sum_{n=1}^{N}e^{-\frac{i}{\hbar}\int_0^t\mathrm{d}t'E_n(t)}\sum_{k=1}^{g_n}\left(-\frac{i}{\hbar}E_n(t)c_{n,k}\,|\psi_{n,k}(\mathbf{R}(t))\rangle+\dot{c}_{n,k}\,|\psi_{n,k}(\mathbf{R})\rangle+c_{n,k}\frac{\partial\,|\psi_{n,k}(\mathbf{R})\rangle}{\partial t}\right)\\ =-\frac{i}{\hbar}\sum_{n=1}^{N}E_n(\mathbf{R})e^{-\frac{i}{\hbar}\int_0^t\mathrm{d}t'E_n(t)}\sum_{k=1}^{g_n}c_{n,k}\,|\psi_{n,k}(\mathbf{R})\rangle\,,\end{aligned} \tag{V.35}$$

and we see that the first term on the left hand side cancels with the right hand side. Multiplying by $\langle\psi_{m,l}(\mathbf{R})|$ on both sides,

$$\sum_{n=1}^{N}e^{-\frac{i}{\hbar}\int_0^t\mathrm{d}t'E_n(t)}\sum_{k=1}^{g_n}\left(\dot{c}_{n,k}\,|\psi_{n,k}(\mathbf{R})\rangle+c_{n,k}\frac{\partial\,|\psi_{n,k}(\mathbf{R})\rangle}{\partial t}\right)=0, \tag{V.36}$$

$$\sum_{n=1}^{N}e^{-\frac{i}{\hbar}\int_0^t\mathrm{d}t'E_n(t)}\sum_{k=1}^{g_n}\left(\dot{c}_{n,k}\delta_{n,m}\delta_{k,l}+c_{n,k}\left\langle\psi_{m,l}(\mathbf{R})\middle|\frac{\partial}{\partial t}\psi_{n,k}(\mathbf{R})\right\rangle\right)=0, \tag{V.37}$$

$$e^{-\frac{i}{\hbar}\int_0^t\mathrm{d}t'E_m(t)}\dot{c}_{m,l}+\sum_{n=1}^{N}e^{-\frac{i}{\hbar}\int_0^t\mathrm{d}t'E_n(t)}\sum_{k=1}^{g_n}c_{n,k}\left\langle\psi_{m,l}(\mathbf{R})\middle|\frac{\partial}{\partial t}\psi_{n,k}(\mathbf{R})\right\rangle=0, \tag{V.38}$$

and in the adiabatic limit[1],

$$e^{-\frac{i}{\hbar}\int_0^t\mathrm{d}t'E_n(t)}\dot{c}_{n,k}=-e^{-\frac{i}{\hbar}\int_0^t\mathrm{d}t'E_n(t)}\sum_{l=1}^{g_n}c_{n,l}\left\langle\psi_{n,k}(\mathbf{R})\middle|\frac{\partial}{\partial t}\psi_{n,l}(\mathbf{R})\right\rangle, \tag{V.39}$$

$$\dot{c}_{n,k}(t)=i\left(\sum_{l=1}^{g_n}i\left\langle\psi_{n,k}(\mathbf{R}(t))\middle|\frac{\partial}{\partial t}\psi_{n,l}(\mathbf{R}(t))\right\rangle\right)c_{n,l}(t). \tag{V.40}$$

[1] Once again, this amounts to restricting the sum over n to the $n=m$ term.

Compared to the Berry phase, the integration is not straightforward, because the quantity $\langle \psi_{n,k}(\mathbf{R}(t)) | \frac{\partial}{\partial t} \psi_{n,l}(\mathbf{R}(t)) \rangle$ is now matrix-valued. To see this, let us write $\mathbf{c}_n$ for the vector column of dimension g_n whose components are the $c_{n,k}$. Let us further define a matrix $A_n(t)$ with matrix elements

$$(A_n(\mathbf{R}(t)))_{kl} = i \left\langle \psi_{n,k}(\mathbf{R}(t)) \middle| \frac{\partial}{\partial t} \psi_{n,l}(\mathbf{R}(t)) \right\rangle, \quad k,l \in \{1,\dots,g_n\}. \tag{V.41}$$

Then we can rewrite equation (V.40) in matrix form as

$$\forall n \in \{1,\dots N\}, \quad \frac{\mathrm{d}}{\mathrm{d}t} \mathbf{c}_n(\mathbf{R}(\mathbf{t})) = i A_n(\mathbf{R}(t)) \mathbf{c}_n(\mathbf{R}(t)) \tag{V.42}$$

For the Berry phase, the energy levels were non-degenerate, and we had $g_n = 1$ for all energy levels $1 \leqslant n \leqslant N$. Thus, in the non-degenerate case the matrix A_n reduced to a one by one matrix, and equation (V.42) was easily integrated. On the other hand, in the general case of degenerate energy levels, A_n is a matrix which may not commute with itself at different times. To express the solution formally, one uses *time-ordering* $\mathcal{T}$, often encountered in quantum field theory [11, 188]. Hence, we can write the solution of equation (V.42) as

$$\mathbf{c}_n(\mathbf{R}(t)) = \mathcal{T} \exp\left(i \int_0^t \mathrm{d}t' \, A_n(\mathbf{R}(t')) \right), \tag{V.43}$$

and writing[1]

$$(A_n(\mathbf{R}(t)))_{kl} = \frac{\mathrm{d}\mathbf{R}}{\mathrm{d}t} \cdot \underbrace{i \langle \psi_{n,k}(\mathbf{R}(t)) | \boldsymbol{\nabla} \psi_{n,l}(\mathbf{R}(t)) \rangle}_{A_n(\mathbf{R})}, \tag{V.44}$$

as before, we have

$$\mathbf{c}_n(\mathbf{R}(t)) = \mathcal{P} \exp\left(i \int_{\mathbf{R}(0)}^{\mathbf{R}(t)} \mathrm{d}\mathbf{R}' \cdot A_n(\mathbf{R}') \right), \tag{V.45}$$

where $\mathcal{P}$ denotes the *path-ordering* of the curves $\mathbf{R}$ traced in parameter space.

Holonomies. The generalisation of loops over manifolds leads to the concept of holonomies, which was first discussed by Simon (1983) [294], and later generalised to non-abelian phases by Wilczek and Zee (1984) [298]. Holonomies describe loops over manifolds that start (and hence end) at some point $\mathbf{R}_0 \in \mathcal{M}$. The holonomies over a manifold form an algebraic structure called a group, and the geometric phases are representations of this group [299, 300].

For the Berry phase, the holonomy group was $U(1)$, so that the initial and final state only differ up to a phase factor, the Berry phase. Clearly, in the general case when the connection A_n is matrix-valued, the holonomy group is not abelian in general, because matrices don't commute.

As before, the quantity $A_n(\mathbf{R})$ defined in equation (V.44) is a connection in the sense of differential geometry. Similar to the abelian case, the Wilczek-Zee connection $A_n(\mathbf{R})$ allows to parallel transport the eigenstates of energy E_n over the manifold $\mathcal{M}$.

3.3) Non-adiabatic generalisations

So far, we have only considered geometric phases arising from adiabatic evolution. This begs the question of whether a concept similar to the geometric phases arises if the evolution is non-adiabatic. As early as 1987, Aharonov and Anandan (1987) [301] introduced a generalisation of the Berry phase for a non-degenerate Hamiltonian with cyclic evolution. The next year, this was extended to the non-abelian case by Anandan (1988) [302], where the requirement of cylic evolution is partly relaxed.

[1] Note that we have almost identical notations between $A_n(\mathbf{R}(t))$ and $A_n(\mathbf{R})$, which differ by the quantity $\dot{\mathbf{R}}$ used to perform the change of variable in the integral.

Non-adiabatic abelian case. The idea put forward by Aharonov and Anandan (1987) [301] to define a non-adiabatic version of the Berry phase is to consider the projective Hilbert space $\Pi_{\mathcal{H}}$, where $\mathcal{H}$ is the original Hilbert space. Indeed, they remarked that for any $|\psi\rangle \in \mathcal{H}$, then $e^{i\phi}|\psi\rangle \in \mathcal{H}$ describes the same physical state, since no measurement[1] can extract the phase $\phi \in \mathbb{R}$. The projective Hilbert space $\Pi_{\mathcal{H}}$ is thus defined as the set of equivalence classes $\left|\overline{\psi}\right\rangle = \left\{|\varphi\rangle\,, \quad \exists\phi \in \mathbb{R}, \quad |\varphi\rangle = e^{i\phi}|\psi\rangle\right\}$, or in other words the set of "rays". Let us call $\Pi : \mathcal{H} \to \Pi_{\mathcal{H}}$ the projection from the Hilbert space to the projective space $\Pi_{\mathcal{H}}$. Then, for any $\phi \in \mathbb{R}$, we have $\Pi(e^{i\phi}|\psi\rangle) = |\psi\rangle$, as illustrated in figure V.2. Note that the Schrödinger equation is satisfied by the states $|\psi\rangle \in \mathcal{H}$ of the Hilbert space, but not the rays $\left|\overline{\psi}\right\rangle$, albeit the latter correspond to the physical states.

Now we follow the approach presented in [303]. We consider a general state $|\psi\rangle \in \mathcal{H}$ which is evolved from $t = 0$ to T along a curve $\mathcal{C}$. To simplify the notations, we note $|\psi(t)\rangle \equiv |\psi(\mathcal{C}(t))\rangle$. Thus, $|\psi(t)\rangle$ traces a curve $\mathcal{C}$ in the Hilbert space $\mathcal{H}$ (see figure V.2), while its projection $\left|\overline{\psi}(t)\right\rangle = \Pi(|\psi(t)\rangle)$ traces a closed[2] curve $\Pi(\mathcal{C})$ in the projective Hilbert space. Since $\left|\overline{\psi}(0)\right\rangle = \left|\overline{\psi}(T)\right\rangle$, then there must exists $\phi \in \mathbb{R}$ such that $|\psi(T)\rangle = e^{i\phi}|\psi(0)\rangle$ (this is pictured as the difference in angles ϕ between $|\psi(0)\rangle$ and $|\psi(T)\rangle$ in figure V.2). We also have at each time $|\psi(t)\rangle = e^{i\gamma(t)}\left|\overline{\psi}(t)\right\rangle$, where γ must be such that $\gamma(T) - \gamma(0) = \phi$. Inserting the former expression into the Schrodinger equation, one finds for γ the equation [303]

$$\frac{\mathrm{d}}{\mathrm{d}t}\gamma = -\frac{1}{\hbar}\left\langle\overline{\psi}(t)\middle|H(t)\middle|\overline{\psi}(t)\right\rangle + i\left\langle\overline{\psi}(t)\middle|\frac{\mathrm{d}}{\mathrm{d}t}\overline{\psi}(t)\right\rangle, \tag{V.46}$$

which after integration gives

$$\gamma(T) = -\frac{1}{\hbar}\int_0^T \mathrm{d}t\,\left\langle\overline{\psi}(t)\middle|H(t)\middle|\overline{\psi}(t)\right\rangle + i\int_0^T \mathrm{d}t\,\left\langle\overline{\psi}(t)\middle|\frac{\mathrm{d}}{\mathrm{d}t}\overline{\psi}(t)\right\rangle. \tag{V.47}$$

By comparison with the adiabatic case, we guess that the first term is the dynamical phase[3], and that the second term is the geometric phase. Indeed, it was shown by Aharonov and Anandan (1987) [301] that the second term does not depend on the time variable, but only on the projective curve $\Pi(\mathcal{C})$. As an example, a non-adiabatic Berry phase was formalised by Tojo and Takeda (2023) [304] for heavy holes in a Si/SiGe structure with both Rashba and Dresselhaus spin-orbit interactions.

Non-adiabatic non-abelian case. We now turn our attention to the non-abelian case, first analysed by Anandan (1988) [302]. We assume that the Hilbert space $\mathcal{H}$ can be decomposed in two orthogonal subspaces $\mathcal{V}$ and $\mathcal{V}^{\intercal}$, so that $\mathcal{H}(t) = \mathcal{V}(t) \oplus \mathcal{V}^{\intercal}(t)$. We need not the evolution of the Hamiltonian H to be cyclic, but we do require that the subspace $\mathcal{V}$ is mapped back onto itself after some run time T, i.e. we impose $\mathcal{V}(0) = \mathcal{V}(T)$. We will need two bases to define the geometrical phases. The first is a smooth instantaneous basis of $\mathcal{V}(t)$, that we note $\{|\varphi_n(t)\rangle\}$, and which satisfies $|\varphi_n(0)\rangle = |\varphi_n(T)\rangle$. The second basis, written $\{|\psi_n(t)\rangle\}$, is chosen to coincide with $\{|\varphi_n(0)\rangle\}$ at $t = 0$, and for subsequent times it evolves according to the Schrödinger equation. Now since both $\{|\varphi_n(t)\rangle\}$ and $\{|\psi_n(t)\rangle\}$ are bases of the same space $\mathcal{V}$, they can be related by some unitary transformation U. In matrix form, we can write this relation $|\boldsymbol{\psi}(t)\rangle = U(t)\,|\boldsymbol{\varphi}(t)\rangle$, where the components of $|\boldsymbol{\psi}(t)\rangle$ ($|\boldsymbol{\varphi}(t)\rangle$) are the $|\psi_n(t)\rangle$ ($|\varphi_n(t)\rangle$).

As usual, inserting the expansion of an arbitrary $|\psi_n(t)\rangle$ in the Schrödinger equation, we find a differential equation for the matrix elements of $U(t)$, and its integration gives [303]

$$U(T) = \mathcal{T}\left\{e^{-i\int_0^T \mathrm{d}t(K(t)-A(t))}\right\} \tag{V.48}$$

where the matrix elements of K and A are

$$K_{nm}(t) = \frac{1}{\hbar}\langle\varphi_n(t)|H(t)|\varphi_m(t)\rangle\,, \quad A_{nm}(t) = i\left\langle\varphi_n(t)\middle|\frac{\mathrm{d}}{\mathrm{d}t}\varphi_m(t)\right\rangle. \tag{V.49}$$

[1] To see this, consider the expectation value $\langle\psi|A|\psi\rangle$ of an observable A associated to a measurement. Defining $|\varphi\rangle = e^{i\phi}|\psi\rangle$, then $\langle\psi|A|\psi\rangle = \langle\varphi|A|\varphi\rangle$ and we see that the phase ϕ does not affect the result.

[2] In the original paper of Aharonov and Anandan (1987) [301], and also in Zhang et al. (2023) [303], no argument is given as to why that is true.

[3] To convince yourself, imagine the adiabatic theorem holds, and notice that $\left\langle\overline{\psi}(t)\middle|H(t)\middle|\overline{\psi}(t)\right\rangle = \langle\psi(t)|H(t)|\psi(t)\rangle$.

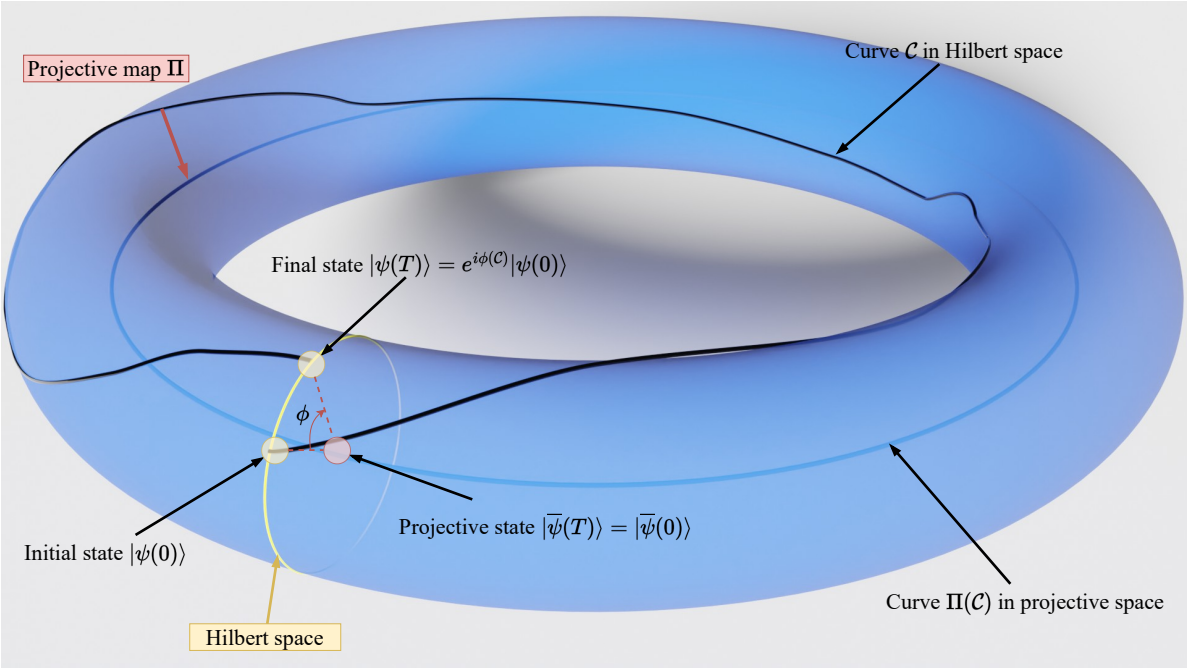


Figure V.2: Illustration of the difference between a Hilbert space and a projective Hilbert space. In the Hilbert space $\mathcal{H}$ (yellow ring), two states can differ by a phase factor and reduce to the same physical state $|\overline{\psi}\rangle$ in the projective Hilbert space $\Pi_{\mathcal{H}}$. A closed loop $\Pi(\mathcal{C})$ in the projective Hilbert space, corresponds to an open loop $\mathcal{C}$ in the Hilbert space, leading to a phase difference the two states in the Hilbert space.

We immediately recognise K as being the non-adiabatic generalisation of the dynamical phase discussed above (compare with the first term of equation (V.47)). Once again, the second matrix A can be shown to be purely geometric, in the sense that it only depends on the loop taken in the subspace $\mathcal{V}$.

Note that the time ordering applies to the total exponential, and the latter cannot simply be factored into two exponentials since the matrix A and K do not, in general, commute[1]. However, in the adiabatic case, the matrix K will commute with A [303], and the we can write

$$U(T) = \mathcal{T}\left\{e^{-i\int_0^T \mathrm{d}t K(t)}\right\}\mathcal{T}\left\{e^{i\int_0^T \mathrm{d}t A(t)}\right\} = \mathcal{T}\left\{e^{-i\int_0^T \mathrm{d}t K(t)}\right\}\mathcal{P}\left\{e^{i\int_{\mathcal{C}} A}\right\}, \tag{V.50}$$

and thus we recover the adiabatic non-abelian case of Wilczek and Zee (1984) [298]. Similarly, taking $\mathcal{V}$ to be a one-dimensional subspace of $\mathcal{H}$, then the matrices A and K reduces to a one by one matrix, and we recover the non-adiabatic abelian phase of Aharonov and Anandan (1987) [301]. Thus, the geometrical phase proposed by Anandan (1988) [302] is the most general geometrical phase.

3.4) Application to quantum computation

As shown above, an interesting property of geometrical phases is that their value depends only on the path taken in the manifold $\mathcal{M}$, or equivalently for cyclic evolutions, on the geometry of $\mathcal{M}$. This property is topological, which makes this phase immune to some decoherence processes. Therefore, encoding quantum information into geometric phases is an attractive option to increase its decoherence time. We can go even further and propose to perform quantum computation using these phases. Below, we shall quickly review, without technical details, the different schemes for performing so-called "geometric" quantum computation.

Terminology. Before starting, we should mention that all the phases described above have geometrical properties. Thus, they are all "geometrical" phases. Moreover, whether the phases

[1] In a recent paper by Yu and Tong (2023) [305], it was actually shown that the evolution operator could always be factored in a holonomic and dynamic part. Since this is a new result, we still follow the standard approach here, where the phases cannot be factored.

are abelian or non-abelian, they all correspond to some holonomy group. However, it seems that abelian holonomies are referred to as geometric phases, while non-abelian holonomies are simply called quantum holonomies [303]. Naturally, quantum computation schemes using geometric phases lead to geometric quantum computation (GQC), while those based on holonomies lead to holonomic quantum computation (HQC).

Adiabatic geometric quantum computation. Most applications of the Berry phases to quantum computation has been the creation of single-qubit phase-shift gates and conditional phase-shift gates for two qubits, see for instance Ekert et al. (2009) [306]. Combined with general single-qubit rotations (which can for instance be performed using standard dynamical evolution), a conditional phase-shift gate is sufficient for performing universal quantum computation. A notable obstacle to the realisation of these phase-shift gates is the dynamical phase, which needs to be removed. There are several methods to do this, such as making sure that the dynamical phases are multiples of 2π, spin echo, or a two-loop technique, which can be used in nuclear magnetic resonance (NMR) [306, 307]. In practice, aside from NMR, single-qubit and two-qubits gates using the Berry phase have also been realised in nitrogen vacancy centers [308].

Non-adiabatic geometric quantum computation. An obvious shortcoming of requiring adiabatic evolution is the long runtime[1]. Indeed, remember the second Di-Vicenzo criteria (introduced in section 4.2 of chapter II), we need the ability to apply several quantum gates to the state within its decoherence time, which a (slow) adiabatic gate is not well-suited for. For this reason, non-adiabatic versions of GQC were first proposed by Xiang-Bin and Keiji (2001) [310] to realise a phase-shift gates in NMR. Later on, universal single-qubit geometric gates were achieved in cold atoms [311], semiconductor quantum dots [312], nitrogen-vacancy centres [313] and superconducting qubits [314–316]. Similar to the adiabatic case, the dynamical phases need to be removed.

Unconventional geometric gates. Alternatively, it was shown that the dynamical phase can, in some settings, be proportional to the geometrical phases. Thus, one does not need to remove the dynamical phase anymore, since it also depends on geometrical features. This is advantageous over conventional phases, since the protocols commonly used to cancel the dynamical phases can introduce additional sources of noise and decoherence. These gates are called *unconventional geometric gates*. This concept was first introduced experimentally with trapped ions by Leibfried et al. (2003) [317], and later formalised by Zhu and Wang (2003) [318]. Shortly after, unconventional geometric gates were experimentally achieved in NMR [319], and other theoretical proposals followed for cavity QED [320–322].

Adiabatic holonomic quantum computation. In adiabatic holonomic quantum computation, one uses the adiabatic evolution of a non-abelian phase, as first described by Wilczek and Zee (1984) [298]. The first proposal by Zanardi and Rasetti (1999) [299] started the field of geometric quantum computation (indeed, their work actually precedes all the abelian schemes discussed above). Zanardi and Rasetti (1999) [299] proposed to encode quantum information in a degenerate eigenspace $\mathcal{V}_n(\mathbf{R}(t))$ of a family of Hamiltonians $H(\mathbf{R}(t))$. Under a cyclic evolution, the eigenstates of $\mathcal{V}_n$ are transformed following a unitary transformation $U_n(\mathcal{C})$ which depends on the loop $\mathcal{C}$ taken by the parameters $\mathbf{R}$. In general, the Wilczek-Zee connection (see equation (V.44)) does not commute for different loops taken in parameter space. Thus, the unitary transformations induced by two different loops do not commute. It can be shown that provided the topology of the parameter space manifold $\mathcal{M}$ is non-trivial, any unitary transformation can be approximated by a sequence of different loops, leading to universal quantum computation [300].

A fully optical proposal was put forward by Pachos and Zanardi (2001) [300], but the most common structure for adiabatic HQC is the tripod, where three ground states $|0\rangle, |1\rangle, |a\rangle$

[1] Lower bounds on the time required to create geometric phases have recently been given by Hörnedal and Sönnerborn (2023) [309].

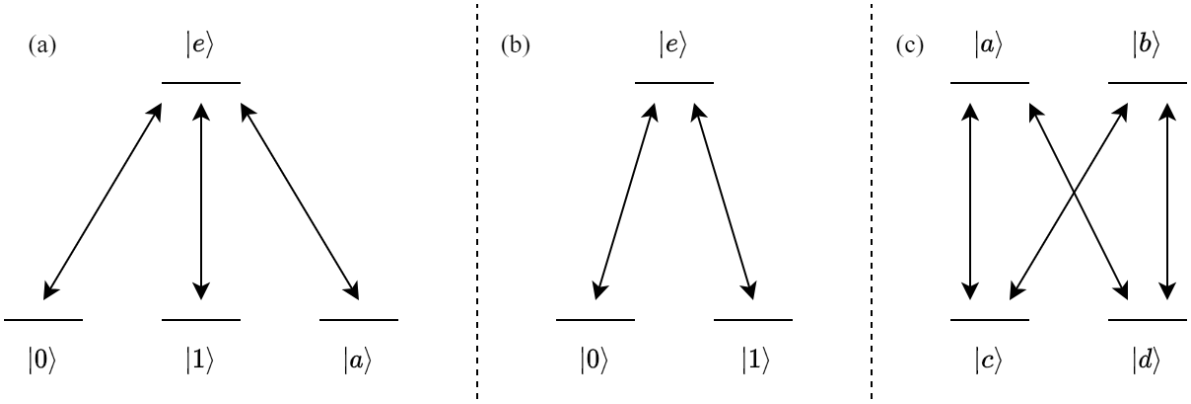


Figure V.3: Schematics of some interesting energy level stuctures to perform holonomic quantum computation. (a) Illustration of the tripod structure used for adiabatic HQC. (b) Illustration of the Λ level structure used for non-adiabatic HQC. (c) Illustration of the four-level structure used for non-adiabatic HQC.

are each coupled to a common excited state $|e\rangle$ (see figure V.3a). The tripod structure is sufficient to perform universal quantum computation [323], and fortunately many physical systems provide such a configuration, such as ion traps [324], neutral atoms [325], and excitons in semiconductors [326, 327]. Aside from the tripod structure, adiabatic holonomic gates were proposed in neutral atoms [328] and semiconductors [329–331].

Non-adiabatic holonomic quantum computation. As noted for adiabatic abelian quantum computation, their adiabatic non-abelian generalisation suffer equally from the long runtime required. Thus, non-adiabatic non-abelian quantum computation is the most promising approach for geometric quantum computation. As previously discussed, non-adiabatic non-abelian geometric phases are the most general type of geometric phases, and naturally many possibilities exist to perform quantum computation with them, see [332] for a recent review.

The first approach consists of using a so-called Λ configuration, which considers three energy levels as pictured in figure V.3b. This configuration can be engineered in superconducting qubits [333, 334], lattices of transmission lines based on transmon qubits [335, 336], nitrogen-vacancy centres [337, 338], NMR [339], trapped ions [340] and quantum dots [341]. When the two lowest energy levels are degenerate, the system has a dark state forming the subspace $\mathcal{V}$ on which quantum information is encoded. Sjoqvist et al. (2012) [342] showed that single-qubit gates could be achieved by performing two single-qubit rotations on different axes, and two-qubit gates could be implemented too. Several alternatives still based on the Λ configuration were later proposed [303] and demonstrated for instance in nitrogen vacancy centres [343] and Rydberg atoms [344]. An alternative configuration is the four-level scheme pictured in figure V.3c, which can for instance be created with superconducting circuits [345], quantum dots [346] or spins in solid-state [347]. Interestingly, a lattice of superconducting qubits in the ultrastrong coupling regime [348] seems to provide immunity to dephasing noise, and be promising for a scalable implementation of holonomic quantum computation.

Finally, a conceptually different method for achieving non-adibatic HQC consists of trying to "speed up" their adiabatic versions, using so-called *shortcut to adiabaticity (STA)* [349–351]. For instance, this was proposed for NV centres by Liang et al. (2016) [352] and later realised by Kleißler, Lazariev, and Arroyo-Camejo (2018) [313]. Alternatively, this was also realised in superconducting qubits by Yan et al. (2019) [353].

4) Gauge theories

Perhaps the most well-known application of gauge theories is to the field of particle physics, where gauge fields are a core concept used for the description of the standard model [354]. However, the ideas of gauge theories extend to other fields of physics such as condensed matter,

quantum mechanics and quantum information. Below, we shall briefly introduce how gauge fields are used in particle physics. Then, we shall discuss the gauge structure of adiabatic and non-adiabatic evolutions, and their connection to geometric phases.

4.1) Gauge symmetry in particle physics

Abelian gauge field: quantum electrodynamics. Let us illustrate how an abelian $U(1)$ gauge theory comes into play for quantum electrodynamics (QED), which describes the interaction of fermions with light. The starting point of QED is the Dirac Lagrangian of a spin half field ψ, which reads [11, 188]

$$\mathcal{L}_{\text{matter}} = \bar{\psi}\big(i\partial\!\!\!/ - m\big)\psi, \tag{V.51}$$

where $\partial\!\!\!/ = \gamma^\mu \partial_\mu$ with γ the Dirac matrices (also called gamma matrices) and m is the mass. One can show that the Euler-Lagrange equations give the Dirac equation $\big(i\partial\!\!\!/ - m\big)\psi = 0$ [188], which in the non-relativistic limit reduces to the Pauli equation [11] discussed in chapter IV. The Dirac lagrangian of equation (V.51) has a *global* $U(1)$ symmetry, i.e. changing $\psi \to e^{i\phi}\psi$ leaves the Lagrangian invariant.

The idea of gauge theories is to promote this global symmetry to a *local symmetry*, by making the phase spacetime dependent. Hence, the transformation of the fields we now consider is

$$\psi(x) \mapsto e^{i\phi(x)}\psi(x) \tag{V.52}$$

where x is the spacetime coordinate. Due to the spacetime dependence, the Dirac Lagrangian is not invariant anymore. The question answered by gauge theories is how the Dirac Lagrangian needs to be modified so that it remains invariant under such a local $U(1)$ symmetry.

The trick is to introduce an abstract field A_μ which transforms as

$$A_\mu(x) \mapsto A_\mu(x) - \frac{1}{q}\partial_\mu \phi(x) \tag{V.53}$$

Using this abstract field, we define a *covariant derivative* $D_\mu = \partial_\mu + iA_\mu$. Replacing simple derivatives by covariant derivatives in the Dirac Lagrangian, we obtain [11]

$$\mathcal{L}_{\text{matter}} = \bar{\psi}\big(iD\!\!\!/ - m\big)\psi = \bar{\psi}\big(i\partial\!\!\!/ - m\big)\psi - q\bar{\psi}\gamma^\mu A_\mu \psi, \tag{V.54}$$

where $D\!\!\!/ = \gamma^\mu D_\mu$. This new Lagrangian is now invariant under the local $U(1)$ symmetry: we see that the price to pay is to couple our fermions to a field (last term of equation (V.54)) following a certain transformation law.

This new field A_μ is called the gauge field, and in the example above its serve to enforce the local $U(1)$ symmetry. From the transformation law of the gauge field, one can guess that A_μ describes the four-potential of electromagnetism. The Lagrangian $\mathcal{L}_{\text{EM}}$ for the electromagnetic field can be expressed in terms of the electromagnetic field tensor $F_{\mu\nu} = \partial_\mu A_\nu - \partial_\nu A_\mu$ [11]. It can be shown that $\mathcal{L}_{\text{EM}} = -\frac{1}{4}F_{\mu\nu}F^{\mu\nu}$, and the Euler-Lagrange equations of motion give the four Maxwell's equations. Thus, considering $\mathcal{L} = \mathcal{L}_{\text{matter}} + \mathcal{L}_{\text{EM}}$, we obtain the Lagrangian for QED, describing the interaction between light and matter. To conclude with this example, we have shown that the gauge field introduced to ensure local $U(1)$ symmetry for spin half particles is nothing but the electromagnetic field.

This procedure has been generalised to non-abelian symmetry groups, leading to Yang-Mills theories [11, 188]. For instance, considering a $SU(3)$ symmetry instead, one obtains the theory of chromodynamics, describing the dynamics of quarks and gluons [188, 354].

4.2) Gauge structure of geometric phases

Gauge field for the Berry phase. Let us return to the geometric phases, and to begin we consider the situation of an abelian geometric phase for a cylic adiabatic evolution. In this setting, the Hamiltonian $H(\mathbf{R}(t))$ only has non-degenerate energy levels $E_n(\mathbf{R}(t))$, and the associated eigenstates $|\psi_n(\mathbf{R}(t))\rangle$ acquire the Berry phase

$$\gamma_n = \oint_{\mathcal{C}} \mathrm{d}\mathbf{R}\cdot A_n(\mathbf{R}) = -\iint_{\Sigma(\mathcal{C})} \mathrm{d}\sigma\,(\boldsymbol{\nabla}\times\mathbf{A}_n)\cdot\mathbf{n}, \tag{V.55}$$

where $A_n(\mathbf{R}) = i\langle\psi_n(\mathbf{R})|\boldsymbol{\nabla}\psi_n(\mathbf{R})\rangle$ is the Berry connection. The right-hand side of the equation above resembles the flux of some magnetic field $\mathbf{B}_n = \boldsymbol{\nabla}\times A_n$, which suggests that $\mathbf{A}_n$ is a gauge field. To check that this is indeed the case, we consider a gauge transformation[1] on the eigenstates

$$|\psi_n(\mathbf{R}(t))\rangle \mapsto e^{i\phi_n(\mathbf{R}(t))}\,|\psi_n(\mathbf{R}(t))\rangle\,, \tag{V.56}$$

where ϕ_n is real-valued. Then, one finds that the transformed gauge field $\mathbf{A}'_n$ is [303]

$$\mathbf{A}'_n(\mathbf{R}) = \mathbf{A}_n(\mathbf{R}) - \boldsymbol{\nabla}\phi_n(\mathbf{R}), \tag{V.57}$$

and hence $\mathbf{A}$ does transform like a gauge potential (compare with the transformation of A_μ for QED in equation (V.53)). Note the dependence of ϕ_n on $\mathbf{R}$, and in this sense the gauge transformation reflects a "local" $U(1)$ symmetry like the one we encountered for QED, and thus we obtained a similar gauge potential. Note that we have n independent gauge fields, one for each energy eigenstate.

Curvature tensor. We can rewrite the components $(\mathbf{B}_n)_{\mu\nu}$ of the magnetic field analogue as $F_n^{\mu\nu} = \partial^\mu A_n^\nu - \partial^\nu A_n^\mu$. This latter expression is akin to the electromagnetic field tensor we discussed for QED, and describes the curvature of the parameter space.

Gauge-invariance. Note that if a cyclic evolution is not performed, then one can gauge away the geometric phase. Thus, it cannot be physical. To see this, simply consider

$$\phi(\mathbf{R}) = \int_{\mathbf{R}(0)}^{\mathbf{R}} \mathrm{d}\mathbf{R}'\cdot A_n(\mathbf{R}'). \tag{V.58}$$

Then, equation (V.57) gives $A'_n(\mathbf{R}) = 0$, and thus the Berry phase vanishes. On the other hand, if the evolution is cyclic, then

$$\gamma_n = \oint_{\mathcal{C}} \mathrm{d}\mathbf{R}\cdot A'_n(\mathbf{R}) = \oint_{\mathcal{C}} \mathrm{d}\mathbf{R}\cdot(\mathbf{A}_n(\mathbf{R}) - \boldsymbol{\nabla}\phi_n(\mathbf{R})) \tag{V.59}$$

$$= \oint_{\mathcal{C}} \mathrm{d}\mathbf{R}\cdot A'_n(\mathbf{R}) - \underbrace{(\phi_n(\mathbf{R}(T)) - \phi_n(\mathbf{R}(0)))}_{=0} \tag{V.60}$$

$$= \oint_{\mathcal{C}} \mathrm{d}\mathbf{R}\cdot A_n(\mathbf{R}), \tag{V.61}$$

and thus the Berry-phase is a gauge-invariant quantity.

Non-abelian case. Let us now consider some eigenspace $\mathcal{V}_n$ of the Hamiltonian H with degeneracy g_n. As we discussed in the previous section, the eigenstates $|\psi_{n,k}(\mathbf{R}(t))\rangle$ of this subspace are related, up to a global dynamical phase factor, by

$$|\psi_{n,k}(\mathbf{R}(T))\rangle = U_n(\mathcal{C})\,|\psi_{n,k}(\mathbf{R}(0))\rangle \tag{V.62}$$

where the unitary matrix U_n is given by

$$U_n(\mathcal{C}) = \mathcal{P}\exp\left(i\int_{\mathcal{C}}\mathrm{d}\mathbf{R}'\cdot A_n(\mathbf{R}')\right) \tag{V.63}$$

for some contour $\mathcal{C}$, and the matrix-valued non-abelian connection

$$(A_n(\mathbf{R}))_{kl} = i\langle\psi_{n,k}(\mathbf{R})|\boldsymbol{\nabla}\psi_{n,l}(\mathbf{R})\rangle\,. \tag{V.64}$$

Compared to the abelian case above, performing a general gauge transformation on the eigenstates amounts to finding a new basis for the eigenspace $\mathcal{V}_n$. The new basis $|\varphi_{n,k}(\mathbf{R}(t))\rangle$ (or

[1] This "gauge transformation" is simply a way to say that we want to choose another set of eigenstates, or basis of the Hamiltonian. Since the eigenspaces of the Hamiltonian are assumed to be non-degenerate, they have dimension one. Thus, the other possible choices of eigenstates must be related to the original one by a scalar. To ensure normalisation, this scalar can only be a phase factor (ϕ_n).

equivalently choice of new eigenstates) must be related by a unitary transformation to the old basis $|\psi_{n,k}(\mathbf{R}(t))\rangle$, and thus we write [96, 303]

$$|\psi_{n,k}(\mathbf{R}(t))\rangle \mapsto |\varphi_{n,k}(\mathbf{R}(t))\rangle = \sum_{l=1}^{g_n} \left(\Phi_n(\mathbf{R}(t))\right)_{kl} |\psi_{n,l}(\mathbf{R}(t))\rangle \,, \tag{V.65}$$

where $(\Phi_n(\mathbf{R}))_{kl}$ are the matrix elements some unitary matrix $\Omega_n(\mathbf{R})$. Then, one can show that the gauge field A_n transforms as [298]

$$A_n(\mathbf{R}(t)) \mapsto A'_n(\mathbf{R}(t)) = \Phi_n^\dagger(\mathbf{R}(t)) A_n(\mathbf{R}(t)) \Phi_n(\mathbf{R}(t)) + i\Phi_n^\dagger(\mathbf{R}(t)) \frac{\mathrm{d}}{\mathrm{d}t} \Phi_n(\mathbf{R}(t)), \tag{V.66}$$

or in terms of the parameter variable $\mathbf{R}$ [96]

$$A_n(\mathbf{R}) \mapsto A'_n(\mathbf{R}) = \Phi_n^\dagger(\mathbf{R}) A_n(\mathbf{R}) \Phi_n(\mathbf{R}) + i\Phi_n^\dagger(\mathbf{R}) \boldsymbol{\nabla} \Phi_n(\mathbf{R}). \tag{V.67}$$

This last transformation law is that of a general non-abelian gauge field, and we can easily check that for the abelian case where $\Phi_n(\mathbf{R}) = e^{i\phi_n(\mathbf{R})}$, we recover the abelian transformation law of equation (V.57). A similar relation can be obtained for a non-adiabatic non-abelian geometric phase [302, 303].

As for the Berry phase, we can attempt to compute the non-abelian holonomy of equation (V.63) for a cyclic evolution using Stoke's theorem, and obtain

$$U_n(\mathcal{C}) = \mathcal{P} \exp\left(i \oint_{\mathcal{C}} \mathrm{d}\mathbf{R}' \cdot A_n(\mathbf{R}') \right) = \mathcal{P} \exp\left(-i \iint_{\boldsymbol{\Sigma}(\mathcal{C})} \mathrm{d}\sigma \, F_n \cdot \mathbf{n} \right), \tag{V.68}$$

where F_n is the gauge field's curvature tensor [96]

$$F_n^{\mu\nu} = \partial^\mu A_n^\nu - \partial^\mu A_n^\nu + i[A_n^\mu, A_n^\nu], \tag{V.69}$$

where the last term denotes a commutator, and we wrote A_n^μ for the matrix defined as

$$(A_n^\mu)_{kl} = i \, \langle \psi_{n,k}(\mathbf{R}) | \partial^\mu \psi_{n,l}(\mathbf{R}) \rangle \,, \tag{V.70}$$

with μ is indexing the component μ of $\mathbf{R}$. The curvature tensor of equation (V.69) has an expression formally identical to that of Yang-Mills theories for non-abelian gauge fields [11, 188] (e.g. the $SU(3)$ gauge theory of quantum chromodynamics [354]). Notice also that in equation (V.69), the commutator vanishes in the abelian case, and then we recover the curvature for the Berry phase or the electromagnetic field [11].

4.3) Further remarks and applications

In the examples above, we saw that the formalism provided by gauge theories is convenient to describe apparently very different physical phenomena. The core idea is that for some local symmetry to exist, a gauge field must be introduced.

Connection with symmetry. For QED and the Berry phase, the symmetry group was $U(1)$, leading to an abelian gauge field. Note that the representation of the group is different in each case: for QED the group acts on spin half fields, while for the Berry phase it acts on state vectors in a Hilbert space.

The other two examples we mentioned are quantum chromodynamics, with symmetry group $SU(3)$, and the non-abelian phases arising under adiabatic evolution. On may wonder what is the underlying symmetry group at play of the latter. The answer is provided by the gauge transformation of equation (V.65), where we see that the states are related by a $g_n \times g_n$ unitary matrix, with g_n the degree of degeneracy of the eigenspace. Thus, the symmetry imposed here is a local $U(g_n)$ symmetry.

Adiabatic gauge potential. Our discussion of the gauge structure of geometric phases has focused on adiabatic evolution. Adiabatic evolution is very convenient for several quantum information processing schemes, such as adiabatic computing, but one drawback is the slowness of the process, which needs to be contrasted with the usually short-lived coherence time of the system. One solution is to speed up adiabatic evolution using *shortcuts to adiabaticity* [349–351, 355–361] that we briefly mentioned for holonomic quantum computation. Among many such shortcuts [351, 355], counterdiabatic driving [357–362] is particularly useful, and can be framed in the language of gauge fields [360, 362, 363]. The idea is to introduce an adiabatic gauge potential, which acts to counteract the term responsible for non-adiabatic evolution. Hence, the gauge theory language is here used to obtain an effective non-adiabatic dynamics.

Synthetic gauge fields. While for QED the gauge field is the "real" electromagnetic field, for the Berry phase one obtains a "synthetic" electromagnetic field, or in other word a synthetic $U(1)$ gauge theory. Interestingly, such a synthetic $U(1)$ gauge field can have properties different from the standard electromagnetic field. For instance, one finds that for a macrospin $\mathbf{S}$ in a (real) magnetic field $\mathbf{B}$, described by the Zeeman Hamiltonian $H = -\mu\mathbf{S}\cdot\mathbf{B}$, the gauge structure is such that the associated synthetic magnetic field correspond to a monopole [96], which is not possible in standard electromagnetism (see chapter III).

In practice, non-trivial synthetic gauge fields are found in many domains of physics [364–366], for instance in spintronics [367], neutral atoms [368], trapped-ions [369], cavity QED [370], or Bose-Einstein condensates [371, 372]. Notably, they can be an important tool to induce topological properties in lattices [373] and non-hermitian systems [374].

Quantum computation. As discussed in the previous section, geometric phases can be used to perform universal quantum computation. Since geometric phases can be formulated in terms of gauge theories, we thus showed a connection between gauge theories and quantum computation. This relation has also been explored in measurement-based quantum computation [375], and it was found that the final result of a computation could be understood as the holonomy of some gauge field. As mentioned in chapter II, quantum walks and quantum cellular automata are alternative models of universal quantum computation. A general non-abelian $U(N)$ gauge symmetry was formulated for discrete-time quantum walks [376, 377] and similar work was performed for cellular automata [378–380]. In particular, imposing such gauge symmetries on cellular automaton was shown to lead to discrete formulations of quantum electrodynamics [381, 382].

5) Discrete gauge-invariant phases

5.1) Connection to a particle in a magnetic field on a lattice

In the previous sections, we introduced several concepts related to geometric phases, and we discussed their relation with $U(n)$ gauge fields. In chapter IV, we claimed that the coupling phases arising from the Zeeman photon-magnon interaction could combine to form $U(1)$ synthetic gauge fields. Here, we shall make this claim more precise by examining the discretised description of a particle in a magnetic field.

The discretisation of the Hamiltonian of a one-dimensional free particle of mass m and momentum p,

$$H = \frac{p^2}{2m}, \tag{V.71}$$

leads to a *tight-binding* model [383]. To simplify the discussion, we consider a single dimension, for which the discretisation of equation (V.71) takes the form

$$H = \sum_k \left(\epsilon a_k^\dagger a_k - t(a_k a_{k+1}^\dagger + a_k^\dagger a_{k+1})\right) \tag{V.72}$$

where ϵ is the on-side energy, t the "hopping" energy, and $a_k, a_k^\dagger$ respectively remove and create a particle at the lattice position indexed by k. In the presence of magnetic field, one needs

to include the vector potential A in equation (V.71), which is given by the minimal coupling replacement we introduced in chapter III. The Hamiltonian becomes

$$H = \frac{(p - qA)^2}{2m} \tag{V.73}$$

where q is the charge of the particle. Providing the vector potential varies slowly compared to the lattice spacing a, the discretisation of this Hamiltonian can be obtained by the *Peierls substitution*[1], which consists of adding a phase

$$\phi_k = a\frac{q}{\hbar}A_k \tag{V.74}$$

to the hopping terms, where A_j the value of the vector potential at the lattice position k. We thus obtain the tight-binding Hamiltonian

$$H = \sum_k \Big(\epsilon a_k^\dagger a_k - t(e^{i\phi_k} a_k a_{k+1}^\dagger + e^{-i\phi_k} a_k^\dagger a_{k+1})\Big). \tag{V.75}$$

We now see that ϕ_k plays a role similar to the coupling phases discovered in chapter IV. In equation (V.75), the phases originate from the presence of a magnetic field. The Hamiltonian of a coupled magnon-photon system with coupling phase φ,

$$H/\hbar = \omega_c c^\dagger c + \omega_m m^\dagger m + g\Big(e^{i\varphi} c m^\dagger + e^{-i\varphi} c^\dagger m\Big), \tag{V.76}$$

takes a formally identical form. Therefore, we can interpret the presence of the coupling phase φ as originating from a *Peierls substitution* of a particle evolving on a lattice, in the presence of a synthetic magnetic field. From our discussion of gauge fields in section 4, a magnetic field is associated with a $U(1)$ gauge field, and thus the magnon-photon coupling phase can be interpreted as arising from a synthetic $U(1)$ gauge field.

5.2) Connection with geometric phases

We now understand that te coupling phases of the magnon/photon coupling combine to create one gauge-invariant phase per loop. This process is reminiscent of geometric phases, and in the original work (neither published nor submitted) of appendix C.4 we consider the possible relations between the discrete and continuous cases.

6) Conclusion

In this chapter, we gave an introduction to the notion of adiabaticity in quantum mechanics, and we briefly discussed some applications of both adiabatic and non-adiabatic physics. We then used the concept of adiabaticity, to describe various geometric phases and discuss their application to quantum computing[2]. This allowed us to understand more precisely how the coupling phases analysed in the previous chapter can be interpreted as inducing synthetic gauge fields.

While the applications of standard geometric phases have been discussed, notice that nothing has been said about possible applications of the discrete phases. As we will see in the next chapter, synthetic gauge fields associated with the discrete phases are an essential element for the creation of non-reciprocal behaviours. Specifically, the second crucial element is the engineering of dissipation, which brings us to the study of dissipative couplings next.

[1] See section 2.2 of [384] for the details on a one-dimensional example, on which the present discussion is based.

[2] Note that non-abelian geometrical phases can also be useful for quantum memories [385] and charge pumping in superconducting devices [386, 387].

Chapter VI

Dissipative couplings and non-reciprocal behaviours

Summary

We describe how dissipative couplings between bosonic modes can appear due to their common coupling to an auxiliary mode or bath. The resulting effective Hamiltonian is shown to be characterised by level attraction, contrary to the usual level repulsion observed for coherent coupling. Next, we consider several experimental realisations of level attraction. We show that while dissipative coupling implies level attraction, the opposite is not necessarily true. In particular, we theoretically show that in a two-tone driving scheme, the observation of level attraction is simply due to interference in the measurement setup, and cannot be attributed to dissipative coupling. Finally, we discuss how the combination of dissipative coupling, coherent coupling, and synthetic gauge fields, can be used to create non-reciprocal behaviour.

Contents

1) Introduction **109**
2) Theory of dissipative coupling and level attraction **110**
2.1 Common coupling to a strongly dissipative mode 111
2.2 Common coupling to a bath 113
2.3 Analysis of the dissipative coupling Hamiltonian 114
3) Observations of level attraction **116**
3.1 Level attraction due to dissipative coupling 116
3.2 Level attraction in other physical systems 117
3.3 Anti-resonances in three-dimensional cavities 117
3.4 Two-tone driving in cavity magnonics 119
4) Engineering non-reciprocal behaviour **119**
4.1 Ring of three bosonic modes 120
4.2 Engineering non-reciprocal interactions in a ring of four bosonic modes 121
4.3 Controlling $U(1)$ gauge fields in loop-coupled systems 121
5) Conclusion **122**

1) Introduction

In the preceding chapters, the physics predominantly revolved around coherent couplings, resulting in the repulsion of energy levels. In this chapter, we consider dissipative couplings instead, which manifest as attraction of the energy levels. As suggested in the last chapter, dissipation is an essential ingredient for the realisation of non-reciprocal behaviour. Hence, the examination of dissipative couplings serves as a natural extension of our research. Apart from their application in achieving non-reciprocity, dissipative couplings are also of fundamental interest due to their connection with open quantum systems, giving rise to non-Hermitian physics.

Some applications of non-hermitian physics. Generally speaking, non-hermitian physics appear due to the coupling of an isolated system to the environment. We already saw an example of this in chapter III with the quantum Langevin equations (QLEs), which we used to model dissipation. This led to the introduction of an imaginary part to the mode's frequencies, leading to a non-hermitian effective[1] Hamiltonian. Non-hermitian physics can be engineered in many physical platforms using Floquet driving [388], but magnetic systems [389] and photonic lattices [390] are particularly convenient for investigating this exotic physics.

To understand some of these exotic behaviours, recall that in quantum mechanics observables are typically associated with Hermitian operators, ensuring real-valued spectra. While this holds for closed quantum systems, in the case of open quantum systems, the associated non-hermitian Hamiltonians allow for spectral singularities to appear. For instance, the non-Hermitian nature of the Hamiltonian allows for the emergence of complex-valued eigenvalues, and in particular the appearance of so-called *exceptional points (EP)*. Exceptional points correspond to the merging of the eigenvalues of the effective Hamiltonian, and provide increased sensibility for quantum sensing applications[2] [391]. Another type of singularity are bound states in the continuum (BIC)[3], with applications in sensing and filtering, notably in high-power scenarios [392]. Besides these practical applications, Floquet engineering allows to create various topological phases of matter (e.g. superconducting, semi-metallic) [393], and exceptional points (EPs) [394]. As an example, in magnonics, Floquet-engineered EPs were used to create diodes and logic gates taking advantages of thermal effects [395].

Furthermore, in various non-hermitian systems, a particular emphasis has been put on PT-symmetry, which leads to real-eigenvalues even though the system is non-hermitian. In PT-symmetric systems, which are omnipresent in photonics [390, 396–399], P corresponds to parity symmetry, and T to time-reversal symmetry [400]. Systems involving PT symmetry have been proposed for various applications, notably magnetometers taking advantage of EPs in cavity magnonics [391].

In practice, the study of PT symmetry, EPs, and BIC are facilitated in systems with dissipative couplings. Furthermore, such non-hermitian systems also have practical applications for quantum information processing, for instance it can be used for chiral Bell-state transfer [401], and enhance entanglement generation near EPs [402]. To summarise, our main motivations for the study of dissipative couplings are the engineering of non-reciprocal behaviour (when combined with synthetic gauge fields), and the creation of non-classical states.

Outline of the chapter. We begin this chapter in section 2 with the theory of dissipative coupling, which originates from an indirect coupling between two modes. The resulting effective Hamiltonians are showed to be described by a non-hermitian Dicke model, whose spectrum describes energy level attraction instead of the usual energy level repulsion. Next, we consider experimental observations of level attraction in section 3. We find that in some experiments, level attraction does originate from dissipative coupling, but this is not always the case. In particular, in optomechanics and two-tone driving, one can observe level attraction in the absence of dissipative coupling. Having surveyed experimental manifestation of level attraction, we finish by a discussion of their application to the creation of non-reciprocal behaviour in section 4.

2) Theory of dissipative coupling and level attraction

Dissipative coupling can be understood as an indirect coupling between two modes, mediated by another mode or a bath. This very general concept was first proposed by Metelmann and Clerk (2015) [403] as a tool to engineer non-reciprocal interactions, and encompasses various experimental realisations. To exemplify this, we derive an effective Hamiltonian leading to

[1] By effective, we mean that this Hamiltonian is such that the dynamics it implies correspond to the dynamics realised in practice. In a sense, this effective Hamiltonian is usually "reverse-engineered" from the equation of motions. See chapter III for an example.

[2] Apart from this application, an interesting connection between geometric phases and EPs exist. More precisely, encircling an EP usually gives rise to non-trivial geometric phases [96].

[3] For a good and short introduction, we also recommend the Wikipedia article on this topic.

dissipative coupling in two different experimental setups. In section 2.1, we examine the case where the indirect dissipative coupling is mediated by a mode, and then in section 2.2 we replace this mode by a one-dimensional waveguide. In both cases the effective Hamiltonian is the same, and we analyse its spectral features in section 2.3.

2.1) Common coupling to a strongly dissipative mode

We consider the system studied by Yu et al. (2019) [404] and pictured in figure VI.1, which consists of two bosonic modes a_1 and a_2 coupling to a common auxiliary mode a_3. The Hamiltonian is $H = H_{\text{free}} + H_I$ where

$$H_{\text{free}} = \sum_{k=1}^{3} \hbar\omega_k a_k^\dagger a_k, \tag{VI.1}$$

$$H_I = \hbar g_1(a_1 a_3^\dagger + \text{h.c}) + \hbar g_2(a_2 a_3^\dagger + \text{h.c}) + \hbar g(a_1 a_2^\dagger + \text{h.c}). \tag{VI.2}$$

Yu et al. (2019) [404] showed that if the dissipation rate $\kappa_3/2\pi$ of a_3 was sufficiently strong, then the indirect coupling between a_1 and a_2 mediated by a_3 is overcome by the dissipation and leads to an imaginary-valued coupling between a_1 and a_2.

The derivation proposed by Yu et al. (2019) [404] consists of first performing a Schrieffer-Wolff transformation[1] to decouple a_3 from a_1 and a_2, and find some indirect coupling between a_1 and a_2. Only then, did they introduce dissipation, but is unclear how this approach can be formally justified[2]. Instead, we are going to use the principle of adiabatic elimination, which is much simpler and easier to justify. We begin by writing the quantum Langevin equations (QLEs) we introduced in chapter III for each mode,

$$\dot{a}_1 = -i\Big(\omega_1 - i\frac{\kappa_1}{2}\Big)a_1 - iga_2 - ig_1 a_3 - \sqrt{\kappa_1}a_1^{\text{in}}, \tag{VI.3}$$

$$\dot{a}_2 = -i\Big(\omega_2 - i\frac{\kappa_2}{2}\Big)a_2 - iga_1 - ig_2 a_3 - \sqrt{\kappa_2}a_2^{\text{in}}, \tag{VI.4}$$

$$\dot{a}_3 = -i\Big(\omega_3 - i\frac{\kappa_3}{2}\Big)a_3 - ig_1 a_1 - ig_2 a_2 - \sqrt{\kappa_3}a_3^{\text{in}}, \tag{VI.5}$$

where $\kappa_k/2\pi$ are the dissipation rates and a_k^{in} the input noise operators. We now assume that the noise has zero mean $\langle a_k^{\text{in}}\rangle = 0$ and we neglect quantum fluctuations, replacing operators by their expectation values. Thus in the frequency domain[3] the QLE become

$$-i\omega\widetilde{a}_1 = -i\Big(\omega_1 - i\frac{\kappa_1}{2}\Big)\widetilde{a}_1 - ig\widetilde{a}_2 - ig_1\widetilde{a}_3, \tag{VI.6}$$

$$\omega\widetilde{a}_2 = \Big(\omega_2 - i\frac{\kappa_2}{2}\Big)\widetilde{a}_2 + g\widetilde{a}_1 + g_2\widetilde{a}_3, \tag{VI.7}$$

$$\Big(\omega - \omega_3 + i\frac{\kappa_3}{2}\Big)\widetilde{a}_3 = g_1\widetilde{a}_1 + g_2\widetilde{a}_2, \tag{VI.8}$$

and in particular we have

$$\widetilde{a}_3 = \frac{g_1\widetilde{a}_1 + g_2\widetilde{a}_2}{\omega - \omega_3 + i\frac{\kappa_3}{2}}. \tag{VI.9}$$

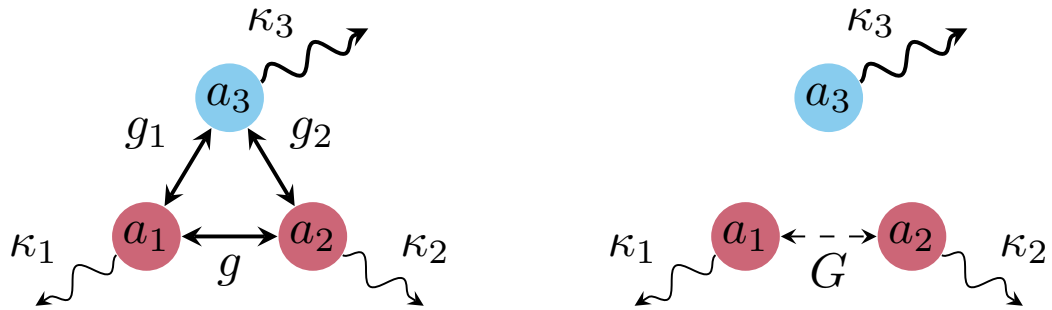
An *adiabatic elimination* of mode a_3 consists of assuming that $|\omega - \omega_3| \ll \frac{\kappa_3}{2}$, so that equation (VI.9) becomes

$$\widetilde{a}_3(\omega) = 2\frac{g_1\widetilde{a}_1(\omega) + g_2\widetilde{a}_2(\omega)}{i\kappa_3}. \tag{VI.10}$$

[1] Recall that we introduced these transformations in chapter III, section 4.2.

[2] To be more precise, it is unclear how to justify that performing a Schrieffer-Wolff transformation first, and then writing the quantum Langevin equations (QLEs), is equivalent to first writing the QLEs, and then performing a Schrieffer-Wolff transformation. Going further, there are two problems involved. Since they add an imaginary part κ_k to the mode's frequencies ω_k, we can guess that dissipation is introduced through QLEs, but this is never mentioned. Assuming this is the case, performing a Schrieffer-Wolff transformation on a non-hermitian Hamiltonian is complicated by the presence of imaginary parts in the mode's frequencies, leading to a non-unitary transformation

[3] Recall that we note $\widetilde{a} = \widetilde{a}(\omega)$ the Fourier transform of an operator a.



(a) Before adiabatic elimination of a_3.

(b) After adiabatic elimination of a_3.

Figure VI.1: Example of the creation of dissipative coupling with three bosonic modes. Modes a_1 and a_2 both couple to the strongly dissipative mode a_3 with coupling strengths $g_1/2\pi$ and $g_2/2\pi$. Additionally, a_1 and a_2 couple to each other with coupling strength $g/2\pi$. Provided the dissipation κ_3 is sufficient, the effective coupling strength $G/2\pi$ between a_1 and a_2 is complex-valued, with its imaginary part contributing to dissipative coupling.

Returning to the time domain, the QLEs are

$$\dot{a}_1(t) = -i\Big(\omega_1 - i\frac{\kappa_1}{2}\Big)a_1(t) - iga_2(t) - ig_1a_3(t), \tag{VI.11}$$

$$\dot{a}_2(t) = -i\Big(\omega_2 - i\frac{\kappa_2}{2}\Big)a_2(t) - iga_1(t) - ig_2a_3(t), \tag{VI.12}$$

$$a_3(t) = 2\frac{g_1a_1(t) + g_2a_2(t)}{i\kappa_3}, \tag{VI.13}$$

where the last equation shows that a_3 depends on the instantaneous values of a_1 and a_2 due to the adiabatic elimination. Replacing a_3 into the first and second equation, we obtain

$$\dot{a}_1 = -i\Big(\omega_1 - i\frac{\kappa_1}{2}\Big)a_1 - iga_2 - 2g_1\frac{g_1a_1 + g_2a_2}{\kappa_3} = -i\left(\omega_1 - i\frac{\kappa_1 + \frac{4g_1^2}{\kappa_3}}{2}\right)a_1 - i\left(g - i\frac{2g_1g_2}{\kappa_3}\right)a_2, \tag{VI.14}$$

$$\dot{a}_2 = -i\Big(\omega_2 - i\frac{\kappa_2}{2}\Big)a_2 - iga_1 - 2g_2\frac{g_1a_1 + g_2a_2}{\kappa_3} = -i\left(\omega_2 - i\frac{\kappa_2 + \frac{4g_2^2}{\kappa_3}}{2}\right)a_2 - i\left(g - i\frac{2g_1g_2}{\kappa_3}\right)a_1, \tag{VI.15}$$

which can be cast into

$$\frac{\mathrm{d}}{\mathrm{d}t}\begin{pmatrix} a_1 \\ a_2 \end{pmatrix} = -\frac{i}{\hbar}H_{\text{eff}}\begin{pmatrix} a_1 \\ a_2 \end{pmatrix} \tag{VI.16}$$

with the effective Hamiltonian

$$H_{\text{eff}}/\hbar = \begin{pmatrix} \omega_1 - i\frac{\widetilde{\kappa}_1}{2} & g - i\Gamma \\ g - i\Gamma & \omega_2 - i\frac{\widetilde{\kappa}_2}{2} \end{pmatrix}, \tag{VI.17}$$

where $\widetilde{\kappa}_1 = \kappa_1 + \frac{4g_1^2}{\kappa_3}$, $\widetilde{\kappa}_2 = \kappa_2 + \frac{4g_2^2}{\kappa_3}$ and $\Gamma = 2\frac{g_1g_2}{\kappa_3}$. We can rewrite this effective Hamiltonian in a more familiar form as

$$H_{\text{eff}} = \hbar\widetilde{\omega}_1a_1^\dagger a_1 + \hbar\widetilde{\omega}_2a_2^\dagger a_2 + \hbar(g - i\Gamma)\Big(a_1a_2^\dagger + a_1^\dagger a_2\Big), \tag{VI.18}$$

where $\widetilde{\omega}_1 = \omega_1 - i\frac{\widetilde{\kappa}_1}{2}$ and $\widetilde{\omega}_2 = \omega_2 - i\frac{\widetilde{\kappa}_2}{2}$. This effective Hamiltonian, we will analyse in section 2.3, describes the open quantum system in the presence of dissipation.

2.2) Common coupling to a bath

A similar albeit different situation is when two bosonic modes are coupled to a common bath instead of a strongly dissipative mode. This leads to the creation of a dissipative coupling Γ between the modes, mediated by the bath. As an example, we consider two bosonic modes coupled to a common waveguide, illustrated in figure VI.2.

Such an experiment can be modelled using two techniques: master equations and quantum Langevin equations. Concerning the former, we refer the reader to [403] and [384] for examples. Here, we shall use the quantum Langevin equations that we introduced in section 5.1 of chapter III. The situation we are trying to model is familiar to waveguide QED scenarios, for which input-output theories have been formalised (see for instance Lalumière et al. (2013) [405]). In such a waveguide, the photons take the form of plane waves travelling along the unconfined direction[1]. These travelling waves can be either left-moving (modes $p_{\leftarrow,\omega}$ in figure VI.2), or right-moving (mode $p_{\rightarrow,\omega}$), and in principle exists for a continuous range of frequencies because of the lack of confinement.

In appendix B.9, we derive the QLEs for two bosonic modes a_k for $k \in \{1,2\}$ and we find

$$\dot{a}_k = -i(\omega_k - i\widetilde{\kappa}_k)a_k - i(g - i\Gamma)a_1 - \sqrt{\gamma_k}p_L^{\text{in}} - \sqrt{\gamma_k}p_R^{\text{in}} \tag{VI.19}$$

where $g/2\pi$ is the coherent coupling strength, $\gamma_i/2\pi$ are the couplings of a_i to the left and right-moving travelling waves in the waveguide, $\widetilde{\kappa}_k = \frac{\kappa_k + 2\gamma_k}{2}$ is the "loaded" dissipation rate which includes the intrinsic ($\kappa_k/2\pi$) and external ($\gamma_i/2\pi$) dissipation channels, $\Gamma = \sqrt{\gamma_1\gamma_2}$ is the dissipative coupling rate, and $p_{L/R}^{\text{in}}$ the travelling waves input operators. Proceeding as in section 5.1.1 of chapter III, we assume that the travelling waves are coherent drives of amplitude $\epsilon \in \mathbb{R}$ and frequency $\omega/2\pi$, and thus we find that the effective Hamiltonian

$$\begin{aligned} H_{\text{eff}} = {} & \hbar\widetilde{\omega}_1 a_1^\dagger a_1 + \hbar\widetilde{\omega}_2 a_2^\dagger a_2 + \hbar(g - i\Gamma)\Big(a_1 a_2^\dagger + a_1^\dagger a_2\Big) \\ & + i\hbar\sqrt{\frac{\gamma_1}{2\pi}}\epsilon\Big(a_1 e^{i\omega t} - a_1^\dagger e^{-i\omega t}\Big) + i\hbar\sqrt{\frac{\gamma_2}{2\pi}}\epsilon\Big(a_2 e^{i\omega t} - a_2^\dagger e^{-i\omega t}\Big) \end{aligned} \tag{VI.20}$$

where $\widetilde{\omega}_k = \omega_k - i\widetilde{\kappa}_k$ recovers the QLEs, and thus it provides a valid description of the physics.

In a rotating frame at the frequency of the drive $\omega/2\pi$, the Hamiltonian becomes

$$\begin{aligned} H_{\text{eff}} = {} & \hbar\widetilde{\Delta}_1 a_1^\dagger a_1 + \hbar\widetilde{\Delta}_2 a_2^\dagger a_2 + \hbar(g - i\Gamma)\Big(a_1 a_2^\dagger + a_1^\dagger a_2\Big) \\ & + \hbar\Big(\mathcal{E}_1^* a_1 - \mathcal{E}_1 a_1^\dagger\Big) + \hbar\Big(\mathcal{E}_1^* a_2 - \mathcal{E}_2 a_2^\dagger\Big) \end{aligned} \tag{VI.21}$$

with $\widetilde{\Delta}_k = \widetilde{\omega}_k - \omega$, $\mathcal{E}_1^* = i\sqrt{\frac{\gamma_1}{2\pi}}\epsilon$ and $\mathcal{E}_2^* = i\sqrt{\frac{\gamma_2}{2\pi}}\epsilon$. The last two terms can be removed using two displacement transformations $D(\alpha) = \exp\Big(\alpha a_1^\dagger - \alpha^* a_1\Big)$ and $D(\beta) = \exp\Big(\beta a_2^\dagger - \beta a^* a_2\Big)$ with[2]

$$\alpha = \frac{(g - i\Gamma)\mathcal{E}_2 - \mathcal{E}_1\widetilde{\Delta}2}{\widetilde{\Delta}1\widetilde{\Delta}2 - (g - i\Gamma)^2}, \tag{VI.22}$$

$$\beta = \frac{(g - i\Gamma)\mathcal{E}_1 - \mathcal{E}_2\widetilde{\Delta}1}{\widetilde{\Delta}1\widetilde{\Delta}2 - (g - i\Gamma)^2}. \tag{VI.23}$$

one finds the effective Hamiltonian

$$H_{\text{eff}} = \hbar\widetilde{\Delta}_1 a_1^\dagger a_1 + \hbar\widetilde{\Delta}_2 a_2^\dagger a_2 + \hbar(g - i\Gamma)\Big(a_1 a_2^\dagger + a_1^\dagger a_2\Big). \tag{VI.24}$$

[1] These "'travelling waves" are simply plane waves of the form $e^{\pm ikx}$, where k is the wave vector and x the unconfined direction.

[2] The details on how to find these values are given in appendix B.10.

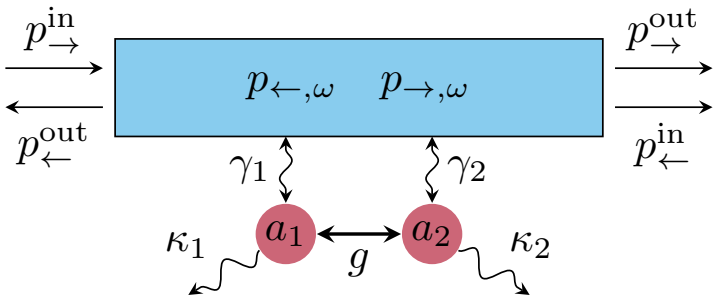


Figure VI.2: Left and right-moving waves in the waveguide, which amounts to considering two baths.

2.3) Analysis of the dissipative coupling Hamiltonian

We saw above that in various experimental setups, a model Hamiltonian for dissipative coupling is given by

$$H_{\text{eff}} = \hbar\widetilde{\omega}_1 a_1^\dagger a_1 + \hbar\widetilde{\omega}_2 a_2^\dagger a_2 + \hbar(g - i\Gamma)\Big(a_1 a_2^\dagger + a_1^\dagger a_2\Big), \tag{VI.25}$$

with $\widetilde{\omega}_k = \omega_k - i\kappa_k$. We note that this effective Hamiltonian is non-hermitian.

Spectrum. Using the technique explained in section 4.1 of chapter III, we find that the spectrum of equation (VI.25) is given by the complex-valued frequencies

$$\widetilde{\omega}_\pm = \frac{\widetilde{\omega}_1 + \widetilde{\omega}_2}{2} \pm \frac{\sqrt{(\widetilde{\omega}_1 - \widetilde{\omega}_2)^2 + 4(g - i\Gamma)^2}}{2}. \tag{VI.26}$$

We notice that when $\Gamma/2\pi = 0$, $\widetilde{\omega}_\pm$ reduces to the standard expression for the polaritons of the Dicke model, leading to level repulsion. More specifically, the real part of $\omega_\pm$ describes repulsion of the energy levels, while the imaginary part of $\omega_\pm$ – which corresponds to linewidths – cross each other. This is illustrated in the first column of figure VI.3. Note that for $\kappa_2 < \kappa_1$, as we chose here, the linewidth of ω_- increases as ω_2 approaches ω_1 (orange dashed line in (b) of figure VI.3). In other words, the linewidth of the lower polaritonic branch attains a maximum on resonance. We conclude that the coherent coupling $g/2\pi$ contributes to level repulsion, and a broadening of the smallest linewidth around the anti-crossing.

On the other hand, let us assume that $g/2\pi = 0$ but $\Gamma/2\pi \neq 0$. Then, the expression of $\widetilde{\omega}_\pm$ simplifies to

$$\widetilde{\omega}_\pm = \frac{\widetilde{\omega}_1 + \widetilde{\omega}_2}{2} \pm \frac{\sqrt{(\widetilde{\omega}_1 - \widetilde{\omega}_2)^2 - 4\Gamma^2}}{2}, \tag{VI.27}$$

which describes energy level attraction (see the second column of figure VI.3). This time, the linewidths of each eigenmode do not cross and are discontinuous. Furthermore, contrary to the case of level repulsion, we see that the linewidth of ω_- has a minimum on resonance.

Finally, in the most general case where both coherent and dissipative couplings co-exist, we observe a hybrid repulsion/attraction of the energy levels depending on the relative magnitudes of $g/2\pi$ and $\Gamma/2\pi$. For instance in figure VI.3, since $g > \Gamma$, we mostly observe an anti-crossing[1]. Nevertheless, the presence of dissipative coupling can be indirectly observed by the evolution of the linewidths of each mode. In the context of cavity magnonics, Yao et al. (2019) [406] and Yao et al. (2019) [407] showed that the "weight" of coherent and dissipative couplings could be monitored through the evolution of the linewidths. Alternatively, the direct observation of level attraction is only possible for purely dissipative coupling, which requires engineering a vanishing coherent coupling $g/2\pi$.

[1]Note however, that if $\Gamma > g$ but $g \neq 0$, we would not observe a crossing of the eigenvalues, which only occur for $g = 0$.

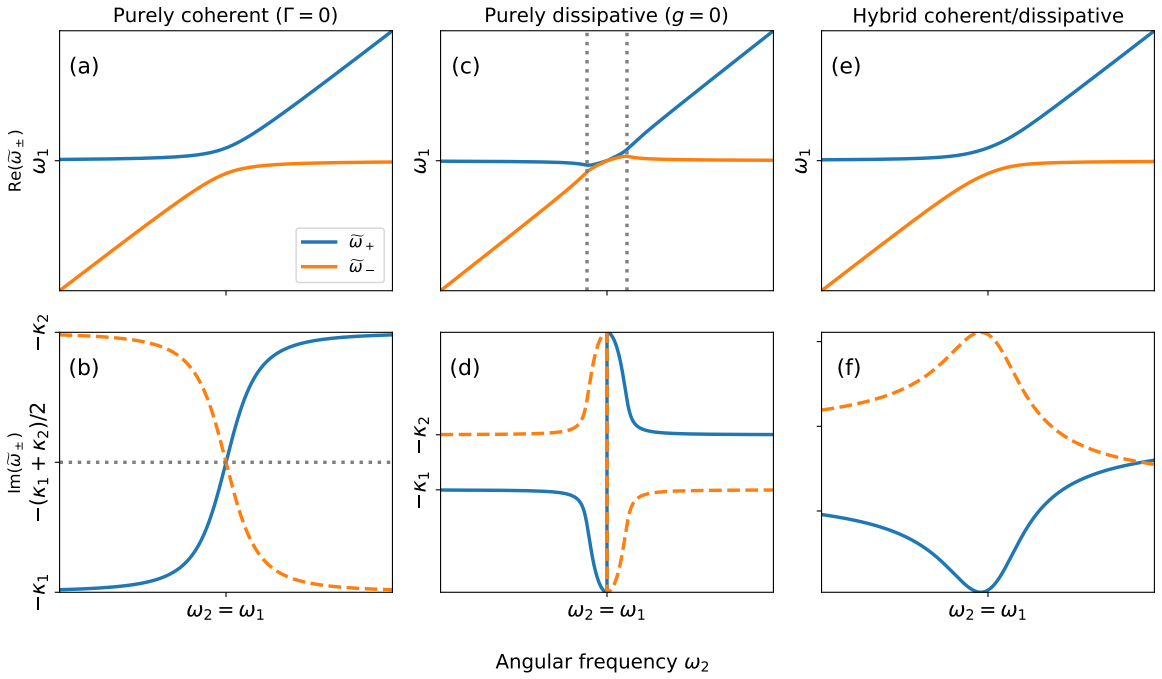


Figure VI.3: Spectrum $\widetilde{\omega}_\pm$ given by equation (VI.26), as a function of ω_2 (abscissa), showing the differences between level repulsion due to the coherent coupling $g/2\pi$, and level attraction induced by dissipative coupling $\Gamma/2\pi$. The parameters are $\omega_1/2\pi = 5$ GHz, $\kappa_1/2\pi = 15$ MHz, $\kappa_2/2\pi = 2$ MHz, $g/2\pi = 50$ MHz and $\Gamma/2\pi = 30$ MHz. The horizontal dashed lines in the top plot of the second columns are located at $\omega_1 \pm 2\Gamma$.

Eigen-modes. When the coupling is purely coherent, we already analysed the resulting eigenmodes in chapter III. Thus, we only discuss the case of dissipative coupling here. Before the regime of level attraction, located between the two vertical gray lines in the second column, eigenmodes are, to a good approximation, mostly made up of a_1 for the blue curve, and a_2 for the orange curve. In the regime of level attraction, the energy levels become degenerate, the two eigenmodes become synchronised [261].

This physics is equivalent to that of two pendulums attached to the same wall. The wall mediates an indirect dissipative coupling between the two pendulums, representing modes a_1 and a_2. During the XVII century, Hyugens observed that even if the two pendulums initially had different frequencies, after some time their oscillations would become identical. He referred to this phenomenon as "the sympathy of two clocks", and it simply corresponds to the phenomenon of level attraction.

Alternative expressions of the effective Hamiltonian. Writing $g - i\Gamma = Ge^{-i\phi}$ where $G \in \mathbb{R}$, we can rewrite equation (VI.25) as

$$H_{\text{eff}} = \hbar\widetilde{\omega}_1 a_1^\dagger a_1 + \hbar\widetilde{\omega}_2 a_2^\dagger a_2 + \hbar G e^{-i\phi}\Big(a_1 a_2^\dagger + a_1^\dagger a_2\Big). \tag{VI.28}$$

Additionally, using e.g. the unitary transformation $U = e^{i\phi a_2^\dagger a_2}$, which maps $a_2 \mapsto e^{-i\phi}a_2$, we obtain

$$H_{\text{eff}} = \hbar\widetilde{\omega}_1 a_1^\dagger a_1 + \hbar\widetilde{\omega}_2 a_2^\dagger a_2 + \hbar G e^{-i\phi}\Big(e^{i\phi}a_1 a_2^\dagger + e^{-i\phi}a_1^\dagger a_2\Big) \tag{VI.29}$$

$$= \hbar\widetilde{\omega}_1 a_1^\dagger a_1 + \hbar\widetilde{\omega}_2 a_2^\dagger a_2 + \hbar G\Big(a_1 a_2^\dagger + e^{-2i\phi}a_1^\dagger a_2\Big). \tag{VI.30}$$

Using this formulation, $\phi = 0$ corresponds to purely coherent coupling, while $\phi = \pi/2$ to purely dissipative coupling. Thus, ϕ parametrises the weight of the coherent and dissipative couplings[1].

[1]Some authors take 2ϕ instead of ϕ to parametrise the effective coupling strength $g - i\Gamma$. Thus using this alternative convention, $\phi = \pi$ corresponds to dissipative coupling (instead of $\phi = \frac{\pi}{2}$ using our convention). Alternatively, some authors take $-\phi$ instead of ϕ to parametrise the system.

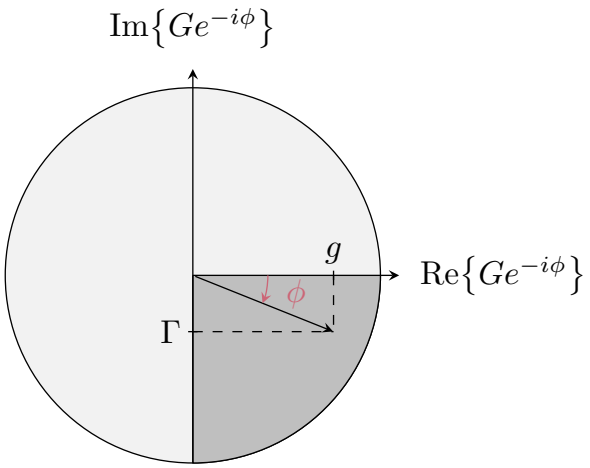


Figure VI.4: Illustration of the contribution of coherent coupling $g/2\pi$ and dissipative coupling $\Gamma/2\pi$ on the effective coupling strength $Ge^{-i\phi} = g - i\Gamma$. Since g and Γ are always positive, the effective coupling strength is confined to the lower right quadrant, leading to the constraint $0 \leqslant \phi \leqslant \frac{\pi}{2}$. The coupling is purely coherent (dissipative) when Γ (g) vanish, or equivalently when $\phi = 0$ ($\phi = \frac{\pi}{2}$).

A hint at non-reciprocity. We note that in the presence of dissipative coupling, the effective Hamiltonian describes a non-reciprocal interaction. To see this more clearly, take the example of a purely dissipatively coupled system by setting $\phi = \frac{\pi}{2}$, we obtain

$$H_{\text{eff}} = \hbar\widetilde{\omega}_1 a_1^\dagger a_1 + \hbar\widetilde{\omega}_2 a_2^\dagger a_2 + \hbar G\Big(a_1 a_2^\dagger - a_1^\dagger a_2\Big). \tag{VI.31}$$

Hence, the process of transferring an excitation from mode 1 to mode 2, described $a_2^\dagger a_1$, has a different phase from the opposite process $a_1^\dagger a_2$. However, the probability of each process is still identical, and given by G. Thus, in a sense, we have not achieved non-reciprocal transmission. We will see in section 4 that the missing ingredient is an alternative path to transfer excitations between the two modes, which requires a loop-coupled system.

3) Observations of level attraction

In the previous section, we explained the mechanism behind dissipative coupling, and we derived a model Hamiltonian. In particular, we saw that for purely dissipative coupling, the spectrum of the open system leads to level attraction. In this section, we examine different experiments in which level attraction has been observed. Importantly, while level attraction can be due to dissipative coupling, sometimes it has a different origin, so that observation of level attraction does not necessarily imply dissipative coupling physics.

3.1) Level attraction due to dissipative coupling

We begin by examining experiments in which level attraction manifested due to dissipative coupling. The two experimental setups described in the previous section, namely the coupling to a common mode, and the coupling to a common bath, were both realised in experiments. Concerning the former, Zhao et al. (2020) [408] created a purely dissipative coupling between two magnon modes, by coupling both of them to a cavity mode. The control of the dissipation of the cavity mode was performed through an antenna coupling to the cavity mode. More specifically, varying the length of the antenna inside the cavity tuned the extrinsic dissipation of the cavity mode, similar to what we observed numerically with COMSOL Multiphysics® in section 5.1 of chapter IV.

The other mechanism, due to the coupling of two modes to a common dissipative bath, has been employed in various experiments in cavity magnonics, using one-dimensional Fabry-Pérot cavities [406, 407, 409], split-ring resonators [410], and cross-line cavities [411–413]. In all of these experiments, a magnon mode and cavity mode both couple to a bath of travelling

waves, or in other words a waveguide. Both the input-output formalism [411, 412] and master equations [413] can be employed to describe this physics. Notably, both methods can be used to obtain an effective Hamiltonian similar to equation (VI.25), leading to energy level attraction.

3.2) Level attraction in other physical systems

Aside from cavity magnonics, level attraction has been observed in optomechanical systems [414], and cavity QED with quantum dots [415]. In these experiments, level attraction is not due to dissipative coupling. Furthermore, level attraction was also theorised to appear in cavity optomagnonics [416] and Bose-Einstein condensates [417], where dissipative coupling does not play a role. Thus, while purely dissipative coupling implies level attraction, the converse is not true.

As an example of how level attraction arises in other systems, let us take the example of Bernier et al. (2018) [414]. In their work, they modelled a multimode optomechanical system based on superconducting cavities with the interaction Hamiltonian

$$H_I = \hbar g(cm + c^\dagger m^\dagger), \tag{VI.32}$$

where m describes a mechanical mode (phonon), and c a cavity photon. This interaction can be diagonalised in the $(c, m^\dagger)$ basis: as a result of using $m^\dagger$ instead of m, the energy of the mechanical mode m is negative. The resulting eigen-frequencies can be shown to be

$$\omega_\pm = \frac{\omega_c + \omega_m}{2} \pm \frac{\sqrt{(\omega_c - \omega_m)^2 - 4g^2}}{2}, \tag{VI.33}$$

which leads to level attraction thanks to the sign factor before the coupling strength. This theoretical prediction of level attraction was experimentally observed in the same paper.

3.3) Anti-resonances in three-dimensional cavities

Another possibility for observing level attraction is with anti-resonances[1] in three-dimensional cavities, as experimentally demonstrated by Rao et al. (2019) [418] by placing a YIG sphere in a cylindrical cavity. In this work, the authors observed level repulsion (attraction) between an anti-resonance and the magnon when the ferromagnetic sphere was placed in a maxima (minima) of the cavity mode's magnetic field. Intuitively, placing the sphere in a maximum of the magnetic field maximises the coherent coupling $g/2\pi$, while placing it in a minima minimises it. Thus, we expect that in such a cavity, the weight of the coherent coupling $g/2\pi$ can be controlled by the location of the YIG sphere, and when $g = 0$ (YIG sphere placed in a node of the magnetic field) the dissipative coupling becomes observable. This begs the question of what produces this dissipative coupling in the first place. Indeed, the cavity confines the electromagnetic field in all three directions, so no travelling waves can exist. Hence, dissipative coupling can only occur due to the presence of a strongly dissipative mode.

Anti-resonances. Some authors have considered anti-resonances to play the role of such strongly dissipative modes. However, this is not quite right, since anti-resonances are not cavity eigenmodes[2]. Indeed, as we showed in section 5.1, the cavity eigenmodes can be predicted using COMSOL Multiphysics® and provided excitation antenna couple to these eigenmodes, they lead to resonances in the transmission. On the other hand, anti-resonances correspond to dips in the transmission amplitude, and they are located at frequencies where no cavity eigenmodes exist. As shown by Rao et al. (2019) [418], their characteristics depends on the excitation antennas, and they only occur due to driving the cavity.

[1] As mentioned in the previous chapters, anti-resonances correspond to a minima in the transmission amplitude (e.g. $|S_{21}|$) of a cavity.

[2] On the other hand, they may be eigenmodes of the open quantum systems consisting of the cavity system and the bath Hamiltonian. The Fano diagonalisation technique (see [419] for an example) can be used to diagonalise the total Hamiltonian, and we may recover the anti-resonances as bound states.

To further understand what anti-resonances are, we now describe two different types of anti-resonances. The first type can be undersdtood classically, by considering two coupled harmonic oscillators, where only one of them is driven. Rao et al. (2019) [418] showed that for two linearly coupled oscillators c and m, with natural frequencies ω_c and ω_m, if one drives oscillator c at ω_m, then c remains static, while m oscillates. Using the formalism of second-quantisation, the Hamiltonian describing this situation is

$$H = \hbar\omega_c c^\dagger c + \hbar\omega_m m^\dagger m + \hbar g\Big(cm^\dagger + c^\dagger m\Big), \tag{VI.34}$$

with $g/2\pi$ the coupling strength. We already calculated an input-output theory for such a Hamiltonian in section 5.2.2. Associating oscillator c to a cavity mode with couplings κ_1, κ_2 to the ports, and m to a magnon mode with intrinsic dissipation κ_m, the transmission coefficient reads (see equation (III.224))

$$S_{21}(\omega) = -i\frac{\sqrt{\kappa_1\kappa_2}(\omega - \widetilde{\omega}_m)}{(\omega - \widetilde{\omega}_c)(\omega - \widetilde{\omega}_m) - g^2}, \tag{VI.35}$$

where $\widetilde{\omega}_c = \omega_c - i\frac{\kappa_1+\kappa_2}{2}$ and $\widetilde{\omega}_m = \omega_m - i\frac{\kappa_m}{2}$. Since the nominator vanishes for $\omega = \omega_m$, we see that the magnon leads to an anti-resonance when the cavity mode is driven at the natural frequency of the magnon. In this case, an anti-resonance appears at the frequency of one of the modes (here the magnon mode).

The second type of anti-resonances arises due to destructive interferences in multimode systems. These anti-resonances do not appear at the frequencies of the cavity eigenmodes, and thus they cannot really be considered as a eigenmode. As an example, let us consider two uncoupled cavity modes, with Hamiltonian

$$H = \hbar\omega_0 c_0^\dagger c_0 + \hbar\omega_1 c_1^\dagger c_1, \tag{VI.36}$$

and let us consider that each cavity mode couples to the input (output) port with coupling rate $\kappa_k/2\pi$ ($\gamma_k/2\pi$). As detailed in appendix B.13, one finds that the transmission coefficient

$$S_{21}(\omega) = -i\frac{\sqrt{\kappa_0\gamma_0}\big(\omega - \omega_1 + i\frac{\kappa_1+\gamma_1}{2}\big) + \sqrt{\kappa_1\gamma_1}\big(\omega - \omega_i + i\frac{\kappa_0+\gamma_0}{2}\big)}{\big(\omega - \omega_0 + i\frac{\kappa_0+\gamma_0}{2}\big)\big(\omega - \omega_1 + i\frac{\kappa_1+\gamma_1}{2}\big)} \tag{VI.37}$$

whose nominator vanishes for $\omega = \omega_r$ where

$$\omega_r = \frac{\sqrt{\kappa_0\gamma_0}\omega_1 + \sqrt{\kappa_1\gamma_1}\omega_0}{\sqrt{\kappa_0\gamma_0} + \sqrt{\kappa_1\gamma_1}}. \tag{VI.38}$$

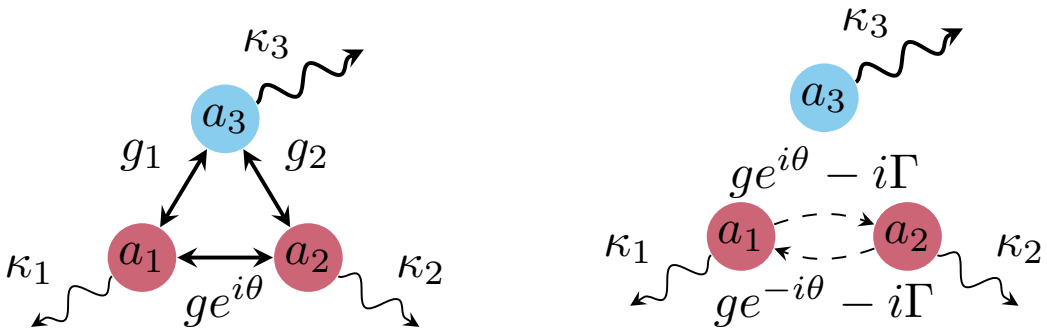
Hence, when two cavity modes are driven simultaneously, an anti-resonance can appear at a frequency different from the natural frequency of each oscillator. We can think of such anti-resonances as the a destructive interference between the two cavity modes, mediated by the drive. In a sense, the two cavity modes are indirectly coupled by the excitation drive.

The origin of level repulsion and attraction with anti-resonances. The origin of level attraction and repulsion with anti-resonances in three-dimensional cavities can be understood using the input-output formalism developed by[1] [279]. The idea is that anti-resonances occur to a phase mismatch between the excitation and detection antennas. This leads to either interferences that manifest as anti-resonances, and their location depends on the coupling to the input and output ports. The characteristics of the anti-resonances were shown to be strongly affected by the loaded quality factors of the cavity eigenmodes.

In particular, [279] used the input-output formalism to derive the transmission coefficient S_{21}. Writing $S_{21} = N(\omega)/D(\omega)$, the behaviour of anti-resonances is given by the equation $N(\omega) = 0$, since it leads to a minimum of transmission. [279] found that the solutions of $N(\omega) = 0$ can be written as

$$\omega_\pm = \frac{\omega_r + \omega_m}{2} \pm \frac{\sqrt{(\omega_r - \omega_m)^2 + 4Ge^{i\phi}}}{2}, \tag{VI.39}$$

[1] At the time of writing this thesis, this reference is unpublished.



(a) Before adiabatic elimination of a_3.

(b) After adiabatic elimination of a_3.

Figure VI.5: Creation of a non-reciprocal interaction by balancing the coherent ($g/2\pi$) and dissipative ($\Gamma/2\pi$) couplings, and adjusting the synthetic gauge field (parametrised by θ). The dissipative mode a_3 is used to mediate the dissipative coupling $\Gamma/2\pi$ between a_1 and a_2.

which can describe both level repulsion and attraction between the magnon (frequency $\omega_m/2\pi$), and the anti-resonance (frequency $\omega_r/2\pi$) depending on the value of ϕ. While the method of [279] does predict the occurrence of level repulsion and attraction depending on experimental parameters, it does not show that dissipative coupling is playing a role. In fact, level attraction with anti-resonances in three-dimensional cavities is solely due to the measurement setup, but the underlying physics remains that of coherent coupling. In the following section, we detail a similar situation in a two-tone driving scheme.

3.4) Two-tone driving in cavity magnonics

We have previously mentioned that both coherent coupling, characterised by level repulsion, and dissipative coupling, characterised by level attraction, have practical applications. While both coherent and dissipative couplings can be engineered, and co-exist, there is no simple mechanism to go from coherent to dissipative coupling physics in-situ. A theoretical proposal by Grigoryan, Shen, and Xia (2018) [420] based on a RLC description of the magnon/photon coupling suggested the possibility to tune a cavity magnonics system between level repulsion and level attraction by driving the magnon, and it was later experimentally realised by [421, 422]. In the original work of appendix C.5, we provide a model based on the input-output formalism to explain the experimental observation of level attraction, and we show that it does not originate from dissipative coupling.

4) Engineering non-reciprocal behaviour

In this section, we finally discuss the application of synthetic gauge fields and dissipative couplings to non-reciprocal interactions. While non-reciprocity is often considered from the transport point of view, there are other possible manifestation. For instance, Wang et al. (2023) [423] demonstrated experimentally a non-reciprocal dispersive pull of the frequencies of a coupled cavity/superconducting qubit system.

Here, we shall focus on non-reciprocal transmission between modes, with the objective of achieve uni-directional quantum information transduction (or in simpler words, a circulator). We begin with the most simple example of a ring of three bosonic modes and follow the analysis of [384]. Next, we investigate how non-reciprocal interactions can be obtained in a ring of four bosonic modes, which we know from [1] and (section 5.2 of chapter IV) can be experimentally implemented in cavity magnonics. We conclude this section by discussing some methods that can be used to control synthetic gauge fields in loop-coupled systems, and we discuss its implementation in a cavity magnonics system.

4.1) Ring of three bosonic modes

We return to the situation of a ring of three bosonic modes a_k studied in section 2.1, but this time we include a gauge-invariant phase θ as pictured in figure VI.5. Formally, the interaction Hamiltonian is now

$$H_I = \hbar g_1(a_1 a_3^\dagger + a_1^\dagger a_3) + \hbar g_2(a_2 a_3^\dagger + a_2^\dagger a_3) + \hbar g(e^{i\theta} a_1 a_2^\dagger + e^{-i\theta} a_1^\dagger a_2). \tag{VI.40}$$

Following section 2.1, the quantum Langevin equations in the semi-classical approximation are

$$\dot{a}_1 = -i\Big(\omega_1 - i\frac{\kappa_1}{2}\Big)a_1 - ige^{-i\theta}a_2 - ig_1 a_3, \tag{VI.41}$$

$$\dot{a}_2 = -i\Big(\omega_2 - i\frac{\kappa_2}{2}\Big)a_2 - ige^{i\theta}a_1 - ig_2 a_3, \tag{VI.42}$$

$$\dot{a}_3 = -i\Big(\omega_3 - i\frac{\kappa_3}{2}\Big)a_3 - ig_1 a_1 - ig_2 a_2, \tag{VI.43}$$

and the adiabatic elimination of a_3 still leads to

$$\widetilde{a}_3(\omega) = 2\frac{g_1\widetilde{a}_1(\omega) + g_2\widetilde{a}_2(\omega)}{i\kappa_3}. \tag{VI.44}$$

Inserting into the QLE for a_1 and a_2, we find

$$\dot{a}_1 = -i(\omega_1 - i\widetilde{\kappa}_1)a_1 - i\Big(ge^{-i\theta} - i\Gamma\Big)a_2, \tag{VI.45}$$

$$\dot{a}_2 = -i(\omega_2 - i\widetilde{\kappa}_2)a_2 - i\Big(ge^{i\theta} - i\Gamma\Big)a_1, \tag{VI.46}$$

where $\Gamma = 2g_1g_2/\kappa_3$ and $\widetilde{\kappa}_k = \kappa_k + \frac{4g_k^2}{\kappa_3}$. Thus, the effective Hamiltonian is

$$H_{\text{eff}} = \hbar\widetilde{\omega}_1 a_1^\dagger a_1 + \hbar\widetilde{\omega}_2 a_2^\dagger a_2 + \underbrace{\Big(ge^{-i\theta} - i\Gamma\Big)a_1^\dagger a_2 + \Big(ge^{i\theta} - i\Gamma\Big)a_1 a_2^\dagger}_{=H_I}, \tag{VI.47}$$

where $\widetilde{\omega}_k = \omega_k - i\widetilde{\kappa}_k$. From there, we see that for $\theta = \frac{\pi}{2}$, the interaction is

$$H_I = (-ig - i\Gamma)a_1^\dagger a_2 + (ig - i\Gamma)a_1 a_2^\dagger \tag{VI.48}$$

and by balancing the coherent and dissipative coupling ($g = \Gamma$) we obtain

$$H_I = -2iga_1^\dagger a_2. \tag{VI.49}$$

In other words, it is possible to transfer an excitation from a_2 to a_1, but the opposite process is forbidden! We thus see that the gauge-invariant phase, or equivalently the synthetic gauge field, is an essential ingredient to achieve non-reciprocal interaction. Note that by setting $\theta = -\frac{\pi}{2}$ instead, we can reverse the direction of the interaction, i.e. we can transfer excitation from a_1 to a_2 but not the other way.

This simple example shows that the recipe to create a non-reciprocal interaction is to first find a loop-coupled system, in which the gauge-invariant phase can be tuned. Then, one needs to create a dissipative coupling, and balance it with the coherent coupling. In other words, we need a tunable synthetic gauge field, and dissipation engineering [384].

Alternatively, we can think of the occurrence of non-reciprocal behaviour through the concept of time-reversal symmetry. Time-reversal corresponds to switching the direction of time $t \mapsto -t$, and physical observables are affected differently by it. For instance, noting T the time reversal operator, the momentum $\mathbf{p}$ changes sign under time-reversal, i.e. $T\mathbf{p}T^{-1} = -\mathbf{p}$, but the position $\mathbf{r}$ is invariant, i.e. $T\mathbf{r}T^{-1} = \mathbf{r}$ [424]. Intuitively, we thus see that breaking time-reversal symmetry can lead to non-reciprocity, due to the transformation law of the momentum operator $\mathbf{p}$. A magnetic field is known to break time-reversal symmetry, and thus it is not surprising that a synthetic $U(1)$ gauge field, for which we can define a synthetic magnetic field, can also break time-reversal symmetry.

4.2) Engineering non-reciprocal interactions in a ring of four bosonic modes

The previous example shows how non-reciprocal interactions can be obtained: we need a coherent coupling, balanced with a dissipative coupling, and a synthetic gauge field. In the original work of appendix C.6, we investigate a system composed of four bosonic modes organised in a ring topology. This system is exactly that theoretically studied in Gardin et al. (2023) [1], and then exprimentally verified in section 5.2 of chapter IV. Thus, having understood the application of synthetic gauge fields, it is only natural to ask whether this could be used in this system.

4.3) Controlling $U(1)$ gauge fields in loop-coupled systems

In section 4.1, we saw that the gauge-invariant phase θ needed to be tuned to achieve non-reciprocal transmission. To conclude this section, we discuss some methods one can use to control the gauge-invariant phase in a loop-coupled system.

Frequency modulation. The first method consists of modulating in time the frequencies of the modes, and has been implemented e.g. with cold atoms [364]. We consider two coupled bosonic modes c and m, where the frequency of m is harmonically modulated. Formally, we consider the Hamiltonian

$$H = \hbar\omega_c c^\dagger c + \hbar(\omega_m + A\cos(\omega_d t + \phi))m^\dagger m + \hbar g(cm^\dagger + c^\dagger m) \tag{VI.50}$$

with $A \in \mathbb{R}$. Using $U = \exp\left(i\theta(t)m^\dagger m\right)$ with $\theta(t) = -\frac{A}{\omega_d}\sin(\omega_d t + \phi)$, we have $m \mapsto me^{-i\theta(t)}$ and

$$i\hbar\dot{U}U^\dagger = i\hbar i\dot{\theta}m^\dagger m = -\hbar A\cos(\omega_d t + \phi)m^\dagger m. \tag{VI.51}$$

Hence the Hamiltonian transforms to[1]

$$H \mapsto H' = UHU^\dagger + i\hbar\dot{U}U^\dagger = \hbar\omega_c c^\dagger c + \hbar\omega_m m^\dagger m + \hbar g\Big(cm^\dagger e^{i\theta(t)} + c^\dagger m e^{-i\theta(t)}\Big) \tag{VI.52}$$

Using the Jacobi-Anger expansion with $x = -\frac{A}{\omega_d}$ and $\varphi = \omega_d t + \phi$

$$e^{ix\sin(\varphi)} = \sum_{n=-\infty}^{\infty} J_n(x)e^{in\varphi}, \tag{VI.53}$$

where J_n is the first kind of Bessel function, we obtain

$$H = \hbar\omega_c c^\dagger c + \hbar\omega_m m^\dagger m + \sum_{n=-\infty}^{\infty} J_n(x)\hbar g\Big(cm^\dagger e^{in\omega_d t}e^{in\phi} + \text{h.c}\Big) \tag{VI.54}$$

Intuitively, as soon as n is greater than 1, we expect the frequencies $n\omega_d$ to be much higher than those of ω_c, ω_m and g, so that we can invoke the rotating wave approximation (RWA). To see this more clearly, we first go to the interaction picture using $U = \exp\big(i\big(\omega_c c^\dagger c + \omega_m m^\dagger m\big)t\big)$, which gives

$$H = \sum_{n=-\infty}^{\infty} J_n(x)\hbar g\Big(cm^\dagger e^{i(\omega_m-\omega_c)t}e^{in\omega_d t}e^{in\phi} + \text{h.c}\Big) \tag{VI.55}$$

As per the rotating wave approximation, the terms oscillating with a frequency $\omega \gg g_c$ can be neglected. To simplify the discussion, we keep only the terms with indices $n = \{0, 1, -1\}$ and obtain

$$\begin{aligned} H/(\hbar g) = {} & J_{-1}(x)cm^\dagger e^{i(\omega_m-\omega_c-\omega_d)t}e^{-i\phi} + J_1(x)cm^\dagger e^{i(\omega_m-\omega_c+\omega_d)t}e^{i\phi} \\ & + J_0(x)cm^\dagger e^{i(\omega_m-\omega_c)t} + \text{h.c} \end{aligned} \tag{VI.56}$$

If for instance one wants the gauge-invariant phase $+\phi$, we set the drive frequency such that $\omega_d = -(\omega_m - \omega_c)$ and thus

$$H/(\hbar g) = J_{-1}(x)cm^\dagger e^{2i\omega_d t}e^{-i\phi} + J_1(x)cm^\dagger e^{i\phi} + J_0(x)cm^\dagger e^{-i\omega_d t} + \text{h.c}, \tag{VI.57}$$

[1] The transformation law of the Hamiltonian is given by equation (A.28) of appendix A.2.

and for $g \ll \omega_d$ the RWA allows to drop the first and last term to finally give

$$H = \hbar g J_1(x)\Big(cm^\dagger e^{i\phi} + e^{-i\phi}c^\dagger m\Big). \tag{VI.58}$$

Here the phase θ is controllable by the phase of the modulation of the frequencies of mode m. Therefore, we phase is controllable.

Frequency modulation in cavity magnonics. This strategy can be readily implemented by driving sphere parallel to the static magnetic field. Assuming this direction is along $\hat{\mathbf{z}}$, then the coupling has a dispersive form (see equation (IV.43)) which reads

$$H_I = \hbar g_z\Big(c + c^\dagger\Big)m^\dagger m, \tag{VI.59}$$

where g_z is the coupling strength given by equation (IV.46), c describes the electromagnetic field, and m the magnon mode. Assuming that the electromagnetic field is a coherent drive of amplitude ϵ at frequency $\omega_d/2\pi$ with a phase ϕ, we have $c \mapsto \langle c\rangle = \epsilon e^{-i\omega_d t}e^{-i\phi}$. Thus, the interaction Hamiltonian becomes

$$H_I = \hbar g_z\Big(c + c^\dagger\Big)m^\dagger m \mapsto 2g_z\epsilon\cos(\omega_d t + \phi)m^\dagger m, \tag{VI.60}$$

which represents a modulation the magnon's frequency.

Coupling modulation. In practice, it is hard to implement successfully the method of frequency modulation because often unwanted sidebands exists [384]. An alternative strategy is the modulation of the coupling strength, which for instance has been used in optomechanics [171] and superconducting circuits [151–153].

Following [384], the model Hamiltonian is

$$H = \hbar\omega_c c^\dagger c + \hbar\omega_m m^\dagger m + 2\hbar g\cos(\omega_d t + \phi)(cm^\dagger + c^\dagger m), \tag{VI.61}$$

which in the interaction picture becomes

$$H = 2\hbar g\cos(\omega_d t + \phi)(e^{i(\omega_m-\omega_c)t}cm^\dagger + e^{-i(\omega_m-\omega_c)t}c^\dagger m). \tag{VI.62}$$

Choosing $\omega_d = \omega_m - \omega_c$ and expanding the cosine,

$$H = \hbar g\Big(e^{i\omega_d t}e^{i\phi} + e^{-i\omega_d t}e^{-i\phi}\Big)(e^{i\omega_d t}cm^\dagger + e^{-i\omega_d t}c^\dagger m) \tag{VI.63}$$

$$= \hbar g(e^{-i\phi}cm^\dagger + e^{i\phi}c^\dagger m) + \hbar g\Big(e^{2i\omega_d t}e^{i\phi}cm^\dagger + e^{-2i\omega_d t}e^{-i\phi}c^\dagger m\Big) \tag{VI.64}$$

and in the limit $g \ll \omega_d$, the last two terms can be dropped under the RWA, and we finally obtain

$$H = \hbar g(e^{-i\phi}cm^\dagger + e^{i\phi}c^\dagger m). \tag{VI.65}$$

5) Conclusion

In this chapter, we have explained how dissipative couplings can be induced between bosonics modes. Conceptually, dissipative coupling is an indirect coupling mediated by a strongly dissipative mode. This dissipative coupling can interfere with an already existent coherent coupling, a synthetic gauge field allows to make them interference destructively, leading to non-reciprocal transmission. From these concepts, we investigated how non-reciprocal transmission could be obtained in the four modes cavity magnonics system studied in chapter IV. While we could not find a method to induce non-reciprocal transmission, we identified future work, and still demonstrated non-reciprocal behaviour.

Looking forward, we will turn our attention to the creation of non-classical states, which can be viewed as resources for quantum information processing. As we previously mentioned,

dissipative couplings, and more generally non-hermitian systems can be beneficial for engineering quantum states. Notably, the non-reciprocal behaviour can lead to to asymmetric entanglement, which from our discussion in chapter II we can guess will lead to quantum steering. Before tackling this interesting topic, we examine the ultrastrong coupling regime in the next chapter. We will see that in this peculiar regime of light/matter interactions, many common approximations fail (most notably the rotating wave approximation), which can be viewed as an opportunity for faster quantum information transduction, and a resource for engineering non-classical states.

Chapter VII

Physics of the ultrastrong coupling regime and beyond

Summary

We discuss the ultrastrong coupling (USC) regime of light/matter interactions, in which common approximations used in quantum optics break down. Therefore, we begin by introducing additional theoretical methods, such as the Hopfield-Bogoliubov diagonalisation and input-output theory, to handle the failing of these assumptions. Once we are able to adequately describe systems in the USC, we turn our attention to the physics resulting from the failure of the aforementioned approximations fail. Finally, we research the case of cavity magnonics in the USC, for which existing light-matter models fail to accurately describe the spectrum. Furthermore, we investigate the possibility of create a cavity-mediated ultrastrong magnon-magnon coupling, useful for quantum information transduction.

Contents

1) Introduction . . . **124**
2) Hopfield-Bogoliubov diagonalisation . . . **126**
2.1 Principles . . . 126
2.2 Applications . . . 127
2.2.1 Diagonalisation of squeezing terms . . . 127
2.2.2 Diagonalisation of the Hopfield model . . . 128
3) Input-output formalism . . . **129**
3.1 Differences with the standard input-output theory . . . 129
3.2 Example: Hopfield model . . . 130
4) Phenomenology of the USC regime . . . **131**
4.1 Virtual excitations and squeezing . . . 131
4.2 Sum rules . . . 132
4.3 Diamagnetic term and its consequences . . . 135
4.4 Gauge invariance . . . 136
5) Cavity magnonics in the USC . . . **136**
6) Cavity-mediated ultrastrong magnon-magnon coupling . . . **136**
7) Conclusion and outlook . . . **137**

1) Introduction

Definition of the ultrastrong and deep strong coupling regimes. In chapter III, we introduced the Rabi and Hopfield models, and assumed the strong coupling (SC) regime, where the coupling strength $g/2\pi$ is greater than the relaxation rates of both light and matter degrees of freedom. The ultra strong coupling (USC) regime, and the related deep strong coupling (DSC) regime, are reached when the coupling strength $g/2\pi$ becomes comparable

to the bare frequencies $\omega/2\pi$ of the subsystems[1] in the cavity. The transition between these regimes is continuous and no exact bounds exist. Still, quantitatively most works[2] agree that the USC regime is entered when $0.1 \lesssim g/\omega < 1$, and the DSC when $1 \lesssim g/\omega$ [428, 429]. Note that the conventional strong coupling (SC) regime is such that $g/\omega < 0.1$. In the ultrastrong coupling regime, the couplings are usually much greater than the relaxation times, so that the cooperativity (introduced in section 4.3 of chapter II) is very high.

In recent years, the ultrastrong coupling regime has been reached in a variety of platforms [428, 429], e.g. intersubband polaritons in semiconductor quantum wells [430], THz photons mediated by a two-dimensional electron gas [431], cavity optomechanics [432], Landau polaritons [433] or circuit QED [434] to name a few[3]. These advancements in experimentally reaching the ultrastrong coupling regime calls for the appropriate development of the theory to describe these systems.

Challenges. Indeed, many standard approximations of quantum optics start to break down at the onset $0.1 \simeq g/\omega$ of the USC regime, and dramatically fail for higher values of g/ω. For instance, the rotating wave approximation (RWA) introduced in chapter III becomes inapplicable [435] and including the counter rotating terms in the Hamiltonian becomes necessary. Similarly, the diamagnetic term[4], often neglected thanks to the Thomas-Reiche-Kuhn sum rule [428, 429, 436], can significantly influence the physics. For instance, the diamagnetic term can hinder the possibility of phase transitions, and is responsible for the counter-intuitive decoupling of light and matter in the DSC regime [437]. Another issue is the two-level system approximation, usually performed on the matter degrees of freedom, which breaks gauge-invariance. As an example, the quantum Rabi model (see equation (III.62)) we derived in chapter III is not gauge-invariant: if one performs a gauge transformation, one finds another model that gives different physical predictions.

The direct applications of the standard quantum optics techniques can lead to unphysical predictions, for instance the emission of photons from the ground state. Thus, the diagonalisation and input-output formalism introduced in chapter III need to be adapted to work in the USC regime. Therefore, the USC regime is also of fundamental interest to the field of light matter interactions.

Motivation. Indeed, the theoretical challenges posed by the ultrastrong coupling regime have connections to quantum field theoretical concepts such as Feynman diagrams [438], symmetry breaking [439, 440], or the dynamical Casimir effect [441], which can be linked to non-adiabatic physics [442]. However, the USC is not just a scientific curiosity, since it can have applications for quantum information processing.

Indeed, the high value of the coupling strength $g/2\pi$ implies faster quantum information transduction [428, 429], and more generally faster quantum information processing, notably for quantum computing. The additional terms that appear in the USC regime (counter-rotating terms and diamagnetic terms) are non-linear, and thus naturally generate entanglement in the system. Therefore, the USC regime can also be beneficial for the creation of non-classical states (see chapter VIII).

Outline. We begin by introducing additional theoretical methods to describe the ultra strong coupling of light and matter. In section 2 we detail how to describe the normal modes of a USC system, and investigate the effects of the counter rotating terms on the polaritons. In section 3, we adapt the input-output formalism to Hamiltonian containing counter rotating and diamagnetic terms. Then in section 4, we discuss in more details some of the physics of the USC regime. The last two sections, sections 5 and 6, consists of original unpublished

[1] It can be the frequency of light, matter, or both.

[2] Notably, some authors use a strict inequality, for instance [425], while [208, 426] uses a looser definition. Note also that some authors impose conditions on both the light and matter frequencies, while others only consider that of light. Note also that other regimes exist [208, 427], but we do not consider them here.

[3] We refer the reader to the reviews [428, 429] for a more exhaustive overview of experiments in the USC regime.

[4] We recall that this term is proportional to the vector potential squared, see equation (III.34) of chapter III.

work concerning cavity magnonics in the USC regime. In section 5 we attempt to derive an effective model for cavity magnonics in the USC regime which agrees with experimental observations, and in section 6 we investigate the possibility of achieve an ultrastrong magnon-magnon coupling mediated by two cavity modes.

2) Hopfield-Bogoliubov diagonalisation

2.1) Principles

We saw in section 4.1 of chapter III how the description of the system in terms of polaritonic frequencies and operators could be obtained by diagonalisation. As a reminder, the method relied on writing a Hamiltonian H in terms of a matrix M and a column vector $\boldsymbol{v}$ of annihilation operators such that $H = \hbar \boldsymbol{v}^\dagger M \boldsymbol{v}$. However, the presence of counter-rotating or diamagnetic terms in the ultra strong coupling makes this method unusable. For instance, the counter-rotating terms, which are of the form cm or $c^\dagger m^\dagger$, cannot be expressed by multiplication of a column vector $\boldsymbol{v} = (c\, m)^t$ and its hermitian conjugate alone. A natural solution consists of artificially[1] doubling the degrees of freedom[2] by including both annihilation and creation operators in $\boldsymbol{v}$. This corresponds to the Hopfield-Bogoliubov method [206], which works for quadratic bosonic Hamiltonians.

We begin by presenting the general *method* of the Hopfield-Bogoliubov diagonalisation, after which we consider two examples[3] of relevance in the coming chapters. We would like to emphasise the word *method* here, because we will not attempt to justify and interpret why the following equations provide the appropriate description of the physics. For more details, we refer the reader to the notes by Michael Stone [443] and chapter 24 of the textbook by Peter Woit [444].

Consider a Hamiltonian dependent on a set of N bosonic annihilation/creation operators $\{a_i\}$, which we organise in a vector $\boldsymbol{a} = \Big(a_1, \dots, a_N\Big)^t$. Our goal is to find the polaritonic operators p_μ and their energy $\hbar\omega_\mu$ such that the Hamiltonian is diagonal. To do that, we define a column vector $\boldsymbol{v}$ composed of the operators a_i and their hermitian conjugate $a_i^\dagger$ as

$$\boldsymbol{v} = \Big(\boldsymbol{a}, \boldsymbol{a}^\dagger\Big)^t. \tag{VII.1}$$

Next, we rewrite the Hamiltonian in a matrix form

$$H = \frac{\hbar}{2} \boldsymbol{v}^\dagger \eta M \boldsymbol{v} \tag{VII.2}$$

where η is a diagonal matrix with the first N diagonal terms equal to $+1$ and the last N diagonal elements equal to -1. We then proceed to diagonalise M and we obtain a set of eigenvectors p_μ with eigenvalues ω_μ. As in chapter III, the eigenvalues $\omega_\mu/2\pi$ give us the spectrum of the system, while the operators p_μ tell us about the hybridisation between the different bosonic modes a_i. Indeed, the operators p_μ are linear combinations of the annihilation operators a_i and $a_i^\dagger$, and are bosonic annihilation operators for the polaritons, with commutation relation $[p_\mu, p_\nu^\dagger] = \delta_{\mu\nu}$. The polaritons come in pairs $p_\mu, p_\mu^\dagger$ with energies $\hbar\omega_\mu$ and $-\hbar\omega_\mu$ respectively. Thus, we can write

$$H = \frac{\hbar}{2} \boldsymbol{v}^\dagger \eta M \boldsymbol{v} = \sum_{\mu=1}^{N} \hbar\omega_\mu p_\mu^\dagger p_\mu - \sum_{\mu=1}^{N} \hbar\omega_\mu p_\mu p_\mu^\dagger. \tag{VII.3}$$

[1] Formally, the size of the matrix to diagonalise doubles. However, as we will see below, the resulting polaritons come in hermitian conjugate pairs with identical eigenvalues up to a sign.

[2] One can see the dagger operators as annihilation operators for the anti-polaritons, just like in Fermi liquid theory one has electrons and holes.

[3] More examples are provided in appendix B.11, based on generalisation of the Hopfield Hamiltonian.

2.2) Applications

2.2.1) Diagonalisation of squeezing terms

As a first example, we consider the following Hamiltonian

$$H = \hbar A a^\dagger a + \hbar B\Big(a^2 + a^{\dagger 2}\Big) \tag{VII.4}$$

with a a bosonic annihilation operator and A, B positive constants, and we will show that the second terms can be interpreted as generating squeezing. The second term of this Hamiltonian is non-linear, but is still quadratic in $a, a^\dagger$, so that the Hopfield-Bogoliubov method can be employed. We rewrite the Hamiltonian as

$$H = \frac{\hbar}{2}\boldsymbol{v}^\dagger \eta M \boldsymbol{v} \tag{VII.5}$$

where $\boldsymbol{v} = \big(a, a^\dagger\big)^t$ and

$$M = \begin{pmatrix} A & 2B \\ -2B & -A \end{pmatrix}. \tag{VII.6}$$

Diagonalisation of M give the spectrum $\omega_\pm = \pm\sqrt{A^2 - 4B^2}$ [17]. Noting b the associated polariton, we thus have

$$H = \hbar A a^\dagger a + \hbar B\Big(a^2 + a^{\dagger 2}\Big) = \hbar\omega_+ b^\dagger b. \tag{VII.7}$$

Squeezing interpretation. We now interpret the operator b as the result of a squeezing operation. We recall the definition of the squeezing operator $S(\eta)$ we introduced in section 2.2.5 of chapter II,

$$S(\eta) = \exp\left[\frac{1}{2}\Big(\eta^* a^2 - \eta a^{\dagger 2}\Big)\right], \tag{VII.8}$$

where $\eta \in \mathbb{C}$ and a is a bosonic annihilation operator. As derived in appendix A.2.2, the action of the squeezing operator on the annihilation operator is given by [17, 34]

$$S(re^{i\theta})^\dagger a S(re^{i\theta}) = a\cosh(r) - a^\dagger e^{i\theta}\sinh(r), \tag{VII.9}$$
$$S(re^{i\theta})^\dagger a^\dagger S(re^{i\theta}) = a^\dagger\cosh(r) - a e^{-i\theta}\sinh(r), \tag{VII.10}$$

where the second equation is obtained by hermitian conjugation of the first.

Let us assume that $b = S(re^{i\theta})^\dagger a S(re^{i\theta})$, and reporting into the diagonal Hamiltonian we find[1]

$$H = \hbar\omega_+ b^\dagger b = \hbar\omega_+\Big(a^\dagger \,\mathrm{ch} - a e^{-i\theta}\,\mathrm{sh}\Big)\Big(a\,\mathrm{ch} - a^\dagger e^{i\theta}\,\mathrm{sh}\Big) \tag{VII.11}$$
$$= \hbar\omega_+ a^\dagger a\,\mathrm{ch}^2 + \hbar\omega_+ a a^\dagger\,\mathrm{sh}^2 - \hbar\omega_+\,\mathrm{ch}\,\mathrm{sh}\Big(a^2 e^{-i\theta} + a^{\dagger 2} e^{i\theta}\Big) \tag{VII.12}$$
$$= \hbar\omega_+ a^\dagger a\big(\mathrm{ch}^2 + \mathrm{sh}^2\big) - \frac{\hbar\omega_+}{2}\,\mathrm{sh}\,2r\Big(a^2 e^{-i\theta} + a^{\dagger 2} e^{i\theta}\Big) \tag{VII.13}$$
$$= \hbar\underbrace{\omega_+\,\mathrm{ch}\,2r}_{=A} a^\dagger a + \hbar\underbrace{\frac{\omega_+\,\mathrm{sh}\,2r}{2}}_{=B}\Big(a^2 e^{-i(\theta+\pi)} + a^{\dagger 2} e^{i(\theta+\pi)}\Big), \tag{VII.14}$$

where we used the bosonic commutation relations of a. Therefore, setting $\theta = \pi$ and choosing r such that $\tanh 2r = \frac{2A}{B}$, we have identified that the terms a^2 + h.c in the Hamiltonian lead to a squeezing transformation. This will prove useful for our study of the generation of non-classical states in the next chapter.

[1] For readability, we write $\mathrm{ch} = \mathrm{ch}\,r = \cosh r$ and $\mathrm{sh} = \mathrm{sh}\,r = \sinh r$.

2.2.2) Diagonalisation of the Hopfield model

We now consider the Hopfield model, which corresponds to a Dicke model in the presence of a diamagnetic term. As previously discussed in chapter III, the Hamiltonian reads

$$H = \hbar\omega_c c^\dagger c + \hbar\omega_m m^\dagger m + \hbar g\Big(c + c^\dagger\Big)\Big(m + m^\dagger\Big) + \hbar D\Big(c + c^\dagger\Big)^2. \tag{VII.15}$$

where c and m are both bosonic annihilation operators. Once again, this Hamiltonian is bosonic and quadratic in c, m and their hermitian conjugates, so that the Hopfield-Bogoliubov method can be applied. Since there are two operators in our system, we define the column vector $\boldsymbol{v}$ by $\boldsymbol{v}^t = \Big(c, m, c^\dagger, m^\dagger\Big)$ and using bosonic commutation relations we rewrite H as

$$\begin{aligned} H &= \frac{\hbar}{2}\omega_c c^\dagger c + \frac{\hbar}{2}\omega_c\Big(cc^\dagger - 1\Big) + \frac{\hbar}{2}\omega_m m^\dagger m + \frac{\hbar}{2}\omega_m\Big(mm^\dagger - 1\Big) && \text{(VII.16)}\\ &\quad + \hbar g\Big(cm + cm^\dagger + c^\dagger m + c^\dagger m^\dagger\Big) + \hbar D\Big(c^2 + cc^\dagger + c^\dagger c + {c^\dagger}^2\Big)\\ &= -\frac{\hbar}{2}(\omega_c + \omega_m) + \frac{\hbar}{2}(\omega_c + 2D)\Big(c^\dagger c + cc^\dagger\Big) + \frac{\hbar}{2}2D\Big(c^\dagger c^\dagger + cc\Big) + \frac{\hbar}{2}\omega_m\Big(m^\dagger m + mm^\dagger\Big)\\ &\quad + \frac{\hbar}{2}g\Big[\Big(c^\dagger m^\dagger + m^\dagger c + cm + mc^\dagger\Big) + \Big(c^\dagger m + m^\dagger c^\dagger + cm^\dagger + mc\Big)\Big] && \text{(VII.17)} \end{aligned}$$

where we have organised the terms such that the matrix formulation is easy to derive. Indeed, neglecting the constant energy offset,

$$H = \tfrac{\hbar}{2}\begin{pmatrix} c^\dagger & m^\dagger & c & m\end{pmatrix}\left(\begin{pmatrix} \omega_c + 2D & 0 & 2D & 0\\ 0 & \omega_m & 0 & 0\\ 2D & 0 & \omega_c + 2D & 0\\ 0 & 0 & 0 & \omega_m\end{pmatrix} + \begin{pmatrix} 0 & g & 0 & g\\ g & 0 & g & 0\\ 0 & g & 0 & g\\ g & 0 & g & 0\end{pmatrix}\right)\begin{pmatrix} c\\ m\\ c^\dagger\\ m^\dagger\end{pmatrix} \tag{VII.18}$$

$$= \frac{\hbar}{2}\boldsymbol{v}^\dagger\begin{pmatrix} \omega_c + 2D & g & 2D & g\\ g & \omega_m & g & 0\\ 2D & g & \omega_c + 2D & g\\ g & 0 & g & \omega_m\end{pmatrix}\boldsymbol{v} \tag{VII.19}$$

$$= \frac{\hbar}{2}\boldsymbol{v}^\dagger\begin{pmatrix} 1 & 0 & 0 & 0\\ 0 & 1 & 0 & 0\\ 0 & 0 & -1 & 0\\ 0 & 0 & 0 & -1\end{pmatrix}\begin{pmatrix} \omega_c + 2D & g & 2D & g\\ g & \omega_m & g & 0\\ -2D & -g & -\omega_c - 2D & -g\\ -g & 0 & -g & -\omega_m\end{pmatrix}\boldsymbol{v} \tag{VII.20}$$

$$= \frac{\hbar}{2}\boldsymbol{v}^\dagger M\eta\boldsymbol{v}. \tag{VII.21}$$

The diagonalisation of M gives the bi-quadratic polaritonic frequencies

$$\omega_\pm^2 = \frac{\omega_c^2 + 4D\omega_c + \omega_m^2}{2} \pm \frac{\sqrt{(\omega_c^2 + 4D\omega_c - \omega_m^2)^2 + 16\omega_c\omega_m g^2}}{2}. \tag{VII.22}$$

and are plotted in figure VII.1. By comparing with the spectrum in the RWA (see equation (III.89)), we see that the trend of energy level repulsion still occurs in the USC regime. The difference between using the RWA and not using it may seem small at the onset of the USC regime ($g/\omega_c = 0.1$), but it is important to pay attention to the order of magnitude of the frequencies here: the observed shift, named the *Bloch-Siegert shift*, is actually around 50 MHz, which is very noticeable experimentally.

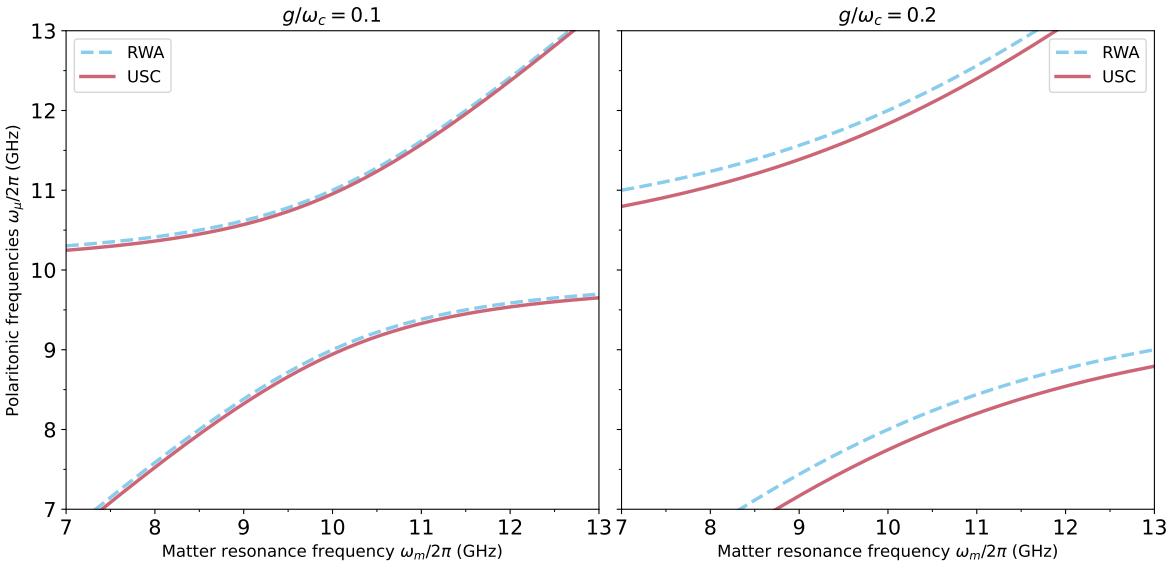


Figure VII.1: Comparison of the spectra of the Dicke model with (dashed blue lines given by equation (VII.22)) and without (solid red lines given by equation (III.89)) the rotating wave approximation, for different values of the coupling strength. In this figure, $\omega_c/2\pi = 10$ GHz.

3) Input-output formalism

In the previous section, we introduced the Hopfield-Bogoliubov method to diagonalise arbitrary quadratic and bosonic Hamiltonians. This analysis considered the system isolated from its environment and this cannot model the experimentally accessible response of a system to e.g. microwave drives. Therefore, to probe systems in the USC, we adapt the input-output formalism introduced in chapter III to the USC regime. We begin by reviewing some of the key differences with the standard approach, and then we illustrate the method on the Hopfield model.

3.1) Differences with the standard input-output theory

To understand why a novel approach to the input-output formalism is needed in the USC, consider the Fourier transform $\mathcal{F}\left[a^\dagger\right](\omega)$ of a bosonic creation operator $a^\dagger$. As shown in appendix A.3, this Fourier transform can be expressed in terms of the Fourier transform of a since $\mathcal{F}\left[a^\dagger\right](\omega) = \mathcal{F}[a]^\dagger(-\omega)$. Thus, in the frequency domain, the inclusion of the counter-rotating terms pushes the system towards negative frequencies. On the other hand, in the standard approach to the quantum Langevin equations and the input-output formalism, the environment is modelled as an infinite number of modes spanning $\pm\infty$. Formally, in chapter III we wrote (see equation (III.151))

$$H_{\text{bath}} = \int_{\mathbb{R}} \mathrm{d}\omega\, \hbar\omega b_\omega^\dagger b_\omega, \tag{VII.23}$$

for the Hamiltonian of a bath. Similarly the interaction of the bath with the cavity was valid for all frequencies $\omega/2\pi \in \mathbb{R}$. This formulation thus allows the cavity system to couple to negative frequency modes representing the environment. As first shown by Ciuti and Carusotto (2006) [225], this is incorrect, since only positive frequencies excitations of the bath are realistic. Thus, in the input-output formalism in the USC, the integration over frequencies are only performed over $\mathbb{R}^+$. As a consequence, it becomes harder to simplify the equations using Fourier transformations, since the integration is not over $\mathbb{R}$, but $\mathbb{R}^+$.

Additionally, in the most general case the Markov approximation[1] is not justified, an issue that can become relevant in the USC. As we will show below, by modifying the expression of the input and output fields, this approximation is not strictly required for the derivation.

[1] Introduced in section 5.1 of chapter III, this approximation consists of assuming that the coupling between the cavity system and the environment is frequency independent.

3.2) Example: Hopfield model

As an example, we consider an input-output theory for the Hopfield Hamiltonian, which we diagonalised in the previous section. We recall that the Hamiltonian reads

$$H_{\text{sys}} = \hbar\omega_c c^\dagger c + \hbar\omega_m m^\dagger m + \hbar g(c+c^\dagger)(m+m^\dagger) + \hbar D(c+c^\dagger)^2 \tag{VII.24}$$

where c (m) is the annihilation operator corresponding to the light (matter) degree of freedom. We consider that the cavity mode c couples to two microwave ports that are used to probe the cavity, while the matter mode couples to another bosonic bath modelling intrinsic dissipation. The details of the derivation are given in appendix B.14, and we merely identify the key steps here.

The first step consists of writing the quantum Langevin equations for all the operators appearing in the Hamiltonian. The equations can be written as

$$\frac{\mathrm{d}c}{\mathrm{d}t} = \frac{1}{i\hbar}[c, H_{\text{sys}}] - \int_{-\infty}^{+\infty} \mathrm{d}t'\, \Gamma_c(t-t')c(t') + F_c(t) \tag{VII.25}$$

$$\frac{\mathrm{d}m}{\mathrm{d}t} = \frac{1}{i\hbar}[m, H_{\text{sys}}] - \int_{-\infty}^{+\infty} \mathrm{d}t'\, \Gamma_m(t-t')m(t') + F_m(t) \tag{VII.26}$$

$$\left(\frac{\mathrm{d}c}{\mathrm{d}t}\right)^\dagger = \frac{1}{i\hbar}\left[c^\dagger, H_{\text{sys}}\right] - \int_{-\infty}^{+\infty} \mathrm{d}t'\, \Gamma_c^*(t-t')c^\dagger(t') + F_c^\dagger(t) \tag{VII.27}$$

$$\left(\frac{\mathrm{d}m}{\mathrm{d}t}\right)^\dagger = \frac{1}{i\hbar}\left[m^\dagger, H_{\text{sys}}\right] - \int_{-\infty}^{+\infty} \mathrm{d}t'\, \Gamma_m^*(t-t')m^\dagger(t') + F_m^\dagger(t) \tag{VII.28}$$

where $\Gamma_{c,m}$ are the memory kernels and $F_{c,m}$ the Langevin forces. The memory kernels involve the frequency-dependent coupling $\kappa(\omega)$ of the cavity mode with the ports. The memory kernels are complex valued, with the real part inducing a broadening of the linewidths, and the imaginary part a shift of the resonance frequencies [225]. The Langevin forces are proportional to the input and output fields. Note that the equations of the creation operators were not needed in the standard approach to the input-output formalism. Similar to the Hopfield-Bogoliubov diagonalisation, it becomes necessary to double the degrees of freedom in the USC, by taking into account the annihilation operators as well as the creation operator.

The system above is non-linear due to the presence of convolutions (second term on the right-hand side). The next step is to consider the frequency domain, in which the system of equations becomes linear. The property $\mathcal{F}\left[a^\dagger\right](\omega) = \mathcal{F}[a]^\dagger(-\omega)$ is used to obtain the system

$$M(\omega)\begin{pmatrix} \widetilde{c}(\omega) \\ \widetilde{m}(\omega) \\ \widetilde{c}^\dagger(-\omega) \\ \widetilde{m}^\dagger(-\omega) \end{pmatrix} = i\begin{pmatrix} \widetilde{F}_c(\omega) \\ \widetilde{F}_m(\omega) \\ \widetilde{F}_c^\dagger(-\omega) \\ \widetilde{F}_m^\dagger(-\omega) \end{pmatrix} \tag{VII.29}$$

where the matrix M involves the Fourier transforms of Γ_c and Γ_m. Inverting this equation, we find

$$\begin{pmatrix} \widetilde{c}(\omega) \\ \widetilde{m}(\omega) \\ \widetilde{c}^\dagger(-\omega) \\ \widetilde{m}^\dagger(-\omega) \end{pmatrix} = G(\omega)\begin{pmatrix} \widetilde{F}_c(\omega) \\ \widetilde{F}_m(\omega) \\ \widetilde{F}_c^\dagger(-\omega) \\ \widetilde{F}_m^\dagger(-\omega) \end{pmatrix} \tag{VII.30}$$

where $G = iM^{-1}$ is analogous to a Green's function. Since $\widetilde{F}_c$ is proportional to the input and output fields, this system provides a first relation between the systems operators c, m and the input and output fields. Combined with the input-output relations, we can solve for the output fields in terms of the input fields to finally obtain

$$\begin{pmatrix} p_{1,\omega}^{\text{out}} \\ p_{2,\omega}^{\text{out}} \end{pmatrix} = U(\omega)\begin{pmatrix} p_{1,\omega}^{\text{in}} \\ p_{2,\omega}^{\text{in}} \end{pmatrix} \tag{VII.31}$$

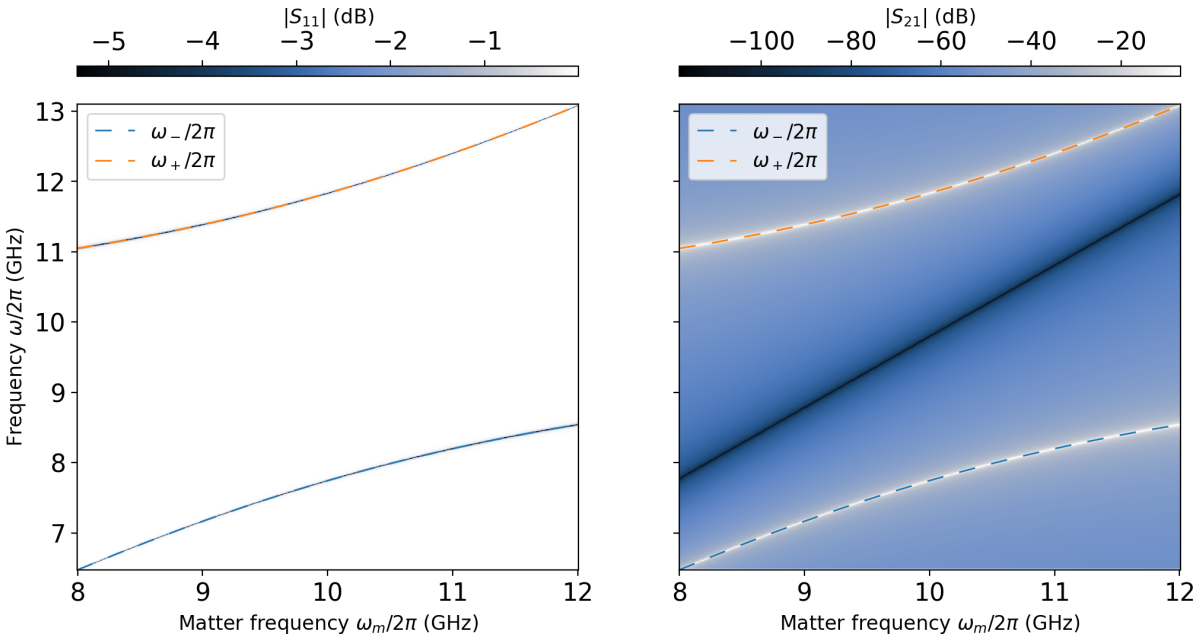


Figure VII.2: Plot of the reflection (left) and transmission (right) coefficient for the Dicke model with intrinsic damping rate $\gamma_c/2\pi = 2$ MHz ($\gamma_m/2\pi = 2$ MHz) for the cavity (magnon) mode, identical coupling to the ports $\gamma_1/2\pi = \gamma_2/2\pi = 10$ MHz. We set $\omega_c/2\pi = 10$ GHz, and $g/2\pi = 1$ GHz giving $g/\omega_c = 0.2$. The theoretical spectra using a Hopfield-Bogoliubov diagonalisation is given by the dashed lines.

where U is a 2×2 matrix and $p^{\text{in}}_{j,\omega}, p^{\text{out}}_{j,\omega}$ are the input and output fields of frequency $\omega/2\pi$ of port $j \in \{1, 2\}$. Noting U_{ij} the matrix elements of U, the reflection and transmission coefficients are given by

$$S_{11}(\omega) = U_{11}(\omega), \tag{VII.32}$$
$$S_{21}(\omega) = U_{21}(\omega), \tag{VII.33}$$

i.e the matrix elements of U.

Using the results derived in appendix B.14, we numerically calculated the reflection and transmission coefficients for parameters identical to that of figure III.6, i.e. and intrinsic cavity (matter) mode damping rate $\gamma_c/2\pi = 2$ MHz ($\gamma_m/2\pi = 1$ MHz), and coupling to the ports $\gamma_1/2\pi = \gamma_2/2\pi = 10$ MHz. The results are plotted in figure VII.2 along with the theoretical spectrum. We see that the resonance dips and transmission resonances follow closely the theoretical spectrum, thus validating our results.

4) Phenomenology of the USC regime

Having introduced the appropriate theoretical tools for the description of USC systems, we now focus on the physics of light/matter interaction models in the USC. We begin by discussing the effects of the counter-rotating terms in the Dicke model. Next, we introduce sum rules in section 4.2, which applied to the quantum Rabi model gives the Thomas-Reiche-Kuhn sum rule. This important result allows to bound the diamagnetic term, and hence justifies its ommision or inclusion in the USC, discussed in section 4.3. Finally, the issue of gauge-invariance is tackled in section 4.4.

4.1) Virtual excitations and squeezing

We consider the Dicke model

$$H = \hbar\omega_c c^\dagger c + \hbar\omega_m m^\dagger m + \hbar g\Big(c + c^\dagger\Big)\Big(m + m^\dagger\Big) \tag{VII.34}$$

and the Tavis-Cummings model

$$H_{\text{RWA}} = \hbar\omega_c c^\dagger c + \hbar\omega_m m^\dagger m + \hbar g\Big(cm^\dagger + c^\dagger m\Big) \tag{VII.35}$$

which results from the application of the rotating wave approximation to the Dicke model. In the Tavis-Cummings model, the total number of excitations in the system, given by the operator $N = c^\dagger c + m^\dagger m$ is a conserved quantity. To derive this, recall from appendix A.1 that we have $[a, a^\dagger a] = a$ and $[a^\dagger, a^\dagger a] = -a^\dagger$ for a bosonic operator a. Therefore, we find that N commutes with the Tavis-Cummings Hamiltonian, i.e. $[N, H_{\text{RWA}}] = 0$. Thus, the Heisenberg equation of motion for N gives $\dot{N} = \frac{1}{i\hbar}[N, H_{\text{RWA}}] = 0$ so that N is constant in time, i.e. a conserved quantity.

The Dicke model, however, does not conserve the total number of excitation because of the counter rotating terms cm and $c^\dagger m^\dagger$. However, the parity of the number of excitations, given by the operator $\Pi = \exp\big(i\pi(c^\dagger c + m^\dagger m)\big)$, is conserved [202, 203]. To intuitively understand the effects of the counter-rotating terms, we can use perturbation theory in $\lambda = \frac{g}{\omega_c + \omega_m}$ using Schrieffer-Wolff transformations, which we introduced in chapter III. Formally, we partition the Dicke model as

$$H = \hbar\omega_c c^\dagger c + \hbar\omega_m m^\dagger m + \hbar g\Big(cm^\dagger + c^\dagger m\Big) + \hbar g\Big(cm + c^\dagger m^\dagger\Big) \tag{VII.36}$$

$$= H_{\text{RWA}} + \hbar g\Big(cm + c^\dagger m^\dagger\Big) \tag{VII.37}$$

and treat the last term (the counter rotating terms) as a perturbation in $\lambda \ll 1$. After some algebra detailed in appendix B.15, we find that to first order in λ, H is transformed to

$$H' = H_{\text{RWA}} - \hbar g\lambda\left[\left(c^\dagger c + \frac{1}{2}\right) + \left(m^\dagger m + \frac{1}{2}\right)\right] - \hbar g\lambda\Big(c^2 + c^{\dagger 2} + m^2 + m^{\dagger 2}\Big) + \mathcal{O}(\lambda) \tag{VII.38}$$

$$= \hbar\omega_c' c^\dagger c + \hbar\omega_m' m^\dagger m + \hbar g\Big(cm^\dagger + c^\dagger m\Big) + \hbar\frac{g^2}{\omega_c + \omega_m}\Big(c^2 + c^{\dagger 2} + m^2 + m^{\dagger 2}\Big) + \mathcal{O}(\lambda), \tag{VII.39}$$

where $\omega_c' = \omega_c - \frac{g^2}{\omega_c + \omega_m}$ and $\omega_m' = \omega_m - \frac{g^2}{\omega_c + \omega_m}$. Hence, we deduce that to first order in perturbation theory, the counter rotating terms renormalise the modes frequencies ($\omega_c'/2\pi$ and $\omega_m'/2\pi$), and introduce non-linear terms c^2, m^2 and their hermitian conjugate. Having interpreted the terms c^2 as squeezing terms in section 2.2.1, we conclude that the counter rotating terms induce a two-mode squeezing of the system [445].

One consequence of this squeezing is that the ground state of the Dicke Hamiltonian, which we note $|G\rangle$ is composed of a superposition of number states of both light and matter. In other words, the expectation value of the number operators for the light ($c^\dagger c$) or matter ($m^\dagger m$) degrees of freedom with respect to the ground state $|G\rangle$ does not vanish. Formally, we have both $\langle G|c^\dagger c|G\rangle \neq 0$ and $\langle G|m^\dagger m|G\rangle \neq 0$. As a result the ground state of the Dicke Hamiltonian exhibits non-vanishing entanglement between light and matter, as recently studied by Miao and Agarwal (2023) [446].

The standard quantum theory of photodetection put forward by Glauber (1963) [447] leads to a photodetection probability proportional to $\langle c^\dagger c\rangle$. Therefore, since $\langle G|c^\dagger c|G\rangle \neq 0$, we expect a non-vanishing detection probability, despite the system being in its ground state. The reason behind this conclusion is that in the ultrastrong coupling regime, the photodection probability is not proportional to $\langle c^\dagger c\rangle$ anymore, as tackled by Di Stefano et al. (2018) [448]. Indeed, the excitations present in the ground state are *virtual excitations*, and contrary to real excitations they cannot be detected. For instance, Ciuti and Carusotto (2006) [225] showed using an input-output theory that for a vacuum input into a cavity QED system, the output of that cavity is still a vacuum, despite the presence of squeezed vacuum inside the cavity. The concept of virtual excitations and their associated virtual quasi-particles has allowed to use some tools of quantum field theory, such as Feynman diagrams, to describe systems in the USC regime [438].

4.2) Sum rules

The Thomas-Reiche-Kuhn sum rule. Sum rules are useful relations between a sum of unknown terms and a known quantity, and have applications in quantum mechanics [436]. Let

us consider a hermitian operator O, and a Hamiltonian H with eigenstates $|\psi_k\rangle$ with energy $\hbar\omega_k$. Then, following Wang (1999) [449] we prove in appendix B.16 that the following sum rule holds

$$\langle\psi_i|[O,[H,O]]|\psi_i\rangle = 2\sum_j (\hbar\omega_j - \hbar\omega_i)|\langle\psi_i|O|\psi_j\rangle|^2. \tag{VII.40}$$

The application of this sum rule to the position operator of a massive particle coupling to an electromagnetic field gives the *Thomas-Reiche-Kuhn sum rule*. To derive it, we begin by expanding the minimal coupling Hamiltonian of this particle, assumed to be of charge q, to find

$$H = \frac{p^2}{2m} - q\frac{pA}{m} + \frac{q^2A^2}{2m}, \tag{VII.41}$$

with A the vector potential, p the momentum of the particle and m its mass. Recalling that $[x,p] = i\hbar$ and $[x,p^2] = 2i\hbar p$ (see appendix A.1), we have

$$[x,[H,x]] = \left[x,\left[\frac{p^2}{2m} - q\frac{pA}{m},x\right]\right] = \left[x,-\frac{i\hbar p}{m} - q\frac{A}{m}(-i\hbar)\right] = \frac{\hbar^2}{m}, \tag{VII.42}$$

and the sum rule above gives

$$\langle\psi_i|[x,[H,x]]|\psi_i\rangle = \frac{\hbar^2}{m} = 2\sum_j (\hbar\omega_j - \hbar\omega_i)|\langle\psi_i|x|\psi_j\rangle|^2. \tag{VII.43}$$

We see that left hand side of Thomas-Reiche-Kuhn sum rule gives a numerical value, which can then be used to estimate the right hand side.

This result is useful to estimate the value of the diamagnetic term in the quantum Rabi model, which we recall reads (equation (III.63))

$$H = \hbar\omega_c c^\dagger c + \frac{1}{2}\hbar\omega_m\sigma_z + \hbar g\left(c + c^\dagger\right)\sigma_x + \hbar D\left(c + c^\dagger\right)^2, \tag{VII.44}$$

where $D = \frac{1}{\hbar}\frac{q^2A_0^2}{2m}$ is the diamagnetic term with A_0 the amplitude of the vector potential, and $g/2\pi$ is the coupling strength. The coupling strength considers the two lowest energy states of the matter degree of freedom,

$$g = \frac{(\omega_1 - \omega_0)A_0}{\hbar}\mu_{01} \tag{VII.45}$$

with $\hbar\omega_m = \hbar(\omega_1 - \omega_0)$ the energy spacing between the two lowest eigenstates (energies $\hbar\omega_0$ and $\hbar\omega_1$), and $\mu_{01} = e\langle\psi_1|x|\psi_0\rangle$ the associated electric dipole moment. More generally, we can have higher energy levels $\hbar\omega_k$ for the matter degree of freedom, and therefore higher-order electric dipole transitions $\mu_{ij} = e\langle\psi_j|x|\psi_i\rangle$ (assumed real for simplicity) between the states of energy $\hbar\omega_i$ and $\hbar\omega_j$. Multiplying the Thomas-Reiche-Kuhn sum rule of equation (VII.43) by the charge e^2, we find [450]

$$\forall i, \quad \sum_j \hbar(\omega_k - \omega_i)\mu_{ij}^2 = \frac{(e\hbar)^2}{2m}, \tag{VII.46}$$

and using this expression for $i = 0$ in the diamagnetic term,

$$\hbar D = \frac{e^2A_0^2}{2m} = \frac{A_0^2}{\hbar}\frac{(e\hbar)^2}{2m} = \frac{A_0^2}{\hbar}\sum_{j\geqslant 1}\hbar(\omega_k - \omega_0)\mu_{0j}^2 \tag{VII.47}$$

$$= \frac{A_0^2}{\hbar}\hbar(\omega_1 - \omega_0)\mu_{01}^2 + \frac{A_0^2}{\hbar}\sum_{j\geqslant 2}\hbar(\omega_k - \omega_0)\mu_{0j}^2 \tag{VII.48}$$

$$= \hbar\frac{\left(\frac{(\omega_1-\omega_0)A_0}{\hbar}\mu_{01}\right)^2}{(\omega_1 - \omega_0)} + \frac{A_0^2}{\hbar}\sum_{j\geqslant 2}\hbar(\omega_k - \omega_0)\mu_{0j}^2 \tag{VII.49}$$

$$= \hbar\frac{g^2}{(\omega_1 - \omega_0)} + \frac{A_0^2}{\hbar}\sum_{j\geqslant 2}\hbar(\omega_k - \omega_0)\mu_{0j}^2 \tag{VII.50}$$

and thus $D \geqslant \frac{g^2}{(\omega_1-\omega_0)}$, which gives a lower bound when a single transition is considered. Recalling that $\hbar\omega_m = \hbar(\omega_1 - \omega_0)$, the Rabi model is therefore often written

$$H = \hbar\omega_c c^\dagger c + \frac{1}{2}\hbar\omega_m\sigma_z + \hbar g\Big(c + c^\dagger\Big)\sigma_x + \hbar\frac{g^2}{\omega_m}\Big(c + c^\dagger\Big)^2, \tag{VII.51}$$

after application of the Thomas-Reiche-Kuhn sum rule. Having an expression for the diamagnetic term allows to analyse the occurrence of phase transitions in the Rabi model [451].

Sum rule for photons. In the preceding Thomas-Reiche-Kuhn sum rule, the matrix elements involved the matter degrees of freedom. A general sum rule, valid for photons at arbitrary light/matter interactions, was proposed by Savasta, Stefano, and Nori [436]. They considered the Hamiltonian $H = H_{\text{light}} + H_{\text{matter}} + H_I$ with H_{light} the Hamiltonian of the electromagnetic field, H_{matter} the Hamiltonian for the matter degrees of freedom, and H_I the light/matter interaction. The eigenstates of H are noted $|\psi_i\rangle$ and have energy ω_i, and they considered a one-dimensional expansion of the vector potential

$$A(x,t) = \sum_n A_n(x) c_n e^{-i\omega_n t} + \text{h.c}, \tag{VII.52}$$

where $A_n(x)$ contains the constants and the mode functions, and c_n are the annihilation operators for the mode n of frequency $\omega_n/2\pi$. The quadratures of the n-th mode are defined as

$$\mathcal{Q}^{(n)} = \frac{c_n + c_n^\dagger}{\sqrt{2}}, \quad \mathcal{P}^{(n)} = i\frac{c_n^\dagger - c_n}{\sqrt{2}}. \tag{VII.53}$$

Introducing the notation $\omega_{ji} = \omega_j - \omega_i$, a general sum rule is

$$\sum_k \frac{\omega_{ki} + \omega_{kj}}{\omega_n} \langle\psi_i|\mathcal{Q}^{(n)}|\psi_k\rangle \langle\psi_k|\mathcal{Q}^{(n)}|\psi_j\rangle = \delta_{ij} \tag{VII.54}$$

provided that $\big[\mathcal{Q}^{(n)}, H\big] = \big[\mathcal{Q}^{(n)}, H_F\big]$ holds. Note that in this sum rule, the matrix elements are taken with respect to the quadratures of light, and that the states are eigenstates of the total light-matter Hamiltonian. A proof of this result is provided in appendix B.18.

As an application of this general sum rule, we consider the Hamiltonian for two coupled bosonic modes c and m given by the Dicke Hamiltonian

$$H = \hbar\omega_c c^\dagger c + \hbar\omega_m m^\dagger m + \hbar g\Big(c + c^\dagger\Big)\Big(m + m^\dagger\Big) = \sum_\mu \hbar\omega_\mu p_\mu^\dagger p_\mu, \tag{VII.55}$$

where we introduced the polariton annihilation operators p_μ diagonalising the Hamiltonian. Since there is a single mode for the cavity, the sum rule reads

$$\sum_\mu \frac{\omega_{\mu i} + \omega_{\mu j}}{\omega_c} \langle\psi_i|\frac{c + c^\dagger}{\sqrt{2}}|\psi_\mu\rangle \langle\psi_\mu|\frac{c + c^\dagger}{\sqrt{2}}|\psi_j\rangle = \delta_{ij}, \tag{VII.56}$$

whre $|\psi_\mu\rangle$ are the energy eigenstates of the polaritons. For $\nu = i = j$, this becomes

$$\sum_\mu \frac{2\omega_{\mu\nu}}{\omega_c}\left|\langle\psi_\nu|\frac{c + c^\dagger}{\sqrt{2}}|\psi_\mu\rangle\right|^2 = 1. \tag{VII.57}$$

We note that $\hbar\omega_k$ is the energy of the full Dicke Hamiltonian, and thus it is non-trivial to evaluate the matrix elements. Indeed, we would like to express $c+c^\dagger$ in terms of the polaritonic operators p_μ, but this relation is complex.

4.3) Diamagnetic term and its consequences

Light-matter decoupling. The presence of a diamagnetic term in a light/matter interaction model can lead to very important physical consequences. One unexpected result, first shown by De Liberato (2014) [437] and then by Garcia-Ripoll, Peropadre, and Liberato (2015) [452], is the decoupling of light and matter far in the ultrastrong coupling regime ($g/\omega_c \simeq 1$). He considered a single matter bosonic modes coupling to several cavity modes, leading to multimode Hopfield model. For significant values of the coupling strength, the diamagnetic terms dominate, and the minimisation of the system's energy leads to the electromagnetic field having vanishing amplitudes at the location of the dipoles. Therefore, the cavity modes do not interact with the matter degrees of freedom, leading to decoupling. This example shows that in the presence of a diamagnetic term, one cannot hope to increase the rate of quantum information exchange between light and matter indefinitely.

Phase transitions. Another interesting effect of the diamagnetic term concerns the possibility of a phase transition in the Dicke model. To see this, let us consider the spectrum of the Dicke model, which from equation (VII.22) (after setting the diamagnetic term $D = 0$) reads

$$\omega_{\pm}^2 = \frac{\omega_c^2 + \omega_m^2}{2} \pm \frac{\sqrt{(\omega_c^2 - \omega_m^2)^2 + 16\omega_c\omega_m g^2}}{2}. \tag{VII.58}$$

The actual polaritonic frequencies are $\sqrt{\omega_{\pm}^2}$, and therefore this latter square root must be defined. For the ω_- solution, this requires the first term of equation (VII.58) to be greater than the second term. Formally, we need

$$\left(\omega_c^2 + \omega_m^2\right)^2 \geqslant (\omega_c^2 - \omega_m^2)^2 + 16\omega_c\omega_m g^2, \tag{VII.59}$$

which after some re-arranging implies

$$g \leqslant g_c = \frac{\sqrt{\omega_c\omega_m}}{2}. \tag{VII.60}$$

When the coupling strength is above the critical value g_c, the eigenvalue become complex valued, and the Dicke Hamiltonian is not applicable. Indeed, at the critical value of the coupling strength, the parity symmetry of the Dicke model is spontaneously broken, and a supperradiant phase transition occurs [199, 200]. In this supperadiant phase, another version of the Dicke model (its superradiant form) should be considered instead, which can be obtained by following the approach[1] developed by Emary and Brandes [202, 203]. The critical observation is that the physics of the standard and supperadiant Dicke model are very different.

However, in the presence of a diamagnetic term, the superradiant phase transition does not occur. To see this, let us restore the diamagnetic term in equation (VII.58). This time, the condition for the square root to be defined is

$$\left(\omega_c^2 + 4D\omega_c + \omega_m^2\right)^2 \geqslant (\omega_c^2 + 4D\omega_c - \omega_m^2)^2 + 16\omega_c\omega_m g^2, \tag{VII.61}$$

which leads to

$$g \leqslant g_c = \frac{\sqrt{(\omega_c + 4D)\omega_m}}{2}. \tag{VII.62}$$

Using the Thomas-Reiche-Kuhn sum rule $D \geqslant \frac{g^2}{\omega_m}$, we find

$$g \leqslant \sqrt{g^2 + \frac{\omega_c\omega_m}{4}} \tag{VII.63}$$

which is always satisfied. Therefore, the presence of a diamagnetic term, combined with the Thomas-Reiche-Kuhn sum rule, prevents the occurrence of the superradiant phase transition.

[1] The trick consists in displacing the bosonic modes as $a \mapsto a + \sqrt{\alpha}$ and $b \mapsto b - \sqrt{\beta}$ with α and β constants to be determined so that the resulting Hamiltonian remains quadratic. However, we need to consider the Dicke Hamiltonian before the first-order expansion of the Holstein-Primakoff transformation. The details of this calculation can be found in [202, 203].

4.4) Gauge invariance

As we saw above, the diamagnetic term originates from the expansion of the minimal coupling Hamiltonian of a particle to the electromagnetic field. The principle of gauge invariance tells us that we could choose another vector potential (corresponding to another gauge) for the derivation of light/matter models. In theory, a gauge transformation should not impact the physical predictions, in particular the possibility of a phase transition.

However, starting from the Rabi model in the Coulomb gauge (see equation (III.63)), De Bernardis et al. (2018) [453] showed that performing a gauge transformation to the dipole gauge led to a model exhibiting different physics. Similarly, Stokes and Nazir (2019) [454] showed that one could interpolate between the Jaynes-Cummings model (which we recall corresponds to the Rabi model under the rotating wave approximation) and the Rabi model by appropriate gauge transformations. This would effectively mean that both models have the same physics, which is a contradiction.

This gauge invariance problem was traced back to the two-level system approximation for the matter degrees of freedom: the Rabi model derived in the Coulomb gauge had already lost its ability to preserve gauge-invariance. Indeed, the truncation of the Hilbert space of a particle in a potential $V(x)$, with x the position operator, introduces a *non-local potential* $V(x,p)$, where p is the momentum of the particle.

Therefore, after truncation of the Hilbert space of the matter degrees of freedom, the minimal coupling replacement should be performed on the kinetic energy term of the particle

$$\frac{p^2}{2m} \mapsto \frac{(p-qA)^2}{2m}, \tag{VII.64}$$

but also on the non-local potentials $V(x,p)$. Such generalised minimal coupling replacements were first introduced by Di Stefano et al. (2019) [450] and applied to the quantum Rabi model. Later, Garziano et al. (2020) [455] applied the same procedure to the Dicke and Hopfield Hamiltonians.

Finally, we would like to mention that time-dependent interactions are another source of gauge ambiguities [456, 457], but we do not discuss these issues here. In summary, issues related to gauge invariance are related to the improper truncation of the degrees of freedom, and time-dependent interactions.

5) Cavity magnonics in the USC

As seen in the previous chapter, new techniques had to be developed to correctly describe the physics of the USC and DSC regimes. These techniques have been abundantly applied to circuit QED and two-dimensional electron gases in quantum wells. On the other hand, these theoretical techniques have not been applied to cavity magnonics system which have demonstrated USC in several experiments [458–465].

Notably, two recent experiments [464, 465] highlighted the fact that the usual Dicke Hamiltonian for describing magnon-photon system fails in the ultrastrong coupling regime. To be more specific, [465] observed that a shift of the magnon resonance frequency $\omega_m/2\pi$ which scaled as g^2/ω_c. In the unpublished original work of appendix C.7, we explore possible reasons for this frequency shift.

6) Cavity-mediated ultrastrong magnon-magnon coupling

As explained in chapters II and IV, cavity magnonics is an interesting platforms for quantum transduction applications. The ultrastrong coupling regime allows to reach faster quantum information exchange rate, and therefore reaching the ultrastrong coupling regime in cavity magnonics promises faster quantum information transduction capabilities. In chapter IV, and more particularly in [1], we explained that cavity modes could act as a bridge to couple two distant YIG samples. This indirect coupling was derived under the rotating wave approximation, which is invalid in the USC regime. Therefore, in the unpublished work of appendix C.8,

we investigate how the indirect coupling is modified in the presence of counter rotating terms, and whether it can reach the ultrastrong coupling regime.

7) Conclusion and outlook

In this chapter, we have generalised the methods introduced in chapter III to treat hybrid light-matter systems in the ultrastrong coupling regime. Notably, we saw that the many approximations that break down in this regime represent an opportunity to explore a rich phenomenology. We also saw that the additional terms presents in the Hamiltonian, such as the counter-rotating terms or the diamagnetic terms, are non-linear, and thus naturally induce squeezing and entanglement. In the following chapter, we shall focus on several methods to create entanglement and non-classical states. We will see that non-linear terms play an important role in the generation of entanglement, illustrating how the ultrastrong coupling regime can be seen as a resource to induce non-classical effects.

Chapter VIII

Engineering non-classical states using non-linear bosonic interactions

Summary

We review several schemes to create non-classical states based on non-linear bosonic interactions. We introduce a pictorial representation which provides a unified understanding of the schemes, and highlights the need for both non-linear and linear interactions. In the original and unpublished work of appendix C.9, we investigate the capability of a non-linear interaction usually neglected in cavity magnonics to create entanglement. The overall discussion, while being general, highlights the potential of cavity magnonics to create entangled state of light and matter due to its many non-linearities and coupling capabilities.

Contents

1) Introduction . . . **138**
2) General principles . . . **139**
2.1 Method and example . . . 139
2.2 Linearisation and strong driving . . . 141
3) Some non-linear bosonic interactions . . . **141**
3.1 Optomechanical interaction . . . 141
3.2 Kerr interactions . . . 143
3.3 Wave mixing . . . 143
3.3.1 Three-wave mixing . . . 143
3.3.2 Parametric and squeezed driving . . . 144
4) Hybrid schemes . . . **144**
5) Enhancing entanglement . . . **147**
6) Conclusion . . . **148**

1) Introduction

In chapter II, we presented some states of interest for quantum information processing, notably squeezed states and Schrödinger cat states. In this chapter, we will now examine different method to create these states, relying on the non-classical measures introduced in chapter II. The focus will be put on-linear bosonic interactions as a source of non-classicality, even though alternatives exist, such as dissipative coupling and discrete variable systems.

We begin this chapter by recalling the general method introduced in chapter II for the computation of bipartite entanglement between two bosonic modes. We illustrate this on the Dicke model in the ultrastrong coupling regime, highlighting its potential for the generation

of non-classical states. Additionally, we outline the linearisation procedure used when dealing with non-linear interactions. Next, in section 3, we review several non-linear interactions and their appearance in various physical platforms. The potential of each interaction for the creation of quantum behaviours is discussed. Notably, we apply methods developed for cavity optomechanics to investigate whether a similar non-linear interaction in cavity magnonics can lead to a novel method to generate bipartite magnon-photon entanglement (original unpublished work discussed in appendix C.9). Building on these different non-linearities, in section 4 we introduce diagrams which allow to easily understand the potential bipartite entanglements which can be created in a hybrid system. Alternatively, this formalism helps in designing scheme to create particular quantum effects, by using two elementary building blocks: non-linear and linear interactions. Finally, in section 5 we succinctly comment on different methods to increase the quality of the generated entanglement. We conclude in section 6.

2) General principles

2.1) Method and example

In section 2.3.2 of chapter II, we introduced several non-classical measures for Gaussian states. The starting point of the discussion was equation (II.59), which reads

$$\dot{\mathbf{u}}(t) = A(t)\mathbf{u}(t) + \mathbf{n}(t), \tag{VIII.1}$$

describing a linear relation between the quadratures of the modes (represented by the vector $\mathbf{u}$) governed by the drift matrix A, and in the presence of noise (represented by the vector $\mathbf{n}$). From our discussion of quantum Langevin equations (QLEs) in chapter III, we now know how to obtain such a relation between the different quadratures of the modes in the presence of noise.

As an example, let us consider the Dicke model with Hamiltonian

$$H = \hbar\omega_c c^\dagger c + \hbar\omega_m m^\dagger m + \hbar g(c + c^\dagger)(m + m^\dagger). \tag{VIII.2}$$

The quantum Langevin equations can be written

$$\dot{c} = -i(\omega_c - i\kappa_c)c - ig(m + m^\dagger) - \sqrt{2\kappa_c}c^{\text{in}} \tag{VIII.3}$$

$$\dot{m} = -i(\omega_m - i\kappa_m)c - ig(c + c^\dagger) - \sqrt{2\kappa_m}m^{\text{in}} \tag{VIII.4}$$

where $\kappa_c/2\pi$ ($\kappa_c/2\pi$) are the dissipation rates[1] of the cavity (magnon) mode, and c^{in} (m^{in}) the associated noise input operator. We define X, Y to be the quadratures of c, x, y the quadratures of m, $X^{\text{in}}, Y^{\text{in}}$ the quadratures of c^{in}, and $x^{\text{in}}, y^{\text{in}}$ the quadratures of m^{in}. Therefore, by appropriate linear combinations of the two QLE above, we find[2]

$$\dot{X} = -\kappa_c X + \omega_c Y - \sqrt{2\kappa_c}X^{\text{in}} \tag{VIII.5}$$

$$\dot{Y} = -\kappa_c Y - \omega_c X - 2gx - \sqrt{2\kappa_c}Y^{\text{in}} \tag{VIII.6}$$

$$\dot{x} = -\kappa_m x + \omega_m y - \sqrt{2\kappa_c}x^{\text{in}} \tag{VIII.7}$$

$$\dot{y} = -\kappa_m y - \omega_m x - 2gX - \sqrt{2\kappa_c}y^{\text{in}} \tag{VIII.8}$$

and therefore we have equation (VIII.1) with $\mathbf{n} = (\sqrt{2\kappa_c}X^{\text{in}}, \sqrt{2\kappa_c}Y^{\text{in}}, \sqrt{2\kappa_m}x^{\text{in}}, \sqrt{2\kappa_m}y^{\text{in}})$, $\mathbf{u} = (X, Y, x, y)^t$, and the drift matrix

$$A = \begin{pmatrix} -\kappa_c & \omega_c & 0 & 0 \\ -\omega_c & -\kappa_c & -2g & 0 \\ 0 & 0 & -\kappa_m & \omega_m \\ -2g & 0 & -\omega_m & -\kappa_m \end{pmatrix}. \tag{VIII.9}$$

[1] Contrary to the conventions used in chapters III and VII, the usual dissipation rate $\kappa/2\pi$ is replaced by $\kappa \mapsto \kappa/2$, as is common in the literature regarding non-classical states. While is just a matter of convention, we must be careful during numerical evolution.

[2] One can use the rules from appendix B.17

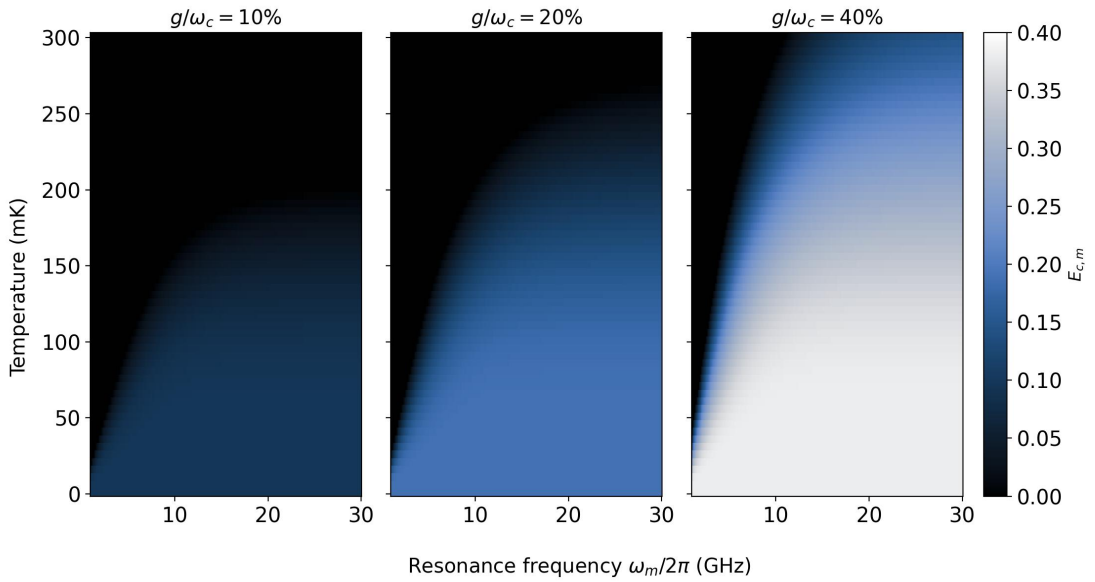


Figure VIII.1: Bipartite entanglement $E_{c,m}$ between the two bosonic modes of the Dicke model for $\omega_c/2\pi = 10$ GHz, $\kappa_c/2\pi = \kappa_m/2\pi = 0.5$ MHz.

Assuming the system is in thermal equilibrium, the noise operators have zero mean ($\langle c^{\text{in}} \rangle = 0$) and the correlations

$$\left\langle c^{\text{in}}(t)c^{\text{in}\dagger}(t') \right\rangle = (N(\omega_c, T) + 1)\delta(t - t'), \quad \left\langle c^{\text{in}\dagger}(t)c^{\text{in}}(t') \right\rangle = N(\omega_c, T)\delta(t - t'), \tag{VIII.10}$$

$$\left\langle c^{\text{in}}(t)c^{\text{in}}(t') \right\rangle = \delta(t - t'), \quad \left\langle c^{\text{in}\dagger}(t)c^{\text{in}\dagger}(t') \right\rangle = \delta(t - t'), \tag{VIII.11}$$

with

$$N(\omega, T) = \frac{1}{e^{\frac{\hbar\omega}{k_b T}} - 1} \tag{VIII.12}$$

the Bose-Einstein distribution, $k_B = 86.17 \times 10^{-3}$ meV/K the Boltzmann constant. This allows us to compute the diffusion matrix $D = (D_{ij})$, which we recall is given by equation (II.61),

$$D_{ij} = \frac{1}{2} \langle n_i n_j + n_j n_i \rangle . \tag{VIII.13}$$

We have

$$\left\langle X^{\text{in}} X^{\text{in}} \right\rangle = \left\langle \left(\frac{c^{\text{in}} + c^{\text{in}\dagger}}{\sqrt{2}} \right) \left(\frac{c^{\text{in}} + c^{\text{in}\dagger}}{\sqrt{2}} \right) \right\rangle = \frac{1}{2} \left\langle c^{\text{in}} \left(c^{\text{in}}\right)^\dagger + \left(c^{\text{in}}\right)^\dagger c^{\text{in}} \right\rangle \tag{VIII.14}$$

$$= \frac{1}{2}(2N(\omega_c, T) + 1) \tag{VIII.15}$$

$$\left\langle Y^{\text{in}} Y^{\text{in}} \right\rangle = -\frac{1}{2} \left\langle \left(c^{\text{in}\dagger} - c^{\text{in}} \right) \left(c^{\text{in}\dagger} - c^{\text{in}} \right) \right\rangle = \frac{1}{2} \left\langle c^{\text{in}} \left(c^{\text{in}}\right)^\dagger + \left(c^{\text{in}}\right)^\dagger c^{\text{in}} \right\rangle \tag{VIII.16}$$

$$= \frac{1}{2}(2N(\omega_c, T) + 1). \tag{VIII.17}$$

and $\left\langle X^{\text{in}} Y^{\text{in}} \right\rangle = \left\langle Y^{\text{in}} X^{\text{in}} \right\rangle = 0$. Therefore, the diffusion matrix is diagonal with

$$D = \begin{pmatrix} \kappa_c(2N(\omega_c, T) + 1) & 0 & 0 & 0 \\ 0 & \kappa_c(2N(\omega_c, T) + 1) & 0 & 0 \\ 0 & 0 & 2N(\omega_\omega, T) + 1 & 0 \\ 0 & 0 & 0 & 2N(\omega_m, T) + 1 \end{pmatrix} \tag{VIII.18}$$

From there, we can now solve the Luypunov equation (equation (II.62)) for the covariance matrix V, and finally extracting the bipartite entanglement between the two modes using the logarithmic negativity.

We numerically solved the Lyapunov equation and extracted the bipartite entanglement $E_{c,m}$ between the two modes and obtained the results of figure VIII.1. We see that a non-negligible entanglement already exists at the frontier between the strong coupling and ultra-strong coupling regime (around $g/\omega_c \simeq 0.1$). The entanglement increases with the coupling strength, and is quite robust with respect to temperature. As the frequency $\omega_m/2\pi$ increases, the thermal occupation of this mode becomes smaller and smaller at a fixed temperature. This is why as $\omega_m/2\pi$ increases, the entanglement survives at higher temperatures. Furthermore, note that that the two modes need not be on resonance for entanglement to exist.

2.2) Linearisation and strong driving

The example above has outlined the different steps involved in the computation of entanglement. However, in the rest of this chapter we will focus on non-linear interactions which will lead to non-linear quantum Langevin equations. Therefore, we will need to linearise the dynamics to put in the form of equation (VIII.1). The linearisation procedure will involve the coherent driving of one of the mode intervening in the non-linear interaction. As shown in section 5.1.1 of chapter III, such a coherent drive of a mode with annihilation operator o can be accounted for by the term (see equation (III.187))

$$H_{\text{drive}} = i\hbar\Omega\left(o^\dagger e^{-i\omega_d t} - o e^{i\omega_d t}\right) \tag{VIII.19}$$

where $\omega_d/2\pi$ is the frequency of the drive, $\Omega = \sqrt{\frac{\kappa P}{2\pi\hbar\omega_d}}$ where P is the power of the drive and $\kappa/2\pi$ its coupling to the mode o. In chapter III, we showed that the effect of this term is to transform a vacuum state $|0\rangle$ into the time-dependent coherent state $|\psi\rangle = e^{-i\omega_d t}|\alpha\rangle$, where $|\alpha\rangle$ is the coherent state defined in equation (II.37) of chapter II. In strong driving limit, where $|\alpha| \gg 1$, then $|\langle o\rangle| \gg 1$ too. We then expand the operator around this steady-state value, and consider the quantum fluctuations operators instead. Formally, we replace $o(t)$ by $o(t) = \langle o\rangle + \delta o(t)$, where δo is the annihilation operator for the quantum fluctuation. This approach is used in all of the non-linear interactions of section 3.

3) Some non-linear bosonic interactions

3.1) Optomechanical interaction

Outline of the theoretical treatment. The first interaction we consider is the one naturally occurring in cavity optomechanics, which we introduced in section 5 of chapter II. The interaction involves a cavity mode and phonons, the quasiparticles associated to quanta of mechanical motion. As previously mentioned, the standard Hamiltonian describing the interaction of a photon (annihilation operator c) and phonon (annihilation operator m) in cavity optomechanics is [162]

$$H = \hbar\omega_c c^\dagger c + \hbar\omega_m m^\dagger m + \hbar g c^\dagger c(m + m^\dagger), \tag{VIII.20}$$

$$= \hbar\omega_c c^\dagger c + \hbar\frac{\omega_m}{2}(p^2 + q^2) + \hbar g\sqrt{2}c^\dagger c q, \tag{VIII.21}$$

where $g/2\pi$ is the coupling strength, and in the second line we used the quadratures q, p of the mechanical mode m. Additionally, a coherent drive of the cavity mode given by equation (VIII.19) is considered.

Considering the system $H + H_{\text{drive}}$, we can derive the quantum Langevin equations (QLEs) for each of the mode in the frame rotating at the frequency of the drive. Formally, introducing the cavity-drive detuning $\Delta = \omega_c - \omega_d$, we obtain [179]

$$\dot{c} = -i(\Delta - i\kappa_c)c + igcq + E + \sqrt{\kappa_c}c^{\text{in}}, \tag{VIII.22}$$

$$\dot{q} = \omega_m p, \tag{VIII.23}$$

$$\dot{p} = -\omega_m q - \kappa_m p + g c^\dagger c + \xi^{\text{in}}, \tag{VIII.24}$$

where we introduced the mechanical noise operator ξ^{in} for the mechanical mode and $\kappa_m/2\pi$ its dissipation rate. The QLEs above are non-linear, as can be seen by examining the right-hand side of equations (VIII.22) and (VIII.24)[1]. Using the method outlined in the previous section, we expand each operator $o \in \{c, q, p\}$ as $o(t) = \langle o \rangle + \delta o(t)$, which decouples the QLE into a set of equations for the steady-state values, and a linear set of equations for the quantum fluctuations. Focusing on the QLEs for the quantum fluctuations, one imposes vacuum fluctuations for the cavity mode, and Brownian noise for the mechanical motion [179]. Afterwards, we can use the standard procedure: computation of the drift and diffusion matrix to solve the Luyapunov equation, giving the steady-state covariance matrix, from which we compute the bipartite entanglement between the mechanical and cavity mode using the logarithmic negativity.

Resulting non-classicality. The optomechanical interaction is non-linear, and was shown to create steady-state entanglement between the cavity and mechanical modes [179]. The resulting bipartite photon-phonon entanglement is non-negligible to a temperature up to 20 K. The existence of entanglement at such a relatively high temperature is linked to the weak dissipation of cavity photons at optical frequencies. Furthermore, Vitali et al. (2007) [179] observed that the optimal cavity-drive detuning Δ for entanglement generation corresponds to $\Delta \simeq \omega_m$, or in other words a red-detuned drive[2]. These predictions were later experimentally verified in cavity optomechanics by Palomaki et al. (2013) [180]. Finally, we note that the optomechanical interaction also induces quantum steering. Therefore, subsequent quantum manipulations of the cavity mode can be used to collapse the mechanical mode into a quantum state.

Application to cavity magnonics. While the optomechanical interaction naturally appears in cavity optomechanics, it can also occur in other systems, notably cavity magnonics. More specifically, similar non-linear interactions arise in three different manner. The first is due to the *magnetostrictive interaction* [257, 466], which leads to a deformation of the sphere's geometry due to the precession of the magnetisation. The deformation of the geometry can be described as a phonon of frequency $\omega/2\pi \simeq 10$ MHz much lower than the GHz frequencies of the magnons. The magnon-phonon coupling is usually very weak, and hence it requires a strong drive of the magnon mode to be activated. Therefore, the magnetostrictive interaction, also called *magnomechanical interaction*, leads to a magnon-phonon interaction very similar to that of optomechanics. Unsuprisingly, the magnetostrictive interaction has been used to generate magnon-phonon entanglement and squeezing [467, 468], by an identical method as the one we described above (based on Vitali et al. (2007) [179]). As detailed in [466], a COMSOL Multiphysics® simulation shows the existence of several mechanical modes. However, so far entanglement generated by the magnostrictive interaction has focused only on the lowest energy vibrational mode.

Alternatively the coupling of magnons to optical photons due to the Faraday effect also leads to an optomechanical interaction [469]. As expected, this allows to create entanglement between microwave magnons and optical light[3] [470]. Furthermore, Sun et al. (2021) [470] showed this non-linear interaction can create quantum steering between magnon and cavity modes. By performing single-photon addition or substraction on a coherent state, we can create Schrödinger cat states of the cavity mode, which due quantum steering allows to collapse the magnon mode in Schrödinger cat states too.

Finally, as we derived in section 4.1 of chapter IV, the Kittel mode of a magnon can couple to the three components of a cavity mode. In particular, for the direction aligned

[1] The non-linearities are respectively in the second and third term of equations (VIII.22) and (VIII.24)

[2] As claimed in section 5 of chapter II, in the red-detuned regime the effective Hamiltonian of equation (II.83) for the quantum fluctuations can be shown to take the form of the Dicke model under the rotating wave approximation, leading to a simple linear coupling [162, 163]. On the other hand, in the opposite blue-detuned regime, the effective Hamiltonian given by equation (II.84) only involves counter rotating terms, which we expect to create entanglement [162, 163]. Therefore, that the red-detuned regime creates entanglement while the blue-detuned regime does not is puzzling.

[3] We recall that by optical light we mean light at optical frequencies.

with the equilibrium magnetisation, the interaction Hamiltonian given by equation (IV.43) takes the form of an optomechanical interaction. We investigate the possibility of generating entanglement using this scheme in the original work of appendix C.9.

3.2) Kerr interactions

Other interesting non-linear interactions are the self-Kerr and cross-Kerr interaction. The self-Kerr interaction describes a non-linear self-interaction with Hamiltonian

$$H_{\text{Kerr}} = \hbar K \left(m^\dagger m\right)^2 = \hbar K m^\dagger m m^\dagger m, \tag{VIII.25}$$

with m the annihilation operator of a bosonic mode. The cross-Kerr interaction between two modes is described by

$$H_{\text{cross-Kerr}} = \hbar K a^\dagger a b^\dagger b, \tag{VIII.26}$$

where a, b are the annihilation operators for the two bosonic modes. The Kerr interactions being non-linear, they indeed induce non-classical behaviours. For instance, the self-Kerr interactions can be used to induce squeezing and sub-Poissonian statistics [471, 472]. As we will see in section 4 this source of non-classicality can be transferred to other modes by coupling to them, leading to bipartite entanglement.

Importantly, these two interactions are found in a variety of physical platforms. For instance, in magnonics self-Kerr interactions[1] arise due to anisotropy [268, 269], while cross-Kerr interactions is possible between the Kittel mode and higher-order magnon modes [474]. Both cross-Kerr and self-Kerr interactions can also be engineered in superconducting circuits [475–477], and can be useful to induce Kerr interactions on other objects. For instance, a superconducting qubit can mediate a cross-Kerr effect between two microwave fields [478]. In the context of quantum computation with photons, a non-linear media can be used to induce a cross-Kerr effect and implement phase shift gates, but the non-linearity is very weak [5, 479, 480].

3.3) Wave mixing

3.3.1) Three-wave mixing

Wave mixing refers to the interaction of three or more bosonic modes. For instance, a three-wave mixing process[2] is described by the interaction Hamiltonian

$$H_I = \hbar g (a_3^\dagger a_2^\dagger a_1 + \text{h.c}), \tag{VIII.27}$$

where $g/2\pi$ is the coupling strength, and a_i ($i \in \{1, 2, 3\}$) are annihilation operators for the bosonic modes. One example of a three-wave mixing process is once again provided by magnons. Indeed, in a YIG sphere, a magnon mode can couple to the whispering gallery modes of the sphere [482], leading to the interaction

$$H_I = \hbar g (m^\dagger a_2^\dagger a_1 + \text{h.c}), \tag{VIII.28}$$

with a_1 the annihilation operator for the π-polarised TE optical mode, and a_2 that of the σ^- polarised mode. The linearisation can once again be obtained by driving a_1 into a coherent state so that $\langle a_1 \rangle = \epsilon$.

Another common example of three-wave mixing is spontaneous parametric down conversion (SPDC), used for instance to create sources of entangled photons for quantum networks [114, 483]. SPDC is obtained by pumping light into a non-linear crystal [480, 483]. In SPDC, a photon of frequency $\omega_1/2\pi$ described by mode a_1 is annihilated to produce two other photons

[1] In cavity magnonics, the self-Kerr coefficient K of equation (VIII.25) verifies $K \propto 1/V_m$ with V_m the volume of the magnetic sample, so that this effect is only observable for small magnets [268, 269]. As for the magnomechanical interaction, the self-Kerr effect in magnons requires a strong drive to be observable and to linearise the dynamics, and therefore it can compete with the magnomechanical interaction [473].

[2] While we only consider a three-wave mixing process here as an example, note that entanglement can also be generated using a four-wave mixing process, see [481] for instance.

described by the modes a_2, a_3 with frequencies $\omega_2/2\pi$ and $\omega_3/2\pi$ such that $\hbar\omega_1 = \hbar\omega_2 + \hbar\omega_3$. In the degenerate case where $\omega_2 = \omega_3$, we can assimilate mode $a_3 = a_2$ to obtain

$$H_I = \hbar g(a_2^{\dagger 2} a_1 + \text{h.c}). \tag{VIII.29}$$

3.3.2) Parametric and squeezed driving

Assuming a_1 is a coherent drive $\langle a_1 \rangle = \alpha e^{-i\omega_d t}$ (see section 5.1.1) and performing a semi-classical approximation, we find

$$H_I = \hbar g(\alpha a_2^{\dagger 2} e^{i\omega_d t} + \text{h.c}), \tag{VIII.30}$$

which is commonly called a *parametric drive* of mode a_2. While the effect of a coherent drive on a bosonic mode is to put into a coherent state, the effect of a parametric drive is to create a squeezed state. To see this, simply rewrite[1] the Hamiltonian above in the frame of the drive to obtain

$$H_I = \hbar g(\alpha a_2^{\dagger 2} + \text{h.c}), \tag{VIII.31}$$

which we already interpreted as a squeezing term in chapter VII (e.g. compare with equation (VII.4)).

Parametric drives are an example of an external non-linearity, which can induce squeezed states without the presence of a non-linearity inside the system. This method has been proposed in cavity optomechanics by Agarwal and Huang (2016) [484]. Another related method consists of driving a mode with a squeezed vacuum state, as considered by Li, Zhu, and Agarwal (2019) [468] in a magnomechanical setup. In this case, the parametric drive Hamiltonian does not need to be included. Instead, we impose correlations functions corresponding to a squeezed vacuum on the input noise operator of the driven mode. As an example, noting a^{in} the input noise operator, we have $\langle a^{\text{in}} \rangle = 0$ (zero mean) and the correlations [485]

$$\left\langle a^{\text{in}\dagger}(t) a^{\text{in}}(t') \right\rangle = \mathcal{N}\delta(t-t'), \quad \left\langle a^{\text{in}}(t) a^{\text{in}\dagger}(t') \right\rangle = (\mathcal{N}+1)\delta(t-t'), \tag{VIII.32}$$

$$\left\langle a^{\text{in}}(t) a^{\text{in}}(t') \right\rangle = \mathcal{M}\delta(t-t'), \quad \left\langle a^{\text{in}\dagger}(t) a^{\text{in}\dagger}(t') \right\rangle = \mathcal{M}^*\delta(t-t'), \tag{VIII.33}$$

with

$$\mathcal{N} = \sinh^2 r + N(\omega_a)\left(\sinh^2 r + \cosh^2 r\right) \tag{VIII.34}$$

$$\mathcal{M} = e^{i\theta} \sinh r \cosh r (1 + 2N(\omega_a)), \tag{VIII.35}$$

and N is the Bose-Einstein distribution given by equation (VIII.12).

4) Hybrid schemes

Approach and limits. So far we have only considered non-linear interactions "by themselves", and described the resulting non-classical states. By introducing additional linear couplings, we can propagate the non-classical correlations created by the non-linearities to other modes. To understand this more simply, we now introduce a graph representation to understand the generation and propagation of non-classical features in a network of bosonic modes. A node represents a bosonic mode, and a straight line between two modes a and b accounts for a linear interaction between them, of the form $H_I = \hbar g(ab^\dagger + \text{h.c})$. On the other hand, the sources of non-linearity are represented by wavy lines as shown in figure VIII.2.

One drawback of the approach described above is that it hides the technical details, such as how the frequency of the modes should be tuned, how strong should the coupling strengths be, or the impact of decoherence. To take into account these details, a full derivation from the quantum Langevin equations to the steady-state covariance matrix is required. Yet, as we show below, this visual formalism will allow us to present a unified understanding of much of the literature based on non-linear bosonic interactions. Note also that for simplicity, we will often consider magnon, phonon and cavity modes, but the following discussion applies to any continuous variable system composed of the same couplings.

[1] Formally, we consider the unitary transformation $\exp\left(i\frac{\omega_d}{2} t a_2^\dagger a_2\right)$.

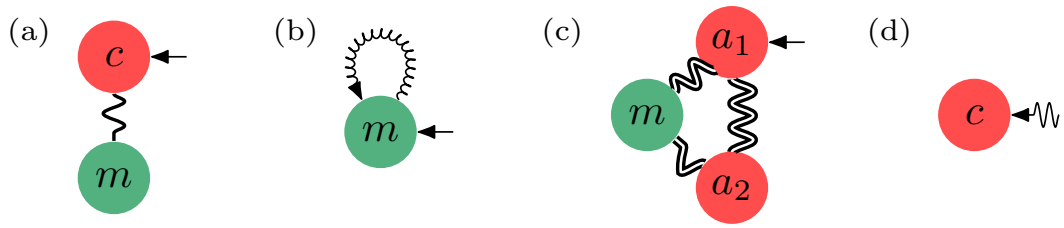


Figure VIII.2: Pictorial representation of various non-linearities. (a) Optomechanical interaction of equation (VIII.20). (b) Self-Kerr interaction of equation (VIII.25). (c) Three-wave mixing process of equation (VIII.27). (d) Parametric or squeezed vacuum drive. Notice the presence of a strong drive (represented by a straight black arrow) on some of the modes in (a-c), necessary to linearise the interaction.

Squeezed driving. The first examples we consider make use of squeezed driving of cavity modes. In the presence of a linear coupling between the cavity mode and another mode, say a magnon mode, the squeezing of the cavity mode can be transferred to the magnon mode when their respective frequencies are identical (i.e. the magnon is on resonance with the cavity mode) [485]. Therefore, squeezed states of an arbitrary bosonic mode can in principle be achieved by linear coupling to an already squeezed mode.

An interesting case is when two magnons modes simultaneously couple to the same cavity mode (see figure VIII.3a), which for instance can be implemented by the three-post re-entrant cavity introduced in chapter IV. In such a setting, it is possible to create both magnon-photon and magnon-magnon entanglement, as shown by Nair and Agarwal (2020) [485]. In the context of cavity magnonics, the two magnon modes are usually the Kittel modes of two distant YIG spheres, separated by macroscopic distances. Therefore, the scheme proposed by Nair and Agarwal (2020) [485] induces entanglement between two spatially distant macroscopic objects.

A variation put forward by Yu, Zhu, and Li (2020) [273] consists of first creating a two-mode squeezed vacuum state, and use it to drive two spatially distant cavities, as illustrated in figure VIII.3b. This scheme first creates entanglement between two cavity modes located in different cavities, which can then be transferred to two magnon modes, for instance hosted by YIG spheres placed inside the two cavities. This time, contrary to the proposal of Nair and Agarwal (2020) [485], the YIG spheres do not couple to the same cavity mode, but still become entangled due to the transfer of non-classical correlations.

A straightforward extension of the scheme of Yu, Zhu, and Li (2020) [273] considers the vibrational modes of the YIG spheres, as pictured in figure VIII.3c [486]. The frequencies of the strong drives of the magnon modes are chosen to be in the red-detuned regime, which linearise the magnon-phonon interaction to a simple linear coupling allowing to propagate entanglement. Therefore, the Li and Gröblacher (2021) [486] showed the distant entanglement of two phonon modes, mediated by the cavity and magnon modes.

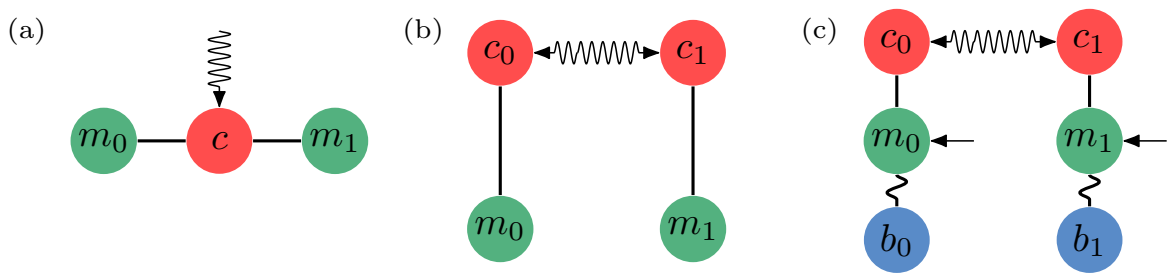


Figure VIII.3: (a) Entanglement between m_0 and m_1 mediated by c, which is driven by a parametric or squeezed drive. (b) Remote entanglement between m_0 and m_1, by driving c_0 and c_1 with a two-mode squeezed drive. (c) Remote entanglement of b_0 and b_1 mediated by the remote entanglement of m_0 and m_1.

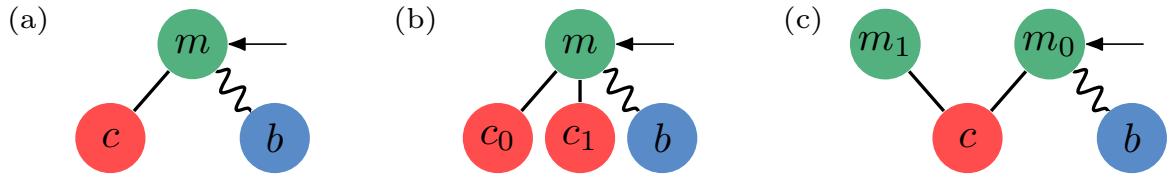


Figure VIII.4: (a) Generation of tripartite magnon-phonon-photon entanglement [467]. (b) Generation of entanglement between two cavity modes in the microwave frequency range [487]. (c) Generation of magnon-magnon entanglement [488].

Optomechanical interaction. We now turn our attention to schemes based on optomechanical interactions, pictured in figure VIII.4. In the first scenario (figure VIII.4a), we consider an optomechanical coupling between a magnon and a phonon due to the magnetostrictive interaction, which from section 3.1 we already know can create entanglement and quantum steering [179, 180, 470]. This setup induces magnon-phonon entanglement, but also magnon-photon and photon-phonon entanglements due to the linear coupling between the magnon and photon [467]. Additionally, it was shown that by an appropriate choice of the frequencies of the magnon and the drive, tripartite photon-magnon-phonon entanglement is achievable [467].

A generalisation of this setup, pictured in figure VIII.4b, was studied by Yu, Shen, and Li (2020) [487], where an additional cavity mode is included. Here, the linear couplings of the cavity modes to the magnon allow to induce entanglement between the two cavity modes at microwave frequencies. In principle, the three-post re-entrant cavity proposed in chapter IV could implement this scheme. One drawback of this scheme is in engineering the frequencies of the cavity modes so that their frequency spacing is of the order of twice that of the phonon mode, i.e. approximately 20 MHz for the lowest order phonon modes of the magnons [487].

Instead of considering two cavity modes, we can also consider two magnon modes in the setting described by figure VIII.4c, which was studied by Li and Zhu (2019) [488]. Unsurprisingly, this allows to generate magnon-magnon entanglement, once again hosted by two spatially distant macroscopic YIG spheres [488].

Other hybrid schemes and looking ahead. It should now be clear that in the schemes presented in figures VIII.3 and VIII.4, one can replace one source of non-linearity by another and create non-classical states. For instance, in figure VIII.4c one can replace the magnon-phonon coupling by a self-Kerr non-linearity, as illustrated in figure VIII.5a and still obtain magnon-magnon entanglement, as shown by Zhang, Scully, and Agarwal (2019) [272].

The different sources of non-linearity we introduced above represent different possible building blocks, which can be arranged using linear couplings to create the desired quantum states. As an example, say we want to generate entanglement between light at microwave frequencies and light at optical frequencies. A natural candidate for this task is the magnon, which can couple to both optical and microwave light. Notably, the coupling to microwave light is linear, while the coupling to light at optical frequencies (optical light) is non-linear. The simplest configuration which involves these three elements is pictured in figure VIII.5b. This setup was analysed by Cai, Liao, and Zhou (2020) [482], which indeed predicted the generation of entanglement between optical and microwave light. Having discussed the elementary "bricks"

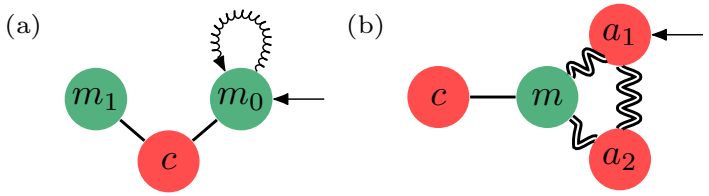


Figure VIII.5: (a) Generation of magnon-magnon entanglement using the self-Kerr effect [272]. (b) Entanglement between microwave and optical light using three-wave mixing [482].

to induce non-classical states, we now turn our attention to the fundamental limits to the quality of entanglement in the next section.

5) Enhancing entanglement

Combination of non-linearities. In this section, we examine how the bipartite entanglement between two bosonic modes can be increased. A simple idea consists of combining different non-linearities together. This idea was verified by Ding et al. (2022) [489], which showed an enhancement of the entanglement from the magnetostrictive interaction when the magnon mode also has a self-Kerr interaction. The same setup can also be used to generate non-reciprocal entanglement [490]. Another example was studied by Hussain, Qamar, and Irfan (2022) [491], which noticed an increased bipartite photon-magnon and photon-phonon entanglements in the presence of a parametric drive of the cavity mode. Zhang et al. (2022) [492] showed a similar enhancement in the case of a squeezed vacuum drive.

The ulstrastrong coupling regime. In section 2, we verified on the Dicke model the presence of significant bipartite entanglement. Therefore, an ultrastrong coupling can be viewed as another resource for the creation of entanglement. However, as discussed in chapter VII, this entanglement is somewhat virtual, since it does not lead to any detectable non-classical feature[1]. One solution to check the effect of the USC on entanglement would be to combine it with other non-linearities, and check for an enhancement. Unfortunately, almost all of the non-linearities considered above require a strong drive, and therefore a rotating frame transformation to make the Hamiltonian time-independent. This cannot be achieved in the presence of counter-rotating terms, such as cm, because they would each pick up a time-dependent phase factor.

Beyond non-linear bosonic interactions. In recent years, several ideas have been put forward to enhance entanglement. One interesting idea is to use coherent feedback loop, as done for instance in [493, 494]. The principle consists of feeding back into the system one of the output, for instance a mechanical motion. Another possibility is to use a PT-symmetric system [495], which we briefly discussed in chapter VI. Ding et al. (2021) [495] considered an open quantum system for which the effective Hamiltonian shows a gain of the cavity mode, instead of dissipation. Combined with the magnetostrictive interaction, an increase in the entanglement was obtained.

Similarly, the dissipative couplings we introduced in chapter VI can be used to generate entanglement, without the presence of any non-linearity in the system. This was used to demonstrate the generation of a magnon Bell state by Yuan et al. (2020) [496]. Dissipative coupling can also be seen as another source of entanglement, which can be combined with other non-linear interactions. As an example, Dong et al. (2023) [497] combined a dissipative coupling with a magnetostrictive interaction, and showed an increase of both entanglement and quantum steering.

Finally, using discrete variable systems offers many possibilities. In the context of cavity magnonics, magnons can couple to superconducting qubits by indirect coupling via a cavity mode: the superconducting qubit couples to light via an electric dipole interaction, leading to a Jaynes-Cummings model (see equation (III.83)), while magnon couple to light using the magnetic dipole interaction. The indirect coupling leads to an effective Jaynes-Cummings model between a superconducting qubit and a magnon [213, 214]. Therefore, all the schemes to create non-classical states in circuit QED are in principles also possible in cavity magnonics. For instance, there are several schemes to create Schrödinger cat states in circuit QED [498–502].

[1] We saw this in the context of the input-output formalism (section 3): even though the ground state of the Dicke model is a two-mode squeezed state, the output of the cavity still corresponds to standard vacuum fluctuations.

6) Conclusion

In this chapter, we have introduced the general principles behind the generation of entanglement and squeezed states based on non-linear bosonic interactions. Notably, we saw that one needs to identify potential sources of non-linearity, and then assemble them together using linear couples to create hybrid quantum states.

We have also highlighted the strength of cavity magnonics for the generation of non-classical states. This potential comes from two capabilities: the presence of several non-linearities, and the possibility of coupling to various other physical platforms, thus making possible the creation of complex entangled states. This is another advantage of considering hybrid systems instead of a single physical platform for quantum information processing, an idea we first hinted at in chapter II. Additionally, cavity magnonics often deals with macroscopic quantum states, such as the Kittel mode in macroscopic magnetic spheres. Therefore, this is an ideal platform for more fundamental studies concerning quantum mechanics, notably concerning whether quantum superpositions hold in the classical realm and more generally the quantum to classical transition [15, 503–505]. It is worth noting, however, that so far there has been no experimental verification of the generated entanglement based on non-linear bosonic interactions.

Finally, we have discussed how in the ultrastrong coupling regime, entanglement naturally comes into play. While combining this with other non-linearities seems hard due to the use of strong driving, we note that the physics can still be simulated using *master equations* [34], a formalism we have not considered in this thesis. Furthermore, master equations are the appropriate tools for dealing with hybrid systems involving discrete variables, such as superconducting qubits. Notably, it would be interesting to investigate a system composed of a cavity mode coupled to a superconducting qubit, where the form is also ultrastongly coupled to a magnon mode. The resulting indirect coupling has not be considered in the literature, and could render the non-classicality induced by the USC regime to be probed through the superconducting qubits. Indeed, so far the quantum regime of cavity magnonics have only been achieved through the indirect coupling with superconducting qubits [213, 214, 506–509].

Chapter IX

Silicon-based quantum computing

Summary

We present the physics of electrons confined on length scale of nanometres in semiconductors. We focus on silicon and provide an introduction to valley physics, as well as the different methods available to model it. Afterwards, we present an overview of charge qubits in silicon double quantum dots and how they can be controlled using non-adiabatic pulses. In this context, we present a proposal for a qubit encoded on the valley states in a single quantum dot, based on the original published work of Gardin et al. (2022) [4].

Contents

1) Introduction **149**
2) Nanostructures and quantum confinement **150**
3) Valley physics in silicon **151**
3.1 Introduction to valley physics 153
3.2 Tight-binding approach 154
3.3 Effective mass approach 156
3.3.1 General case 157
3.3.2 Flat quantum well 158
4) Charge qubits **159**
4.1 Standard charge qubits 159
4.2 Valley qubits 160
5) Conclusion **161**

1) Introduction

In this last chapter, we turn our attention to semiconductor-based nanostructures, which have applications spanning both classical and quantum technologies. Notable classical applications include light-emitting diodes (LEDs), solar cells, or quantum dot displays. On the quantum side, semiconducting nanostructures can be used for single-photon sources [112, 116–121, 510] and detectors [123–131], or single-electron quantum pumps for quantum metrology [511–518].

Another major application of semiconductor nanostructures is quantum computing, which is the topic we will focus on in this chapter. Indeed, with an appropriate design these nanostructures can trap electrons (or holes), leading to an isolated and controllable electronic quantum system. As an example, in the context of cavity magnonics we consider an ensemble of spins, and therefore their collective excitations. Conversely, in a semiconductor (electron) spin qubit, the confinement of the electron provided by the nanostructure allows to isolate a single spin degree of freedom and manipulate it. Furthermore, building qubits in semiconductor nanostructures is appealing due to the existence of an advanced semiconductor industry with well-established fabrication processes. Indeed, similar techniques can be used to notably create silicon based qubits, which are promising for scalability and integration density [519–523], contrary to say trapped ions.

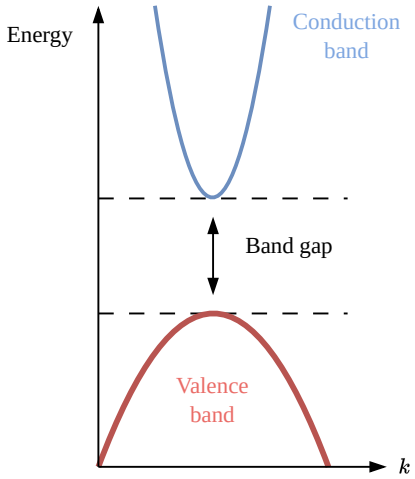


Figure IX.1: Schematic of the (filled) valence and conduction bands (respectively red and blue) as a function of crystal momentum k.

We begin in section 2 by discussing the physics of quantum confinement, and we introduce two particular structures of interest for quantum computing: Si/Si_xGe_{1-x} heterostructures and quantum dots (QDs). In this chapter we focus on silicon, which is one of the most important material of the semiconductor industry. For silicon, solely considering the physics of nanostructures and the standard degrees of freedom (charge, spin or orbital) is not sufficient. Indeed, additional *valley physics*, introduced in section 3, come into play in various silicon-based devices. Then, in section 4, we review silicon charge qubits, and notably we propose in Gardin et al. (2022) [4] (available in appendix C.10) a potential valley qubit based on a single quantum dot. We conclude in section 5

2) Nanostructures and quantum confinement

Zero-dimensional confinement: bulk semiconductors. We begin by considering the behaviour of electrons in a bulk semiconductor material, in the absence of an electromagnetic field. Due to the presence of the underlying periodic lattice structure on which the electron live, the electronic states are organised in different energy bands separated by an energy gap [262, 383]. Of particular interest are the *valence and conduction bands* as pictured in figure IX.1. The minimum of the conduction band is approximately quadratic, with a dispersion relation

$$E(\mathbf{k}) = \frac{\hbar^2 \mathbf{k}^2}{2m^*} = \frac{\hbar^2}{2m^*}\left(k_x^2 + k_y^2 + k_z^2\right), \tag{IX.1}$$

where m^* is the effective mass of the material, which is adjusted to fit the curvature of the conduction band. This dispersion relation is similar to that of a free particle of mass m^*, with plane waves eigenstates $\psi_{\mathbf{k}}(\mathbf{r}) = e^{i\mathbf{k}\cdot\mathbf{r}}$. At first sight this is surprising since this indicates that the electrons do not feel any potential and are delocalised over the lattice, despite the presence of the periodic ion core potentials.

Nevertheless, *Bloch's theorem* [262, 383] tells us that electrons indeed mostly behave like plane waves in a periodic potential, regardless of how strong[1] this potential is. The actual eigenstates are of the form $\psi_{\mathbf{k}}(\mathbf{r}) = u_{\mathbf{k}}(\mathbf{r})e^{i\mathbf{k}\cdot\mathbf{r}}$, where the corrections $u_{\mathbf{k}}(\mathbf{r})$ are called the Bloch functions and have the same periodicity as that of the potential. The dispersion relation of equation (IX.1) still hold, and the momentum k can take a continuous range of values due to the absence of confinement.

One-dimensional confinement: quantum wells. Quantum mechanics at the undergraduate level tells us that for a particle of mass m confined to an infinite quantum well of width

[1] Note that the valence electrons somewhat screen the Coulomb potential from the ion cores, so that this potential is not as strong as it may seem.

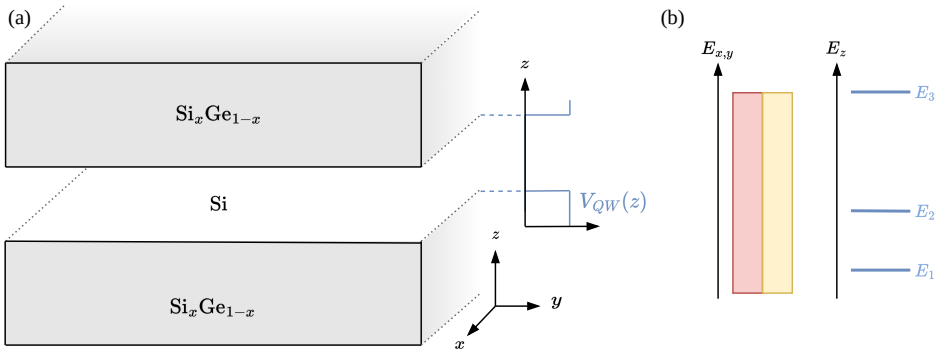


Figure IX.2: Schematic of a Si/Si_xGe_{1-x} heterostructure and its associated energy level structure. The electrons in the silicon layer are unconfined in the x and y direction, leading to a continuous energy spectrum. On the other hand, the confinement in the z direction due to the Si_xGe_{1-x} layers create a quantum well potential, leading to quantised energy levels in this direction.

L, its energies are quantised as [33]

$$E_n = \frac{\hbar^2}{2m}\left(\frac{n\pi}{L}\right)^2, \tag{IX.2}$$

where $n \geqslant 1$ is an integer. The same result hold for an electron confined in a semiconductor material, provided we replace the electron's mass m_e by its effective mass m^* in the direction of confinement.

To see this, assume that an electron is confined in a Si/Si_xGe_{1-x} heterostructure made of different layers of silicon and silicon-germanium, as pictured in figure IX.2. A concentration $x = 0.2$ is typical of these nanostructures, leading to a confinement of the electron in the z direction, effectively creating a quantum well. If we consider plane waves $e^{\pm ik_z z}$ along this direction, imposing that the wave function vanishes on the Si/Si_xGe_{1-x} interfaces lead to a quantisation of k_z which reads $k_z = \frac{n\pi}{L}$. Therefore, the energy spectrum is only quantised in the z direction, while it takes continuous values in the x and y directions. Note that as $L \to \infty$, the confinement effectively disappear and we recover a quasi-continuous spectrum for the z direction too.

Two-dimensional confinement: nanowires. A straigthforward extension of the quantum well is that of a nanowire, in which the electrons are now confined to two dimensions, as illustrated in figure IX.3. A common implementation are silicon nanowire on a silicon oxide (SiO_2) substrate, which can be used for silicon qubits but also single-electron quantum pump [285]. In such a structure, the electrons are still free to move along one axis, while their states are quantised in the other two confined dimensions.

Three-dimensional confinement: quantum dots. Naturally, confinement along the last free dimension leads to a completely isolated quantum system. Such systems are called quantum dots (QDs), and can be created by a dopant atom such as phosphorus into silicon, or through electrostatic gates patterned on a nanowire (in green in figures IX.3a to IX.3c) or a Si/Si_xGe_{1-x} heterostructure (see the left side of figure IX.4). The three-dimensional confinement leads to completely discrete energy levels, akin to those of atomic levels. Therefore, electrons in quantum dots can sometimes be referred to as *artificial atoms*. Usually, the energy level spacing ΔE of the dot (also called the orbital energy spacing) is of the order of a few meV, which can be tuned by the electrostatic gates.

3) Valley physics in silicon

Aside from the physics originating from confinement, in silicon one also needs to consider the valley degrees of freedom, which arise due to the symmetries of the crystal. In this section, we

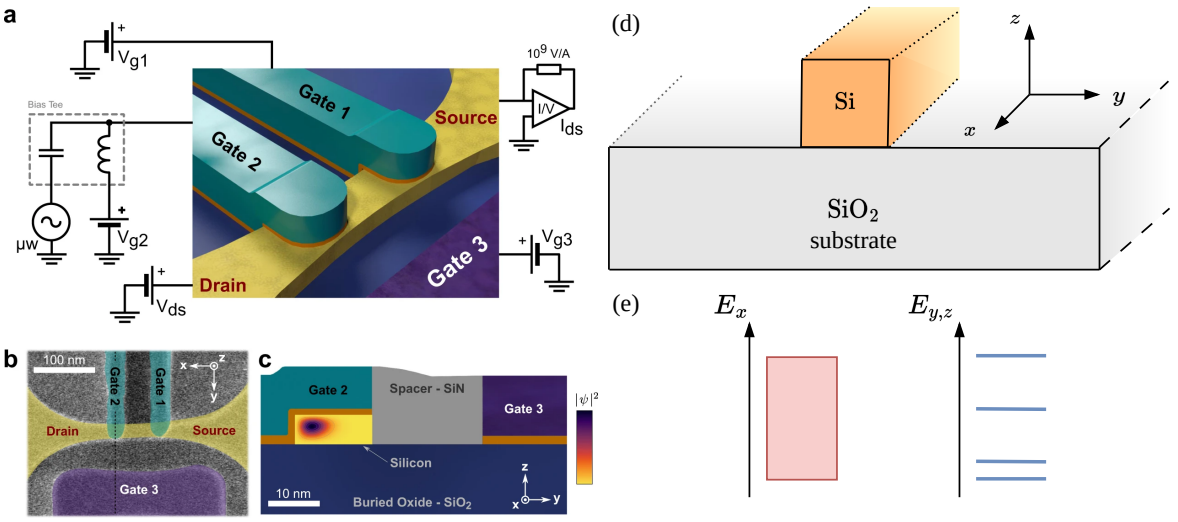


Figure IX.3: (a-c) Figure 1 of Corna et al. (2018) [524] licensed under CC BY 4.0 [140], showing a nanowire device used in a silicon spin qubit. (d) Schematic of a silicon nanowire on a SiO_2 substrate, where only one dimension (x) is unconfined. (e) Energy diagram of a nanowire, with discrete energy levels in the y and z directions and continuous spectrum in x due to the lack of confinement.

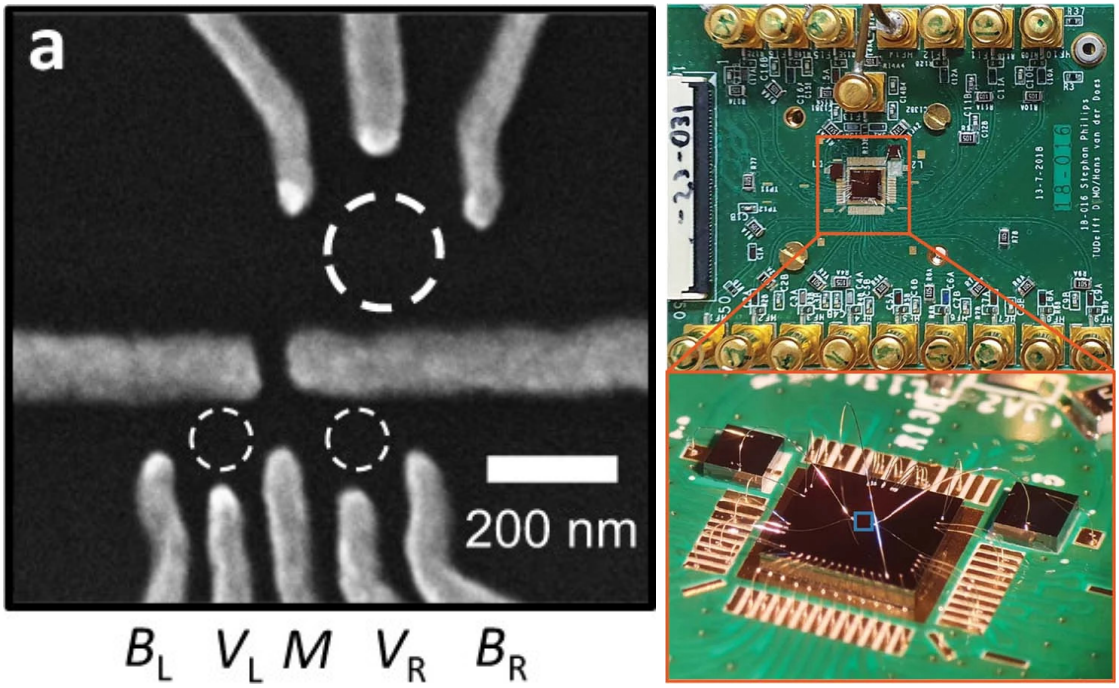
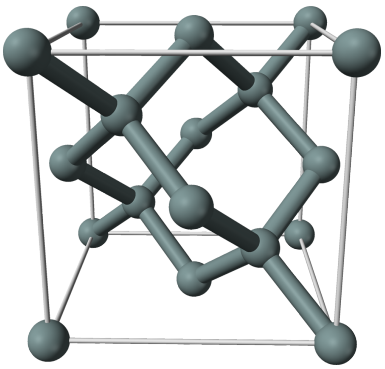


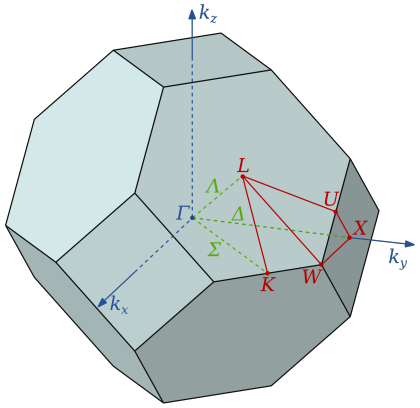
Figure IX.4: Left: figure 1a of Penthorn, Schoenfield, and Rooney (2019) [525], licensed under CC BY 4.0 [140], showing a scanning electron micrograph of a double quantum dot (dashed circles at the bottom) defined by electrostatic gates patterned on a Si/SiGe heterostructure. Right: figure 7b of Philips et al. (2022) [526], showing the integration of six-qubit quantum processor on a chip. Licensed under CC BY 4.0 [140].

explore this valley physics in silicon[1], starting by a general discussion of the origin and some of its properties. Then, we discuss two complementary effective models for valleys in silicon, namely the tight-binding and effective mass methods.

[1]Note that other materials can exhibit valley physics, such as graphene.



(a) Face-centred cubic lattice, from [529].



(b) Brillouin zone of the face-centred cubic lattice, from [530].

Figure IX.5: (a) Crystal structure of silicon, corresponding to a face-centred cubic lattice [527]. (b) The Brillouin zone of silicon [527].

3.1) Introduction to valley physics

Origin of valleys. The crystal structure of silicon is that of a face-centred cubic Bravais lattice, which is pictured in figure IX.5a. The associated the Brillouin zone (reciprocal space) is illustrated in figure IX.5b, where several points of interest (notably Γ and X) are illustrated.

The band structure of bulk silicon is plotted in figure IX.6, where the conduction and valence bands are separated by the grey area. We observe that silicon is an indirect bandgap material, since the minimum of the conduction band is not centred in $k = 0$ (corresponding to the Γ point, see figure IX.5b), but around the X point at $k_0 = 0.85\frac{2\pi}{a}$ with $a = 0.5431$ nm the lattice constant of silicon [527]. The minimum of the conduction band is actually composed of six degenerate minima due to six crystallographic axes [528]. These minima are referred to as *valleys* [528].

Evolution of the valleys with confinement. The six-fold degeneracy of the valleys correspond to bulk silicon only, and in the presence of confinement the valleys evolve as described

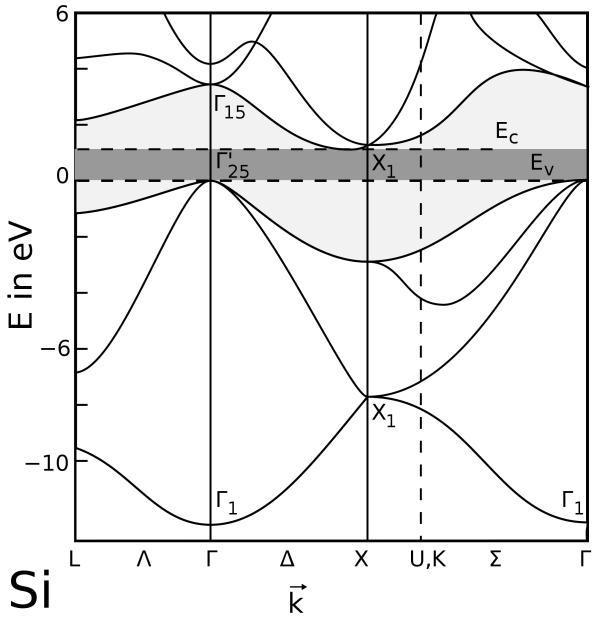


Figure IX.6: Bandstructure of bulk silicon in recriprocal space. The gray area denotes the energy gap between the valence band (bottom) and the conduction band (top). The points in reciprocal space on the abscissa are illustrated in figure IX.5b. Image from [531], licensed under CC BY-SA 2.5 [532].

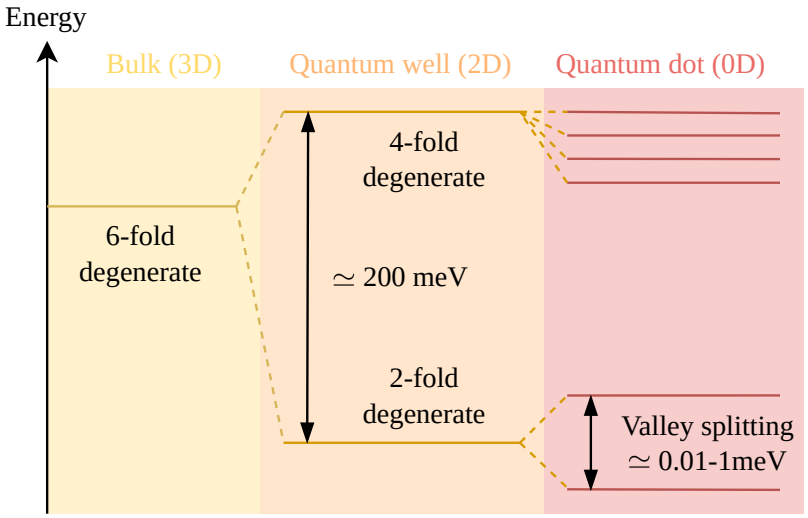


Figure IX.7: Evolution of the valleys in silicon with different degrees of confinement. Inspired from figure 7a of Zwanenburg et al. (2013) [527]

in figure IX.7. Indeed, in the presence of confinement in one direction as in a quantum well, the six-fold degeneracy is broken into a low energy two-fold degeneracy, and a four-fold degeneracy of higher energy (middle of figure IX.7). A significant energy gap (of around 200 meV for Si/Si_xGe_{1-x} heterostructures [527]) exists between the two-fold and four-fold degenerate valleys, and therefore the relevant physics is that of the lowest two valley states. Finally, in the presence of strain, additional confinements or electric fields (e.g. in a quantum dot created by gates in a Si/Si_xGe_{1-x} heterostructure), the remaining two-fold valley degeneracy is further broken [527], leading to a *valley splitting* ΔE_v.

The valley splitting is strongly dependent on atomistic details of the nanostructure, notably disorder which is ubiquitous in Si_xGe_{1-x} heterostructures [527]. Indeed, Si_xGe_{1-x} is a disordered alloy, in which the distribution of the silicon and germanium atoms is random. As a consequence, the wave function can penetrate into the buffer in different manners depending on the exact atomic details of the interface. Additionally, the position of the atoms is not exactly ordered because the silicon and germanium atoms can have different bond lengths. Further, the concentration of silicon and germanium atoms is not precisely known. The miscuts and randomness of Si_xGe_{1-x} have strong consequences on the values of the valley splitting.

Mixing of orbital and valley degrees of freedom. The lowest two valley states[1] represent additional degrees of freedom for the electrons, aside from their usual orbital and spin degrees of freedom. In the absence of coupling between the valley and orbitals, the spectrum of the valley states combines with that of the orbitals and spins. As an example, we show in figure IX.8 the combination of the valley and orbital degrees of freedom in the absence of magnetic field (and therefore we neglect the spin degrees of freedom) in a quantum dot formed in a Si/Si_xGe_{1-x} heterostructure.

3.2) Tight-binding approach

As previously explained, the valley splitting is very sensitive to atomistic details, and therefore the best method consists of using large scale tight-binding calculations include many electronic bands. Notably, this can be performed using NEMO 3D's 20 band $sp^3d^5s^*$ model [533]. However, using these computationally expensive softwares complicates the understanding of the underlying valley physics, hence the idea of using simplified effective models. One such model was provided by two papers [534, 535] by Boykin et al.[2].

[1] The lowest two valley states can sometimes be referred to as *pseudo-spins* in the literature, due to them offering exactly two additional degrees of freedom like spin.

[2] The model was first introduced by Boykin et al. (2004) [534] and showed remarkable agreement with NEMO 3D simulations. Then, Boykin et al. (2004) [535] analysed analytically the model and clarified the

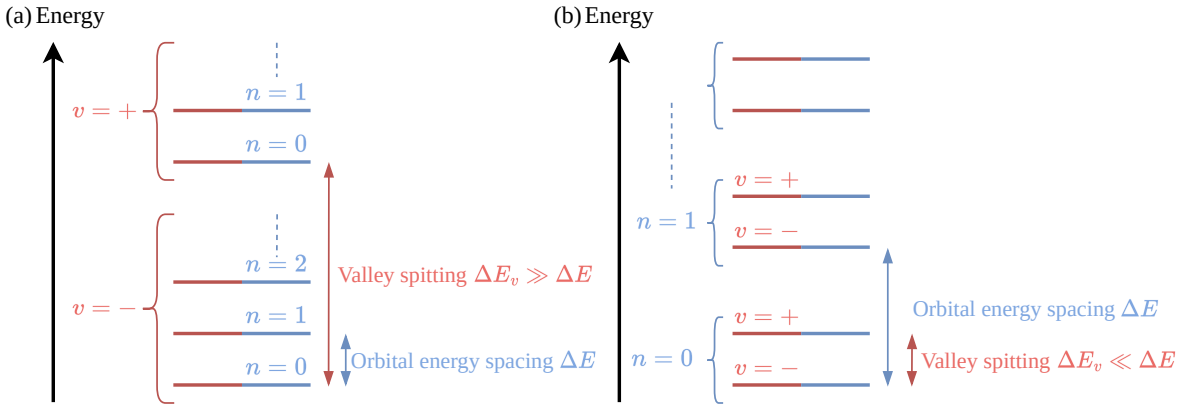


Figure IX.8: Combination of the valley and orbital degrees of freedom depending on the relative magnitudes of the valley splitting ΔE_v and orbital energy spacing ΔE. In this figure, we have neglected spin, and assumed a constant orbital energy spacing ΔE, for instance due to a harmonic quantum dot potential. The two lowest valley states are indexed by the quantum number $v = \pm$, while the orbitals are indexed by $n \in \mathbb{N}$. Inspired from figure 9 of Zwanenburg et al. (2013) [527].

The approach of Boykin et al. (2004) [535] consists of considering the simplest tight-binding model which reproduces the dispersion relation $E(k)$ of the two lowest valley states. As shown in Zwanenburg et al. (2013) [527], a one-band model with nearest-neighbour hopping cannot reproduce the dispersion relation of the silicon valleys. Instead, the next possibility is to consider nearest-neighbour and second nearest-neighbour couplings. Formally, Boykin et al. (2004) [535] considers a quantum well of $2N+1$ atoms and noting $|n\rangle$ the position eigenstate for atom n, we consider the tight-binding Hamiltonian

$$H = \sum_n \epsilon \left|n\right\rangle \left\langle n\right| + (t_1 \left|n+1\right\rangle \left\langle n\right| + t_2 \left|n+2\right\rangle \left\langle n\right| + \text{h.c}), \tag{IX.3}$$

where ϵ is the on-side energy, t_1 the nearest neighbour hopping, and t_2 the second nearest neighbour hopping. To begin, we consider there is one atom per unit cell, the length of the latter being $\frac{a}{4}$ [535] with a [534]. By imposing periodic boundary conditions on the coefficients C_n of a trial wave function $|\psi\rangle = \sum_n C_n |n\rangle$, inserting $|\psi\rangle$ into H leads to the dispersion relation

$$E(k) = \epsilon + 2t_1 \cos(ka) + 2t_2 \cos(2ka), \tag{IX.4}$$

where $-\frac{\pi}{a} \leqslant k \leqslant \frac{\pi}{a}$ [535].

Next, as detailed in Boykin et al. (2004) [535], this one-band model can be interpreted by a basis change as tight-binding model containing two atoms per unit cell (which is now of length $\frac{a}{2}$). Using this alternative formulation, we obtain a two-band model with dispersion relation

$$E_\pm(k) = \epsilon \pm 2t_1 \cos\left(\frac{ka}{2}\right) + 2t_2 \cos(ka). \tag{IX.5}$$

Importantly, for $t_1 = 0.683$ eV, $t_2 = 0.612$ eV and $\epsilon = 3$ eV, the lowest band of $E_\pm(k)$ has a minimum at $k_0 = 0.82\frac{2\pi}{a}$ (compared to $k_0 = 0.85\frac{2\pi}{a}$ for real silicon [527]), and the curvature suggests an effective mass[1] $m_l = 0.91 m_e$ as observed in silicon. In other words, the dispersion relation obtained from this two-band tight-binding model reproduces the dispersion relation of the valleys in bulk, as testified by comparing figures IX.6 and IX.9.

The next step consist of imposing hardwall boundary conditions on the coefficient C_n, leading to one-dimensional confinement as in a quantum well. In matrix notation, the eigenvalue

valley physics.

[1] In theory the effective mass can vary with the position, but in Si/Si_xGe_{1-x} heterostructure this variation is negligible [527].

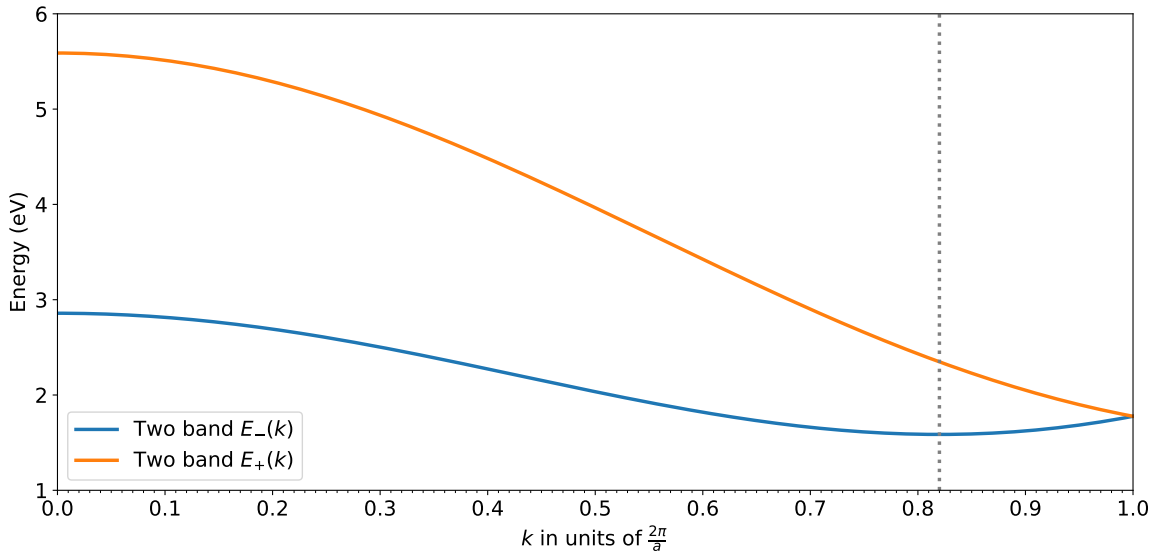


Figure IX.9: Plot of the dispersion relation of equation (IX.5) of the two-band tight-binding model of [534, 535], reproducing the behaviour of the two lowest bands of figure IX.6 between Γ ($k = 0$) and X ($k = \frac{2\pi}{a}$). The lowest band has a minimum at $k_0 = 0.82\frac{2\pi}{a}$ (marked by the vertical dashed line) similar to silicon.

problem consists of diagonalising equation (IX.3) given by

$$H = \begin{pmatrix} \epsilon & t_1 & t_2 & 0 & \dots & \dots & 0 \\ t_1 & \epsilon & t_1 & t_2 & 0 & \ddots & \cdots \\ t_2 & t_1 & \epsilon & t_1 & t_2 & \ddots & \cdots \\ 0 & \ddots & \ddots & \ddots & \ddots & \ddots & 0 \\ \cdots & \ddots & t_2 & t_1 & \epsilon & t_1 & t_2 \\ \cdots & \ddots & 0 & t_2 & t_1 & \epsilon & t_1 \\ 0 & \dots & \dots & 0 & t_2 & t_1 & \epsilon \end{pmatrix}. \tag{IX.6}$$

As expected from such a confinement, the wave functions adopt a sine-like envelope similar to that found in infinite quantum wells. However, due to valley physics, the two lowest energy wave functions exhibit fast modulations on atomic distances, of the order of $k_0 = \frac{2\pi}{a}$ [527], as pictured in figure IX.10. This rather simple tight-binding model allows to estimate the evolution of the valley splitting with the width of the quantum well or in the presence of an electric field, which we will use to model a valley qubit in appendix C.10. As mentioned in the supplemental material of Zwanenburg et al. [527], Boykin's two band model overpredicts the valley splitting by around two order of magnitudes, compared to measurement on real devices. The origin of this discrepancy is due to the incorrect assumption of a flat quantum well, without taking into account the disordered Si_xGe_{1-x} buffers.

3.3) Effective mass approach

The tight-binding method presented above is simple and allows to give analytical results for the valley splitting in the case of a flat quantum well, as studied by Boykin et al. (2004) [535]. However, in more complicated geometries ubiquitous of Si/Si_xGe_{1-x} heterostructures, these analytical results fail. In these situations, effective mass theories developed in [536–538] can be used to complement the tight-binding method. Effective mass theories neglect atomistic details, since their are only valid for slowly varying potentials V such that $V(\mathbf{r})/|\boldsymbol{\nabla} V(\mathbf{r})| \gg a$, where a is the crystalline lattice constant of silicon [537]. This may sound problematic, since valley physics is strongly dependent on atomistic details. The solution is to incorporate an

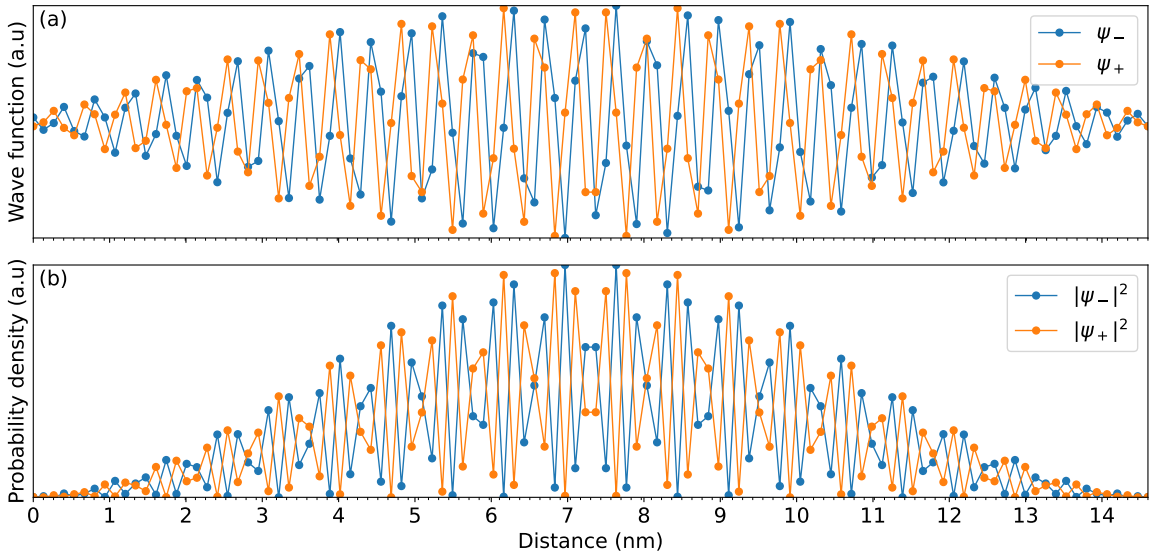


Figure IX.10: Plot of (a) the wavefunctions and (b) probability densities of the two lowest energy (valley) states for a quantum well of 110 atoms, corresponding to 14.6 nm. The minor xticks correspond to atomic lattice points.

empirical valley coupling potential V_v in the form of a delta function, producing a atomistic-like perturbation. To illustrate this, we first present the method in the general case, and then we illustrate it on two limiting cases for which an analytical solution is available.

3.3.1) General case

Let us note $F_n(x,z)$ the eigenstates of the (unperturbed) Hamiltonian of a typical Si/Si$_x$Ge$_{1-x}$ heterostructure,

$$H_0 = -\frac{\hbar^2}{2m_l}\frac{\partial^2}{\partial z^2} - \frac{\hbar^2}{2m_t}\left(\frac{\partial^2}{\partial x^2} + \frac{\partial^2}{\partial y^2}\right) + V_{\text{QW}}(z) + V_{\text{QD}}(x,y), \tag{IX.7}$$

where $m_l = 0.92m_e$ ($m_t = 0.19m_e$) is the longitudinal (transverse) effective mass of electrons in silicon, V_{QW} is the confinement potential of a quantum well in the z direction, and V_{QD} is two-dimensional quantum dot potential. These functions are also called "envelope functions". Following, [537, 538], we can define an effective Hamiltonian $H = H_0 + V_v$ from the unperturbed Hamiltonian using a valley coupling potential V_v, which we treat as a perturbation. In an effective mass theory, the valley coupling potential takes the form of a Dirac function located at the interface. For instance, for an interface located at position z_0, we write:

$$V_v = v_v \delta(z - z_0) \tag{IX.8}$$

where v_v is a constant that can be determined by experiments or a tight-binding theory. Note that the quantum well in z has two interfaces, but it is sufficient to include only one of the interface to describe the physics, as explained in [538].

We note $E_{\widetilde{n}}$ the eigenstates of H. Note that the change in index, $\widetilde{n}$ instead of the orbital number n, reflects the mixing of orbitals and valleys. We can define an unperturbed basis set that we write as follows:

$$|n,v\rangle = |n\rangle \otimes |v\rangle = e^{ik_0 vz} F_n(x,y,z) \tag{IX.9}$$

where the index $n \in \mathbb{N}$ denotes the orbital levels (from both the x and z axis) while $v \in \{-1,1\}$ refers to the two lowest z valleys centered around $k_0 \simeq 0.82\frac{2\pi}{a}$. Note that the fast oscillating Bloch functions $u_k(r)$ have not been included. We can use this unperturbed basis to expand the wavefunctions. In other words, the wavefunctions we are looking for are linear combinations of the unperturbed basis.

The method to use the effective mass theory is as follows:

1. solve for the envelope functions $F_n(x, y, z)$ using the unperturbed Hamiltonian H_0
2. evaluate the matrix elements $\langle n', v'|H|n, v\rangle$ with $H = H_0 + V_v$
3. diagonalize the effective Hamiltonian H, with the eigenvectors indicating how to combine the envelope functions

Note that the size of the effective Hamiltonian is not too big. Indeed, since we only consider the two lowest valleys in the z direction, the size of this Hamiltonian will grow as $2n$ with n the number of orbital energies we want to include. The part with the heaviest computational requirement is in solving for the envelope functions when diagonalizing the unperturbed Hamiltonian H_0.

3.3.2) Flat quantum well

To illustrate the results obtained using the effective mass formalism, and connect it with the results of the tight-binding approach, we consider the case of a flat infinite quantum well. We assume that the width of the quantum well is such that the orbital number n of the electrons is determined by the eigenstates of the quantum dot potential, which we note $f_n(x, y)$, while that of the of the quantum well potential is $g(z)$. Therefore, the eigenfunctions of the unperturbed Hamiltonian H_0 are $F_n(x, y, z) = f_n(x, y)g(z)$.

For a flat quantum well, we can readily use the formula[1] of Friesen and Coppersmith (2010) [538] which give the matrix elements

$$\langle n', v|H|n, v\rangle = \delta_{n,n'}\left(\epsilon_n + v_v g(z_0)^2\right), \tag{IX.10}$$

$$\langle n', -v|H|n, v\rangle = v_v g(z_0)^2 e^{2ivk_0z_0} \iint \mathrm{d}x'\,\mathrm{d}y'\, f_{n'}(x', y')f_n(x', y') \tag{IX.11}$$

$$= \delta_{n,n'} v_v g(z_0)^2 e^{2ivk_0z_0}. \tag{IX.12}$$

Following the notation of the [537], we can define

$$\Delta_0 = v_v g(z_0)^2, \tag{IX.13}$$

$$\Delta_1 = v_v g(z_0)^2 e^{2ivk_0z_0}. \tag{IX.14}$$

Then, the effective Hamiltonian H can be written as a diagonal block matrix, with blocks H_n of size 2×2 defined as

$$H_n = \begin{pmatrix} \langle n, -1|H|n, -1\rangle & \langle n, -1|H|n, 1\rangle \\ \langle n, 1|H|n, -1\rangle & \langle n, 1|H|n, 1\rangle \end{pmatrix} = \begin{pmatrix} \epsilon_n + \Delta_0 & \Delta_1 \\ \Delta_1^* & \epsilon_n + \Delta_0 \end{pmatrix}. \tag{IX.15}$$

The diagonalisation of H_n gives the eigenenergies

$$\epsilon_n^- = \epsilon_n + \Delta_0 - |\Delta_1|, \tag{IX.16}$$

$$\epsilon_n^+ = \epsilon_n + \Delta_0 + |\Delta_1| \tag{IX.17}$$

which are hence separated by $|\Delta_1|$, representing the valley splitting. It is easy to check that one can choose the eigenvectors

$$\alpha_- = \frac{-1}{2i}\begin{pmatrix} e^{ik_0z_0} \\ -e^{-ik_0z_0} \end{pmatrix}, \quad \alpha_+ = \frac{1}{2}\begin{pmatrix} e^{ik_0z_0} \\ e^{-ik_0z_0} \end{pmatrix}, \tag{IX.18}$$

[1] The case of a flat quantum well corresponds to using $\theta = 0$ in the formula of Friesen and Coppersmith (2010) [538].

which match with the ones from reference [537]. Hence, the wave-functions corresponding to eigenvectors α_- and α_+ are

$$|n,-1\rangle = \frac{-1}{2i}\left(e^{ik_0z_0}f_n(x,y)g(z)e^{-ik_0z} - e^{-ik_0z_0}f_n(x,y)g(z)e^{ik_0z}\right) \tag{IX.19}$$

$$= \frac{-1}{2i}\left(e^{-ik_0(z-z_0)} - e^{ik_0(z-z_0)}\right) f_n(x,y)g(z) \tag{IX.20}$$

$$= \sin(k_0(z-z_0))f_n(x,y)g(z), \tag{IX.21}$$

$$|n,1\rangle = \frac{1}{2}\left(e^{ik_0z_0}f_n(x,y)g(z)e^{-ik_0z} + e^{-ik_0z_0}f_n(x,y)g(z)e^{ik_0z}\right)$$

$$= \frac{1}{2}\left(e^{-ik_0(z-z_0)} + e^{ik_0(z-z_0)}\right) f_n(x,y)g(z) \tag{IX.22}$$

$$= \cos(k_0(z-z_0))f_n(x,y)g(z). \tag{IX.23}$$

From these expressions, we can interpret the plots of the wave functions obtained using the tight-binding model in figure IX.10. We see that the envelope $F_n(x,y,z) = f_n(x,y)g(z)$ is the same for both eigenstates. The envelope function is modulated on the order of k_0, with a dephasing of $\frac{\pi}{2}$ between the two valley states.

Finally, it worth noticing that in the case where there is no valley coupling ($v_v = 0$), we have $\Delta_0 = \Delta_1 = 0$, and the blocks H_n of equation (IX.15) become diagonal [537, 538]

$$H_n = \begin{pmatrix} \epsilon_n & 0 \\ 0 & \epsilon_n \end{pmatrix}. \tag{IX.24}$$

In this case, each orbital level ϵ_n is doubly degenerate, and the associated eigenvectors are $\alpha_- = (1 \quad 0)^t$ and $\alpha_+ = (0 \quad 1)^t$ corresponding to the unperturbed eigenstates $|n,-1\rangle = f_n(x)g(z)e^{-ik_0z}$ and $|n,1\rangle = f_n(x)g(z)e^{ik_0z}$. Notably, the probability densities are identical since the phase factor vanishes using the modulus square $|\psi|^2$.

4) Charge qubits

4.1) Standard charge qubits

We now consider an alternative realisation of qubit in silicon based on the charge degree of freedom. Charge qubits use a single electron in double quantum dot (DQD) for their operation. The computational basis consists in bonding and antibonding combination of the states $|L\rangle$ and $|R\rangle$, which encode whether the electron is in the left dot ($|L\rangle$) or right dot ($|R\rangle$). This hybridization of $|L\rangle$ and $|R\rangle$ stems from a non-zero tunneling rate t between the two dots, hence delocalizing the electron in the two dots.

An effective Hamiltonian describing this system is given by [539]

$$H = \frac{\epsilon}{2}\sigma_z + t\sigma_x = \begin{pmatrix} \frac{\epsilon}{2} & t \\ t & -\frac{\epsilon}{2} \end{pmatrix}, \tag{IX.25}$$

where ϵ is the detuning energy between each dot and t is the inter-dot tunnelling rate. The resulting eigenvalues $E_\pm$ are

$$E_\pm = \pm\frac{\sqrt{\epsilon^2 + 4t^2}}{2} \tag{IX.26}$$

As a function of the detuning ϵ between the two dots, the spectrum exhibits an anticrossing with a gap $2t$ as shown in figure IX.11. Coherent control of the resulting qubit can be achieved through different pulses varying the detuning ϵ between the dots. Some of these pulses are adiabatic, while others are non-adibatic (on the order of the hundreds of picoseconds), and amount to performing Landau-Zener transitions, first discussed in chapter V. The initialisation of the qubit can be performed by relaxation by tuning the system either in the $|L\rangle$ or $|R\rangle$

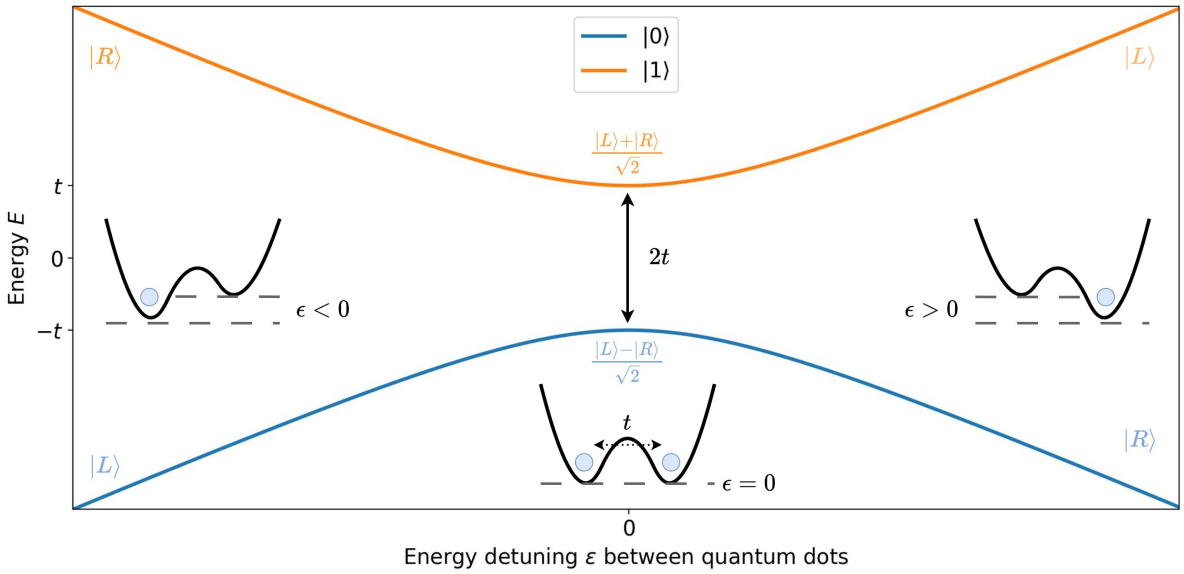


Figure IX.11: Energy diagram of a charge qubit, made up of a single electron in a double quantum dot. The tunnelling rate between the two dots is t, and corresponds to the coupling between the two dots, determining the energy splitting.

configuration. For the readout, charge sensing is used, for instance using another quantum dot or a quantum point contact [528, 539].

The strengths of the charge qubit are their fast control (using non-adiabatic pulses), and the easiness of their readout. Unfortunately, a major drawback is their sensitivity to *charge noise*, leading to very poor decoherence times. Indeed, charge noise leads to fluctuations of the energy levels of the quantum dot, which can originate from the $1/f$ noise of the dielectrics used in the device, or the Johnson-Nyquist noise from control gates [521, 528]. As a consquence, as of 2021, the best reported decoherence time of a charge qubit was 7 ns for a single-qubit gate time of 0.1 ns and single-qubit fidelity of 86 % [93, 540]. In principle, the short decoherence time can be overcome by decreasing the operation time, but doing so require non-adiabatic pulses that cannot be generated with high-enough fidelity with current pulse generators [541]. Indeed, because precise timing of such pulses is necessary, non-adiabatic control is less resilient against control errors than the adiabatic counterpart [521], leading to poor gate fidelities. Despite this disadvantage, charge qubits can still be used for charge sensing, which is notably used to readout spin qubits.

4.2) Valley qubits

Valley qubit based on a double quantum dot. As discussed in section 3, valley physics comes into play in silicon nanostructure. The valleys represent additional degrees of freedom onto which quantum information can be encoded. This idea has been explored [525, 542]. The principle of operation is very similar to that of standard charge qubits. In Schoenfield, Freeman, and Jiang (2017) [542], a small valley splitting exists in the left quantum dot only, while in Penthorn, Schoenfield, and Rooney (2019) [525] a valley splitting exist in each of the two dots. The associated energy diagrams are plotted in figure IX.12, where $|L_\pm\rangle$ ($|R_\pm\rangle$) labels the $\pm$ valley state of the electron in the left (right) dot.

Schoenfield, Freeman, and Jiang (2017) [542] demonstrated coherent Rabi oscillations between the two valley states $|L_\pm\rangle$, while Penthorn, Schoenfield, and Rooney (2019) [525] demonstrated two-axis coherent control of a qubit encoded on $|L_\pm\rangle$. An attractive feature of such an encoding of the qubit on the valley states is the experimentally observed resilience against charge noise. Indeed, contrary to standard charge qubits, the energy levels of the valley states do not fluctuate as much due to applied voltages, leading to an improved decoherence time of the order of a few nanoseconds.

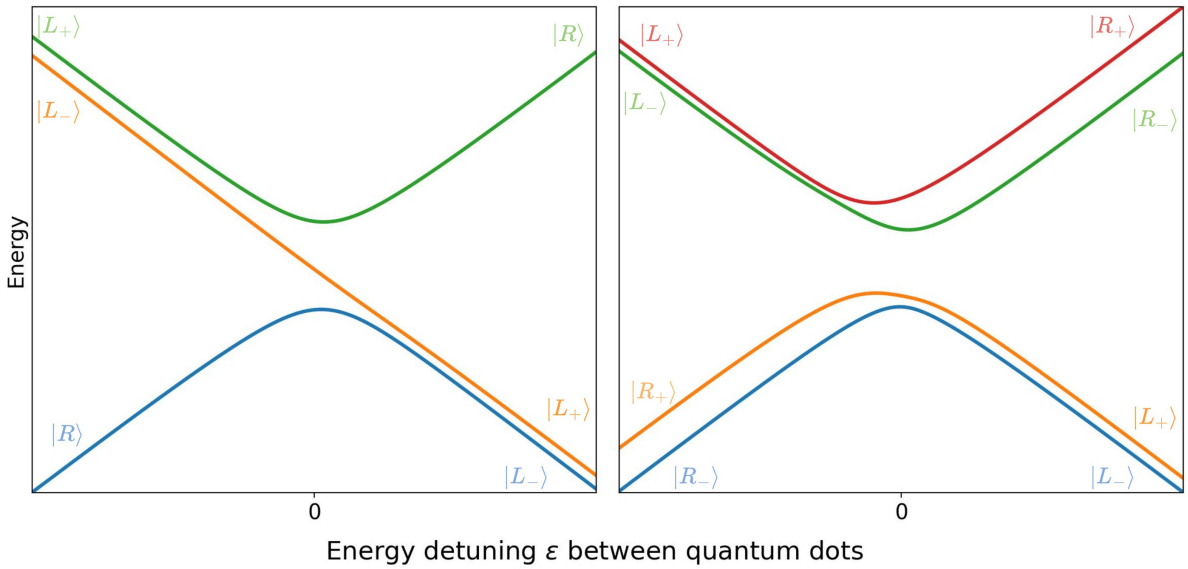


Figure IX.12: Energy diagram of the valley qubits proposed by Schoenfield, Freeman, and Jiang (2017) [542] (left) and Penthorn, Schoenfield, and Rooney (2019) [525] (right).

Interface steps and non-adiabatic valley qubit. The previous examples of charge qubits show that in principle, it is sufficient to have a two-level system with controllable parameters to induce fast single-qubit rotations using appropriate non-adiabatic pulses. The valleys states are appealing to encode quantum information due to their improved immunity against charge noise. However, the prediction of the valley splitting is complicated due to its dependence on microscopic details. One imperfection which can affect the valley splitting is the presence of atomic steps at the interface of a Si/Si_xGe_{1-x} heterostructure. These "miscuts" of the silicon layer are typical of Si/Si_xGe_{1-x} nanostructures [543–546].

In the original published work Gardin et al. (2022) [4] available in appendix C.10, we showed that the presence of a single interface step led to a coupling between the two valley states in a Si/Si_xGe_{1-x} heterostructure. Intuitively, this can be understood by the fact that before and after the step, the states are less and more confined, respectively, and also have differing valley splitting. As a result, an anti-crossing opens, and we discovered that the energy gap can be controlled using an applied static electric field. These elements show that a valley qubits encoded in a single quantum dot may be possible, and that control can be achieved using non-adiabatically using electric fields only. The valley physics was obtained using the tight-binding model presented in section 3, and was further verified by a 40 band $sp^3d^5s^*$ model in NEMO 3D. While the precise origin and characterisation of the anti-crossing has not been carried out, this work contributes to the understanding of valley physics and silicon-based quantum computing.

5) Conclusion

In this chapter, we have introduced silicon physics and the associated theoretical treatment (tight-binding and effective mass) to model it. This allowed us to explore valley physics and lay the foundations for a novel valley qubit in a single quantum dot [4]. To complete this qubit proposal, it is desirable to derive an effective Hamiltonian modelling the anti-crossing between the valley states. This would allow to explore the possibility of performing arbitrary single-qubit operations by engineering appropriate non-adiabatic pulses, even though the timescales required may be beyond what is currently feasible. Another important possible continuation of our work would be the computation of the relaxation rate T_1 of the valley states, for instance following the method of Tahan and Joynt (2014) [547].

Our discussion of silicon-based quantum computing focused on charge qubits, which have the advantage of fast operation using non-adiabatic pulses, at the price of poor gate fidelities. While fast quantum operations are desirable to limit the effect of decoherence, we see there

there exists a trade-off between fast computation time and fidelity of operation. It is worth mentioning that several alternative silicon qubits, based on the spin degree of freedom, have been demonstrated [548]. Notably, spins of silicon electrons has very high decoherence time, because of weak spin orbit coupling, and the availability of isotopes with zero nuclear spins.

Chapter X

Conclusion and perspectives

1) Summary of contributions

In this thesis, we began by examining several quantum technologies (chapter II), and identified several resources on which they relied on. We then focused on a subset of these, namely coherent control, quantum information transduction, and the engineering of non-classical and non-reciprocal behaviours, in the context of cavity magnonics and silicon nanostructures.

After introducing the formalism for the study of light-matter interactions in chapter III, we found in [1, 2] (chapter IV) that the Zeeman magnon-photon coupling phases could steer a cavity magnonics system towards either dark mode physics (useful for quantum memory applications [227]), or cavity-mediated coupling (for quantum information transduction). In chapter V, through our study of geometric phases, we understood that the coupling phases give rise to a synthetic $U(1)$ gauge field, whose value is characterised by a gauge invariant phase θ. Therefore, in chapter VI we studied its potential applications and showed that it can be used make coherent and dissipative couplings interfere. In turn, such interference allowed the creation of non-reciprocal interactions, which can be useful for quantum communication.

Furthermore, using the theoretical foundations developed in chapters III and IV, we provided a theoretical model for a two-tone driving scheme which was initially thought to be able to access both the applications of coherent and dissipative couplings on-demand in a single versatile platform. Notably, our understanding of dissipative coupling developed in chapter VI permitted us to clarify the physics at play in this scheme.

In chapter VII, we attempted to theoretically explain the deviation between the numerical/experimental data observed in Bourcin et al. (2023) [465], and the those predicted by the Dicke model, which is the standard model for cavity magnonics systems [267]. In that same chapter, we highlighted the potential of the ultrastrong coupling regime for faster quantum information transduction, and the creation of non-classical states. Concerning the latter, we examined several proposals based on non-linear bosonic interactions in chapter VIII, highlighting their essential elements. From these insights, we proposed a potentially new method to create magnon-photon entanglement in cavity magnonics, but we could not validate whether this scheme works.

Finally, in chapter IX, we examined the physics of nanostructures and valley physics in silicon. Combining these two different elements with non-adiabatic physics (developed in chapter V in the context of geometric phases), we showed in Gardin et al. (2022) [4] that a qubit based on the valley degrees of freedom could potentially be created in a miscut Si/Si_xGe_{1-x} heterostructure. Interestingly, unlike other charge qubits, this proposal considers a single quantum dot, and could benefit for the resilience of valley states to charge noise (recall that the main limitation of charge qubits is their sensibility to charge noise), while still allowing fast all-electrical control.

Among the different physical resources we focused on, we saw that cavity magnonics was a useful platform for several of them, while semiconductor nanostructures only exemplified one (coherent control). Note that this does not mean that semiconductor nanostructures are "inferior" to cavity magnonics with respect to quantum information processing, but instead that the topics we focused on were naturally more suited to cavity magnonics rather than

silicon-based nanostructures.

2) Outstanding work

Additional theoretical tools and methods. First of all, we would like to mention further theoretical methods of interest for future work. In chapter II, we discussed several quantum information processing schemes, and identified various "quantum primitives" useful for their realisation. Among these primitives, we saw that genuine quantum states, such as squeezed states, are an interesting resource for many quantum technologies. While we introduced several measures of non-classicality, we left out quasi-probability distributions [34]. Contrary to standard probability distributions which only take positive values, quasi-probability distributions such as the Wigner functions can also become negative, accounting for non-classical behaviour. Furthermore, we have circumvented the use of density operators to describe mixed states. However, this formalism is very useful in quantum information processing, for example for quantum state tomography, the visualisation of decoherence on the Bloch sphere, and the characterisation of entanglement (notably in discrete variables using the Von Neumann entanglement entropy [5]).

Additionally, the formalism of master equations [34] is a powerful method to treat open quantum systems, and can complement the shortcomings of quantum Langevin equations. For instance, they allow to simulate the time-domain dynamics of dissipative quantum systems beyond the mean-field treatment. In practice, this can be used to model semiconductor qubits in the presence of dissipative processes such as relaxation or dephasing. Similarly, the coupling of magnons to superconducting qubits can be used to create single magnons [549–552] or cat states [553, 554]. Importantly, all these proposals use master equations for the modelling. Additionally, master equations can be adapted to work in the ultrastrong coupling regime [207, 555–557], and therefore they can be used to study the enhancement of entanglement without using a rotating frame transformation[1].

Geometric phases, synthetic gauge fields, and their applications. Gauge theories are a universal concept, and naturally appear in various fields of physics. In this thesis, we encountered the notion of gauge during our description of quantum light, and the discussion of geometric phases. Indeed, we saw that quantum electrodynamics (QED) is a $U(1)$ gauge theory, and therefore gauge theory intervenes in the description of light-matter interaction (discussed in chapters III and VII). On the other hand, geometric phases are associated with a gauge theory of the parameter space of the quantum system, explained in chapter V.

In chapter IV, and more specifically in [1], we showed that the coupling phases in cavity magnonics could be used to create a synthetic $U(1)$ gauge field, characterised by a single gauge-invariant phase θ. We noticed that both geometric phases and the discrete synthetic $U(1)$ gauge field arise due to a common underlying gauge symmetry broken by the presence of an interaction loop. This feature led us to explore, in appendix C.4, the possible connections between the gauge-invariant phase θ (resulting from the coupling phases in cavity magnonics) and standard geometric phases. While the relations between the two warrants further study, we can already see that applications of geometric phases (robust quantum control for quantum computation) cannot be achieved with the cavity magnonics coupling phases.

One reason is that the gauge-invariant phase θ associated with the synthetic $U(1)$ gauge field is static, even though it can be tuned by the cavity geometry, as shown theoretically in Gardin et al. (2023) [1] and experimentally in Gardin et al. (2024) [2]. Additionally, as mentioned in section 4.3, tunability could be achieved through coupling strength or resonance frequency modulations. Concerning the latter, an interesting possibility is to drive the magnetic sample along the equilibrium direction. This can be done using a loop antenna placed around a YIG sphere (as considered in the two-tone driving scheme of appendix C.5 for instance), and orienting the loop so that the generated AC magnetic field is aligned with the

[1] Recall that in chapter VIII we mentioned that carrying out these transformations does not simplify the Hamiltonian in the presence of counter rotating terms.

static magnetic field $\mathbf{H}_0$ used to tune the magnon's resonance frequency. However, the coupling of the YIG sphere to the magnetic field generated by a loop antenna requires further investigations, notably to predict the coupling[1]. Furthermore, as noted above, the artificial $U(1)$ gauge field has applications for quantum memories and quantum information transduction. Therefore, the in-situ control of the gauge invariant parameter θ could prove useful to tune the system between these two applications.

Finally, we note that θ effectively parametrises the value of the gauge field in a single loop. More generally, we can imagine creating a lattice of k loops, where each loop is associated with a gauge-invariant phase θ_k indicating the value of the gauge field on each loop. Such a network would create a spatially-dependent gauge field, which has been proposed in cavity optomechanics [558]. In cavity magnonics, this could potentially be performed by coupling cavity modes together, which requires further investigation.

3) Future directions

Integration of cavity magnonics systems on a chip. We demonstrated that cavity magnonics is promising for a variety of applications, but an important shortcoming concerns its miniaturisation and integration with other platforms. Indeed, the cavity magnonics implementations we focused on in this thesis are rather bulky, since they comprise three-dimensional cavities and the presence of a (reasonable albeit still) large magnetic field used to tune the resonance frequency of the magnon. Therefore, to build useful devices in the future, it appears necessary to integrate cavity magnonics system on a chip, for example by using planar structures compatible with other physical platforms. Notably, the integration with silicon chips would facilitate the integration with photonics, circuit QED, or semiconductor qubits. Furthermore, because of the low temperatures required to reach the quantum regime of magnonics (to the milli-Kelvin to a few hundreds milli-Kelvin for microwave frequencies), superconducting cavities seem to be especially promising since they are particularly suited for operating at low temperatures.

Relation between chirality, synthetic gauge fields, and non-reciprocity. Over the course of this thesis, we have explained how to obtain non-reciprocal behaviour by combining a synthetic gauge field with dissipation. It is worth mentioning that while these elements can induce non-reciprocity, they are not the only ingredients. Indeed, another possibility is to engineer chiral behaviour in a hybrid system. As an example, in cavity magnonics one can create chiral cavity modes, which by coupling to the magnon modes induce chiral magnon modes and create non-reciprocal behaviours [559, 560]. Therefore, it would be interesting to explore the interplay between synthetic gauge fields and chirality, notably the strength of the resulting non-reciprocity. As an example, we note that in optomechanics a network of synthetic gauge fields can be created [558], and is related to the creation of chiral edge states.

Real two-tone driving. Coherent couplings are useful for quantum information transduction, while dissipative couplings can be used to create non-reciprocal behaviours. Therefore, the ability of having both in a single platform is of interest. While the two-tone driving proposal studied in appendix C.5 was shown not to lead to dissipative coupling physics, it remains an interesting direction to achieve the in-situ control of the weight of the coherent and/or dissipative couplings. Such a scheme would allow to obtain non-reciprocal behaviours and quantum information transduction behaviours on-demand in a single platform. So far, in cavity magnonics dissipative couplings have almost exclusively been obtained by coupling a cavity and magnon mode indirectly through travelling waves, and hence it is towards such systems that one should turn its attention in the future.

Applications of the ultrastrong coupling regime. We discussed the ultrastrong coupling regime of light-matter interactions in chapter VII, which can be used for faster quantum

[1] Such a modelling could in principle be performed using COMSOL Multiphysics®, and will complement the work started in appendix C.2.

information transduction as well as the generation of non-classical states. Concerning the latter, we saw in chapter VIII that a difficulty was the combination of the ultrastrong coupling regime with schemes based on non-linear bosonic interactions. As mentioned above, this difficulty could potentially be circumvented by using master equations to model the hybrid system.

A related future direction concerns the extraction of the virtual particles contained in the ground state of USC systems. Indeed, as discussed in section 4.1 of chapter VII, in the USC the eigenstates $|\psi_\mu\rangle$ are strongly hybridised light-matter states containing a non-vanishing number of light and matter quasiparticles. However, these excitations are *virtual*, since they cannot be detected outside of the USC system. Several schemes have been put forward for the detection and extraction of these virtual particles, such as the introduction of a two-level system as a detector, or the time-modulation of resonance frequencies or coupling strengths. These schemes are reminiscent of the dynamical Casimir effect [207, 441, 557, 561–566]. Notably, the time-dependent resonance frequency modulation method could be implemented in cavity magnonics by two means. The first concerns the modulation of the magnon frequency through the applied static magnetic field. However, the variation in the magnetic field amplitudes must be non-adiabatic to extract virtual excitations, which is experimentally challenging. Instead, it may be feasible to drive a YIG sphere along the direction parallel to the static magnetic field to modulate its resonance frequency[1]. Recall that we have already discussed this method above concerning the dynamical tuning of synthetic gauge fields. Nevertheless, it is worth mentioning that time-dependent interactions are another source of gauge ambiguities [456, 457], a topic we have not tackled here.

Furthermore, while the inclusion of a diamagnetic term for the magnons seems to agree with USC cavity magnonics experimental data, we are still unable to provide a good justification for the inclusion of this term. Two possible routes should be explored, namely the investigation of a sum rule for the magnon-photon Dicke model, and the quantisation of the electromagnetic field in a magnetic medium. Indeed, concerning the latter, we note that in chapter III we considered the quantisation of the electromagnetic field in arbitrary dielectrics, assuming a scalar magnetic permeability μ_r. However, as mentioned during our investigation of the ultrastrong coupling regime in cavity magnonics (see chapter VII and appendix C.7), using this expression in magnetic materials is incorrect, because the magnetic permeability tensor μ is not unity (e.g. see the Polder susceptibility tensor of equation (IV.83)). Therefore, to obtain a consistent theory of light interacting with magnetic material, we need to quantise the electromagnetic field in a magnetic medium, for instance following [567, 568].

Non-classicality in cavity magnonics. In chapter VIII, we presented several principles and schemes to generate non-classical states. While we only focused on non-linear bosonic interactions, other possibilities exist, notably using discrete variable systems. Furthermore, while our focus has been on Gaussian processes, non-Gaussian schemes also exist [569], and the resulting states can exhibit stronger entanglement than Gaussian schemes [570, 571]. Therefore, the investigation of non-Gaussian entanglement seems like a relevant direction, notably in cavity magnonics which has so far only focused on Gaussian entanglement.

Furthermore, it is worth recalling that so far, only the schemes based on the magnon-superconducting qubit indirect coupling has been demonstrated experimentally. Notably, to the best of our knowledge, none of the schemes based on non-linear bosonic interactions presented in chapter VIII have been experimentally (in cavity magnonics) verified at the time of writing. Despite this lack of experimental verification, we note that the magnon-phonon coupling due to the magnetostrictive interaction (see section 3.1 of chapter VIII) by itself has been demonstrated experimentally by Zhang et al. (2016) [466]. Therefore, all the schemes based on this interaction could also potentially be verified experimentally. In particular, the calculation of the phonon modes of a YIG sphere can be performed numerically using COMSOL Multiphysics®, and can be extended to arbitrary geometries[2].

[1] Note that this could potentially induce a magnetostrictive interaction, discussed in chapter VIII, with the sphere's vibrational mode.

[2] Notably for optomechanical cavities, see for instance the supplementary material of [432].

Silicon qubits and non-adiabatic quantum pumps. In chapter IX, we studied silicon charge qubits based on double quantum dots. In Gardin et al. (2022) [4] (see appendix C.10), we proposed a non-adiabatic valley qubit based on the valley degrees of freedom in a silicon-germanium heterostructure. This proposal is reminiscent of single-electron quantum pumps [511–518], which aim at trapping a single electron at a time in a quantum dot, with the objective of producing a single-electron source. Indeed, the operation of single-electron quantum pumps can be modelled by a quantum dot whose centre moves in space, similar to what was done by Yamahata et al. (2019) [285]. Such single-electron sources, akin to single-photon sources, are useful for quantum metrology and sensing, since they can produce the most precise current sources.

However, as shown in [285] and [4] (appendix C.10), when the pumping frequency is high enough, the movement of the quantum dot induces transitions towards higher excited states, which tunnel out of the dot faster than the ground state. As a result, typically the accuracy of the quantum pump decreases at high pumping frequencies. Therefore, in principle using a tighter quantum dot would allow to limit non-adiabatic transitions at higher pumping frequencies, as demonstrated numerically by our work [4]. Therefore, aside from the development of qubits based on [4], another research direction consists of optimising single-electron pumps so that they can operate at high pumping frequencies, in the non-adiabatic regime.

Appendix A

Theoretical reminders

A.1) Operator identities

In this appendix, we note q and p the canonical position and momentum operators. For $i \in \{1, 2, 3\}$ the Pauli matrices σ_i are defined as

$$\sigma_1 = \begin{pmatrix} 0 & 1 \\ 1 & 0 \end{pmatrix}, \quad \sigma_2 = \begin{pmatrix} 0 & -i \\ i & 0 \end{pmatrix}, \quad \sigma_3 = \begin{pmatrix} 1 & 0 \\ 0 & -1 \end{pmatrix}. \tag{A.1}$$

Fundamental commutation relation and notations. The fundamental commutation relation is

$$[q, p] = i\hbar \tag{A.2}$$

where $[q, p] = qp - pq$ denote the commutator of q and p. The anticommutator is defined as $\{q, p\} = qp + pq = \{p, q\}$. Using the commutation relation, we can write

$$\{q, p\} = i\hbar + 2pq = 2qp - i\hbar. \tag{A.3}$$

Formulas for commutators of products. We now introduce formulas from which we will derive other commutation relations

$$[A, BC] = [A, B]C + B[A, C] \tag{A.4}$$
$$[AB, C] = [A, C]B + A[B, C] \tag{A.5}$$
$$[AB, CD] = A[B, C]D + [A, C]BD + CA[B, D] + C[A, D]B. \tag{A.6}$$

Position-momentum identities. We can then derive the following identities:

$$\begin{aligned}
[q, p^2] &= [q, p]p + p[q, p] = 2i\hbar p \\
[p, q^2] &= [p, q]q + q[p, q] = -2i\hbar q \\
[p^2, q^2] &= [p^2, q]q + q[p^2, q] = -i\hbar pq - i\hbar qp = -2i\hbar\{q, p\} \\
[pq, q] &= [p, q]q + p[q, q] = -i\hbar q \\
[pq, q^2] &= [pq, q]q + q[pq, q] = -2i\hbar q^2 \\
[pq, p] &= [p, p]q + p[q, p] = i\hbar p \\
[pq, p^2] &= [pq, p]p + p[pq, p] = 2i\hbar p^2 \\
[qp, p] &= [q, p]p + x[p, p] = i\hbar p \\
[qp, q] &= [q, q]p + q[p, q] = -i\hbar q \\
[qp, p^2] &= [qp, p]p + p[qp, p] = 2i\hbar p^2 \\
[qp, q^2] &= [qp, q]q + q[qp, q] = -2i\hbar q^2
\end{aligned}$$

Identities for bosonic operators. Using the commutation relation $[a, a^\dagger] = 1$ for bosonic annihilation a and creation operators $a^\dagger$, we can show by induction that for any integer n,

$$\left[a, {a^\dagger}^n\right] = n{a^\dagger}^{n-1}, \quad \left[a^\dagger, a^n\right] = -na^{n-1}. \tag{A.7}$$

We also have the identities

$$[a, a^\dagger a] = a, \quad [a, aa^\dagger] = a, \quad [a^\dagger, a^\dagger a] = -a^\dagger. \tag{A.8}$$

Pauli matrices identities. Before giving the identities, we introduce the spin raising and lowering operators

$$\sigma_+ = \frac{1}{2}(\sigma_1 + i\sigma_2) = \begin{pmatrix} 0 & 1 \\ 0 & 0 \end{pmatrix}, \quad \sigma_- = \frac{1}{2}(\sigma_1 - i\sigma_2) = \begin{pmatrix} 0 & 0 \\ 1 & 0 \end{pmatrix}. \tag{A.9}$$

We then have the identities

$$[\sigma_i, \sigma_j] = 2i\epsilon_{ijk}\sigma_k, \quad \{\sigma_i, \sigma_j\} = 2\delta_{ij}I_2, \tag{A.10}$$

$$[\sigma_+, \sigma_1] = \sigma_3, \quad [\sigma_+, \sigma_2] = i\sigma_3, \quad [\sigma_+, \sigma_3] = -2\sigma_+, \tag{A.11}$$

$$[\sigma_-, \sigma_1] = -\sigma_3, \quad [\sigma_-, \sigma_2] = i\sigma_3, \quad [\sigma_-, \sigma_3] = 2\sigma_-, \tag{A.12}$$

$$[\sigma_+, \sigma_-] = \sigma_3, \tag{A.13}$$

$$\sigma_i^2 = I_2, \quad \left(\sigma^\pm\right)^2 = 0 \tag{A.14}$$

$$\sigma_+\sigma_- = \frac{1}{2}(1 + \sigma_z), \quad \sigma_-\sigma_+ = \frac{1}{2}(1 - \sigma_z) \tag{A.15}$$

Baker-Campbell-Hausdorff formula. A special case of Baker-Campbell-Hausdorff formula gives, for two operators X and Y,

$$e^X Y e^{-X} = Y + [X, Y] + \frac{1}{2!}[X, [X, Y]] + \frac{1}{3!}[X, [X, [X, Y]]] + \ldots, \tag{A.16}$$

or more concisely

$$e^X Y e^{-X} = \sum_{n=0}^{\infty} \frac{\left[X^{(n)}, Y\right]}{n!} \tag{A.17}$$

where we note $\left[(X)^{(n)}, Y\right]$ the n-th iterated commutator defined as

$$\left[X^{(0)}, Y\right] \equiv Y, \quad \left[X^{(1)}, Y\right] = [X, Y] = XY - YX \tag{A.18}$$

$$\left[X^{(2)}, Y\right] = [X, [X, Y]], \quad \left[X^{(3)}, Y\right] = \left[X, \left[X^{(2)}, Y\right]\right] \tag{A.19}$$

and so on.

Application to bosonic operators. For an annihilation operator a following bosonic commutation relation $\left[a, a^\dagger\right] = 1$ and $\varphi \in \mathbb{C}$, we use equation (A.17) with $X = \varphi a^\dagger a$ and $Y = a$. Recalling that $[a^\dagger a, a] = -a$ gives

$$e^{\varphi a^\dagger a} a e^{-\varphi a^\dagger a} = a + [\varphi a^\dagger a, a] + \frac{1}{2!}[\varphi a^\dagger a, [\varphi a^\dagger a, a]] + \frac{1}{3!}[\varphi a^\dagger a, [\varphi a^\dagger a, [\varphi a^\dagger a, a]]] + \ldots \tag{A.20}$$

$$= a - \varphi a + \frac{1}{2!}[\varphi a^\dagger a, -\varphi a] + \frac{1}{3!}[\varphi a^\dagger a, [\varphi a^\dagger a, -\varphi a]] + \ldots \tag{A.21}$$

$$= a - \varphi a - \frac{\varphi^2}{2!}[a^\dagger a, a] - \frac{\varphi^2}{3!}[\varphi a^\dagger a, [a^\dagger a, -a]] + \ldots \tag{A.22}$$

$$= a - \varphi a + \frac{\varphi^2}{2!}a + \frac{\varphi^3}{3!}[a^\dagger a, a] + \ldots \tag{A.23}$$

$$= a + (-\varphi)a + \frac{(-\varphi)^2}{2!}a + \frac{(-\varphi)^3}{3!}a + \ldots \tag{A.24}$$

$$= a\sum_{k=0}^{\infty} \frac{(-\varphi)^k}{k!} = ae^{-\varphi}, \tag{A.25}$$

and similarly $e^{\varphi a^\dagger a} a^\dagger e^{-\varphi a^\dagger a} = \left(e^{\varphi a^\dagger a} a e^{-\varphi a^\dagger a}\right)^\dagger = a^\dagger e^{i\varphi}$.

Invariance of the number operator. Note that the number operator $a^\dagger a$ is unaffected by the transformation, since

$$e^{\varphi a^\dagger a} a^\dagger a e^{-\varphi a^\dagger a} = e^{\varphi a^\dagger a} a^\dagger e^{-\varphi a^\dagger a} e^{\varphi a^\dagger a} a e^{-\varphi a^\dagger a} = a^\dagger e^{i\varphi} a e^{-i\varphi} \tag{A.26}$$

$$= a^\dagger a. \tag{A.27}$$

Case of operators that commute. Additionally, for any operator O that commutes with X, i.e $[X, O] = 0$, then O is unaffected by the transformation, i.e $e^X O e^{-X} = O$, due to the vanishing of the iterated commutators in the Baker–Campbell–Hausdorff formula (equation (A.17)).

A.2) Unitary transformations

A time-dependent unitary transformation U maps a Hamiltonian H to H' such that

$$H \mapsto H' = UHU^\dagger + i\hbar \dot{U} U^\dagger. \tag{A.28}$$

This corresponds to the so-called rotating frame transformations. For a time-independent unitary transformation, $H' = UHU^\dagger$, we simply refer to it as a change of frame. The Baker–Campbell–Hausdorff formula given by equation (A.17) is useful for computing the transformed Hamiltonian, which we recall read

$$e^X Y e^{-X} = \sum_{n=0}^{\infty} \frac{\left[X^{(n)}, Y\right]}{n!}. \tag{A.29}$$

Note that the Baker–Campbell–Hausdorff formula ensures that $e^X e^{-X} = 1$ for any operator X. However, for $U = e^X$ to be unitary, we need $X^\dagger = -X$.

A.2.1) Displacement transformation

We define the displacement operator associated with a bosonic operator a as [17, 34, 190]

$$D(\alpha) = \exp\left(\alpha a^\dagger - \alpha^* a\right), \tag{A.30}$$

where $\alpha \in \mathbb{C}$. Note that $D(-\alpha) = D(\alpha)^{-1} = D(\alpha)^\dagger$. Defining $X = \alpha a^\dagger - \alpha^* a$, the action of $D(\alpha)$ on a is[1]

$$D(\alpha)^\dagger a D(\alpha) = a - \left[\alpha a^\dagger - \alpha^* a, a\right] + \sum_{n=2}^{\infty} \frac{\left[-X^{(n)}, a\right]}{n!} \tag{A.31}$$

$$= a + \alpha, \tag{A.32}$$

from which we deduce

$$D(\alpha)^\dagger a^\dagger D(\alpha) = a^\dagger + \alpha^*. \tag{A.33}$$

Note that by using the Baker-Campbell-Hausdorff formula, we have

$$D(\alpha) D(\beta) = e^{\frac{1}{2}(\alpha\beta^* - \alpha^*\beta)} D(\alpha + \beta), \tag{A.34}$$

so that two consecutive displacement transformations are the sum of the displacements, up to a phase factor.

[1] From equation (A.28), the Hamiltonian transforms to $UHU^\dagger$ under a time-independent unitary transformation U. Here, we chose $U = D(\alpha)^\dagger = e^{-X}$.

A.2.2) Squeezing transformation

The squeezing operator for a bosonic annihilation operator a is defined as [17, 34]

$$S(\eta) = \exp\left\{\frac{1}{2}\left(\eta^* a^2 - \eta {a^\dagger}^2\right)\right\}. \tag{A.35}$$

Action on the creation annihilation operators. Let use define $X = -\frac{1}{2}\left(\eta^* a^2 - \eta {a^\dagger}^2\right)$, so that $S(\eta) = e^{-X}$ and X is anti-hermitian. From equation (A.7) we deduce $[a^2, a^\dagger] = 2a$ and $[{a^\dagger}^2, a] = -2a^\dagger$. Thus,

$$[X, a] = \left[\frac{\eta}{2}{a^\dagger}^2, a\right] = -\eta a^\dagger, \tag{A.36}$$

$$\left[X^{(2)}, a\right] = \left[X, -\eta a^\dagger\right] = \left[-\frac{\eta^*}{2}a^2, -\eta a^\dagger\right] = |\eta|^2 a. \tag{A.37}$$

This suggests the formulas

$$\left[X^{(2k)}, a\right] = |\eta|^{2k} a, \quad \left[X^{(2k+1)}, a\right] = -\eta|\eta|^{2k} a^\dagger, \tag{A.38}$$

which are true to $k = 0$ since $\left[X^{(0)}, a\right] \equiv a$. Furthermore, if the formulas above are true for some $k \geq 0$, then

$$\left[X^{(2k+2)}, a\right] = \left[X, \left[X^{(2k+1)}, a\right]\right] = -\eta|\eta|^{2k}\left[X, a^\dagger\right] = -\eta|\eta|^{2k}\left[-\frac{\eta^*}{2}a^2, a^\dagger\right] = |\eta|^{2(k+1)} a, \tag{A.39}$$

$$\left[X^{(2k+3)}, a\right] = \left[X, \left[X^{(2k+2)}, a\right]\right] = |\eta|^{2(k+1)}\left[\frac{\eta}{2}{a^\dagger}^2, a\right] = -\eta|\eta|^{2(k+1)} a^\dagger, \tag{A.40}$$

and thus the formula are true for $k+1$. By induction, they hold for all $k \geq 0$.

Now using the Baker–Campbell–Hausdorff formula of equation (A.17) we have

$$e^X a e^{-X} = \sum_{n=0}^{\infty} \frac{\left[X^{(n)}, a\right]}{n!} = \sum_{k=0}^{\infty} \frac{\left[X^{(2k)}, a\right]}{(2k)!} + \sum_{k=0}^{\infty} \frac{\left[X^{(2k+1)}, a\right]}{(2k+1)!} \tag{A.41}$$

$$= \sum_{k=0}^{\infty} \frac{|\eta|^{2k}}{(2k)!} a - \eta \sum_{k=0}^{\infty} \frac{|\eta|^{2k}}{(2k+1)!} a^\dagger \tag{A.42}$$

$$= a\cosh(|\eta|) - \frac{\eta}{|\eta|} a^\dagger \sinh(|\eta|). \tag{A.43}$$

Writing $\eta = re^{i\theta}$, we obtain [17]

$$S(re^{i\theta})^\dagger a S(re^{i\theta}) = a\cosh(r) - e^{i\theta} a^\dagger \sinh(r) \tag{A.44}$$

and by hermitian conjugation,

$$S(re^{i\theta})^\dagger a^\dagger S(re^{i\theta}) = a^\dagger \cosh(r) - e^{-i\theta} a \sinh(r). \tag{A.45}$$

A.3) Fourier transforms

Fourier transforms can be defined in different ways depending on the user's background (engineer, mathematician, physicist...) and the specific application considered. The two sources of variations are the normalisation constant and the variables used in the exponential.

This section fixes the convention used for the Fourier transforms used in this thesis. The most common properties are then derived using this definition.

Definition of the Fourier transform. We will use the following definition of the Fourier transform in the rest of this document:

$$\tilde{a}(\omega) = \int_{\mathbb{R}} \mathrm{d}t e^{i\omega t} a(t) \tag{A.46}$$

Fourier transform of hermitian conjugates. We have the following property for the Fourier transform of dagger operators:

$$\mathcal{F}\Big[a^\dagger\Big](\omega) = \mathcal{F}[a]^\dagger(-\omega). \tag{A.47}$$

Indeed, we can write

$$\begin{aligned}\mathcal{F}[a]^\dagger(\omega) &= \left(\int_{\mathbb{R}} \mathrm{d}t e^{i\omega t} a(t)\right)^\dagger && \text{(A.48)}\\ &= \int_{\mathbb{R}} \mathrm{d}t e^{-i\omega t} a^\dagger(t) && \text{(A.49)}\\ &= \mathcal{F}\Big[a^\dagger\Big](-\omega). && \text{(A.50)}\end{aligned}$$

Starting from the last line and flipping the sign of ω, we find $\mathcal{F}\big[a^\dagger\big](\omega) = \mathcal{F}[a]^\dagger(-\omega)$ as claimed.

Fourier transform of time derivatives.

$$\begin{aligned}\widetilde{\dot{a}}(\omega) &= \int_{\mathbb{R}} \mathrm{d}t e^{i\omega t} \frac{\mathrm{d}a}{\mathrm{d}t}\\ &= \underbrace{\big[e^{i\omega t} a(t)\big]_{\mathbb{R}}}_{\to 0} - i\omega \int_{\mathbb{R}} \mathrm{d}t e^{i\omega t} a(t)\\ &= -i\omega \widetilde{a}(\omega)\end{aligned}$$

Fourier transform of time derivatives of hermitian conjugates.

$$\begin{aligned}\mathcal{F}\Big[\dot{a}^\dagger\Big](\omega) &= \left(\mathcal{F}[\dot{a}](-\omega)\right)^\dagger\\ &= \left((-i\omega\widetilde{a}(\omega))(-\omega)\right)^\dagger\\ &= (+i\omega\widetilde{a}(-\omega))^\dagger\\ &= -i\omega\widetilde{a}^\dagger(-\omega) && \text{(A.51)}\end{aligned}$$

Fourier transform of Heaviside distribution. From Wikipedia, the Fourier transform of the the Heaviside function is (performing $\omega \mapsto -\omega$ because of the difference in the definition of the Fourier transform):

$$\begin{aligned}\widetilde{\Theta}(\omega) &= \frac{1}{2}\left(\delta\Big(\frac{\omega}{2\pi}\Big) + \frac{i}{\pi}\mathrm{p.v}\frac{1}{\frac{\omega}{2\pi}}\right) = \frac{1}{2}\left(\delta\left(\frac{1}{2\pi}\omega\right) + \frac{i}{\pi}\mathrm{p.v}\frac{2\pi}{\omega}\right) = \frac{1}{2}\left(\frac{1}{\frac{1}{2\pi}}\delta(\omega) + \frac{2\pi i}{\pi}\mathrm{p.v}\frac{1}{\omega}\right)\\ &= \pi\delta(\omega) + i\mathrm{p.v}\frac{1}{\omega} && \text{(A.52)}\end{aligned}$$

were we used the dilatation property of the Dirac's delta function.

Appendix B

Supplemental calculations

This appendix contains some (lengthy) derivations whose results I use in the main text.

B.1) Commutation relations of the input fields

We recall that we defined the input fields as

$$c_{\text{in}}(t) = \frac{1}{\sqrt{2\pi}} \int_{\mathbb{R}} \mathrm{d}\omega \, e^{-i\omega(t-t_0)} b_\omega(t_0). \tag{B.1}$$

where $\left[b_\omega, b^\dagger_{\omega'}\right] = \delta(\omega - \omega')$. Then,

$$\begin{aligned}
\left[b_{\text{in}}(t), b^\dagger_{\text{in}}(t')\right] &= \frac{1}{2\pi} \iint_{\mathbb{R}^2} \mathrm{d}\omega \, \mathrm{d}\omega' \, e^{-i\omega(t-t_0)} e^{i\omega'(t'-t_0)} \left[b_\omega, b^\dagger_{\omega'}\right] && \text{(B.2)} \\
&= \frac{1}{2\pi} \int_{\mathbb{R}} \mathrm{d}\omega \, e^{-i\omega(t-t_0)+i\omega(t'-t_0)} && \text{(B.3)} \\
&= \frac{1}{2\pi} \int_{\mathbb{R}} \mathrm{d}\omega \, e^{-i\omega(t-t')} && \text{(B.4)} \\
&= \delta(t-t'). && \text{(B.5)}
\end{aligned}$$

B.2) Coherent drives and displacement transformations

B.2.1) Cavity driven by a coherent drive

The calculations that follow show that one can perform a unitary transformation that removes the term due to the coherent drive.

B.2.1.1) Empty cavity

Consider the Hamiltonian of a cavity driven at $\omega_d/2\pi$,

$$H = \hbar\Delta_c c^\dagger c + \hbar\Omega(c + c^\dagger), \tag{B.6}$$

with $\Delta_c = \omega_c - \omega_d$. We treat the drive as a perturbation V. We consider $\Lambda = \lambda(c - c^\dagger)$ with λ to BE determineD[2]. The Schrieffer-Wolff condition is

$$\begin{aligned}
V + [\Lambda, H_0] &= \hbar\Omega(c + c^\dagger) + \left[\lambda(c - c^\dagger), \hbar\Delta_c c^\dagger c\right] && \text{(B.7)} \\
&= \hbar\Omega(c + c^\dagger) + \hbar\Delta_c\lambda\Big(c + c^\dagger\Big), && \text{(B.8)}
\end{aligned}$$

so we need $\lambda = -\frac{\Omega}{\Delta_c}$.

[2]Note that $\Lambda^\dagger = -\Lambda$, which ensures the transformation is unitary.

The resulting Hamiltonian is

$$H' = H_0 + \frac{1}{2}[\Lambda, V] + \frac{1}{2}[\Lambda, [\Lambda, V]] + \mathcal{O}(\Lambda^3) \tag{B.9}$$
$$= \hbar\Delta_c c^\dagger c + \frac{1}{2}\Big[\lambda(c - c^\dagger), \hbar\Omega(c + c^\dagger)\Big] \tag{B.10}$$
$$= \hbar\Delta_c c^\dagger c + \frac{\hbar\Omega\lambda}{2}(1 + 1) \tag{B.11}$$
$$= \hbar\Delta_c c^\dagger c - \hbar\frac{\Omega^2}{\Delta_c}. \tag{B.12}$$

Note that the transformation is exact, since higher-order commutators vanish. Moreover, notice that $U = e^\Lambda$ has the form of a displacement operator.

B.2.1.2) Cavity with linear coupling to a bosonic mode

Consider the following cavity system driven at $\omega_d/2\pi$,

$$H = \hbar\Delta_c c^\dagger c + \hbar\Delta_m m^\dagger m + \hbar g\Big(cm^\dagger + c^\dagger m\Big) + \hbar\Omega(c + c^\dagger), \tag{B.13}$$

with $\Delta_c = \omega_c - \omega_d$ and $\Delta_m = \omega_m - \omega_d$. We treat the drive as a perturbation V. We consider $\Lambda = \lambda(c - c^\dagger)$ with λ to be determined. The Schrieffer-Wolff condition is

$$V + [\Lambda, H_0] = \hbar\Omega(c + c^\dagger) + \Big[\lambda(c - c^\dagger), \hbar\Delta_c c^\dagger c\Big] + \Big[\lambda(c - c^\dagger), \hbar g\Big(cm^\dagger + c^\dagger m\Big)\Big] \tag{B.14}$$
$$= \hbar\Omega(c + c^\dagger) + \hbar\Delta_c\lambda\Big(c + c^\dagger\Big) + \hbar\lambda g\Big(m + m^\dagger\Big), \tag{B.15}$$

which clearly cannot vanish in general since it involves different operators.

Let us consider $\Lambda = \lambda_c(c - c^\dagger) + \lambda_m(m - m^\dagger)$ instead. Then,

$$\begin{aligned} V + [\Lambda, H_0] &= \hbar\Omega(c + c^\dagger) \\ &\quad + \Big[\lambda_c(c - c^\dagger), \hbar\Delta_c c^\dagger c\Big] + \Big[\lambda_c(c - c^\dagger), \hbar g\Big(cm^\dagger + c^\dagger m\Big)\Big] \\ &\quad + \Big[\lambda_m(m - m^\dagger), \hbar\Delta_m m^\dagger m\Big] + \Big[\lambda_m(m - m^\dagger), \hbar g\Big(cm^\dagger + c^\dagger m\Big)\Big] \qquad \text{(B.16)} \\ &= \hbar\Omega(c + c^\dagger) \\ &\quad + \hbar\Delta_c\lambda_c\Big(c + c^\dagger\Big) + \hbar\lambda_c g\Big(m + m^\dagger\Big) \\ &\quad + \hbar\Delta_m\lambda_m\Big(m + m^\dagger\Big) + \hbar\lambda_m g\Big(c + c^\dagger\Big) \qquad \text{(B.17)} \\ &= \hbar\Big[(\Omega + \Delta_c\lambda_c + \lambda_m g)(c + c^\dagger) + (\lambda_c g + \Delta_m\lambda_m)(m + m^\dagger)\Big]. \qquad \text{(B.18)} \end{aligned}$$

Imposing $V + [\Lambda, H_0] = 0$ (Schrieffer-Wolff condition) leads to

$$\begin{cases} \Delta_c\lambda_c + g\lambda_m + \Omega = 0 \\ \Delta_m\lambda_m + g\lambda_c = 0 \end{cases}, \quad \begin{cases} \lambda_c = -\frac{\Delta_m}{g}\lambda_m \\ \Big(-\frac{\Delta_c\Delta_m}{g} + g\Big)\lambda_m = -\Omega \end{cases}, \quad \begin{cases} \lambda_m = \frac{g\Omega}{\Delta_c\Delta_m - g^2} \\ \lambda_c = \frac{-\Delta_m\Omega}{\Delta_c\Delta_m - g^2} \end{cases}. \tag{B.19}$$

The resulting Hamiltonian is

$$H' = H_0 + \frac{1}{2}[\Lambda, V] + \frac{1}{2}[\Lambda, [\Lambda, V]] + \mathcal{O}(\Lambda^3) \tag{B.20}$$
$$= \hbar\Delta_c c^\dagger c + \hbar\Delta_m m^\dagger m + \hbar g\Big(cm^\dagger + c^\dagger m\Big) + \frac{1}{2}\Big[\lambda(c - c^\dagger), \hbar\Omega(c + c^\dagger)\Big] \tag{B.21}$$
$$= \hbar\Delta_c c^\dagger c + \hbar\Delta_m m^\dagger m + \hbar g\Big(cm^\dagger + c^\dagger m\Big) - \hbar\frac{\Omega^2}{\Delta_c}. \tag{B.22}$$

Note that the transformation is exact, since higher-order commutators vanish.

B.2.1.3) Empty cavity with complex coupling to the drive

Consider the Hamiltonian of a cavity driven at $\omega_d/2\pi$,

$$H = \hbar\Delta_c c^\dagger c + \hbar\Big(\epsilon c + \epsilon^* c^\dagger\Big), \tag{B.23}$$

with $\Delta_c = \omega_c - \omega_d$ and $\epsilon \in \mathbb{C}$. As before, we consider $\Lambda = \lambda(c - c^\dagger)$ where $\lambda \in \mathbb{R}$, so that $\Lambda^\dagger = -\Lambda$. The Schrieffer-Wolff condition reads

$$V + [\Lambda, H_0] = \hbar\Big(\epsilon c + \epsilon^* c^\dagger\Big) + \Big[\lambda(c - c^\dagger), \hbar\Delta_c c^\dagger c\Big] \tag{B.24}$$

$$= \hbar\Big(\epsilon c + \epsilon^* c^\dagger\Big) + \hbar\Delta_c\lambda\Big(c + c^\dagger\Big). \tag{B.25}$$

We see that this expression cannot vanish if $\lambda \in \mathbb{R}$.

Instead, we promote λ to a complex number and consider $\Lambda = (\lambda c - \lambda^* c^\dagger)$ where we verify that $\Lambda^\dagger = -\Lambda$. The Schrieffer-Wolff condition is modified as

$$V + [\Lambda, H_0] = \hbar\Big(\epsilon c + \epsilon^* c^\dagger\Big) + \Big[(\lambda c - \lambda^* c^\dagger), \hbar\Delta_c c^\dagger c\Big] \tag{B.26}$$

$$= \hbar\Big(\epsilon c + \epsilon^* c^\dagger\Big) + \hbar\Delta_c\Big(\lambda c + \lambda^* c^\dagger\Big). \tag{B.27}$$

We now have an equivalent condition for making this expression vanish, that is $\lambda = \frac{-\epsilon}{\Delta_c}$, and this matches with the condition found when the coupling to the drive was real.

The resulting Hamiltonian is

$$H' = H_0 + \frac{1}{2}[\Lambda, V] + \frac{1}{2}[\Lambda, [\Lambda, V]] + \mathcal{O}(\Lambda^3) \tag{B.28}$$

$$= \hbar\Delta_c c^\dagger c + \frac{1}{2}\Big[(\lambda c - \lambda^* c^\dagger), \hbar\Big(\epsilon c + \epsilon^* c^\dagger\Big)\Big] \tag{B.29}$$

$$= \hbar\Delta_c c^\dagger c + \frac{\hbar}{2}(\lambda\epsilon^* + \lambda^*\epsilon) \tag{B.30}$$

$$= \hbar\Delta_c c^\dagger c - \hbar\frac{|\epsilon|^2}{\Delta_c}. \tag{B.31}$$

Note that the transformation is exact, since higher order commutators vanish.

B.3) Indirect coupling in a ring of three bosonic modes

A natural generalisation of the previous system is that of a ring of three bosonic mode, pictured in figure B.1. Since this system is now loop-coupled, there exists a gauge-invariant phase θ, which we can focus on the coupling between the two cavity modes. Formally, we now consider the interaction Hamiltonian

$$H_I = \hbar g_0\Big(c_0 m^\dagger + c_0^\dagger m\Big) + \hbar g_1\Big(c_1 m^\dagger + c_1^\dagger m\Big) + \hbar g_c\Big(e^{i\theta} c_0 c_1^\dagger + e^{-i\theta} c_0^\dagger c_1\Big). \tag{B.32}$$

We generalise the Schrieffer-Wolff transformation by considering

$$\Lambda = \lambda_0\Big(c_0 m^\dagger - c_0^\dagger m\Big) + \lambda_1\Big(c_1 m^\dagger - c_1^\dagger m\Big) + \lambda_c\Big(c_0 c_1^\dagger - c_0^\dagger c_1\Big). \tag{B.33}$$

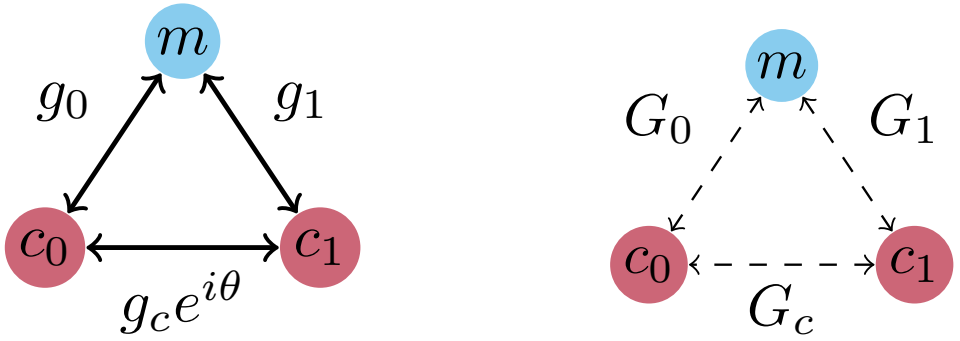
We now have

$$[\Lambda, H_0] = \hbar(\omega_0 - \omega_m)\lambda_0\Big(c_0 m^\dagger + c_0^\dagger m\Big) + \hbar(\omega_1 - \omega_m)\lambda_1\Big(c_1 m^\dagger + c_1^\dagger m\Big) \tag{B.34}$$

$$+ \Big[\lambda_c\Big(c_0 c_1^\dagger - c_0^\dagger c_1\Big), \hbar\omega_0 c_0 c_0^\dagger + \hbar\omega_1 c_1^\dagger c_1 + \hbar\omega_m m^\dagger m\Big]$$

$$= \hbar(\omega_0 - \omega_m)\lambda_0\Big(c_0 m^\dagger + c_0^\dagger m\Big) + \hbar(\omega_1 - \omega_m)\lambda_1\Big(c_1 m^\dagger + c_1^\dagger m\Big) \tag{B.35}$$

$$+ \hbar(\omega_0 - \omega_1)\lambda_c\Big(c_0 c_1^\dagger + c_0^\dagger c_1\Big),$$



(a) General regime. (b) Dispersive regime

Figure B.1: Indirect coupling in a ring of three bosonic modes.

so that the Schrieffer-Wolff condition imposes

$$\lambda_0 = \frac{g_0}{\Delta_0}, \quad \Delta_0 = \omega_m - \omega_0, \tag{B.36}$$

$$\lambda_1 = \frac{g_1}{\Delta_1}, \quad \Delta_1 = \omega_m - \omega_1, \tag{B.37}$$

$$\lambda_c = \frac{g_c}{\Delta_c}, \quad \Delta_c = \omega_1 - \omega_0. \tag{B.38}$$

The first iterated commutator becomes

$$\begin{aligned}
[\Lambda, V] &= 2\hbar\lambda_0 g_0\Big(c_0^\dagger c_0 + m^\dagger m\Big) + 2\hbar\lambda_1 g_1\Big(c_1^\dagger c_1 + m^\dagger m\Big) - \hbar(\lambda_0 g_1 + \lambda_1 g_0)\Big(c_0 c_1^\dagger + c_0^\dagger c_1\Big) \\
&\quad + \hbar\Big[\lambda_0\Big(c_0 m^\dagger - c_0^\dagger m\Big) + \lambda_1\Big(c_1 m^\dagger - c_1^\dagger m\Big), g_c\Big(e^{i\theta} c_0 c_1^\dagger + e^{-i\theta} c_0^\dagger c_1\Big)\Big] \qquad \text{(B.39)} \\
&\quad + \hbar\Big[\lambda_c\Big(c_0 c_1^\dagger - c_0^\dagger c_1\Big), g_0\Big(c_0 m^\dagger + c_0^\dagger m\Big) + g_1\Big(c_1 m^\dagger + c_1^\dagger m\Big) + g_c\Big(e^{i\theta} c_0 c_1^\dagger + e^{-i\theta} c_0^\dagger c_1\Big)\Big] \\
&= 2\hbar\lambda_0 g_0\Big(c_0^\dagger c_0 + m^\dagger m\Big) + 2\hbar\lambda_1 g_1\Big(c_1^\dagger c_1 + m^\dagger m\Big) - \hbar(\lambda_0 g_1 + \lambda_1 g_0)\Big(c_0 c_1^\dagger + c_0^\dagger c_1\Big) \\
&\quad + \hbar g_c\lambda_0\Big(e^{-i\theta} c_1 m^\dagger + e^{i\theta} c_1^\dagger m\Big) + \hbar g_c\lambda_1\Big(e^{i\theta} c_0 m^\dagger + e^{-i\theta} c_0^\dagger m\Big) \qquad \text{(B.40)} \\
&\quad + \hbar\lambda_c g_0\Big(c_1^\dagger m + c_1 m^\dagger\Big) + \hbar\lambda_c g_1\Big(-c_0 m^\dagger - c_0^\dagger m\Big) + \hbar\lambda_c g_c\Big(e^{-i\theta}\Big[c_0 c_1^\dagger, c_0^\dagger c_1\Big] - e^{i\theta}\Big[c_0^\dagger c_1, c_0 c_1^\dagger\Big]\Big) \\
&= 2\hbar\lambda_0 g_0\Big(c_0^\dagger c_0 + m^\dagger m\Big) + 2\hbar\lambda_1 g_1\Big(c_1^\dagger c_1 + m^\dagger m\Big) - \hbar(\lambda_0 g_1 + \lambda_1 g_0)\Big(c_0 c_1^\dagger + c_0^\dagger c_1\Big) \\
&\quad + \hbar g_c\lambda_0\Big(e^{-i\theta} c_1 m^\dagger + e^{i\theta} c_1^\dagger m\Big) + \hbar g_c\lambda_1\Big(e^{i\theta} c_0 m^\dagger + e^{-i\theta} c_0^\dagger m\Big) \qquad \text{(B.41)} \\
&\quad + \hbar\lambda_c g_0\Big(c_1 m^\dagger + c_1^\dagger m\Big) - \hbar\lambda_c g_1\Big(c_0 m^\dagger + c_0^\dagger m\Big) + 2\hbar\cos\theta\lambda_c g_c\Big(c_1^\dagger c_1 + c_0^\dagger c_0\Big) \\
&= 2\hbar\lambda_0 g_0\Big(c_0^\dagger c_0 + m^\dagger m\Big) + 2\hbar\lambda_1 g_1\Big(c_1^\dagger c_1 + m^\dagger m\Big) + 2\hbar\cos\theta\lambda_c g_c\Big(c_1^\dagger c_1 + c_0^\dagger c_0\Big) \\
&\quad - \hbar\lambda_c g_1\Big(c_0 m^\dagger + c_0^\dagger m\Big) + \hbar g_c\lambda_1\Big(e^{i\theta} c_0 m^\dagger + e^{-i\theta} c_0^\dagger m\Big) \qquad \text{(B.42)} \\
&\quad + \hbar\lambda_c g_0\Big(c_1 m^\dagger + c_1^\dagger m\Big) + \hbar g_c\lambda_0\Big(e^{-i\theta} c_1 m^\dagger + e^{i\theta} c_1^\dagger m\Big) \\
&\quad - \hbar(\lambda_0 g_1 + \lambda_1 g_0)\Big(c_0 c_1^\dagger + c_0^\dagger c_1\Big),
\end{aligned}$$

so that the transformed Hamiltonian to first order is

$$\begin{aligned}
H' &= \hbar\omega_0' c_0 c_0^\dagger + \hbar\omega_1' c_1^\dagger c_1 + \hbar\omega_m' m^\dagger m \\
&\quad + \hbar(G_0 c_0 m^\dagger + G_0^* c_0^\dagger m) + \hbar(G_1 c_1 m^\dagger + G_1^* c_1^\dagger m) - \hbar G_c(c_0 c_1^\dagger + c_0^\dagger c_1),
\end{aligned} \tag{B.43}$$

with the angular frequencies

$$\omega_0' = \omega_0 + \frac{g_0^2}{\omega_m - \omega_0} + \frac{g_c^2}{\omega_1 - \omega_0}, \tag{B.44}$$

$$\omega_1' = \omega_1 + \frac{g_1^2}{\omega_m - \omega_1} + \frac{g_c^2}{\omega_1 - \omega_0}, \tag{B.45}$$

$$\omega_m' = \omega_m + \frac{g_0^2}{\omega_m - \omega_0} + \frac{g_1^2}{\omega_m - \omega_1} \tag{B.46}$$

and the indirect couplings

$$G_0 = \frac{g_1 g_c e^{i\theta}}{2}\left(\frac{1}{\Delta_1} - \frac{1}{\Delta_c}\right) = \frac{\Delta_c - \Delta_1}{2}\frac{g_1 g_c e^{i\theta}}{\Delta_1 \Delta_c}, \tag{B.47}$$

$$G_1 = \frac{\Delta_0 + \Delta_c}{2}\frac{g_0 g_c e^{-i\theta}}{\Delta_0 \Delta_c}, \tag{B.48}$$

$$G_c = \frac{\Delta_0 + \Delta_1}{2}\frac{g_0 g_1}{\Delta_0 \Delta_1}. \tag{B.49}$$

B.4) Normalisation of the mode functions of the electromagnetic field

We consider the expressions[1]

$$\mathbf{E} = i\sqrt{\frac{\hbar\omega_c}{2\epsilon_0}}\left(c - c^\dagger\right)\mathbf{u} \tag{B.50}$$

$$\mathbf{H} = \frac{1}{\mu_0}\sqrt{\frac{\hbar}{2\omega_c\epsilon_0}}(c + c^\dagger)\nabla \times \mathbf{u} \tag{B.51}$$

of the electromagnetic field. Then, using equation (IV.48) and replacing in equation (B.50),

$$\mathbf{E} = i\sqrt{\frac{\hbar\omega_c}{2\epsilon_0}}\left(c - c^\dagger\right)\frac{\mathbf{E}}{\sqrt{\int_{V_c} |\mathbf{E}|^2 \,\mathrm{d}^3 r}} \tag{B.52}$$

$$\sqrt{\int_{V_c} |\mathbf{E}|^2 \,\mathrm{d}^3 r} = i\sqrt{\frac{\hbar\omega_c}{2\epsilon_0}}\left(c - c^\dagger\right) \tag{B.53}$$

$$\int_{V_c} |\mathbf{E}|^2 \,\mathrm{d}^3 r = -\frac{\hbar\omega_c}{2\epsilon_0}\left(-cc^\dagger - c^\dagger c + c^2 + \left(c^\dagger\right)^2\right) \tag{B.54}$$

$$\int_{V_c} \frac{1}{2}\epsilon_0 |\mathbf{E}|^2 \,\mathrm{d}^3 r = \frac{\hbar\omega_c}{4}\left(1 + c^\dagger c + c^\dagger c\right) - \frac{\hbar\omega_c}{4}\left(c^2 + \left(c^\dagger\right)^2\right) \tag{B.55}$$

$$= \frac{\hbar\omega_c}{2}\left(c^\dagger c + \frac{1}{2}\right) - \frac{\hbar\omega}{4}\left(c^2 + \left(c^\dagger\right)^2\right) \tag{B.56}$$

Similarly, remembering that $\mu_0\epsilon_0 = \frac{1}{c^2}$, we use equation (IV.49) in equation (B.51) and obtain

$$\mathbf{H} = \frac{1}{\mu_0}\sqrt{\frac{\hbar}{2\omega_c\epsilon_0}}(c + c^\dagger)\frac{\omega}{c}\frac{\mathbf{H}}{\sqrt{\int_{V_c} |\mathbf{H}|^2 \,\mathrm{d}^3 r}} \tag{B.57}$$

$$\int_{V_c} |\mathbf{H}|^2 \,\mathrm{d}^3 r = \frac{1}{\mu_0^2}\frac{\hbar}{2\omega_c\epsilon_0}\frac{\omega^2}{c^2}\left(cc^\dagger + c^\dagger c + c^2 + \left(c^\dagger\right)^2\right) \tag{B.58}$$

$$\int_{V_c} \frac{1}{2}\mu_0 |\mathbf{H}|^2 \,\mathrm{d}^3 r = \frac{\hbar\omega_c}{4}\left(2c^\dagger c + 1 + c^2 + \left(c^\dagger\right)^2\right) \tag{B.59}$$

$$= \frac{\hbar\omega_c}{2}\left(c^\dagger c + \frac{1}{2}\right) + \frac{\hbar\omega}{4}\left(c^2 + \left(c^\dagger\right)^2\right) \tag{B.60}$$

[1] Here, the expression of $\mathbf{E}$ is guessed by analogy.

Hence we obtain the result

$$\int_{V_c}\left(\frac{1}{2}\epsilon_0\mathbf{E}^2+\frac{1}{2}\mu_0\mathbf{H}^2\right)\mathrm{d}^3\mathbf{r}=\hbar\omega_c\left(c^\dagger c+\frac{1}{2}\right), \tag{B.61}$$

i.e we see that each mode k is associated to a harmonic oscillator.

The previous calculation approximated the electromagnetic field as a single mode. Formally, one could perform a similar calculation using an index k describing the mode, and obtain

$$\int_{V_c}\left(\frac{1}{2}\epsilon_0\mathbf{E}_k^2+\frac{1}{2}\mu_0\mathbf{H}_k^2\right)\mathrm{d}^3\mathbf{r}=\hbar\omega_k\left(c_k^\dagger c_k+\frac{1}{2}\right). \tag{B.62}$$

This can be proven by using the formulation of [187] of the electromagnetic field in terms of position and momentum coordinates.

B.5) Derivation of the Zeeman interaction

B.5.1) Orbital angular momentum

We follow [194], and consider a charge q in an electromagnetic field. The Zeeman term can be obtained by expanding the Hamiltonian after the minimal coupling replacement $\mathbf{p}\mapsto\mathbf{p}-q\mathbf{A}$. We have

$$H=\frac{1}{2m}\left[\frac{\hbar}{i}\boldsymbol{\nabla}-q\mathbf{A}\right]^2+q\phi \tag{B.63}$$

where $\mathbf{A}$ is the three-vector potential and ϕ the scalar electrostatic potential. Expanding the kinetic term and using the Coulomb gauge $\boldsymbol{\nabla}\cdot\mathbf{A}=0$, we *incorrectly* obtain

$$H=\frac{-\hbar^2}{2m}\nabla^2-\frac{\hbar}{i}\frac{q}{2m}[\boldsymbol{\nabla}\cdot\mathbf{A}+\mathbf{A}\cdot\boldsymbol{\nabla}]+\left[\frac{q^2}{2m}A^2+q\phi\right] \tag{B.64}$$

$$=\frac{-\hbar^2}{2m}\nabla^2-\frac{\hbar}{i}\frac{q}{2m}\mathbf{A}\cdot\boldsymbol{\nabla}+\frac{q^2}{2m}A^2+q\phi. \tag{B.65}$$

However, a small mistake has crept in, because the Schrödinger equation acts on wave functions, which we have neglected. Indeed, to be exact we instead have

$$H=\frac{-\hbar^2}{2m}\nabla^2\psi-\frac{\hbar}{i}\frac{q}{2m}[\boldsymbol{\nabla}\cdot(\mathbf{A}\psi)+\mathbf{A}\cdot\boldsymbol{\nabla}\psi]+\left[\frac{q^2}{2m}A^2+q\phi\right]\psi \tag{B.66}$$

$$=\frac{-\hbar^2}{2m}\nabla^2\psi-\frac{\hbar}{i}\frac{q}{2m}[(\boldsymbol{\nabla}\cdot\mathbf{A})\psi+2\mathbf{A}\cdot\boldsymbol{\nabla}\psi]+\left[\frac{q^2}{2m}A^2+q\phi\right]\psi \tag{B.67}$$

$$=\frac{-\hbar^2}{2m}\nabla^2\psi-\frac{\hbar}{i}\frac{q}{m}\mathbf{A}\cdot\boldsymbol{\nabla}\psi+\left[\frac{q^2}{2m}A^2+q\phi\right]\psi, \tag{B.68}$$

or

$$H=\frac{-\hbar^2}{2m}\nabla^2-\frac{\hbar}{i}\frac{q}{m}\mathbf{A}\cdot\boldsymbol{\nabla}+\frac{q^2}{2m}A^2+q\phi \tag{B.69}$$

for short. Notice the factor of 2 appearing in the second term compared to equation (B.65). Next, recall that for any vectors $\mathbf{a},\mathbf{b}$ and $\mathbf{c}$, we have the formula $\mathbf{a}\times(\mathbf{b}\times\mathbf{c})=(\mathbf{a}\cdot\mathbf{c})\mathbf{b}-(\mathbf{a}\cdot\mathbf{b})\mathbf{c}$. Hence, for a uniform magnetic flux density $\mathbf{B}(\mathbf{r})=B$, we have

$$\boldsymbol{\nabla}\times(\mathbf{B}\times\mathbf{r})=(\boldsymbol{\nabla}\cdot\mathbf{r})\mathbf{B}-(\boldsymbol{\nabla}\cdot\mathbf{B})\mathbf{r} \tag{B.70}$$

$$=\left(\frac{\partial x^i}{\partial x^i}\right)\mathbf{B}-(\mathbf{B}\cdot\boldsymbol{\nabla})\mathbf{r} \tag{B.71}$$

$$=3\mathbf{B}-B_i\hat{\mathbf{x}}_\mathbf{i}\frac{\partial x^i}{\partial x^i} \tag{B.72}$$

$$=3\mathbf{B}-\mathbf{B}=2\mathbf{B} \tag{B.73}$$

Since $\boldsymbol{\nabla} \times \mathbf{A} = \mathbf{B}$, we see from the calculation above that $\mathbf{A} = \frac{1}{2}\mathbf{B} \times \mathbf{r}$. Using the identity $\mathbf{a} \cdot (\mathbf{b} \times \mathbf{c}) = (\mathbf{a} \times \mathbf{b}) \cdot \mathbf{c}$, we can rewrite the Hamiltonian above as

$$H = \frac{-\hbar^2}{2m}\nabla^2 - \frac{\hbar}{i}\frac{q}{2m}(\mathbf{B} \times \mathbf{r}) \cdot \boldsymbol{\nabla} + \frac{q^2}{2m}A^2 + q\phi \tag{B.74}$$

$$= \frac{-\hbar^2}{2m}\nabla^2 - \frac{\hbar}{i}\frac{q}{2m}\mathbf{B} \cdot [\mathbf{r} \times \boldsymbol{\nabla}] + \frac{q^2}{2m}A^2 + q\phi \tag{B.75}$$

$$= \frac{-\hbar^2}{2m}\nabla^2 - \frac{q}{2m}\mathbf{B} \cdot [\mathbf{r} \times \mathbf{p}] + \frac{q^2}{2m}A^2 + q\phi \tag{B.76}$$

$$= \frac{-\hbar^2}{2m}\nabla^2 - \frac{q}{2m}(\mathbf{B} \cdot \mathbf{L}) + \frac{q^2}{2m}A^2 + q\phi \tag{B.77}$$

$$= \frac{-\hbar^2}{2m}\nabla^2 - \boldsymbol{\mu} \cdot \mathbf{B} + \frac{q^2}{2m}A^2 + q\phi \tag{B.78}$$

In particular, if no potential is present, we obtain:

$$H = \frac{-\hbar^2}{2m}\nabla^2 - \boldsymbol{\mu} \cdot \mathbf{B} + \frac{q^2}{2m}A^2. \tag{B.79}$$

Finally, note that in the case of an electron, we obtain $\boldsymbol{\mu} = \gamma_L \mathbf{L}$, with the gyromagnetic ratio $\gamma_L = \frac{-e}{2m_e} = -14$ GHz/T, e the elementary electric charge and m_e the mass of the electron.

B.5.2) Spin orbital angular momentum

The Pauli equation reads

$$i\hbar\frac{\partial}{\partial t}|\psi\rangle = H|\psi\rangle, \tag{B.80}$$

where the Hamiltonian is given by

$$H = \frac{1}{2m}\boldsymbol{\sigma} \cdot (\mathbf{p} - q\mathbf{A})^2 + q\phi. \tag{B.81}$$

Here, ϕ is the electric scalar potential, $\mathbf{A}$ is the usual vector potential, q, m are the charge/mass of the particle, $\boldsymbol{\sigma} = (\sigma_x, \sigma_y, \sigma_z)$ are the Pauli matrices and $\mathbf{p} = (p_x, p_y, p_z)$ is the momentum operator. This can be simplified using the Pauli vector identity, which for two vectors $\mathbf{a}, \mathbf{b}$ reads

$$(\boldsymbol{\sigma} \cdot \mathbf{a})(\boldsymbol{\sigma} \cdot \mathbf{b}) = \mathbf{a} \cdot \mathbf{b} + i\boldsymbol{\sigma} \cdot (\mathbf{a} \times \mathbf{b}). \tag{B.82}$$

As a consequence, we can rewrite equation (B.81) as

$$H = \frac{1}{2m}\Big((\mathbf{p} - q\mathbf{A})^2 + i\boldsymbol{\sigma} \cdot [(\mathbf{p} - q\mathbf{A}) \times (\mathbf{p} - q\mathbf{A})]\Big) + q\phi. \tag{B.83}$$

We now look into simplifying the term $[(\mathbf{p} - q\mathbf{A}) \times (\mathbf{p} - q\mathbf{A})]$. To avoid errors, we should remember that this term is applied to a scalar function ψ. Recalling the vector identity $\nabla \times (\mathbf{A}\psi) = \psi\nabla \times \mathbf{A} + (\boldsymbol{\nabla}\psi) \times \mathbf{A}$ and $\mathbf{p} = \frac{\hbar}{i}\boldsymbol{\nabla}$, we can write

$$[(\mathbf{p} - q\mathbf{A}) \times (\mathbf{p} - q\mathbf{A})]\psi = \big[\mathbf{p} \times \mathbf{p} + q^2\mathbf{A} \times \mathbf{A} - q\mathbf{p} \times \mathbf{A} - q\mathbf{A} \times \mathbf{p}\big]\psi \tag{B.84}$$

$$= -q[\mathbf{p} \times \mathbf{A} + \mathbf{A} \times \mathbf{p}]\psi \tag{B.85}$$

$$= iq\hbar[\boldsymbol{\nabla} \times \mathbf{A} + \mathbf{A} \times \boldsymbol{\nabla}]\psi \tag{B.86}$$

$$= iq\hbar[\boldsymbol{\nabla} \times (\mathbf{A}\psi) + \mathbf{A} \times (\boldsymbol{\nabla}\psi)] \tag{B.87}$$

$$= iq\hbar[\psi\nabla \times \mathbf{A} + (\boldsymbol{\nabla}\psi) \times \mathbf{A} - (\boldsymbol{\nabla}\psi) \times \mathbf{A}] \tag{B.88}$$

$$= iq\hbar\psi(\boldsymbol{\nabla} \times \mathbf{A}) \tag{B.89}$$

$$= iq\hbar\psi\mathbf{B} \tag{B.90}$$

Finally, the Hamiltonian can be rewritten in a form that making apparent the Zeeman term due to spin angular momentum,

$$H = \frac{1}{2m}\Big((\mathbf{p} - q\mathbf{A})^2 - q\hbar\boldsymbol{\sigma} \cdot \mathbf{B}\Big) + q\phi. \tag{B.91}$$

For an electron, neglecting the scalar potential ($\phi = 0$), we can recast the Hamiltonian in the form of [262], which reads

$$H = \frac{(p + e\mathbf{A})^2}{2m} + g_L \mu_B \mathbf{B} \cdot \boldsymbol{\sigma} + V(r) \tag{B.92}$$

where $g_L \simeq 2$ is the electron's Landé g-factor and $\mu_B = \hbar \frac{e}{2m_e}$ is the Bohr magneton. Defining the magnetic moment due to spin as $\boldsymbol{\mu} = -g_L \mu_B \boldsymbol{\sigma}$, we deduce that the Zeeman energy due to spin is $-\boldsymbol{\mu} \cdot \mathbf{B}$, formally identical to the Zeeman energy for orbital angular momentum.

B.6) Derivation of the magnon Hamiltonian

We consider the Hamiltonian equation (IV.27) which reads

$$H = -\frac{1}{2}\frac{J}{\hbar^2} \sum_{\langle i,j \rangle} \mathbf{S}_i \cdot \mathbf{S}_j - \frac{g\mu_B B_0}{\hbar} \sum_i S_i^z. \tag{B.93}$$

Expression with the spin raising and lowering operators. We introduce the local spin raising and lowering operators $S_i^{\pm} = S_i^x \pm i S_i^y$ where the index i still indicates a specific lattice site. We can then rewrite the $\mathbf{S}_i \cdot \mathbf{S}_j$ term of equation (IV.27) above as $\frac{1}{2}\Big([S_i^+ S_j^- + S_i^- S_j^+\Big) + S_i^z S_j^z$. Indeed, we have

$$S_i^+ S_j^- = (S_i^x + iS_i^y)\Big(S_j^x - iS_j^y\Big) = S_i^x S_j^x - iS_i^x S_j^y + iS_i^y S_j^x + S_i^y S_j^y. \tag{B.94}$$

Similarly,

$$S_i^- S_j^+ = S_i^x S_j^x + iS_i^x S_j^y - iS_i^y S_j^x + S_i^y S_j^y. \tag{B.95}$$

Hence, using the two equations above,

$$\begin{aligned} \frac{1}{2}\Big(S_i^+ S_j^- + S_i^- S_j^+\Big) + S_i^z S_j^z = &= S_i^x S_j^x + S_i^y S_j^y + S_i^z S_j^z && \text{(B.96)} \\ &= (S_i^x \hat{\mathbf{x}} + S_i^y \hat{\mathbf{y}} + S_i^z \hat{\mathbf{z}}) \cdot \Big(S_j^x \hat{\mathbf{x}} + S_j^y \hat{\mathbf{y}} + S_j^z \hat{\mathbf{z}}\Big) && \text{(B.97)} \\ &= \mathbf{S}_i \cdot \mathbf{S}_j, && \text{(B.98)} \end{aligned}$$

and we rewrite equation (IV.27) as[1]

$$H = -\frac{1}{2}\frac{J}{\hbar^2} \sum_{\langle i,j \rangle} \left[\frac{1}{2}\Big(S_i^+ S_j^- + S_i^- S_j^+\Big) + S_i^z S_j^z\right] - \frac{g\mu_B B_0}{\hbar} \sum_i S_i^z. \tag{B.99}$$

Holstein-Primakoff transformation. When the number of excitation is small, the Hamiltonian can be expressed in terms of bosonic operators using a Holstein-Primakoff transformation. We follow the standard approach, see references [94, 194, 214, 269, 572].

The Holstein-Primakoff transformation we consider is

$$S_i^+ = \hbar\sqrt{2s}\sqrt{1 - \frac{m_i^\dagger m_i}{2s}} m_i, \tag{B.100}$$

$$S_i^- = \hbar m_i^\dagger \sqrt{2s}\sqrt{1 - \frac{m_i^\dagger m_i}{2s}}, \tag{B.101}$$

$$S_i^z = \hbar\Big(s - m_i^\dagger m_i\Big), \tag{B.102}$$

[1] In the literature, it is possible to encounter Hamiltonians in which a single pair of $S_i^{\pm}$ operators appear, e.g Rameshti et al. [94]. This form is obtained using the commutator $\left[S_i^-, S_j^+\right]$ and neglecting a constant energy shift.

where s is the *maximum value* of the spin at each site i (without units), and m_i is the bosonic operator counting the number of spin excitation at site i. Note the presence of $\hbar$ since $S_i^{\pm}, S_i^z$ have units of angular momentum and the m_i are dimensionless.

The ground state of a ferromagnet corresponds to all the spins aligned with each other. It can be shown that the energy cost of flipping a single spin in the lattice requires an energy of the order of the Curie temperature [266]. For instance, for Yttrium-Iron-Garnet, the Curie temperature is 559 K [194], which is far above room temperature. Therefore, it is a good approximation to consider that the number of flipped spins is small compared to the total number N of spins. Therefore we assume that for most lattice positions, $\frac{m_i^\dagger m_i}{2s} \ll 1$, even there may be some locations where this does not hold. This allows to approximate the operators $S_i^{\pm}$ by expanding the square root as

$$S_i^+ \simeq \hbar\sqrt{2s} m_i, \tag{B.103}$$

$$S_i^- \simeq \hbar\sqrt{2s} m_i^\dagger. \tag{B.104}$$

Inserting equations (B.102) to (B.104) into equation (B.99) reads

$$\begin{aligned} H = &-\frac{1}{2}\frac{J}{\hbar^2}\sum_{\langle i,j\rangle}\left[\frac{\left(\hbar\sqrt{2s}\right)^2}{2}\left(m_i m_j^\dagger + m_i^\dagger m_j\right) + \hbar^2\left(s - m_i^\dagger m_i\right)\left(s - m_j^\dagger m_j\right)\right] \\ &+ g\mu_B B_0 \sum_i \left(m_i^\dagger m_i - s\right) \end{aligned} \tag{B.105}$$

and to second order in m_i,

$$\begin{aligned} H = &E_0 + g\mu_B B_0 \sum_i^N m_i^\dagger m_i \\ &- \frac{1}{2}Js\sum_{\langle i,j\rangle}\left(m_i m_j^\dagger + m_i^\dagger m_j\right) + \frac{1}{2}Js\sum_{\langle i,j\rangle}\left(m_i^\dagger m_i + m_j^\dagger m_j\right) + \mathcal{O}(m^3) \end{aligned} \tag{B.106}$$

where the energy offset is

$$E_0 = -g\mu_B B_0 sN - \frac{1}{2}Js\sum_{\langle i,j\rangle} s \tag{B.107}$$

$$= -g\mu_B B_0 sN - \frac{1}{2}Js\sum_i Zs \tag{B.108}$$

$$= -g\mu_B B_0 sN - \frac{1}{2}JNZs^2, \tag{B.109}$$

where Z is the number of nearest neighbours, and N the number of spins.

Diagonalisation in reciprocal space. The Hamiltonian of equation (B.106) is composed of nearest-neighbour interaction terms, similar to those encountered in tight-binding models (see chapter IX). Additionally, as previously discussed, the energy cost of flipping a single spin is very high, so we expect the low-energy excitations to be formed of small deviations from the ground states. Such solutions can be obtained by considering collective spin excitations in reciprocal space. Therefore, we introduce[1] the magnon annihilation operator with wave vector $\mathbf{k}$ by

$$m_{\mathbf{k}} = \frac{1}{\sqrt{N}}\sum_j^N e^{-i\mathbf{k}\cdot\mathbf{r}_j} m_j \tag{B.110}$$

with $\mathbf{r}_i$ the position of the i-th site of the crystal. It is easy to show that the bosonic commutation relations are preserved in reciprocal space[2], so that we have $\left[m_{\mathbf{k}}, m_{\mathbf{k}'}^\dagger\right] = \delta_{\mathbf{k},\mathbf{k}'}$. Replacing

[1] Taking a positive sign in the exponential gives an equivalent definition, and does not change the result.

[2] As a reminder, we have $\frac{1}{N}\sum_j^N e^{i(\mathbf{k}-\mathbf{k}')\cdot\mathbf{r}_j} = \delta_{\mathbf{k},\mathbf{k}'}$.

the position-space operators using the inverse Fourier transform, the Hamiltonian is rewritten[1]

$$\begin{aligned}
H &= E_0 + g\mu_B B_0 \sum_i^N \frac{1}{N} \sum_{\mathbf{k},\mathbf{k}'} m_{\mathbf{k}}^\dagger m_{\mathbf{k}'} e^{i(\mathbf{k}-\mathbf{k}')\cdot\mathbf{r}_i} \\
&\quad - \frac{1}{2} Js \sum_{\langle i,j\rangle} \frac{1}{N} \sum_{\mathbf{k},\mathbf{k}'} \left(m_{\mathbf{k}} m_{\mathbf{k}'}^\dagger e^{-i\mathbf{k}\cdot\mathbf{r}_i} e^{i\mathbf{k}'\cdot\mathbf{r}_j} + m_{\mathbf{k}}^\dagger m_{\mathbf{k}'} e^{i\mathbf{k}\cdot\mathbf{r}_i} e^{-i\mathbf{k}'\cdot\mathbf{r}_j} \right) \\
&\quad + \frac{1}{2} Js \sum_{\langle i,j\rangle} \frac{1}{N} \sum_{\mathbf{k},\mathbf{k}'} \left(m_{\mathbf{k}}^\dagger m_{\mathbf{k}'} e^{i(\mathbf{k}-\mathbf{k}')\cdot\mathbf{r}_i} + m_{\mathbf{k}}^\dagger m_{\mathbf{k}'} e^{i(\mathbf{k}-\mathbf{k}')\cdot\mathbf{r}_j} \right) \qquad \text{(B.111)} \\
&= E_0 + g\mu_B B_0 \sum_{\mathbf{k}} m_{\mathbf{k}}^\dagger m_{\mathbf{k}} \\
&\quad - \frac{1}{2} Js \sum_{\mathbf{k},\mathbf{k}'} \left(m_{\mathbf{k}} m_{\mathbf{k}'}^\dagger \frac{1}{N} \sum_{\langle i,j\rangle} e^{-i\mathbf{k}\cdot\mathbf{r}_i} e^{i\mathbf{k}'\cdot\mathbf{r}_j} + m_{\mathbf{k}}^\dagger m_{\mathbf{k}'} \frac{1}{N} \sum_{\langle i,j\rangle} e^{i\mathbf{k}\cdot\mathbf{r}_i} e^{-i\mathbf{k}'\cdot\mathbf{r}_j} \right) \qquad \text{(B.112)} \\
&\quad + \frac{1}{2} Js \sum_{\mathbf{k},\mathbf{k}'} m_{\mathbf{k}}^\dagger m_{\mathbf{k}'} \frac{1}{N} \sum_{\langle i,j\rangle} \left(e^{i(\mathbf{k}-\mathbf{k}')\cdot\mathbf{r}_i} + e^{i(\mathbf{k}-\mathbf{k}')\cdot\mathbf{r}_j} \right)
\end{aligned}$$

We rewrite the sum $\sum_{\langle i,j\rangle}$ over nearest neighbours as $\sum_{\langle i,\boldsymbol{\delta}\rangle}$, such that $\mathbf{r_i} = \mathbf{r}_i + \boldsymbol{\delta}$. Note that $\boldsymbol{\delta}$ does not depend on i, because it represents the possible vectors going to the nearest neighbours in a unit cell, and therefore it is identical for any lattice position. Further defining $\gamma_{\mathbf{k}} = \frac{1}{Z}\sum_{\boldsymbol{\delta}} e^{-i\mathbf{k}\cdot\boldsymbol{\delta}}$, with Z the coordination number of the lattice (number of nearest neighbours), we obtain

$$\begin{aligned}
H &= E_0 + g\mu_B B_0 \sum_{\mathbf{k}} m_{\mathbf{k}}^\dagger m_{\mathbf{k}} \\
&\quad - \frac{1}{2} Js \sum_{\mathbf{k},\mathbf{k}'} \left(m_{\mathbf{k}} m_{\mathbf{k}'}^\dagger \frac{1}{N} \sum_{\langle i,\boldsymbol{\delta}\rangle} e^{-i\mathbf{k}\cdot\mathbf{r}_i} e^{i\mathbf{k}'\cdot\mathbf{r}_i} e^{i\mathbf{k}'\cdot\boldsymbol{\delta}} + m_{\mathbf{k}}^\dagger m_{\mathbf{k}'} \frac{1}{N} \sum_{\langle i,\boldsymbol{\delta}\rangle} e^{i\mathbf{k}\cdot\mathbf{r}_i} e^{-i\mathbf{k}'\cdot\mathbf{r}_i} e^{-i\mathbf{k}'\cdot\boldsymbol{\delta}} \right) \qquad \text{(B.113)} \\
&\quad + \frac{1}{2} Js \sum_{\mathbf{k},\mathbf{k}'} m_{\mathbf{k}}^\dagger m_{\mathbf{k}'} \frac{1}{N} \sum_{\langle i,\boldsymbol{\delta}\rangle} \left(e^{i(\mathbf{k}-\mathbf{k}')\cdot\mathbf{r}_i} + e^{i(\mathbf{k}-\mathbf{k}')\cdot(\mathbf{r}_i+\boldsymbol{\delta})} \right) \\
&= E_0 + g\mu_B B_0 \sum_{\mathbf{k}} m_{\mathbf{k}}^\dagger m_{\mathbf{k}} \\
&\quad - \frac{1}{2} Js \sum_{\mathbf{k},\mathbf{k}'} \left[m_{\mathbf{k}} m_{\mathbf{k}'}^\dagger \left(\frac{1}{N} \sum_i e^{-i(\mathbf{k}-\mathbf{k}')\cdot\mathbf{r}_i} \right) \left(\sum_{\boldsymbol{\delta}} e^{i\mathbf{k}'\cdot\boldsymbol{\delta}} \right) + m_{\mathbf{k}}^\dagger m_{\mathbf{k}'} \left(\frac{1}{N} \sum_i e^{i(\mathbf{k}-\mathbf{k}')\cdot\mathbf{r}_i} \right) \left(\sum_{\boldsymbol{\delta}} e^{-i\mathbf{k}'\cdot\boldsymbol{\delta}} \right) \right] \qquad \text{(B.114)} \\
&\quad + \frac{1}{2} Js \sum_{\mathbf{k},\mathbf{k}'} m_{\mathbf{k}}^\dagger m_{\mathbf{k}'} \left[\left(\frac{1}{N} \sum_i e^{i(\mathbf{k}-\mathbf{k}')\cdot\mathbf{r}_i} \right) \left(\sum_{\boldsymbol{\delta}} 1 \right) + \left(\frac{1}{N} \sum_i e^{i(\mathbf{k}-\mathbf{k}')\cdot\mathbf{r}_i} \right) \left(\sum_{\boldsymbol{\delta}} e^{i(\mathbf{k}-\mathbf{k}')\cdot\boldsymbol{\delta}} \right) \right] \\
&= E_0 + g\mu_B B_0 \sum_{\mathbf{k}} m_{\mathbf{k}}^\dagger m_{\mathbf{k}} \\
&\quad - \frac{1}{2} Js \sum_{\mathbf{k}} \left(m_{\mathbf{k}} m_{\mathbf{k}}^\dagger \sum_{\boldsymbol{\delta}} e^{i\mathbf{k}\cdot\boldsymbol{\delta}} + m_{\mathbf{k}}^\dagger m_{\mathbf{k}} \sum_{\boldsymbol{\delta}} e^{-i\mathbf{k}\cdot\boldsymbol{\delta}} \right) \qquad \text{(B.115)} \\
&\quad + \frac{1}{2} Js \sum_{\mathbf{k}} m_{\mathbf{k}}^\dagger m_{\mathbf{k}} 2Z \\
&= E_0 + (g\mu_B B_0 + JsZ) \sum_{\mathbf{k}} m_{\mathbf{k}}^\dagger m_{\mathbf{k}} - \frac{1}{2} JsZ \sum_{\mathbf{k}} \left(\gamma_{-\mathbf{k}} m_{\mathbf{k}} m_{\mathbf{k}}^\dagger + \gamma_{\mathbf{k}} m_{\mathbf{k}}^\dagger m_{\mathbf{k}} \right) \qquad \text{(B.116)} \\
&= E_0 + (g\mu_B B_0 + JsZ) \sum_{\mathbf{k}} m_{\mathbf{k}}^\dagger m_{\mathbf{k}} - \frac{1}{2} JsZ \sum_{\mathbf{k}} \left(\gamma_{-\mathbf{k}} + (\gamma_{\mathbf{k}} + \gamma_{-\mathbf{k}}) m_{\mathbf{k}}^\dagger m_{\mathbf{k}} \right) \qquad \text{(B.117)}
\end{aligned}$$

[1] Note that i denotes both the imaginary number and an index here, but the context makes distinguishing between them easy.

For a crystal with a centre of symmetry, $\gamma_{-\mathbf{k}} = \gamma_{\mathbf{k}}$, and we finally obtain

$$H = \left[E_0 - \frac{1}{2}JsZ\sum_{\mathbf{k}}\gamma_{\mathbf{k}}\right] + \sum_{\mathbf{k}}[g\mu_B B_0 + JsZ(1-\gamma_{\mathbf{k}})]m_{\mathbf{k}}^\dagger m_{\mathbf{k}} \tag{B.118}$$

$$= E_0' + \sum_{\mathbf{k}}\hbar\omega_{\mathbf{k}} m_{\mathbf{k}}^\dagger m_{\mathbf{k}} \tag{B.119}$$

with the unobservable energy offset E_0' and the dispersion relation $\omega_{\mathbf{k}}$. Note that $E_0' = E_0$, since $\sum_{\mathbf{k}}\gamma_{\mathbf{k}} = 0$. This can be shown using the fact that each component of the wave vector $\mathbf{k}$ is quantised as e.g. $k_x = \frac{2\pi n_x}{L_x}$ with $n_x \in \mathbb{N}$, and using the discrete Fourier transform property $\sum_{n=0}^{L_x-1} e^{i\frac{2\pi n_x}{L_x}a} = \delta_{a,0}$.

Dispersion relation for a cubic lattice in the long-wavelength limit. For a cubic lattice[1], there are 6 nearest-neighbour so $Z = 6$. The lattice constant a is the same in all directions, so that

$$\gamma_{\mathbf{k}} = \frac{1}{Z}\sum_{\boldsymbol{\delta}} e^{-i\mathbf{k}\cdot\boldsymbol{\delta}} = \frac{1}{6}\left(e^{-ik_x a} + e^{ik_x a} + e^{-ik_y a} + e^{ik_y a} + e^{-ik_z a} + e^{ik_z a}\right) \tag{B.120}$$

$$= \frac{1}{3}(\cos k_x a + \cos k_y a + \cos k_z a). \tag{B.121}$$

In the long-wavelength limit, the norm of the wave vector is small compared to the lattice constant $ak \ll 1$, and expanding the cosines to first order we obtain [94, 194, 257]

$$\hbar\omega_{\mathbf{k}} = \hbar\omega_0 + 2Jsa^2k^2 \tag{B.122}$$

with $\hbar\omega_0 = g\mu_B B_0$.

B.7) Derivation of the Polder susceptibility tensor

The LLG equation reads

$$\dot{\mathbf{m}} = -\gamma\mu_0(\mathbf{M}_S \times (\mathbf{H}_0 + \mathbf{h}) + \mathbf{m}\times\mathbf{H}_0) + \frac{\alpha}{M_s}\mathbf{M}_S \times \dot{\mathbf{m}}, \tag{B.123}$$

and to simplify the forthcoming calculations, we introduce

$$S = \begin{pmatrix} 0 & -1 \\ 1 & 0 \end{pmatrix}, \tag{B.124}$$

which has the properties $S^2 = -1$ and hence $S^{-1} = -S$. Note that the action of S on a column vector $(a,b)^t$ is $S(a,b)^t = (-b,a)^t$. Finally, recall that the inverse of a 2×2 matrix

$$N = \begin{pmatrix} a & b \\ c & d \end{pmatrix} \tag{B.125}$$

is simply given by

$$N^{-1} = \frac{1}{|N|}\begin{pmatrix} d & -b \\ -c & a \end{pmatrix} = \frac{1}{ad-bc}\begin{pmatrix} d & -b \\ -c & a \end{pmatrix}, \tag{B.126}$$

with $|N|$ the determinant of the matrix N.

[1] Also called a cubic "P" or cubic-primitive lattice [262]

B.7.1) Without demagnetisation fields

In vector form

$$\begin{pmatrix}\dot{m}_x\\ \dot{m}_y\\ \dot{m}_z\end{pmatrix} = -\gamma\mu_0\begin{pmatrix}0\\0\\M_S\end{pmatrix}\times\begin{pmatrix}h_x\\h_y\\H_0\end{pmatrix} - \gamma\mu_0\begin{pmatrix}m_x\\m_y\\0\end{pmatrix}\times\begin{pmatrix}0\\0\\H_0\end{pmatrix} + \frac{\alpha}{M_S}\begin{pmatrix}0\\0\\M_S\end{pmatrix}\times\begin{pmatrix}\dot{m}_x\\\dot{m}_y\\0\end{pmatrix} \tag{B.127}$$

$$= -\gamma\mu_0\begin{pmatrix}-M_S h_y\\M_s h_x\\0\end{pmatrix} - \gamma\mu_0\begin{pmatrix}m_y H_0\\-m_x H_0\\0\end{pmatrix} + \frac{\alpha}{M_S}\begin{pmatrix}-M_S\dot{m}_y\\M_s\dot{m}_x\\0\end{pmatrix} \tag{B.128}$$

from which we see that we can neglect the $\hat{\mathbf{z}}$ component. Defining $\omega_M = \gamma\mu_0 M_S$ and $\omega_0 = \gamma\mu_0 H_0$, we have

$$\frac{\mathrm{d}}{\mathrm{d}t}\begin{pmatrix}\dot{m}_x\\\dot{m}_y\end{pmatrix} = -\omega_M\begin{pmatrix}-h_y\\h_x\end{pmatrix} + \omega_0\begin{pmatrix}-m_y\\m_x\end{pmatrix} + \alpha\frac{\mathrm{d}}{\mathrm{d}t}\begin{pmatrix}-m_y\\m_x\end{pmatrix}. \tag{B.129}$$

In frequency space,

$$-i\omega\begin{pmatrix}m_x\\m_y\end{pmatrix} = -\omega_M\begin{pmatrix}-h_y\\h_x\end{pmatrix} + (\omega_0 - i\alpha\omega)\begin{pmatrix}-m_y\\m_x\end{pmatrix}, \tag{B.130}$$

$$(i\omega + (\omega_0 - i\alpha\omega)S)\begin{pmatrix}m_x\\m_y\end{pmatrix} = \omega_M S\begin{pmatrix}h_x\\h_y\end{pmatrix}, \tag{B.131}$$

$$\begin{pmatrix}h_x\\h_y\end{pmatrix} = \frac{1}{\omega_M}\left(-i\omega S - (\omega_0 - i\alpha\omega)S^2\right)\begin{pmatrix}m_x\\m_y\end{pmatrix}, \tag{B.132}$$

$$\begin{pmatrix}h_x\\h_y\end{pmatrix} = \frac{1}{\omega_M}\underbrace{\begin{pmatrix}\omega_0 - i\alpha\omega & i\omega\\ -i\omega & \omega_0 - i\alpha\omega\end{pmatrix}}_{=N}\begin{pmatrix}m_x\\m_y\end{pmatrix}. \tag{B.133}$$

The determinant of N is simply $(\omega_0 - i\alpha\omega)^2 - \omega^2$, and computing the inverse of the matrix N gives the Polder susceptibility tensor

$$\chi = \begin{pmatrix}u & -iv\\ iv & u\end{pmatrix} \tag{B.134}$$

with

$$u = \frac{\omega_M(\omega_0 - i\alpha\omega)}{(\omega_0 - i\alpha\omega)^2 - \omega^2}, \tag{B.135}$$

$$v = \frac{\omega_M\omega}{(\omega_0 - i\alpha\omega)^2 - \omega^2}. \tag{B.136}$$

These results are in agreement with [275, 277, 573–577].

B.7.2) Including demagnetising factors

The inclusion of the demagnetisation factors follows a similar derivation up to equation (B.133), which read

$$\begin{pmatrix}h_x\\h_y\end{pmatrix} = \frac{1}{\omega_M}\begin{pmatrix}\omega_0 - i\alpha\omega & i\omega\\ -i\omega & \omega_0 - i\alpha\omega\end{pmatrix}\begin{pmatrix}m_x\\m_y\end{pmatrix}. \tag{B.137}$$

We now introduce the demagnetisation fields through the replacements

$$h_x \mapsto h_x - N_x m_x, \tag{B.138}$$
$$h_y \mapsto h_y - N_y m_y, \tag{B.139}$$
$$H_0 \mapsto H_0 - N_z M_s, \tag{B.140}$$

and in particular we notice that $\omega_0 \mapsto \omega_0 - N_z\omega_M$. We obtain

$$\begin{pmatrix} h_x \\ h_y \end{pmatrix} - \begin{pmatrix} N_x m_x \\ N_y m_y \end{pmatrix} = \frac{1}{\omega_M}\begin{pmatrix} \omega_0 - N_z\omega_M - i\alpha\omega & i\omega \\ -i\omega & \omega_0 - N_z\omega_M - i\alpha\omega \end{pmatrix}\begin{pmatrix} m_x \\ m_y \end{pmatrix}, \tag{B.141}$$

$$\begin{pmatrix} h_x \\ h_y \end{pmatrix} = \frac{1}{\omega_M}\underbrace{\begin{pmatrix} \omega_0 + (N_x - N_z)\omega_M - i\alpha\omega & i\omega \\ -i\omega & \omega_0 + (N_y - N_z)\omega_M - i\alpha\omega \end{pmatrix}}_{=N}\begin{pmatrix} m_x \\ m_y \end{pmatrix} \tag{B.142}$$

The determinant of N is modified to

$$|N| = (\omega_0 + (N_x - N_z)\omega_M - i\alpha\omega)(\omega_0 + (N_y - N_z)\omega_M - i\alpha\omega) - \omega^2 \tag{B.143}$$

and we deduce the Polder susceptibility tensor

$$\chi = \begin{pmatrix} u_y & -iv \\ iv & u_x \end{pmatrix} \tag{B.144}$$

with, for $j \in \{x, y\}$,

$$u_j = \frac{\omega_M(\omega_0 + (N_j - N_z)\omega_M - i\alpha\omega)}{(\omega_0 + (N_x - N_z)\omega_M - i\alpha\omega)(\omega_0 + (N_y - N_z)\omega_M - i\alpha\omega) - \omega^2}, \tag{B.145}$$
$$v = \frac{\omega_M\omega}{(\omega_0 + (N_x - N_z)\omega_M - i\alpha\omega)(\omega_0 + (N_y - N_z)\omega_M - i\alpha\omega) - \omega^2}. \tag{B.146}$$

Note that by further neglecting the terms of order α^2, we obtain

$$u_j = \frac{\omega_M(\omega_0 + (N_j - N_z)\omega_M - i\alpha\omega)}{\omega_m^2 - \omega^2 - i\alpha\omega(2(\omega_0 - N_z\omega_M) + (N_x + N_y)\omega_M)}, \tag{B.147}$$
$$v = \frac{\omega_M\omega}{\omega_m^2 - \omega^2 - i\alpha\omega(2(\omega_0 - N_z\omega_M) + (N_x + N_y)\omega_M)}, \tag{B.148}$$

with

$$\omega_m^2 = (\omega_0 + (N_x - N_z)\omega_M)(\omega_0 + (N_y - N_z)\omega_M). \tag{B.149}$$

This is in agreement with section 2.2 of [226].

B.7.3) Pertubation along the equilibrium direction

We assume that the perturbating RF field has a component along $\hat{\mathbf{z}}$. The LLG equation in vector form becomes

$$\begin{pmatrix} \dot{m}_x \\ \dot{m}_y \\ \dot{m}_z \end{pmatrix} = -\omega_M\begin{pmatrix} 0 \\ 0 \\ 1 \end{pmatrix} \times \begin{pmatrix} h_x \\ h_y \\ H_0 + h_z \end{pmatrix} - \gamma\mu_0\begin{pmatrix} m_x \\ m_y \\ m_z \end{pmatrix} \times \begin{pmatrix} 0 \\ 0 \\ H_0 + h_z \end{pmatrix} + \alpha\begin{pmatrix} 0 \\ 0 \\ 1 \end{pmatrix} \times \begin{pmatrix} \dot{m}_x \\ \dot{m}_y \\ \dot{m}_z \end{pmatrix} \tag{B.150}$$

$$= -\omega_M\begin{pmatrix} -h_y \\ h_x \\ 0 \end{pmatrix} - \omega_0\begin{pmatrix} m_y \\ -m_x \\ 0 \end{pmatrix} - \gamma\mu_0\begin{pmatrix} m_y h_z \\ -m_x h_z \\ 0 \end{pmatrix} + \alpha\begin{pmatrix} -\dot{m}_y \\ \dot{m}_x \\ 0 \end{pmatrix}. \tag{B.151}$$

We see that m_z is a constant, and to first order in small quantities, the third term vanishes, so we recover the usual susceptibility tensor.

Instead, let us assume that h_z is not a small quantity. We return to the LLG equation

$$\frac{\mathrm{d}\mathbf{M}}{\mathrm{d}t} = -\gamma\mu_0\mathbf{M}\times\mathbf{H} + \frac{\alpha}{M_s}\left(\mathbf{M}\times\frac{\mathrm{d}\mathbf{M}}{\mathrm{d}t}\right) \tag{B.152}$$

and separating $\mathbf{M}(t) = M_s\hat{\mathbf{z}} + \mathbf{m}(t)$ and $\mathbf{H}(t) = H_0\hat{\mathbf{z}} + \mathbf{h}(t)$,

$$\begin{aligned}\begin{pmatrix}\dot{m}_x\\ \dot{m}_y\\ \dot{m}_z\end{pmatrix} &= -\omega_M\begin{pmatrix}0\\0\\1\end{pmatrix}\times\begin{pmatrix}h_x\\h_y\\H_0+h_z\end{pmatrix} - \gamma\mu_0\begin{pmatrix}m_x\\m_y\\m_z\end{pmatrix}\times\begin{pmatrix}h_x\\h_y\\H_0+h_z\end{pmatrix} \\ &\quad + \alpha\begin{pmatrix}0\\0\\1\end{pmatrix}\times\begin{pmatrix}\dot{m}_x\\\dot{m}_y\\\dot{m}_z\end{pmatrix} + \frac{\alpha}{M_S}\begin{pmatrix}m_x\\m_y\\m_z\end{pmatrix}\times\begin{pmatrix}\dot{m}_x\\\dot{m}_y\\\dot{m}_z\end{pmatrix}\end{aligned} \tag{B.153}$$

$$\begin{aligned}&= -\omega_M\begin{pmatrix}-h_y\\h_x\\0\end{pmatrix} - \gamma\mu_0\begin{pmatrix}m_y(H_0+h_z) - m_zh_y\\ m_zh_x - m_x(H_0+h_z)\\ m_xh_y - m_yh_x\end{pmatrix} \\ &\quad + \alpha\begin{pmatrix}-\dot{m}_y\\\dot{m}_x\\0\end{pmatrix} + \frac{\alpha}{M_S}\begin{pmatrix}m_y\dot{m}_z - m_z\dot{m}_y\\ m_z\dot{m}_x - m_x\dot{m}_z\\ m_x\dot{m}_y - m_y\dot{m}_x\end{pmatrix}.\end{aligned} \tag{B.154}$$

This is a nonlinear system of differential equations. If we assume that the quantities $\mathbf{h}, \mathbf{m}$ are small in the $\hat{\mathbf{x}}, \hat{\mathbf{y}}$ components, we can neglect their product, and write

$$\begin{aligned}\begin{pmatrix}\dot{m}_x\\\dot{m}_y\\\dot{m}_z\end{pmatrix} &= -\omega_M\begin{pmatrix}-h_y\\h_x\\0\end{pmatrix} - \gamma\mu_0\begin{pmatrix}m_y(H_0+h_z) - m_zh_y\\ m_zh_x - m_x(H_0+h_z)\\ 0\end{pmatrix} \\ &\quad + \alpha\begin{pmatrix}-\dot{m}_y\\\dot{m}_x\\0\end{pmatrix} + \frac{\alpha}{M_S}\begin{pmatrix}m_y\dot{m}_z - m_z\dot{m}_y\\ m_z\dot{m}_x - m_x\dot{m}_z\\ 0\end{pmatrix},\end{aligned} \tag{B.155}$$

and from the last line we see that m_z is a constant. Focusing on the first two components, we can write

$$\begin{aligned}\begin{pmatrix}\dot{m}_x\\\dot{m}_y\end{pmatrix} &= -\omega_M\begin{pmatrix}-h_y\\h_x\end{pmatrix} - \gamma\mu_0\begin{pmatrix}m_y(H_0+h_z) - m_zh_y\\ m_zh_x - m_x(H_0+h_z)\end{pmatrix} \\ &\quad + \alpha\begin{pmatrix}-\dot{m}_y\\\dot{m}_x\end{pmatrix} + \frac{\alpha}{M_S}\begin{pmatrix}-m_z\dot{m}_y\\ m_z\dot{m}_x\end{pmatrix}\end{aligned} \tag{B.156}$$

which we can reduce to

$$\begin{pmatrix}\dot{m}_x\\ \dot{m}_y\end{pmatrix} = -(\omega_M+\gamma\mu_0 m_z)\begin{pmatrix}-h_y\\ h_x\end{pmatrix} + (\omega_0+\gamma\mu_0 h_z)\begin{pmatrix}-m_y\\ m_x\end{pmatrix} + \alpha\Big(1+\frac{m_z}{M_S}\Big)\begin{pmatrix}-\dot{m}_y\\ \dot{m}_x\end{pmatrix} \tag{B.157}$$

$$\Big(1-\alpha\Big(1+\frac{m_z}{M_S}\Big)S\Big)\begin{pmatrix}\dot{m}_x\\ \dot{m}_y\end{pmatrix} = -(\omega_M+\gamma\mu_0 m_z)S\begin{pmatrix}h_x\\ h_y\end{pmatrix} + (\omega_0+\gamma\mu_0 h_z)S\begin{pmatrix}m_x\\ m_y\end{pmatrix}, \tag{B.158}$$

$$(\omega_0+\omega_z)\begin{pmatrix}m_x\\ m_y\end{pmatrix} - \Big(-S-\alpha\Big(1+\frac{m_z}{M_S}\Big)\Big)\begin{pmatrix}\dot{m}_x\\ \dot{m}_y\end{pmatrix} = \omega'_M\begin{pmatrix}h_x\\ h_y\end{pmatrix}, \tag{B.159}$$

with $\omega_z = \gamma\mu_0 h_z$ and $\omega'_M = \omega_M + \gamma\mu_0 m_z$. In frequency space,

$$\Big(\omega_0+\omega_z - i\omega\Big[S+\alpha\Big(1+\frac{m_z}{M_S}\Big)\Big]\Big)\begin{pmatrix}m_x\\ m_y\end{pmatrix} = \omega'_M\begin{pmatrix}h_x\\ h_y\end{pmatrix}, \tag{B.160}$$

$$\frac{1}{\omega'_M}\begin{pmatrix}\omega_0+\omega_z - i\omega\alpha\Big(1+\frac{m_z}{M_S}\Big) & i\omega\\ -i\omega & \omega_0+\omega_z - i\omega\alpha\Big(1+\frac{m_z}{M_S}\Big)\end{pmatrix}\begin{pmatrix}m_x\\ m_y\end{pmatrix} = \begin{pmatrix}h_x\\ h_y\end{pmatrix}. \tag{B.161}$$

Introducing the demagnetisation fields with

$$h_x \mapsto h_x - N_x m_x, \tag{B.162}$$

$$h_y \mapsto h_y - N_y m_y, \tag{B.163}$$

$$H_0 \mapsto H_0 - N_z M_s, \tag{B.164}$$

we obtain $\mathbf{Nm} = \mathbf{h}$ with

$$\mathbf{N} = \frac{1}{\omega'_M}\begin{pmatrix}\omega_0 - N_z\omega_M + \omega_z + \omega'_M N_x - i\omega\alpha\Big(1+\frac{m_z}{M_S}\Big) & i\omega\\ -i\omega & \omega_0 - N_z\omega_M + \omega_z + \omega'_M N_y - i\omega\alpha\Big(1+\frac{m_z}{M_S}\Big)\end{pmatrix} \tag{B.165}$$

We see that m_z is a constant fitting parameter that modifies the susceptibility tensor. In a sense, this amounts to modifying the saturation magnetisation.

B.8) Equation for the magnetic field in a medium

In what follows a $\cdot$ symbol indicates matrix multiplication between a matrix on the left side, and a vector (in bold) on the right side. We start from the Maxwell-Ampère equation in the absence of source

$$\boldsymbol{\nabla}\times\mathbf{H} = \frac{\partial\mathbf{D}}{\partial t}, \tag{B.166}$$

and using the linear relationships

$$\mathbf{D} = \underline{\epsilon}\cdot\mathbf{E}, \quad \mathbf{B} = \underline{\mu}\cdot\mathbf{H} \tag{B.167}$$

we obtain

$$\boldsymbol{\nabla}\times\big(\underline{\mu}^{-1}\cdot\mathbf{B}\big) = \underline{\epsilon}\cdot\frac{\partial\mathbf{E}}{\partial t}, \tag{B.168}$$

$$\epsilon_0\underline{\epsilon}^{-1}\cdot\big(\boldsymbol{\nabla}\times\big(\mu_0\underline{\mu}^{-1}\cdot\mathbf{B}\big)\big) = \epsilon_0\mu_0\frac{\partial\mathbf{E}}{\partial t}, \tag{B.169}$$

$$\boldsymbol{\nabla}\times\big[\epsilon_0\underline{\epsilon}^{-1}\cdot\big(\boldsymbol{\nabla}\times\big(\mu_0\underline{\mu}^{-1}\cdot\mathbf{B}\big)\big)\big] = \frac{1}{c^2}\frac{\partial}{\partial t}\boldsymbol{\nabla}\times\mathbf{E}, \tag{B.170}$$

$$\boldsymbol{\nabla}\times\big[\epsilon_0\underline{\epsilon}^{-1}\cdot\big(\boldsymbol{\nabla}\times\big(\mu_0\underline{\mu}^{-1}\cdot\mathbf{B}\big)\big)\big] + \frac{1}{c^2}\frac{\partial^2\mathbf{B}}{\partial t^2} = 0, \tag{B.171}$$

where for the last line we used the Maxwell-Faraday equation $\boldsymbol{\nabla} \times \mathbf{E} = -\frac{\partial \mathbf{B}}{\partial t}$. From there, defining $k^2 = \omega^2/c^2$ we obtain

$$\boldsymbol{\nabla} \times \left[\epsilon_0 \underline{\epsilon}^{-1} \cdot \left(\boldsymbol{\nabla} \times \left(\mu_0 \underline{\mu}^{-1} \cdot \mathbf{B}\right)\right)\right] + k^2 \mathbf{B} = 0, \tag{B.172}$$

or alternatively by multiplying n^2 with $n = \sqrt{\epsilon_r \mu_r}$ the refractive index, ϵ_r the relative dielectric constant, and μ_r the relative permeability,

$$\boldsymbol{\nabla} \times \left[\epsilon_0 \epsilon_r \underline{\epsilon}^{-1} \cdot \left(\boldsymbol{\nabla} \times \left(\mu_0 \mu_r \underline{\mu}^{-1} \cdot \mathbf{B}\right)\right)\right] + k_n^2 \mathbf{B} = 0, \tag{B.173}$$

where $k_n = nk$. Note that the equation above has a sign difference from equation (20) of [94].

B.9) Input-output theory for two bosonic modes coupling to a common waveguide

Quantum Langevin equations. We consider the coupling of two bosons to a common bath. To model a waveguide, we simply need to consider two baths, one for travelling photons in each direction. If one is only interested in the transmission, then only a single travelling photon mode is needed. Following Lalumière et al. (2013) [405], we write the general Hamiltonian for the waveguide as

$$H_{\text{bath}} = \int_0^\infty \mathrm{d}\omega\, \hbar\omega \left(p_{L,\omega}^\dagger p_{L,\omega} + p_{R,\omega}^\dagger p_{R,\omega}\right) \tag{B.174}$$

where $p_{L,\omega}$ ($p_{R,\omega}$) describes left (right) moving photons in the waveguide. The interaction with the two bosonic modes are given by

$$H_{\text{sys–bath}} = \sum_{k=1}^{2} \int \mathrm{d}\omega\, i\hbar \left[\sqrt{\frac{\kappa_{L,k}}{2\pi}} \left(a_k p_{L,\omega}^\dagger - a_k^\dagger p_{L,\omega}\right) + \sqrt{\frac{\kappa_{R,k}}{2\pi}} \left(a_k p_{R,\omega}^\dagger - a_k^\dagger p_{R,\omega}\right)\right] \tag{B.175}$$

Note that formally, this amounts to considering that two distinct baths each couple to two modes.

After writing the Heisenberg equation of motion for $p_{L,\omega}$, we find the formal solution

$$p_{L,\omega}(t) = p_{L,\omega}(t_0) e^{-i\omega(t-t_0)} + \sum_{k=1}^{2} \sqrt{\frac{\kappa_{L,k}}{2\pi}} \int_{t_0}^{t} \mathrm{d}t'\, a_k(t') e^{-i\omega(t-t')}, \tag{B.176}$$

leading to the input-output relation

$$p_L^{\text{out}} = p_L^{\text{in}} + \sum_k \sqrt{\kappa_{L,k}} a_k, \tag{B.177}$$

with

$$p_L^{\text{in}}(t) = \lim_{t_0 \to -\infty} \frac{1}{\sqrt{2\pi}} \int \mathrm{d}\omega\, e^{-i\omega(t-t_0)} p_{L,\omega}(t_0), \quad p_L^{\text{out}}(t) = \lim_{t_1 \to +\infty} \frac{1}{\sqrt{2\pi}} \int \mathrm{d}\omega\, e^{-i\omega(t-t_1)} p_{L,\omega}(t_1). \tag{B.178}$$

We have analogous relations for the right-moving field. The QLEs for the two modes a_k and $a_{k'}$ (with $k \neq k'$) coupling to the waveguide can then be written

$$\dot{a}_k = -i\omega_k - iga_{k'} - \int \mathrm{d}\omega \left(\sqrt{\frac{\kappa_{L,k}}{2\pi}} p_{L,\omega} + \sqrt{\frac{\kappa_{R,k}}{2\pi}} p_{R,\omega} \right) \tag{B.179}$$

$$= -i\omega_k a_k - iga_{k'} - \sqrt{\kappa_{L,k}} p_L^{\mathrm{in}} - \sqrt{\kappa_{R,k}} p_R^{\mathrm{in}} - \sum_l \int \mathrm{d}\omega \int_{t_0}^{t} \mathrm{d}t' \left(\sqrt{\frac{\kappa_{L,k}}{2\pi}} \sqrt{\frac{\kappa_{L,l}}{2\pi}} + \sqrt{\frac{\kappa_{R,k}}{2\pi}} \sqrt{\frac{\kappa_{R,l}}{2\pi}} \right) a_l(t') e^{-i\omega} \tag{B.180}$$

$$= -i\omega_k a_k - iga_{k'} - \sqrt{\kappa_{L,k}} p_L^{\mathrm{in}} - \sqrt{\kappa_{R,k}} p_R^{\mathrm{in}} - \sum_l \int_{t_0}^{t} \mathrm{d}t' \left(\sqrt{\kappa_{L,k}\kappa_{L,l}} + \sqrt{\kappa_{R,k}\kappa_{R,l}} \right) a_l(t') \delta(t - t') \tag{B.181}$$

$$= -i\omega_k a_k - iga_{k'} - \sqrt{\kappa_{L,k}} p_L^{\mathrm{in}} - \sqrt{\kappa_{R,k}} p_R^{\mathrm{in}} - \sum_l \left(\frac{\sqrt{\kappa_{L,k}\kappa_{L,l}}}{2} + \frac{\sqrt{\kappa_{R,k}\kappa_{R,l}}}{2} \right) a_l(t) \tag{B.182}$$

$$= -i\left(\omega_k - i\frac{\kappa_{L,k} + \kappa_{R,k}}{2} \right) a_k - \left(ig + \frac{\sqrt{\kappa_{L,k}\kappa_{L,k'}} + \sqrt{\kappa_{R,k}\kappa_{R,k'}}}{2} \right) a_{k'} - \sqrt{\kappa_{L,k}} p_L^{\mathrm{in}} - \sqrt{\kappa_{R,k}} p_R^{\mathrm{in}} \tag{B.183}$$

Transmission coefficient with the input-output formalism. In the frequency domain, the equation above becomes

$$\omega \widetilde{a}_k = \left(\omega_k - i\frac{\kappa_{L,k} + \kappa_{R,k}}{2} \right) \widetilde{a}_k + \left(g - i\frac{\sqrt{\kappa_{L,k}\kappa_{L,k'}} + \sqrt{\kappa_{R,k}\kappa_{R,k'}}}{2} \right) \widetilde{a}_{k'} - i\sqrt{\kappa_{L,k}} \widetilde{p}_L^{\mathrm{in}} - i\sqrt{\kappa_{R,k}} \widetilde{p}_R^{\mathrm{in}}, \tag{B.184}$$

$$\widetilde{\Delta_k} \widetilde{a}_k = \underbrace{\left(g - i\frac{\sqrt{\kappa_{L,k}\kappa_{L,k'}} + \sqrt{\kappa_{R,k}\kappa_{R,k'}}}{2} \right)}_{=K_{kk'}} \widetilde{a}_{k'} \underbrace{-i\sqrt{\kappa_{L,k}} \widetilde{p}_L^{\mathrm{in}} - i\sqrt{\kappa_{R,k}} \widetilde{p}_R^{\mathrm{in}}}_{=P_k}. \tag{B.185}$$

Note that $K_{12} = K_{21} = K$. Using specific indices, we obtain the system

$$\begin{cases} \widetilde{\Delta_1} \widetilde{a}_1 = K\widetilde{a}_2 + P_1 \\ \widetilde{\Delta_2} \widetilde{a}_2 = K\widetilde{a}_1 + P_2 \end{cases} \tag{B.186}$$

which gives

$$\widetilde{\Delta_1}\widetilde{\Delta_2}\widetilde{a}_1 = K(K\widetilde{a}_1 + P_2) + \widetilde{\Delta_2} P_1, \tag{B.187}$$

$$\left(\widetilde{\Delta_1}\widetilde{\Delta_2} - K^2 \right) \widetilde{a}_1 = KP_2 + \widetilde{\Delta_2} P_1, \tag{B.188}$$

$$\widetilde{a}_1 = \frac{KP_2 + \widetilde{\Delta_2} P_1}{\widetilde{\Delta_1}\widetilde{\Delta_2} - K^2}, \tag{B.189}$$

and a_2 can be obtained from the equation above by exchanging the indices 1 and 2. We have

$$S_{21} = \frac{p_R^{\mathrm{out}}}{p_R^{\mathrm{in}}} = \frac{p_R^{\mathrm{in}} + \sum_k \sqrt{\kappa_{R,k}} a_k}{p_R^{\mathrm{in}}} = 1 + \sqrt{\kappa_{R,1}} \frac{K\frac{P_2}{p_R^{\mathrm{in}}} + \widetilde{\Delta_2}\frac{P_1}{p_R^{\mathrm{in}}}}{\widetilde{\Delta_1}\widetilde{\Delta_2} - K^2} + \sqrt{\kappa_{R,2}} \frac{K\frac{P_1}{p_R^{\mathrm{in}}} + \widetilde{\Delta_1}\frac{P_2}{p_R^{\mathrm{in}}}}{\widetilde{\Delta_1}\widetilde{\Delta_2} - K^2}. \tag{B.190}$$

so that the transmission from the left to the right is given by assuming $p_L^{\mathrm{in}} = 0$, and reads

$$S_{21} = 1 - i\frac{\sqrt{\kappa_{R,1}}\left(K\sqrt{\kappa_{R,2}} + \widetilde{\Delta_2}\sqrt{\kappa_{R,1}} \right) + \sqrt{\kappa_{R,2}}\left(K\sqrt{\kappa_{R,1}} + \widetilde{\Delta_1}\sqrt{\kappa_{R,2}} \right)}{\widetilde{\Delta_1}\widetilde{\Delta_2} - K^2} \tag{B.191}$$

$$= 1 - i\frac{\kappa_{R,1}\widetilde{\Delta_2} + \kappa_{R,2}\widetilde{\Delta_1} + 2\sqrt{\kappa_{R,1}\kappa_{R,2}}K}{\widetilde{\Delta_1}\widetilde{\Delta_2} - K^2} \tag{B.192}$$

$$= 1 - i\frac{\kappa_{R,1}\widetilde{\Delta_2} + \kappa_{R,2}\widetilde{\Delta_1} + 2\sqrt{\kappa_{R,1}\kappa_{R,2}}(g - i\Gamma)}{\widetilde{\Delta_1}\widetilde{\Delta_2} - (g - i\Gamma)^2} \tag{B.193}$$

We can rewrite the transmission as a single fraction to identify the singularities, i.e.

$$S_{21} = \frac{\widetilde{\Delta_1}\widetilde{\Delta_2} - (g-i\Gamma)^2 - i\kappa_{R,1}\widetilde{\Delta_2} - i\kappa_{R,2}\widetilde{\Delta_1} - 2i\sqrt{\kappa_{R,1}\kappa_{R,2}}(g-i\Gamma)}{\widetilde{\Delta_1}\widetilde{\Delta_2} - (g-i\Gamma)^2} \tag{B.194}$$

Resonances of the transmission. The resonances of the transmission are characterised by the zeros of the denominator, i.e. by the condition

$$(\omega - \widetilde{\omega}_1)(\omega - \widetilde{\omega}_2) - (g-i\Gamma)^2 = 0, \tag{B.195}$$

with complex-valued solutions

$$\widetilde{\omega}_\pm = \frac{\widetilde{\omega}_1 + \widetilde{\omega}_2}{2} \pm \frac{\sqrt{(\widetilde{\omega}_1 - \widetilde{\omega}_2)^2 + 4(g-i\Gamma)^2}}{2}. \tag{B.196}$$

Anti-resonances of the transmission. The anti-resonances are characterised instead by the zeros of the nominator, which corresponds to

$$(\omega - \widetilde{\omega}_1)(\omega - \widetilde{\omega}_2) - (g-i\Gamma)^2 - i\kappa_{R,1}(\omega - \widetilde{\omega}_2) - i\kappa_{R,2}(\omega - \widetilde{\omega}_1) - 2i\sqrt{\kappa_{R,1}\kappa_{R,2}}(g-i\Gamma) = 0 \tag{B.197}$$

$$\omega^2 - (\widetilde{\omega}_1 + \widetilde{\omega}_2)\omega + \widetilde{\omega}_1\widetilde{\omega}_2 - (g-i\Gamma)^2 - i(\kappa_{R,1}+\kappa_{R,2})\omega + i\kappa_{R,1}\omega_2 + i\kappa_{R,2}\omega_1 - 2i\sqrt{\kappa_{R,1}\kappa_{R,2}}(g-i\Gamma) = 0 \tag{B.198}$$

$$\omega^2 - (\widetilde{\omega}_1 + i\kappa_{R,1} + \widetilde{\omega}_2 + i\kappa_{R,2})\omega + (\widetilde{\omega}_1 + i\kappa_{R,1})(\widetilde{\omega}_2 + i\kappa_{R,2}) + \kappa_{R,1}\kappa_{R,2} - (g-i\Gamma)^2 - 2i\sqrt{\kappa_{R,1}\kappa_{R,2}}(g-i\Gamma) = 0 \tag{B.199}$$

$$\omega_\pm = \frac{\widetilde{\omega}_1 + i\kappa_{R,1} + \widetilde{\omega}_2 + i\kappa_{R,2}}{2} \pm \frac{\sqrt{(\widetilde{\omega}_1 + i\kappa_{R,1} - \widetilde{\omega}_2 - i\kappa_{R,2})^2 + 4\Big[(g-i\Gamma)^2 + 2i(g-i\Gamma)\sqrt{\kappa_{R,1}\kappa_{R,2}} - \kappa_{R,1}\kappa_{R,2}\Big]}}{2} \tag{B.200}$$

$$\omega_\pm = \frac{\widetilde{\Omega}_1 + \widetilde{\Omega}_2}{2} \pm \frac{\sqrt{\Big(\widetilde{\Omega}_1 - \widetilde{\Omega}_2\Big)^2 + 4\Big[(g-i\Gamma)^2 + 2i(g-i\Gamma)\sqrt{\kappa_{R,1}\kappa_{R,2}} - \kappa_{R,1}\kappa_{R,2}\Big]}}{2} \tag{B.201}$$

B.10) Simplification of the effective Hamiltonian for two bosonics modes coupled to a common waveguide

We introduce $G = g - i\Gamma$ and rewrite the effective Hamiltonian as

$$H_{\text{eff}}/\hbar = \widetilde{\Delta}_1 a_1^\dagger a_1 + \widetilde{\Delta}_2 a_2^\dagger a_2 + G\Big(a_1 a_2^\dagger + a_1^\dagger a_2\Big) + \mathcal{E}_1^* a_1 + \mathcal{E}_1 a_1^\dagger + \mathcal{E}_2^* a_2 + \mathcal{E}_2 a_2^\dagger \tag{B.202}$$

Recalling that the displacement transformations $D(\alpha) = \exp\Big(\alpha a_1^\dagger - \alpha^* a_1\Big)$ and $D(\beta) = \exp\Big(\beta a_2^\dagger - \beta a^* a_2\Big)$ transform $a_1 \mapsto a_1 + \alpha$ and $a_2 \mapsto a_2 + \beta$ (see appendix A.2.1), we obtain

$$\begin{aligned} H_{\text{eff}}/\hbar \mapsto H_{\text{eff}}/\hbar' = {} & \widetilde{\Delta}_1 a_1^\dagger a_1 + \widetilde{\Delta}_2 a_2^\dagger a_2 + G\Big(a_1 a_2^\dagger + a_1^\dagger a_2\Big) \\ & + \widetilde{\Delta}_1\alpha^* a_1 + \widetilde{\Delta}_1\alpha a_1^\dagger + \widetilde{\Delta}_2\beta^* a_2 + \widetilde{\Delta}_2\beta a_2^\dagger \\ & + G\Big(\alpha a_2^\dagger + \beta^* a_1 + \alpha^* a_2 + \beta a_1^\dagger\Big) + \mathcal{E}_1^* a_1 + \mathcal{E}_1 a_1^\dagger + \mathcal{E}_2^* a_2 + \mathcal{E}_2 a_2^\dagger, \end{aligned} \tag{B.203}$$

and grouping the terms we obtain

$$\begin{aligned} H_{\text{eff}}/\hbar' = {} & \widetilde{\Delta}_1 a_1^\dagger a_1 + \widetilde{\Delta}_2 a_2^\dagger a_2 + G\Big(a_1 a_2^\dagger + a_1^\dagger a_2\Big) \\ & + \Big(\widetilde{\Delta}_1\alpha^* + G\beta^* + \mathcal{E}_1^*\Big)a_1 + \Big(\widetilde{\Delta}_2\beta^* + G\alpha^* + \mathcal{E}_2^*\Big)a_2 \\ & + \Big(\widetilde{\Delta}_1\alpha + G\beta + \mathcal{E}_1\Big)a_1^\dagger + \Big(\widetilde{\Delta}_2\beta + G\alpha + \mathcal{E}_2\Big)a_2^\dagger. \end{aligned} \tag{B.204}$$

To eliminate the last four terms, we need to find α and β such that

$$\begin{cases} \widetilde{\Delta}_1\alpha + G\beta + \mathcal{E}_1 = 0 \\ \widetilde{\Delta}_2\beta + G\alpha + \mathcal{E}_2 \end{cases}, \quad \begin{cases} \widetilde{\Delta}_1\widetilde{\Delta}_2\alpha + G(-G\alpha - \mathcal{E}_2) + \widetilde{\Delta}_2\mathcal{E}_1 = 0 \\ \widetilde{\Delta}_2\beta = -G\alpha - \mathcal{E}_2 \end{cases}, \tag{B.205}$$

$$\begin{cases} \left(\widetilde{\Delta}_1\widetilde{\Delta}_2 - G^2\right)\alpha = G\mathcal{E}_2 - \mathcal{E}_1\widetilde{\Delta}_2 \\ \left(\widetilde{\Delta}_1\widetilde{\Delta}_2 - G^2\right)\beta = G\mathcal{E}_1 - \mathcal{E}_2\widetilde{\Delta}_1 \end{cases}, \quad \begin{cases} \alpha = \frac{G\mathcal{E}_2 - \mathcal{E}_1\widetilde{\Delta}_2}{\widetilde{\Delta}_1\widetilde{\Delta}_2 - G^2} \\ \beta = \frac{G\mathcal{E}_1 - \mathcal{E}_2\widetilde{\Delta}_1}{\widetilde{\Delta}_1\widetilde{\Delta}_2 - G^2} \end{cases} \tag{B.206}$$

B.11) Additional examples of Hopfield–Bogoliubov transformation

B.11.1) Hopfield model with several cavity modes

We consider a generalised multimode Hopfield model from De Liberato (2014) [437]. The Hamiltonian includes several light modes, each with an associated diamagnetic term. To simplify the notations, we will note $\omega_0 = \omega_b$ the matter mode. The Hamiltonian we consider is

$$H = \hbar\omega_0 b^\dagger b + \sum_n \hbar\omega_n a_n^\dagger a_n + \sum_n \hbar\Omega_n (b^\dagger + b)(a_n^\dagger + a_n) + \sum_{m,n} \hbar\frac{\Omega_n\Omega_m}{\omega_0}(a_n^\dagger + a_n)(a_m^\dagger + a_m) \tag{B.207}$$

where b is the only matter degree of freedom, a_n are the cavity modes and $\Omega_n/2\pi$ the coupling strength between b and a_n. We consider $\boldsymbol{a} = (a_1, \dots, a_N)$ to be a column vector, which we embed in a larger column vector $\boldsymbol{v}$ defined as

$$\boldsymbol{v} = \left(b, \boldsymbol{a}, b^\dagger, \left(\boldsymbol{a}^\dagger\right)^t\right)^t \tag{B.208}$$

where ^{t} indicates the matrix transpose. Next we express H_{LM} in terms of $\boldsymbol{v}$ as follows. First, we expand the interaction terms and use the bosonic commutation relations to symmetrize the Hamiltonian.

$$\begin{aligned} H = {} & \frac{\hbar}{2}\omega_0\left(b^\dagger b + bb^\dagger\right) + \sum_n \frac{\hbar}{2}\omega_n\left(a_n^\dagger a_n + a_n a_n^\dagger\right) - \overbrace{\frac{\hbar}{2}\left(\omega_0 + \sum_n \omega_n\right)}^{=\mathcal{E}} \\ & + \sum_n \frac{\hbar}{2}\Omega_n\left(\left(b^\dagger a_n^\dagger + b^\dagger a_n + b a_n^\dagger + b a_n\right) + \left(b^\dagger a_n^\dagger + b^\dagger a_n + b a_n^\dagger + b a_n\right)\right) \\ & + \sum_{m,n} \frac{\hbar}{2}\frac{2\Omega_n\Omega_m}{\omega_0}\left(a_n^\dagger a_m^\dagger + a_n^\dagger a_m + a_n a_m^\dagger + a_m a_n\right) \end{aligned} \tag{B.209}$$

and we discard the unobservable energy offset $\mathcal{E}$. Then, we arrange the terms in an order making explicit a matrix multiplication:

$$\begin{aligned} H = {} & \frac{\hbar}{2}\omega_0\left(b^\dagger b + bb^\dagger\right) + \sum_n \frac{\hbar}{2}\omega_n\left(a_n^\dagger a_n + a_n a_n^\dagger\right) \\ & + \frac{\hbar}{2}\sum_n \Omega_n\left(b^\dagger a_n + b^\dagger a_n^\dagger + a_n^\dagger b + a_n^\dagger b^\dagger + b a_n + b a_n^\dagger + a_n b + a_n b^\dagger\right) \\ & + \frac{\hbar}{2}\sum_{m,n} \frac{2\Omega_n\Omega_m}{\omega_0}\left(a_n^\dagger a_m + a_n^\dagger a_m^\dagger + a_n a_m + a_n a_m^\dagger\right) \end{aligned} \tag{B.210}$$

Finally, colouring to easily identify them in matrix form:

$$\begin{aligned} H = &\frac{\hbar}{2}\omega_0\left(b^\dagger b + bb^\dagger\right) + \sum_n \frac{\hbar}{2}\omega_n\left(a_n^\dagger a_n + a_n a_n^\dagger\right) \\ &+ \frac{\hbar}{2}\sum_n \Omega_n\left(b^\dagger a_n + b^\dagger a_n^\dagger + a_n^\dagger b + a_n^\dagger b^\dagger + b a_n + b a_n^\dagger + a_n b + a_n b^\dagger\right) \\ &+ \frac{\hbar}{2}\sum_{m,n} \frac{2\Omega_n\Omega_m}{\omega_0}\left(a_n^\dagger a_m + a_n^\dagger a_m^\dagger + a_n a_m + a_n a_m^\dagger\right) \end{aligned} \tag{B.211}$$

$$= \frac{\hbar}{2}\left(b^\dagger, a_1^\dagger, \dots, a_N^\dagger, b, a_1, \dots, a_N\right) M \begin{pmatrix} b \\ a_1 \\ \vdots \\ a_N \\ b^\dagger \\ a_1^\dagger \\ \vdots \\ a_N^\dagger \end{pmatrix} \tag{B.212}$$

with

$$M = \begin{pmatrix} \omega_0 & \Omega_1 & \dots & \Omega_N & 0 & \Omega_1 & \dots & \Omega_N \\ \Omega_1 & \omega_1 + \frac{2\Omega_1\Omega_1}{\omega_0} & \dots & \frac{2\Omega_1\Omega_N}{\omega_0} & \Omega_1 & \frac{2\Omega_1\Omega_1}{\omega_0} & \dots & \frac{2\Omega_1\Omega_N}{\omega_0} \\ \vdots & \vdots & \ddots & \vdots & \vdots & \vdots & & \vdots \\ \Omega_N & \frac{2\Omega_N\Omega_1}{\omega_0} & \dots & \omega_N + \frac{2\Omega_N\Omega_N}{\omega_0} & \Omega_N & \frac{2\Omega_N\Omega_1}{\omega_0} & \dots & \frac{2\Omega_N\Omega_N}{\omega_0} \\ 0 & \Omega_1 & \dots & \Omega_N & \omega_0 & \Omega_1 & \dots & \Omega_N \\ \Omega_1 & \frac{2\Omega_1\Omega_1}{\omega_0} & \dots & \frac{2\Omega_1\Omega_N}{\omega_0} & \Omega_1 & \omega_1 + \frac{2\Omega_1\Omega_1}{\omega_0} & \dots & \frac{2\Omega_1\Omega_N}{\omega_0} \\ \vdots & \vdots & & \vdots & \vdots & \vdots & \ddots & \vdots \\ \Omega_N & \frac{2\Omega_N\Omega_1}{\omega_0} & \dots & \frac{2\Omega_N\Omega_N}{\omega_0} & \Omega_N & \frac{2\Omega_N\Omega_1}{\omega_0} & \dots & \omega_N + \frac{2\Omega_N\Omega_N}{\omega_0} \end{pmatrix} \tag{B.213}$$

B.11.2) Multimode Hopfield model

We consider a generalisation of De Liberato (2014) [437] in which we include N cavity and M matter modes, with diamagnetic terms. The Hamiltonian we consider is[1]

$$H = \sum_n \hbar\omega_{a,n} a_n^\dagger a_n + \sum_m \hbar\omega_{b,m} b_m^\dagger b_m + \sum_{n,m} \hbar g_{nm}(a_n^\dagger + a_n)(b_m^\dagger + b_m) + \sum_{n,m} \hbar d_{nm}(a_n^\dagger + a_n)(a_m^\dagger + a_m) \tag{B.214}$$

where b_m are the matter degrees of freedom and a_n are the cavity modes. We consider the row vectors $\boldsymbol{a} = (a_0, a_1, \dots, a_{N-1})^t$ and $\boldsymbol{b} = (b_0, b_1, \dots, b_{M-1})^t$ that we embed in $\boldsymbol{v}$ as

$$\boldsymbol{v} = \left(\boldsymbol{a}, \boldsymbol{b}, \boldsymbol{a}^\dagger, \boldsymbol{b}^\dagger\right)^t \tag{B.215}$$

where ^{t} indicates the matrix transpose. The goal is to find the matrix M such that

$$H = \frac{\hbar}{2}\boldsymbol{v}^\dagger \eta M \boldsymbol{v} \tag{B.216}$$

[1] We have left out the initial and final values of the indices for readability. The cavity modes range from 0 to $N-1$ and the matter modes from 0 to $M-1$.

where $\eta = \sigma_z \otimes I_{N+M}$ and I_k is the $k \times k$ identity matrix.

In De Liberato (2014) [437], there is a single matter mode b_0 and $d_{nm} = \frac{g_{n,0}g_{m,0}}{\omega_{b,0}}$. The corresponding matrix M was given by

$$M = \begin{pmatrix} \omega_{a,n}\delta_{n,m} + \frac{2g_{n,0}g_{m,0}}{\omega_{b,0}} & g^t_{n,0} & \frac{2g_{n,0}g_{m,0}}{\omega_{b,0}} & g^t_{n,0} \\ g_{n,0} & \omega_{b,0} & g_{n,0} & 0 \\ -\frac{2g_{n,0}g_{m,0}}{\omega_{b,0}} & -g^t_{n,0} & -\omega_{a,n}\delta_{n,m} - \frac{2g_{n,0}g_{m,0}}{\omega_{b,0}} & -g^t_{n,0} \\ -g_{n,0} & 0 & -g_{n,0} & -\omega_{b,0} \end{pmatrix}. \tag{B.217}$$

Hence we deduce that the generalisation is

$$M = \begin{pmatrix} \omega_{a,n}\delta_{nm} + 2d_{n,m} & g_{nm} & 2d_{n,m} & g_{nm} \\ g^t_{nm} & \omega_{b,n}\delta_{nm} & g^t_{nm} & 0 \\ -2d_{n,m} & -g_{nm} & -\omega_{a,n}\delta_{n,m} - 2d_{n,m} & -g_{nm} \\ -g^t_{nm} & 0 & -g^t_{nm} & -\omega_{b,n}\delta_{nm} \end{pmatrix}. \tag{B.218}$$

Implementation. The matrix above can be decomposed in blocks that make the implementation easier. First, we define

$$\mathcal{W} = \mathrm{diag}\,(\omega_{a,n}, \omega_{b,m}), \quad W = \begin{pmatrix} \mathcal{W} & \\ & -\mathcal{W} \end{pmatrix} \tag{B.219}$$

where $\mathcal{W}$ is a $(N+M) \times (N+M)$ matrix. Then, defining $\mathcal{G} = (g_{n,m})_{0 \leqslant n \leqslant N-1, 0 \leqslant m \leqslant M-1}$ a $N \times M$ matrix and $\mathcal{D} = (d_{n,m})_{0 \leqslant n,m \leqslant N-1}$ a $N \times N$ matrix, we can write M as

$$M = W + \begin{pmatrix} 1 & 1 \\ -1 & -1 \end{pmatrix} \otimes \begin{pmatrix} 2\mathcal{D} & \mathcal{G} \\ \mathcal{G}^t & 0 \end{pmatrix}. \tag{B.220}$$

Strong coupling limit. For low coupling strengths, we can perform the rotating wave approximation (RWA) and neglect the diamagnetic terms. Then, the Hopfield matrix reads

$$M = \begin{pmatrix} \omega_{a,n}\delta_{nm} & g_{nm} & 0 & 0 \\ g^t_{nm} & \omega_{b,n}\delta_{nm} & 0 & 0 \\ 0 & 0 & -\omega_{a,n}\delta_{n,m} & -g_{nm} \\ 0 & 0 & -g^t_{nm} & -\omega_{b,n}\delta_{nm} \end{pmatrix}. \tag{B.221}$$

B.11.3) Another multimode Hopfield model

The Hopfield-Bogoliubov method can be used to diagonalise any Hamiltonian of the form

$$H = \sum_{n=0}^{N-1} \hbar\omega_{a,n} a^\dagger_n a_n + \sum_{n,m=0}^{N-1} \hbar g_{nm}(a^\dagger_n + a_n)(a^\dagger_m + a_m) \tag{B.222}$$

where a_n are bosonic modes. We consider the row vector $\boldsymbol{v} = (a_0, a_1, \ldots, a_{N-1})^t$ with ^{t} indicating the matrix transpose. The goal is to find the matrix M such that

$$H = \frac{\hbar}{2}\mathbf{v}^\dagger \eta M \mathbf{v} \tag{B.223}$$

where $\eta = \sigma_z \otimes I_N$.

In De Liberato (2014) [437], there is a single matter mode b_0 and $d_{nm} = \frac{g_{n,0}g_{m,0}}{\omega_{b,0}}$. The corresponding matrix M was given by

$$M = \begin{pmatrix} \omega_{a,n}\delta_{n,m} + \frac{2g_{n,0}g_{m,0}}{\omega_{b,0}} & g^t_{n,0} & \frac{2g_{n,0}g_{m,0}}{\omega_{b,0}} & g^t_{n,0} \\ g_{n,0} & \omega_{b,0} & g_{n,0} & 0 \\ -\frac{2g_{n,0}g_{m,0}}{\omega_{b,0}} & -g^t_{n,0} & -\omega_{a,n}\delta_{n,m} - \frac{2g_{n,0}g_{m,0}}{\omega_{b,0}} & -g^t_{n,0} \\ -g_{n,0} & 0 & -g_{n,0} & -\omega_{b,0} \end{pmatrix}. \tag{B.224}$$

Hence we deduce that the generalisation is

$$M = \begin{pmatrix} \omega_{a,n}\delta_{nm} + 2d_{n,m} & g_{nm} & 2d_{n,m} & g_{nm} \\ g^t_{nm} & \omega_{b,n}\delta_{nm} & g^t_{nm} & 0 \\ -2d_{n,m} & -g_{nm} & -\omega_{a,n}\delta_{n,m} - 2d_{n,m} & -g_{nm} \\ -g^t_{nm} & 0 & -g^t_{nm} & -\omega_{b,n}\delta_{nm} \end{pmatrix}. \tag{B.225}$$

Implementation. The matrix above can be decomposed in blocks that make the implementation easier. First, we define

$$\mathcal{W} = \mathrm{diag}\left(\omega_{a,n}, \omega_{b,m}\right), \quad W = \begin{pmatrix} \mathcal{W} & \\ & -\mathcal{W} \end{pmatrix} \tag{B.226}$$

where $\mathcal{W}$ is a $(N+M)\times(N+M)$ matrix. Then, defining $\mathcal{G} = (g_{n,m})_{0\leqslant n\leqslant N-1, 0\leqslant m\leqslant M-1}$ a $N\times M$ matrix and $\mathcal{D} = (d_{n,m})_{0\leqslant n,m\leqslant N-1}$ a $N\times N$ matrix, we can write M as

$$M = W + \begin{pmatrix} 1 & 1 \\ -1 & -1 \end{pmatrix} \otimes \begin{pmatrix} 2\mathcal{D} & \mathcal{G} \\ \mathcal{G}^t & 0 \end{pmatrix}. \tag{B.227}$$

Strong coupling limit. For low coupling strengths, we can perform the rotating wave approximation (RWA) and neglect the diamagnetic terms. Then, the Hopfield matrix reads

$$M = \begin{pmatrix} \omega_{a,n}\delta_{nm} & g_{nm} & 0 & 0 \\ g^t_{nm} & \omega_{b,n}\delta_{nm} & 0 & 0 \\ 0 & 0 & -\omega_{a,n}\delta_{n,m} & -g_{nm} \\ 0 & 0 & -g^t_{nm} & -\omega_{b,n}\delta_{nm} \end{pmatrix}. \tag{B.228}$$

B.12) Heisenberg equation of motions of the averages of the harmonic oscillator

Let us note $\xi : t \mapsto \xi(t)$ the trajectory of the centre of the harmonic potential. In the classical case, the potential is $V(x,t) = \frac{1}{2}m\omega^2(x(t) - \xi(t))^2$. Following the first quantisation procedure[1], we replace the variable x by the position operator $\hat{x} : \psi \mapsto x\psi$. Similarly, we replace the function ξ by the operator $\hat{\xi}(t) : \psi \mapsto \xi(t)\psi$. The potential operator becomes

$$\hat{V} = \frac{1}{2}m\omega^2(x - \xi(t))^2 = \frac{1}{2}m\omega^2\hat{x}^2 + \frac{1}{2}m\omega^2\hat{\xi}^2 + \frac{1}{2}m\omega^2\left\{\hat{x}, \hat{\xi}\right\}$$

where $\{\}$ is the notation for the anti-commutator[2]. Since $\hat{\xi}$ only multiplies the wave function by a time-dependent constant, it commutes[3] with the position operator (note that we also have

[1] A pedagogical introduction of first quantisation is given in section 6.1 of Gambini and Pullin (2011) [578].
[2] The anti-commutator of two operators A and B is defined as $\{A, B\} = AB + BA$.
[3] The commutator of two operators A and B is defined as $[A, B] = AB - BA$.

$\left[\hat{\xi},\hat{p}\right]=0$ since $\xi(t)$ does not depend on x, so is unaffected by the derivative in the momentum operator $\hat{p}=\frac{\hbar}{i}\frac{\mathrm{d}}{\mathrm{d}x}$). Hence, the potential simplifies and we can write the Hamiltonian as

$$\hat{H}=\frac{\hat{p}^2}{2m}+\frac{1}{2}m\omega^2\hat{x}^2+\frac{1}{2}m\omega^2\hat{\xi}(t)^2-m\omega^2\hat{x}\hat{\xi}(t). \tag{B.229}$$

The Heisenberg equation of motion for any operator $\hat{A}$ reads

$$\frac{\mathrm{d}\left\langle\hat{A}\right\rangle}{\mathrm{d}t}=\left\langle\frac{\partial\hat{A}}{\partial t}+\frac{1}{i\hbar}\left[\hat{A},\hat{H}\right]\right\rangle. \tag{B.230}$$

Setting $\hat{A}=\hat{p}$ and using some commutators from appendix A.1,

$$\begin{aligned}
\frac{\mathrm{d}\left\langle\hat{p}\right\rangle}{\mathrm{d}t}=&\left\langle\frac{\partial\hat{p}}{\partial t}+\frac{1}{i\hbar}\left[\hat{p},\hat{H}\right]\right\rangle\\
=&\left\langle 0+\frac{1}{i\hbar}\left[\hat{p},\hat{H}\right]\right\rangle\\
=&\frac{1}{i\hbar}\left\langle\left[\hat{p},\frac{\hat{p}^2}{2m}\right]+\left[\hat{p},\frac{1}{2}m\omega^2\hat{x}^2\right]+\left[\hat{p},\frac{1}{2}m\omega^2\hat{\xi}(t)^2\right]-\left[\hat{p},m\omega^2\hat{x}\hat{\xi}(t)\right]\right\rangle\\
=&\frac{1}{i\hbar}\left\langle 0+\frac{1}{2}m\omega^2\left[\hat{p},\hat{x}^2\right]+0-m\omega^2\xi(t)\left[\hat{p},\hat{x}\right]\right\rangle\\
=&\frac{1}{i\hbar}\left\langle m\omega^2\frac{-2i\hbar\hat{x}}{2}+m\omega^2\xi(t)i\hbar\right\rangle\\
=&m\omega^2\left(\xi(t)-\left\langle\hat{x}\right\rangle(t)\right).
\end{aligned}$$

Similarly for $\hat{x}$,

$$\begin{aligned}
\frac{\mathrm{d}\left\langle\hat{x}\right\rangle}{\mathrm{d}t}=&\left\langle\frac{\partial\hat{x}}{\partial t}+\frac{1}{i\hbar}\left[\hat{x},\hat{H}\right]\right\rangle\\
=&\frac{1}{i\hbar}\left\langle\left[\hat{x},\hat{H}\right]\right\rangle\\
=&\frac{1}{i\hbar}\left\langle\left[\hat{x},\frac{\hat{p}^2}{2m}\right]+\left[\hat{x},\frac{1}{2}m\omega^2\hat{x}^2\right]+\left[\hat{x},\frac{1}{2}m\omega^2\hat{\xi}(t)^2\right]-\left[\hat{x},m\omega^2\hat{x}\hat{\xi}(t)\right]\right\rangle\\
=&\frac{1}{i\hbar}\left\langle\frac{2i\hbar\hat{p}}{2m}+0+0+0\right\rangle\\
=&\frac{\left\langle\hat{p}\right\rangle}{m}.
\end{aligned}$$

By deriving this last equality with respect to time, we obtain

$$\frac{\mathrm{d}^2\left\langle\hat{x}\right\rangle}{\mathrm{d}t^2}=\frac{1}{m}\frac{\mathrm{d}\left\langle\hat{p}\right\rangle}{\mathrm{d}t}=\omega^2\left(\xi(t)-\left\langle\hat{x}\right\rangle(t)\right).$$

This last equality can be rewritten as the equation of a classical harmonic oscillator driven by an external excitation $\xi(t)$:

$$\frac{\mathrm{d}^2\left\langle\hat{x}\right\rangle}{\mathrm{d}t^2}+\omega^2\left\langle\hat{x}\right\rangle=\omega^2\xi(t). \tag{B.231}$$

B.13) Input-output for two cavity modes

We consider the Hamiltonian

$$H=\hbar\omega_0c_0^\dagger c_0+\hbar\omega_1c_1^\dagger c_1, \tag{B.232}$$

and the QLE for c_i reads

$$\dot{c}_i(t)=-i\left(\omega_i-i\frac{\kappa_i+\gamma_i}{2}\right)-\sqrt{\kappa_i}p_1^{\mathrm{in}}(t)-\sqrt{\gamma_i}p_2^{\mathrm{in}}(t). \tag{B.233}$$

The frequency-space solution is

$$\widetilde{c}_i(\omega) = -i\frac{\sqrt{\kappa_i}p_1^{\text{in}}(\omega) + \sqrt{\gamma_i}p_2^{\text{in}}(\omega)}{\omega - \omega_i + i\frac{\kappa_i+\gamma_i}{2}} \tag{B.234}$$

which describes a Lorentzian response of each of the cavity modes. The input-output relations are

$$p_1^{\text{out}} = p_1^{\text{in}} + \sum_i \sqrt{\kappa_i}c_i \tag{B.235}$$

$$p_2^{\text{out}} = p_2^{\text{in}} + \sum_i \sqrt{\gamma_i}c_i \tag{B.236}$$

Using a semi-classical approximation, the transmission coefficient reads

$$S_{21}(\omega) = \left.\frac{p_2^{\text{out}}}{p_1^{\text{in}}}\right|_{p_2^{\text{in}}=0} = \frac{\sqrt{\gamma_0}\,\widetilde{c}_0|_{p_2^{\text{in}}=0} + \sqrt{\gamma_1}\,\widetilde{c}_1|_{p_2^{\text{in}}=0}}{p_1^{\text{in}}} \tag{B.237}$$

$$= -i\frac{\sqrt{\kappa_0\gamma_0}}{\widetilde{\Delta}_0} - i\frac{\sqrt{\kappa_1\gamma_1}}{\widetilde{\Delta}_1} \tag{B.238}$$

$$= -i\left(\frac{\sqrt{\kappa_0\gamma_0}\widetilde{\Delta}_1 + \sqrt{\kappa_1\gamma_1}\widetilde{\Delta}_0}{\widetilde{\Delta}_0\widetilde{\Delta}_1}\right) \tag{B.239}$$

where we introduced $\widetilde{\Delta}_i = \omega - \omega_i + i\frac{\kappa_i+\gamma_i}{2}$. An anti-resonance can occur if the real part of the nominator vanishes, which corresponds to

$$\sqrt{\kappa_0\gamma_0}(\omega - \omega_1) + \sqrt{\kappa_1\gamma_1}(\omega - \omega_0) = 0, \tag{B.240}$$

$$(\sqrt{\kappa_0\gamma_0} + \sqrt{\kappa_1\gamma_1})\omega = \sqrt{\kappa_0\gamma_0}\omega_1 + \sqrt{\kappa_1\gamma_1}\omega_0, \tag{B.241}$$

$$\omega_r = \frac{\sqrt{\kappa_0\gamma_0}\omega_1 + \sqrt{\kappa_1\gamma_1}\omega_0}{\sqrt{\kappa_0\gamma_0} + \sqrt{\kappa_1\gamma_1}}. \tag{B.242}$$

Note that if one of the mode does not couple to the receiving antenna (i.e. $\gamma_i = 0$), then we observe an anti-resonance at a resonance?

B.14) Input-output theory of the Hopfield model in the USC

In this appendix, we derive an input-output theory for two coupled bosonic modes (annihilation operators c and m) in the ultrastrong coupling regime by following Ciuti and Carusotto (2006) [225]. We consider a total of four bosonic baths, two to model the coupling of the cavity mode to microwave ports, and two others to model the intrinsic dissipation of the cavity and matter mode. Thus, the bath Hamiltonian is[1]

$$\begin{aligned} H_{\text{bath}} = &\sum_{j=1,2}\int_{\mathbb{R}^+} \mathrm{d}\omega\left[\hbar\omega p_{j,\omega}^\dagger p_{j,\omega} + i\hbar\Big(\kappa_j(\omega)p_{j,\omega}c^\dagger - \kappa_j^*(\omega)p_{j,\omega}^\dagger c\Big)\right] \\ &+ \int_{\mathbb{R}^+} \mathrm{d}\omega\left[\hbar\omega\alpha_\omega^\dagger\alpha_\omega + i\hbar\Big(\kappa_\alpha(\omega)\alpha_\omega c^\dagger - \kappa_\alpha^*(\omega)\alpha_\omega^\dagger c\Big)\right] \\ &+ \int_{\mathbb{R}^+} \mathrm{d}\omega\left[\hbar\omega\beta_\omega^\dagger\beta_\omega + i\hbar\Big(\kappa_\beta(\omega)\beta_\omega m^\dagger - \kappa_\beta^*(\omega)\beta_\omega^\dagger m\Big)\right] \end{aligned} \tag{B.243}$$

where in the first term we have the baths corresponding to the microwave ports, and the remaining terms model intrinsic losses. The total Hamiltonian is $H = H_{\text{bath}} + H_{\text{sys}}$ where

$$H_{\text{sys}} = \hbar\omega_c c^\dagger c + \hbar\omega_m m^\dagger m + \hbar g(c + c^\dagger)(m + m^\dagger) + \hbar D(c + c^\dagger)^2 \tag{B.244}$$

is the Hopfield model. The overall system is pictured in figure B.2.

[1] Contrary to Ciuti and Carusotto (2006) [225], we adopt a continuous formulation for the baths. This does not impact the results.

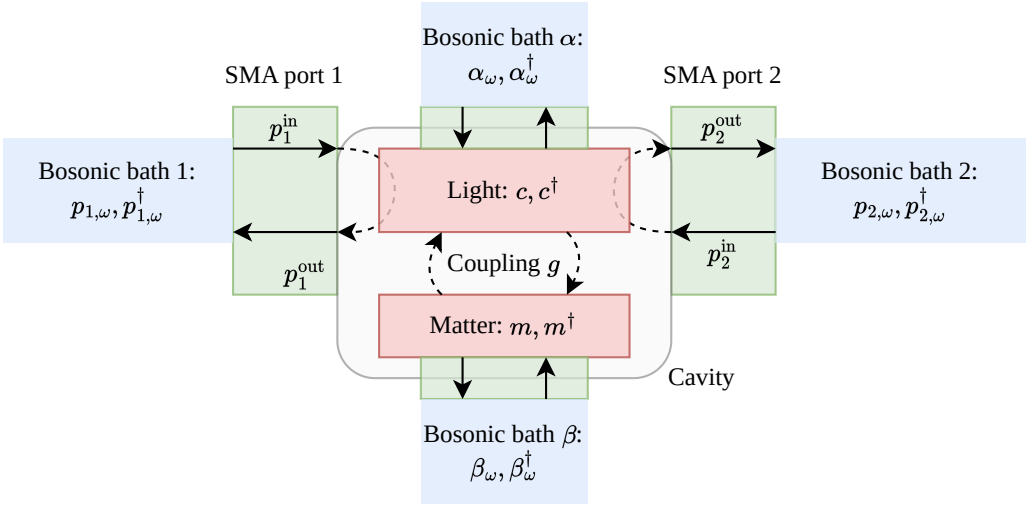


Figure B.2: Schematic of the system modelled in this appendix. The baths α, β model intrinsic dissipation (radiative losses), while two other baths couple to the cavity mode to model microwave excitation and probe drives.

B.14.1) Quantum Langevin equations in the time domain

Equation of motion for the bath operators. For the bath operator modelling the intrinsic dissipation of the cavity mode,

$$\frac{\mathrm{d}\alpha_\omega}{\mathrm{d}t} = \frac{1}{i\hbar}[\alpha_\omega, H] = -i\omega\alpha_\omega - \kappa_\alpha^*(\omega)c \tag{B.245}$$

with formal solution

$$\alpha_\omega(t) = e^{-i\omega(t-t_0)}\alpha_\omega(t_0) - \kappa_\alpha^*(\omega)\int_{t_0}^{t}\mathrm{d}t'\, e^{-i\omega(t-t')}c(t') \tag{B.246}$$

By analogy, we deduce

$$\beta_\omega(t) = e^{-i\omega(t-t_0)}\beta_\omega(t_0) - \kappa_\beta^*(\omega)\int_{t_0}^{t}\mathrm{d}t'\, e^{-i\omega(t-t')}m(t') \tag{B.247}$$

$$p_{j,\omega}(t) = e^{-i\omega(t-t_0)}p_{j,\omega}(t_0) - \kappa_j^*(\omega)\int_{t_0}^{t}\mathrm{d}t'\, e^{-i\omega(t-t')}c(t'), \quad j \in \{1,2\}, \tag{B.248}$$

for the other bath operators.

Langevin force and memory kernel. We have

$$\int_{\mathbb{R}^+}\mathrm{d}\omega\,\kappa_\alpha(\omega)\alpha_\omega = \int_{\mathbb{R}^+}\mathrm{d}\omega\,\kappa_\alpha(\omega)e^{-i\omega(t-t_0)}\alpha_\omega(t_0) - \int_{\mathbb{R}^+}\mathrm{d}\omega\,|\kappa_\alpha(\omega)|^2\int_{t_0}^{t}\mathrm{d}t'\, e^{-i\omega(t-t')}c(t') \tag{B.249}$$

$$= \underbrace{\int_{\mathbb{R}^+}\mathrm{d}\omega\,\kappa_\alpha(\omega)e^{-i\omega t}\alpha_\omega^{\text{in}}}_{=F_\alpha(t)} - \int_{\mathbb{R}^+}\mathrm{d}\omega\,|\kappa_\alpha(\omega)|^2\int_{-\infty}^{t}\mathrm{d}t'\, e^{-i\omega(t-t')}c(t') \tag{B.250}$$

$$= F_\alpha(t) - \int_{-\infty}^{+\infty}\mathrm{d}t'\,\Theta(t-t')\underbrace{\int_{\mathbb{R}^+}\mathrm{d}\omega\,|\kappa_\alpha(\omega)|^2 e^{-i\omega(t-t')}}_{\Gamma_\alpha(t-t')}c(t') \tag{B.251}$$

$$= F_\alpha(t) - \int_{-\infty}^{+\infty}\mathrm{d}t'\,\Gamma_\alpha(t-t')c(t') \tag{B.252}$$

$$= F_\alpha(t) - [\Gamma_\alpha * c](t) \tag{B.253}$$

where $*$ indicates convolution, $\alpha_\omega^{\text{in}} = \lim_{t_0 \to -\infty} e^{i\omega t_0}\alpha_\omega(t_0)$, and we extended[1] the upper bound of the time integral to ∞ while taking the limit $t_0 \to -\infty$. F_α and Γ_α are the Langevin force and memory kernel associated to the bath operator α. A similar calculus gives

$$\int_{\mathbb{R}^+} \mathrm{d}\omega\, \kappa_\beta(\omega)\beta_\omega = F_\beta(t) - [\Gamma_\beta * m]\,(t), \tag{B.254}$$

$$\int_{\mathbb{R}^+} \mathrm{d}\omega\, \kappa_j(\omega)p_{j,\omega} = F_j(t) - [\Gamma_j * c]\,(t), \quad j \in \{1,2\}. \tag{B.255}$$

Expression of c with the memory kernels and Langevin forces. The equation of motion of c gives

$$\frac{\mathrm{d}c}{\mathrm{d}t} = \frac{1}{i\hbar}[c, H] = \frac{1}{i\hbar}[c, H_{\text{sys}}] + \int_{\mathbb{R}^+} \mathrm{d}\omega \left(\kappa_\alpha(\omega)\alpha_\omega + \sum_j \kappa_j(\omega)p_{j,\omega} \right). \tag{B.256}$$

and using equations (B.253) and (B.255),

$$\frac{\mathrm{d}c}{\mathrm{d}t} = \frac{1}{i\hbar}[c, H_{\text{sys}}] + F_\alpha(t) + F_1(t) + F_2(t) - (\Gamma_\alpha * c)(t) - (\Gamma_1 * c)(t) - (\Gamma_2 * c)(t). \tag{B.257}$$

We expand the commutator to obtain

$$\begin{aligned}\frac{\mathrm{d}c}{\mathrm{d}t} &= -i\omega_c c - ig(m + m^\dagger)) + \frac{D}{i}\left[c, (c + c^\dagger)^2\right] \\ &\quad + F_\alpha(t) + F_1(t) + F_2(t) - (\Gamma_\alpha * c)(t) - (\Gamma_1 * c)(t) - (\Gamma_2 * c)(t)\end{aligned} \tag{B.258}$$

Expanding $(c+c^\dagger)^2 = c^2 + cc^\dagger + c^\dagger c + {c^\dagger}^2$ and using the results of appendix A.1, $\left[c, (c + c^\dagger)^2\right] = 2c + 2c^\dagger$, and thus

$$\begin{aligned}\frac{\mathrm{d}c}{\mathrm{d}t} &= -i\omega_c c - ig(m + m^\dagger)) - 2iD(c + c^\dagger) \\ &\quad + F_\alpha(t) + F_1(t) + F_2(t) - (\Gamma_\alpha * c)(t) - (\Gamma_1 * c)(t) - (\Gamma_2 * c)(t).\end{aligned} \tag{B.259}$$

Expression of m with the memory kernels and Langevin forces. Referring to figure B.2, the matter degree of freedom do not couple to the baths, and thus we have

$$\frac{\mathrm{d}m}{\mathrm{d}t} = \frac{1}{i\hbar}[m, H_{\text{sys}}] + \int_{\mathbb{R}^+} \mathrm{d}\omega\, \kappa_\beta(\omega)\beta_\omega = \frac{1}{i\hbar}[m, H_{\text{sys}}] + F_\beta(t) - [\Gamma_\beta * m]\,(t) \tag{B.260}$$

$$= -i\omega_m m - ig(c + c^\dagger) + F_\beta(t) - [\Gamma_\beta * m]\,(t). \tag{B.261}$$

Final non-linear system in the time-domain. By taking the hermitian conjugate of equations (B.259) and (B.261), we finally obtain

$$\begin{aligned}\dot{c} &= -i\omega_c c - ig(m + m^\dagger)) - 2iD(c + c^\dagger) \\ &\quad + F_\alpha(t) + F_1(t) + F_2(t) - (\Gamma_\alpha * c)(t) - (\Gamma_1 * c)(t) - (\Gamma_2 * c)(t)\end{aligned} \tag{B.262}$$

$$\dot{m} = -i\omega_m m - ig(c + c^\dagger) + F_\beta(t) - [\Gamma_\beta * m]\,(t) \tag{B.263}$$

$$\begin{aligned}(\dot{c})^\dagger &= i\omega_c c^\dagger + ig(m + m^\dagger) + 2iD(c + c^\dagger) \\ &\quad + F_\alpha^\dagger(t) + F_1^\dagger(t) + F_2^\dagger(t) - \left(\Gamma_\alpha^* * c^\dagger\right)(t) - \left(\Gamma_1^* * c^\dagger\right)(t) - \left(\Gamma_2^* * c^\dagger\right)(t)\end{aligned} \tag{B.264}$$

$$(\dot{m})^\dagger = i\omega_m m^\dagger + ig(c + c^\dagger) + F_\beta^\dagger(t) - \left[\Gamma_\beta^* * m^\dagger\right](t). \tag{B.265}$$

This system of equation involves convolutions which are non-linear in the time domain. However, they become simple products in the frequency domain.

[1] This can be done for sufficiently well-behaved functions. As in chapter III, we assume this is the case.

B.14.2) Quantum Langevin equations in the frequency domain

Frequency space equations of the matter degree of freedom. In frequency space, equation (B.263) becomes

$$-i\omega\widetilde{m}(\omega) = -i\omega_m\widetilde{m}(\omega) - ig(\widetilde{c}(\omega) + \widetilde{c}^\dagger(-\omega)) + \widetilde{F}_\beta(\omega) - \widetilde{\Gamma}_\beta(\omega)\widetilde{m}(\omega), \tag{B.266}$$

$$0 = -ig\widetilde{c}(\omega) + i\Big(\omega - \omega_m + i\widetilde{\Gamma}_\beta(\omega)\Big)\widetilde{m}(\omega) - ig\widetilde{c}^\dagger(-\omega) + \widetilde{F}_\beta(\omega), \tag{B.267}$$

$$-g\widetilde{c}(\omega) + \Big(\omega - \omega_m + i\widetilde{\Gamma}_\beta(\omega)\Big)\widetilde{m}(\omega) - g\widetilde{c}^\dagger(-\omega) - i\widetilde{F}_\beta(\omega) = 0. \tag{B.268}$$

while equation (B.265) becomes

$$-i\omega\widetilde{m}^\dagger(-\omega) = i\omega_m\widetilde{m}^\dagger(-\omega) + ig(\widetilde{c}(\omega) + \widetilde{c}^\dagger(-\omega)) + \widetilde{F}^\dagger_\beta(-\omega) - \widetilde{\Gamma}^*_\beta(-\omega)\widetilde{m}^\dagger(-\omega), \tag{B.269}$$

$$ig\widetilde{c}(\omega) + i\Big(\omega + \omega_m + i\widetilde{\Gamma}^*_\beta(-\omega)\Big)\widetilde{m}^\dagger(-\omega) + ig\widetilde{c}^\dagger(-\omega) + \widetilde{F}^\dagger_\beta(-\omega) = 0, \tag{B.270}$$

$$g\widetilde{c}(\omega) + g\widetilde{c}^\dagger(-\omega) + \Big(\omega + \omega_m + i\widetilde{\Gamma}^*_\beta(-\omega)\Big)\widetilde{m}^\dagger(-\omega) - i\widetilde{F}^\dagger_\beta(-\omega) = 0. \tag{B.271}$$

Equations (B.268) and (B.271) can be summarised by the matrix equation

$$\begin{pmatrix} -g & \omega - \omega_m + i\widetilde{\Gamma}_\beta(\omega) & -g & 0 \\ g & 0 & g & \omega + \omega_m + i\widetilde{\Gamma}^*_\beta(-\omega) \end{pmatrix} \begin{pmatrix} \widetilde{c}(\omega) \\ \widetilde{m}(\omega) \\ \widetilde{c}^\dagger(-\omega) \\ \widetilde{m}^\dagger(-\omega) \end{pmatrix} = i \begin{pmatrix} \widetilde{F}_\beta(\omega) \\ \widetilde{F}^\dagger_\beta(-\omega) \end{pmatrix} \tag{B.272}$$

We now consider the light degrees of freedom to obtain two more equations.

Frequency space equations of the light degree of freedom. In Fourier space, equation (B.262) becomes

$$\begin{aligned} -i\omega\widetilde{c}(\omega) = -i(\omega_c + 2D)\widetilde{c}(\omega) - ig\Big(\widetilde{m}(\omega) + \widetilde{m}^\dagger(-\omega)\Big) - 2iD\widetilde{c}^\dagger(-\omega) \\ + \widetilde{F}_\alpha(\omega) + \widetilde{F}_1(\omega) + \widetilde{F}_2(\omega) - \Big(\widetilde{\Gamma}_\alpha(\omega) + \widetilde{\Gamma}_1(\omega) + \widetilde{\Gamma}_2(\omega)\Big)\widetilde{c}(\omega) \end{aligned} \tag{B.273}$$

$$\begin{aligned} i\Big(\omega - \omega_c - 2D + i\Big[\widetilde{\Gamma}_\alpha(\omega) + \widetilde{\Gamma}_1(\omega) + \widetilde{\Gamma}_2(\omega)\Big]\Big)\widetilde{c}(\omega) - ig\widetilde{m}(\omega) \\ -2iD\widetilde{c}^\dagger(-\omega) - ig\widetilde{m}^\dagger(-\omega) + \widetilde{F}_\alpha(\omega) + \widetilde{F}_1(\omega) + \widetilde{F}_2(\omega) \end{aligned} = 0 \tag{B.274}$$

$$\begin{aligned} \Big(\omega - \omega_c - 2D + i\Big[\widetilde{\Gamma}_\alpha(\omega) + \widetilde{\Gamma}_1(\omega) + \widetilde{\Gamma}_2(\omega)\Big]\Big)\widetilde{c}(\omega) \\ -g\widetilde{m}(\omega) - 2D\widetilde{c}^\dagger(-\omega) - g\widetilde{m}^\dagger(-\omega) \end{aligned} = i\Big(\widetilde{F}_\alpha(\omega) + \widetilde{F}_1(\omega) + \widetilde{F}_2(\omega)\Big) \tag{B.275}$$

while equation (B.264) comes out as

$$\begin{aligned} -i\omega\widetilde{c}^\dagger(-\omega) = i(\omega_c + 2D)\widetilde{c}^\dagger(-\omega) + ig\Big(\widetilde{m}(\omega) + \widetilde{m}^\dagger(-\omega)\Big) + 2iD\widetilde{c}(\omega) \\ + \widetilde{F}^\dagger_\alpha(-\omega) + \widetilde{F}^\dagger_1(-\omega) + \widetilde{F}^\dagger_2(-\omega) - \Big(\widetilde{\Gamma}^*_\alpha(-\omega) + \widetilde{\Gamma}^*_1(-\omega) + \widetilde{\Gamma}^*_2(-\omega)\Big)\widetilde{c}^\dagger(-\omega), \end{aligned} \tag{B.276}$$

$$\begin{aligned} i\Big(\omega + \omega_c + 2D + i\Big[\widetilde{\Gamma}^*_\alpha(-\omega) + \widetilde{\Gamma}^*_1(-\omega) + \widetilde{\Gamma}^*_2(-\omega)\Big]\Big)\widetilde{c}^\dagger(-\omega) \\ +ig\widetilde{m}(\omega) + 2iD\widetilde{c}(\omega) + ig\widetilde{m}^\dagger(-\omega) + \widetilde{F}^\dagger_\alpha(-\omega) + \widetilde{F}^\dagger_1(-\omega) + \widetilde{F}^\dagger_2(-\omega) \end{aligned} = 0, \tag{B.277}$$

$$\begin{aligned} 2D\widetilde{c}(\omega) + g\widetilde{m}(\omega) + g\widetilde{m}^\dagger(-\omega) \\ \Big(\omega + \omega_c + 2D + i\Big[\widetilde{\Gamma}^*_\alpha(-\omega) + \widetilde{\Gamma}^*_1(-\omega) + \widetilde{\Gamma}^*_2(-\omega)\Big]\Big)\widetilde{c}^\dagger(-\omega) \end{aligned} = i\Big(\widetilde{F}^\dagger_\alpha(-\omega) + \widetilde{F}^\dagger_1(-\omega) + \widetilde{F}^\dagger_2(-\omega)\Big). \tag{B.278}$$

Using equations (B.275) and (B.278) we can complete equation (B.272) to obtain

$$M\begin{pmatrix}\widetilde{c}(\omega)\\ \widetilde{m}(\omega)\\ \widetilde{c}^\dagger(-\omega)\\ \widetilde{m}^\dagger(-\omega)\end{pmatrix} = i\begin{pmatrix}\widetilde{F}_\alpha(\omega)+\widetilde{F}_1(\omega)+\widetilde{F}_2(\omega)\\ \widetilde{F}_\beta(\omega)\\ \widetilde{F}_\alpha^\dagger(-\omega)+\widetilde{F}_1^\dagger(-\omega)+\widetilde{F}_2^\dagger(-\omega)\\ \widetilde{F}_\beta^\dagger(-\omega)\end{pmatrix} \tag{B.279}$$

where

$$M = \begin{pmatrix}\omega-\omega_c-2D+i\left[\widetilde{\Gamma}_\alpha(\omega)+\widetilde{\Gamma}_1(\omega)+\widetilde{\Gamma}_2(\omega)\right] & -g & -2D & -g\\ -g & \omega-\omega_m+i\widetilde{\Gamma}_\beta(\omega) & -g & 0\\ 2D & g & \omega+\omega_c+2D+i\left[\widetilde{\Gamma}^*_\alpha(-\omega)+\widetilde{\Gamma}^*_1(-\omega)+\widetilde{\Gamma}^*_2(-\omega)\right] & g\\ g & 0 & g & \omega+\omega_m+i\widetilde{\Gamma}^*_\beta(-\omega)\end{pmatrix} \tag{B.280}$$

B.14.3) Input-output relations and frequency domain Langevin forces and memory kernels

Input output relations. Rewriting equation (B.246) as

$$e^{i\omega t}\alpha_\omega(t) = e^{i\omega t_0}\alpha_\omega(t_0) - \kappa^*_\alpha(\omega)\int_{t_0}^{t}\mathrm{d}t'\, e^{i\omega t'}c(t') \tag{B.281}$$

and taking the limits $t_0\to\infty$ and $t\to+\infty$ we obtain the input-output relation

$$\alpha^{\text{out}}_\omega = \alpha^{\text{in}}_\omega - \kappa^*_\alpha(\omega)\widetilde{c}(\omega) \tag{B.282}$$

where we defined the output field as $\alpha^{\text{out}}_\omega = \lim_{t\to+\infty} e^{i\omega t}\alpha_\omega(t)$. We have similar input-output relations for the other bath operators.

Frequency space Langevin forces and memory kernels. To solve the matrix equation above, we need the frequency domain expression of the Langevin forces and memory kernels. For the memory kernel, we find

$$\begin{aligned}
\widetilde{\Gamma}_\alpha(\omega) &= \int_{\mathbb{R}}\mathrm{d}t\, e^{i\omega t}\int_{\mathbb{R}^+}\mathrm{d}\omega'\left|\kappa_\alpha(\omega')\right|^2\Theta(t)e^{-i\omega' t} && \text{(B.283)}\\
&= \int_{\mathbb{R}^+}\mathrm{d}\omega'\left|\kappa_\alpha(\omega')\right|^2\int_{\mathbb{R}}\mathrm{d}t\,\Theta(t)e^{i(\omega-\omega')t} && \text{(B.284)}\\
&= \int_{\mathbb{R}^+}\mathrm{d}\omega'\left|\kappa_\alpha(\omega')\right|^2\widetilde{\Theta}(\omega-\omega') && \text{(B.285)}\\
&= \int_{\mathbb{R}^+}\mathrm{d}\omega'\left|\kappa_\alpha(\omega')\right|^2\left(\pi\delta(\omega-\omega')+i\mathrm{PV}\frac{1}{\omega-\omega'}\right) && \text{(B.286)}\\
&= \pi|\kappa_\alpha(\omega)|^2 + i\mathrm{PV}\int_{\mathbb{R}^+}\mathrm{d}\omega'\,\frac{|\kappa_\alpha(\omega')|^2}{\omega-\omega'} && \text{(B.287)}
\end{aligned}$$

where PV stands for the Cauchy principal value. We have similar results for $\widetilde{\Gamma}_\beta$ and $\widetilde{\Gamma}_{1,2}$. For the Langevin force, we have

$$\begin{aligned}
\widetilde{F}_\alpha(\omega) &= \int_{\mathbb{R}}\mathrm{d}t e^{i\omega t}\int_{\mathbb{R}^+}\mathrm{d}\omega'\,\kappa_\alpha(\omega')e^{-i\omega' t}\alpha^{\text{in}}_{\omega'} && \text{(B.288)}\\
&= \int_{\mathbb{R}^+}\mathrm{d}\omega'\,\kappa_\alpha(\omega')\alpha^{\text{in}}_{\omega'}\int_{\mathbb{R}}\mathrm{d}t e^{i(\omega-\omega')t} && \text{(B.289)}\\
&= 2\pi\int_{\mathbb{R}^+}\mathrm{d}\omega'\,\kappa_\alpha(\omega')\alpha^{\text{in}}_{\omega'}\delta(\omega-\omega') && \text{(B.290)}\\
&= \pi\kappa_\alpha(\omega)\alpha^{\text{in}}_\omega && \text{(B.291)}
\end{aligned}$$

where we used equation (III.167).

B.14.4) Relation between the output and input fields in frequency space

Let use now assume that we solve and write the solution of equation (B.279) as

$$\begin{pmatrix} \widetilde{c}(\omega) \\ \widetilde{m}(\omega) \\ \widetilde{c}^\dagger(-\omega) \\ \widetilde{m}^\dagger(-\omega) \end{pmatrix} = G(\omega) \begin{pmatrix} \widetilde{F}_\alpha(\omega) + \widetilde{F}_1(\omega) + \widetilde{F}_2(\omega) \\ \widetilde{F}_\beta(\omega) \\ \widetilde{F}_\alpha^\dagger(-\omega) + \widetilde{F}_1^\dagger(-\omega) + \widetilde{F}_2^\dagger(-\omega) \\ \widetilde{F}_\beta^\dagger(-\omega) \end{pmatrix} \tag{B.292}$$

with $G(\omega) = iM^{-1}(\omega)$.

Using equation (B.292) for positive ω, we have:

$$\widetilde{c}(\omega > 0) = G_{11}(\omega)\Big(\widetilde{F}_\alpha(\omega) + \widetilde{F}_1(\omega) + \widetilde{F}_2(\omega)\Big) + G_{12}(\omega)\widetilde{F}_\beta(\omega) \tag{B.293}$$

$$= \pi G_{11}(\omega)\big[\kappa_\alpha(\omega)\alpha_\omega^{\text{in}} + \kappa_1(\omega)p_{1,\omega}^{\text{in}} + \kappa_2(\omega)p_{2,\omega}^{\text{in}}\big] + \pi G_{12}(\omega)\kappa_\beta(\omega)\beta_\omega^{\text{in}} \tag{B.294}$$

Using the input-output relation

$$p_{1,\omega}^{\text{out}} = p_{1,\omega}^{\text{in}} - \kappa_1^*(\omega)\widetilde{c}(\omega), \tag{B.295}$$

we have

$$\frac{p_{1,\omega}^{\text{in}} - p_{1,\omega}^{\text{out}}}{\kappa_1^*(\omega)} = \pi G_{11}(\omega)\big[\kappa_\alpha(\omega)\alpha_\omega^{\text{in}} + \kappa_1(\omega)p_{1,\omega}^{\text{in}} + \kappa_2(\omega)p_{2,\omega}^{\text{in}}\big] + \pi G_{12}(\omega)\kappa_\beta(\omega)\beta_\omega^{\text{in}} \tag{B.296}$$

After rearranging the terms, we have

$$\frac{p_{1,\omega}^{\text{out}}}{\kappa_1^*(\omega)} = \frac{p_{1,\omega}^{\text{in}}}{\kappa_1^*(\omega)} - \pi G_{11}(\omega)\kappa_\alpha(\omega)\alpha_\omega^{\text{in}} - \pi G_{11}(\omega)\sum_j \kappa_j(\omega)p_{j,\omega}^{\text{in}} - \pi G_{12}(\omega)\kappa_\beta(\omega)\beta_\omega^{\text{in}} \tag{B.297}$$

and finally

$$\begin{aligned} p_{1,\omega}^{\text{out}} = &\Big(1 - G_{11}(\omega)\pi|\kappa_1(\omega)|^2\Big)p_{1,\omega}^{\text{in}} - G_{11}(\omega)\pi\kappa_1^*(\omega)\kappa_2(\omega)p_{2,\omega}^{\text{in}} \\ &- \pi\kappa_1^*(\omega)\big[G_{11}(\omega)\kappa_\alpha(\omega)\alpha_\omega^{\text{in}} + G_{12}(\omega)\kappa_\beta(\omega)\beta_\omega^{\text{in}}\big]. \end{aligned} \tag{B.298}$$

By symmetry between $p_{1,\omega}$ and $p_{2,\omega}$ we deduce that $p_{2,\omega}^{\text{out}}$ can be obtained by exchanging the indices 1 and 2 in the expression of $p_{1,\omega}^{\text{out}}$ above. Thus, we arrive the linear relation

$$\begin{pmatrix} p_{1,\omega}^{\text{out}} \\ p_{2,\omega}^{\text{out}} \end{pmatrix} = U(\omega)\begin{pmatrix} p_{1,\omega}^{\text{in}} \\ p_{2,\omega}^{\text{in}} \end{pmatrix} + \pi\begin{pmatrix} \kappa_1^*(\omega) \\ \kappa_2^*(\omega) \end{pmatrix}\big[G_{11}(\omega)\kappa_\alpha(\omega)\alpha_\omega^{\text{in}} + G_{12}(\omega)\kappa_\beta(\omega)\beta_\omega^{\text{in}}\big] \tag{B.299}$$

with

$$U(\omega) = \begin{pmatrix} 1 - G_{11}(\omega)\pi|\kappa_1(\omega)|^2 & G_{11}(\omega)\pi\kappa_1^*(\omega)\kappa_2(\omega) \\ G_{11}(\omega)\pi\kappa_2^*(\omega)\kappa_1(\omega) & 1 - G_{11}(\omega)\pi|\kappa_2(\omega)|^2 \end{pmatrix} \tag{B.300}$$

B.14.5) Reflection and transmission coefficients

We note the state of the baths $|\psi\rangle = |\psi_1\rangle\,|\psi_2\rangle\,|\psi_\alpha\rangle\,|\psi_\beta\rangle$, where the indices on the kets denote the bath. Each bath is composed of an infinity of modes, for instance

$$|\psi_1\rangle = \prod_{\omega=0}^{\infty} |\psi_\omega\rangle\,, \tag{B.301}$$

where $|\psi_\omega\rangle$ is the state of the bath mode with annihilation operator $p_{1,\omega}$. In the following we assume that the baths modelling intrinsic dissipation are such that for all frequencies $\omega/2\pi$, we have $\langle\psi_\alpha|\alpha_\omega^{\text{in}}|\psi_\alpha\rangle = \langle\psi_\beta|\beta_\omega^{\text{in}}|\psi_\beta\rangle = 0$. Furthermore, when either port 1 or port 2 are in a

coherent state, we mean that only a single mode of frequency $\omega/2\pi$ is in a coherent state (for example $\langle\psi_1|p^{\text{in}}_{1,\omega}|\psi_1\rangle = \alpha$ if port 1 is in a coherent state $|\alpha\rangle$).

Using equation (B.299), and noting U_{ij} the matrix elements of U, the reflection is

$$S_{11}(\omega) = \left.\frac{\left\langle p^{\text{out}}_{1,\omega}\right\rangle}{\left\langle p^{\text{in}}_{1,\omega}\right\rangle}\right|_{\left\langle p^{\text{in}}_{2,\omega}\right\rangle=0} = U_{11}(\omega) \tag{B.302}$$

while the transmission is

$$S_{21}(\omega) = \left.\frac{\left\langle p^{\text{out}}_{2,\omega}\right\rangle}{\left\langle p^{\text{in}}_{1,\omega}\right\rangle}\right|_{\left\langle p^{\text{in}}_{1,\omega}\right\rangle=0} = U_{21}(\omega) \tag{B.303}$$

B.15) Bloch-Siegert corrections to the Dicke model

We partition the Dicke model as

$$H = \hbar\omega_c c^\dagger c + \hbar\omega_m m^\dagger m + \hbar g(c + c^\dagger)(m + m^\dagger) \tag{B.304}$$

$$= \underbrace{\hbar\omega_c c^\dagger c + \hbar\omega_m m^\dagger m}_{=H_0} + \underbrace{\hbar g\Big(cm^\dagger + c^\dagger m\Big)}_{=H_I} + \underbrace{\hbar g\Big(cm + c^\dagger m^\dagger\Big)}_{=V}. \tag{B.305}$$

We take the Schrieffer-Wolff transformation $U = e^\Lambda$ with

$$\Lambda = \lambda\Big(c^\dagger m^\dagger - cm\Big) \tag{B.306}$$

and $\lambda = \frac{g}{\omega_c+\omega_m}$ and we assume $\lambda \ll 1$.

Recalling $[c^\dagger, c^\dagger c] = -c^\dagger$, $[c, c^\dagger c] = c$ and $[AB, CD] = A[B, C]D + [A, C]BD + CA[B, D] + C[A, D]B$,

$$[\Lambda, H_0] = \hbar\lambda\Big[c^\dagger m^\dagger - cm, \omega_c c^\dagger c + \omega_m m^\dagger m\Big] \tag{B.307}$$

$$= \hbar\lambda\Big(-\omega_c\Big(c^\dagger m^\dagger + cm\Big) - \omega_m\Big(c^\dagger m^\dagger + cm\Big)\Big) \tag{B.308}$$

$$= -V, \tag{B.309}$$

$$[\Lambda, H_I] = \hbar g\lambda\Big[c^\dagger m^\dagger - cm, cm^\dagger + c^\dagger m\Big] \tag{B.310}$$

$$= \hbar g\lambda\Big(-m^{\dagger 2} - c^{\dagger 2} - \big(c^2 + m^2\big)\Big) \tag{B.311}$$

$$= -\hbar g\lambda\Big(c^2 + c^{\dagger 2} + m^2 + m^{\dagger 2}\Big), \tag{B.312}$$

$$[\Lambda, V] = \hbar g\lambda\Big[c^\dagger m^\dagger - cm, c^\dagger m^\dagger + cm\Big] \tag{B.313}$$

$$= \hbar g\lambda\Big(\Big[c^\dagger m^\dagger, cm\Big] - \Big[cm, c^\dagger m^\dagger\Big]\Big) = 2\hbar g\lambda\Big[c^\dagger m^\dagger, cm\Big] \tag{B.314}$$

$$= 2\hbar g\lambda\Big(-m^\dagger m - cc^\dagger\Big) \tag{B.315}$$

$$= 2\hbar g\lambda\Big(-m^\dagger m - c^\dagger c - 1\Big) \tag{B.316}$$

$$= -2\hbar g\lambda\left[\left(c^\dagger c + \frac{1}{2}\right) + \left(m^\dagger m + \frac{1}{2}\right)\right] \tag{B.317}$$

Going to the first order in λ requires second order in Λ since $[\Lambda, H_0]$ is 0-th order. The Baker-Campbell-Hausdorff formula gives

$$e^{\Lambda} H e^{-\Lambda} = H + [\Lambda, H] + \frac{1}{2!}[\Lambda, [\Lambda, H]] + \mathcal{O}(\lambda) \tag{B.318}$$

$$= H_0 + H_I + V + [\Lambda, H_0] + [\Lambda, H_I] + [\Lambda, V] + \frac{1}{2!}[\Lambda, [\Lambda, H]] + \mathcal{O}(\lambda) \tag{B.319}$$

$$= H_0 + H_I + [\Lambda, H_I] + [\Lambda, V] + \frac{1}{2!}[\Lambda, [\Lambda, H_0]] + \underbrace{\frac{1}{2!}[\Lambda, [\Lambda, H_I + V]]}_{\mathcal{O}(\lambda^2)} + \mathcal{O}(\lambda) \tag{B.320}$$

$$= H_0 + H_I - \hbar g\lambda\Big(c^2 + {c^\dagger}^2 + m^2 + {m^\dagger}^2\Big) - 2\hbar g\lambda\left[\left(c^\dagger c + \frac{1}{2}\right) + \left(m^\dagger m + \frac{1}{2}\right)\right] + \frac{1}{2!}[\Lambda, -V] + \mathcal{O}(\lambda) \tag{B.321}$$

$$= H_0 + H_I - \hbar g\lambda\left[\left(c^\dagger c + \frac{1}{2}\right) + \left(m^\dagger m + \frac{1}{2}\right)\right] - \hbar g\lambda\Big(c^2 + {c^\dagger}^2 + m^2 + {m^\dagger}^2\Big) + \mathcal{O}(\lambda) \tag{B.322}$$

$$= \hbar\omega_c' c^\dagger c + \hbar\omega_m' m^\dagger m + \hbar g\Big(cm^\dagger + c^\dagger m\Big) \tag{B.323}$$

$$+ \hbar\frac{g^2}{\omega_c + \omega_m}\Big(c^2 + {c^\dagger}^2 + m^2 + {m^\dagger}^2\Big) + \mathcal{O}(\lambda), \tag{B.324}$$

where $\omega_c' = \omega_c - \frac{g^2}{\omega_c+\omega_m}$ and $\omega_m' = \omega_m - \frac{g^2}{\omega_c+\omega_m}$.

B.16) Proof of the standard sum rule

We follow Wang (1999) [449], and we note $|\psi_k\rangle$ the eigenstates with energy $\hbar\omega_k$ the total Hamiltonian H, i.e. $H|\psi_k\rangle = \hbar\omega_k|\psi_k\rangle$. We consider a hermitian operator A, and following the notations of appendix A.1 we note $\left[H, A^{(n)}\right]$ the n-th iterated commutator of A with the Hamiltonian.

We first note that we have on the one hand

$$\left(\left[H, A^{(1)}\right]\right)^\dagger = (HA - AH)^\dagger = [A, H] = -\left[H, A^{(1)}\right], \tag{B.325}$$

and on the other hand, inserting a resolution of the identity $1 = \sum_k |\psi_k\rangle\langle\psi_k|$

$$\langle\psi_i|\left[H, A^{(1)}\right]|\psi_j\rangle = \langle\psi_i|HA - AH|\psi_j\rangle \tag{B.326}$$

$$= \sum_k \left(\delta_{ki}\hbar\omega_k\langle\psi_k|A|\psi_j\rangle - \delta_{kj}\hbar\omega_j\langle\psi_i|A|\psi_k\rangle\right) \tag{B.327}$$

$$= (\hbar\omega_i - \hbar\omega_j)\langle\psi_i|A|\psi_j\rangle. \tag{B.328}$$

We can prove by induction that equations (B.325) and (B.328) generalise to

$$\left(\left[H, A^{(k)}\right]\right)^\dagger = (-1)^k\left[H, A^{(k)}\right] \tag{B.329}$$

$$\langle\psi_i|\left[H, A^{(k)}\right]|\psi_j\rangle = (\hbar\omega_i - \hbar\omega_j)^k\langle\psi_i|A|\psi_j\rangle. \tag{B.330}$$

for $k \geqslant 1$. Indeed, we have

$$\left(\left[H, A^{(k+1)}\right]\right)^\dagger = \left(H\left[H, A^{(k)}\right] - \left[H, A^{(k)}\right]H\right)^\dagger \tag{B.331}$$

$$= \left(\left[H, A^{(k)}\right]\right)^\dagger H - H\left(\left[H, A^{(k)}\right]\right)^\dagger \tag{B.332}$$

$$= (-1)^k\left(\left[H, A^{(k)}\right]H - H\left[H, A^{(k)}\right]\right) = (-1)^{k+1}\left[H, A^{(k+1)}\right], \tag{B.333}$$

and

$$\langle\psi_i|\Big[H,A^{(k+1)}\Big]|\psi_j\rangle = \langle\psi_i|H\Big[H,A^{(k)}\Big]-\Big[H,A^{(k)}\Big]H|\psi_j\rangle \tag{B.334}$$

$$= \sum_l \Big(\delta_{li}\hbar\omega_l \langle\psi_l|\Big[H,A^{(k)}\Big]|\psi_j\rangle - \delta_{lj}\hbar\omega_j \langle\psi_i|\Big[H,A^{(k)}\Big]|\psi_l\rangle\Big) \tag{B.335}$$

$$= (\hbar\omega_i-\hbar\omega_j)\langle\psi_i|\Big[H,A^{(k)}\Big]|\psi_j\rangle \tag{B.336}$$

$$= (\hbar\omega_i-\hbar\omega_j)^{k+1}\langle\psi_i|[H,A]|\psi_j\rangle\,. \tag{B.337}$$

Using the properties of equations (B.329) and (B.330), we find

$$\langle\psi_i|\Big[A,\Big[H,A^{(k)}\Big]\Big]|\psi_i\rangle = \sum_j \Big(\langle\psi_i|A|\psi_j\rangle\,\langle\psi_j|\Big[H,A^{(k)}\Big]|\psi_i\rangle - \langle\psi_i|\Big[H,A^{(k)}\Big]|\psi_j\rangle\,\langle\psi_j|A|\psi_i\rangle\Big) \tag{B.338}$$

$$= \sum_j \Big(\langle\psi_i|A|\psi_l\rangle(\hbar\omega_j-\hbar\omega_i)^k\langle\psi_j|A|\psi_i\rangle - (\hbar\omega_i-\hbar\omega_j)^k|\langle\psi_i|A|\psi_j\rangle|^2\Big) \tag{B.339}$$

$$= \sum_j \Big(1-(-1)^k\Big)(\hbar\omega_j-\hbar\omega_i)^k|\langle\psi_i|A|\psi_j\rangle|^2 \tag{B.340}$$

Evaluating in $k=1$ gives the desired sum rule

$$\langle\psi_i|[A,[H,A]]|\psi_i\rangle = 2\sum_j(\hbar\omega_j-\hbar\omega_i)|\langle\psi_i|A|\psi_j\rangle|^2. \tag{B.341}$$

B.17) A shortcut to computing the equation of motion of quadratures

Assume that an operator a follows an equation of the form

$$\dot{a} = (-\kappa-i\omega)a+(\gamma-ig)a^\dagger \tag{B.342}$$

$$= -i(\omega-i\kappa)a - i(g+i\gamma)a^\dagger \tag{B.343}$$

with $\kappa,\omega,g,\gamma\in\mathbb{R}$ and the dot indicates a time derivative. Defining the quadratures $x=(a+a^\dagger)/\sqrt{2}$ and $y=i(a^\dagger-a)/\sqrt{2}$, we take the appropriate linear combination of the equation for a above and obtain

$$\dot{x} = \frac{\big((-\kappa-i\omega)a+(\gamma-ig)a^\dagger\big)+\big((-\kappa+i\omega)a^\dagger+(\gamma+ig)a\big)}{\sqrt{2}} \tag{B.344}$$

$$= -\kappa x+\omega y+\gamma x-gy, \tag{B.345}$$

$$\dot{y} = i\frac{(-\kappa+i\omega)a^\dagger+(\gamma+ig)a-(-\kappa-i\omega)a-(\gamma-ig)a^\dagger}{\sqrt{2}} \tag{B.346}$$

$$= -\kappa y-\omega x-\gamma y-gx, \tag{B.347}$$

which tells us how an operator is transformed into a quadrature depending on the "complexness" of its coefficient.

Note that these rules can be generalised if other operators are present. For instance, consider

$$\dot{a} = (-\kappa-i\omega)a - ig\Big(b+b^\dagger\Big), \tag{B.348}$$

with b another operator. Defining the quadratures for b as $X=(b+b^\dagger)/\sqrt{2}$ and $Y=i(b^\dagger-b)/\sqrt{2}$, we obtain

$$\dot{x} = -\kappa x+\omega y, \tag{B.349}$$

$$\dot{y} = -\kappa y-\omega x-2gX. \tag{B.350}$$

B.18) Proof of the sum rule for interacting photons

In this appendix, we prove the sum rule given in equation (VII.54). To prove this result, first remember that the conjugate momentum for the electromagnetic field is $\Pi = \epsilon_0 \dot{A}$. Thus,

$$\Pi = \epsilon_0 \dot{A} = \frac{\epsilon_0}{i\hbar}[A, H]. \tag{B.351}$$

From there, we find that

$$\begin{aligned}
\langle\psi_i|\Pi|\psi_j\rangle &= \frac{\epsilon_0}{i\hbar}(\langle\psi_i|AH|\psi_j\rangle - \langle\psi_i|HA|\psi_j\rangle) && \text{(B.352)}\\
&= \frac{\epsilon_0}{i\hbar}\sum_k (\langle\psi_i|A|\psi_k\rangle\langle\psi_k|H|\psi_j\rangle - \langle\psi_i|H|\psi_k\rangle\langle\psi_k|A|\psi_j\rangle) && \text{(B.353)}\\
&= \frac{\epsilon_0}{i}\sum_k (\langle\psi_i|A|\psi_k\rangle\delta_{kj}\omega_j - \delta_{ik}\omega_k\langle\psi_k|A|\psi_j\rangle) && \text{(B.354)}\\
&= \frac{\epsilon_0}{i}(\omega_j - \omega_i)\langle\psi_i|A|\psi_j\rangle && \text{(B.355)}\\
&= i\epsilon_0\omega_{ij}\langle\psi_i|A|\psi_j\rangle, && \text{(B.356)}
\end{aligned}$$

which corresponds to equation (3) in the original paper [436]. Additionally,

$$\begin{aligned}
\dot{\mathcal{Q}}^{(n)} &= \frac{1}{i\hbar}\Big[\mathcal{Q}^{(n)}, H\Big] = \frac{1}{i\hbar}\Big[\mathcal{Q}^{(n)}, H_F\Big] && \text{(B.357)}\\
&= \frac{1}{i\hbar}\frac{1}{\sqrt{2}}\left[c_n + c_n^\dagger, \sum_k \hbar\omega_k c_k^\dagger c_k\right] = \frac{\omega_n}{i}\frac{c_n - c_n^\dagger}{\sqrt{2}} = \omega_n \mathcal{P}^{(n)}. && \text{(B.358)}
\end{aligned}$$

Hence, the commutation relation between the quadratures of mode n reads

$$\begin{aligned}
i &= \Big[\mathcal{Q}^{(n)}, \mathcal{P}^{(n)}\Big] = \frac{1}{\omega_n}\Big[\mathcal{Q}^{(n)}, \dot{\mathcal{Q}}^{(n)}\Big] = \frac{1}{i\hbar\omega_n}\Big[\mathcal{Q}^{(n)}, \Big[\mathcal{Q}^{(n)}, H_F\Big]\Big] = \frac{1}{i\hbar\omega_n}\Big[\mathcal{Q}^{(n)}, \Big[\mathcal{Q}^{(n)}, H\Big]\Big] && \text{(B.359)}\\
&= \frac{1}{i\hbar\omega_n}\Big[\mathcal{Q}^{(n)}, \mathcal{Q}^{(n)}H - H\mathcal{Q}^{(n)}\Big] && \text{(B.360)}\\
&= \frac{1}{i\hbar\omega_n}\Big({\mathcal{Q}^{(n)}}^2 H - \mathcal{Q}^{(n)}H\mathcal{Q}^{(n)} - \mathcal{Q}^{(n)}H\mathcal{Q}^{(n)} + H{\mathcal{Q}^{(n)}}^2\Big). && \text{(B.361)}
\end{aligned}$$

Taking the matrix elements and inserting the identity[1],

$$\begin{aligned}
\delta_{ij} &= \frac{-1}{\hbar\omega_n}\langle\psi_i|{\mathcal{Q}^{(n)}}^2 H - 2\mathcal{Q}^{(n)}H\mathcal{Q}^{(n)} + H{\mathcal{Q}^{(n)}}^2|\psi_j\rangle && \text{(B.362)}\\
&= \frac{-1}{\hbar\omega_n}\left(\sum_k \langle\psi_i|{\mathcal{Q}^{(n)}}^2|\psi_k\rangle\delta_{kj}\hbar\omega_j + \delta_{ik}\hbar\omega_k\langle\psi_k|{\mathcal{Q}^{(n)}}^2|\psi_j\rangle - 2\langle\psi_i|\mathcal{Q}^{(n)}H|\psi_k\rangle\langle\psi_k|\mathcal{Q}^{(n)}|\psi_j\rangle\right) && \text{(B.363)}\\
&= \frac{-1}{\hbar\omega_n}\left(\langle\psi_i|{\mathcal{Q}^{(n)}}^2|\psi_j\rangle\hbar\omega_j + \hbar\omega_i\langle\psi_i|{\mathcal{Q}^{(n)}}^2|\psi_j\rangle - 2\sum_k \hbar\omega_k\langle\psi_i|\mathcal{Q}^{(n)}|\psi_k\rangle\langle\psi_k|\mathcal{Q}^{(n)}|\psi_j\rangle\right) && \text{(B.364)}\\
&= \frac{1}{\omega_n}\sum_k \Big(2\omega_k\langle\psi_i|\mathcal{Q}^{(n)}|\psi_k\rangle\langle\psi_k|\mathcal{Q}^{(n)}|\psi_j\rangle - (\omega_j + \omega_i)\langle\psi_i|\mathcal{Q}^{(n)}|\psi_k\rangle\langle\psi_k|\mathcal{Q}^{(n)}|\psi_j\rangle\Big) && \text{(B.365)}\\
&= \sum_k \frac{\omega_{ki} + \omega_{kj}}{\omega_n}\langle\psi_i|\mathcal{Q}^{(n)}|\psi_k\rangle\langle\psi_k|\mathcal{Q}^{(n)}|\psi_j\rangle && \text{(B.366)}
\end{aligned}$$

as announced.

[1] Remember that $I = \sum_k |\psi_k\rangle\langle\psi_k|$.

Appendix C

Original works

This appendix contains the original works that have been undertaken during this thesis. As required by the University of Adelaide, each work is preceded by a *statement of authorship*, outlining the contributions of the authors.

Contents

C.1) Manifestation of the coupling phase in microwave cavity magnonics **207**
C.2) Using COMSOL Multiphysics® to model hybrid magnon-photon systems **224**
C.3) Engineering synthetic gauge fields through the coupling phases in cavity magnonics . . **238**
C.4) Discrete (geometric) phases in loop-coupled bosonic systems **254**
C.5) Level attraction from interferences in two-tone driving **260**
C.6) Engineering non-reciprocal behaviour in a ring of four bosonic modes **281**
C.7) Effective Hamiltonian for the ultrastrong magnon-photon Zeeman coupling **289**
C.8) Cavity-mediated ultrastrong magnon-magnon coupling **299**
C.9) Study of the optomechanical coupling between a cavity photon and a magnon **304**
C.10) Nonadiabatic quantum control of valley states in silicon **312**

C.1) Manifestation of the coupling phase in microwave cavity magnonics

Statement of Authorship

Title of Paper	Manifestation of the Coupling Phase in Microwave Cavity Magnonics
Publication Status	☑ Published ☐ Accepted for Publication ☐ Submitted for Publication ☐ Unpublished and Unsubmitted work written in manuscript style
Publication Details	Physical Review Applied , Vol. 19, No. 5, 2023-05

Principal Author

Name of Principal Author (Candidate)	Alan Gardin
Contribution to the Paper	Analysed experimental data and developed a theoretical model, which once generalised led to thetheoretical discussion in the paper. Wrote the manuscript, and carried out the theoretical calculations.
Overall percentage (%)	60
Certification:	This paper reports on original research I conducted during the period of my Higher Degree by Research candidature and is not subject to any obligations or contractual agreements with a thi inclusion in this thesis. I am the primary author of this paper.
Signature	Date 22/01/2024

Co-Author Contributions

By signing the Statement of Authorship, each author certifies that:

i. the candidate's stated contribution to the publication is accurate (as detailed above);

ii. permission is granted for the candidate in include the publication in the thesis; and

iii. the sum of all co-author contributions is equal to 100% less the candidate's stated contribution.

Name of Co-Author	Jeremy Bourhill
Contribution to the Paper	Proposed a cavity design and measured it, leading to the idea of a coupling phase. Read and provided comments on the manuscript.
Signature	Date 05/02/2024

Name of Co-Author	Vincent Vlaminck
Contribution to the Paper	Proposed a cavity design and measured it, leading to the idea of a coupling phase. Read and provided comments on the manuscript.
Signature	Date 02/02/2024

Name of Co-Author	Christian Person		
Contribution to the Paper	Managed and gave directions to the project. Read and provided comments on the manuscript.		
Signature		Date	01/02/2024

Name of Co-Author	Christophe Fumeaux		
Contribution to the Paper	Managed and gave directions to the project. Read and provided comments on the manuscript.		
Signature		Date	01/02/2024

Name of Co-Author	Vincent Castel		
Contribution to the Paper	Managed and gave directions to the project. Proposed a cavity design and measured it, leading to the idea of a coupling phase. Read and provided comments on the manuscript.		
Signature		Date	01/02/2024

Name of Co-Author	Giuseppe Tettamanzi		
Contribution to the Paper	Managed and gave directions to the project. Read and provided comments on the manuscript.		
Signature		Date	01/02/2024

PHYSICAL REVIEW APPLIED **19,** 054069 (2023)

Manifestation of the Coupling Phase in Microwave Cavity Magnonics

Alan Gardin,[1,2,3,*] Jeremy Bourhill,[2,4] Vincent Vlaminck,[2,3] Christian Person,[2,3] Christophe Fumeaux,[5] Vincent Castel,[2,3] and Giuseppe C. Tettamanzi[1,6]

[1] *School of Physics, The University of Adelaide, Adelaide, SA 5005, Australia*
[2] *IMT Atlantique, Technopole Brest-Iroise, CS 83818, Brest Cedex 3 29238, France*
[3] *Lab-STICC (UMR 6285), CNRS, Technopole Brest-Iroise, CS 83818, Brest Cedex 3 29238, France*
[4] *ARC Centre of Excellence for Engineered Quantum Systems and ARC Centre of Excellence for Dark Matter Particle Physics, Department of Physics, University of Western Australia, 35 Stirling Highway, Crawley, Western Australia 6009, Australia*
[5] *School of Electrical and Electronic Engineering, The University of Adelaide, Adelaide, SA 5005, Australia*
[6] *School of Chemical Engineering and Advanced Materials, The University of Adelaide, Adelaide, SA 5005, Australia*

(Received 11 January 2023; revised 1 February 2023; accepted 14 April 2023; published 22 May 2023)

The interaction between microwave photons and magnons is well understood and originates from the Zeeman coupling between spins and a magnetic field. Interestingly, the magnon-photon interaction is accompanied by a phase factor, which can usually be neglected. However, under the rotating wave approximation, if two magnon modes simultaneously couple with two cavity resonances, this phase cannot be ignored as it changes the physics of the system. We consider two such systems, each differing by the sign of one of the magnon-photon coupling strengths. This simple difference, originating from the various coupling phases in the system, is shown to preserve, or destroy, two potential applications of hybrid photon-magnon systems, namely dark-mode memories and cavity-mediated coupling. The observable consequences of the coupling phase in this system is akin to the manifestation of a discrete Pancharatnam-Berry phase, which may be useful for quantum information processing and the creation of nonreciprocal devices using proper cavity engineering.

DOI: 10.1103/PhysRevApplied.19.054069

I. INTRODUCTION

Magnons are quasiparticles associated with the collective excitation of spins in magnetic materials. Magnons in ferrimagnetic insulators such as yttrium iron garnet (YIG) are promising for information transduction, due to their ability to couple to a plethora of systems, such as mechanical resonators or optical and microwave photonic modes [1,2]. The emerging field of cavity magnonics focuses on the photon-magnon interaction confined within cavities at microwave or optical frequencies [3–5]. In the microwave domain, strong and ultrastrong coherent coupling have been demonstrated [6–10], with the latter even reachable at room temperature [11].

Owing to this flexibility, indirect coupling of two noninteracting systems by an auxiliary mode has been investigated in Refs. [12–18]. For instance, two macroscopically distant magnetic samples in a cavity can indirectly couple by using the cavity photons as a bridge [15–21]. Notably, in this configuration some eigenmodes are "dark," in the sense that they do not lead to an experimental signature when probing the system. This dark-mode physics can be used to create dark-mode gradient memories as experimentally demonstrated in Zhang *et al.* [21]. Another example of cavity-mediated coupling is the coupling of a magnon with a superconducting qubit, again mediated by a common cavity mode [22,23]. This versatile configuration motivated studies of quantum magnonics [24], with proposals for single-magnon sources [25,26], multimagnon blockade [27], single-shot detection of a single magnon [28] and quantum sensing of magnons [29].

These applications rely on the coupling between microwave photons and magnons, which physically originates from the Zeeman coupling between the spins in the ferrimagnetic material and the cavity's rf magnetic field [30]. Adopting a quantum formalism to describe this coupling allows for the precise computation of the coupling strength based on microscopic parameters and the cavity geometry [31]. Interestingly, the coherent magnon-photon coupling term resulting from the Zeeman coupling term is accompanied by a phase factor. This phase, different from that in dissipative magnon-photon coupling, has never been discussed explicitly in the cavity magnonics

*alan.gardin@adelaide.edu.au

 © 2023 American Physical Society

literature, probably due to its inconspicuous nature in the systems considered so far.

The main contribution of this paper is to highlight how the coupling phases can become relevant in systems composed of several magnon and cavity modes. To that effect, we begin by explaining the origin of the coupling phase between a microwave photon and a magnon in Sec. II. In Sec. III, we introduce a hybrid system composed of two YIG spheres, each coupling to two magnetic eigenmodes of a microwave cavity. We show that the various magnon-photon coupling phases in such a system lead to an observable quantity θ parametrizing the Hamiltonian. To illustrate the impact of the physical phase θ, we study the physics of such a system in Sec. IV, and find that both cavity-mediated coupling and dark-mode physics are θ dependent.

II. COUPLING PHASE BETWEEN A MICROWAVE PHOTON AND A MAGNON

A. Free Hamiltonian

In this section, we consider the interaction between one YIG sphere and one magnetic eigenmode of a microwave cavity. The geometry of the cavity fixes the resonance frequency $\omega_c/2\pi$ of the magnetic mode $\mathbf{H}$. These two quantities can be obtained by solving Maxwell's equations, for instance using an electromagnetic finite-element modeling software such as COMSOL Multiphysics®.

The lowest-order magnetostatic mode in the YIG sphere (the Kittel mode, $\mathbf{k} = 0$) corresponds to a collective precession of the spins, which can be described using a macroscopic spin [32,33]. Whilst higher-order standing-wave modes (for $\mathbf{k} \neq 0$) exist [34], we focus on the fundamental uniform mode in this work. For a spherical YIG sample, the ferromagnetic resonance (FMR) frequency $\omega_m/2\pi$ can be tuned by an applied static magnetic field $\mathbf{H}_0 = H_0\hat{\mathbf{z}}$ as $\omega_m = \gamma|\mathbf{H}_0|$, with γ the gyromagnetic ratio.

After quantization of the electromagnetic field, the cavity mode takes the form of a quantized harmonic oscillator $\hbar\omega_c c^\dagger c$, described using bosonic annihilation and creation operators c and $c^\dagger$, respectively. Provided the number of magnons is negligible compared to the number of spins in the YIG, we can describe the magnon by a bosonic annihilation operator m after a Holstein-Primakoff transformation [35], leading to a harmonic oscillator for the magnon mode [34]. The resulting free Hamiltonian (i.e., without interactions) is the sum of two quantized harmonic oscillators

$$H_{\text{free}} = \hbar\omega_c c^\dagger c + \hbar\omega_m m^\dagger m, \tag{1}$$

describing the cavity and magnon mode, respectively. Note that these operators commute.

B. Interaction term

The magnetic mode in the cavity, $\mathbf{H}$, couples to the macrospin of the YIG sphere by a Zeeman interaction. Assuming the cavity mode $\mathbf{H}$ has no z dependence (for instance, by considering a re-entrant cavity [30,31,36,37]), the interaction term reads (details in Appendix A)

$$H_I = \hbar g e^{i\varphi}\left(c + c^\dagger\right) m^\dagger + \hbar g e^{-i\varphi}\left(c + c^\dagger\right) m, \tag{2}$$

where the coupling strength $g/2\pi > 0$ and coupling phase $\varphi > 0$ are real numbers. The coupling strength has the well-known expression [30,31]

$$\frac{g}{2\pi} = \eta\sqrt{\omega_c}\frac{\gamma}{4\pi}\sqrt{\frac{\mu}{g_L\mu_B}\mu_0\hbar n_s}, \tag{3}$$

where μ_B is the Bohr magneton, $\mu = 5\mu_B$ the magnetic moment of YIG, $g_L = 2$ the Landé g factor, μ_0 the magnetic permeability of vacuum, $n_s = 4.22 \times 10^{27}\ \text{m}^{-3}$ the spin density of YIG, and the so-called form factor

$$\eta = \sqrt{\frac{\left(\int_{V_m}\mathbf{H}\cdot\hat{\mathbf{x}}d^3r\right)^2 + \left(\int_{V_m}\mathbf{H}\cdot\hat{\mathbf{y}}d^3r\right)^2}{V_m\int_{V_c}|\mathbf{H}|^2d^3r}}, \tag{4}$$

with V_c the volume of the cavity and V_m the volume of the magnetic sample. On the other hand, the coupling phase φ reads

$$\varphi = \arg\widetilde{H}, \tag{5}$$

where

$$\widetilde{H} = \int_{V_m}\mathbf{H}\cdot\hat{\mathbf{x}}d^3r + i\int_{V_m}\mathbf{H}\cdot\hat{\mathbf{y}}d^3r. \tag{6}$$

From the definition of $\widetilde{H}$, we see that the coupling phase depends on the orientation of the cavity's magnetic mode $\mathbf{H}$ traversing the magnetic sample.

For moderate values of the coupling strength $g/2\pi$, we can perform the rotating-wave approximation (RWA) and neglect the counter-rotating terms $cm + c^\dagger m^\dagger$ in Eq. (2), so that the interaction simplifies to

$$H_I = \hbar g\left(e^{i\varphi}cm^\dagger + e^{-i\varphi}c^\dagger m\right), \tag{7}$$

which is valid in the strong coupling regime ($g/\omega_c < 0.1$), but not in the ultrastrong coupling regime ($g/\omega_c \geqslant 0.1$) [11]. We refer the reader to Refs. [38–40] for details about the ultrastrong coupling regime and the applicability of the RWA. In the remainder of this paper, we always apply the RWA, and consider Eq. (7) instead of Eq. (2).

To conclude this section, we would like to mention that the coupling phase φ is fundamentally different from

the phase factor used to model dissipative couplings [41], or two-tone driving experiments [42–44]. Indeed, the magnon-photon dissipative coupling can be modeled as

$$H_{I,\text{dissipative}} = \hbar J(cm^\dagger + e^{i\phi}c^\dagger m), \tag{8}$$

where J and ϕ are constants. We notice that this term is not Hermitian, contrary to Eq. (7), and leads to complex eigenvalues. This is at the origin of the spectral signature of dissipatively coupled systems, which is the attraction of energy levels. Conversely, a Hermitian system guarantees real eigenvalues, and the coupling manifests as the standard level repulsion instead, or in other words, an anticrossing in the spectrum.

III. EXAMPLE WITH A PHYSICAL PHASE

The previous section highlights the presence of a coupling phase φ for each magnon-photon coupling term. In this section, we consider a system under the rotating-wave approximation composed of two identical YIG spheres, each coupling to two magnetic eigenmodes of the cavity. The free Hamiltonian of the previous section is naturally generalized to

$$H_{\text{free}} = \hbar\omega_{c,0}c_0^\dagger c_0 + \hbar\omega_{c,1}c_1^\dagger c_1 + \hbar\omega_{m,0}m_0^\dagger m_0 + \hbar\omega_{m,1}m_1^\dagger m_1, \tag{9}$$

where the c_k describe the two magnetic eigenmodes of the cavity, and m_k the two magnon modes associated with each YIG sphere. Again, the operators c_k and m_k all commute with each other, as they describe independent harmonic oscillators. We introduce the notations ω_o and δ_o for each operator $o \in \{c, m\}$ as

$$\omega_o = \frac{\omega_{o,0} + \omega_{o,1}}{2}, \quad \delta_o = \frac{\omega_{o,1} - \omega_{o,0}}{2}, \tag{10}$$

so that

$$\omega_{o,0} = \omega_o - \delta_o, \quad \omega_{o,1} = \omega_o + \delta_o. \tag{11}$$

The microwave cavity design determines the two resonances of the cavity modes, and hence the detuning δ_c between them and the average cavity resonance ω_c. For the magnons, the applied magnetic field $\mathbf{H}_0$ tunes the average magnon frequency $\omega_m = \gamma|\mathbf{H_0}|$, whilst the magnon detuning δ_m can be created by a permanent magnet or a coil placed near the YIG spheres (such a setup was used in Ref. [21], for instance).

Assuming that both magnon modes couple with the same coupling strength g_k to the cavity mode c_k, the interaction Hamiltonian under the RWA is generalized to

$$H_I = \hbar g_0 e^{i\varphi_{00}} c_0 m_0^\dagger + \hbar g_0 e^{i\varphi_{01}} c_0 m_1^\dagger + \hbar g_1 e^{i\varphi_{10}} c_1 m_0^\dagger + \hbar g_1 e^{i\varphi_{11}} c_1 m_1^\dagger + \text{h.c.}, \tag{12}$$

and h.c. denotes the omitted Hermitian conjugate terms. This interaction Hamiltonian can be simplified by focusing all the coupling phases into one term (see Fig. 1) using unitary transformations (we recall some elementary properties of unitary transformations in Appendix B). The transformed interaction Hamiltonian is

$$H_{I,\theta} = \hbar g_0 c_0 m_0^\dagger + \hbar g_0 c_0 m_1^\dagger + \hbar g_1 c_1 m_0^\dagger + \hbar g_1 e^{i\theta} c_1 m_1^\dagger + \text{h.c.}, \tag{13}$$

with $\theta = \varphi_{11} - \varphi_{01} - (\varphi_{10} - \varphi_{00})$. The "physical phase" θ is reminiscent of a discrete Pancharatnam-Berry phase, a

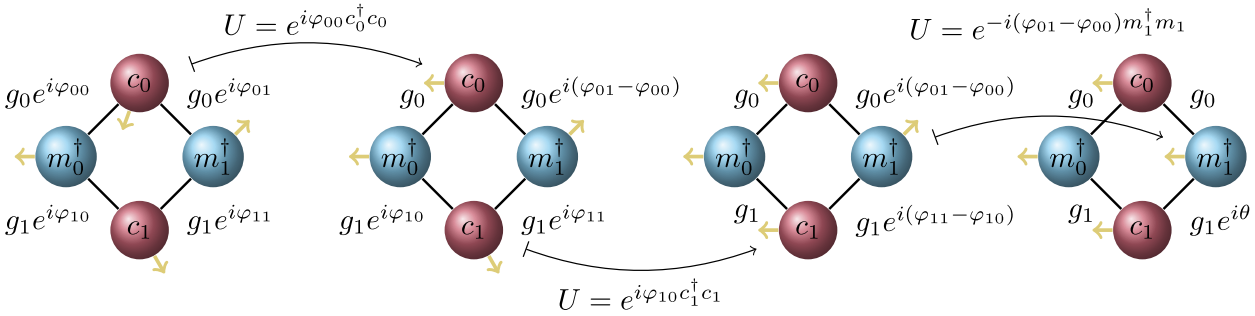


FIG. 1. Illustration of the appearance of a physical phase θ when two magnon modes m_0, m_1 (blue circles) both couple to two cavity modes c_0, c_1 (red circles). The black lines between each circle represent a coupling described by Eq. (7) (the Hermitian conjugate term is omitted for readability). The coupling phase measures the difference in orientation of the yellow arrows coming out of each circle. By moving to an appropriate reference frame using a unitary transformation, we can align the yellow arrows of two interacting modes, hence removing the coupling phase. We successively (from left to right) rotate the cavity mode c_0, the cavity mode c_1, and finally the magnon mode m_1 to align the yellow arrows with that of m_0. After successive rotation of the operators, all yellow arrows point in the same direction, and yet a physical phase $\theta = \varphi_{11} - \varphi_{01} - (\varphi_{10} - \varphi_{00})$ remains. Note that the free Hamiltonian is unaffected by the successive rotation of the modes, see Appendix B.

gauge-invariant geometrical phase factor originating from the existence of a local $U(1)$ gauge degree of freedom for each state involved in a loop in some parameter space [45]. This $U(1)$ gauge is nothing but a choice of phase, which in our system is the coupling phase located on the black lines of Fig. 1. The various coupling phases are linked to each other through the circles, forming a loop—leading to an observable physical phase θ.

To conclude this section, we note that most systems studied in the literature consist of single magnon-photon systems, or several magnon modes coupling to a single cavity mode. In particular, setups comprised of two magnon modes coupling to one cavity mode have attracted interest for indirect coupling and dark-mode physics [15–17,19–21], as well as the generation of entangled states [46–48]. In these cases, the coupling phases do not lead to a physical phase, as we show in Appendix C. This is in stark contrast with the system proposed here.

IV. INFLUENCE OF THE PHYSICAL PHASE

We now highlight the θ-dependent physics of the system described in the previous section, i.e.,

$$H_\theta = H_{\text{free}} + H_{I,\theta}, \tag{14}$$

with H_{free} and $H_{I,\theta}$ given by Eqs. (9) and (13). While θ could in principle take any value in $[0, 2\pi]$, we focus our analysis on $\theta = 0$ and $\theta = \pi$, differing only in the sign of the coupling strength of the last term.

A. Diagonalization method

The coupling between the photonic and matter degrees of freedom described by Eq. (13) leads to the appearance of quasiparticles known as polaritons. Polaritons are hybridized light-matter states and, in the context of cavity magnonics, they are known as cavity magnon polaritons (CMP) [3,49]. Diagonalization of the system allows one to find the frequencies of the polaritons, as well as their composition in terms of the operators c_k for the cavity modes, and the operators m_k for the magnon modes. All the modes of the system being bosonic, diagonalization can be achieved by writing $H_\theta = \hbar v^\dagger H v$ with $v = (c_0, c_1, m_0, m_1)^t$ (^{t} indicates matrix transposition) and

$$A = \begin{pmatrix} \omega_{c,0} & 0 & g_0 & g_0 \\ 0 & \omega_{c,1} & g_1 & g_1 e^{-i\theta} \\ g_0 & g_1 & \omega_{m,0} & 0 \\ g_0 & g_1 e^{i\theta} & 0 & \omega_{m,1} \end{pmatrix}. \tag{15}$$

After diagonalization of A, the eigenvectors give the polaritonic operators p_μ, while the eigenvalues give the polaritonic frequencies $\omega_\mu/2\pi$. The polaritons can be expressed in terms of the initial operators as

$$p_\mu = u_{\mu 0} c_0 + u_{\mu 1} c_1 + v_{\mu 2} m_0 + v_{\mu 3} m_1, \tag{16}$$

where the coefficients u (v) are the first (last) two components of the eigenvectors of A.

We note that in general, diagonalizing A amounts to solving a polynomial equation of degree four, namely

$$\det(A - \omega_\mu I_4) = 0, \tag{17}$$

where I_4 is the 4×4 identity matrix. Whilst analytical solutions exist, they are rather unpleasant and do not clarify the physics.

B. Spectrum and cavity-mediated coupling

1. Spectral features

We numerically diagonalized Eq. (15) for $\theta = 0$ and $\theta = \pi$ in Fig. 2. The coherent magnon-photon couplings manifest as two anticrossings, each located near the resonance of the associated cavity mode (i.e., at $\omega_c \pm \delta_c$). We observe that the value of the physical phase θ seems to have an impact only when $\delta_m = 0$, since as δ_m increases the cases $\theta = 0$ and $\theta = \pi$ become less distinguishable.

Interestingly, it appears that when $\delta_m = 0$ and $\omega_m = \omega_c$, the eigenvalues ω_1 and ω_2 cross for $\theta = 0$ [Fig. 2(a)], but

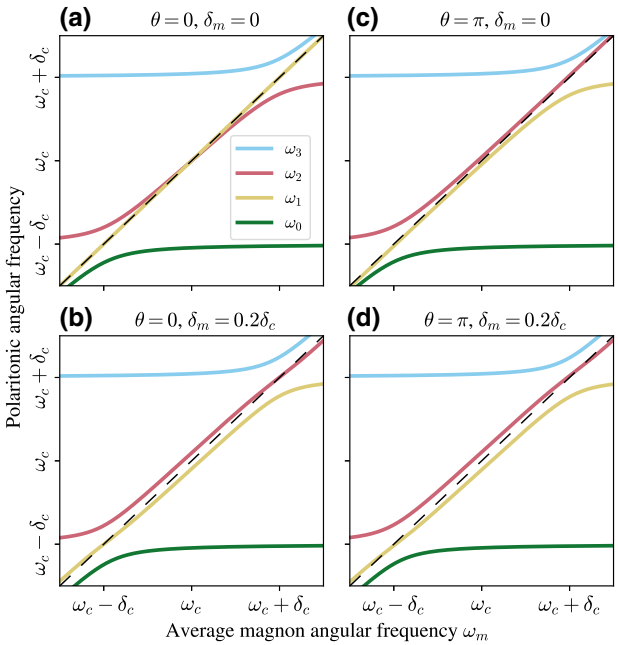


FIG. 2. Numerical spectra of H_θ for $\theta = 0$ and $\theta = \pi$ as a function of the average magnon frequency $\omega_m/2\pi$, for two values of the magnon detuning δ_m. Parameters are $\omega_{c,0} = 4$ GHz, $\omega_{c,1} = 6$ GHz, and $g_0 = g_1 = 0.03\omega_c$. The dashed line corresponds to $\omega = \omega_m$. The legend in (a) is common to (b),(c) and (d).

do not for $\theta = \pi$ [Fig. 2(c)]. Repulsion between energy levels is usually the signature of a coupling phenomenon, while level crossing is indicative of the absence of coupling. This suggests that at $\omega_m = \omega_c$, the eigenmodes associated with ω_1 and ω_2 couple for $\theta = \pi$, but do not for $\theta = 0$.

2. Analysis in the dispersive regime

To clarify this spectral feature, we consider the dispersive regime, where both magnons are assumed to be far detuned from both cavity modes. Defining the detuning $\Delta_{kk'} = \omega_{m,k'} - \omega_{c,k}$ between the cavity mode c_k and the magnon mode $m_{k'}$, the dispersive limit corresponds to $|\Delta_{kk'}| \gg g_k$ for all $k, k' \in \{0, 1\}$. Under this approximation, we can employ a Schrieffer-Wolff transformation to perform first-order perturbation theory in $|g_k/\Delta_{kk'}| \ll 1$ (see Appendix D). We find that the magnon modes being significantly detuned from the cavity modes, the photon-magnon couplings are negligible, and the cavity and magnon modes decouple from each other [see Eq. (D5)]. However, virtual photons still mediate a magnon-magnon interaction, which for $\omega_m = \omega_c$, is described by the effective Hamiltonian (again, see Appendix D for details)

$$H'_{\text{magnons}} = \hbar\omega'_{m,0} m_0^\dagger m_0 + \hbar\omega'_{m,1} m_1^\dagger m_1 + \hbar\left(G_\theta m_0 m_1^\dagger + \text{h.c.}\right), \tag{18}$$

where the frequencies of the magnons are shifted due to the cavity modes as

$$\omega'_{m,k} = \omega_c + \frac{g_0^2}{\Delta_{0k}} + \frac{g_1^2}{\Delta_{1k}} \tag{19}$$

and the indirect magnon-magnon coupling $G_\theta/2\pi$ is

$$G_\theta = \frac{\delta_c}{\delta_c^2 - \delta_m^2}\left(g_0^2 - e^{i\theta} g_1^2\right). \tag{20}$$

We first note that while G_θ is complex valued (and can become purely imaginary), the effective Hamiltonian Eq. (18) is still Hermitian, guaranteeing real eigenvalues. The magnitude of G_θ characterizes the strength of the magnon-magnon coupling, and predicts level repulsion of the eigenmodes of Eq. (18). However, for $g_0 = g_1$ and $\theta = 0$, the magnons do not interact since G_θ vanishes, leading to crossing of the energy levels. Note that the crossing of eigenvalues reflects $G_\theta = 0$, and should not be confused with level attraction in dissipatively coupled systems (which we recall is associated with non-Hermitian Hamiltonians).

3. Cavity-mediated coupling

To verify our analysis, we numerically plot ω_1 and ω_2 by diagonalizing Eq. (15) at $\omega_m = \omega_c$ in Fig. 3. We observe

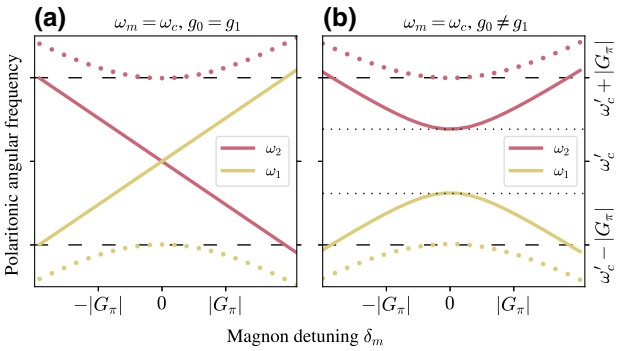


FIG. 3. Numerical spectra of H_θ for $\theta = 0$ (solid lines), and $\theta = \pi$ (dots) as a function of the magnon detuning δ_m at $\omega_m = \omega_c$. The dashed lines are at $\omega'_c \pm |G_\pi|$ while the dotted lines are at $\omega'_c \pm |G_0|$, with G_θ evaluated using Eq. (20) for $\delta_m = 0$. We set $g_0 = g_1 = 0.01\omega_c$ in (a), $g_0 = 0.01\omega_{c,0}$ and $g_1 = 0.01\omega_{c,1}$ in (b). The definition of ω'_c is per the main text. Other parameters and legend are as in Fig. 2.

the crossing of the solid lines (corresponding to $\theta = 0$), while the dots ($\theta = \pi$) anticross. The situation changes if we set $g_0 \neq g_1$ as shown in Fig. 3, and now we observe level repulsion for both $\theta = 0$ and $\theta = \pi$. This behavior is exactly the one we infer in the dispersive regime. Note that our analysis of the dispersive regime is valid if $|g_k/\Delta_{kk'}| \ll 1$. At $\omega_m = \omega_c$, this is equivalent to imposing $g_0, g_1 \ll |\delta_c - \delta_m|$, which the parameters employed in Fig. 3 satisfy. Regardless of the values of g_0 and g_1, Fig. 3 shows that the frequency gap between the eigenmodes of Eq. (18) is minimal when $\omega'_{m,0} = \omega'_{m,1}$, i.e., $\delta_m = 0$. The location of this minimum gap is given by $\omega'_c = \omega_c + (g_0^2 - g_1^2)/\delta_c$ due to the frequency shift of the magnon modes described by Eq. (19).

Physically, Eq. (20) highlights an interference effect between the magnon-magnon couplings contributed by each cavity mode. This interference can be constructive for $\theta = \pi$, or destructive for $\theta = 0$, and we always have $|G_\pi| > |G_0|$. In particular, if $g_0 = g_1$, the cavity-mediated coupling between the magnons completely vanishes for $\theta = 0$. We conclude that the case $\theta = 0$ is always detrimental to indirectly couple two spatially distant magnons, while the case $\theta = \pi$ is beneficial. This conclusion highlights the relevance of the physical phase θ for multimode cavity-mediated coupling applications.

C. Dark-mode physics

1. Rotated magnon basis

After having looked at the spectrum, we now turn our attention to the eigenmodes of H_θ. The physics will be more easily understood by considering a rotated magnon

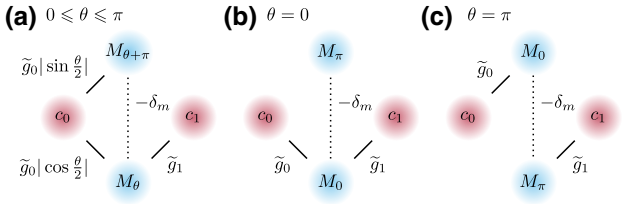


FIG. 4. Schematic of the interactions present in H_θ in the rotated magnon basis [see Eqs. (22) and (23)] for (a) arbitrary θ, (b) $\theta = 0$, (c) $\theta = \pi$. The black lines are labeled by the magnitude of the couplings, and the dotted black line represents the possibility of vanishing δ_m. Note that $M_0 = M_{2\pi}$.

basis $M_\theta, M_{\theta+\pi}$, defined by

$$M_\theta = \frac{m_0 + e^{-i\theta} m_1}{\sqrt{2}}. \tag{21}$$

It is easy to prove that, since m_0 and m_1 commute with each other, so do M_θ and $M_{\theta+\pi}$. Note that $M_0 = M_{2\pi}$ corresponds to co-rotating magnons (i.e., both magnons precess in phase) while M_π corresponds to counter-rotating magnons (precessing out of phase). In this basis, the free Hamiltonian Eq. (9) now reads

$$\begin{aligned} H_{\text{free}} = {} & \hbar\omega_{c,0} c_0^\dagger c_0 + \hbar\omega_{c,1} c_1^\dagger c_1 \\ & + \hbar\omega_m M_\theta^\dagger M_\theta + \hbar\omega_m M_{\theta+\pi}^\dagger M_{\theta+\pi} \\ & - \delta_m \left(M_\theta M_{\theta+\pi}^\dagger + \text{h.c.} \right), \end{aligned} \tag{22}$$

while the interaction Hamiltonian Eq. (13) reads

$$\begin{aligned} H_{I,\theta} = {} & \hbar\widetilde{g}_0 e^{-i\theta/2} c_0 \left(\cos\frac{\theta}{2} M_\theta - i \sin\frac{\theta}{2} M_{\theta+\pi} \right)^\dagger \\ & + \hbar\widetilde{g}_1 c_1 M_\theta^\dagger + \text{h.c.}, \end{aligned} \tag{23}$$

where we introduce the notation $\widetilde{g}_k = \sqrt{2} g_k$. The different interaction pathways between the modes are illustrated in Fig. 4(a).

Notably, if $\delta_m = 0$, H_θ describes the interaction between four different modes, while for $\theta = 0$ it separates into a three-mode system $\{c_0, c_1, M_0\}$ and a one-mode system $\{M_\pi\}$, and for $\theta = \pi$ it separates into two two-mode systems $\{c_0, M_0\}$ and $\{c_1, M_\pi\}$. In particular, for $\delta_m = 0$ and $\theta = 0$ [Fig. 4(b)], we see that M_π does not couple to any other mode.

2. Dark-mode definition

The presence of such an uncoupled eigenmode is reminiscent of dark-mode physics. Dark (bright) states are states that weakly (strongly) couple with the readout mechanism. Due to their weak coupling, these states benefit from an increased lifetime over their bright counterpart, and hence are interesting candidates for storing information. Dark and bright modes are defined similarly, but refer to the associated polaritonic mode in continuous variable systems.

The definition of a dark mode given above is dependent on the mechanism used to probe the system. Since here we are interested in photon-magnon hybridization, we consider a detection based on a microwave transmission experiment mediated by photons. As a consequence, we expect that any eigenmode coupling with cavity modes will indirectly couple to the readout medium, hence acquiring an experimental signature. This scenario is similar to that encountered in previous studies of dark-mode physics in cavity magnonics [17–21,50].

To illustrate our discussion of dark modes, we now consider the transmission through the cavity (S_{21} parameter), experimentally obtained by attaching a vector network analyzer to the two ports of a cavity. This can be modeled using the input-output formalism [51], which couples the system to the environment. The derivation of the input-output theory is rather lengthy, so we refer the reader to Appendix E for more details. We consider that each cavity mode c_k couples to a photonic bath with coupling rate $\sqrt{\gamma/2\pi}$ and we set $\gamma = 5$ MHz. We further introduce the intrinsic dissipation $\kappa = 1$ MHz of the cavity (due to its finite quality factor) and magnon modes (Gilbert damping) through $\widetilde{\omega}_{o,k} = \omega_{o,k} - i\kappa$. Other parameters are as in Fig. 2. Note that the system is now an open quantum system, and effectively becomes non-Hermitian due to the inclusion of the intrinsic damping. However, for weak coupling to the environment, the physics of the system remains the same.

3. Dark-mode physics

The numerical results of the input-output theory are plotted in Fig. 5. Given the definition of a dark mode given above, we conclude that for $\theta = 0$, M_π is dark, since it is uncoupled to cavity modes. This is indeed what we observe in Fig. 5(a): comparing to the spectrum in Fig. 2, the polaritonic frequency $\omega_1/2\pi$ associated with M_π does not give a maximum of transmission, unlike the other frequencies. This is in contrast with Fig. 5(c), in which all the polaritonic frequencies lead to maxima of transmissions. Indeed, for $\theta = \pi$, M_π couples to c_1. Hence, since all the eigenmodes for $\theta = \pi$ couple to photons, we conclude that strictly speaking, there are no dark modes for $\theta = \pi$.

These observations rely on both magnon modes having identical resonance frequencies, i.e., $\delta_m = 0$. If this symmetry is broken by setting $\delta_m \neq 0$, an alternative interaction pathway between M_π and M_0 opens (see Fig. 4), regardless of the value of θ. Since M_0 couples to the cavity modes, then M_π will also couple to the cavity modes through M_0. As a consequence, we expect M_π to acquire

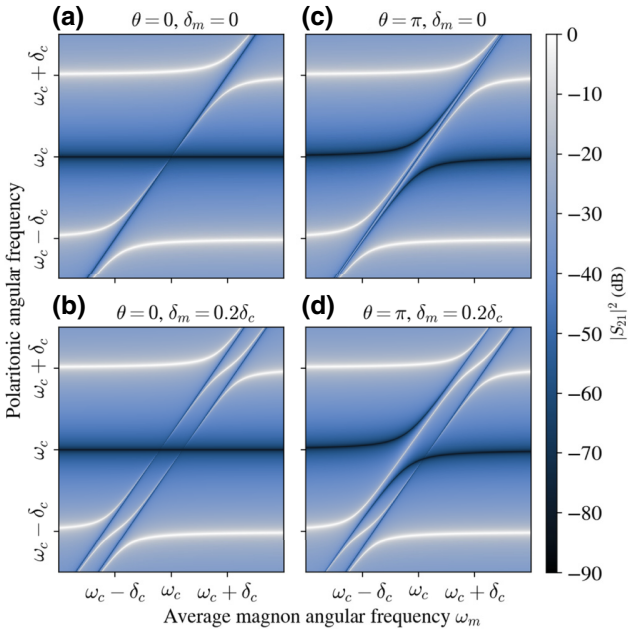


FIG. 5. Numerical calculation of the microwave transmission through the system obtained using an input-output theory for H_θ at different magnon detuning δ_m. See the main text for the parameters. In (a) we see that the spectral line associated to ω_1 (see Fig. 2) does not lead to a maximum of transmission, contrary to (b)–(d). This shows that the eigenmode associated with ω_1 is a dark mode.

an experimental signature if $\delta_m \neq 0$. This theoretical prediction is supported numerically by Figs. 5(b) and 5(d). We note that this phenomenon of the illumination of a dark mode by symmetry breaking was already discussed by Ref. [20] in the interaction picture.

To conclude this section, we comment on the presence of two types of antiresonances. The first type corresponds to dark diagonal lines, which follow the FMR of the YIG spheres. They are the result of destructive interference between the FMR and the rf magnetic mode of the cavity, as explained by Ref. [52]. The other type is due to destructive interference between the two cavity modes, and corresponds to the dark horizontal lines centred around $\omega_c = \omega_{c,0} + \omega_{c,1}/2$. These antiresonances are uncoupled for $\theta = 0$ (straight line for all ω_m), while for $\theta = \pi$ an anticrossing appears. This phenomenon can be explained by the fact that for $\theta = 0$, both cavity modes couple to M_0 with equal coupling strengths, while the situation is different for $\theta = \pi$ (see Fig. 4). Had we set $g_0 \neq g_1$, the antiresonance due to the cavity modes would have also coupled near the FMR for $\theta = 0$.

V. CONCLUSION

To summarize our results, we show that the interaction between a microwave photon and a magnon in a cavity is always associated with a coupling phase, which is different from that in dissipatively coupled systems. In most cases studied in the literature, this coupling phase can be omitted because of the simple topology of the interaction diagrams. Indeed, we trace the manifestation of the coupling phase to the presence of loops in the interaction diagrams (as illustrated by Fig. 6), a phenomenon similar to a discrete Pancharatnam-Berry phase. To illustrate that the physics is dependent on the coupling phase, we consider a model composed of two cavity modes and two magnon modes, parametrized by the physical phase θ. For different values of θ, we find different behaviors with respect to two potential applications of cavity magnonics: one case is advantageous for cavity-mediated coupling but cannot be used for dark-mode memories ($\theta = \pi$), and vice versa for the other case ($\theta = 0$). We note that while we show results only for $\theta = 0$ and $\theta = \pi$, our analytical derivations are still parametrized by a general θ, and hence apply to intermediate cases. In fact, values of θ between 0 and π continuously interpolate between the results presented in this paper (see the cavity-mediated coupling strength of Eq. (20), for example).

One could question whether there are simpler models in which there is a physical phase. In theory, any system in which there are n interactions between n bosonic modes, with one being a microwave photon-magnon interaction, leads to a physical phase. One such example was considered by Zhan *et al.* [19], where two ferromagnetic bilayers couple to a common cavity mode, but can also directly couple together thanks to the interlayer exchange interaction. This results in a triangular-shaped interaction diagram, so that in principle, a physical phase should parametrize their Hamiltonian. However, it is unclear how the impact of the physical phase could be experimentally verified in such a system. First, achieving different coupling phases for each ferromagnetic bilayer is a challenging experimental task, since the two layers need to be close to each other but be penetrated by the same cavity mode with a different angle (see Eq. (5)). Furthermore, as noted by the authors of Zhan *et al.* [19], the experimental verification of their analysis requires smaller magnon damping rates than currently reported in experiments.

Instead, the model introduced in Sec. III should be experimentally accessible using re-entrant cavity designs. Indeed, previous experimental results demonstrated the tunability of the frequencies of the cavity modes, with values of the coupling strengths compatible with the RWA [31,36,37]. Placing two YIG spheres in a re-entrant cavity with three post (also called pillar) should allow implementation of the two cases $\theta = 0$ and $\theta = \pi$ discussed here, and will be the subject of a separate investigation.

Finally, we point out that similar discrete gauge-invariant phases have been considered in different systems, such as arrays of superconducting qubits [53] or optomechanical systems [54–60]. It was shown that under certain conditions, this discrete phase was a manifestation

of a synthetic gauge field [61,62], which led to broken time-reversal symmetry and the creation of nonreciprocal devices. Hence, the engineering of cavities to achieve specific physical phases appears an exciting research direction. The design of such cavities will consist in controlling the relative orientation of the magnetic modes traversing the magnetic samples, as described by Eq. (5). Finally, we note that we consider only a rather simple model in which a physical phase manifests. For instance, considering an additional cavity mode would lead to the appearance of two physical phases, for which the physics is yet to be explored. More generally, the existence of discrete Pancharatnam-Berry phases in microwave cavity magnonics may find applications in quantum information processing and nonreciprocal devices.

ACKNOWLEDGMENTS

We acknowledge financial support from Thales Australia and Thales Research and Technology. This work is part of the research program supported by the European Union through the European Regional Development Fund (ERDF), the Ministry of Higher Education and Research, the Brittany region through the CPER SpaceTechDroneTech, and the ANR project ICARUS (22-CE24-0008-01). We thank Tyler Whittaker, Thomas Kong, and Ross Monaghan for reading the paper and providing useful comments. The scientific color map *oslo* [63] is used in this study to prevent visual distortion of the data and exclusion of readers with colorvision deficiencies [64].

APPENDIX A: PHOTON-MAGNON COUPLING TERM

In this Appendix, we show that the interaction term between a microwave cavity mode c and a magnon mode m can be expressed as

$$H_I = \hbar g e^{i\varphi}(c + c^\dagger)m^\dagger + \text{h.c.}, \tag{A1}$$

with g and φ positive real numbers. This derivation is valid in the macrospin approximation [32,33] and provided the number of magnon excitations is small compared to the number of spins.

Our starting point is the Supplemental Material of Ref. [30]. In particular, it is shown that in the macrospin approximation the interaction term is given by

$$\begin{aligned} H_I = {} & \hbar g^x \left(c + c^\dagger\right)\left(m + m^\dagger\right) + \hbar i g^y \left(c + c^\dagger\right)\left(m - m^\dagger\right) \\ & + \hbar g^z \left(c + c^\dagger\right) m^\dagger m + \hbar \Omega^z \left(c + c^\dagger\right) \end{aligned} \tag{A2}$$

with

$$g^x = -\frac{\gamma}{2cV_m}\sqrt{\frac{\hbar\omega_c S}{\epsilon_0}}\frac{\int_{V_m}\mathbf{H}\cdot\hat{\mathbf{x}}d^3r}{\sqrt{\int_{V_c}|\mathbf{H}|^2d^3r}}, \tag{A3}$$

$$g^y = \frac{\gamma}{2cV_m}\sqrt{\frac{\hbar\omega_c S}{\epsilon_0}}\frac{\int_{V_m}\mathbf{H}\cdot\hat{\mathbf{y}}d^3r}{\sqrt{\int_{V_c}|\mathbf{H}|^2d^3r}}, \tag{A4}$$

$$g^z = \frac{\gamma}{cV_m}\sqrt{\frac{\hbar\omega_c}{2\epsilon_0}}\frac{\int_{V_m}\mathbf{H}\cdot\hat{\mathbf{z}}d^3r}{\sqrt{\int_{V_c}|\mathbf{H}|^2d^3r}}, \tag{A5}$$

$$\Omega^z = -\frac{\gamma S}{cV_m}\sqrt{\frac{\hbar\omega_c}{2\epsilon_0}}\frac{\int_{V_m}\mathbf{H}\cdot\hat{\mathbf{z}}d^3r}{\sqrt{\int_{V_c}|\mathbf{H}|^2d^3r}}, \tag{A6}$$

where γ is the gyromagnetic ratio, V_m the volume of the magnetic sample, V_c the volume of the cavity, ω_c the resonance of the cavity, $S = \mu/(g_L\mu_B)N_S$ the total spin number of the macrospin operator, μ the magnetic moment of the magnetic sample, $g_L = 2$ the Landé g factor, μ_B the Bohr magneton, N_s the number of spins in the magnetic sample, c the speed of light in vacuum, ϵ_0 the permittivity of vacuum, and $\mathbf{H}$ the magnetic mode of the cavity.

Assuming that the magnetic mode has no z dependence, $g^z = \Omega^z = 0$ and Eq. (A2) can be written as $H_I = \hbar\left(g^x - ig^y\right)\left(c + c^\dagger\right)m^\dagger + \text{h.c.}$ with

$$g^x - ig^y = -\frac{\gamma}{2cV_m}\sqrt{\frac{S\hbar\omega_c}{\epsilon_0}}\frac{\int_{V_m}\mathbf{H}\cdot\hat{\mathbf{x}}d^3r + i\int_{V_m}\mathbf{H}\cdot\hat{\mathbf{y}}d^3r}{\sqrt{\int_{V_c}|\mathbf{H}|^2d^3r}} \tag{A7}$$

$$= -\frac{\gamma}{2}\sqrt{\frac{\mu_0 S\hbar\omega_c}{V_m}}\frac{\widetilde{H}}{\sqrt{V_m\int_{V_c}|\mathbf{H}|^2d^3r}}, \tag{A8}$$

where we use $\mu_0\epsilon_0 = 1/c^2$ and we recognize the quantity $\widetilde{H} = \int_{V_m}\mathbf{H}\cdot\hat{\mathbf{x}}d^3r + i\int_{V_m}\mathbf{H}\cdot\hat{\mathbf{y}}d^3r$ defined in Eq. (6) of the main text. We introduce $\mathbf{H}$ as a cavity mode, which means that it is the solution of an eigenvalue problem for the electromagnetic field obeying Maxwell's equations in the cavity. By definition, $-\mathbf{H}$ is also a solution to this eigenvalue problem, and hence Eq. (A8) is still valid after replacing $\mathbf{H} \mapsto -\mathbf{H}$. This removes the inconvenient minus sign Eq. (A8) so that we can now write

$$H_I = \frac{\hbar\gamma}{2}\sqrt{\frac{\mu_0 S\hbar\omega_c}{V_m}}\frac{\widetilde{H}}{\sqrt{V_m\int_{V_c}|\mathbf{H}|^2d^3r}}\left(c + c^\dagger\right)m^\dagger + \text{h.c.} \tag{A9}$$

$$= \frac{\hbar\gamma}{2}\sqrt{\frac{\mu_0 S\hbar\omega_c}{V_m}}\eta e^{i\theta}\left(c + c^\dagger\right)m^\dagger + \text{h.c.}, \tag{A10}$$

where we define

$$\eta = \frac{|\widetilde{H}|}{\sqrt{V_m \int_{V_c} |\mathbf{H}|^2 d^3r}} \tag{A11}$$

$$= \sqrt{\frac{\left(\int_{V_m} \mathbf{H}\cdot\hat{\mathbf{x}} d^3r\right)^2 + \left(\int_{V_m} \mathbf{H}\cdot\hat{\mathbf{y}} d^3r\right)^2}{V_m \int_{V_c} |\mathbf{H}|^2 d^3r}}, \tag{A12}$$

and $\varphi = \arg \widetilde{H}$ as announced in the main text.

To derive the expression of the coupling strength $g/2\pi$ as per the main text, we follow [31] and write $S = \mu/(g_L\mu_B)N_s = \mu/(g_L\mu_B)n_sV_m$ with n_s the spin density of the magnetic sample. Equation (A10) is then rewritten

$$H_I = \hbar g e^{i\varphi}\left(c + c^\dagger\right) m^\dagger + \text{h.c.}, \tag{A13}$$

with

$$g/2\pi = \eta\sqrt{\omega_c}\frac{\gamma}{4\pi}\sqrt{\frac{\mu}{g_L\mu_B}\mu_0\hbar n_s}. \tag{A14}$$

APPENDIX B: UNITARY TRANSFORMATIONS

A time-dependent unitary transformation U maps a Hamiltonian H to H' such that

$$H \mapsto H' = UHU^\dagger + i\hbar\dot{U}U^\dagger. \tag{B1}$$

This corresponds to the so-called rotating-frame transformations. For a time-independent unitary transformation, $H' = UHU^\dagger$, we simply refer to it as a change of frame. The Baker-Campbell-Hausdorff formula is useful for computing the transformed Hamiltonian, it reads

$$e^X Y e^{-X} = \sum_{n=0}^{\infty} \frac{\left[X^{(n)}, Y\right]}{n!}, \tag{B2}$$

where X and Y are operators, and we note $\left[(X)^{(n)}, Y\right]$ the nth iterated commutator defined as

$$\left[X^{(0)}, Y\right] \equiv Y, \quad \left[X^{(1)}, Y\right] = [X, Y] = XY - YX, \tag{B3}$$

$$\left[X^{(2)}, Y\right] = [X, [X, Y]], \quad \left[X^{(3)}, Y\right] = \left[X, \left[X^{(2)}, Y\right]\right] \tag{B4}$$

and so on.

For an annihilation operator a following bosonic commutation relation $\left[a, a^\dagger\right] = 1$ and $\varphi \in \mathbb{R}$, the unitary transformation $U = e^{i\varphi a^\dagger a}$ transforms a and $a^\dagger$ as

$$UaU^\dagger = e^{i\varphi a^\dagger a} a e^{-i\varphi a^\dagger a} = a e^{-i\varphi}, \tag{B5}$$

$$Ua^\dagger U^\dagger = a^\dagger e^{i\varphi}. \tag{B6}$$

The associated number operator $a^\dagger a$ is unaffected by the transformation, since

$$Ua^\dagger aU^\dagger = Ua^\dagger U^\dagger UaU^\dagger = a^\dagger e^{i\varphi} a e^{-i\varphi} \tag{B7}$$

$$= a^\dagger a, \tag{B8}$$

where $U^\dagger U = I$ since U is unitary.

Additionally, for any operator O that commutes with $a^\dagger a$, i.e $\left[a^\dagger a, O\right] = 0$, then O is unaffected by the transformation, i.e., $UOU^\dagger = O$, due to the vanishing of the iterated commutators in the Baker-Campbell-Hausdorff formula [Eq. (B2)].

APPENDIX C: RELEVANCE OF THE PHASE FACTOR

1. Removal of the coupling phase for a magnon-photon system

In the simple case of a single cavity-mode coupling to a single magnon mode, the Hamiltonian is $H = H_{\text{free}} + H_I$ defined by Eqs. (1) and (7). In light of Fig. 6, we can choose to rotate the cavity mode by φ using $U_c = e^{i\varphi c^\dagger c}$. Formally, $H_{\text{free}} \mapsto H'_{\text{free}} = H_{\text{free}}$ is unchanged while

$$H_I \mapsto H'_I = e^{i\varphi c^\dagger c}\left(\hbar g e^{i\varphi} c m^\dagger + \text{h.c.}\right) e^{-i\varphi c^\dagger c} \tag{C1}$$

$$= \hbar g e^{i\varphi}\left(e^{i\theta c^\dagger c} c e^{-i\varphi c^\dagger c}\right)\left(e^{i\theta c^\dagger c} m^\dagger e^{-i\varphi c^\dagger c}\right) + \text{h.c.} \tag{C2}$$

$$= \hbar g e^{i\varphi}\left(c e^{-i\varphi}\right) m^\dagger + \text{h.c.} \tag{C3}$$

$$= \hbar g c m^\dagger + \text{h.c.} \tag{C4}$$

hence removing the coupling phase φ. Pictorially, this is illustrated on the right of Fig. 6, where we see that the yellow arrow of mode c has changed orientation, and is now pointing in the same direction as that of mode m. Alternatively, as illustrated in Fig. 6, we can rotate the magnon mode instead, using $U_m = e^{-i\varphi m^\dagger m}$, which yields the same result, albeit with a different final orientation of the yellow arrows.

The fact that φ is absent after a change of frame implies that it cannot be physical. Similarly, note that the two extremal cases $\varphi = 0$ and $\varphi = \pi$ differ only by the sign of the coupling strength, and hence we deduce that its polarity does not affect the physics.

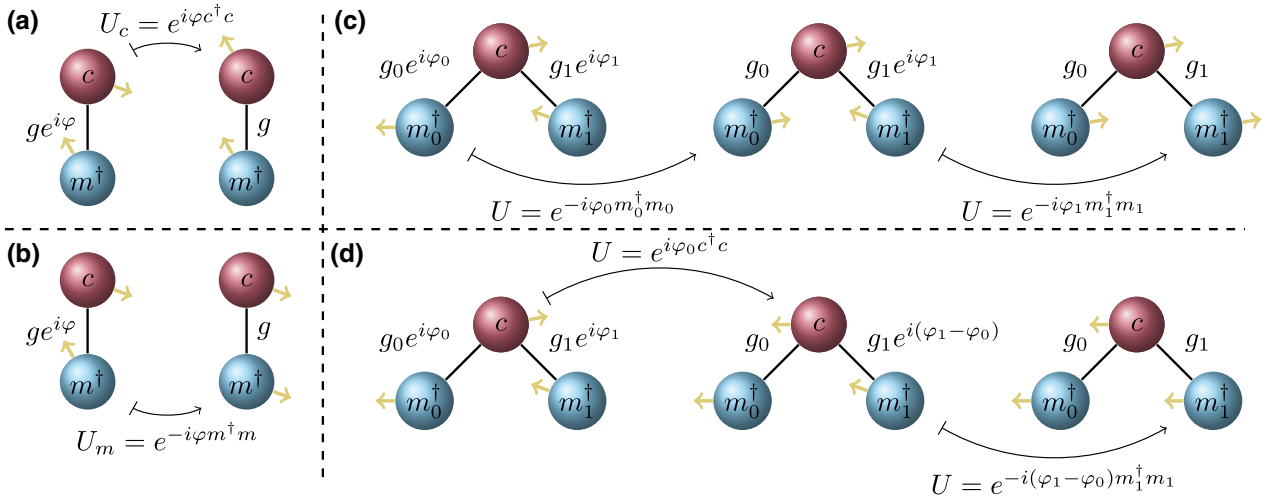


FIG. 6. Example diagrams showing coupling phase removal by unitary transformations. The conventions used are that of Fig. 1. (a) Rotation of the cavity mode c using $U_c = e^{i\varphi c^\dagger c}$. The magnon mode m is unaffected. (b) Rotation of the magnon mode m using $U_m = e^{-i\varphi m^\dagger m}$. (c) Rotation of both magnon modes using $U = e^{-i\varphi_j m_j^\dagger m_j}$ for $j \in \{0, 1\}$. (d) Rotation of the cavity mode c using $U = e^{i\varphi_0 c^\dagger c}$ and the magnon mode m_1 using $U = e^{-i(\varphi_1 - \varphi_0) m_1^\dagger m_1}$.

2. Removal of the coupling phase for two magnons coupling to a common cavity mode

We now assume that an additional magnon mode couples to the cavity mode, as considered in many works [15–17,19–21,46–48]. We also note that since all modes are bosonic, this scenario is equivalent to one where a single magnon mode couples to two cavity modes, as considered, e.g., by Ref. [52]. The Hamiltonian is $H = H_{\text{free}} + H_I$ with

$$H_{\text{free}} = \hbar\omega_c c^\dagger c + \hbar\omega_{m,0} m_0^\dagger m_0 + \hbar\omega_{m,1} m_1^\dagger m_1, \tag{C5}$$

$$H_I = \hbar g_0 e^{i\varphi_0} c m_0^\dagger + \hbar g_1 e^{i\varphi_1} c m_1^\dagger + \text{h.c.}, \tag{C6}$$

and is illustrated in Fig. 6.

One simple possibility to remove the coupling phases φ_i is to successively rotate m_i using $U_{m_i} = e^{-i\varphi_i m_i^\dagger m_i}$ for $i \in \{0, 1\}$ (Fig. 6). While this is the simplest method, we could also rotate the cavity mode c (Fig. 6), for instance to remove φ_0 using $U_c = e^{i\varphi_0 c^\dagger c}$, but then the coupling to the second magnon is also affected and reads $\hbar g_1 e^{i(\varphi_1 - \varphi_0)} c m_1^\dagger + \text{h.c.}$ Applying $U_{m_1} = e^{-i(\varphi_1 - \varphi_0) m_1^\dagger m_1}$ removes the remaining phase.

Formally, it appears that the coupling phases are again unimportant for the resulting physics. While the physics is unchanged, we would like to mention that the *interpretation* of the physics is as follows: the rotated frame is not the laboratory frame. As an example, Ref. [20] studied the specific case of $\varphi_0 = \varphi_1 = 0$ and $g_0 = g_1 = g$, and found that $M_- = (m_0 - m_1)/\sqrt{2}$ was the only dark mode of the system. If we were to consider $g_0 = -g_1 = g$ instead (obtained by applying $U = e^{-i\pi m_1^\dagger m_1}$ for instance), we would find that the dark mode is transformed to $M_+ = (m_0 + m_1)/\sqrt{2}$ in this frame. Still, the spectrum and other physical predictions of Ref. [20] would all hold.

3. Two cavity modes and two magnon modes

We note that the removal of the coupling phases in the previous examples is facilitated by the fact that the interaction diagrams have open ends: the rotation of the modes at the ends of the interaction chain would at most affect one edge. Having a closed loop, however, removes this freedom, resulting in an observable physical phase θ. We believe the hybrid system introduced in Sec. III is the simplest system with an interaction loop involving a magnon-photon interaction, which could be experimentally accessible.

APPENDIX D: EFFECTIVE HAMILTONIAN IN THE DISPERSIVE REGIME

For the purpose of this section, we adopt different notations for convenience. The model studied in the main text can be written as $H_\theta = H_{\text{free}} + H_I$

$$H_{\text{free}} = \sum_{k=0}^{1} \hbar\omega_{c,k} c_k^\dagger c_k + \hbar\omega_{m,k} m_k^\dagger m_k \tag{D1}$$

$$H_I = \sum_{k,k'=0}^{1} \hbar g_{kk'} c_k m_{k'}^\dagger + \text{h.c.}, \tag{D2}$$

with $g_{0k'} = g_0$, $g_{10} = g_1$, and $g_{11} = g_1 e^{i\theta}$. We hence assume that $g_{kk'} \in \mathbb{C}$ in this section, even though we are mostly interested in the cases $\theta = 0$ or π, for which the $g_{kk'}$ become real. We also introduce the detuning $\Delta_{kk'} = \omega_{m,k'} - \omega_{c,k}$ between the cavity mode c_k and the magnon mode $m_{k'}$. In the rest of this section, we assume that the magnons are significantly detuned from the both cavity mode such that $|\lambda_{kk'}| \ll 1$ with $\lambda_{kk'} = g_{kk'}/\Delta_{kk'}$ for $k, k' \in \{0, 1\}$.

To find the effective Hamiltonian in this regime, we employ a Schrieffer-Wolff transformation [65] to treat H_I as a perturbation of H_{free}. Using the unitary transformation $U = e^{\Lambda}$ with

$$\Lambda = \sum_{k,k'} \left(\lambda_{kk'} c_k m_{k'}^\dagger - \lambda_{kk'}^* c_k^\dagger m_{k'} \right), \tag{D3}$$

we have $H_I + [\Lambda, H_{\text{free}}] = 0$ and the Baker-Campbell-Hausdorff formula [see Eq. (B2)] gives $H'_\theta = e^{\Lambda} H_\theta e^{-\Lambda} = H_{\text{free}} + \frac{1}{2}[\Lambda, H_I]$ to first order in $|\lambda|$.

After using commutator identities, we find the commutator

$$\begin{aligned}[\Lambda, H_I] = 2\hbar \sum_k \left[\left(\sum_l \frac{|g_{lk}|^2}{\Delta_{lk}} \right) m_k^\dagger m_k - \left(\sum_l \frac{|g_{kl}|^2}{\Delta_{kl}} \right) c_k^\dagger c_k \right] \\ + \hbar \sum_{k \neq k'} \left[\left(\sum_l \lambda_{lk'} g_{lk}^* \right) m_k m_{k'}^\dagger + \text{h.c.} \right] \\ - \hbar \sum_{k \neq k'} \left[\left(\sum_l \lambda_{kl} g_{k'l}^* \right) c_k c_{k'}^\dagger + \text{h.c.} \right] + \text{cst.}\end{aligned} \tag{D4}$$

The constant originates from using the bosonic commutation relations for the operators c_k, m_k. Hence, after applying $U = e^{\Lambda}$, we obtain the effective Hamiltonian

$$\begin{aligned}H'_\theta = \sum_k \hbar\omega'_{c,k} c_k^\dagger c_k + \hbar\omega'_{m,k} m_k^\dagger m_k \\ + \sum_{k \neq k'} \left(\kappa_{kk'} c_k c_{k'}^\dagger + \text{h.c.} \right) + \sum_{k \neq k'} \left(G_{kk'} m_k m_{k'}^\dagger + \text{h.c.} \right)\end{aligned} \tag{D5}$$

with shifted resonances

$$\omega'_{c,k} = \omega_{c,k} - \sum_{k'} \frac{|g_{kk'}|^2}{\Delta_{kk'}}, \tag{D6}$$

$$\omega'_{m,k} = \omega_{m,k} + \sum_{k'} \frac{|g_{k'k}|^2}{\Delta_{k'k}}, \tag{D7}$$

photon-photon couplings

$$\kappa_{kk'} = -\sum_l \frac{g_{kl} g_{k'l}^*}{2\Delta_{kl}}, \tag{D8}$$

and magnon-magnon couplings

$$G_{kk'} = \sum_l \frac{g_{lk'} g_{lk}^*}{2\Delta_{lk'}}. \tag{D9}$$

The effective Hamiltonian highlights the decoupling of the photonic and matter degrees of freedom in the dispersive regime: light and matter do not interact anymore. However, we obtain a photon-photon coupling mediated by virtual magnons, and magnon-magnon couplings mediated by virtual photons.

Concentrating on the magnon modes, and setting $\omega_m = \omega_c$, we obtain the effective Hamiltonian for the magnons

$$H'_m = \sum_k \hbar\omega'_{m,k} m_k^\dagger m_k + \hbar \left(G_\theta m_0 m_1^\dagger + \text{h.c.} \right), \tag{D10}$$

with $G_\theta = G_{01} + G_{10}^*$ and shifted magnon frequencies

$$\omega'_{m,0} = \omega_c + \frac{\left(g_0^2 + g_1^2\right)\delta_m + \left(g_0^2 - g_1^2\right)\delta_c}{\delta_c^2 - \delta_m^2}, \tag{D11}$$

$$\omega'_{m,1} = \omega_c - \frac{\left(g_0^2 + g_1^2\right)\delta_m - \left(g_0^2 - g_1^2\right)\delta_c}{\delta_c^2 - \delta_m^2}. \tag{D12}$$

APPENDIX E: DETAILS OF THE INPUT-OUTPUT THEORY

In the main text, we consider the transmission of the cavity by microwave photons. In this Appendix, we derive an analytical expression of the transmission of the cavity using the input-output formalism [51]. We note that similar results can be obtained employing the loop theory introduced in Ref. [66]. In the following, we assume that we replace $\omega_{o,k} \mapsto \omega_{o,k} - i\kappa$ for $o_k \in \{c, m\}, k \in \{0, 1\}$ with κ the intrinsic dissipation rate.

1. Bath modeling

We model the environment with a bosonic bath Hamiltonian H_{bath} with operators a_ω and b_ω for the left and right side of the cavity. It reads

$$H_{\text{bath}} = \int_{-\infty}^{\infty} d\omega \left(\hbar\omega a_\omega^\dagger a_\omega + \hbar\omega b_\omega^\dagger b_\omega \right). \tag{E1}$$

The interaction between the bath and the cavity is

$$H_{\text{sys bath}} = i\hbar \int_{-\infty}^{\infty} d\omega \left(\sum_{k=0}^{1} c_k \left(\kappa_{a,k} a_\omega^\dagger + \kappa_{b,k} b_\omega^\dagger \right) + \text{h.c.} \right), \tag{E2}$$

where we define $\sqrt{\gamma_{o,k}/2\pi} = \kappa_{o,k}$ for the bath operators $o \in \{a, b\}$. The frequency independence of the coupling to the bath corresponds to a memory-less environment (first Markov approximation [51]). The Heisenberg equation of motion for the bath operators $o \in \{a, b\}$ is

$$\dot{o}_\omega = -\frac{i}{\hbar}\left[o_\omega, H_{\text{bath}} + H_{\text{sys bath}}\right] = -i\omega o_\omega + \sum_k \kappa_{o,k} c_k, \tag{E3}$$

with the formal solutions

$$o_\omega(t) = o_\omega(t_0)e^{-i\omega(t-t_0)} + \sum_k \kappa_{o,k}\int_{t_0}^{t} dt' c_k(t')e^{-i\omega(t-t')} \tag{E4}$$

for $t_0 < t$ and

$$o_\omega(t) = o_\omega(t_1)e^{-i\omega(t-t_1)} - \sum_k \kappa_{o,k}\int_{t}^{t_1} dt' c_k(t')e^{-i\omega(t-t')} \tag{E5}$$

for $t < t_1$.

2. System for the cavity modes in frequency space

We now define the input fields

$$o^{\text{in}}(t) = \frac{1}{\sqrt{2\pi}}\int d\omega e^{-i\omega(t-t_0)} o_\omega(t_0) \tag{E6}$$

and using the solution of Eq. (E4) for $t_0 < t$ we have

$$\kappa^*_{o,k}\int_{\mathbb{R}} d\omega o_\omega(t) = \sqrt{\gamma^*_{o,k}}o^{\text{in}}(t) + \sum_{k'}\frac{\sqrt{\gamma^*_{o,k}\gamma_{o,k'}}}{2}c_{k'}(t). \tag{E7}$$

We adopt the notations of Appendix D and write the interaction term $H_I = \sum_{k,k'=0}^{1} g_{kk'}c_k m^\dagger_{k'} + \text{h.c.}$ The Heisenberg equation for the cavity modes at $t_0 < t$ reads

$$\begin{aligned}\dot{c}_k &= -\frac{i}{\hbar}\left[c_k, H_{\text{sys}} + H_{\text{sys bath}}\right] \\ &= -i\omega_{c,k}c_k - i\sum_{k'} g_{kk'}m_{k'} - \sum_{o\in\{a,b\}}\sqrt{\gamma^*_{o,k}}o^{\text{in}}(t) \\ &\quad - \sum_{o\in\{a,b\},k'}\frac{\sqrt{\gamma^*_{o,k}\gamma_{o,k'}}}{2}c_{k'}(t)\end{aligned} \tag{E8}$$

while that for the magnon modes is

$$\dot{m}_k = -\frac{i}{\hbar}\left[m_k, H_{\text{sys}}\right] = -i\omega_{m,k}m_k - i\sum_{k'} g_{k'k}c_{k'}. \tag{E9}$$

In frequency space,

$$-i\omega\tilde{m}_k = -i\omega_{m,k}\tilde{m}_k - i\sum_{k'} g_{k'k}\tilde{c}_{k'}, \tag{E10}$$

which gives

$$\tilde{m}_k = \frac{\sum_{k'} g_{k'k}\tilde{c}_{k'}}{\omega - \omega_{m,k}}. \tag{E11}$$

At this stage, it is convenient to introduce the detunings

$$\Delta_{o,k} = \omega - \omega_{o,k}, \quad o \in \{c, m\},\ k \in \{0, 1\}. \tag{E12}$$

The cavity modes in Fourier space then read

$$\Delta_{c,k}\tilde{c}_k + \sum_{o\in\{a,b\},k'}\left(i\frac{\sqrt{\gamma^*_{o,k}\gamma_{o,k'}}}{2} - \sum_l \frac{g_{kl}g_{k'l}}{\Delta_{m,l}}\right)\tilde{c}_{k'} + \sum_{o\in\{a,b\}} i\sqrt{\gamma^*_{o,k}}\tilde{o}^{\text{in}} = 0. \tag{E13}$$

Separating the terms $k = k'$ and $k \neq k'$, we obtain the system

$$A_0\tilde{c}_0 + B_{01}\tilde{c}_1 + \sum_{o\in\{a,b\}} O_{o,0}\tilde{o}^{\text{in}} = 0, \tag{E14}$$

$$B_{10}\tilde{c}_0 + A_1\tilde{c}_1 + \sum_{o\in\{a,b\}} O_{o,1}\tilde{o}^{\text{in}} = 0, \tag{E15}$$

with the solutions

$$\tilde{c}_0 = \sum_{o\in\{a,b\}}\frac{O_{o,0}A_1 - O_{o,1}B_{01}}{B_{10}B_{01} - A_0A_1}\tilde{o}^{\text{in}}, \tag{E16}$$

$$\tilde{c}_1 = \sum_{o\in\{a,b\}} -\frac{O_{o,0}B_{10} - O_{o,1}A_0}{B_{10}B_{01} - A_0A_1}\tilde{o}^{\text{in}} \tag{E17}$$

and

$$A_k = \left(\Delta_{c,k} + i\sum_{o\in\{a,b\}}\frac{|\gamma_{o,k}|}{2}\right)\Delta_{m,0}\Delta_{m,1} - g^2_{k0}\Delta_{m,1} - g^2_{k1}\Delta_{m,0}, \tag{E18}$$

$$B_{kk'} = i\left(\sum_{o\in\{a,b\}}\frac{\sqrt{\gamma^*_{o,k}\gamma_{o,k'}}}{2}\right)\Delta_{m,0}\Delta_{m,1} - g_{k0}g_{k'0}\Delta_{m,1} - g_{k1}g_{k'1}\Delta_{m,0}, \tag{E19}$$

$$O_{o,k} = i\sum_{o\in\{a,b\}}\sqrt{\gamma^*_{o,k}}\Delta_{m,0}\Delta_{m,1}. \tag{E20}$$

3. Input-output relations

We now define the output field

$$o^{\text{out}}(t) = \frac{1}{\sqrt{2\pi}} \int d\omega e^{-i\omega(t-t_1)} o_\omega(t_1), \tag{E21}$$

and using the solution at $t < t_1$ we have

$$\kappa_{o,k}^* \int_{\mathbb{R}} d\omega o_\omega(t) = \sqrt{\gamma_{o,k}^*} o^{\text{out}}(t) - \sum_{k'} \frac{\sqrt{\gamma_{o,k}^* \gamma_{o,k'}}}{2} c_{k'}(t), \tag{E22}$$

which combined with Eq. (E7) leads to input-output relations

$$\tilde{o}^{\text{out}} - \tilde{o}^{\text{in}} = \sum_k \sqrt{\gamma_{o,k}} \tilde{c}_k \tag{E23}$$

valid for each bath operator $o \in \{a, b\}$.

4. Transmission

The transmission through the system can be defined as

$$S_{21} = \left. \frac{\left\langle \tilde{b}^{\text{out}} \right\rangle}{\left\langle \tilde{a}^{\text{in}} \right\rangle} \right|_{\left\langle \tilde{b}^{\text{in}} \right\rangle = 0} = \frac{\sum_k \sqrt{\gamma_{b,k}} \left\langle \tilde{c}_k \right\rangle}{\left\langle \tilde{a}^{\text{in}} \right\rangle}, \tag{E24}$$

where we use the input-output relations. Using Eqs. (E16) and (E17), we obtain

$$S_{21} = \sqrt{\gamma_{b,0}} \frac{O_{a,0} A_1 - O_{a,1} B_{01}}{B_{10} B_{01} - A_0 A_1} - \sqrt{\gamma_{b,1}} \frac{O_{a,0} B_{10} - O_{a,1} A_0}{B_{10} B_{01} - A_0 A_1}. \tag{E25}$$

[1] X. Zhang, C.-L. Zou, L. Jiang, and H. X. Tang, Cavity magnomechanics, Sci. Adv. **2**, (2016).

[2] D. Lachance-Quirion, Y. Tabuchi, A. Gloppe, K. Usami, and Y. Nakamura, Hybrid quantum systems based on magnonics, Applied Physics Express **12**, 070101 (2019).

[3] M. Harder and C.-M. Hu, Cavity spintronics: An early review of recent progress in the study of magnon–photon level repulsion, Solid State Phys., 47,.

[4] M. Harder, B. M. Yao, Y. S. Gui, and C.-M. Hu, Coherent and dissipative cavity magnonics, J. Appl. Phys. **129**, 201101 (2021).

[5] B. Z. Rameshti, S. V. Kusminskiy, J. A. Haigh, K. Usami, D. Lachance-Quirion, Y. Nakamura, C.-M. Hu, H. X. Tang, G. E. Bauer, and Y. M. Blanter, Cavity magnonics, Phys. Rep. 979, 1 (2021)., ArXiv:2106.09312

[6] X. Zhang, C.-L. Zou, L. Jiang, and H. X. Tang, Strongly Coupled Magnons and Cavity Microwave Photons, Phys. Rev. Lett. **113**, 156401 (2014).

[7] J. Bourhill, N. Kostylev, M. Goryachev, D. L. Creedon, and M. E. Tobar, Ultrahigh cooperativity interactions between magnons and resonant photons in a YIG sphere, Phys. Rev. B **93**, 144420 (2016).

[8] M. Goryachev, W. G. Farr, D. L. Creedon, Y. Fan, M. Kostylev, and M. E. Tobar, High-Cooperativity Cavity QED with Magnons at Microwave Frequencies, Phys. Rev. Appl. **2**, 054002 (2014).

[9] I. Golovchanskiy, N. Abramov, V. Stolyarov, A. Golubov, M. Y. Kupriyanov, V. Ryazanov, and A. Ustinov, Approaching Deep-Strong On-Chip Photon-to-Magnon Coupling, Phys. Rev. Appl. **16**, 034029 (2021).

[10] I. A. Golovchanskiy, N. N. Abramov, V. S. Stolyarov, M. Weides, V. V. Ryazanov, A. A. Golubov, A. V. Ustinov, and M. Y. Kupriyanov, Ultrastrong photon-to-magnon coupling in multilayered heterostructures involving superconducting coherence via ferromagnetic layers, Sci. Adv. **7**, (2021).

[11] G. Bourcin, J. Bourhill, V. Vlaminck, and V. Castel, Strong to ultra-strong coherent coupling measurements in a yig/cavity system at room temperature, (2022), ArXiv:2209.14643.

[12] P. Hyde, L. Bai, M. Harder, C. Match, and C.-M. Hu, Indirect coupling between two cavity modes via ferromagnetic resonance, Appl. Phys. Lett. **109**, 152405 (2016).

[13] N. Crescini, C. Braggio, G. Carugno, A. Ortolan, and G. Ruoso, Coherent coupling between multiple ferrimagnetic spheres and a microwave cavity at millikelvin temperatures, Phys. Rev. B **104**, 064426 (2021).

[14] K. An, R. Kohno, A. Litvinenko, R. Seeger, V. Naletov, L. Vila, G. de Loubens, J. B. Youssef, N. Vukadinovic, G. Bauer, A. Slavin, V. Tiberkevich, and O. Klein, Bright and Dark States of Two Distant Macrospins Strongly Coupled by Phonons, Phys. Rev. X **12**, 011060 (2022).

[15] N. J. Lambert, J. A. Haigh, S. Langenfeld, A. C. Doherty, and A. J. Ferguson, Cavity-mediated coherent coupling of magnetic moments, Phys. Rev. A **93**, 021803 (2016).

[16] B. Z. Rameshti and G. E. W. Bauer, Indirect coupling of magnons by cavity photons, Phys. Rev. B **97**, 014419 (2018).

[17] V. L. Grigoryan and K. Xia, Cavity-mediated dissipative spin-spin coupling, Phys. Rev. B **100**, 014415 (2019).

[18] P.-C. Xu, J. W. Rao, Y. S. Gui, X. Jin, and C.-M. Hu, Cavity-mediated dissipative coupling of distant magnetic moments: Theory and experiment, Phys. Rev. B **100**, 094415 (2019).

[19] X. Zhan, Y. Zhang, X. Yan, and Y. Xiao, Bright and dark modes of exchange-coupled ferromagnetic bilayers in a microwave cavity, J. Appl. Phys. **130**, 123901 (2021).

[20] J. M. P. Nair, D. Mukhopadhyay, and G. S. Agarwal, Cavity-mediated level attraction and repulsion between magnons, Phys. Rev. B **105**, 214418 (2022).

[21] X. Zhang, C.-L. Zou, N. Zhu, F. Marquardt, L. Jiang, and H. X. Tang, Magnon dark modes and gradient memory, Nat. Commun. **6**,.

[22] Y. Tabuchi, S. Ishino, A. Noguchi, T. Ishikawa, R. Yamazaki, K. Usami, and Y. Nakamura, Coherent coupling between a ferromagnetic magnon and a superconducting qubit, Science **349**, 405 (2015).

[23] Y. Tabuchi, S. Ishino, A. Noguchi, T. Ishikawa, R. Yamazaki, K. Usami, and Y. Nakamura, Quantum

magnonics: The magnon meets the superconducting qubit, C. R. Phys. **17**, 729 (2016).

[24] H. Yuan, Y. Cao, A. Kamra, R. A. Duine, and P. Yan, Quantum magnonics: When magnon spintronics meets quantum information science, Phys. Rep. **965**, 1 (2022).

[25] Z.-X. Liu, H. Xiong, and Y. Wu, Magnon blockade in a hybrid ferromagnet-superconductor quantum system, Phys. Rev. B **100**, 134421 (2019).

[26] J. kun Xie, S. li Ma, and F. li Li, Quantum-interference-enhanced magnon blockade in an yttrium-iron-garnet sphere coupled to superconducting circuits, Phys. Rev. A **101**, 042331 (2020).

[27] K. Wu, W. Xue Zhong, G. Ling Cheng, and A. Xi Chen, Phase-controlled multimagnon blockade and magnon-induced tunneling in a hybrid superconducting system, Phys. Rev. A **103**, 052411 (2021).

[28] D. Lachance-Quirion, S. P. Wolski, Y. Tabuchi, S. Kono, K. Usami, and Y. Nakamura, Entanglement-based single-shot detection of a single magnon with a superconducting qubit, Science **367**, 425 (2020).

[29] S. Wolski, D. Lachance-Quirion, Y. Tabuchi, S. Kono, A. Noguchi, K. Usami, and Y. Nakamura, Dissipation-Based Quantum Sensing of Magnons with a Superconducting Qubit, Phys. Rev. Lett. **125**, 117701 (2020).

[30] G. Flower, M. Goryachev, J. Bourhill, and M. E. Tobar, Experimental implementations of cavity-magnon systems: From ultra strong coupling to applications in precision measurement, New J. Phys. **21**, 095004 (2019).

[31] J. Bourhill, V. Castel, A. Manchec, and G. Cochet, Universal characterization of cavity–magnon polariton coupling strength verified in modifiable microwave cavity, J. Appl. Phys. **128**, 073904 (2020).

[32] O. O. Soykal and M. E. Flatté, Size dependence of strong coupling between nanomagnets and photonic cavities, Phys. Rev. B **82**, 104413 (2010).

[33] O. O. Soykal and M. E. Flatté, Strong Field Interactions Between a Nanomagnet and a Photonic Cavity, Phys. Rev. Lett. **104**, 077202 (2010).

[34] D. D. Stancil and A. Prabhakar, *Spin Waves* (Springer, US, 2009).

[35] T. Holstein and H. Primakoff, Field dependence of the intrinsic domain magnetization of a ferromagnet, Phys. Rev. **58**, 1098 (1940).

[36] N. C. Carvalho, Y. Fan, and M. E. Tobar, Piezoelectric tunable microwave superconducting cavity, Rev. Sci. Instrum. **87**, 094702 (2016).

[37] M. E. Tobar and M. Goryachev, Microwave frequency magnetic field manipulation systems and methods and associated application instruments, apparatus and system (2019).

[38] P. Forn-Díaz, L. Lamata, E. Rico, J. Kono, and E. Solano, Ultrastrong coupling regimes of light-matter interaction, Rev. Mod. Phys. **91**, 025005 (2019).

[39] A. Frisk Kockum, A. Miranowicz, S. De Liberato, S. Savasta, and F. Nori, Ultrastrong coupling between light and matter, Nat. Rev. Phys. **1**, 19 (2019).

[40] A. Le Boité, Theoretical methods for ultrastrong light–matter interactions, Adv. Quantum Technol. **3**, 1900140 (2020).

[41] Y.-P. Wang and C.-M. Hu, Dissipative couplings in cavity magnonics, J. Appl. Phys. **127**, 130901 (2020).

[42] V. L. Grigoryan, K. Shen, and K. Xia, Synchronized spin-photon coupling in a microwave cavity, Phys. Rev. B **98**, 024406 (2018).

[43] I. Boventer, M. Kläui, R. Macêdo, and M. Weides, Steering between level repulsion and attraction: broad tunability of two-port driven cavity magnon-polaritons, New J. Phys. **21**, 125001 (2019).

[44] I. Boventer, C. Dörflinger, T. Wolz, R. Macêdo, R. Lebrun, M. Kläui, and M. Weides, Control of the coupling strength and linewidth of a cavity magnon-polariton, Phys. Rev. Res. **2**, 013154 (2020).

[45] R. Resta, Manifestations of Berry's phase in molecules and condensed matter, J. Phys.: Condens. Matter **12**, R107 (2000).

[46] J. Li and S.-Y. Zhu, Entangling two magnon modes via magnetostrictive interaction, New J. Phys. **21**, 085001 (2019).

[47] Z. Zhang, M. O. Scully, and G. S. Agarwal, Quantum entanglement between two magnon modes via Kerr nonlinearity driven far from equilibrium, Phys. Rev. Res. **1**, 023021 (2019).

[48] J. M. P. Nair and G. S. Agarwal, Deterministic quantum entanglement between macroscopic ferrite samples, Appl. Phys. Lett. **117**, 084001 (2020).

[49] M. Harder, L. Bai, C. Match, J. Sirker, and C. Hu, Study of the cavity-magnon-polariton transmission line shape, Sci. Chin. Phys., Mech. Astron. **59**, (2016).

[50] M. X. Bi, X. H. Yan, Y. Xiao, and C. J. Dai, Magnon dark mode in a strong driving microwave cavity, J. Appl. Phys. **126**, 173902 (2019).

[51] C. W. Gardiner and M. J. Collett, Input and output in damped quantum systems: Quantum stochastic differential equations and the master equation, Phys. Rev. A **31**, 3761 (1985).

[52] M. Harder, P. Hyde, L. Bai, C. Match, and C.-M. Hu, Spin dynamical phase and antiresonance in a strongly coupled magnon-photon system, Phys. Rev. B **94**, 054403 (2016).

[53] J. Koch, A. A. Houck, K. L. Hur, and S. M. Girvin, Time-reversal-symmetry breaking in circuit-QED-based photon lattices, Phys. Rev. A **82**, 043811 (2010).

[54] M. Schmidt, S. Kessler, V. Peano, O. Painter, and F. Marquardt, Optomechanical creation of magnetic fields for photons on a lattice, Optica **2**, 635 (2015).

[55] F. Ruesink, M.-A. Miri, A. Alù, and E. Verhagen, Nonreciprocity and magnetic-free isolation based on optomechanical interactions, Nat. Commun. **7**, (2016).

[56] N. R. Bernier, L. D. Tóth, A. Koottandavida, M. A. Ioannou, D. Malz, A. Nunnenkamp, A. K. Feofanov, and T. J. Kippenberg, Nonreciprocal reconfigurable microwave optomechanical circuit, Nat. Commun. **8**, (2017).

[57] K. Fang, J. Luo, A. Metelmann, M. H. Matheny, F. Marquardt, A. A. Clerk, and O. Painter, Generalized non-reciprocity in an optomechanical circuit via synthetic magnetism and reservoir engineering, Nat. Phys. **13**, 465 (2017).

[58] J. P. Mathew, J. del Pino, and E. Verhagen, Synthetic gauge fields for phonon transport in a nano-optomechanical system, Nat. Nanotechnol. **15**, 198 (2020).

[59] Y. Chen, Y.-L. Zhang, Z. Shen, C.-L. Zou, G.-C. Guo, and C.-H. Dong, Synthetic Gauge Fields in a Single Optomechanical Resonator, Phys. Rev. Lett. **126**, 123603 (2021).

[60] Z. Shen, Y.-L. Zhang, Y. Chen, Y.-F. Xiao, C.-L. Zou, G.-C. Guo, and C.-H. Dong, Nonreciprocal Frequency Conversion and Mode Routing in a Microresonator, Phys. Rev. Lett. **130**, 013601 (2023).

[61] M. Aidelsburger, S. Nascimbene, and N. Goldman, Artificial gauge fields in materials and engineered systems, C. R. Phys. **19**, 394 (2018).

[62] A. Clerk, Introduction to quantum non-reciprocal interactions: From non-Hermitian Hamiltonians to quantum master equations and quantum feedforward schemes, SciPost Phys. Lect. Notes (2022),.

[63] F. Crameri, Scientific colour maps (2021).

[64] F. Crameri, G. E. Shephard, and P. J. Heron, The misuse of colour in science communication, Nat. Commun. **11**, (2020).

[65] J. R. Schrieffer and P. A. Wolff, Relation between the Anderson and Kondo Hamiltonians, Phys. Rev. **149**, 491 (1966).

[66] H. Y. Yuan, W. Yu, and J. Xiao, Loop theory for input-output problems in cavities, Phys. Rev. A **101**, 043824 (2020).

C.2) Using COMSOL Multiphysics® to model hybrid magnon-photon systems

Statement of Authorship

Title of Paper	Using COMSOL Multiphysics to model hybrid magnon-photon systems
Publication Status	☐ Published ☐ Accepted for Publication ☐ Submitted for Publication ☑ Unpublished and Unsubmitted w ork w ritten in manuscript style
Publication Details	

Principal Author

Name of Principal Author (Candidate)	Alan Gardin		
Contribution to the Paper	Performed theoretical and numerical calculations. Analysed numerical data and wrote the manuscript.		
Overall percentage (%)	50		
Certification:	This paper reports on original research I conducted during the period of my Higher Degree by Research candidature and is not subject to any obligations or contractual agreements with a th train its inclusion in this thesis. I am the primary author of this paper.		
Signature		Date	22/01/2024

Co-Author Contributions

By signing the Statement of Authorship, each author certifies that:

i. the candidate's stated contribution to the publication is accurate (as detailed above);

ii. permission is granted for the candidate in include the publication in the thesis; and

iii. the sum of all co-author contributions is equal to 100% less the candidate's stated contribution.

Name of Co-Author	Christian Person		
Contribution to the Paper	Read and provided comments on the manuscript.		
Signature		Date	18/03/2024

Name of Co-Author	Christophe Fumeaux		
Contribution to the Paper	Read and provided comments on the manuscript.		
Signature		Date	17/03/2024

Name of Co-Author	Giuseppe Tettamanzi		
Contribution to the Paper	Read and provided comments on the manuscript.		
Signature		Date	17-03-2024

Name of Co-Author	Vincent Castel		
Contribution to the Paper	Read and provided comments on the manuscript.		
Signature		Date	18/03/2024

Using COMSOL Multiphysics® to model hybrid magnon/photon systems

Alan Gardin,[1,2,*] Christophe Fumeaux,[3] Christian Person,[1] Giuseppe C. Tettamanzi,[4] and Vincent Castel[1]

[1] *IMT Atlantique, Lab-STICC, UMR CNRS 6285, F-29238 Brest, France*
[2] *School of Physics, The University of Adelaide, Adelaide SA 5005, Australia*
[3] *School of Electrical Engineering and Computer Science, The University of Queensland, Brisbane QLD 4072, Australia*
[4] *School of Chemical Engineering and Advanced Materials, The University of Adelaide, Adelaide SA 5005, Australia*

Cavity magnonics is the study of the interaction between magnons, the quantas of spin wave excitation in magnetic materials, and photons confined to a cavity. The dominant coupling mechanism between magnons and photons at microwave frequencies is the Zeeman interaction, which naturally depends on the photonic density of states inside the cavity. In this tutorial, we give a pedagogical introduction to using COMSOL Multiphysics® to model hybrid magnon/photon system in the microwave frequency range. Using the example of re-entrant cavities, we discuss (1) the engineering of cavity resonances, (2) the impact of the excitation antennas on the quality factors, (3) the calculation of the S-parameters of cavities, with and without a magnet, and (4) the calculation of the coupling strength.

CONTENTS

I. Introduction 1

II. Theory 2
A. Electromagnetic field in a cavity 2
B. The Kittel mode 2
C. Experimental characterisation 3

III. Eigenmode analysis 4
A. Main steps 5
B. Study of a two-post re-entrant cavity 6

IV. Frequency domain analysis 7
A. Setting up excitation antennas 7
B. Influence of the geometry of the antenna 8

V. Modelling coupled magnon/photon systems 10
A. Transmission spectrum 10
B. Coupling strength 11

VI. Conclusion 11

Acknowledgments 12

References 12

I. INTRODUCTION

a. Context and problem statement. In cavity magnonics, the electromagnetic field distribution plays an important role. One key aspect concerns the magnon/photon coupling, which strongly depends on the distribution of the magnetic field in the cavity. For instance, it is best to have a locally uniform magnetic field in the location of the magnetic sample, so that only the Kittel mode is excited. Additionally, to optimise the coupling strength and potentially reach the ultrastrong coupling regime and beyond, it is necessary to concentrate the electromagnetic field as much as possible into the magnetic sample. Such optimisations can be performed using COMSOL Multiphysics®.

Furthermore, often measurements are performed by a reflection or transmission experiment, which again is mediated by the electromagnetic field. The engineering of the excitation antenna, and their impact on cavity magnonics application can again be studied using COMSOL Multiphysics®.

b. Contribution and scope. In this work, we demonstrate how the RF module of COMSOL Multiphysics®, a finite element modelling software, can be used to engineer and optimise cavity magnonics platforms. We focus our discussion on three-dimensional cavities operating in microwave frequencies between 1 to 20 GHz. Additionally, the only magnetic sample we shall consider is a Yttrium-Iron-Garnet (YIG) sphere, and we will only examine the lowest-order spin wave mode of YIG, the so-called Kittel mode. We shall further assume that a static magnetic field $\mathbf{H}_0 = H_0\hat{\mathbf{z}}$ is applied along the $\hat{\mathbf{z}}$ axis. We will also assume the Coulomb gauge $\boldsymbol{\nabla}\cdot\mathbf{A} = 0$ (with $\mathbf{A}$ the vector potential) throughout the paper. The emphasis is put on an intuitive understanding, rather than mathematical rigour. Version 6.1 of COMSOL Multiphysics® is used throughout.

c. Outline. We begin by some theoretical reminders in section II. Notably, we introduce the mode decomposition of the electromagnetic field inside a cavity, and the coupling of magnons with microwave photons. Next, in section III, we discuss the eigenmode analysis using COMSOL Multiphysics® by using the example of a two-post re-entrant cavity.

* alan.gardin@imt-atlantique.fr

II. THEORY

A. Electromagnetic field in a cavity

a. Mode decomposition In this first paragraph, we would like to provide some intuition on why the electromagnetic field can be decomposed as a discrete set of independent "modes", when it is confined to a cavity. One way to understand this is to consider the wave equation for the vector potential $\mathbf{A}$, from which the electric and magnetic field can be obtained from

$$\mathbf{E} = -\frac{\partial \mathbf{A}}{\partial t}, \quad \mathbf{B} = \boldsymbol{\nabla} \times \mathbf{A}. \tag{1}$$

In the Coulomb gauge, one can prove by combining Maxwell's equations that $\mathbf{A}$ satisfies the standard wave equation

$$\left(\boldsymbol{\nabla}^2 - \frac{n^2}{c^2}\frac{\partial^2}{\partial t^2}\right)\mathbf{A}(\mathbf{r}, t) = 0 \tag{2}$$

with $n = \sqrt{\epsilon_r \mu_r}$ the refractive index, and ϵ_r (μ_r) the relative electric permittivity (magnetic permeability) of the medium. This well-known equation can be solved by separation of variables, and for instance the solution can be written in terms of plane waves

$$\mathbf{A}(\mathbf{r}, t) = \int \mathrm{d}k \left(c_k e^{i(\mathbf{k}\cdot\mathbf{r} - \omega_k t)} + c_k^* e^{-i(\mathbf{k}\cdot\mathbf{r} - \omega_k t)}\right) \tag{3}$$

with $k = n\frac{\omega_k}{c}$ is a continuous variable (and thus we have a continuous set of associated frequencies ω_k), and c_k complex-valued constants. A plane wave basis is adapted for free space, but in the presence of metallic boundaries, the wave vectors can only take discrete values.

Let us take the example of a cubic cavity of length L. If we note $\hat{\mathbf{n}}$ the unit vector normal to an interface, then the electric and magnetic fields satisfy the boundary conditions [1]

$$\hat{\mathbf{n}} \times (\mathbf{E}_{\text{out}} - \mathbf{E}_{\text{in}}) = 0, \quad \hat{\mathbf{n}} \cdot (\mathbf{B}_{\text{out}} - \mathbf{B}_{\text{in}}) = 0. \tag{4}$$

Since these conditions are valid at all times, then necessarily we have $e^{i(\mathbf{k}\cdot\mathbf{r})} = 0$ on the boundaries, which leads to the conditions

$$k_x = n_x \frac{2\pi}{L}, \quad k_y = n_y \frac{2\pi}{L}, \quad k_z = n_z \frac{2\pi}{L}, \tag{5}$$

where n_x, n_y, n_z are integers. Thus, we see that confining the electromagnetic field in a certain region of space led to a discrete set of modes, and we can rewrite

$$\mathbf{A}(\mathbf{r}, t) = \sum_k \left(c_k e^{-i\omega_k t} + c_k^* e^{i\omega_k t}\right)\mathbf{u}_k(\mathbf{r}), \tag{6}$$

where $\mathbf{u}_k$ are the spatial mode functions satisfying the Helmholtz equation

$$(\boldsymbol{\nabla}^2 + k^2)\mathbf{u}_k = 0. \tag{7}$$

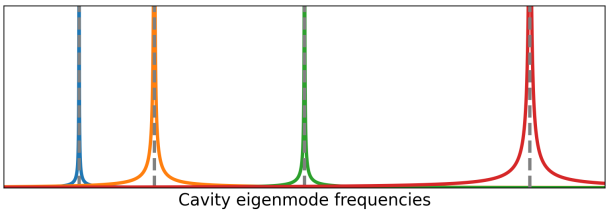


FIG. 1. Illustration of the broadening of the energy levels in a practical cavity. Ideally, the mode decomposition described by eq. (6) leads to a discrete set of frequencies, illustrated by the vertical dashed lines. However, in practice each cavity mode has a finite lifetime broadening the frequencies as shown by the solid lines. The larger the broadening, the higher the dissipation, which corresponds to a reduced lifetime.

b. Losses In an ideal cavity made of a perfect electric conductor, then the modes have an infinite lifetime, since there are no losses. However in practice, the cavity modes dissipates their energy to the environment, for instance due to radiative losses in the cavity walls, or interaction with the matter inside of the cavity. The effect of dissipation is to broaden the energy levels, giving them a finite linewidth. Formally, a cavity mode of frequency $\omega_c/2\pi$ acquires a finite linewidth by including an imaginary part $\omega_c \mapsto \omega_c - i\frac{\kappa_c}{2}$, which can be derived e.g. using quantum Langevin equations [2, 3]. The broadening of energy levels is illustrated in fig. 1.

c. Effect of dielectrics The electromagnetic field wants to go to regions with higher dielectric constants. For instance, if one places a dielectric where the electromagnetic field has a maximum, then it will lower this eigenmode's frequency. Indeed, we will have made it easier for the mode to exists in the same location, so it requires less energy, and by $E = \hbar\omega$ if E is lowered then ω is lowered.

B. The Kittel mode

a. Definition and dynamics Yttrium-iron-garnet can be thought of as a spin ensemble, described by local angular momenta vectors $\mathbf{s}_i$, with i indexing a spatial location in the lattice. We focus on the lowest-order mode, the Kittel model, which corresponds to all spins precessing in phase. Thus, we can model the YIG sphere with a macrospin vector $\mathbf{S} = \sum_i \mathbf{s}_i$. The macrospin can be linked to the magnetisation $\mathbf{M}$ by

$$\mathbf{M} = \frac{\gamma_S}{V_m}\mathbf{S}, \tag{8}$$

where $\gamma_S/2\pi = 28.04$ GHz/T is the gyromagnetic ratio for spins, and V_m the volume of the YIG sample. The dynamics of the magnetisation in the presence of a magnetic field $\mathbf{H}$ is described by the Landau-Lifschitz-Gilbert

equation

$$\frac{\mathrm{d}\mathbf{M}}{\mathrm{d}t} = -\gamma_S \mu_0 \mathbf{M} \times \mathbf{H} + \frac{\alpha}{M_s}\left(\mathbf{M} \times \frac{\mathrm{d}\mathbf{M}}{\mathrm{d}t}\right) \tag{9}$$

where $\mathbf{M}_s$ is the saturation magnetisation, and α is the phenomenological Gilbert damping constant (for YIG, usually $10^{-5} \leqslant \alpha \leqslant 10^{-4}$).

b. Response to a small magnetic field The Landau-Lifschitz-Gilbert equation can be linearised in the presence of a small time-dependent magnetic field $\mathbf{h}$. From now on, we assume that a static magnetic field $\mathbf{H}_0$ is applied along the $\hat{\mathbf{z}}$ axis, and we take $\mathbf{h}$ to be orthogonal to $\mathbf{H}_0$, i.e. $\mathbf{h}$ only has components in $\hat{\mathbf{x}}$ and $\hat{\mathbf{y}}$. The static magnetic field leads to a saturation magnetisation M_S oriented along $\hat{\mathbf{z}}$, while the small time-dependent magnetic field $\mathbf{h}$ leads to a deviation $\mathbf{m} = \chi\mathbf{h}$ of the magnetisation from equilibrium, where, for a spherical magnetic sample [4],

$$\chi = \begin{pmatrix} u & -iv & 0 \\ iv & u & 0 \\ 0 & 0 & 0 \end{pmatrix} \tag{10}$$

is the magnetic susceptibility with

$$u = \frac{\omega_M(\omega_0 - i\alpha\omega)}{(\omega_0 - i\alpha\omega)^2 - \omega^2}, \tag{11}$$

$$v = \frac{\omega_M \omega}{(\omega_0 - i\alpha\omega)^2 - \omega^2}. \tag{12}$$

where $\omega_M = \gamma_S \mu_0 M_S$, $\omega_0 = \gamma_S \mu_0 H_0$, $\gamma/2\pi$ the gyromagnetic ratio of an electron, μ_0 the magnetic permeability of vacuum, M_S the saturation magnetisation, α the Gilbert damping. Recalling that $\mathbf{B} = \mu_0(\mathbf{H} + \mathbf{M})$, we have $\mathbf{B} = \mu\mathbf{H}$ with $\mu = \mu_0(1 + \chi)$ the magnetic permeability tensor.

c. Details of the interaction Using a microscopic model and a second-quantised formalism, it can be shown that the coupling strength to a collective spin precession (Kittel mode) is [5, 6]

$$\frac{g}{2\pi} = \eta\sqrt{\omega_c}A, \tag{13}$$

where $\omega_c/2\pi$ is the cavity resonance frequency,

$$A = \frac{\gamma_S}{4\pi}\sqrt{\frac{\mu}{g_L \mu_B}\mu_0 \hbar n_s} \tag{14}$$

is a constant with $\gamma_S = 28$ GHz/T the gyromagnetic ratio μ_B the Bohr magneton, $\mu = 5\mu_B$ the magnetic moment of YIG, $n_s = 6.22 \times 10^{27}$ m^{-3} is the spin density of Yttrium-Iron-Garnet [6], $\hbar$ is the reduced Planck constant, and η is the filling-factor

$$\eta = \sqrt{\frac{\left(\int_{V_m} \mathrm{d}^3\mathbf{r}\, \mathbf{h}(\mathbf{r}) \cdot \hat{\mathbf{x}}\right)^2 + \left(\int_{V_m} \mathrm{d}^3\mathbf{r}\, \mathbf{h}(\mathbf{r}) \cdot \hat{\mathbf{y}}\right)^2}{V_m \int_{V_c} \mathrm{d}^3\mathbf{r}\, |\mathbf{h}(\mathbf{r})|^2}} \tag{15}$$

where V_c (V_m) is the volume of the cavity (magnetic sample).

d. Spectral features The coupling between photons and magnons leads to a novel quasi-particles called a polariton. The physics of a magnon coupled to a photon is essentially that of two coupled harmonic oscillators [4, 5], and the resulting polaritons can also be interpreted as a harmonic oscillator. Noting $\omega_c/2\pi$ ($\omega_m/2\pi$) the frequencies of the cavity mode (magnon mode), and $g/2\pi$ the coupling strength between them, we find that the frequencies $\omega_\pm/2\pi$ of the polaritons are given by [4]

$$\omega_\pm = \frac{\omega_c + \omega_m}{2} \pm \frac{\sqrt{(\omega_c - \omega_m)^2 + 4g^2}}{2}. \tag{16}$$

C. Experimental characterisation

a. Electric and magnetic antennas The characterisation of a cavity magnonics is often performed through the measure of the reflection or transmission coefficient of the cavity. This implies the ability to couple a measuring device to the cavity modes. This can be done in two ways: through an electric field, or a magnetic field. Depending on which method is used, an electric or magnetic antenna need to be inserted into the cavity. Examples of electric and magnetic antennas are pictured in fig. 2. The main difference is that electric antennas are "open", while magnetic antennas are closed. As a consequence, magnetic antennas can be referred to as "loop antennas" in some works.

To fix terminology, it is common to employ the term "probe" instead of antenna. Here, we shall use the term antenna when it is used as an emitter (i.e. we want to excite some eigenmode of the cavity), and probe when the antenna is used as a receiver. For instance, if there are two ports labelled 1 and 2, then to compute S_{21}, port 1 is a probe and port 2 an antenna.

b. Input-output formalism The input-output formalism [2] is a useful tool to derive expressions for the reflection and transmission coefficient of the cavity. We refer the reader to [2–4, 7, 8] for the derivation, and we

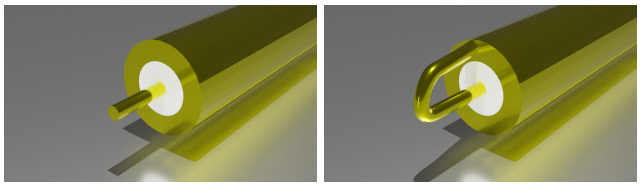


FIG. 2. Example of antennas used to excite the cavity modes, where we can distinguish the inner and outer conductor made of copper (yellowish), and the dielectric between them (white). (a) Detailed view of an electric antenna, made by letting the inner conductor of a coaxial cable be longer than the dielectric and outer conductor. (b) Detailed view of a magnetic (or loop) antenna, made by soldering the inner conductor back onto the outer conductor. The inner conductor could also be soldered onto the cavity, but it makes it harder to change and reuse the antennas for another cavity.

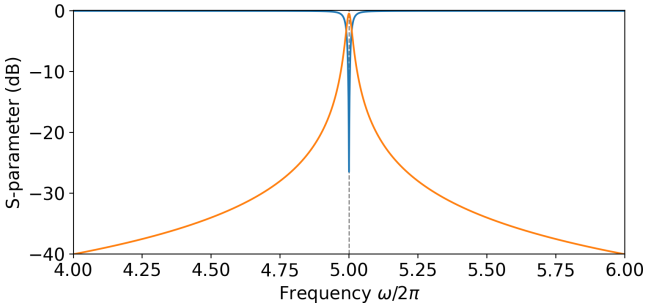


FIG. 3. Plot of the reflection amplitude $|S_{11}|$ (blue) and transmission amplitude $|S_{21}|$ (orange) squared given by eqs. (17) and (18). The parameters used are typical of cavity magnonics systems: $\omega_c/2\pi = 5$ GHz, $\kappa_c/2\pi = 1$ MHz, and $\kappa_1/2\pi = \kappa_2/2\pi = 10$ MHz.

only quote the results here. For a single cavity mode of frequency $\omega_c/2\pi$ coupling to two antennas with coupling rates $\kappa_1/2\pi$ and $\kappa_2/2\pi$,

$$S_{11}(\omega) = 1 - i\frac{\kappa_1}{\omega - \omega_c + i\frac{\kappa_c+\kappa_1+\kappa_2}{2}}, \tag{17}$$

$$S_{21}(\omega) = -i\frac{\sqrt{\kappa_1\kappa_2}}{\omega - \omega_c + i\frac{\kappa_c+\kappa_1+\kappa_2}{2}}, \tag{18}$$

where $\kappa_c/2\pi$ is the intrinsic dissipation rate of the cavity mode.

In practice, these reflection and transmission amplitudes can be measured by a vector network analyser (VNA). However, VNAs measure powers, proportional to amplitudes squared, and give the result in dB. For instance, a reflection S_{11}^{dB} as given by a VNA is usually

$$S_{11}^{\mathrm{dB}} = 10\log_{10}\left(|S_{11}|^2\right) = 20\log_{10}\left(|S_{11}|\right), \tag{19}$$

while technically the quantity $|S_{11}|$ in decibel is given by $10\log_{10}(|S_{11}|)$ instead. Usually, an experimental plot of the reflection or transmission amplitude thus corresponds to $|S_{11}|^2$ instead of $|S_{11}|$, but it is common to simply label such plots by e.g. $|S_{11}|$ instead of $|S_{11}|^2$, while still referring to them as amplitudes. We shall do the same here.

In fig. 3, we plot the reflection and transmission "amplitudes" given by eqs. (17) and (18). We observe that the reflection has a dip at the cavity mode's frequency, while the transmission has a maximum at the cavity mode's frequency. The imaginary part in the denominators of the reflection and transmission contributes to a finite linewidth of the cavity resonance, where we see it has contributions from the intrinsic damping ($\kappa_c/2\pi$), as well as from the coupling to the ports ($\kappa_1/2\pi$ and $\kappa_2/2\pi$). We further see that the amplitude of the resonances depend on the material (through the intrinsic losses characterised by $\kappa_c/2\pi$) and the coupling to the ports.

c. Quality factors Quality factors are measures of the losses in a system. One often distinguishes between three quality factors: the internal (or unloaded) quality factor Q_i, the external (or coupling) quality factor Q_e, and the loaded quality factor Q_l. The internal quality factor Q can be defined as

$$Q_i = \frac{\omega_c}{\kappa_c}, \tag{20}$$

and describe the ratio of the average energy stored by the average energy loss per radian [9]. The external quality Q_e factor accounts for the losses due to coupling the environment, for instance the excitation antennas. Thus, $Q_e = \frac{\omega_c}{\kappa_1+\kappa_2}$. Finally, the loaded quality factor Q_l is the experimentally available quantity, and accounts for both the internal and coupling losses [9]. In terms of the internal and external quality factors, it reads

$$\frac{1}{Q_l} = \frac{1}{Q_i} + \frac{1}{Q_e} = \frac{\kappa_c + \kappa_1 + \kappa_2}{\omega_c}. \tag{21}$$

In microwave cavities, quality factors are typically of the order of 10^2 to 10^5. Finish this, cite references. The design of the antennas affects the external quality factor, and will be discussed in section III.

d. Reflection and transmission coefficients for coupled magnon/photon Using the input-output formalism when the cavity mode couples to the magnon, we find [4, 7, 8]

$$S_{11}(\omega) = 1 - i\frac{\kappa_1\left(\omega - \omega_m + i\frac{\kappa_m}{2}\right)}{\left(\omega - \omega_c + i\frac{\kappa_c+\kappa_1+\kappa_2}{2}\right)\left(\omega - \omega_m + i\frac{\kappa_m}{2}\right) - g^2}, \tag{22}$$

$$S_{21}(\omega) = -i\frac{\sqrt{\kappa_1\kappa_2}\left(\omega - \omega_m + i\frac{\kappa_m}{2}\right)}{\left(\omega - \omega_c + i\frac{\kappa_c+\kappa_1+\kappa_2}{2}\right)\left(\omega - \omega_m + i\frac{\kappa_m}{2}\right) - g^2}, \tag{23}$$

where $g/2\pi$ is the coupling strength of eq. (13), $\omega_m/2\pi$ is the magnon's resonance frequency, and $\kappa_m/2\pi$ its intrinsic dissipation rate.

e. Experimental setup The standard measurement setup is pictured in fig. 5, and comprises four elements, (1) the cavity, (2) the magnetic sample placed inside the cavity, (3) an electromagnet to apply the static magnetic field $\mathbf{H}_0$, which tunes the magnon frequency, and (4) a vector network analyser to measure the transmission/reflection of the cavity system.

The spectrum obtained by reflection of transmission follows the hybridised frequencies $\omega_\pm/2\pi$ described by eq. (16). Additional information about experimental setups can be found in references [4, 10–12].

III. EIGENMODE ANALYSIS

The COMSOL Multiphysics® software [13] can be used to compute numerically the eigenmodes of a cavity using the RF module. The first step is to perform a CAD modelling of the cavity in COMSOL Multiphysics®. The second step involves setting up the proper materials for

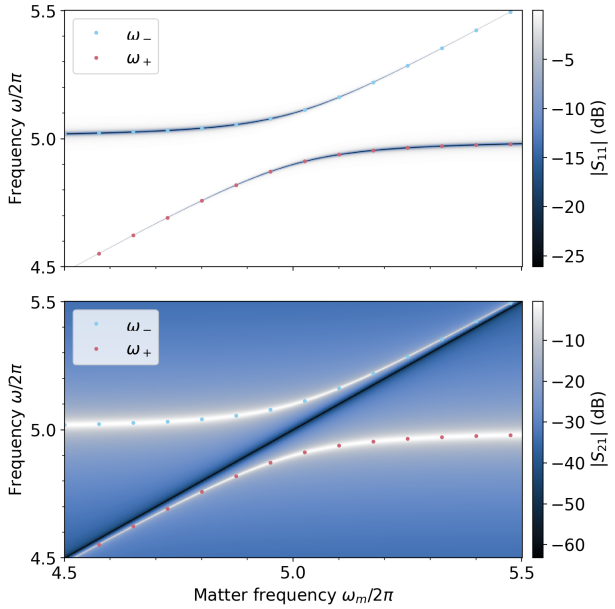


FIG. 4. Plot of the reflection amplitude $|S_{11}|$ and transmission amplitude $|S_{21}|$ given by eqs. (22) and (23). The parameters used are identical to fig. 3, with the coupling strength $g/2\pi = 100$ MHz.

each component of the system. The final step consists of adjusting the parameters for the eigensolver, such as the mesh refinement or the eigenvalue search method.

It is necessary to understand the limitations of this software to critically assess its results. In the following, we begin by successively examining the influence of each step described above on the output given by COMSOL Multiphysics®. We take the example of a two-post re-entrant cavity based on the design studied in [6], and pictured in fig. 6.

A. Main steps

a. Modelling method The first step is to model the cavity, which can be done directly in COMSOL Multiphysics®, or by importing standard 3D modelling files such as `.STEP` or `.STL` files. At microwave frequencies, the skin depth is negligible for good conductors such as copper. Thus, if we are not interested in the losses, we can simply model the interior of the cavity. Often, there are several ways of performing the modelling, and in general the methods are equivalent. Here, we chose to create three cylinders for respectively the cavity and the two posts, and then we subtract the two posts from the cavity.

The material inside the cavity is set as air. For the YIG sphere, we define a blank material with $\epsilon_r = 15$ and $\mu_r = 1$ [14]. The cavity itself is a perfect electric conductor, which is the default.

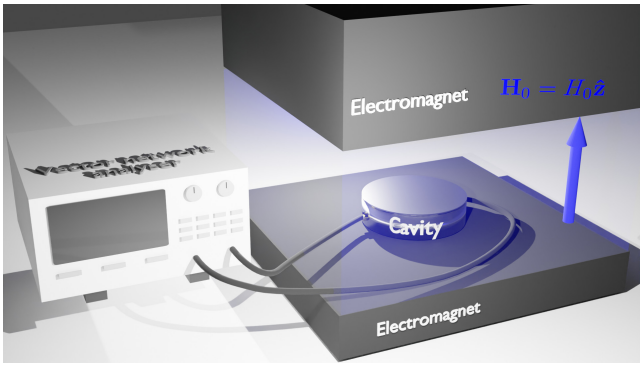


FIG. 5. Standard experimental setup to characterise a cavity magnonics system. The cylindrical cavity is connected to the vector network analyser with coaxial cables to measure the reflection and transmission coefficients. An electromagnet is used to create a tunable static magnetic field $\mathbf{H}_0$ to tune the ferromagnetic resonance frequency $\omega_m/2\pi$ of the magnon.

b. Material and losses The choice of material affect the boundary conditions. However, as we previously stated, for good conductors the finite conductivity makes the fields leak into the cavity walls only weakly. Thus, we expect the frequency and field distribution of the eigenmodes to be mostly determined by the geometry of the cavity, and not the material (unless of course we choose an unrealistically lossy material).

Simply changing the material of the cavity to copper changes neither the frequency nor the quality factor of the mode. This is due to the default *perfect electric conductor* (PEC) condition set by COMSOL Multiphysics®, which effectively disregards the material. Instead, one needs to add an *impedance boundary condition* so that the material is taken into account. As a consequence, we observe a small real-valued shift in the frequency, a small imaginary part, and a finite quality factor. To model the roughness of the cavity, one can simply diminish the conductivity of the material used, which we will increase the losses.

c. Influence of the mesh Using an appropriate mesh is a critical step of finite element modelling. By default, the mesh is "Physics-controlled", which means that COMSOL Multiphysics® automatically creates the mesh, with a user-controlled global refinement. Another option is to start from an automatic mesh defined by COMSOL Multiphysics®, and then refine it manually around regions of interest, such as the YIG sphere. Note that so-called "singularities" can happen if some abrupt geometries are not properly smoothed [15].

d. Solver As described in the COMSOL Multiphysics® manual [16], there are several ways of searching for eigenmodes. When one searches for eigenmodes around a certain frequencies, then

- *Closest in absolute value*: search for solutions that are closest to the given frequency in absolute value
- *Larger real part* to search for eigenvalues with a

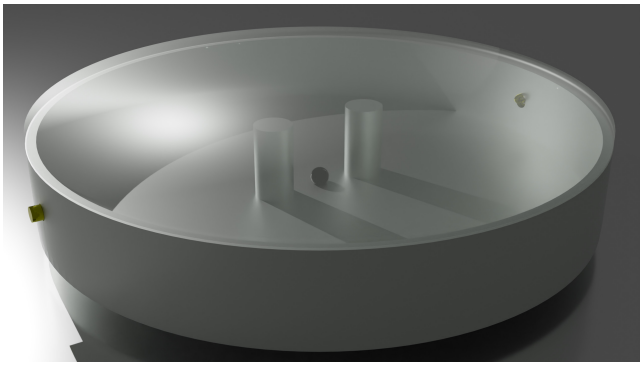


FIG. 6. The two-post cavity used in the examples, where the lid has been made transparent to observe the interior. By default, the radius of the cavity is 15 mm and its height 5 mm. The posts have a radius of 1 mm and are separated by a distance of 2.72 mm, from centre to centre. The height of the posts is 4.850 mm, corresponding to a gap of 150 μm between the top of the posts and the lid. Note the presence of a YIG sphere of radius 0.235 μm between the posts, placed at a height of 335 μm from the bottom of the cavity.

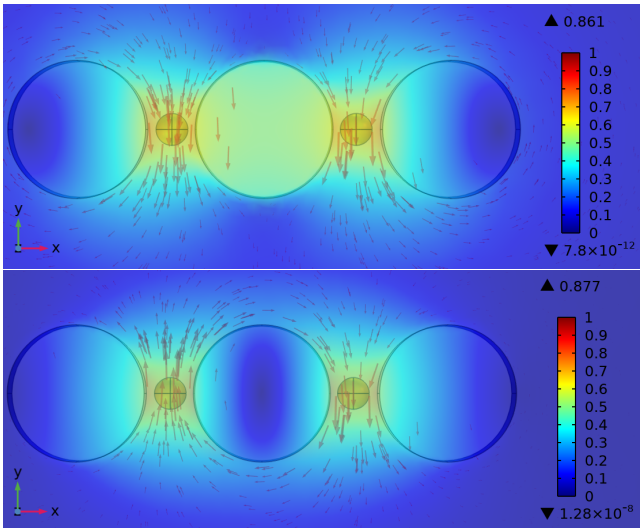


FIG. 7. Magnetic field distribution of (a) the dark mode and (b) the dark mode, obtained using an eigenmode analysis of COMSOL Multiphysics®.

larger real part than the shift value

- *Smaller real part*: to search for eigenvalues with a smaller real part than the shift value

Similar options exists for the imaginary part too.

Note that the initial value used for the solver can affect the results. For instance, with default settings, looking for eigenmodes around 1 Ghz or 3 GHz gave the same values for the eigenfrequencies and the magnetic fields, but the associated quality factors could differ by several orders of magnitude.

B. Study of a two-post re-entrant cavity

We now illustrate how COMSOL Multiphysics® can be used to tune the frequency of two eigenmodes in the cavity pictured in fig. 6, first proposed in [12] for cavity magnonics. These two eigenmodes are referred to as dark and bright modes [12], and their field distribution is shown in fig. 7. While we focus on the lowest-order magnon mode (Kittel mode), higher-order modes exist and can be excited when the cavity mode's magnetic field $\mathbf{h}$ is not uniform over the YIG sphere. Thus, we can notice that the bright mode is preferred for coupling to a YIG sphere, because between the posts, its field distribution if more uniform than that of the dark mode.

Next, we successively study the impact of several geometric parameters on the resonance frequencies of the dark and bright modes in fig. 8: the radius of the cavity, the height of the cavity, the distance between the posts, the radius of the posts, the distance between the top of the posts and the lid, and the difference of height between two posts, when all the other parameters are fixed to values given in fig. 6. The different trends observed give different knobs to tune the resonances frequencies of these two modes. Note that figs. 8(b), 8(c) and 8(e) mirror the results obtained by [12].

For instance, we see that varying the distance between the posts (fig. 8(c)) significantly tunes the frequency of the bright mode, while keeping the frequency of the dark mode almost identical. On the other hand, varying the radius of the cavity, the height of the cavity, or the radius of the posts allow to tune the frequencies of both modes in similar proportions.

Importantly, we see that the frequencies of the modes are very sensible to the height of the posts: indeed, variations of the order of μm lead to variations of the frequencies in the GHz range. For a range of micrometers, the roughness of the material used can come into play. This suggests that polishing the lid of the cavity can have an importance on the resonance frequencies of a re-entrant cavity.

Because the electric field is strongest at the top of the posts, we can interpret changing the radius of the posts as varying the capacitance. An alternative way of changing this capacitance is through the distance between the lid the posts. The formula for the capacitance of two parallel plates of surface A, separated by a distance d with a material of relative permittivity ϵ_r in between is

$$C = \epsilon_0 \epsilon_r \frac{A}{d}. \tag{24}$$

Thus, increasing the distance d between the posts and the lid reduces the capacitance, while increasing the radius of the posts increases it. Figures 8(d) and 8(e) thus show that the eigen-frequencies have an inverse relationship with the capacitance.

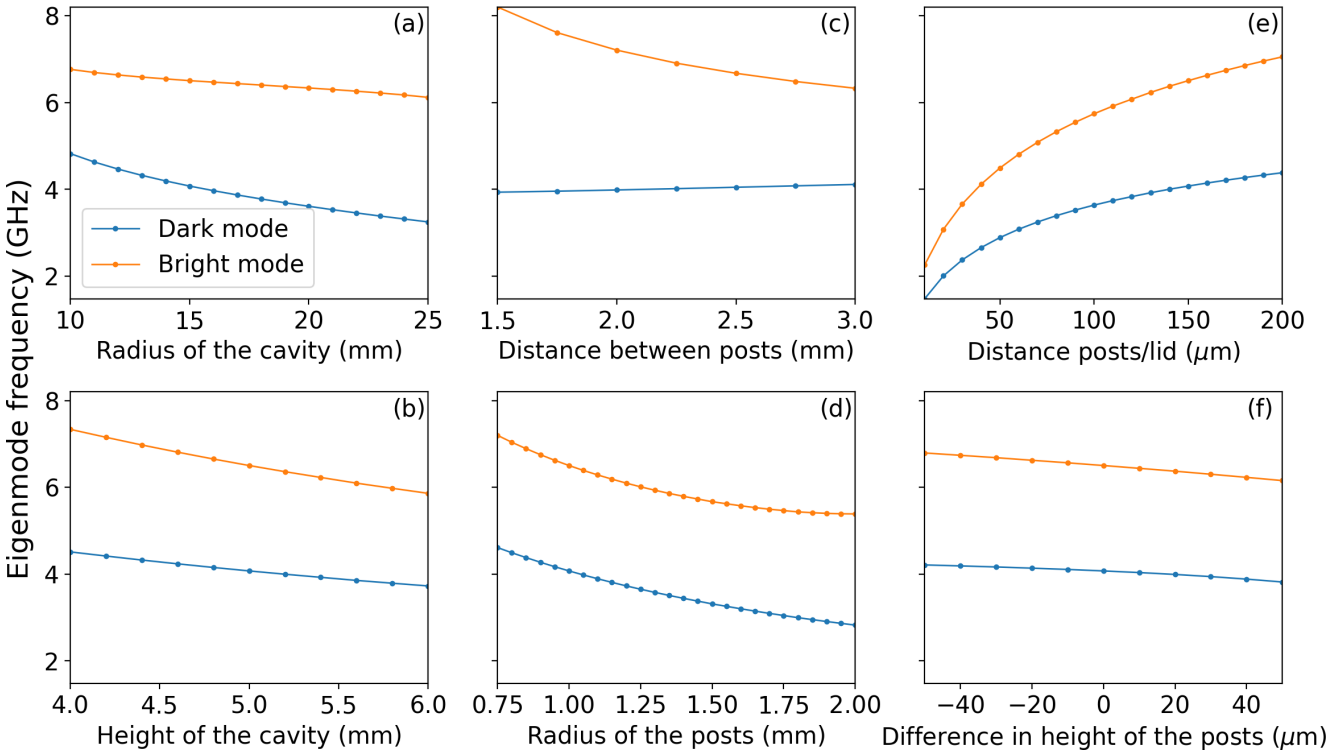


FIG. 8. (a) Evolution of the resonance frequencies of the dark and bright modes as a function of the cavity radius. (b) Evolution of the resonance frequencies of the dark and bright modes as a function of the height of the cavity. (c) Evolution of the resonance frequencies of the dark and bright modes as a function of the distance between the posts radius. (d) Evolution of the resonance frequencies of the dark and bright modes as a function of radius of the posts. (e) Evolution of the resonance frequencies of the dark and bright modes as a function of the gap between the posts and the lid. (f) Evolution of the resonance frequencies of the dark and bright modes as a function of the difference in height of the posts. In each plot, only one parameter is changed, while the others are set to the values of fig. 6.

IV. FREQUENCY DOMAIN ANALYSIS

So far, we have somewhat been studying an idealised cavity, since it was isolated from the environment. We now turn our attention to the response of a cavity to an excitation, characterised by the S-parameters. Such an analysis corresponds to a *frequency domain* study in COMSOL Multiphysics®. This type of study necessitates setting up excitation ports attached to an electric or magnetic antenna, which can be of two kinds: *lumped ports* and *ports* [17]. Lumped ports are simpler, and are based on a lumped element description of the ports in terms of voltage, current and impedance. Ports, on the other hand, directly consider the electromagnetic field, which is more complicated by also more precise.

A. Setting up excitation antennas

a. Lumped ports According to the documentation of the RF module [17], a lumped port is appropriate for modelling the connection to a transmission line, such as a coaxial cable. There are three relevant variables for a lumped port: its voltage V, its current I, and its impedance $Z = \frac{V}{I}$. In COMSOL Multiphysics®, the voltage V is calculated by a line integral of the electric field between the conductors defining the port. The price to pay for such simplicity is that the reflection and transmission can be less precise than a calculation using the electromagnetic field.

For a lumped port, COMSOL Multiphysics® allows to specify a phase only if one chooses a voltage excitation. To find the voltage associated with a certain power, we can use the relation $P = VI = V^2/Z$. Most of the time, the impedance of the port is $Z_0 = 50\,\Omega$, which allows specifying the excitation voltage at the port from the desired power.

In COMSOL Multiphysics®, we can access the equations and variables used for the computation of certain simulation results [18]. To introduce how the S-parameter are computed, let us assume a cavity with two ports 1 and 2. If port 1 is excited by a voltage V_{in} with a phase ϕ, then the equations used by COMSOL Multiphysics® are [17]

$$S_{11} = \frac{V_1 - V_{\text{in}} e^{i(\phi_1+\varphi)}}{V_{\text{in}} e^{i(\phi_1+\varphi)}}, \quad S_{21} = \frac{V_2}{V_{\text{in}} e^{i(\phi_1+\varphi)}} \tag{25}$$

where φ is an unspecified phase.

b. Ports We assume that two ports attached to a cavity are connected to a coaxial cable, and hence we need to select "coaxial cable" as the terminal type in COMSOL Multiphysics®. A coaxial cable has a different number of modes, and here we consider the lowest order mode (corresponding to the signal propagating in the cable). We note $\mathbf{E}_{\text{mode},j} = \sum_{\mathbf{v}\in\{\hat{\mathbf{x}},\hat{\mathbf{y}},\hat{\mathbf{z}}\}} \mathbf{E}_{\text{mode},j,\mathbf{v}}\mathbf{v}$ the tangential component of the electric mode of the coaxial cable associated with port j. Similarly, we define $\mathbf{E}_{\text{inside}}$ to be the tangential component of the electric field inside the cavity.

For instance, the calculation of the transmission parameter S_{21} involves the variable

$$S_{2x} = \frac{\int_{A_2} \mathrm{d}^2\mathbf{r}\, \mathbf{E}_{\text{inside}}(\mathbf{r}) \cdot \mathbf{E}^*_{\text{mode},2}(\mathbf{r})}{\int_{A_2} \mathrm{d}^2\mathbf{r}\, |E_{\text{mode},2}(\mathbf{r})|^2}, \tag{26}$$

where A_2 is the area of the port (dielectric) and $\cdot$ denotes the usual (component-wise) dot product of two vectors. To better understand this expression, it is convenient to define a "scalar product" of two fields $\mathbf{E}_k, \mathbf{E}_l$ as

$$\langle \mathbf{E}_k | \mathbf{E}_l \rangle_{A_2} = \int_{A_1} \mathrm{d}^2\mathbf{r}\, \mathbf{E}_k(\mathbf{r}) \cdot \mathbf{E}_l(\mathbf{r})^*. \tag{27}$$

Then, we can rewrite S_{2x} as

$$S_{2x} = \frac{\langle \mathbf{E}_{\text{inside}} | \mathbf{E}_{\text{mode},2} \rangle_{A_2}}{\langle \mathbf{E}_{\text{mode},2} | \mathbf{E}_{\text{mode},2} \rangle_{A_2}}. \tag{28}$$

We observe that this definition characterises the overlap (nominator) between the EM mode in the coaxial cable, and the EM field in the cavity, up to a normalisation factor (denominator).

On the other hand, if we examine the reflection parameter S_{11}, we can observe that it involves computing

$$S_{1x} = \frac{\left\langle \mathbf{E}_{\text{inside}} - \mathbf{E}_{\text{mode},1} e^{i\phi} \middle| \mathbf{E}_{\text{mode},1} \right\rangle_{A_1}}{\langle \mathbf{E}_{\text{mode},1} | \mathbf{E}_{\text{mode},1} \rangle_{A_1}} \tag{29}$$

$$= \frac{\langle \mathbf{E}_{\text{inside}} | \mathbf{E}_{\text{mode},1} \rangle_{A_1}}{\langle \mathbf{E}_{\text{mode},1} | \mathbf{E}_{\text{mode},1} \rangle_{A_1}} - e^{i\phi}. \tag{30}$$

In a sense, at each port boundary, we have

$$E_{\text{inside},r} = E_{\text{mode},r} + E_{\text{reflected},r}. \tag{31}$$

This is why for reflection parameters, we compute the overlap with $E_{\text{inside},r} - E_{\text{mode},r}e^{i\phi}$ instead of $E_{\text{mode},r}$.

In COMSOL Multiphysics®, the design of the ports boils down to creating three cylinders, one for the innner conductor, one for the dielectric, and one for the outer conductor. The radiuses of each of these parts can be obtained from the datasheet of the coaxial cable being used. To check for mistakes, note that COMSOL Multiphysics® proposes to compute the impedance of the ports, and it should be close to the standard 50 Ω if the geometry and dielectric constant have been set appropriately.

c. Multiple excitations We note that the definition used for the transmission of ports, should, *a priori*, still be appropriate if there are multiple excitations. Indeed, if we consider 3 ports, with port 1 and 3 being active, then the transmission through port 2 should still be described by the normalised overlap between the field in the cavity, and the mode of the coaxial cable.

On the other hand, the transmission for lumped ports depends on the input voltage. Maybe it is sufficient to consider the sum of the voltages as input. But also maybe not: if we think of the cavity as a circuit, the different excitations due to the antennas may be inserted at different points of the circuit. Clearly, this leads to a non-trivial modification of the transmission parameter.

Note that if the system is linear, we can simply compute the S parameters separately to compute the transmission in the presence of multiple excitations.

B. Influence of the geometry of the antenna

a. Type of antenna and spatial location The field distribution of the eigenmode we want to couple to helps in choosing whether an electric or magnetic antenna should be used. For instance, in a cylindrical cavity, it may be easier to couple to electric fields, rather than magnetic fields, so an electric antenna is preferred. This is partly due to the location of the antenna: if it is placed in a node of the field we want to couple to, then no energy energy transfer will be possible. Hence, the location of the antennas should be considered carefully to excite the modes of interest.

As an example, [19] used the CST software to numerically compute the transmission through a empty cylindrical cavity of radius 12.5 mm and height of $h = 35$ mm. with electrical antenna. As shown in fig. 9, the eigenmodes did produce resonances, but importantly the location of the antenna changed the quality factors, and affected the presence of anti-resonnances.

To check the impact of electric versus magnetic antennas, we modelled the cavity used by [19] in COMSOL Multiphysics® and we varied both the height ($h/2$ or $h/4$ with $h = 35$mm the height of the cavity) and the type (electric or magnetic) of the antenna. The results are presented in fig. 10, and we observe that magnetic antennas couple better to the cavity modes. Indeed, the quality factor is larger, and the transmission amplitude higher. Additionally, we notice that some cavity mdoes were not excited with electric antennas (for instance the eigenmode near 9 GHz), but they are with magnetic antennas.

b. Geometric details and impact on the eigenmodes One may be tempted to optimise the geometry of the antenna to obtain a perfect circular loop, and thus maximise the coupling. However, this is, in general, a mistake. The purpose of the antennas is to inject microwaves inside the cavity, but we do not want the antennas to be resonant (and hence it is unnecessary to make the

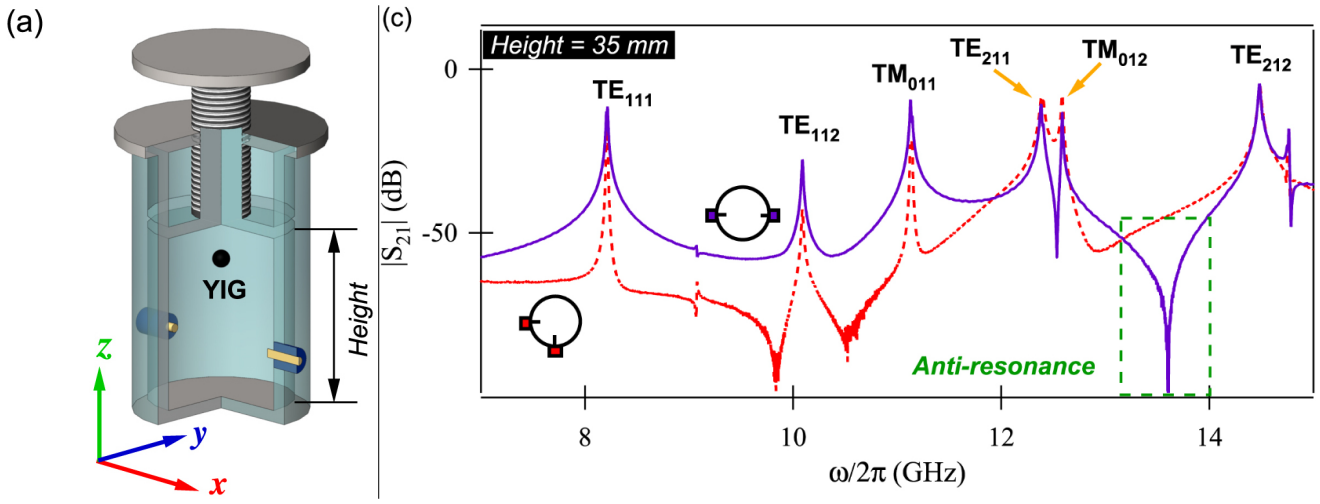


FIG. 9. Figures 2a and 2c of [19] reproduced under the CC Attribution 3.0 license [20]. On the left, the cylindrical cavity used in the simulations. On the right, the results of the CST simulation for different location of the electric antennas.

loop antenna's radiuses to match with the wavelengths of the injected microwave). Indeed, maximising the couplings to the ports leads to a much wider linewidth, which would complicate the measurement of a coupled magnon/photon spectrum for instance.

Intuitively, the antennas can be considered as a small perturbation of the eigenmodes inside the cavity. The more the antennas protrude inside the cavity, the more the eigenmodes are perturbed, because the geometry of the cavity is affected. Furthermore, the quality factor decreases as the length of the antennas inside the cavity increases. On the other hand, increasing the length of the antenna also increases the couplings between the ports and the eigenmodes, e.g. $\kappa_1/2\pi$ for port 1, which results in higher transmission amplitude.

To check this, we used an eigenmode analysis for various lengths of the magnetic antenna protruding inside the 2-post cavity. The results are shown in fig. 12, and we only show the quality factors here because we found the frequencies to vary at most by 3MHz for the dark mode, and 4MHz for the bright mode. Additionally,

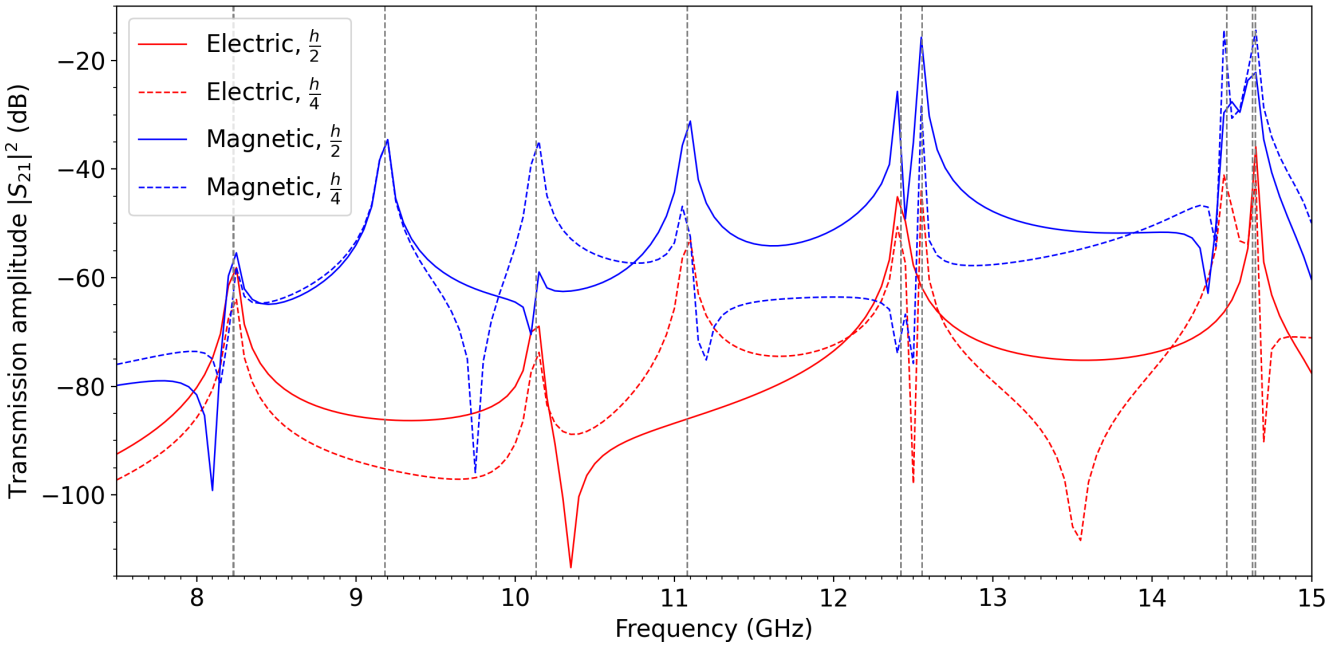


FIG. 10. Results of the frequency domain COMSOL Multiphysics® simulations for different types of antenna, and different height placements. Electric antennas are shown in blue, while magnetic antennas are shown in red. The solid (dashed) lines correspond to the antennas being placed at $h/2$ mm ($h/4$), where h is the cavity height. The vertical dashed lines correspond to the frequencies found using an eigenmode analysis.

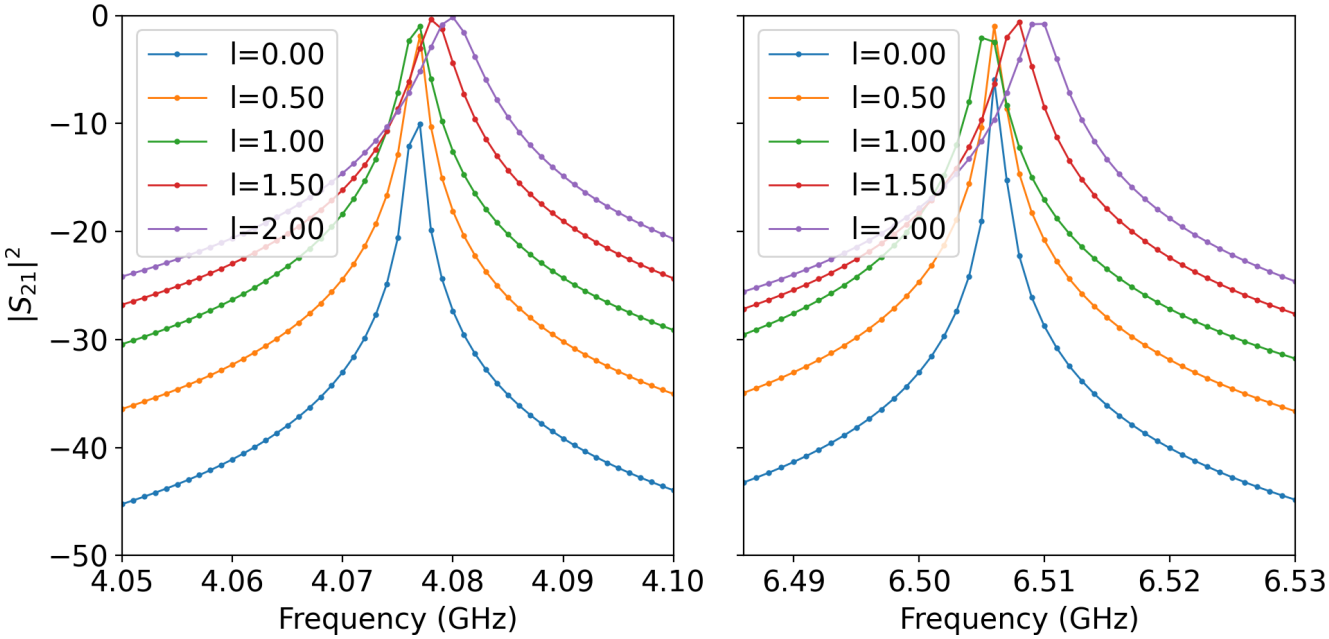


FIG. 11. Results of the frequency domain COMSOL Multiphysics® simulations for in the two-posts cavity for different lengths of antenna.

in fig. 11 we performed a frequency domain simulation around the resonances of the dark and bright modes. We see that as the length of the antenna gets longer, the quality factor diminishes, which confirms the results of the eigenmode analysis of fig. 12. Furthermore, we can observe a higher transmission amplitude (due to the smaller quality factor), and a small shift of the resonance frequencies.

c. Reliability As for an eigenmode analysis, the mesh needs to be refined enough to lead to physical and accurate results. As an example of the potential problems that can appear, let us consider that for a sufficiently refined mesh, we find a resonance at $\omega_c/2\pi = 5$ GHz, both from an eigenmode analysis and a frequency domain analysis. Let us assume the frequency domain analysis was performed between 4 GHz and 6 GHz. With a mesh of insufficient quality, a that same frequency domain analysis between 4 and 6 GHz can exhibit anti-resonances, i.e. dips in the transmission amplitude, that do not appear with an appropriate mesh.

Similarly, for a coarse mesh, the location of the resonance can fluctuate, for instance depending on the bounds used for the frequency domain analysis (e.g. starting the analysis at 4.5 GHz instead of 4 GHz). Note that in theory, the location of the resonances should be identical to that given by an eigenmode analysis, provided the eigenmode analysis included the antennas. However, non-invasive antennas are usually small perturbations to the cavity, so if an eigenmode analysis is performed without the antennas, as we did previously, the frequency shift of the resonances should remain modest.

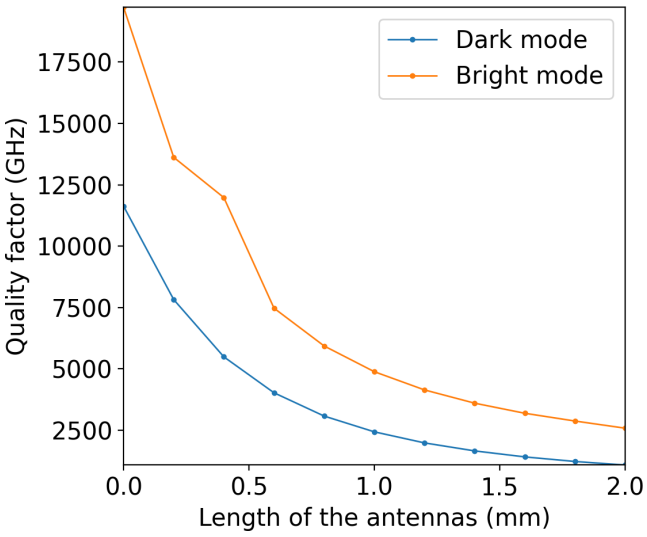


FIG. 12. Evolution of the quality factor for different lengths of antenna protruding inside the cavity.

V. MODELLING COUPLED MAGNON/PHOTON SYSTEMS

A. Transmission spectrum

COMSOL Multiphysics® also allows to model a standard experiment of cavity magnonics, where one measures the reflection (and transmission) parameters as a function of the static magnetic field $\mathbf{H}_0$. The method consists of performing a *frequency domain analysis*, as

described in the previous section, but this time including the magnetic sample in the simulation. To include the magnetic sample, and its response to the applied static magnetic field, one needs to change its relative permeability from scalar to the matrix μ which depends on the susceptibility tensor eq. (10). A good starting point to implement this in practice is the *Three-port ferrite circulator* example for the RF module [21], which neglects the ferrite losses. Another example which does include the losses is the *Impedance Matching of a Lossy Ferrite 3-Port Circulator* [22]. Note that we need to put in the internal field viewed by the sphere, which along $\hat{\mathbf{z}}$ is $\mathbf{H}_0 - N_{zz}M_s$ with $N_{zz} = 1/3$ and $M_s \simeq 0.190$ T.

This method has shown good agreement with experimental data, even in the ulstrastrong coupling regime [23].

B. Coupling strength

The coupling strength can be calculated in two ways. The first involves computing the form-factor using an eigenmode of frequency domain analysis. Indeed, the form-factor η appearing in the expression of the coupling strength of eq. (13) can be written

$$\eta = \sqrt{\frac{\left(\widetilde{H}_x\right)^2 + \left(\widetilde{H}_y\right)^2}{V_m \int_{V_c} \mathrm{d}^3 r \, |\mathbf{h}(\mathbf{r})|^2}} \tag{32}$$

where

$$\widetilde{H}_j = \int_{V_m} \mathrm{d}^3 r \, \mathbf{h}(\mathbf{r}) \cdot \hat{\mathbf{j}}, \tag{33}$$

for $j \in \{x, y\}$. COMSOL Multiphysics®computes $\mathbf{h}$ in phasor form as

$$\mathbf{h}(\mathbf{r}) = \sum_{j=x,y,z} |\mathbf{h}_j(\mathbf{r})| e^{i\varphi_j(\mathbf{r})} \hat{\mathbf{j}}, \tag{34}$$

with the total field being $\mathbf{h}(\mathbf{r}, t) = \mathbf{h}(\mathbf{r}) e^{-i\omega t}$. In a sense, COMSOL Multiphysics® computes the Heisenberg picture representation of the electromagnetic field. When computing $\widetilde{H}_j$, one should consider the "real" field, which can be obtained from $\mathbf{h}(\mathbf{r}, t)$ by taking the real part. Hence,

$$\widetilde{H}_j = \int_{V_m} \mathrm{d}^3 r \, \mathrm{Re}\Big\{ |\mathbf{h}_j(\mathbf{r})| e^{i\varphi_j(\mathbf{r})} e^{-i\omega t} \Big\} \tag{35}$$

$$= \int_{V_m} \mathrm{d}^3 r \, |\mathbf{h}_j(\mathbf{r})| \cos\left(\omega t - \varphi_j(\mathbf{r})\right). \tag{36}$$

Unfortunately, in many situations the phases φ_j are not homogeneous in the domain of the magnetic sample, so that we cannot simply ignore them. We thus need to evaluate $\widetilde{H}_j$ over a whole period $\frac{\omega}{2\pi}$. Using $\cos(a-b) = \cos a \cos b + \sin a \sin b$,

$$\widetilde{H}_j = \int_{V_m} \mathrm{d}^3 r \, |\mathbf{h}_j(\mathbf{r})| [\cos\omega t \cos\varphi_j(\mathbf{r}) + \sin\omega t \sin\varphi_j(\mathbf{r})] \tag{37}$$

$$= \cos(\omega t) \int_{V_m} \mathrm{d}^3 r \, |\mathbf{h}_j(\mathbf{r})| \cos\varphi_j(\mathbf{r}) \tag{38}$$

$$+ \sin(\omega t) \int_{V_m} \mathrm{d}^3 r \, |\mathbf{h}_j(\mathbf{r})| \sin\varphi_j(\mathbf{r}).$$

Defining

$$R_j = \int_{V_m} \mathrm{d}^3 r \, |\mathbf{h}_j(\mathbf{r})| \cos\varphi_j(\mathbf{r}), \tag{39}$$

$$I_j = \int_{V_m} \mathrm{d}^3 r \, |\mathbf{h}_j(\mathbf{r})| \sin\varphi_j(\mathbf{r}), \tag{40}$$

for $j = x, y$, we have

$$\left(\widetilde{H}_i\right)^2 = \cos^2\omega t R_j^2 + \sin^2\omega_t I_j^2 + \sin 2\omega t R_j I_j, \tag{41}$$

and hence

$$\left(\widetilde{H}_x\right)^2 + \left(\widetilde{H}_y\right)^2 = \cos^2\omega t\big(R_x^2 + R_y^2\big) + \sin^2\omega_t\big(I_x^2 + I_y^2\big) + \sin 2\omega t(R_x I_x + R_y I_y). \tag{42}$$

Thus, we can compute the integrals R_j and I_j in COMSOL Multiphysics®, and then deduce the trend of η, and hence $g/2\pi$ over a period $2\pi/\omega$.

Alternatively, we can use eq. (16) to fit a transmission spectrum obtained using a frequency domain analysis. Then, when $\omega_c = \omega_m$, the gap between the frequencies $\omega_\pm$ is $2g$, giving the coupling strength. However, this method is much more computationally expensive because one needs to run a frequency domain simulations for several values of the applied magnetic field $\mathbf{H}_0$.

VI. CONCLUSION

Through a series of examples, we have given directions on how COMSOL Multiphysics® can be used to engineering cavities for cavity magnonics applications. Notably, we showed how several quantities of interest in cavity magnonics can be modelled, investigated and then optimised using COMSOL Multiphysics®. These include the coupling of the excitation antennas to the cavity modes, the field distribution and its frequency, the coupling strength, and the reflection or transmission spectrum in a presence of a static magnetic field.

We would also like to mention that a frequency domain analysis is time-consuming. A possible solution to this problem is to expand the electromagnetic field's Green function in terms of the eigenmodes, as proposed in [24]. Then, in principle, one needs to perform a single eigenmode analysis to then perform frequency domain simulations. Indeed, the electromagnetic eigenmodes do not

depend on the applied static magnetic field. However, one may need a large number of eigenmodes to build the Green's function. Another potential problem is that an eigenmode analysis requires more RAM than frequency domain simulations.

Finally, we would like to mention that in principle COMSOL can be used to compute the frequency-dependence of the coupling of the cavity modes to the ports. Indeed, in the standard input-output theory, one makes a Markov approximation and neglects this frequency dependence. As a consequence, even far from resonance this non-vanishing coupling can effect experimental observables such as anti-resonances [25]. Looking at the model interaction Hamiltonian between the ports and the cavity mode in the input-output formalism, we see that it is linear in the creation and annihilation operators of the cavity modes and environment [2]. This suggests an overlap integral over frequency of the electromagnetic field of the cavity modes and that of the coaxial cable making up the ports. Regardless of the exact expression, it is likely that the computation of these overlap integrals can be numerically computed using COMSOL.

ACKNOWLEDGMENTS

We acknowledge financial support from Thales Australia and Thales Research and Technology. The scientific colour map *oslo* [26] is used in this study to prevent visual distortion of the data and exclusion of readers with colourvision deficiencies [27].

[1] B. Z. Rameshti, S. V. Kusminskiy, J. A. Haigh, K. Usami, D. Lachance-Quirion, Y. Nakamura, C.-M. Hu, H. X. Tang, G. E. Bauer, and Y. M. Blanter, Cavity magnonics (2021), arXiv:2106.09312 [cond-mat.mes-hall].

[2] C. W. Gardiner and M. J. Collett, Input and output in damped quantum systems: Quantum stochastic differential equations and the master equation, Physical Review A **31**, 3761 (1985).

[3] A. A. Clerk, M. H. Devoret, S. M. Girvin, F. Marquardt, and R. J. Schoelkopf, Introduction to quantum noise, measurement, and amplification, Reviews of Modern Physics **82**, 1155–1208 (2010).

[4] M. Harder and C.-M. Hu, Cavity spintronics: An early review of recent progress in the study of magnon–photon level repulsion, Solid State Physics , 47–121 (2018).

[5] G. Flower, M. Goryachev, J. Bourhill, and M. E. Tobar, Experimental implementations of cavity-magnon systems: from ultra strong coupling to applications in precision measurement, New Journal of Physics **21**, 095004 (2019).

[6] J. Bourhill, V. Castel, A. Manchec, and G. Cochet, Universal characterization of cavity–magnon polariton coupling strength verified in modifiable microwave cavity, Journal of Applied Physics **128**, 073904 (2020).

[7] M. Harder, B. M. Yao, Y. S. Gui, and C.-M. Hu, Coherent and dissipative cavity magnonics, Journal of Applied Physics **129**, 201101 (2021).

[8] H. Y. Yuan, W. Yu, and J. Xiao, Loop theory for input-output problems in cavities, Physical Review A **101**, 043824 (2020).

[9] D. Pozar, *Microwave Engineering, 4th Edition* (Wiley, 2011).

[10] W. G. Farr, D. L. Creedon, M. Goryachev, K. Benmessai, and M. E. Tobar, Ultrasensitive microwave spectroscopy of paramagnetic impurities in sapphire crystals at millikelvin temperatures, Phys. Rev. B **88**, 224426 (2013).

[11] M. Goryachev, W. G. Farr, D. L. Creedon, and M. E. Tobar, Spin-photon interaction in a cavity with time-reversal symmetry breaking, Phys. Rev. B **89**, 224407 (2014).

[12] M. Goryachev, W. G. Farr, D. L. Creedon, Y. Fan, M. Kostylev, and M. E. Tobar, High-cooperativity cavity qed with magnons at microwave frequencies, Phys. Rev. Applied **2**, 054002 (2014).

[13] S. COMSOL AB, Stockholm, Comsol multiphysics® (2020).

[14] W. Yu, J. Wang, H. Yuan, and J. Xiao, Prediction of attractive level crossing via a dissipative mode, Physical Review Letters **123**, 227201 (2019).

[15] L. Andersson, *Fillet Away Your Electromagnetic Field Singularities* (2014).

[16] COMSOL, *COMSOL Multiphysics 6.1 Reference Manual*, COMSOL (2022).

[17] COMSOL, *RF Module User's Guide, COMSOL 6.1*, COMSOL (2022).

[18] Under "Model Builder", select "Show More Options..." and enable *Equation View* [28].

[19] J. W. Rao, C. H. Yu, Y. T. Zhao, Y. S. Gui, X. L. Fan, D. S. Xue, and C.-M. Hu, Level attraction and level repulsion of magnon coupled with a cavity anti-resonance, New Journal of Physics **21**, 065001 (2019).

[20] C. Commons, Creative commons attribution 3.0 license.

[21] COMSOL, *Three-Port Ferrite Circulator*, COMSOL ().

[22] COMSOL, *Impedance Matching of a Lossy Ferrite 3-Port Circulator*, COMSOL ().

[23] G. Bourcin, J. Bourhill, V. Vlaminck, and V. Castel, Strong to ultrastrong coherent coupling measurements in a YIG/cavity system at room temperature, Physical Review B **107**, 214423 (2023).

[24] P. Y. Chen, D. J. Bergman, and Y. Sivan, Generalizing normal mode expansion of electromagnetic green's tensor to open systems, Physical Review Applied **11**, 044018 (2019).

[25] G. Bourcin, A. Gardin, J. Bourhill, V. Vlaminck, and V. Castel, Level attraction in a quasi-closed cavity, unpublished (2024).

[26] F. Crameri, Scientific colour maps (2021).

[27] F. Crameri, G. E. Shephard, and P. J. Heron, The misuse of colour in science communication, Nature Communications **11**, 10.1038/s41467-020-19160-7 (2020).

[28] COMSOL, *Viewing and Accessing the Equations and Variables for Physics Feature Nodes*, COMSOL ().

C.3) Engineering synthetic gauge fields through the coupling phases in cavity magnonics

Statement of Authorship

Title of Paper	Engineering synthetic gauge fields through the coupling phases in cavity magnonics
Publication Status	☒ Published ☐ Accepted for Publication ☐ Submitted for Publication ☐ Unpublished and Unsubmitted work written in manuscript style
Publication Details	arXiv, 2023-12-08 **Phys. Rev. Applied 21, 064033**

Principal Author

Name of Principal Author (Candidate)	Alan Gardin
Contribution to the Paper	Proposed a cavity design to obtain different synthetic gauge fields, performed the theoretical calculations, wrote the manuscript, analysed the experimental and numerical data.
Overall percentage (%)	60
Certification:	This paper reports on original research I conducted during the period of my Higher Degree by Res subject to any obligations or contractual agreements with a thir inclusion in this thesis. I am the primary author of this paper.
Signature	Date 22/01/2024

Co-Author Contributions

By signing the Statement of Authorship, each author certifies that:

i. the candidate's stated contribution to the publication is accurate (as detailed above);

ii. permission is granted for the candidate in include the publication in the thesis; and

iii. the sum of all co-author contributions is equal to 100% less the candidate's stated contribution.

Name of Co-Author	Guillaume Bourcin
Contribution to the Paper	Checked all the calculations, read the manuscript and provided comments on his structure. Proposed a cavity design for the creation of a non-trivial synthetic gauge field.
Signature	Date 05/02/2024

Name of Co-Author	Jeremy Bourhill
Contribution to the Paper	Proposed the original cavity design and measured it. Read the manuscript and provided comments.
Signature	Date 05/02/2024

Name of Co-Author	Vincent Vlaminck		
Contribution to the Paper	Proposed the original cavity design and measured it. Read the manuscript and provided comments.		
Signature		Date	02/02/2024

Name of Co-Author	Christian Person		
Contribution to the Paper	Read the manuscript and provided comments on his structure.		
Signature		Date	01/02/2024

Name of Co-Author	Christophe Fumeaux		
Contribution to the Paper	Read the manuscript and provided comments on his structure.		
Signature		Date	01/02/2024

Name of Co-Author	Giuseppe Tettamanzi		
Contribution to the Paper	Managed the project, read the manuscript and provided comments on his structure, checked calculations.		
Signature		Date	01/02/2024

Name of Co-Author	Vincent Castel		
Contribution to the Paper	Proposed the original cavity design and measured it. Optimised the initial cavity design, performed numerical simulations using COMSOL, carried out the measurements. Managed the project, read the manuscript, and provided comments on his structure.		
Signature		Date	01/02/20

Engineering synthetic gauge fields through the coupling phases in cavity magnonics

Alan Gardin,[1,2,*] Guillaume Bourcin,[2] Jeremy Bourhill,[3] Vincent Vlaminck,[2] Christian Person,[2] Christophe Fumeaux,[4] Giuseppe C. Tettamanzi,[1,5] and Vincent Castel[2]

[1] *School of Physics, The University of Adelaide, Adelaide, SA 5005, Australia*
[2] *Lab-STICC, UMR CNRS 6285, IMT Atlantique, Brest F-29238, France*
[3] *ARC Centre of Excellence for Engineered Quantum Systems and ARC Centre of Excellence for Dark Matter Particle Physics, Department of Physics, University of Western Australia, 35 Stirling Highway, Crawley, WA 6009, Australia*
[4] *School of Electrical Engineering and Computer Science, The University of Queensland, Brisbane, QLD 4072, Australia*
[5] *School of Chemical Engineering and Advanced Materials, The University of Adelaide, Adelaide, SA 5005, Australia*

(Received 13 December 2023; revised 6 May 2024; accepted 17 May 2024; published 13 June 2024)

Cavity magnonics, which studies the interaction of light with magnetic systems in a cavity, is a promising platform for quantum transducers and quantum memories. At microwave frequencies, the coupling between a cavity photon and a magnon, the quasiparticle of a spin-wave excitation, is a consequence of the Zeeman interaction between the cavity's magnetic field and the magnet's macroscopic spin. For each photon-magnon interaction, a coupling phase factor exists, and this is often neglected in simple systems; however, in "loop-coupled" systems, where there are at least as many couplings as modes, the coupling phases become relevant for the physics and lead to synthetic gauge fields. We present experimental evidence of the existence of such coupling phases by considering two spheres made of yttrium-iron-garnet and two different re-entrant cavities. We predict numerically the values of the coupling phases, and we find good agreement between the theory and the experimental data. These results show that in cavity magnonics, one can engineer synthetic gauge fields, which can be useful for cavity-mediated coupling and engineering dark-mode physics.

DOI: 10.1103/PhysRevApplied.21.064033

I. INTRODUCTION

Magnons are the quasiparticles associated with the elementary excitation of a spin wave in a magnetically ordered material, such as the ferrimagnet yttrium-iron-garnet (YIG). The field of cavity magnonics, or spin cavitronics, aims to use the interactions of photons in a cavity with magnons for both classical technologies (e.g., radio-frequency circulators or isolators, and spintronics [1–10]) and quantum technologies [11–13]. Magnons are notably promising for quantum transduction [14] due to their capability to couple to phonons [15], optical and microwave photons, and superconducting qubits [16–19]. The coupling with microwave photons has been particularly fruitful, and there have been demonstrations of coherent coupling [20], indirect coupling [21,22], ultrastrong coherent coupling [23–27], dissipative coupling [28–36], the tuning between level repulsion and attraction [37,38], a dark-mode memory [39], and nonreciprocal effects [36,40–42].

Physically, all of these results involve the photon-magnon coupling, which originates from the Zeeman interaction between the magnetic dipole moment of a magnet and a magnetic field. This interaction is characterized by a coupling strength and a coupling phase, which can both be chosen to be real positive numbers. As recently shown in Ref. [43], in most simple systems, the coupling phases can be ignored since they do not affect the physics; however, in "loop-coupled" systems [42,44–49], where there are at least as many couplings as modes, neglecting the coupling phases can lead to an erroneous description of the physics. Notably, in the context of cavity magnonics, it has been theoretically shown that the coupling phases can steer the system toward either dark-mode physics (which is useful for quantum memories [39]) or the enhancement of cavity-mediated coupling by taking advantage of several cavity modes [43] (which is useful for quantum information transduction).

*Corresponding author: alan.gardin@adelaide.edu.au

 © 2024 American Physical Society

However, so far, no experimental evidence of the coupling phases has been reported, despite their striking impact on cavity-magnonics applications. To bridge this gap, we propose two re-entrant three-post cavities, in which multiple cavity modes simultaneously couple to two magnon modes, creating loop-coupled systems. We experimentally measure a first cavity in which the physics is characterized by a single physical phase $\theta = \pi$, which makes it fall within the theoretical analysis of a previous work [43]. In contrast, in the second cavity, the physics is determined by two physical phases $\theta_1 = 0$ and $\theta_2 = \pi$. In both cavities, we predict theoretically the values of the physical phases and find good agreement with our experiments.

In Sec. II, we introduce the coupling phases, and how one can reduce them to the so-called *physical phases* characterizing the physics using unitary transformations. Importantly, we interpret these physical phases as parametrizing a synthetic $U(1)$ gauge field (or synthetic magnetic field), allowing our work to be connected to the wider literature. Next, in Sec. III, we introduce a cavity with a physical phase $\theta = \pi$, which is supported by both theory and experiment. In Sec. IV, we perform a similar analysis, but this time on a cavity leading to the physical phases $\theta_1 = \pi$ and $\theta_2 = 0$. We conclude in Sec. V.

II. INTRODUCTION TO THE MAGNON-PHOTON COUPLING PHASE

We adopt a second-quantized formalism for the description of the cavity (annihilation operator c_k) and magnon modes (annihilation operator m_l after performing the Holstein-Primakoff transformation [50] on the macrospin operator [51]). The ferromagnetic resonance frequency of the magnons is tuned by a static applied magnetic field $\mathbf{H}_0 = H_0\hat{\mathbf{z}}$. The coupling between the cavity mode c_k and the magnon mode m_l is characterized by a coupling strength $g_{kl}/2\pi$ and a coupling phase φ_{kl} defined as [43,51]

$$g_{kl}/2\pi = \eta_{kl}\sqrt{\omega_k}\frac{\gamma}{4\pi}\sqrt{\frac{\mu}{g_L\mu_B}\hbar\mu_0 n_s}, \tag{1}$$

$$\varphi_{kl} = \arg\left\{\int_{V_m} \mathrm{d}^3 r \mathbf{h}_k(\mathbf{r})\cdot\hat{\mathbf{x}} + i\int_{V_m} \mathrm{d}^3 r \mathbf{h}_k(\mathbf{r})\cdot\hat{\mathbf{y}}\right\}, \tag{2}$$

where $\gamma/2\pi = 28$ GHz/T is the gyromagnetic ratio, $\mu = 5\mu_B$ is the magnetic moment of a unit cell of YIG, μ_B is the Bohr magneton, μ_0 is the magnetic permeability of vacuum, $g_L = 2$ is the Landé g-factor, $n_s = 4.22\times 10^{23}$ m^{-3} is the spin density of YIG [52], $\mathbf{h}_k$ is the magnetic field vector of the cavity mode k, V_m is the volume of the YIG spheres, and

$$\eta_{kl} = \sqrt{\frac{\left(\int_{V_m} \mathrm{d}^3 r \mathbf{h}_k(\mathbf{r})\cdot\hat{\mathbf{x}}\right)^2 + \left(\int_{V_m} \mathrm{d}^3 r \mathbf{h}_k(\mathbf{r})\cdot\hat{\mathbf{y}}\right)^2}{V_m\int_{V_c}\mathrm{d}^3 r|\mathbf{h}_k(\mathbf{r})|^2}} \tag{3}$$

is the filling factor, in which V_c is the volume of the cavity.

The interaction Hamiltonian between the cavity mode c_k and the magnon mode m_l reads [43]

$$H_I = \hbar g_{kl}\left(e^{i\varphi_{kl}}c_k m_l^\dagger + e^{-i\varphi_{kl}}c_k^\dagger m_l\right), \tag{4}$$

in which we used the rotating-wave approximation, which is valid provided $(g_{kl}/\omega_k) < 10\%$ [53,54]. Note that the interaction Hamiltonian (4) is Hermitian and results from the coherent coupling between photons and magnons. This is in stark contrast with dissipative couplings [11,12], in which the interaction is non-Hermitian and results from an indirect coupling [55] of the magnons and photons through a strongly dissipative mode [28,29], or traveling wave reservoir [30–36].

Formally, recall that the unitary transformation $U = e^{i\varphi c^\dagger c}$ transforms the operator c as $c \mapsto e^{-i\varphi}c$, and that unitary transformations amount to a change of basis. Thus, the transformations $U_{c_k} = e^{i\varphi_{kl}c_k^\dagger c_k}$ and $U_{m_l} = e^{-i\varphi_{kl}m_l^\dagger m_l}$ can both remove the coupling phase from Eq. (4). Physically, this means that there exists a basis in which the coupling phase vanishes, so we might as well set it to zero to simplify the study of the physics. In other words, this amounts to changing the reference phase.

The situation is more complicated when one considers several simultaneous couplings. Naturally, any isolated bosonic mode has a local phase degree of freedom [corresponding to a $U(1)$ symmetry] since, for example, the mapping $c \mapsto e^{-i\varphi}c$ does not change its Hamiltonian; however, couplings between modes constrain these local phase choices, which can break this symmetry. For instance, the coupling of Eq. (4) "locks" the local phase choices of c_k and m_l together, but we are still free to rotate either c_k (using U_{c_k}) or m_l (using U_{m_l}) to remove the coupling phase. In other words, we have two phase degrees of freedom, but there is only one constraint between them; however, when the number of couplings (constraints) is greater than or equal to the number of modes (degrees of freedom), we cannot remove all the coupling phases, and they become relevant for the physics.

To illustrate this concept, let us consider the example of two magnon modes simultaneously coupling to three cavity modes, as illustrated in Fig. 1. We can eliminate the coupling phases between m_1 and the cavity modes in Fig. 1(a) using

$$U_{c_k} = e^{i\varphi_{k1}c_k^\dagger c_k}, \quad k \in \{1,2,3\}, \tag{5}$$

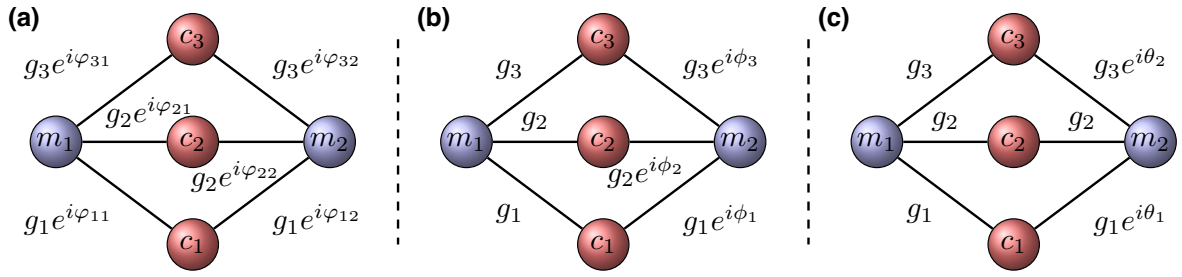


FIG. 1. Simplification of the physics of a system composed of two magnon modes m_1 and m_2 (in blue) coupling equally and simultaneously to three cavity modes c_1, c_2, and c_3 (in red). (a) The system in which all the coupling phases remain. (b) After unitarily transforming the cavity modes using Eq. (5), the physics is determined only by three phases $\phi_k = \varphi_{k2} - \varphi_{k1}$, accounting for the difference in coupling for each cavity mode $k \in \{1, 2, 3\}$. (c) After rotating m_2 using Eq. (6), we are left with two physical phases $\theta_1 = \phi_1 - \phi_2$ and $\theta_2 = \phi_3 - \phi_2$.

and we obtain Fig. 1(b). Next, we rotate m_2 with

$$U_{c_k} = e^{i\phi_2 m_2^\dagger m_2}, \tag{6}$$

and we finally obtain two *physical phases* θ_1 and θ_2 characterizing the physics [see Fig. 1(c)].

Therefore, in the system of Fig. 1, we have six couplings and five modes, leading to two physical phases. If the two magnons couple to only two cavity modes (e.g., by setting $g_3 = 0$), we have as many constraints as degrees of freedom, and the system is characterized by a single physical phase.

To conclude this section, we would like to mention that a physical phase effectively parametrizes an artificial (or synthetic) $U(1)$ gauge field. Indeed, Eq. (4) can be interpreted as the interaction Hamiltonian of a charged particle on a lattice in the presence of a static magnetic field (see Refs. [46,56] for instance). These artificial gauge fields have been proposed for several physical systems, such as neutral atoms [57,58], circuit QED [46,55,59], and cavity optomechanics [47–49]. Electrodynamics is naturally a $U(1)$ gauge theory, and therefore, by analogy, an artificial $U(1)$ gauge field leads to synthetic electromagnetism. Notably, an artificial magnetic field can be used to break time-reversal symmetry in systems where the presence of a "natural" magnetic field is problematic, such as in circuit QED [46]. In turn, synthetic gauge fields can be used to create nonreciprocal behaviors by balancing coherent and dissipative couplings through reservoir engineering [55,56,60], and there have been proposals for circuit QED [46,55,59] and cavity optomechanics [47–49]. Framing the effect of the coupling phases in cavity magnonics in terms of synthetic gauge fields allows a connection to be made with all the aforementioned works; however, it is worth noting that the associated applications may not be so relevant for cavity magnonics, because a static magnetic field is already present. Still, as shown in Ref. [43], the coupling phases, or the associated synthetic gauge field, can lead to distinct physics in cavity magnonics; therefore, their study remains of practical interest.

III. A SINGLE PHYSICAL PHASE

A. Cavity design

The first cavity we consider, called cavity π, is pictured in Fig. 2(a) and contains three posts. It is based on the design of a two-post re-entrant cavity from Refs. [23,24], and it possesses similar eigenmodes. The distributions of the magnetic fields of the two cavity eigenmodes of interest were simulated using COMSOL Multiphysics® [see Figs. 2(c) and 2(e)]. The magnetic fields of these two cavity eigenmodes are concentrated between the posts, where we place two identical YIG spheres of diameter 470 μm. Importantly, the magnetic fields of the eigenmodes are either in the same or opposite directions at the sphere locations, which leads to different coupling phases. This difference can also be understood by considering the strength and direction of the electric field, which is concentrated between the tops of the posts and the lid [see Figs. 2(b) and 2(d)]. For instance, the electric field of the first cavity eigenmode [see Fig. 2(b)] is localized only on the left and right posts, but with opposing directions [which, by the right-hand rule, agrees with the circulation of the magnetic field shown in Fig. 2(c)]. Conversely, for the second cavity eigenmode, the electric field is nonzero on top of each post, albeit with different intensities and orientations, and this leads to the magnetic field of Fig. 2(e).

B. Prediction of the physical phase

The numerical evaluation of the coupling strengths and coupling phases [given by Eqs. (1) and (2)] can be performed using eigenmode analysis in COMSOL Multiphysics, the results of which are summarized in Table I. Recall that the first index corresponds to the cavity mode, while the second is for the magnon mode. For the magnon modes, $l = 1$ ($l = 2$) corresponds to the left (right) YIG sphere. We first note that the coupling phases indeed follow

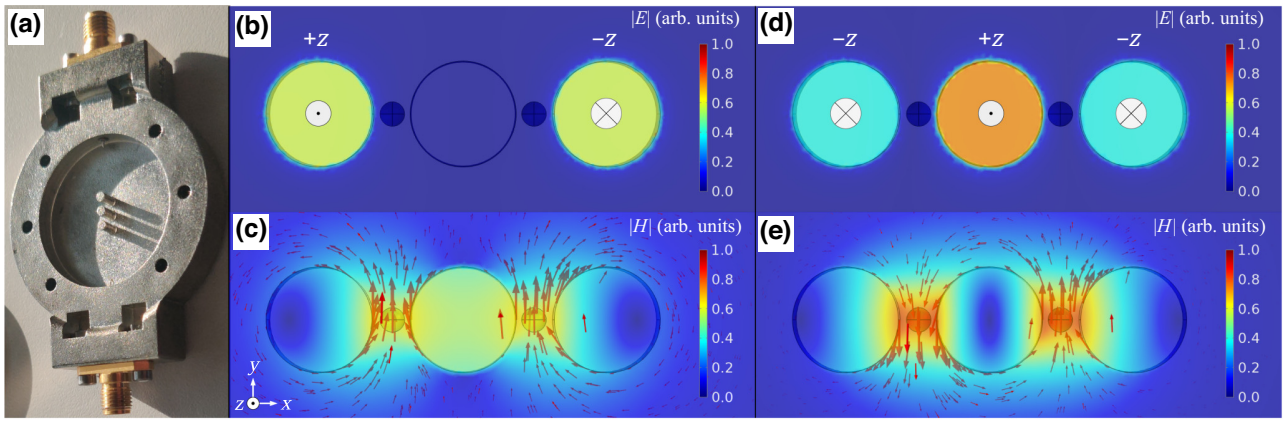


FIG. 2. (a) Three-post re-entrant cavity π used in the experiment. The lid of the cavity is not shown. (b),(c) Electric and magnetic field norms, simulated using COMSOL Multiphysics, of the first eigenmode c_1 (frequency $\omega_{c,1}/2\pi = 4.524$ GHz) of cavity π. (d),(e) Electric and magnetic field distributions, simulated using COMSOL, of the second eigenmode c_2 (frequency $\omega_{c,2}/2\pi = 6.378$ GHz) of cavity π. For each mode, the magnetic field is maximal between the posts, where the YIG spheres are placed, while the electric field is concentrated between the top of the posts and the lid of the cavity. The vectors are only shown for the magnetic field.

the directions of the two cavity eigenmodes' magnetic fields shown in Fig. 2. Furthermore, we observe that both YIG spheres couple with the same coupling strength to each cavity mode, as can be expected from the symmetry of the problem. Hence, from now on, we set $g_{11} = g_{12} = g_1$ and $g_{21} = g_{22} = g_2$. Assuming both YIG spheres to be perfectly identical, the Hamiltonian of the system is $H_\pi = H_{\text{free}} + H_I$, with

$$H_{\text{free}} = \sum_{k=1}^{2} \hbar\omega_{c,k} c_k^\dagger c_k + \sum_{l=1}^{2} \hbar\omega_m m_l^\dagger m_l, \tag{7}$$

where $\omega_m = \gamma H_0$ is the ferromagnetic resonance frequency of the lowest-order magnon modes (Kittel mode) and

$$\begin{aligned} H_I = {} & \hbar g_1 e^{-i\frac{\pi}{2}} c_1 m_1^\dagger + \hbar g_1 e^{-i\frac{\pi}{2}} c_1 m_2^\dagger \\ & + \hbar g_2 e^{i\frac{\pi}{2}} c_2 m_1^\dagger + \hbar g_2 e^{-i\frac{\pi}{2}} c_2 m_2^\dagger + \text{H.c.}, \end{aligned} \tag{8}$$

in which H.c. indicates the Hermitian conjugate terms. This system falls within the example of Fig. 1 by setting $g_3 = 0$, from which we deduce that after the unitary transformations, the interaction Hamiltonian can be written as

$$\begin{aligned} H_I = {} & \hbar g_1 c_1 m_1^\dagger + \hbar g_1 e^{i\theta_1} c_1 m_2^\dagger \\ & + \hbar g_2 c_2 m_1^\dagger + \hbar g_2 c_2 m_2^\dagger + \text{H.c.}, \end{aligned} \tag{9}$$

with $\theta_1 = \varphi_{12} - \varphi_{11} - (\varphi_{22} - \varphi_{21}) = \pi$; hence the name "cavity π" for the cavity.

The values of the coupling strengths and of the physical phase can be verified by the transmission amplitude $|S_{21}|$ through the cavity. Hence, in Appendix A, we present a frequency-domain simulation using COMSOL Multiphysics to numerically compute $|S_{21}|$ as a function of the magnon resonance frequency $\omega_m/2\pi$, and the results have good agreement with the eigenmode results of Table I.

C. Experimental results

The three-post cavity π design was 3D printed and then metallized. Using a vector network analyzer, we measured the transmission through the cavity when the static magnetic field $\mathbf{H}_0$ was swept to tune ω_m, and we obtained the data shown in Fig. 3. The hybridized photon-magnon polariton frequencies are predicted by the spectrum of $H_\pi = H_{\text{free}} + H_I$, with H_{free} given by Eq. (7) and H_I given by Eq. (9), and these are plotted on top of the color map with $\theta_1 = \pi$ as suggested by Table I, but with the adjusted parameters $g_1/2\pi = 81$ MHz and $g_2/2\pi = 120$ MHz instead. We attribute the difference between theory and experiment for the coupling strengths to the imperfection of the 3D printing and metallization processes. In particular, the three posts of cavity π are not completely cylindrical, which changes the focusing of the magnetic field between them.

TABLE I. Numerical calculation of the coupling strengths g_{kl} and coupling phases φ_{kl} of cavity π using COMSOL Multiphysics.

Coupling strength (MHz)		Coupling phase (rad)	
$g_{11}/2\pi$	139	φ_{11}	$-\frac{\pi}{2}$
$g_{12}/2\pi$	139	φ_{12}	$-\frac{\pi}{2}$
$g_{21}/2\pi$	207	φ_{21}	$+\frac{\pi}{2}$
$g_{22}/2\pi$	207	φ_{22}	$-\frac{\pi}{2}$

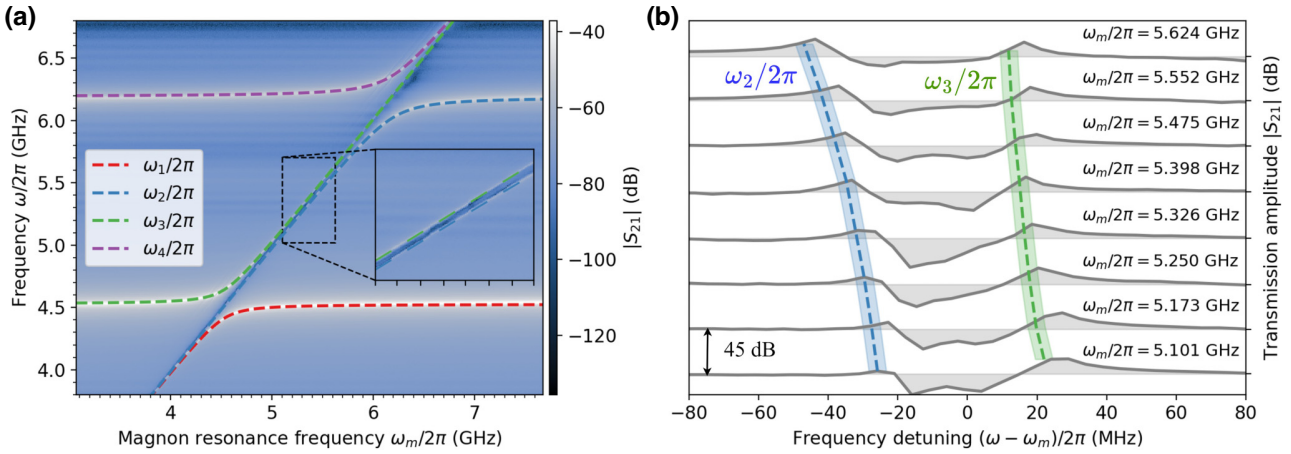


FIG. 3. (a) Experimental transmission amplitude $|S_{21}|$ of cavity π, along with the theoretical spectrum in dashed lines. The fit parameters are $\omega_{c,1}/2\pi = 4.527$ GHz, $\omega_{c,2}/2\pi = 6.19$ GHz, $g_1/2\pi = 81$ MHz, $g_2/2\pi = 120$ MHz, and $\theta_1 = \pi$. Inset: enlargement of $5.1 \leq \omega_m/2\pi \leq 5.62$ GHz, and $5.02 \leq \omega/2\pi \leq 5.7$ GHz, showing that the hybridized photon-magnon polariton frequencies $\omega_2/2\pi$ and $\omega_3/2\pi$ do not cross. The ticks on the base of the inset indicate the $\omega_m/2\pi$ cuts plotted in (b). (b) Line cuts for different values of $\omega_m/2\pi$ of the transmission amplitude $|S_{21}|$ with the spectrum in dashed lines. The width of $\omega_/2\pi$ and $\omega_3/2\pi$ show the uncertainty ± 2.5 MHz in frequency. For each line cut, the average value of the transmission is used to define the horizontal line from which the coloring begins: this allows resonances and antiresonances to be distinguished. All the transmission-line cuts are separated by 45 dB. The legend for the spectrum is common to (a) and (b).

Nevertheless, we note that while the observed coupling strengths are lower than the theoretical values, the prediction for θ_1 remains valid. Indeed, as shown in Ref. [43], the frequencies $\omega_2/2\pi$ and $\omega_3/2\pi$ cross for $\theta_1 = 0$, whereas they do not for $\theta_1 = \pi$. Figure 3(b) and the inset of Fig. 3(a) confirm the existence of a frequency gap between $\omega_2/2\pi$ and $\omega_3/2\pi$, which is the signature of the indirect coupling between both magnons, simultaneously mediated by the two cavity modes [43]. In other words, this spectral feature demonstrates the coherent coupling between two spatially distant YIG spheres mediated by the two cavity modes, despite the relatively high-frequency detuning. Note that if we instead had $\theta_1 = 0$, the indirect magnon-magnon coupling induced by each cavity mode would interfere destructively.

The coherent coupling of a cavity mode to two YIG spheres leads to an enhancement of the frequency gap at the anticrossings by $\sqrt{2}$; i.e., the gap is given by $2\sqrt{2}g$ instead of $2g$ [43,61], which we verify in Appendix B by comparison with measurements with a single YIG sphere. In addition, by examining the linewidths, we measured $\kappa_1/2\pi = 15 \pm 2.5$ MHz and $\kappa_2/2\pi = 22.5 \pm 2.5$ MHz for the linewidths of the cavity modes, and $\kappa_m/2\pi = 5 \pm 2.5$ MHz for the YIG spheres.

IV. ANALYSIS OF TWO PHYSICAL PHASES

A. Cavity $\pi 0$ design

Using cavity π, we showed the existence of a single physical phase $\theta_1 = \pi$. In this section, we examine the possibility of obtaining a different value for the physical phase. In the previous cavity, the origin of the difference in circulation of the magnetic field between the posts can be understood by examining the distribution of the electric field. Following this principle, we engineered another three-post re-entrant cavity to obtain two different values $\theta = 0$ and $\theta = \pi$ for the physical phases in a unique cavity. This is achieved by making the radius of the center post (0.75 mm) larger than that of the other two posts (0.5 mm), as shown in Fig. 4. As a result of this difference in the radii, the electric field intensity is stronger on the center post than on the other two [see Fig. 4(a)]. This leads to the appearance of another cavity eigenmode of frequency $\omega_{c,2}/2\pi = 7.525$ GHz, in which the magnetic field distribution rotates solely around the center post, as shown in Fig. 4(b). Interestingly, the other two cavity eigenmodes observed for cavity π remain, but their frequencies are modified as $\omega_{c,1}/2\pi \mapsto \omega_{c,1}/2\pi = 6.544$ GHz and $\omega_{c,2}/2\pi \mapsto \omega_{c,3}/2\pi = 8.567$ GHz.

B. Prediction of the physical phases

The resulting system consists of three cavity eigenmodes, each coupling to the two YIG spheres. The coupling strengths and coupling phases were computed using COMSOL Multiphysics, and the results are listed in Table II. Once again, given the symmetry of the problem, both YIG spheres couple with almost equal coupling strength to each cavity eigenmode, so we set $g_{11} = g_{12} = g_1 = 130$ MHz, $g_{21} = g_{22} = g_2 = 150$ MHz, and $g_{31} = g_{32} = g_3 = 104$ MHz. The system thus obtained is that described in Sec. II, and using Fig. 1, we deduce that the

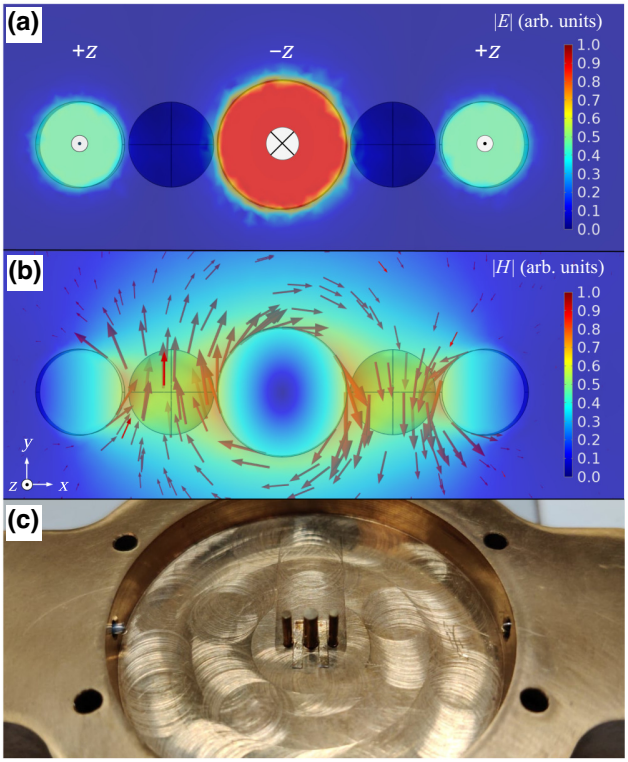


FIG. 4. (a) Electric and (b) magnetic field distributions, simulated using COMSOL Multiphysics, of the second eigenmode c_2 of cavity $\pi 0$. The two eigenmodes of cavity π still exist but have different frequencies. (c) Three-post re-entrant cavity $\pi 0$. In contrast to cavity π, the three posts do not have the same radius, leading to the creation of an additional cavity mode, as shown in (a),(b).

physics is characterized by two coupling phases θ_1 and θ_2. Using Table II, we predict $\theta_1 = \varphi_{12} - \varphi_{11} - (\varphi_{22} - \varphi_{21}) = \pi$ and $\theta_2 = \varphi_{32} - \varphi_{31} - (\varphi_{22} - \varphi_{21}) = 0$; hence the name "cavity $\pi 0$." The results of the frequency-domain simulation are presented in Appendix A, and they agree with the eigenmode analysis of Table II.

TABLE II. Numerical calculation of the coupling strengths g_{kl} and coupling phases φ_{kl} of cavity $\pi 0$ using COMSOL Multiphysics.

Coupling strength (MHz)		Coupling phase (rad)	
$g_{11}/2\pi$	130	φ_{11}	$-\frac{\pi}{2}$
$g_{12}/2\pi$	127	φ_{12}	$-\frac{\pi}{2}$
$g_{21}/2\pi$	148	φ_{21}	$+\frac{\pi}{2}$
$g_{22}/2\pi$	150	φ_{22}	$-\frac{\pi}{2}$
$g_{31}/2\pi$	103	φ_{31}	$+\frac{\pi}{2}$
$g_{32}/2\pi$	104	φ_{32}	$-\frac{\pi}{2}$

C. Experimental results

For cavity π of Sec. III, we did not have precise qualitative agreement with the theoretical predictions due to the additive manufacturing process of the cavity. Thus, we adopted a different strategy for cavity $\pi 0$: we used brass cylinders with a calibrated height to create the posts, and we machined the rest of the cavity from brass. In re-entrant cavities, the eigenmodes are very sensitive to the distance between the top of the posts and the lid. Hence, by using posts with identical heights, we ensured that the potential errors in the distance between the posts and the lid are uniform.

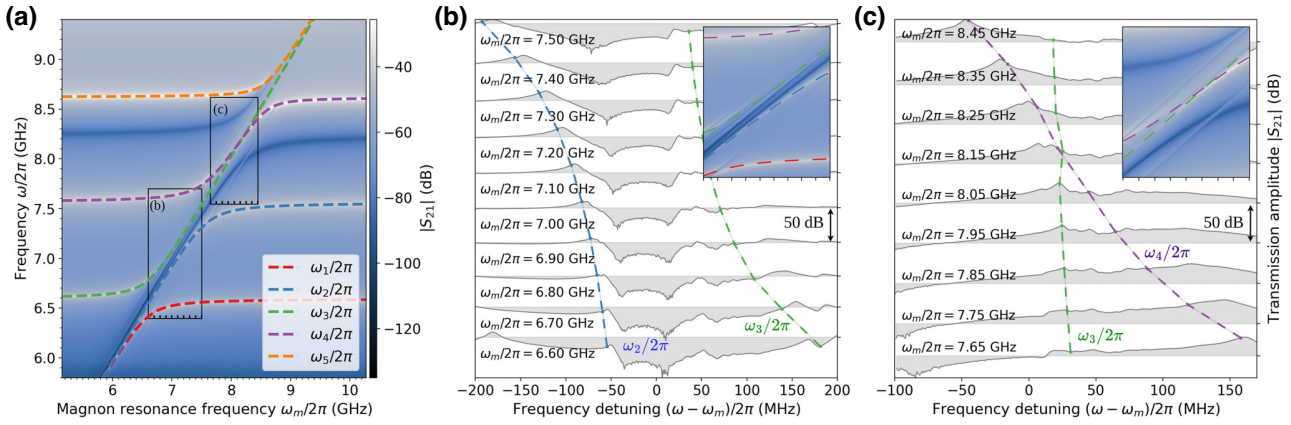


FIG. 5. (a) Experimental transmission amplitude ($|S_{21}|$) of cavity $\pi 0$, with the theoretical spectrum in dashed lines. The two rectangles show the data ranges used in (b),(c), with the ticks on the bottom indicating the $\omega_m/2\pi$ cuts. (b),(c) Transmission-amplitude cuts for different $\omega_m/2\pi$ values, with the spectrum in dashed lines. As in Fig. 3(b), the average value of the transmission is used to define the horizontal line from which the coloring begins. The fit parameters are indicated in Table II with the cavity resonances $\omega_{c,1}/2\pi = 6.594$ GHz, $\omega_{c,2}/2\pi = 7.562$ GHz, and $\omega_{c,3}/2\pi = 8.619$ GHz. The legend is common to all three subfigures, and the curves are all offset by 50 dB.

The experimental data, along with the polariton spectrum, are plotted in Fig. 5. This time, the fit parameters exactly correspond to those given in Table II, which indicates that the construction of the cavity matches very well with the COMSOL design. As for cavity π, the physical phase $\theta_1 = \pi$ suggests that the eigenfrequencies do not cross between the first two anticrossings, which is indeed confirmed by Fig. 5(b). On the other hand, having $\theta_2 = 0$ should lead to a crossing of the eigenfrequencies between the second and third anticrossings [43]; however, when $\theta_2 = 0$, one of the polaritons is a magnonic dark mode [39,43], which does not lead to a resonance in the transmission amplitude [61]. Thus, as seen in Fig. 5(c), we merely observe a single resonance peak moving as $\omega_m/2\pi$ is varied. This is verified using the input-output formalism [62] in Appendix C.

Compared with cavity π, we notice the appearance of higher-order magnon modes, which manifest as anticrossings located away from the magnon resonance $\omega_m/2\pi$. The excitation of these higher-order magnonic modes can be explained by the fact that the spheres used in this experiment are larger (radius of 0.5 mm, similar to the radius of the left and right posts; see Fig. 4), and thus the cavity modes' magnetic fields of Fig. 4(b) are less uniform over the spheres. The presence of a higher-order magnon mode can be verified by placing a single YIG sphere in cavity $\pi 0$ (see Fig. 9 in Appendix B). Finally, as shown in Appendix B, we also observe the $\sqrt{2}$ enhancement of the frequency gap at the anticrossings due to the coherent coupling of the two distant spin ensembles. The measured linewidths of the cavity modes are $\kappa_1/2\pi = 17 \pm 0.5$ MHz, $\kappa_2/2\pi = 42.5 \pm 0.5$ MHz, and $\kappa_3/2\pi = 20 \pm 0.5$ MHz. For the YIG spheres, we found the linewidths $\kappa_m/2\pi = 5 \pm 0.5$ MHz.

V. CONCLUSION

To summarize our results, we have proposed using three-post re-entrant cavities to engineer the coupling phases, and this leads to the engineering of synthetic gauge fields. The experimental data were shown to match with numerical predictions based on the theory developed in Ref. [43]. Depending on the value of the physical phase θ, which parametrizes the physics, we observe either a cavity-mediated magnon-magnon coupling ($\theta = \pi$) or dark-mode physics ($\theta = 0$). These findings are relevant for indirect coupling applications [14,21,22], dark-mode memories [39], and the creation of nonreciprocal behaviors [55,56,60]. While we focused on the the two cases $\theta \in \{0, \pi\}$, intermediate values of θ can be engineered using additional posts, as theoretically demonstrated in Appendix D.

Concerning indirect coupling, we verified the $\sqrt{2}$ enhancement of the coupling strength due to having two distant macroscopic spin ensembles coherently coupling with the cavity mode. In the case of $\theta = \pi$, the magnon-magnon coupling extends in the dispersive regime, where both magnons are strongly detuned from the cavity modes. As shown in Ref. [43], this results from the constructive interference of the cavity-mediated coupling by both cavity modes (while for $\theta = 0$, the cavity-mediated couplings interfere destructively). It was shown that the dispersive regime is advantageous for sensing applications based on magnons (i.e., magnetometry [63] or dark-matter detection [64]), so these schemes could benefit from engineering of the coupling phases.

This flexibility in the cavity-mediated coupling can also be useful for coupling magnons with superconducting transmon qubits through the cavity modes, which has so far only been demonstrated in rectangular cavities [16–19]. Indeed, such qubits couple to the electric field of the cavity modes, which in re-entrant cavities is focused on top of the posts [see Figs. 2(b), 2(d), and 4(a)]. The existence of several cavity modes, which may or may not couple to the magnons, is thus interesting for developing quantum information processing.

Finally, note that here the gauge-invariant phase θ parametrizing the synthetic gauge field is fixed by the coupling phases, which are themselves uniquely determined by the geometry of the cavity; nonetheless, tunability could be achieved by modulating the frequencies of one or more magnons [56], for instance by directly driving a YIG sphere using a loop generating a magnetic field parallel to the static magnetic field. Hence, in principle, re-entrant cavities can be used to engineer a loop-coupled system, and by tuning the gauge-invariant phases, either through cavity engineering or driving the YIG spheres, we

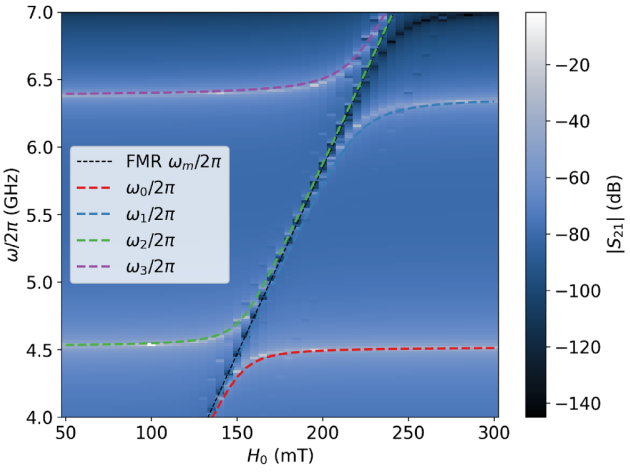


FIG. 6. Frequency-domain simulation, using COMSOL Multiphysics, of the transmission through cavity π. The spectra predicted using the eigenmode analysis of COMSOL Multiphysics are plotted on top, with the eigenfrequencies given in Fig. 2 and the other parameters given by Table I.

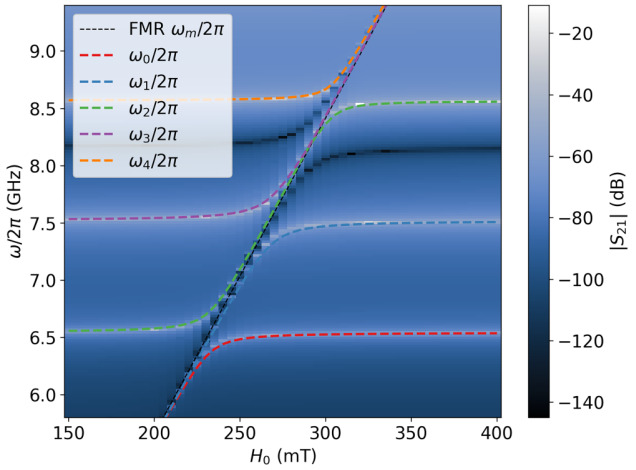


FIG. 7. Frequency-domain simulation, using COMSOL Multiphysics, of the transmission through cavity $\pi 0$. The spectra predicted using the eigenmode analysis of COMSOL Multiphysics are plotted on top, with the eigenfrequencies given in Sec. IV of the main text and the other parameters given by Table II.

could steer the system toward either cavity-mediated or dark-mode memory applications on demand.

ACKNOWLEDGMENTS

We would like to thank Bernard Abiven, mechanic at IMT Atlantique, for building cavity $\pi 0$. We acknowledge financial support from Thales Australia and Thales Research and Technology. This work is part of the research program supported by the European Union through the European Regional Development Fund (ERDF), by the Ministry of Higher Education and Research, Brittany and Rennes Métropole, through the CPER SpaceTech DroneTech, by Brest Métropole, and the ANR projects ICARUS and MagFunc. Jeremy Bourhill is funded by the Australian Research Council Centre of Excellence for Engineered Quantum Systems, CE170100009 and the Centre of Excellence for Dark Matter Particle Physics,

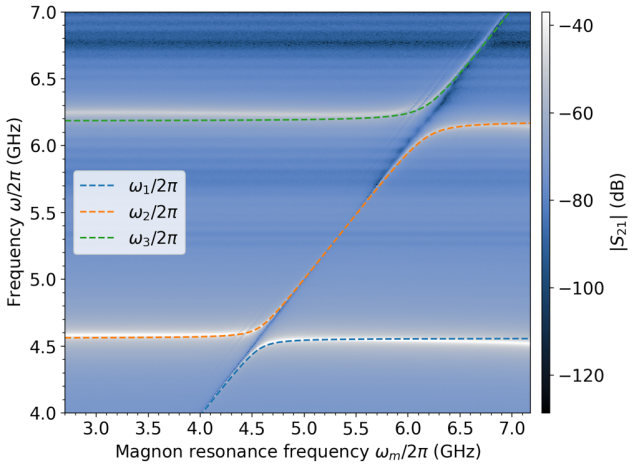


FIG. 8. Experimental transmission amplitude ($|S_{21}|$) of cavity π loaded with a single YIG sphere instead of two, with the theoretical spectrum in colored lines. The fit parameters are identical to those of Fig. 3(a) except for a shift of the first cavity mode, which was instead set to $\omega_{c,1}/2\pi = 4.56$ GHz.

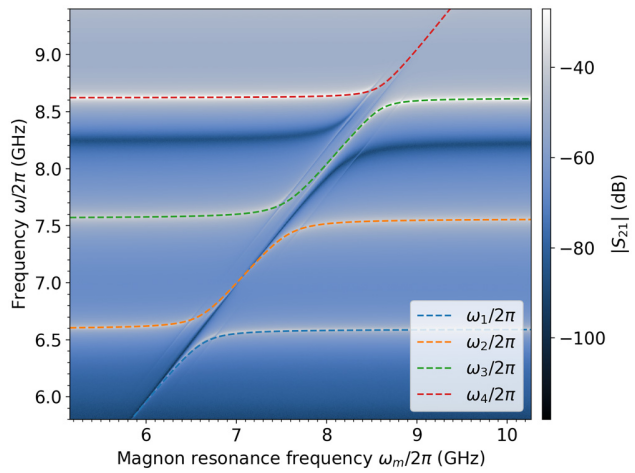


FIG. 9. Experimental transmission amplitude ($|S_{21}|$) of cavity $\pi 0$ loaded with a single YIG sphere instead of two, with the theoretical spectrum in colored lines. The fit parameters are exactly the same as those in Fig. 5.

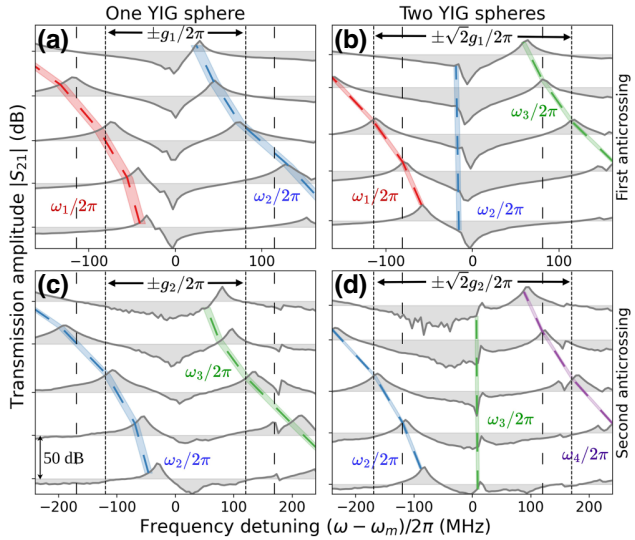


FIG. 10. Experimental transmission amplitude $|S_{21}|$ of cavity π for (a),(b) the first anticrossing and (c),(d) the second anticrossing. In the left column, we show the results for a single YIG sphere present in the cavity, while in the right column we show the case of two YIG spheres. From bottom to top, the line cuts in each subfigure are shown at $\omega_m \in \{\omega_{c,k} - 2g_k, \omega_{c,k} - g_k, \omega_{c,k}, \omega_{c,k} + g_k, \omega_{c,k} + 2g_k\}$. In all the subfigures, the curves are offset by 50 dB.

CE200100008. The scientific color map *oslo* [65] is used in this study to prevent visual distortion of the data and exclusion of readers with color-vision deficiencies [66].

APPENDIX A: SIMULATION RESULTS

In this appendix, we compare the simulation results of the eigenmode and frequency-domain analyses of COMSOL Multiphysics. The eigenmode simulations give the values of the coupling strengths and physical phases presented in Tables I and II, while the frequency-domain simulations give the transmission coefficient S_{21}. We use the results of the eigenmode analysis to plot the spectrum on top of the frequency-domain simulations, and we obtain good agreement, as shown in Fig. 6 for cavity π and Fig. 7 for cavity $\pi 0$.

Importantly, the frequency-domain COMSOL Multiphysics simulations only include the Kittel mode for the magnons and not higher-order modes; therefore, the presence of crossings (anticrossings) of the polaritonic frequencies for $\theta = 0$ ($\theta = \pi$) observed cannot be due to the presence of higher-order modes.

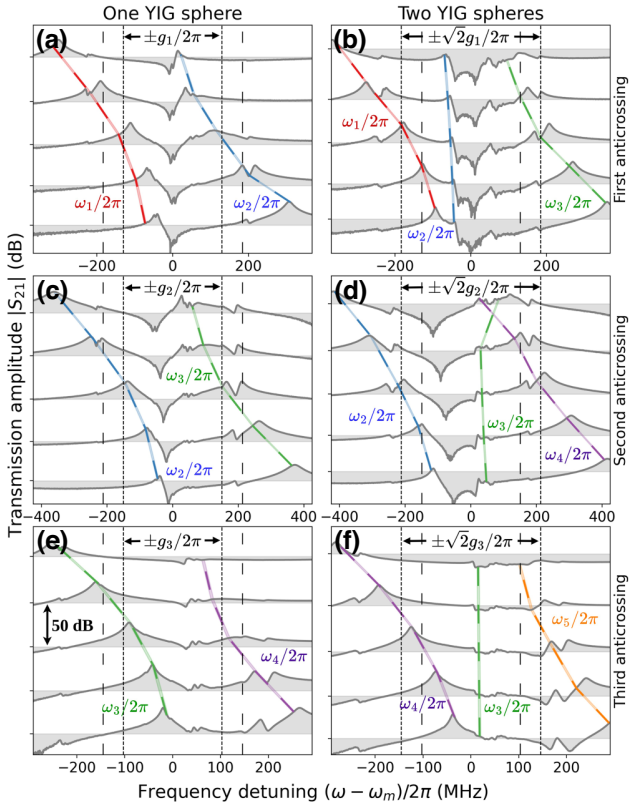


FIG. 11. Experimental transmission amplitude $|S_{21}|$ of cavity $\pi 0$ for (a),(b) the first anticrossing, (c),(d) the second anticrossing, and (e),(f) the third anticrossing. The line cuts are identical to those of Fig. 10.

APPENDIX B: COHERENT COUPLING OF TWO DISTANT SPHERES

The coherent coupling of N YIG spheres to a cavity mode leads to an enhancement by $\sqrt{N}$ of the frequency gap when the magnons are on resonance with the cavity mode [39]. To check that this was indeed the case, we removed one of the YIG spheres and measured cavities π and $\pi 0$ again. The experimental results are given in Fig. 8 for cavity π and in Fig. 9 for cavity $\pi 0$. We can notice the presence of higher-order magnon modes in both figures, which are characterized by diagonal lines parallel to the Kittel mode's frequency $\omega/2\pi$.

In Fig. 10, we compare the anticrossings for cavity π when a single YIG sphere is loaded in the cavity [Figs. 10(a) and 10(c)], versus two YIG spheres

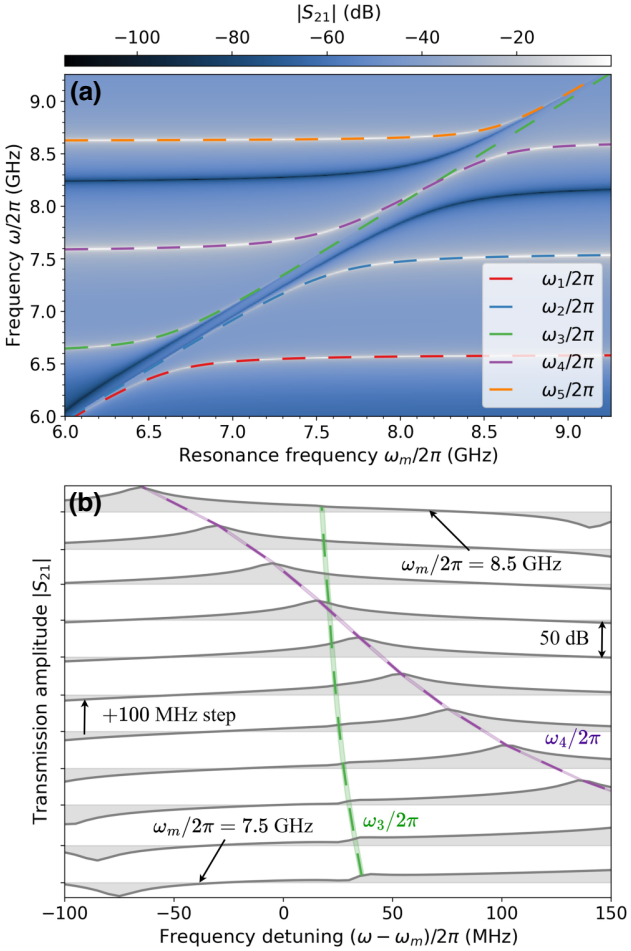


FIG. 12. Input-output modeling of the transmission amplitude $|S_{21}|$ through cavity $\pi 0$. (a) Transmission amplitude reproducing the experimental results of Fig. 5(a). (b) Cuts from $\omega_m/2\pi = 7.5$ GHz (bottom) up to $\omega_m/2\pi = 8.5$ GHz, in steps of 100 MHz, of the transmission amplitude $|S_{21}|$. These results mirror the experimental data of Fig. 5(c) and show the crossing of eigenvalues characteristic of $\theta_1 = 0$.

[Figs. 10(b) and 10(d)]. The dashed colored lines track the polariton frequencies, and these are seen to follow the resonance peaks. In particular, the third line cut corresponds to the magnon(s) being on resonance with the cavity mode, for which the anticrossing frequency gap is minimum. We see that in the case of a single YIG sphere, this frequency gap is given by $2g_k/2\pi$ (first column), whereas for two YIG spheres, the gap is $2\sqrt{2}g_k/2\pi$ (second column).

We carried out the same analysis for cavity $\pi 0$, as shown in Fig. 11, and the $\sqrt{2}$ enhancement was also verified. In Fig. 11(f), the vertical lines indicating $\pm\sqrt{2}g_3$ seem to be offset to the left. Note that if a YIG sphere is removed, the system is no longer loop coupled, and thus the effects of the coupling phases disappear.

APPENDIX C: INPUT-OUTPUT THEORY

The main objective of this appendix is to show that the dark mode arising for $\theta_2 = 0$ in cavity $\pi 0$ does not lead to a resonance in the transmission spectrum. To model the transmission amplitude $|S_{21}|$ through the cavity, we use the input-output formalism [62], for which there is abundant literature (see Refs. [11–13] for instance). The derivation is rather lengthy [43], and we therefore only describe the main steps here and refer the reader to Ref. [67] for more details.

To model the intrinsic dissipation of the magnon modes in the YIG spheres, we couple each of them to a bosonic bath with a real-valued and frequency-independent coupling rate $\kappa_m/2\pi = 5$ MHz (assumed to be identical for both YIG spheres). For the cavity modes, we only need to consider the two ports of the cavity, from which the S parameters are measured; therefore, we assume that the cavity mode c_i couples to two bosonic baths with frequency-independent coupling rates $\kappa_{ij}e^{i\phi_{ij}}/2\pi$, where $j \in \{1,2\}$ indexes the bath. Note that the phases ϕ_{ij} are necessary to reproduce the antiresonance behaviors, as recently shown in Ref. [67].

We use $\kappa_{1j}/2\pi = 1$ MHz, $\kappa_{2j}/2\pi = 3$ MHz, and $\kappa_{3j}/2\imath = 2$ MHz for $j \in \{1,2\}$. The values of the phases ϕ_{ij} can be obtained by examining the direction of the magnetic field (for instance, using an eigenmode analysis in COMSOL Multiphysics) coupled to the probes used to inject and measure the microwaves inside the cavity [67]. We set $\phi_{1j} = \pi_{3j} = \pi$ for $j \in \{1,2\}$ n $\phi_{21} = \pi$ and $\phi_{22} = 0$. Furthermore, the features of antiresonances depend on several cavity modes, and to properly model the lowest-frequency antiresonance, we included a lower-frequency cavity mode with frequency $\omega_0/2\pi = 3$ GHz and the negative coupling rates $\kappa_{01}/2\pi = \kappa_{02}/2\pi = -5$ MHz to the ports. For the cavity resonance frequencies and coupling strengths, we use the same values as for Fig. 5.

The results are plotted in Fig. 12, and we note, in particular, that Fig. 12(a) successfully reproduces Fig. 5(a). In Fig. 12(b), we reproduce Fig. 5(c) in the absence of higher-order magnon modes. As a consequence, the tracking of the polaritonic frequencies is simplified, and we verify the crossing of the eigenvalues. Notably, $\omega_3/2\pi$ does not lead to a resonance near the crossing, since it corresponds to a magnon dark mode, as theoretically predicted in Ref. [43].

APPENDIX D: ENGINEERING ARBITRARY PHYSICAL PHASES

The objective of this investigation was to design a cavity capable of introducing a nontrivial phase between consecutive modes while operating in the strong-coupling regime. To that effect, we developed a re-entrant cavity with five posts, which additionally ensures uniform coupling strength across multiple YIG spheres. Furthermore, the phase relationship between the two modes is contingent upon the positioning of four posts within the cavity,

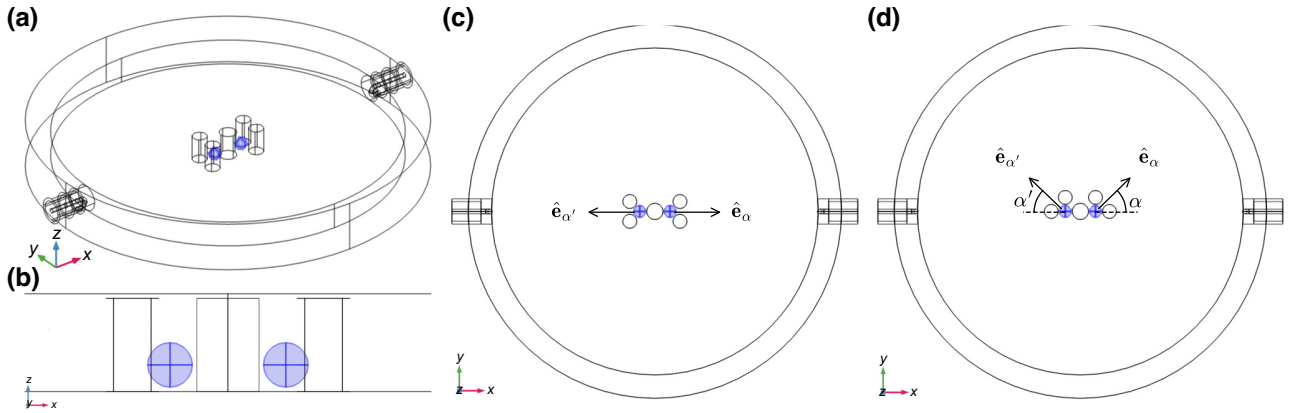


FIG. 13. Representation of the proposed re-entrant cavity (a) in three dimensions, (b) in the (z,x) plane enlarged to view the gap d between the tops of the posts and the lid, (c) in the (x,y) plane with the directions $\hat{\mathbf{e}}_\alpha, \hat{\mathbf{e}}_{\alpha'}$ represented, where $\hat{\mathbf{e}}_{\alpha'}$ is the mirror symmetry of $\hat{\mathbf{e}}_\alpha$ with respect to the (y,z) plane, and (d) in the (x,y) plane with the direction $\hat{\mathbf{e}}_\alpha$ making an angle α with respect to the x axis. The two YIG spheres are represented in blue.

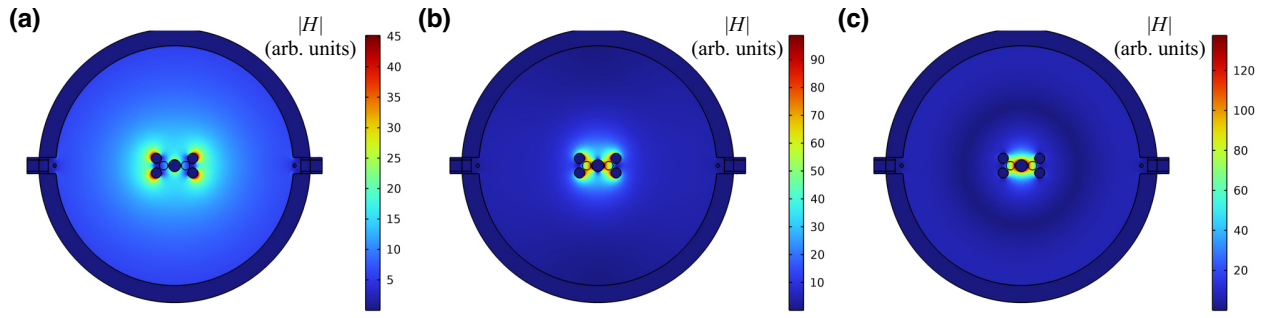


FIG. 14. Representation of the $|H|$ field of the first three cavity modes in the (x, y) plane at the z coordinate of the center of the YIG spheres.

as demonstrated in our analysis. By manipulating the positions of these posts, it is feasible to fine-tune the coupling phase by adjusting the gap between the top of the post and the cavity lid.

The cavity dimensions were optimized to maximize the coupling strength for each YIG sphere and to ensure that the phase falls within the range $[n(\pi/4), (n+1)(\pi/4)]$ with $n \in \mathbb{Z}$ by tuning an angle α, as detailed in the following. As depicted in Fig. 13, the cavity is cylindrical and features five cylindrical posts. The cavity has a radius of 14 mm and a height of 2.25 mm. All posts have the same height, which depends on the value of the gap d; thus, the post height is $2.25 - d$. Positioned at the center of the cavity is a fixed post with a radius of 0.7 mm. The two YIG spheres are located on either side of the center post along the x axis, with a spacing of 0.1 mm from the center post. Four additional posts are situated at the periphery of each YIG sphere, spaced 0.1 mm from the spheres. These peripheral posts are symmetrically positioned with respect to the y axis, which passes through the center of the cavity. The radius of the peripheral posts is 0.6 mm. Relative to the direction $\hat{e}_\alpha$, the two peripheral posts on the right-hand side of the cavity are positioned at $\pm 45°$. In addition, the direction $\hat{e}_\alpha$ forms an angle α with the x axis, ranging from $0°$ to $45°$, allowing the tuning of the coupling phases.

The norms of the cavity modes' magnetic fields are depicted in Fig. 14 for the first three modes of the cavity. We focus on the second and third modes due to their high filling factor η [see Eq. (3)], which are quite similar for both modes and spheres, as illustrated in Table III. This table presents the eigenfrequencies $\omega/2\pi$ of the first three modes of the cavity, along with the filling factors η_L and η_R for the YIG spheres on the left- and right-hand sides, respectively. In addition, the associated coupling strengths g_L and g_R are provided. The values are given for an angle $\alpha = 0°$ and a gap $d = 50$ μm.

Table IV presents similar characteristics for the two modes of interest, along with the averaged H-field direction inside each YIG sphere and the coupling phase. It is observed that the coupling strength slightly decreases from $\alpha = 0°$ to $\alpha = 45°$, whereas the difference in coupling strength between mode 1 and mode 2 slightly increases; however, the coupling strength remains relatively constant, ranging from 4.2% to 5.7%. The coupling phase varies between $129°$ and $180°$ for α ranging from $45°$ to $0°$, allowing for measurements with a nontrivial physical phase between $135°$ and $180°$.

TABLE III. Characteristics of the first three cavity modes for $d = 50$ μm.

Mode	$\omega/2\pi$ (GHz)	η_L	η_R	g_L/ω	g_R/ω
0	4.02	0.018	0.019	0.011	0.012
1	8.29	0.125	0.123	0.055	0.056
2	12.03	0.144	0.145	0.055	0.055

TABLE IV. Characteristics of the cavity modes versus α for $d = 50$ μm.

α (°)	$\omega/2\pi$ (GHz)	η_L	η_R	g_L/ω	g_R/ω	ϕ_L (°)	ϕ_R (°)	θ (°)
0	8.29	0.125	0.123	0.057	0.056	90	90	180
	12.03	0.144	0.145	0.055	0.055	−90	90	
5	8.29	0.125	0.122	0.057	0.056	−91	−88	170
	12.09	0.141	0.142	0.053	0.053	−86	87	
10	8.27	0.125	0.122	0.057	0.055	−92	−87	160
	12.07	0.139	0.140	0.053	0.053	−82	83	
15	8.33	0.124	0.122	0.056	0.055	86	95	151
	12.09	0.134	0.134	0.050	0.051	−79	80	
20	8.38	0.124	0.120	0.056	0.055	85	96	144
	12.07	0.130	0.130	0.049	0.049	−76	78	
25	8.48	0.122	0.121	0.055	0.054	−97	−83	139
	12.05	0.126	0.125	0.047	0.047	−76	77	
30	8.54	0.122	0.119	0.055	0.054	83	98	133
	12.03	0.121	0.121	0.046	0.046	−74	75	
35	8.62	0.121	0.119	0.054	0.053	−98	−81	131
	11.99	0.119	0.119	0.045	0.045	106	−105	
40	8.74	0.121	0.118	0.054	0.052	81	99	130
	11.97	0.115	0.115	0.044	0.044	−73	74	
45	8.90	0.120	0.118	0.053	0.052	−99	−80	128
	11.96	0.112	0.112	0.042	0.042	−74	74	

TABLE V. Characteristics of the cavity modes versus d for $\alpha = 45°$.

d (μm)	$\omega/2\pi$ (GHz)	η_L	η_R	g_L/ω	g_R/ω	ϕ_L (°)	ϕ_R (°)	θ (°)
5	3.34	0.123	0.116	0.088	0.083	80	102	146
	4.67	0.154	0.157	0.093	0.095	97	−95	
10	4.63	0.124	0.115	0.075	0.070	−100	−78	147
	6.45	0.155	0.158	0.080	0.082	97	−94	
25	6.88	0.122	0.118	0.061	0.059	−100	−79	144
	9.61	0.156	0.158	0.066	0.067	98	−97	
50	8.90	0.120	0.118	0.053	0.052	−99	−80	129
	11.95	0.112	0.112	0.043	0.043	−74	74	
100	10.84	0.112	0.110	0.045	0.044	82	98	90
	12.77	0.051	0.051	0.019	0.019	−53	53	

Table V presents the same information for a fixed angle of 45° while varying the gap d from 100 to 5 μm. This demonstrates that measurements with a nontrivial phase can be conducted within the range 90° to 135°.

[1] S. A. Wolf, D. D. Awschalom, R. A. Buhrman, J. M. Daughton, S. von Molnar, M. L. Roukes, A. Y. Chtchelkanova, and D. M. Treger, Spintronics: A spin-based electronics vision for the future, Science **294**, 1488 (2001).

[2] A. V. Chumak, V. I. Vasyuchka, A. A. Serga, and B. Hillebrands, Magnon spintronics, Nat. Phys. **11**, 453 (2015).

[3] G. Csaba, Á. Papp, and W. Porod, Perspectives of using spin waves for computing and signal processing, Phys. Lett. A **381**, 1471 (2017).

[4] A. V. Chumak, A. A. Serga, and B. Hillebrands, Magnonic crystals for data processing, J. Phys. D: Appl. Phys. **50**, 244001 (2017).

[5] A. V. Chumak, Fundamentals of magnon-based computing, arXiv:1901.08934.

[6] A. Barman, *et al.*, The 2021 magnonics roadmap, J. Phys.: Condens. Matter **33**, 413001 (2021).

[7] A. Mahmoud, F. Ciubotaru, F. Vanderveken, A. V. Chumak, S. Hamdioui, C. Adelmann, and S. Cotofana, Introduction to spin wave computing, J. Appl. Phys. **128**, 161101 (2020).

[8] S. Bhatti, R. Sbiaa, A. Hirohata, H. Ohno, S. Fukami, and S. Piramanayagam, Spintronics based random access memory: A review, Mater. Today **20**, 530 (2017).

[9] A. V. Chumak, *et al.*, Advances in magnetics roadmap on spin-wave computing, IEEE Trans. Magn. **58**, 1 (2022). working paper or preprint

[10] J. Grollier, D. Querlioz, K. Y. Camsari, K. Everschor-Sitte, S. Fukami, and M. D. Stiles, Neuromorphic spintronics, Nat. Electron. **3**, 360 (2020).

[11] M. Harder, B. M. Yao, Y. S. Gui, and C.-M. Hu, Coherent and dissipative cavity magnonics, J. Appl. Phys. **129**, 201101 (2021).

[12] B. Z. Rameshti, S. V. Kusminskiy, J. A. Haigh, K. Usami, D. Lachance-Quirion, Y. Nakamura, C.-M. Hu, H. X. Tang, G. E. Bauer, and Y. M. Blanter, Cavity magnonics, arXiv:2106.09312.

[13] H. Yuan, Y. Cao, A. Kamra, R. A. Duine, and P. Yan, Quantum magnonics: When magnon spintronics meets quantum information science, Phys. Rep. **965**, 1 (2022).

[14] D. Lachance-Quirion, Y. Tabuchi, A. Gloppe, K. Usami, and Y. Nakamura, Hybrid quantum systems based on magnonics, Appl. Phys. Express **12**, 070101 (2019).

[15] X. Zhang, C.-L. Zou, L. Jiang, and H. X. Tang, Cavity magnomechanics, Sci. Adv. **2**, e1501286 (2016).

[16] Y. Tabuchi, S. Ishino, A. Noguchi, T. Ishikawa, R. Yamazaki, K. Usami, and Y. Nakamura, Coherent coupling between a ferromagnetic magnon and a superconducting qubit, Science **349**, 405 (2015).

[17] Y. Tabuchi, S. Ishino, A. Noguchi, T. Ishikawa, R. Yamazaki, K. Usami, and Y. Nakamura, Quantum magnonics: The magnon meets the superconducting qubit, C. R. Phys. **17**, 729 (2016). quantum microwaves / Micro-ondes quantiques.

[18] D. Lachance-Quirion, Y. Tabuchi, S. Ishino, A. Noguchi, T. Ishikawa, R. Yamazaki, and Y. Nakamura, Resolving quanta of collective spin excitations in a millimeter-sized ferromagnet, Sci. Adv. **3**, e1603150 (2017).

[19] D. Lachance-Quirion, S. P. Wolski, Y. Tabuchi, S. Kono, K. Usami, and Y. Nakamura, Entanglement-based single-shot detection of a single magnon with a superconducting qubit, Science **367**, 425 (2020).

[20] N. Crescini, C. Braggio, G. Carugno, A. Ortolan, and G. Ruoso, Coherent coupling between multiple ferrimagnetic spheres and a microwave cavity at millikelvin temperatures, Phys. Rev. B **104**, 064426 (2021).

[21] N. J. Lambert, J. A. Haigh, S. Langenfeld, A. C. Doherty, and A. J. Ferguson, Cavity-mediated coherent coupling of magnetic moments, Phys. Rev. A **93**, 021803 (2016).

[22] P. Hyde, L. Bai, M. Harder, C. Match, and C.-M. Hu, Indirect coupling between two cavity modes via ferromagnetic resonance, Appl. Phys. Lett. **109**, 152405 (2016).

[23] M. Goryachev, W. G. Farr, D. L. Creedon, Y. Fan, M. Kostylev, and M. E. Tobar, High-cooperativity cavity QED with magnons at microwave frequencies, Phys. Rev. Appl. **2**, 054002 (2014).

[24] N. Kostylev, M. Goryachev, and M. E. Tobar, Superstrong coupling of a microwave cavity to yttrium iron garnet magnons, Appl. Phys. Lett. **108**, 062402 (2016).

[25] I. A. Golovchanskiy, N. N. Abramov, V. S. Stolyarov, A. A. Golubov, M. Y. Kupriyanov, V. V. Ryazanov, and A. V. Ustinov, Approaching deep-strong on-chip photon-to-magnon coupling, Phys. Rev. Appl. **16**, 034029 (2021).

[26] I. A. Golovchanskiy, N. N. Abramov, V. S. Stolyarov, M. Weides, V. V. Ryazanov, A. A. Golubov, A. V. Ustinov, and M. Y. Kupriyanov, Ultrastrong photon-to-magnon coupling in multilayered heterostructures involving superconducting coherence via ferromagnetic layers, Sci. Adv. **7**, eabe8638 (2021).

[27] G. Bourcin, J. Bourhill, V. Vlaminck, and V. Castel, Strong to ultra-strong coherent coupling measurements in a YIG/cavity system at room temperature, arXiv:2209.14643.

[28] W. Yu, J. Wang, H. Y. Yuan, and J. Xiao, Prediction of attractive level crossing via a dissipative mode, Phys. Rev. Lett. **123**, 227201 (2019).

[29] J. Zhao, Y. Liu, L. Wu, C.-K. Duan, Y. x. Liu, and J. Du, Observation of anti-$\mathcal{PT}$-symmetry phase transition in the magnon-cavity-magnon coupled system, Phys. Rev. Appl. **13**, 014053 (2020).

[30] M. Harder, Y. Yang, B. M. Yao, C. H. Yu, J. W. Rao, Y. S. Gui, R. L. Stamps, and C.-M. Hu, Level attraction due to dissipative magnon-photon coupling, Phys. Rev. Lett. **121**, 137203 (2018).

[31] B. Bhoi, B. Kim, S.-H. Jang, J. Kim, J. Yang, Y.-J. Cho, and S.-K. Kim, Abnormal anticrossing effect in photon-magnon coupling, Phys. Rev. B **99**, 134426 (2019).

[32] Y. Yang, J. W. Rao, Y. S. Gui, B. M. Yao, W. Lu, and C.-M. Hu, Control of the magnon-photon level attraction in a planar cavity, Phys. Rev. Appl. **11**, 054023 (2019).

[33] B. Yao, T. Yu, X. Zhang, W. Lu, Y. Gui, C.-M. Hu, and Y. M. Blanter, The microscopic origin of magnon-photon level attraction by traveling waves: Theory and experiment, Phys. Rev. B **100**, 214426 (2019).

[34] B. Yao, T. Yu, Y. S. Gui, J. W. Rao, Y. T. Zhao, W. Lu, and C.-M. Hu, Coherent control of magnon radiative damping with local photon states, Commun. Phys. **2**, 161 (2019).

[35] Z. Lu, X. Mi, Q. Zhang, Y. Sun, J. Guo, Y. Tian, S. Yan, and L. Bai, Interference induced microwave transmission in the YIG-microstrip cavity system, J. Magn. Magn. Mater. **540**, 168457 (2021).

[36] Y.-P. Wang, J. W. Rao, Y. Yang, P.-C. Xu, Y. S. Gui, B. M. Yao, J. Q. You, and C.-M. Hu, Nonreciprocity and unidirectional invisibility in cavity magnonics, Phys. Rev. Lett. **123**, 127202 (2019).

[37] I. Boventer, M. Kläui, R. Macedo, and M. Weides, Steering between level repulsion and attraction: Broad tunability of two-port driven cavity magnon-polaritons, New J. Phys. **21**, 125001 (2019).

[38] I. Boventer, C. Dorflinger, T. Wolz, R. Macedo, R. Lebrun, M. Klaui, and M. Weides, Control of the coupling strength and linewidth of a cavity magnon-polariton, Phys. Rev. Res. **2**, 013154 (2020).

[39] X. Zhang, C.-L. Zou, N. Zhu, F. Marquardt, L. Jiang, and H. X. Tang, Magnon dark modes and gradient memory, Nat. Commun. **6**, 8914 (2015).

[40] X. Li, J. Li, X. Cheng, and G. Li, Nonreciprocal transmission in a four-mode cavity magnonics system, Laser Phys. Lett. **19**, 095208 (2022).

[41] N. Zhu, X. Han, C.-L. Zou, M. Xu, and H. X. Tang, Magnon-photon strong coupling for tunable microwave circulators, Phys. Rev. A **101**, 043842 (2020).

[42] C. Kong, J. Liu, and H. Xiong, Nonreciprocal microwave transmission under the joint mechanism of phase modulation and magnon Kerr nonlinearity effect, Front. Phys. **18**, 12501 (2022).

[43] A. Gardin, J. Bourhill, V. Vlaminck, C. Person, C. Fumeaux, V. Castel, and G. C. Tettamanzi, Manifestation of the coupling phase in microwave cavity magnonics, Phys. Rev. Appl. **19**, 054069 (2023).

[44] S. Zheng, F. Sun, Y. Lai, Q. Gong, and Q. He, Manipulation and enhancement of asymmetric steering via interference effects induced by closed-loop coupling, Phys. Rev. A **99**, 022335 (2019).

[45] J. Huang, D.-G. Lai, and J.-Q. Liao, Controllable generation of mechanical quadrature squeezing via dark-mode engineering in cavity optomechanics, Phys. Rev. A **108**, 013516 (2023).

[46] J. Koch, A. A. Houck, K. L. Hur, and S. M. Girvin, Time-reversal-symmetry breaking in circuit-QED-based photon lattices, Phys. Rev. A **82**, 043811 (2010).

[47] N. R. Bernier, L. D. Tóth, A. Koottandavida, M. A. Ioannou, D. Malz, A. Nunnenkamp, A. K. Feofanov, and T. J. Kippenberg, Nonreciprocal reconfigurable microwave optomechanical circuit, Nat. Commun. **8**, 604 (2017).

[48] K. Fang, J. Luo, A. Metelmann, M. H. Matheny, F. Marquardt, A. A. Clerk, and O. Painter, Generalized non-reciprocity in an optomechanical circuit via synthetic magnetism and reservoir engineering, Nat. Phys. **13**, 465 (2017).

[49] Y. Chen, Y.-L. Zhang, Z. Shen, C.-L. Zou, G.-C. Guo, and C.-H. Dong, Synthetic gauge fields in a single optomechanical resonator, Phys. Rev. Lett. **126**, 123603 (2021).

[50] T. Holstein and H. Primakoff, Field dependence of the intrinsic domain magnetization of a ferromagnet, Phys. Rev. **58**, 1098 (1940).

[51] G. Flower, M. Goryachev, J. Bourhill, and M. E. Tobar, Experimental implementations of cavity-magnon systems: From ultra strong coupling to applications in precision measurement, New J. Phys. **21**, 095004 (2019).

[52] J. Bourhill, V. Castel, A. Manchec, and G. Cochet, Universal characterization of cavity–magnon polariton coupling strength verified in modifiable microwave cavity, J. Appl. Phys. **128**, 073904 (2020).

[53] A. Frisk Kockum, A. Miranowicz, S. De Liberato, S. Savasta, and F. Nori, Ultrastrong coupling between light and matter, Nat. Rev. Phys. **1**, 19 (2019).

[54] A. Le Boité, Theoretical methods for ultrastrong light–matter interactions, Adv. Quantum Technol. **3**, 1900140 (2020).

[55] A. Metelmann and A. A. Clerk, Nonreciprocal photon transmission and amplification via reservoir engineering, Phys. Rev. X **5**, 021025 (2015).

[56] A. Clerk, Introduction to quantum non-reciprocal interactions: From non-Hermitian Hamiltonians to quantum master equations and quantum feedforward schemes, SciPost Phys Lect. Notes **44**, 44 (2022).

[57] Y.-J. Lin, R. L. Compton, K. Jiménez-García, J. V. Porto, and I. B. Spielman, Synthetic magnetic fields for ultracold neutral atoms, Nature **462**, 628 (2009).

[58] J. Dalibard, F. Gerbier, G. Juzeliūnas, and P. Ohberg, Colloquium: Artificial gauge potentials for neutral atoms, Rev. Mod. Phys. **83**, 1523 (2011).

[59] K. M. Sliwa, M. Hatridge, A. Narla, S. Shankar, L. Frunzio, R. J. Schoelkopf, and M. H. Devoret, Reconfigurable Josephson circulator/directional amplifier, Phys. Rev. X **5**, 041020 (2015).

[60] S.-A. Biehs and G. S. Agarwal, Enhancement of synthetic magnetic field induced nonreciprocity via bound states in the continuum in dissipatively coupled systems, Phys. Rev. B **108**, 035423 (2023).

[61] J. M. P. Nair, D. Mukhopadhyay, and G. S. Agarwal, Cavity-mediated level attraction and repulsion between magnons, Phys. Rev. B **105**, 214418 (2022).

[62] C. W. Gardiner and M. J. Collett, Input and output in damped quantum systems: Quantum stochastic differential equations and the master equation, Phys. Rev. A **31**, 3761 (1985).
[63] N. Crescini, G. Carugno, and G. Ruoso, Phase-modulated cavity magnon polaritons as a precise magnetic field probe, Phys. Rev. Appl. **16**, 034036 (2021).
[64] G. Flower, J. Bourhill, M. Goryachev, and M. E. Tobar, Broadening frequency range of a ferromagnetic axion haloscope with strongly coupled cavity–magnon polaritons, Phys. Dark Universe **25**, 100306 (2019).
[65] F. Crameri, Scientific colour maps, 2021.
[66] F. Crameri, G. E. Shephard, and P. J. Heron, The misuse of colour in science communication, Nat. Commun. **11**, 5444 (2020).
[67] G. Bourcin, A. Gardin, J. Bourhill, V. Vlaminck, and V. Castel, Level attraction in a quasi-closed cavity, arXiv:2402.06258.

C.4) Discrete (geometric) phases in loop-coupled bosonic systems

Statement of Authorship

Title of Paper	Discrete (geometric) phases in loop-coupled bosonic systems
Publication Status	☐ Published ☐ Accepted for Publication ☐ Submitted for Publication ☑ Unpublished and Unsubmitted w ork w ritten in manuscript style
Publication Details	

Principal Author

Name of Principal Author (Candidate)	Alan Gardin
Contribution to the Paper	Performed theoretical calculation and wrote the manuscript.
Overall percentage (%)	80
Certification:	This paper reports on original research I conducted during the period of my Higher Degree by Research candidature and is not subject to any obligations or contractual agreements with a ain its inclusion in this thesis. I am the primary author of this paper.
Signature	Date: 22/01/2024

Co-Author Contributions

By signing the Statement of Authorship, each author certifies that:

i. the candidate's stated contribution to the publication is accurate (as detailed above);

ii. permission is granted for the candidate in include the publication in the thesis; and

iii. the sum of all co-author contributions is equal to 100% less the candidate's stated contribution.

Name of Co-Author	Christian Person
Contribution to the Paper	Read and provided comments on the manuscript.
Signature	Date: 18/03/2024

Name of Co-Author	Christophe Fumeaux
Contribution to the Paper	Read and provided comments on the manuscript.
Signature	Date: 13/03/2024

Name of Co-Author	Vincent Castel		
Contribution to the Paper	Read and provided comments on the manuscript.		
Signature		Date	18/03/2024

Name of Co-Author	Giuseppe Tettamanzi		
Contribution to the Paper	Read and provided comments on the manuscript.		
Signature		Date	18-03-2024

Discrete (geometric) phases in loop-coupled bosonic systems

Alan Gardin,[1,2,3,*] Christian Person,[2,3] Christophe Fumeaux,[4] Vincent Castel,[2,3] and Giuseppe C. Tettamanzi[5]

[1] *School of Physics, The University of Adelaide, Adelaide SA 5005, Australia*
[2] *IMT Atlantique, Technopole Brest-Iroise, CS 83818, 29238 Brest Cedex 3, France*
[3] *Lab-STICC (UMR 6285), CNRS, Technopole Brest-Iroise, CS 83818, 29238 Brest Cedex 3, France*
[4] *School of Electrical and Electronic Engineering, The University of Adelaide, Adelaide SA 5005, Australia*
[5] *School of Chemical Engineering and Advanced Materials, The University of Adelaide, Adelaide SA 5005, Australia*

In linear loop-coupled bosonic systems, the coupling phases become a gauge-invariant quantity, a process reminiscent of the Pancharatnam and Berry phases. In this work, we explore the possible connections between these discrete phases and standard geometrical phases.

I. INTRODUCTION

Since the first formal discussion of geometric phases by Berry in 1984 [1], this concept has found numerous applications in physics. Following Berry's paper, the connection to holonomies was discussed by Simon [2], and the Berry's phase was understood as being a particular case of an adiabatic abelian holonomy. Quickly, geometrical phases were generalised, first to adiabatic non-abelian holonomies [3], then to non-adiabatic abelian holonomies [4], and finally to non-adiabatic non-abelian holonomies [5]. In all of these works, the geometrical phase occur due to the variation of some parameter $\mathbf{R} \in \mathcal{M}$ of an Hamiltonian $H(\mathbf{R})$, over some loop in the manifold $\mathcal{M}$ defining the parameter space. Furthermore, the focus is placed on the states $|\psi\rangle$ of the system, and the phase it can acquire over the evolution of the parameter $\mathbf{R}$.

On the other hand, a gauge-invariant phase can appear in loop-coupled bosonic systems, which are systems in which the interaction graph between the modes contains a loop. In the particular case of a linear coupling between bosons, the coupling phases, which can usually be discarded, can become observable, as recently shown for two magnon modes and two microwave cavity modes [6]. Similar discrete phases have been examined from a practical point of view in circuit QED [7] and optomechanical systems [8–11]. It seems that their major application is the creation of non-reciprocal behaviour [7–10, 12–14], at the condition of an appropriate engineering of dissipation [12]. Furthermore, it seems that non-reciprocal behaviour carry over to the quantum regime, see e.g. the prediction of asymmetric steering in a non-linear loop-coupled system of three bosons [15].

Despite these interesting applications, it is unclear how much of the literature on geometric phases can be applied to the discrete gauge-invariant phases occurring in loop-coupled bosonic systems. The aim of this paper is to attempt to fill this gap. We begin by reviewing the basics of geometric phases in section II. Next, we introduce a generic linearly coupled bosonic model in section III, and explain how the coupling loops lead to discrete gauge-invariant phases. It is well known that geometric phases are associated with gauge fields. Thus, in section IV, we compare the gauge structures of standard geometric phases with that of the bosonic model of section III. Notably, we find an analogy between the time-parametrisation of kets, and the bosonic mode index in our model. For regular geometric phases, the energy spectrum affects whether the phase is associated with an abelian or non-abelian gauge field. Consequently, we examine the spectrum of our model in section V. Finally, an interesting concept in gauge theories is that of symmetry breaking, which leads to the appearance of massless gauge bosons (Goldstone theorem). We consider such a possibility in section VI. We conclude in section VII, also presenting an outline of future work.

II. A QUICK REVIEW OF ADIABATIC GEOMETRIC PHASES

We consider a Hamiltonian H parametrised by a real vector $\mathbf{R} \in \mathcal{M}$. The parameters are themselves time-dependent. We note $\mathcal{V}_n$ the eigenspaces of the Hamiltonian with energy E_n and dimension g_n, where $1 \leqslant n \leqslant N$. Thus, a general solution of the Schrodinger equation can be written

$$|\psi(\mathbf{R}(t))\rangle = \sum_{n=1}^{N} \sum_{k=1}^{g_n} c_{n,k}(t)\, |\psi_{n,k}(\mathbf{R}(t))\rangle\,, \tag{1}$$

where the $c_{n,k}$ are complex-valued coefficients. We restrict ourselves to the case of an adiabatic cylic evolution with runtime T, so that $\mathbf{R}(0) = \mathbf{R}(T)$. Then, one can show that an initial eigenstates $|\psi_{n,k}(0)\rangle$ evolves to

$$|\psi_{n,k}(t)\rangle = e^{-\frac{i}{\hbar}\int_0^T \mathrm{d}t' E_n(t')} \mathcal{P}\left\{ \exp\left(i \oint_{\mathcal{C}} \mathrm{d}A_n \right) \right\} \tag{2}$$

where $\mathcal{P}$ denotes path-ordering, and A_n is a matrix with elements

$$(A_n)_{kl} = i\, \langle \psi_{n,k}(\mathbf{R}(t)) | \boldsymbol{\nabla} \psi_{n,l}(\mathbf{R}(t)) \rangle\,, \tag{3}$$

where $\boldsymbol{\nabla}$ acts on the parameters $\mathbf{R}$.

* alan.gardin@adelaide.edu.au

III. DISCRETE GAUGE-INVARIANT PHASES

We now introduce a simple bosonic model leading to the appearance of observables phases when the system is loop-coupled. We consider a set of N bosonic modes a_k with frequencies $\omega_k/2\pi$, described by the Hamiltonian

$$H_0 = \sum_{k=1}^{N} \hbar\omega_k a_k^\dagger a_k. \tag{4}$$

Any unitary transformation $U = e^{i\phi a_k^\dagger a_k}$ leaves this Hamiltonian invariant. Thus, for each k, we are free redefine $a_k \mapsto a_k e^{-i\phi_k}$, which corresponds to a $U(1)$ symmetry. More specifically, for N uncoupled bosonic modes, we have N such $U(1)$ symmetries.

We consider a linear coupling (beam-splitter) between bosonic modes,

$$H_I = \frac{1}{2}\sum_{k\neq l}^{N} \hbar g_{gk}(e^{i\varphi_{kl}} a_k a_l^\dagger + \text{h.c}) \tag{5}$$

where the factor of $\frac{1}{2}$ accounts for double counting, and h.c denotes the hermitian conjugate terms. The total Hamiltonian $H = H_0 + H_I$ thus describes a lattice of coupled bosons, with potential long-range coupling.

For $N = 2$ bosons, the interactions reads

$$H_I = \hbar g(e^{i\varphi} a_1 a_2^\dagger + \text{h.c}) \tag{6}$$

with g the coupling strength, φ the coupling phase. In this simple case, the coupling phase φ can be eliminated by leveraging the gauge degree of freedom of a_1 or a_2. For instance, we can rotate a_1 using the unitary transformation $e^{i\varphi a_1^\dagger a_1}$. Having used the phase freedom of a_1 to remove the coupling phase, in a sense there is only a single phase freedom remaining (that of a_2). Thus, the interaction term constrains the intrinsic $U(1)$ gauge of freedom of a_1 and a_2: the original two phase degrees of freedom have been reduced to a single $U(1)$ symmetry.

Generalising, we guess that if there are as many couplings as there are of modes, then no phase degrees of freedom remain, and the coupling phases cannot be eliminated. As an example, consider a ring of $N = 3$ coupled bosonic modes, where the interaction Hamiltonian is now

$$\begin{aligned} H_I = \hbar g_1(e^{i\varphi_1} a_1 a_2^\dagger + \text{h.c}) + \hbar g_2\Big(e^{i\varphi_2} a_2 a_3^\dagger + \text{h.c}\Big) \\ + \hbar g_3\Big(e^{i\varphi_3} a_3 a_1^\dagger + \text{h.c}\Big). \end{aligned} \tag{7}$$

Rotating the bosonic modes using $e^{i\varphi_1 a_1^\dagger a_1}$ and $e^{-i\varphi_2 a_3^\dagger a_3}$ the coupling phases are focused in the last term, giving

$$\begin{aligned} H_I = \hbar g_1(a_1 a_2^\dagger + \text{h.c}) + \hbar g_2\Big(a_2 a_3^\dagger + \text{h.c}\Big) \\ + \hbar g_3\Big(e^{i(\varphi_3+\varphi_2+\varphi_1)} a_3 a_1^\dagger + \text{h.c}\Big), \end{aligned} \tag{8}$$

and thus the coupling phases cannot be gauged away. Indeed, such a ring of bosons is "loop-coupled", which formally means that there are as many couplings as there are of modes. As a consequence, the coupling phases can combine to form a gauge invariant (and hence observable) phase $\phi = \varphi_1 + \varphi_2 + \varphi_3$.

If we return to an arbitrary lattice of bosonic modes, we see that any loop within this lattice leads to a gauge invariant phase ϕ. We refer to these gauge invariant phases, resulting from the underlying coupling phases, as discrete phases in what follows. For a particle evolving on a lattice, the presence of a magnetic field can be taken into account through the Peierls substitution, and we refer the reader to the supplementary material of [7] for an introduction, or section 2.2 of [12]. Formally, we can interpret eq. (5) as the Hamiltonian of such a particle, with the operators $a_k^\dagger$ corresponding to the creation of a particle at the lattice site k. Using this interpretation, the phases can be thought of as the values of the synthetic vector potential [7, 11] at each lattice point. Therefore, a spatially dependent vector potential can be created by adjusting these phases.

IV. GAUGE STRUCTURE

We saw above that there is an intrinsic $U(1)$ symmetry for any uncoupled bosonic mode. This symmetry is to be compared to that of any state vector $|\psi\rangle$ in quantum mechanics. Indeed, for any $|\psi\rangle$ in some Hilbert space $\mathcal{H}$, then for any real constant ϕ, $e^{i\phi}|\psi\rangle$ describes the same physical state. It is common to introduce rays, which are equivalence classes of state vectors up to some phase factor. Formally, the equivalence class of $|\psi\rangle \in \mathcal{H}$ lives in the projective Hilbert space $\Pi_{\mathcal{H}}$, composed of the sets of $\overline{|\psi\rangle} = \{|\varphi\rangle\,, \quad \exists\phi \in \mathbb{R},\ |\varphi\rangle = e^{i\phi}|\psi\rangle\}$.

This local gauge invariance of any state vector $|\psi\rangle \in \mathcal{H}$ is at the origin of the geometric phases consider by Berry, Wilczek and Zee [1, 3]. Indeed, consider a loop $\mathbf{R} : [0,1] \to \mathcal{M}$ in parameter space, with the path taken in $\mathcal{M}$ is $\mathcal{C}$. Then the states induced by this curve, $|\psi(\mathbf{R}(t))\rangle$, acquire a phase difference between their endpoints $|\psi(\mathbf{R}(1))\rangle = e^{i\gamma(\mathbf{R})}|\psi(\mathbf{R}(0))\rangle$, because even though neighbouring states remain in phase (parallel transport condition), a macroscopic phase difference accumulates, leading to a geometric phase [16]. In a sense, the geometric phase accounts for the fact that the state has indeed evolved, and can be thought of as a kind of memory.

The appearance of a discrete phase in the bosonic model can be understood similarly. Here, the curve $\mathbf{R}(t)$ is indicated by the discrete index k of the bosonic mode, and the loop $\mathcal{C}$ one takes to vary the parameters $\mathbf{R}$ corresponds to a path taken through the couplings between the modes. In other words, a choice of loop $\mathcal{C}$ in the discrete model amounts to choosing a set of bosonic modes connected by the linear couplings. Another way to think about this is that a loop in a lattice of bosons corresponds to a path that an excitation (or quasiparticle) can take to propagate through the lattice.

V. EFFECTS OF SPECTRUM

When discussing geometric phases, one often distinguishes between the abelian and non-abelian cases. The abelian case corresponds to the situation where all the eigenspace of the Hamiltonian have dimension one, i.e. there are no degeneracies. This corresponds to a $U(1)$ symmetry, which is naturally abelian. If one allows for degeneracies, then the symmetry is $U(g_n)$, where g_n is the dimension of the eigenspace n. Of course, the group $U(g_n)$ is non-abelian once $g_n \geqslant 2$.

In our bosonic model, each mode has an energy $\hbar\omega_k$, and the energy levels do not affect the appearance of the discrete phases. Still, we naturally expect that given a loop $\mathcal{C}$ over the lattice, the phase acquired by an excitation propagating along this loop would be affected by the energies of the modes.

On the other hand, we can imagine stacking all the bosons a_k into a single column vector $\mathbf{a}$, and thus rewrite the Hamiltonian as

$$H = \mathbf{a}^\dagger \hbar\Omega \mathbf{a} + \mathbf{a}^\dagger \hbar G \mathbf{a}, \tag{9}$$

where $\Omega = \mathrm{diag}\{\omega_1, \dots, \omega_N\}$ and G is the matrix of couplings. We can now consider the space spanned by $\mathbf{a}$. When $\forall i \in \{1, \dots, N\}, \omega_i = \omega$, then this space is somewhat a degenerate space. It would be interesting to consider the time-evolution of these operators, and see if a geometric phase can arise. Moving forward, we note that it is very likely that the proper tool to use is the path integral, suggested by the work of [17] on the geometric phase formulation for second-quantisation.

VI. SYMMETRY BREAKING

As explained in section III, in a sense adding couplings between the bosonic modes gradually breaks their intrinsic $U(1)$ symmetries. In gauge field theories, the spontaneous symmetry breaking leads to the appearance of massless gauge bosons. Naturally, we examine if parallels can be drawn with our bosonic model.

A. Example: real scalar ϕ^4 theory

We first recall the basic idea of symmetry breaking in gauge field theories. We consider e.g. a massive scalar field ϕ, with Lagrangian

$$\mathcal{L} = \frac{1}{2}\partial_\mu\phi\partial^\mu\phi + \frac{1}{2}m^2\phi^2, \tag{10}$$

and we couple it to some potential V. The standard example is the so-called "mexican hat" potential, which for instance can be obtained taking $V(\phi) = -\frac{1}{4}\lambda\phi^4$. In this case, the theory has an unstable "false vacuum" for $\phi = 0$, which can be guessed by trying to minimise the Lagrangian with respect to ϕ. With this procedure, one also finds two other minima at $v = \pm\sqrt{m^2/\lambda}$. The idea is then to expand the Lagrangian around the "true" physical vacuum, by a change of variable $\varphi = \phi \pm v$. Often, this vacuum is degenerate as it is here, and associated with some symmetry group. Choosing one such vacuum, for instance taking $\varphi = \phi - v$, we find after the change of variable that the Lagrangian is

$$\mathcal{L} = \frac{1}{2}\partial_\mu\varphi\partial^\mu\varphi + \lambda v^2\varphi^2 + \lambda v\varphi^3 - \frac{1}{4}\lambda\varphi^4, \tag{11}$$

and thus a mass term has appeared.

B. Discrete case

For our bosonic model, it is not clear at first sight what the potential is. However, one can write the creation and annihilation operators in terms of the quadratures q and p, that behave like position and momentum operators. Thus, inverting

$$q_k = \frac{a_k + a_k^\dagger}{\sqrt{2}}, \quad p_k = i\frac{a_k^\dagger - a_k}{\sqrt{2}}, \tag{12}$$

we obtain

$$a_k\sqrt{2} = q_k + ip_k, \quad a_k^\dagger\sqrt{2} = q_k - ip_k, \tag{13}$$

and then the Hamiltonian of a single boson reads

$$H_0 = \hbar\omega_k a_k^\dagger a_k = \hbar\omega_k(q_k^2 + p_k^2) \tag{14}$$

after using $[q_k, p_k] = i$ and discarding a constant energy offset. We thus recover the standard picture of an harmonic oscillator with parabolic potential $\propto q_k^2$.

We may then attempt to expand the linear coupling terms between bosons of eq. (5), but we would like to argue that this is unnecessary. Indeed, the total Hamiltonian is quadratic in creation and annihilation operators, and thus it can be diagonalised with a Hopfield-Bogoliubov transformation. After diagonalisation, the Hamiltonian simply takes the form of a sum of uncoupled bosons,

$$H = \sum_\mu \hbar\omega_\mu p_\mu^\dagger p_\mu. \tag{15}$$

The resulting system being uncoupled, we have little change of obtaining some symmetry breaking behaviour.

VII. CONCLUSION

To make the connection to the geometric phases, it should be possible to define a discrete gauge field, and from it a flux. This flux, which is the surface integral in parameter space of the curvature tensor, is the only observable quantity. Thus, being able to define a flux is an important step. Ref [7] may help: they provide a

comparison of the discrete vs continuous case. However, they do not discuss geometric phases, which is the main point of our work.

Alternatively, the discrete phases can be understood as originating from a Peierls substitution [18], which is usually used for a lattice under a magnetic field.

Generally speaking, chiral behaviour involves the coupling along one direction, but not the other [19], which is naturally connected to non-reciprocal behaviour. This, the connection of discrete phases – which are involved in the creation of non-reciprocal phenomena – with chirality warrants further research. Indeed, we note that a bosonic superposition of the form

$$\frac{a_1 + e^{i\theta} a_2}{\sqrt{2}}, \tag{16}$$

can be an eigenmode of a ring made up of four bosons [6]. In ref [20], the authors referred to such an eigenmode a as chiral mode, despite the different physical meaning attached to the phase θ. Moreover, chiral transfer was proposed using a lattice of superconducting qubits in [7], where discrete phases came into play.

It is interesting to note that geometric phases, when they can be observable, cannot be associated with a standard quantum-mechanical observable, i.e. an hermitian operator [16]. The underlying idea is that the smooth family of Hamiltonian which leads to a geometric phase, hides the fact that the system is somewhat "coupled" to the environment in such a way that a parametrisation of the Hamiltonian is possible. Thus, we can understand the appearance of a geometric phase as "the price to pay" for a such a continuous description of a family of Hamiltonians [16]. Whether this remains true for discrete phases is an interesting question.

[1] M. V. Berry, Quantal phase factors accompanying adiabatic changes, Proc. Roy. Soc. Lond. A **392**, 45 (1984).
[2] B. Simon, Holonomy, the quantum adiabatic theorem, and berry's phase, Physical Review Letters **51**, 2167 (1983).
[3] F. Wilczek and A. Zee, Appearance of gauge structure in simple dynamical systems, Physical Review Letters **52**, 2111 (1984).
[4] Y. Aharonov and J. Anandan, Phase change during a cyclic quantum evolution, Physical Review Letters **58**, 1593 (1987).
[5] J. Anandan, Non-adiabatic non-abelian geometric phase, Physics Letters A **133**, 171 (1988).
[6] A. Gardin, J. Bourhill, V. Vlaminck, C. Person, C. Fumeaux, V. Castel, and G. C. Tettamanzi, Manifestation of the coupling phase in microwave cavity magnonics, Physical Review Applied **19**, 054069 (2023), arXiv:2212.05389 [quant-ph].
[7] J. Koch, A. A. Houck, K. L. Hur, and S. M. Girvin, Time-reversal-symmetry breaking in circuit-QED-based photon lattices, Physical Review A **82**, 043811 (2010).
[8] N. R. Bernier, L. D. Tóth, A. Koottandavida, M. A. Ioannou, D. Malz, A. Nunnenkamp, A. K. Feofanov, and T. J. Kippenberg, Nonreciprocal reconfigurable microwave optomechanical circuit, Nature Communications **8**, 10.1038/s41467-017-00447-1 (2017).
[9] K. Fang, J. Luo, A. Metelmann, M. H. Matheny, F. Marquardt, A. A. Clerk, and O. Painter, Generalized non-reciprocity in an optomechanical circuit via synthetic magnetism and reservoir engineering, Nature Physics **13**, 465 (2017).
[10] F. Ruesink, J. P. Mathew, M.-A. Miri, A. Alù, and E. Verhagen, Optical circulation in a multimode optomechanical resonator, Nature Communications **9**, 10.1038/s41467-018-04202-y (2018).
[11] M. Schmidt, S. Kessler, V. Peano, O. Painter, and F. Marquardt, Optomechanical creation of magnetic fields for photons on a lattice, Optica **2**, 635 (2015).
[12] A. Clerk, Introduction to quantum non-reciprocal interactions: from non-hermitian hamiltonians to quantum master equations and quantum feedforward schemes, SciPost Physics Lecture Notes 10.21468/scipostphyslectnotes.44 (2022).
[13] S.-A. Biehs, P. Rodriguez-Lopez, M. Antezza, and G. S. Agarwal, Nonreciprocal heat flux via synthetic fields in linear quantum systems, Physical Review A **108**, 042201 (2023), arXiv:2305.18066 [quant-ph].
[14] S.-A. Biehs and G. S. Agarwal, Enhancement of synthetic magnetic field induced nonreciprocity via bound states in the continuum in dissipatively coupled systems, Physical Review B **108**, 035423 (2023), arXiv:2305.14945 [cond-mat.mes-hall].
[15] S. Zheng, F. Sun, Y. Lai, Q. Gong, and Q. He, Manipulation and enhancement of asymmetric steering via interference effects induced by closed-loop coupling, Physical Review A **99**, 022335 (2019).
[16] R. Resta, Manifestations of berry's phase in molecules and condensed matter, Journal of Physics: Condensed Matter **12**, R107 (2000).
[17] S. Deguchi and K. Fujikawa, Second-quantized formulation of geometric phases, Physical Review A **72**, 012111 (2005).
[18] J. Larson, E. Sjöqvist, and P. Öhberg, *Conical Intersections in Physics* (Springer International Publishing, 2020).
[19] P. Lodahl, S. Mahmoodian, S. Stobbe, A. Rauschenbeutel, P. Schneeweiss, J. Volz, H. Pichler, and P. Zoller, Chiral quantum optics, Nature **541**, 473 (2017).
[20] V. L. Grigoryan and K. Xia, Cavity-mediated dissipative spin-spin coupling, Physical Review B **100**, 014415 (2019).

C.5) Level attraction from interferences in two-tone driving

Statement of Authorship

Title of Paper	Level attraction due to interferences: the case of two-tone driving
Publication Status	☐ Published ☐ Accepted for Publication ☒ Submitted for Publication ☐ Unpublished and Unsubmitted w ork w ritten in manuscript style
Publication Details	arXiv:2404:17108

Principal Author

Name of Principal Author (Candidate)	Alan Gardin
Contribution to the Paper	Performed theoretical calculations, analysed experimental and numerical data and wrote the manuscript.
Overall percentage (%)	75
Certification:	This paper reports on original research I conducted during the period of my Higher Degree by Research candidature and is not subject to any obligations or contractual agreements with a third party that would constrain its inclusion in this thesis. I am the primary author of this paper.
Signature	Date 22/01/2024

Co-Author Contributions

By signing the Statement of Authorship, each author certifies that:

i. the candidate's stated contribution to the publication is accurate (as detailed above);

ii. permission is granted for the candidate in include the publication in the thesis; and

iii. the sum of all co-author contributions is equal to 100% less the candidate's stated contribution.

Name of Co-Author	Guillaume Bourcin
Contribution to the Paper	Checked the theoretical calculations and helped eliminate other physical explanations. Read and provided comments on the manuscript.
Signature	Date 03/12/2024

Name of Co-Author	Christian Person
Contribution to the Paper	Read and provided comments on the manuscript.
Signature	Date 18/03/2024

Name of Co-Author	Christophe Fumeaux		
Contribution to the Paper	Read and provided comments on the manuscript.		
Signature		Date	17/03/2024

Name of Co-Author	Romain Lebrun		
Contribution to the Paper	Read and provided comments on the manuscript.		
Signature		Date	

Name of Co-Author	Isabella Boventer		
Contribution to the Paper	Carried out experiments and analysed experimental data. Read and provided comments on the manuscript.		
Signature		Date	15/03/2023

Name of Co-Author	Giuseppe Tettamanzi		
Contribution to the Paper	Read and provided comments on the manuscript.		
Signature		Date	

Name of Co-Author	Vincent Castel		
Contribution to the Paper	Carried out experiments and numerical calculations. Read and provided comments on the manuscript.		
Signature		Date	12/03/2024

Name of Co-Author	Christophe Fumeaux		
Contribution to the Paper	Read and provided comments on the manuscript.		
Signature		Date	

Name of Co-Author	Romain Lebrun		
Contribution to the Paper	Read and provided comments on the manuscript.		
Signature		Date	12/03/2024

Name of Co-Author	Isabella Boventer		
Contribution to the Paper	Carried out experiments and analysed experimental data. Read and provided comments on the manuscript.		
Signature		Date	

Name of Co-Author	Giuseppe Tettamanzi		
Contribution to the Paper	Read and provided comments on the manuscript.		
Signature		Date	19/03/2024

Name of Co-Author	Vincent Castel		
Contribution to the Paper	Carried out experiments and numerical calculations. Read and provided comments on the manuscript.		
Signature		Date	12/03/2024

Level attraction from interference in two-tone driving

Alan Gardin,[1,2,*] Guillaume Bourcin,[2] Christian Person,[2] Christophe Fumeaux,[3] Romain Lebrun,[4] Isabella Boventer,[4] Giuseppe C. Tettamanzi,[5] and Vincent Castel[2]

[1] *School of Physics, Chemistry and Earth Sciences, The University of Adelaide, Adelaide SA 5005, Australia*
[2] *IMT Atlantique, Lab-STICC, UMR CNRS 6285, F-29238 Brest, France*
[3] *School of Electrical Engineering and Computer Science, The University of Queensland, Brisbane QLD 4072, Australia*
[4] *Unité Mixte de Physique, CNRS, Thales, Université Paris-Saclay, 91767 Palaiseau, France*
[5] *School of Chemical Engineering, Discipline of Materials Engineering, The University of Adelaide, Adelaide SA 5005, Australia*

Coherent and dissipative couplings, respectively characterised by energy level repulsion and attraction, each have different applications for quantum information processing. Thus, a system in which both coherent and dissipative couplings are tunable on-demand and in-situ is tantalising. A first step towards this goal is the two-tone driving of two bosonic modes, whose experimental signature was shown to exhibit controllable level repulsion and attraction by changing the phase and amplitude of one drive. However, whether the underlying physics is that of coherent and dissipative couplings has not been clarified, and cannot be concluded solely from the measured resonances (or anti-resonances) of the system. Here, we show how the physics at play can be analysed theoretically. Combining this theory with realistic finite-element simulations, we deduce that the observation of level attraction originates from interferences due to the measurement setup, and not dissipative coupling. Beyond the clarification of a novel origin for level attraction attributed to interference, our work demonstrate how effective Hamiltonians can be derived to appropriately describe the physics.

Introduction. The coherent coupling between two systems corresponds to the coherent exchange of energy between them, and is characterised by energy level repulsion (also known as normal-mode splitting or an anti-crossing). This phenomenon is ubiquitous in physics, spanning the classical coupling of two harmonic oscillators [1] to the coupling of bosonic quasi-particles with two-level systems [2] or other bosonic modes [3]. With respect to quantum information processing, coherent coupling allows to convert quantum information between light and solid-state degrees of freedom, and is therefore an elementary building block of quantum communication [4–6]. On the other hand, dissipative coupling [7–9], characterised by energy level attraction instead, arises due to the indirect coupling of two modes mediated by a common reservoir [10–12] (e.g. a strongly dissipative auxiliary mode [13], a photonic environment [14–16], metallic leads [17]). The merging of energy levels characterising dissipative couplings leads to exceptional points [18–21], which can be useful for topological energy transfer [22], and improved sensitivity for quantum metrology and quantum sensing applications [23, 24]. Furthermore, balancing coherent and dissipative couplings, using dissipation engineering and synthetic gauge fields for instance, allows to break time-reversal symmetry and thus create non-reciprocal devices [10–12, 25–28]. Therefore, building a system in which both coherent and dissipative couplings co-exist and are tunable would be useful to access all the aforementioned applications in a unique versatile platform.

Such a system, due to the presence of both coherent and dissipative couplings, should have an energy spectrum exhibiting both level repulsion and level attraction. Two reflection experiments [29, 30], in which two coherently-coupled bosonic modes were simultaneously driven, suggested such an energy level structure (and hence the presence of coherent and dissipative couplings). Indeed, it is usually expected that the response of a system to excitations at frequencies close to their normal modes leads to resonances (or anti-resonances), with various possible line shapes informing on the underlying physics [31, 32]. However, inspection of the experimental signature alone is not sufficient because it may not be related to the energy levels. For instance, while dissipative coupling implies level attraction in a variety of platforms such as optomechanics [33], Aharonov-Bohm interferometers [17] or semiconductor microcavities [16], alternative physics can also lead to level attraction, as exemplified in optomechanics [34] or spinor condensates [35]. For all these reasons, the physics at play in two-tone driving remains unclear.

In this letter, we model a two-tone driving experiment, similar to those of [29, 30]. Our starting point is the Hamiltonian of two coherently coupled bosonic modes, whose spectrum is that of level repulsion. To model the two-tone driving and the experimentally accessible quantities, we use quantum Langevin equations (QLEs) and the input-output formalism [36]. This theoretical treatment allows to find an analytical expression for the experimental signature, where both level repulsion and attraction can occur. Importantly, we show analytically and using finite element simulations, that level attraction can be attributed to an anti-resonance due to the destructive interference between the reflection and transmission coef-

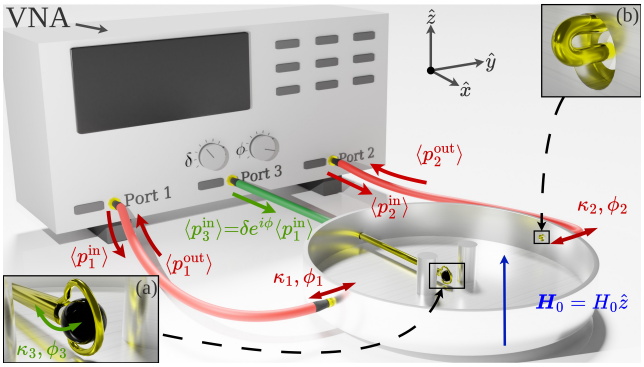


FIG. 1. Schematic of a two-tone driving experiment using a two-post re-entrant cavity [37] loaded with a ferromagnetic sphere made of Yttrium-Iron-Garnet. Ports 1 and 3 are always active and drive respectively the cavity and magnon modes. The cavity is connected to a vector network analyser (VNA) to measure the reflection at Port 1 and the transmission through Port 2. Inset (a): the YIG sphere is placed at the centre of a loop made by soldering the inner and outer conductor of a coaxial cable, itself placed between the two posts where the cavity mode's magnetic field is strongest. In the picture, the loop is in the (x, z) plane, and the YIG sphere is biased along $\hat{\mathbf{z}}$ by the static magnetic field $\mathbf{H}_0$. Inset (b): antenna used to excite the cavity modes.

ficients. To clarify the physics, we derive the open-system effective Hamiltonian of the two-tone driven system, and show that the physics remains exclusively that of coherent coupling, despite the observation of level attraction.

Quantum Langevin equations. We consider the experimental setup of fig. 1, where a ferromagnetic sphere made of Yttrium-Iron-Garnet (YIG) is placed inside a microwave cavity. The second-quantised Hamiltonian of the system enclosed inside the cavity is that of the lowest-order magnon mode (quantised spin wave) coupled to a single cavity mode, described by [9]

$$H_{\rm sys} = \hbar\omega_c c^\dagger c + \hbar\omega_m m^\dagger m + \hbar\big(gcm^\dagger + g^* c^\dagger m\big), \quad (1)$$

where $g/2\pi$ is the (complex) coherent coupling strength [38, 39] between the cavity mode (operators $c, c^\dagger$) and the magnon mode (operators $m, m^\dagger$). The frequency of the cavity mode $\omega_c/2\pi$ is fixed by the cavity's geometry, while the ferromagnetic resonance of the magnon is tuned by a static magnetic field $\mathbf{H}_0 = H_0\hat{\mathbf{z}}$ as $\omega_m = \gamma|\mathbf{H}_0|$ where $\gamma/2\pi = 28$ GHz/T is the gyromagnetic ratio.

The quantum Langevin equations (QLEs) allow to model the coupling of the cavity system described by eq. (1) to the environment, to model intrinsic dissipation or external drives. To model the intrinsic damping of the cavity mode c and the magnon mode m, we assume that they each couple to a different bosonic bath with coupling constants $\kappa_c/2\pi$ and $\kappa_m/2\pi$. As per fig. 1, the cavity system described by eq. (1) is coupled to three ports p_i, labelled from 1 to 3, where the first two ports couple only to the cavity mode (with real-valued coupling constants $\kappa_1/2\pi$ and $\kappa_2/2\pi$ and phases ϕ_1, ϕ_2 [40]) and the third couples only to the magnon mode (real-valued coupling constant $\kappa_3/2\pi$ with phase ϕ_3). Physically, the coupling of the magnon to port 3 is due to the Zeeman interaction with the magnetic field created by the loop of port 3. The QLE for the cavity and magnon modes then read [41]

$$\dot{c} = -i\widetilde{\omega}_c c - ig^* m - \sqrt{\kappa_c}c^{\rm in} - \sqrt{\kappa_1}e^{i\phi_1}p_1^{\rm in} - \sqrt{\kappa_2}e^{i\phi_2}p_2^{\rm in}, \quad (2)$$

$$\dot{m} = -i\widetilde{\omega}_m m - igc - \sqrt{\kappa_m}m^{\rm in} - \sqrt{\kappa_3}e^{i\phi_3}p_3^{\rm in}, \quad (3)$$

where $\widetilde{\omega}_c = \omega_c - i\frac{\kappa_c+\kappa_1+\kappa_2}{2}$ and $\widetilde{\omega}_m = \omega_m - i\frac{\kappa_m+\kappa_3}{2}$. In the QLEs, $c^{\rm in}$ and $m^{\rm in}$ account for intrinsic damping and have zero mean $\langle c^{\rm in}\rangle = \langle m^{\rm in}\rangle = 0$, while $p_i^{\rm in}$ represent the coupling to the ports.

Two-tone reflection and transmission. We now assume that $p_1^{\rm in}$ and $p_3^{\rm in}$ correspond to coherent drives at the same frequency, albeit with a phase and amplitude difference written $\langle p_3^{\rm in}\rangle = \delta e^{i\phi}\langle p_1^{\rm in}\rangle$. We also perform a semi-classical approximation and neglect quantum fluctuations, which amounts to only considering expectation values. Using the input-output formalism [41], the reflection at Port 1 when Port 3 is active is found to be

$$r_1(\omega) = \frac{\langle p_1^{\rm out}\rangle|_{\langle p_2^{\rm in}\rangle=0}}{\langle p_1^{\rm in}\rangle} \quad (4)$$

$$= 1 - i\sqrt{\kappa_1}\frac{\widetilde{\Delta}_m\sqrt{\kappa_1} + g^*\sqrt{\kappa_3}e^{i(\phi_3-\phi_1)}\delta e^{i\phi}}{\widetilde{\Delta}_c\widetilde{\Delta}_m - |g|^2} \quad (5)$$

where $\widetilde{\Delta}_c = \omega - \widetilde{\omega}_c$ and $\widetilde{\Delta}_m = \omega - \widetilde{\omega}_m$. By comparing with the expressions of the standard S-parameters [41], we note that the reflection r_1 can also be written $r_1(\omega) = S_{11} + \delta e^{i\phi}S_{13}$ which is expected given the linearity of the problem.

For $\delta \neq 0$, the reflection coefficient r_1 can be greater than one, because it is only normalised to the input power from Port 1, thus neglecting that of Port 3. Following the setup of fig. 1, and taking the power out of Port 1 as a reference, the VNA outputs a power $1 + \delta^2$, so we can renormalise the reflection to $R_1(\omega) = \frac{1}{\sqrt{1+\delta^2}}r_1(\omega)$. Similarly, we can calculate the normalised transmission coefficient through Port 2 when both Port 1 and Port 3 are active, and we find [42]

$$T_2(\omega) = \frac{1}{\sqrt{1+\delta^2}}\frac{\langle p_2^{\rm out}\rangle|_{\langle p_2^{\rm in}\rangle=0}}{\langle p_1^{\rm in}\rangle} = \frac{S_{21} + \delta e^{i\phi}S_{23}}{\sqrt{1+\delta^2}}. \quad (6)$$

We plot $|R_1|$ in fig. 2 and $|T_2|$ in fig. 3 with the parameters $\omega_c/2\pi = 10$ GHz, $|g|/2\pi = 20$ MHz, $\kappa_c/2\pi = \kappa_m/2\pi = 1$ MHz, $\kappa_1/2\pi = \kappa_2/2\pi = 10$ MHz, $\kappa_3/2\pi = 5$ MHz, $\varphi = -\pi/2$ and $\phi_1 = \phi_2 = \phi_3 = 0$. The reflection R_1 exhibits controllable level repulsion and attraction depending on the amplitude δ of the drives and the dephasing ϕ, mirroring the experimental results of [29, 30]. On

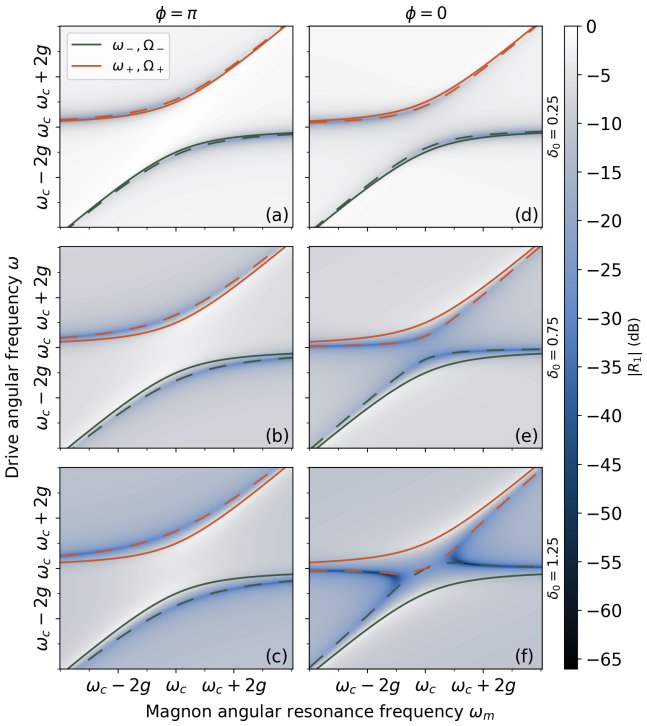


FIG. 2. Normalised reflection amplitude $|R_1|$ at Port 1 for increasing values of $\delta_0 = \frac{\sqrt{\kappa_1\kappa_3}}{|g|}\delta$ from top to bottom, and a dephasing $\phi = \pi$ (first column) and $\phi = 0$ (second column) between the drives of Port 1 and Port 3. The solid lines correspond to the real part of the zeros $\widetilde{\omega}_\pm$ of the denominator of R_1, given by eq. (9), while the dashed lines correspond to the zeros $\widetilde{\Omega}_\pm$ of the nominator of R_1.

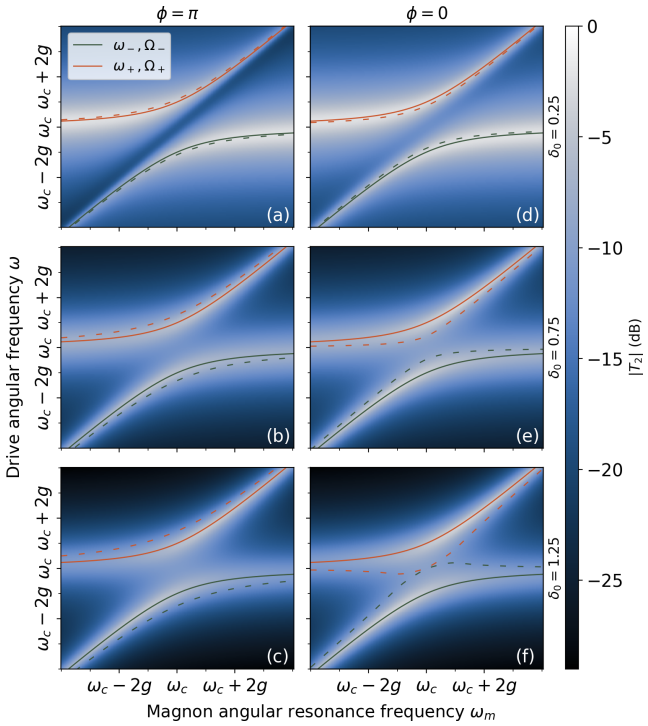


FIG. 3. Normalised transmission amplitude $|T_2|$ through Port 2 for $\phi = \pi$ and $\phi = 0$, and increasing values of δ_0 from top to bottom. The parameters used are identical to those of fig. 2.

the other hand, we notice that the transmission T_2 only shows level repulsion, despite the system being driven in exactly the same way: between R_1 and T_2, only the measurement location changes, and thus the physics should be the same.

Analysis of the two-tone reflection coefficient. An advantage of the input-output formalism is that it allows us to understand analytically the spectral features of fig. 2. Indeed, by writing $r_1(\omega) = N(\omega)/D(\omega)$ in terms of a nominator N and a denominator D, the denominator can be factorised as

$$D(\omega) = \omega^2 - (\widetilde{\omega}_c + \widetilde{\omega}_m)\omega + \widetilde{\omega}_c\widetilde{\omega}_m - |g|^2 \tag{7}$$
$$= (\omega - \widetilde{\omega}_+)(\omega - \widetilde{\omega}_-) \tag{8}$$

where

$$\widetilde{\omega}_\pm = \frac{\widetilde{\omega}_c + \widetilde{\omega}_m}{2} \pm \frac{\sqrt{(\widetilde{\omega}_c - \widetilde{\omega}_m)^2 + 4|g|^2}}{2} \tag{9}$$

are the complex-valued solutions of the quadratic eq. (7).

On the other hand, the nominator N can be written as

$$N(\omega) = \omega^2 - (\widetilde{\omega}'_c + \widetilde{\omega}_m)\omega + \widetilde{\omega}'_c\widetilde{\omega}_m - G^2 \tag{10}$$

where we defined $\widetilde{\omega}'_c = \widetilde{\omega}_c + i\kappa_1$ and

$$G = |g|\sqrt{1 + \frac{\sqrt{\kappa_1\kappa_3}}{|g|}\delta e^{i(\phi+\phi_3-\phi_1+\frac{\pi}{2}-\arg g)}}, \tag{11}$$

with $\arg g$ is the phase of the complex number g. Comparing eqs. (7) and (10), we see that the nominator can be factored similarly to the denominator as $N(\omega) = (\omega - \widetilde{\Omega}_+(\delta,\phi))(\omega - \widetilde{\Omega}_-(\delta,\phi))$, where the complex frequencies $\widetilde{\Omega}_\pm(\delta,\phi)$ are formally identical to eq. (9), after replacing $\omega_c \mapsto \omega'_c$ and $|g| \mapsto G$. Finally, we obtain

$$r_1(\omega) = \frac{\Big(\omega - \widetilde{\Omega}_+(\delta,\phi)\Big)\Big(\omega - \widetilde{\Omega}_-(\delta,\phi)\Big)}{(\omega - \widetilde{\omega}_+)(\omega - \widetilde{\omega}_-)}. \tag{12}$$

For small dissipation rates κ_i, the imaginary part of $\widetilde{\omega}_\pm$ is small compared to its real part. Therefore, in eq. (12), when ω is close to $\omega_\pm = \mathrm{Re}\{\widetilde{\omega}_\pm\}$, the denominator $|D|$ of $|R_1|$ almost vanishes, leading to a resonance behaviour (maxima) of $|R_1|$. Furthermore, $\omega_\pm$ corresponds to the spectrum of the Hamiltonian of eq. (1), and hence this resonance behaviour is expected to give information about the spectrum of the closed-system. As shown by the solid lines in figs. 2 and 3, the spectrum is that of coherent coupling, characterised by energy level repulsion with an angular frequency gap $2|g|$. Hence, the denominator of $|R_1|$, or equivalently its resonances, does inform on the underlying physics.

The situation is different for the nominator N of R_1, which leads to anti-resonances.Indeed, while the expressions of $\widetilde{\omega}_\pm$ and $\widetilde{\Omega}_\pm$ are formally identical, the effective coupling strength $G/2\pi$ for $\widetilde{\Omega}_\pm$ is complex-valued (while it is real-valued, $|g|/2\pi$, for $\widetilde{\omega}_\pm$) which can lead to level attraction. To see this more clearly, it is convenient to introduce the effective amplitude $\delta_0 = \frac{\sqrt{\kappa_1\kappa_3}}{|g|}\delta$ and the effective phase $\phi_0 = \phi_1 - \phi_3 + \arg g - \frac{\pi}{2}$ of Port 3. We can then rewrite eq. (11) as

$$G = g\sqrt{1 + \delta_0 e^{i(\phi-\phi_0)}}. \tag{13}$$

Therefore, when $\phi - \phi_0 = 0$ the effective coupling strength $G/2\pi$ is real-valued and increases as δ_0 increases, leading to an increase in level repulsion (see the dashed lines in the first column of fig. 2). On the other hand, when $\phi - \phi_0 = \pi$, the effective coupling strength is real-valued when $\delta_0 < 1$ and diminishes when δ_0 increases. Eventually, when $\delta_0 > 1$, the coupling strength becomes purely imaginary due to taking the square root of a negative number, leading to level attraction. In the limiting case where $\delta_0 = 1$, we have $G = 0$ and we obtain two uncoupled anti-resonances. As can be seen from the dashed lines in fig. 2, these spectral features indeed correspond to anti-resonances (minima of $|R_1|$) at the frequencies $\Omega_\pm$. Physically, these frequencies $\Omega_\pm$ are determined by the interference between the nominators of S_{11} and S_{13} since $r_1(\omega) = S_{11} + \delta e^{i\phi} S_{13}$. Hence, the input-output formalism shows that while the denominator of $|R_1|$ informs on the physics, the nominator is interference-based. Furthermore, the denominators of both R_1 and T_2 are identical [42], leading to similar resonant behaviour following the coherent coupling spectrum. However, their anti-resonance behaviours differ because their nominators differ [42].

Numerical finite element results. The input-output formalism provides interesting insights thanks to the resulting analytical expressions. However, it remains a toy-model of a two-tone driving experiment. Instead, a realistic modelling, taking into account the geometry of the cavity and of the ports, can be perfomed using COMSOL Multiphysics®, a finite element modelling software. We use a two-post re-entrant cavity [43, 44], similar to that sketched in fig. 1, in which the loop antenna of Port 3 is inserted from the bottom of the cavity [45]. At the location of the YIG sphere, the cavity mode's magnetic field is purely along the $\hat{\mathbf{x}}$ axis [37]. In our analysis, we assumed that Port 3 does not couple to the cavity mode, which requires us to orient the loop antenna so that it generates a magnetic field orthogonal to the cavity mode. Thus, noting $\hat{\mathbf{n}}$ the normal to the plane of the loop, we need $\hat{\mathbf{n}}$ to be in the (x, z) plane. Furthermore, since only the components orthogonal to the static magnetic field $H_0\hat{\mathbf{z}}$ contribute to the coupling between Port 3 and the magnon, $\kappa_3/2\pi$ is maximum when $\hat{\mathbf{n}} = \hat{\mathbf{y}}$.

We first numerically calculated the S parameters for different values of $\mathbf{H}_0$ using COMSOL [45]. From these two S parameters, we can plot R_1 and T_2 after normalising $r_1(\omega) = S_{11} + \delta e^{i\phi} S_{13}$ and $t_2(\omega) = S_{21} + \delta e^{i\phi} S_{23}$, and we obtain the results of fig. 4, which successfully reproduce the input-output theory results of figs. 2 and 3. As a further verification, we also performed a fully two-tone experiment in COMSOL for $\delta = 12$, and the results were identical to those of the second and fourth rows of fig. 4.

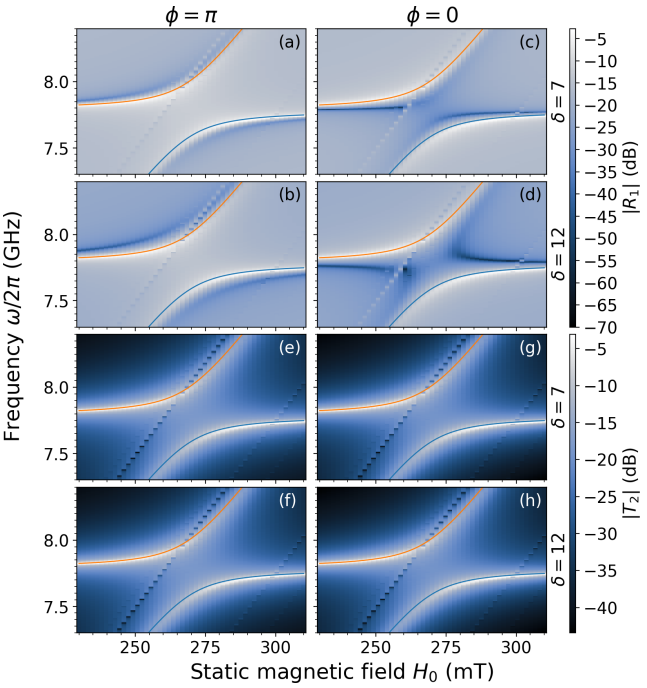


FIG. 4. Plots of the normalised reflection and transmission amplitudes $|R_1|, |T_2|$ using the numerical values of the S parameters obtained using COMSOL. Note that contrary to fig. 2 we varied the amplitude δ at Port 3 instead of the effective amplitude δ_0, because the latter depends on the unknown parameters κ_1, κ_3.

Effective Hamiltonian for the open system. We have now confirmed that the resonances of R_1 and T_2 follow energy level repulsion, suggesting coherent coupling physics. However, one may worry that the physics of the two-tone driven system is different from the physics of the closed-system Hamiltonian of eq. (1), which does not include the coherent drives. To derive the effective Hamiltonian, we write the QLEs eqs. (2) and (3) in the semi-classical approximation where operators are replaced by their expectation values. Recalling that $\langle c^{\text{in}} \rangle = \langle m^{\text{in}} \rangle = 0$, the QLEs read

$$\dot{c} = -i\widetilde{\omega}_c c - igm - \sqrt{\kappa_1} e^{i\phi_1} p_1^{\text{in}} - \sqrt{\kappa_2} e^{i\phi_2} p_2^{\text{in}}, \tag{14}$$

$$\dot{m} = -i\widetilde{\omega}_m m - igc - \sqrt{\kappa_3} e^{i\phi_3} p_3^{\text{in}}. \tag{15}$$

In both a reflection and transmission measurement, port 2 is not driven, so we set $p_2^{\text{in}} = 0$. On the other hand, p_1^{in} and p_3^{in} correspond to coherent drives at frequency $\omega/2\pi$ with amplitudes $\mathcal{E}$ and $\delta e^{i\phi}\mathcal{E}$. Thus, further defin-

ing $\mathcal{E}_1 = \sqrt{\kappa_1/2\pi}e^{i\phi_1}\mathcal{E}$ and $\mathcal{E}_3 = \sqrt{\kappa_3/2\pi}e^{i\phi_3}\mathcal{E}\delta e^{i\phi}$, the QLEs become [41]

$$\dot{c} = -i\widetilde{\omega}_c c - igm - \mathcal{E}_1 e^{-i\omega t}, \tag{16}$$

$$\dot{m} = -i\widetilde{\omega}_m m - igc - \mathcal{E}_3 e^{-i\omega t}. \tag{17}$$

From these equations, we find that the effective non-hermitian Hamiltonian (recall that $\widetilde{\omega}_c, \widetilde{\omega}_m \in \mathbb{C}$)

$$\begin{aligned} H_{\text{eff}} = \hbar\widetilde{\omega}_c c^\dagger c + \hbar\widetilde{\omega}_m m^\dagger m + \hbar\big(gcm^\dagger + g^* c^\dagger m\big) \\ + i\hbar\big(\mathcal{E}_1 c e^{i\omega t} - \text{h.c}\big) + i\hbar\big(\mathcal{E}_3 m e^{i\omega t} - \text{h.c}\big) \end{aligned} \tag{18}$$

where h.c stands for the hermitian conjugate terms, gives Heisenberg equations of motion identical to eqs. (16) and (17). Thus, the physics described by eq. (18) is identical to that given by the QLEs. After a rotating frame transformation to remove the time-dependence and displacement operations [46], this Hamiltonian is unitarily equivalent to

$$H'_{\text{eff}} = -\hbar\widetilde{\Delta}_c c^\dagger c - \hbar\widetilde{\Delta}_m m^\dagger m + \hbar\big(gcm^\dagger + g^* c^\dagger m\big). \tag{19}$$

Physical interpretation and conclusion. Formally similar to the closed-system Hamiltonian of eq. (1), this effective Hamiltonian describes a coherent coupling physics, with a spectrum corresponding to level repulsion. Since H'_{eff} describes the physics of the cavity system in the presence of coherent drives, we conclude that the physics of two-tone driving indeed corresponds to coherent coupling, even though the reflection coefficient can show level attraction due to interference-based anti-resonances. Therefore, the anti-resonance frequencies $\Omega_\pm/2\pi$ (dashed lines in fig. 2) do not correspond to the spectrum of the system, which are instead given by $\omega_\pm/2\pi$ (solid lines in fig. 2).

While here the anti-resonances leading to level attraction come from interferences between S_{11} and S_{13}, anti-resonances can also appear in one-tone driven systems as experimentally demonstrated by Rao *et al.* [47]. Notably, these anti-resonances can exhibit different coupling behaviour recently analysed by [40], and suggest energy level repulsion and attraction with a magnon mode. These behaviours are associated with the numerators of the transmission coefficient, and therefore they are not associated to a physical coherent and dissipative coupling (even though they do allow to fit experimental data). Importantly, it is incorrect to derive an effective Hamiltonian from this numerator alone, as it is not associated with a physical dynamics.

To conclude, we have showed that when two bosonic modes are simultaneously driven, the resonances in reflection and transmission indeed inform on the normal modes of the system, while the observed anti-resonances are due to interference physics, and are unrelated to the coupled system. We note that while this two-tone driving does not correspond to the in-situ control of coherent and dissipative couplings, achieving it is still a relevant research direction. Finally, while we considered a cavity magnonics system as a physical realisation of two coupled bosonic modes, many other systems, such as intersubband polaritons [48] or cavity optomechanics in the red-detuned regime [49], reduce to a similar Hamiltonian (the Dicke model [50] after employing the Holstein-Primakoff transformation [51] and the rotating wave approximation [52]). Hence, the derivations employed here are very general and may prove useful to analyse the physics in other open systems.

We acknowledge financial support from Thales Australia and Thales Research and Technology. This work is part of the research program supported by the European Union through the European Regional Development Fund (ERDF), by the Ministry of Higher Education and Research, Brittany and Rennes Métropole, through the CPER SpaceTech DroneTech, by Brest Métropole, and the ANR projects ICARUS (ANR-22-CE24-0008) and MagFunc (ANR-20-CE91-0005). The scientific colour map *oslo* [53] was used to prevent visual distortion of the data and exclusion of readers with colourvision deficiencies [54].

* alan.gardin@adelaide.edu.au

[1] L. Novotny, Strong coupling, energy splitting, and level crossings: A classical perspective, American Journal of Physics **78**, 1199 (2010).

[2] C. Weisbuch, M. Nishioka, A. Ishikawa, and Y. Arakawa, Observation of the coupled exciton-photon mode splitting in a semiconductor quantum microcavity, Physical Review Letters **69**, 3314 (1992).

[3] J. M. Dobrindt, I. Wilson-Rae, and T. J. Kippenberg, Parametric normal-mode splitting in cavity optomechanics, Physical Review Letters **101**, 263602 (2008).

[4] N. Gisin and R. Thew, Quantum communication, Nature Photonics **1**, 165 (2007).

[5] H. J. Kimble, The quantum internet, Nature **453**, 1023 (2008).

[6] D. Lachance-Quirion, Y. Tabuchi, A. Gloppe, K. Usami, and Y. Nakamura, Hybrid quantum systems based on magnonics, Applied Physics Express **12**, 070101 (2019).

[7] C. Lu, B. Turner, Y. Gui, J. Burgess, J. Xiao, and C.-M. Hu, An experimental demonstration of level attraction with coupled pendulums, American Journal of Physics **91**, 585 (2023).

[8] Y.-P. Wang and C.-M. Hu, Dissipative couplings in cavity magnonics, Journal of Applied Physics **127**, 130901 (2020).

[9] M. Harder, B. M. Yao, Y. S. Gui, and C.-M. Hu, Coherent and dissipative cavity magnonics, Journal of Applied Physics **129**, 201101 (2021).

[10] Y.-P. Wang, J. W. Rao, Y. Yang, P.-C. Xu, Y. S. Gui, B. M. Yao, J. Q. You, and C.-M. Hu, Nonreciprocity and unidirectional invisibility in cavity magnonics, Physical Review Letters **123**, 127202 (2019).

[11] A. Metelmann and A. A. Clerk, Nonreciprocal photon transmission and amplification via reservoir engineering,

Physical Review X **5**, 021025 (2015).
[12] A. Clerk, Introduction to quantum non-reciprocal interactions: from non-hermitian hamiltonians to quantum master equations and quantum feedforward schemes, SciPost Physics Lecture Notes 10.21468/scipostphyslectnotes.44 (2022).
[13] W. Yu, J. Wang, H. Y. Yuan, and J. Xiao, Prediction of attractive level crossing via a dissipative mode, Physical Review Letters **123**, 227201 (2019).
[14] B. Yao, T. Yu, Y. S. Gui, J. W. Rao, Y. T. Zhao, W. Lu, and C.-M. Hu, Coherent control of magnon radiative damping with local photon states, Communications Physics **2**, 10.1038/s42005-019-0264-z (2019).
[15] B. Yao, T. Yu, X. Zhang, W. Lu, Y. Gui, C.-M. Hu, and Y. M. Blanter, The microscopic origin of magnon-photon level attraction by traveling waves: Theory and experiment, Physical Review B **100**, 214426 (2019).
[16] O. Bleu, K. Choo, J. Levinsen, and M. M. Parish, Dissipative light-matter coupling and anomalous dispersion in nonideal cavities, Physical Review A **109**, 023707 (2024).
[17] B. Kubala and J. Konig, Flux-dependent level attraction in double-dot aharonov-bohm interferometers, Physical Review B **65**, 245301 (2002).
[18] W. D. Heiss, The physics of exceptional points, Journal of Physics A: Mathematical and Theoretical **45**, 444016 (2012).
[19] D. Zhang, X.-Q. Luo, Y.-P. Wang, T.-F. Li, and J. Q. You, Observation of the exceptional point in cavity magnon-polaritons, Nature Communications **8**, 10.1038/s41467-017-01634-w (2017).
[20] G.-Q. Zhang and J. Q. You, Higher-order exceptional point in a cavity magnonics system, Physical Review B **99**, 054404 (2019).
[21] H. M. Hurst and B. Flebus, Non-hermitian physics in magnetic systems, Journal of Applied Physics **132**, 10.1063/5.0124841 (2022), arXiv:2209.03946 [cond-mat.mes-hall].
[22] H. Xu, D. Mason, L. Jiang, and J. G. E. Harris, Topological energy transfer in an optomechanical system with exceptional points, Nature **537**, 80 (2016).
[23] Y. Cao and P. Yan, Exceptional magnetic sensitivity of pt-symmetric cavity magnon polaritons, Physical Review B **99**, 214415 (2019).
[24] T. Yu, H. Yang, L. Song, P. Yan, and Y. Cao, Higher-order exceptional points in ferromagnetic trilayers, Physical Review B **101**, 144414 (2020).
[25] J. Koch, A. A. Houck, K. L. Hur, and S. M. Girvin, Time-reversal-symmetry breaking in circuit-QED-based photon lattices, Physical Review A **82**, 043811 (2010).
[26] K. M. Sliwa, M. Hatridge, A. Narla, S. Shankar, L. Frunzio, R. J. Schoelkopf, and M. H. Devoret, Reconfigurable josephson circulator/directional amplifier, Physical Review X **5**, 041020 (2015).
[27] K. Fang, J. Luo, A. Metelmann, M. H. Matheny, F. Marquardt, A. A. Clerk, and O. Painter, Generalized non-reciprocity in an optomechanical circuit via synthetic magnetism and reservoir engineering, Nature Physics **13**, 465 (2017).
[28] X. Huang, C. Lu, C. Liang, H. Tao, and Y.-C. Liu, Loss-induced nonreciprocity, Light: Science & Applications **10**, 30 (2021).
[29] I. Boventer, M. Kläui, R. Macêdo, and M. Weides, Steering between level repulsion and attraction: broad tunability of two-port driven cavity magnon-polaritons, New Journal of Physics **21**, 125001 (2019).
[30] I. Boventer, C. Dorflinger, T. Wolz, R. Macedo, R. Lebrun, M. Klaui, and M. Weides, Control of the coupling strength and linewidth of a cavity magnon-polariton, Physical Review Research **2**, 013154 (2020).
[31] A. Barnthaler, S. Rotter, F. Libisch, J. Burgdorfer, S. Gehler, U. Kuhl, and H.-J. Stockmann, Probing decoherence through fano resonances, Physical Review Letters **105**, 056801 (2010).
[32] M. F. Limonov, M. V. Rybin, A. N. Poddubny, and Y. S. Kivshar, Fano resonances in photonics, Nature Photonics **11**, 543 (2017).
[33] Q. Lu, J. Guo, Y.-L. Zhang, Z. Fu, L. Chen, Y. Xiang, and S. Xie, Level attraction due to dissipative phonon–phonon coupling in an opto-mechano-fluidic resonator, ACS Photonics **10**, 699 (2023).
[34] N. R. Bernier, L. D. Tóth, A. K. Feofanov, and T. J. Kippenberg, Level attraction in a microwave optomechanical circuit, Physical Review A **98**, 023841 (2018).
[35] N. R. Bernier, E. G. Dalla Torre, and E. Demler, Unstable avoided crossing in coupled spinor condensates, Physical Review Letters **113**, 065303 (2014).
[36] C. W. Gardiner and M. J. Collett, Input and output in damped quantum systems: Quantum stochastic differential equations and the master equation, Physical Review A **31**, 3761 (1985).
[37] J. Bourhill, V. Castel, A. Manchec, and G. Cochet, Universal characterization of cavity–magnon polariton coupling strength verified in modifiable microwave cavity, Journal of Applied Physics **128**, 073904 (2020).
[38] G. Flower, M. Goryachev, J. Bourhill, and M. E. Tobar, Experimental implementations of cavity-magnon systems: from ultra strong coupling to applications in precision measurement, New Journal of Physics **21**, 095004 (2019).
[39] A. Gardin, J. Bourhill, V. Vlaminck, C. Person, C. Fumeaux, V. Castel, and G. C. Tettamanzi, Manifestation of the coupling phase in microwave cavity magnonics, Physical Review Applied **19**, 054069 (2023), arXiv:2212.05389 [quant-ph].
[40] G. Bourcin, A. Gardin, J. Bourhill, V. Vlaminck, and V. Castel, Level attraction in a quasi-closed cavity, (2024), type: article, arxiv:2402.06258 [quant-ph].
[41] See supplemental material at [url] for the derivation of the quantum langevin equation and the input-output theory.
[42] See supplemental material at [url] for the expression of the transmission and its plot.
[43] M. Goryachev, W. G. Farr, D. L. Creedon, Y. Fan, M. Kostylev, and M. E. Tobar, High-cooperativity cavity qed with magnons at microwave frequencies, Phys. Rev. Applied **2**, 054002 (2014).
[44] N. Kostylev, M. Goryachev, and M. E. Tobar, Superstrong coupling of a microwave cavity to yttrium iron garnet magnons, Applied Physics Letters **108**, 062402 (2016).
[45] See supplemental material at [url] for more details on the cavity used in the simulations and its characterisation.
[46] See supplemental material at [url] for the details of the transformations.
[47] J. W. Rao, C. H. Yu, Y. T. Zhao, Y. S. Gui, X. L. Fan, D. S. Xue, and C.-M. Hu, Level attraction and level repulsion of magnon coupled with a cavity anti-resonance, New Journal of Physics **21**, 065001 (2019).

[48] C. Ciuti, G. Bastard, and I. Carusotto, Quantum vacuum properties of the intersubband cavity polariton field, Physical Review B **72**, 115303 (2005).
[49] M. Aspelmeyer, T. J. Kippenberg, and F. Marquardt, Cavity optomechanics, Reviews of Modern Physics **86**, 1391 (2014).
[50] K. Hepp and E. H. Lieb, On the superradiant phase transition for molecules in a quantized radiation field: the dicke maser model, Annals of Physics **76**, 360 (1973).
[51] T. Holstein and H. Primakoff, Field dependence of the intrinsic domain magnetization of a ferromagnet, Phys. Rev. **58**, 1098 (1940).
[52] A. Le Boité, Theoretical methods for ultrastrong light–matter interactions, Advanced Quantum Technologies **3**, 1900140 (2020), https://onlinelibrary.wiley.com/doi/pdf/10.1002/qute.201900140.
[53] F. Crameri, Scientific colour maps (2021).
[54] F. Crameri, G. E. Shephard, and P. J. Heron, The misuse of colour in science communication, Nature Communications **11**, 10.1038/s41467-020-19160-7 (2020).

Supplementary information for "Level attraction from interference in two-tone driving"

Alan Gardin, Guillaume Bourcin, Christian Person, Christophe Fumeaux,
Romain Lebrun, Isabella Boventer, Giuseppe C. Tettamanzi, and Vincent Castel

CONTENTS

Derivation of the quantum Langevin equations 1

Calculation of the reflection at Port 1 3

Expression of the reflection at Port 1 with standard S-parameters 5

Calculation of the transmission 5

Expression of the reflection at Port 2 and the transmission at Port 1 6

Effective coupling strength and crosstalk 6

Simplification of the effective Hamiltonian 7

Finite element modelling results 8

References 11

Derivation of the quantum Langevin equations

System definition. In this note, we derive the quantum Langevin equations of the coupled magnon/photon cavity system under the rotating wave approximation, which is valid for $|g| \ll \omega_c, \omega_m$ [1, 2], where $g/2\pi$ is the coupling strength. We recall that the most general Hamiltonian describing a coupled magnon-photon system reads [3]

$$H_{\text{sys}} = \hbar\omega_c c^\dagger c + \hbar\omega_m m^\dagger m + \hbar(gcm^\dagger + g^* c^\dagger m), \tag{1}$$

where $g/2\pi$ is complex-valued due to potential coupling phases [4].

The intrinsic losses of the cavity and magnon modes (respectively due to radiative losses and the Gilbert damping) can be modelled by coupling to two bosonic baths described by the Hamiltonians

$$H_{\text{bath,intrinsic}} = \int_{\mathbb{R}} \mathrm{d}\omega\, \hbar\omega a_\omega^\dagger a_\omega + \int_{\mathbb{R}} \mathrm{d}\omega\, \hbar\omega b_\omega^\dagger b_\omega, \tag{2}$$

$$H_{\text{cav–bath,intrinsic}} = \int_{\mathbb{R}} \mathrm{d}\omega\, i\hbar\sqrt{\frac{\kappa_c}{2\pi}}\left(ca_\omega^\dagger - c^\dagger a_\omega\right) + \int_{\mathbb{R}} \mathrm{d}\omega\, i\hbar\sqrt{\frac{\kappa_m}{2\pi}}\left(cb_\omega^\dagger - c^\dagger b_\omega\right). \tag{3}$$

Here, we have assumed frequency-independent (Markov approximation) and real-valued coupling rates $\kappa_c/2\pi, \kappa_m/2\pi$ to the baths.

Additionally, the cavity system is coupled to the environment through three ports, used to inject and sense microwave fields. We label them as Port 1, Port 2, and Port 3. To model the coupling of the magnon and cavity modes to the ports, we again couple them to a bosonic bath, but this time we allow the coupling rates to be complex-valued to model potential dephasing of the microwaves through the coaxial cables or due to the antenna geometry [5]. Therefore, we assume that the cavity mode couples to Ports 1 and 2 with coupling constants $\kappa_1/2\pi, \kappa_2/2\pi$, and phases ϕ_1, ϕ_2, while the magnon couples to Port 3 only, with coupling constant $\kappa_3/2\pi$ and phase ϕ_3. For the sake of completeness, we further consider that the cavity mode can couple to Port 3 with coupling constant $\zeta\kappa_3/2\pi$ and phase ϕ_3', where ζ

a dimensionless constant. The continuous-frequency bosonic bath of port i is described by creation and annihilation operators $p_{i,\omega}^\dagger, p_{i,\omega}$ with Hamiltonian

$$H_{\text{bath,ports}} = \sum_{i=1}^{3} \int_{\mathbb{R}} \mathrm{d}\omega\, \hbar\omega p_{i,\omega}^\dagger p_{i,\omega}. \tag{4}$$

while the interaction between the bath and the cavity system is modelled by

$$\begin{aligned} H_{\text{cav–bath,ports}} = &\int_{\mathbb{R}} \mathrm{d}\omega\, i\hbar\sqrt{\frac{\kappa_1}{2\pi}}\Big(cp_{1,\omega}^\dagger e^{-i\phi_1} - c^\dagger p_{1,\omega} e^{i\phi_1}\Big) + \int_{\mathbb{R}} \mathrm{d}\omega\, i\hbar\sqrt{\frac{\kappa_2}{2\pi}}\Big(cp_{2,\omega}^\dagger e^{-i\phi_2} - c^\dagger p_{2,\omega} e^{i\phi_2}\Big) \\ &+ \int_{\mathbb{R}} \mathrm{d}\omega\, i\hbar\sqrt{\frac{\kappa_3}{2\pi}}\Big(mp_{3,\omega}^\dagger e^{-i\phi_3} - m^\dagger p_{3,\omega} e^{i\phi_3}\Big) + \int_{\mathbb{R}} \mathrm{d}\omega\, i\hbar\sqrt{\frac{\zeta\kappa_3}{2\pi}}\Big(cp_{3,\omega}^\dagger e^{-i\phi_3} - c^\dagger p_{3,\omega} e^{i\phi_3'}\Big). \end{aligned} \tag{5}$$

Thus, the total Hamiltonian of the joint cavity system and environment is

$$H = H_{\text{sys}} + H_{\text{bath,intrinsic}} + H_{\text{cav–bath,intrinsic}} + H_{\text{bath,ports}} + H_{\text{cav–bath,ports}}. \tag{6}$$

Equation of motions. The Heisenberg equation of motion for $p_{1,\omega}$ is

$$\dot{p}_{1,\omega}(t) = -i\omega p_{1,\omega}(t) + \sqrt{\frac{\kappa_1}{2\pi}} e^{-i\phi_1} c(t). \tag{7}$$

The formal solution for an arbitrary $t_0 < t$ is

$$p_{1,\omega}(t) = e^{-i\omega(t-t_0)} p_{1,\omega}(t_0) + \int_{t_0}^{t} \mathrm{d}t'\, \sqrt{\frac{\kappa_1}{2\pi}} e^{-i\phi_1} c(t') e^{-i\omega\left(t-t'\right)}, \tag{8}$$

and by analogy we deduce that

$$p_{2,\omega}(t) = e^{-i\omega(t-t_0)} p_{2,\omega}(t_0) + \int_{t_0}^{t} \mathrm{d}t'\, \sqrt{\frac{\kappa_2}{2\pi}} e^{-i\phi_2} c(t') e^{-i\omega\left(t-t'\right)}, \tag{9}$$

$$p_{3,\omega}(t) = e^{-i\omega(t-t_0)} p_{3,\omega}(t_0) + \int_{t_0}^{t} \mathrm{d}t'\, \sqrt{\frac{\kappa_3}{2\pi}} e^{-i\phi_3} m(t') e^{-i\omega\left(t-t'\right)} + \int_{t_0}^{t} \mathrm{d}t'\, \sqrt{\frac{\zeta\kappa_3}{2\pi}} e^{-i\phi_3'} c(t') e^{-i\omega\left(t-t'\right)}, \tag{10}$$

$$a_\omega(t) = e^{-i\omega(t-t_0)} a_\omega(t_0) + \int_{t_0}^{t} \mathrm{d}t'\, \sqrt{\frac{\kappa_c}{2\pi}} c(t') e^{-i\omega\left(t-t'\right)}, \tag{11}$$

$$b_\omega(t) = e^{-i\omega(t-t_0)} b_\omega(t_0) + \int_{t_0}^{t} \mathrm{d}t'\, \sqrt{\frac{\kappa_m}{2\pi}} m(t') e^{-i\omega\left(t-t'\right)}. \tag{12}$$

Taking $t_0 \to -\infty$ and using $\int_{-\infty}^{t} \mathrm{d}t'\, f(t')\delta(t-t') = \frac{1}{2} f(t)$, the Heisenberg equation of motion for m is

$$\dot{m}(t) = -i\omega_m m(t) - igc(t) - \sqrt{\frac{\kappa_m}{2\pi}} \int_{\mathbb{R}} \mathrm{d}\omega\, b_\omega(t) - \sqrt{\frac{\kappa_3}{2\pi}} e^{i\phi_3} \int_{\mathbb{R}} \mathrm{d}\omega\, p_{3,\omega}(t) \tag{13}$$

$$\begin{aligned} &= -i\omega_m m(t) - igc(t) - \sqrt{\kappa_m} m^{\text{in}}(t) - \frac{\kappa_m}{2\pi} \int_{t_0\to-\infty}^{t} \mathrm{d}t'\, m(t') \int_{\mathbb{R}} \mathrm{d}\omega\, e^{-i\omega\left(t-t'\right)} \\ &\quad - \sqrt{\kappa_3} e^{i\phi_3} p_3^{\text{in}}(t) - \frac{\kappa_3}{2\pi} \int_{t_0\to-\infty}^{t} \mathrm{d}t' \Big(m(t') + e^{i(\phi_3-\phi_3')}\sqrt{\zeta} c(t')\Big) 2\pi\delta(t-t') \end{aligned} \tag{14}$$

$$= -i\widetilde{\omega}_m m(t) - \Big(ig + e^{i(\phi_3-\phi_3')}\sqrt{\zeta}\frac{\kappa_3}{2}\Big) c(t) - \sqrt{\kappa_m} m^{\text{in}}(t) - \sqrt{\kappa_3} e^{i\phi_3} p_3^{\text{in}}(t), \tag{15}$$

with $\widetilde{\omega}_m = \omega_m - i\frac{\kappa_m+\kappa_3}{2}$,

$$p_i^{\text{in}}(t) = \lim_{t_0\to-\infty} \frac{1}{\sqrt{2\pi}} \int_{\mathbb{R}} \mathrm{d}\omega\, e^{-i\omega(t-t_0)} p_{i,\omega}(t_0), \tag{16}$$

and

$$c^{\text{in}}(t) = \lim_{t_0\to-\infty} \frac{1}{\sqrt{2\pi}} \int_{\mathbb{R}} \mathrm{d}\omega\, e^{-i\omega(t-t_0)} a_\omega(t_0), \quad m^{\text{in}}(t) = \lim_{t_0\to-\infty} \frac{1}{\sqrt{2\pi}} \int_{\mathbb{R}} \mathrm{d}\omega\, e^{-i\omega(t-t_0)} b_\omega(t_0). \tag{17}$$

Similarly, the Heisenberg equation of motion for c reads

$$\begin{aligned}\dot{c}(t) &= -i\omega_c c(t) - ig^* m(t) - \sqrt{\frac{\kappa_c}{2\pi}}\int_{\mathbb{R}} \mathrm{d}\omega\, a_\omega(t) \\ &\quad - \sqrt{\frac{\kappa_1}{2\pi}}e^{i\phi_1}\int_{\mathbb{R}} \mathrm{d}\omega\, p_{1,\omega}(t) - \sqrt{\frac{\kappa_2}{2\pi}}e^{i\phi_2}\int_{\mathbb{R}} \mathrm{d}\omega\, p_{2,\omega}(t) - \sqrt{\frac{\zeta\kappa_3}{2\pi}}e^{i\phi_3'}\int_{\mathbb{R}} \mathrm{d}\omega\, p_{3,\omega}(t) \qquad (18)\\ &= -i\omega_c c(t) - ig^* m(t) - e^{i(\phi_3'-\phi_3)}\sqrt{\zeta}\frac{\kappa_3}{2}m(t) - \frac{\kappa_c+\kappa_1+\kappa_2+\zeta\kappa_3}{2}c(t) \\ &\quad - \sqrt{\kappa_c}c^{\mathrm{in}}(t) - \sqrt{\kappa_1}e^{i\phi_1}p_1^{\mathrm{in}}(t) - \sqrt{\kappa_2}e^{i\phi_2}p_2^{\mathrm{in}}(t) - \sqrt{\zeta\kappa_3}e^{\phi_3'}p_3^{\mathrm{in}}(t) \qquad (19)\\ &= -i\widetilde{\omega}_c c(t) - \widetilde{g}' m(t) - \sqrt{\kappa_c}c^{\mathrm{in}}(t) - \sqrt{\kappa_1}e^{i\phi_1}p_1^{\mathrm{in}}(t) - \sqrt{\kappa_2}e^{i\phi_2}p_2^{\mathrm{in}}(t) - \sqrt{\zeta\kappa_3}e^{i\phi_3'}p_3^{\mathrm{in}}(t). \qquad (20)\end{aligned}$$

where we defined $\widetilde{\omega}_c = \omega_c - i\frac{\kappa_c+\kappa_1+\kappa_2+\zeta\kappa_3}{2}$ and $\widetilde{g}' = g^* - i\sqrt{\zeta}\frac{\kappa_3}{2}e^{i(\phi_3'-\phi_3)}$. Similarly defining $\widetilde{g} = g - i\sqrt{\zeta}\frac{\kappa_3}{2}e^{i(\phi_3-\phi_3')}$, we can rewrite the Heisenberg equation of motions as

$$\dot{m} = -i\widetilde{\omega}_m m - \widetilde{g}c - \sqrt{\kappa_m}m^{\mathrm{in}}(t) - \sqrt{\kappa_3}e^{i\phi_3}p_3^{\mathrm{in}}(t), \qquad (21)$$

$$\dot{c} = -i\widetilde{\omega}_c c - i\widetilde{g}' m - \sqrt{\kappa_c}c^{\mathrm{in}}(t) - \sqrt{\kappa_1}e^{i\phi_1}p_1^{\mathrm{in}}(t) - \sqrt{\kappa_2}e^{i\phi_2}p_2^{\mathrm{in}}(t) - \sqrt{\zeta\kappa_3}e^{i\phi_3'}p_3^{\mathrm{in}}(t), \qquad (22)$$

which are the QLEs given in the main text.

Calculation of the reflection at Port 1

Frequency-space solutions. We now perform a semi-classical approximation, and replace operators by their expectation value. Recalling that $\langle c^{\mathrm{in}}\rangle = \langle m^{\mathrm{in}}\rangle = 0$, the QLEs simplify to

$$\dot{m} = -i\widetilde{\omega}_m m - i\widetilde{g}c - \sqrt{\kappa_3}e^{i\phi_3}p_3^{\mathrm{in}}(t), \qquad (23)$$

$$\dot{c} = -i\widetilde{\omega}_c c - i\widetilde{g}' m - \sqrt{\kappa_1}e^{i\phi_1}p_1^{\mathrm{in}}(t) - \sqrt{\kappa_2}e^{i\phi_2}p_2^{\mathrm{in}}(t) - \sqrt{\zeta\kappa_3}e^{i\phi_3'}p_3^{\mathrm{in}}(t), \qquad (24)$$

and in frequency space,

$$-i\omega\widetilde{m} = -i\widetilde{\omega}_m\widetilde{m} - i\widetilde{g}\widetilde{c} - \sqrt{\kappa_3}e^{i\phi_3}\widetilde{p}_3^{\mathrm{in}}, \qquad (25)$$

$$-i\widetilde{\Delta}_c\widetilde{c} = -i\widetilde{g}'\widetilde{m} - \sqrt{\kappa_1}e^{i\phi_1}\widetilde{p}_1^{\mathrm{in}} - \sqrt{\kappa_2}e^{i\phi_2}\widetilde{p}_2^{\mathrm{in}} - \sqrt{\zeta\kappa_3}e^{i\phi_3'}\widetilde{p}_3^{\mathrm{in}}, \qquad (26)$$

with $\widetilde{\Delta}_c = \omega - \widetilde{\omega}_c$ and $\widetilde{\Delta}_m = \omega - \widetilde{\omega}_m$. In particular, the first equation gives

$$\widetilde{m} = \frac{\widetilde{g}\widetilde{c} - i\sqrt{\kappa_3}e^{i\phi_3}\widetilde{p}_3^{\mathrm{in}}}{\widetilde{\Delta}_m}, \qquad (27)$$

which inserted in the second equation leads to

$$\widetilde{c} = \frac{\widetilde{g}'\widetilde{m} - i\sqrt{\kappa_1}e^{i\phi_1}\widetilde{p}_1^{\mathrm{in}} - i\sqrt{\kappa_2}e^{i\phi_2}\widetilde{p}_2^{\mathrm{in}} - i\sqrt{\zeta\kappa_3}e^{i\phi_3'}\widetilde{p}_3^{\mathrm{in}}}{\widetilde{\Delta}_c} \qquad (28)$$

$$\widetilde{c} = \frac{-i}{A(\omega)}\Big[\widetilde{\Delta}_m\sqrt{\kappa_1}e^{i\phi_1}\widetilde{p}_1^{\mathrm{in}} + \widetilde{\Delta}_m\sqrt{\kappa_2}e^{i\phi_2}\widetilde{p}_2^{\mathrm{in}} + \Big(\widetilde{g}'e^{i\phi_3} + \sqrt{\zeta}e^{i\phi_3'}\widetilde{\Delta}_m\Big)\sqrt{\kappa_3}\widetilde{p}_3^{\mathrm{in}}\Big] \qquad (29)$$

where $A(\omega) = \widetilde{\Delta}_c\widetilde{\Delta}_m - \widetilde{g}\widetilde{g}'$.

Input-output relations. To derive the input-output relations, we first write the formal solution of $p_{1,\omega}$ for $t < t_1$ as

$$p_{1,\omega}(t) = e^{-i\omega(t-t_1)}p_{1,\omega}(t_1) - \int_t^{t_1}\mathrm{d}t'\,\sqrt{\frac{\kappa_1}{2\pi}}e^{-i\phi_1}c(t')e^{-i\omega\left(t-t'\right)}. \qquad (30)$$

and we have on the one hand

$$\int_{\mathbb{R}}\mathrm{d}\omega\, p_{1,\omega}(t) = \sqrt{2\pi}\Big(p_1^{\mathrm{in}}(t) + \frac{\sqrt{\kappa_1}}{2}e^{-i\phi_1}c(t)\Big), \qquad (31)$$

and on the other

$$\int_{\mathbb{R}} \mathrm{d}\omega\, p_{1,\omega}(t) = \sqrt{2\pi}\left(p_{1,\omega}^{\mathrm{out}}(t) - \frac{\sqrt{\kappa_1}}{2}e^{-i\phi_1}c(t)\right), \tag{32}$$

so that the input-output relation is

$$p_1^{\mathrm{out}}(t) = p_1^{\mathrm{in}}(t) + \sqrt{\kappa_1}e^{-i\phi_1}c(t). \tag{33}$$

We can similarly derive

$$p_2^{\mathrm{out}}(t) = p_2^{\mathrm{in}}(t) + \sqrt{\kappa_2}e^{-i\phi_2}c(t), \tag{34}$$

$$p_3^{\mathrm{out}}(t) = p_3^{\mathrm{in}}(t) + \sqrt{\kappa_3}e^{-i\phi_3}m(t) + \sqrt{\zeta\kappa_3}e^{-i\phi_3'}c(t). \tag{35}$$

Modelling coherent drives. To examine the reflection and transmission, we consider that p_1, coupling to the cavity mode, is a coherent drive at frequency $\omega_d/2\pi$. Such a coherent drive is expected to reproduce the classical dynamics through the use of coherent states [6]. Formally, the state space for p_1 is the product of the Fock space of the bath operators $p_{1,\omega}$ for each frequency $\omega/2\pi$. Formally, the state of the bath is the tensor product $\bigotimes_{\omega\in\mathbb{R}}|\psi_\omega\rangle$, where $|\psi_\omega\rangle$ is the state of the bosonic mode described by the annihilation operator $p_{1,\omega}$. If we assume a coherent drive, then only the mode of frequency $\omega_d/2\pi$ has a non-vanishing number of excitation, which we take to be a coherent state $|\mathcal{E}_{\omega_d}\rangle$. Formally, $|\psi_\omega\rangle = |0\rangle$ if $\omega \neq \omega_d$, and $|\psi_\omega\rangle = |\mathcal{E}_{\omega_d}\rangle$ if $\omega = \omega_d$. Hence, $\langle p_1\rangle = \langle\mathcal{E}_{\omega_d}|p_1|\mathcal{E}_{\omega_d}\rangle = \mathcal{E}_{\omega_d} \in \mathbb{C}$, since we recall that coherent states are eigenstates of annihilation operators [6]. We make a similar approximation for Port 3 driving the magnon, albeit with a different amplitude and phase, and hence $\langle p_3\rangle = \delta e^{i\phi}\mathcal{E}_{\omega_d}$.

A convenient choice for the coherent state $\mathcal{E}_{\omega_d}$ is $\mathcal{E}_{\omega_d} = \lim_{t_0\to-\infty}\alpha e^{-i\omega_d t_0}$ with $\mathcal{E}\in\mathbb{R}$. Indeed, in the time-domain this gives for instance

$$\begin{aligned}
\left\langle p_1^{\mathrm{in}}(t)\right\rangle &= \langle\mathcal{E}_{\omega_d}|p_1^{\mathrm{in}}(t)|\mathcal{E}_{\omega_d}\rangle && (36)\\
&= \lim_{t_0\to-\infty}\left\langle \alpha e^{i\omega_d t_0}\middle|\frac{1}{\sqrt{2\pi}}\int_{\mathbb{R}}\mathrm{d}\omega\, e^{-i\omega(t-t_0)}p_{1,\omega}(t_0)\middle|\mathcal{E}e^{-i\omega_d t_0}\right\rangle && (37)\\
&= \lim_{t_0\to-\infty}\left\langle \mathcal{E}e^{i\omega_d t_0}\middle|\frac{1}{\sqrt{2\pi}}e^{-i\omega_d(t-t_0)}\alpha e^{-i\omega_d t_0}\middle|\mathcal{E}e^{-i\omega_d t_0}\right\rangle && (38)\\
&= \frac{\mathcal{E}}{\sqrt{2\pi}}e^{-i\omega_d t} && (39)
\end{aligned}$$

where in the third line we used the fact that a coherent state is an eigenstate of the annihilation operator, and that $p_{1,\omega}\left|\mathcal{E}e^{-i\omega_d t_0}\right\rangle = 0$ if $\omega\neq\omega_d$.

Expression of the reflection coefficient. From $\left\langle p_1^{\mathrm{in}}(t)\right\rangle = \frac{\mathcal{E}}{\sqrt{2\pi}}e^{-i\omega_d t}$, we see that $\left\langle \widetilde{p}_1^{\mathrm{in}}(\omega)\right\rangle = \mathcal{E}\delta(\omega-\omega_d)$. Thus, assimilating ω to the frequency of the drive, the reflection at Port 1 reads

$$\begin{aligned}
r_1(\omega) = \left.\frac{\widetilde{p}_1^{\mathrm{out}}}{\widetilde{p}_1^{\mathrm{in}}}\right|_{\widetilde{p}_2^{\mathrm{in}}=0} &= 1 + \sqrt{\kappa_1}e^{-i\phi_1}\frac{\widetilde{c}|_{\widetilde{p}_2^{\mathrm{in}}=0}}{\widetilde{p}_1^{\mathrm{in}}} && (40)\\
&= 1 - i\sqrt{\kappa_1}\frac{\widetilde{\Delta}_m\sqrt{\kappa_1}}{A(\omega)} - i\sqrt{\kappa_1}e^{-i\phi_1}\frac{\left(\widetilde{g}'e^{i\phi_3} + \sqrt{\zeta}e^{i\phi_3'}\widetilde{\Delta}_m\right)\sqrt{\kappa_3}}{A(\omega)}\frac{\widetilde{p}_3^{\mathrm{in}}}{\widetilde{p}_1^{\mathrm{in}}} && (41)\\
&= 1 - i\sqrt{\kappa_1}\frac{\widetilde{\Delta}_m\sqrt{\kappa_1} + \left(\widetilde{g}'e^{i(\phi_3-\phi_1)} + \sqrt{\zeta}e^{i(\phi_3'-\phi_1)}\widetilde{\Delta}_m\right)\sqrt{\kappa_3}\delta e^{i\phi}}{A(\omega)} && (42)
\end{aligned}$$

Notice that for $\kappa_3 = 0$, i.e. only the cavity mode is driven, the expression for the reflection reduces to the S_{11} parameter.

Normalisation. For a standard coherent state $|\mathcal{E}\rangle$, the mean number of particle is given by $|\mathcal{E}|^2$. Here, the unit of the ports $\langle p_k\rangle$ are $\sqrt{\omega}$, which can be seen by considering the quantum Langevin equations. Hence, for the ports, $|\mathcal{E}|^2$ is a number of photons per second, which can be linked with the power of the drive P by

$$\mathcal{E} = \sqrt{\frac{P}{\hbar\omega_d}}. \tag{43}$$

Given that $\langle p_3\rangle = \delta e^{i\phi}\langle p_1\rangle$, we deduce that the power difference between Port 1 and Port 3 is given by δ^2, which allows to renormalise the expression of the reflection and transmission.

Expression of the reflection at Port 1 with standard S-parameters

In this note, we derive the expressions of the standard S-parameters, when only one port is active at a time. Assuming that port 3 is not active, i.e. $\langle p_3^{\rm in}\rangle = 0$ (which corresponds to $\delta = 0$), the reflection r_1 and transmission t_2 coefficients of eqs. (42) and (50) reduce to

$$S_{11}(\omega) = 1 - i\frac{\widetilde{\Delta}_m\kappa_1}{\widetilde{\Delta}_c\widetilde{\Delta}_m - \widetilde{g}\widetilde{g}'}, \tag{44}$$

$$S_{21}(\omega) = -i\frac{\widetilde{\Delta}_m\sqrt{\kappa_1\kappa_2}e^{i(\phi_1-\phi_2)}}{\widetilde{\Delta}_c\widetilde{\Delta}_m - \widetilde{g}\widetilde{g}'}. \tag{45}$$

which are the standard S parameters for a two-port cavity. Note that by symmetry we also have

$$S_{12}(\omega) = -i\frac{\widetilde{\Delta}_m\sqrt{\kappa_1\kappa_2}e^{i(\phi_2-\phi_1)}}{\widetilde{\Delta}_c\widetilde{\Delta}_m - \widetilde{g}\widetilde{g}'}, \quad S_{22}(\omega) = 1 - i\frac{\widetilde{\Delta}_m\kappa_2}{\widetilde{\Delta}_c\widetilde{\Delta}_m - \widetilde{g}\widetilde{g}'}. \tag{46}$$

Similarly, using eq. (29) we find

$$S_{13}(\omega) = \left.\frac{\widetilde{p}_1^{\rm out}}{\widetilde{p}_3^{\rm in}}\right|_{\widetilde{p}_1^{\rm in}=\widetilde{p}_2^{\rm in}=0} = \sqrt{\kappa_1}e^{-i\phi_1}\frac{\widetilde{c}|_{\widetilde{p}_1^{\rm in}=\widetilde{p}_2^{\rm in}=0}}{\widetilde{p}_3^{\rm in}} = -i\sqrt{\kappa_1\kappa_3}\frac{\widetilde{g}'e^{i(\phi_3-\phi_1)} + \sqrt{\zeta}e^{i(\phi_3'-\phi_1)}\widetilde{\Delta}_m}{A(\omega)}, \tag{47}$$

and hence

$$r_1(\omega) = S_{11} + \delta e^{i\phi}S_{13} = 1 - i\sqrt{\kappa_1}\frac{\widetilde{\Delta}_m\sqrt{\kappa_1} + \left(\widetilde{g}'e^{i(\phi_3-\phi_1)} + \sqrt{\zeta}e^{i(\phi_3'-\phi_1)}\widetilde{\Delta}_m\right)\sqrt{\kappa_3}\delta e^{i\phi}}{A(\omega)} \tag{48}$$

which matches with the equation given in the main text for $\zeta = 0$.

Calculation of the transmission

Using the results of the input-output theory above, the transmission through Port 2 when Port 1 and 3 are active is calculated to be

$$t_2(\omega) = \left.\frac{\widetilde{p}_2^{\rm out}}{\widetilde{p}_1^{\rm in}}\right|_{\widetilde{p}_2^{\rm in}=0} = \sqrt{\kappa_2}e^{-i\phi_2}\frac{\widetilde{c}|_{\widetilde{p}_2^{\rm in}=0}}{\widetilde{p}_1^{\rm in}} \tag{49}$$

$$= -i\sqrt{\kappa_2}\frac{\widetilde{\Delta}_m\sqrt{\kappa_1}e^{i(\phi_1-\phi_2)} + \left(\widetilde{g}'e^{i(\phi_3-\phi_2)} + \sqrt{\zeta}e^{i(\phi_3'-\phi_2)}\widetilde{\Delta}_m\right)\sqrt{\kappa_3}\delta e^{i\phi}}{A(\omega)}. \tag{50}$$

Thus, the normalised transmission at Port 2 is $T_2 = \frac{1}{\sqrt{1+\delta^2}}t_2$.

Expression with S parameters. Furthermore, from eq. (47), we see that S_{23} can be obtained from S_{13} by replacing $(\kappa_1, \phi_1) \mapsto (\kappa_2, \phi_2)$, and thus we have

$$S_{23}(\omega) = \left.\frac{\widetilde{p}_2^{\rm out}}{\widetilde{p}_3^{\rm in}}\right|_{\widetilde{p}_1^{\rm in}=\widetilde{p}_2^{\rm in}=0} = \sqrt{\kappa_2}e^{-i\phi_2}\frac{\widetilde{c}|_{\widetilde{p}_1^{\rm in}=\widetilde{p}_2^{\rm in}=0}}{\widetilde{p}_3^{\rm in}} = -i\sqrt{\kappa_2\kappa_3}\frac{\widetilde{g}'e^{i(\phi_3-\phi_2)} + \sqrt{\zeta}e^{i(\phi_3'-\phi_2)}\widetilde{\Delta}_m}{A(\omega)}. \tag{51}$$

Hence, comparing eq. (50) with eqs. (45) and (51) we conclude that $t_2 = S_{21} + \delta e^{i\phi}S_{23}$.

Zeros of the nominator. The zeros of the nominator of T_2 are given by

$$(\omega - \widetilde{\omega}_m)\left[\sqrt{\kappa_1}e^{i(\phi_1-\phi_2)} + \sqrt{\zeta\kappa_3}e^{i(\phi_3'-\phi_2)}\delta e^{i\phi}\right] + \left(g^* - i\sqrt{\zeta}\frac{\kappa_3}{2}e^{i(\phi_3'-\phi_3)}\right)e^{i(\phi_3-\phi_2)}\sqrt{\kappa_3}\delta e^{i\phi} = 0 \tag{52}$$

i.e.

$$\omega = \widetilde{\omega}_m + \frac{\left(g^* - i\sqrt{\zeta}\frac{\kappa_3}{2}e^{i(\phi_3'-\phi_3)}\right)e^{i\phi_3}\sqrt{\kappa_3}\delta e^{i\phi}}{\sqrt{\kappa_1}e^{i\phi_1} + \sqrt{\zeta\kappa_3}e^{i\phi_3'}\delta e^{i\phi}}. \tag{53}$$

Expression of the reflection at Port 2 and the transmission at Port 1

In the main text, we only consider that Port 1 is being driven, while Port 2 is passive and used as a probe. In this note, we exchange the role of Port 1 and Port 2 to check that the results are identical. Thus, we now have $\langle p_2^{\rm in}(t)\rangle = \frac{\mathcal{E}}{\sqrt{2\pi}} e^{-i\omega_d t}$, $\langle p_3^{\rm in}\rangle = \delta e^{i\phi}\langle p_1^{\rm in}\rangle$, and $\langle p_2^{\rm in}\rangle = 0$. The reflection at Port 2 is

$$r_2(\omega) = \left.\frac{\widetilde{p}_2^{\rm out}}{\widetilde{p}_2^{\rm in}}\right|_{\widetilde{p}_1^{\rm in}=0} = 1 + \sqrt{\kappa_2}e^{-i\phi_2}\frac{\widetilde{c}|_{\widetilde{p}_1^{\rm in}=0}}{\widetilde{p}_2^{\rm in}} \tag{54}$$

$$= 1 - i\sqrt{\kappa_2}\frac{\widetilde{\Delta}_m\sqrt{\kappa_2} + \left(\widetilde{g}' e^{i(\phi_3-\phi_2)} + \sqrt{\zeta}e^{i(\phi_3'-\phi_2)}\widetilde{\Delta}_m\right)\sqrt{\kappa_3}\delta e^{i\phi}}{A(\omega)}, \tag{55}$$

and hence it is formally identical to r_1 after replacing the index 1 by 2. For the transmission through Port 1,

$$t_1(\omega) = \left.\frac{\widetilde{p}_1^{\rm out}}{\widetilde{p}_2^{\rm in}}\right|_{\widetilde{p}_1^{\rm in}=0} = \sqrt{\kappa_1}e^{-i\phi_1}\frac{\widetilde{c}|_{\widetilde{p}_1^{\rm in}=0}}{\widetilde{p}_2^{\rm in}} \tag{56}$$

$$= -i\sqrt{\kappa_1}\frac{\widetilde{\Delta}_m\sqrt{\kappa_2}e^{i(\phi_2-\phi_1)} + \left(\widetilde{g}' e^{i(\phi_3-\phi_1)} + \sqrt{\zeta}e^{i(\phi_3'-\phi_1)}\widetilde{\Delta}_m\right)\sqrt{\kappa_3}\delta e^{i\phi}}{A(\omega)}. \tag{57}$$

Effective coupling strength and crosstalk

For non-vanishing coupling of Port 3 to the cavity mode, $\zeta \neq 0$, we recall that the reflection coefficient given by eq. (42) is

$$r_1(\omega) = \frac{N(\omega)}{D(\omega)} = 1 - i\sqrt{\kappa_1}\frac{\widetilde{\Delta}_m\sqrt{\kappa_1} + \left(\widetilde{g}' e^{i(\phi_3-\phi_1)} + \sqrt{\zeta}e^{i(\phi_3'-\phi_1)}\widetilde{\Delta}_m\right)\sqrt{\kappa_3}\delta e^{i\phi}}{A(\omega)} \tag{58}$$

$$= \frac{\widetilde{\Delta}_c\widetilde{\Delta}_m - \widetilde{g}\widetilde{g}' - i\kappa_1\widetilde{\Delta}_m - i\widetilde{g}'\sqrt{\kappa_1\kappa_3}e^{i(\phi_3-\phi_1)}\delta e^{i\phi} - i\widetilde{\Delta}_m\sqrt{\zeta}\sqrt{\kappa_1\kappa_3}e^{i(\phi_3'-\phi_1)}\delta e^{i\phi}}{\widetilde{\Delta}_c\widetilde{\Delta}_m - \widetilde{g}\widetilde{g}'}. \tag{59}$$

The nominator is

$$N(\omega) = \omega^2 - (\widetilde{\omega}_c + \widetilde{\omega}_m)\omega + \widetilde{\omega}_c\widetilde{\omega}_m - \widetilde{g}\widetilde{g}' - i\kappa_1(\omega - \widetilde{\omega}_m) - i\widetilde{g}'\sqrt{\kappa_1\kappa_3}\delta e^{i(\phi+\phi_3-\phi_1)} - i(\omega-\widetilde{\omega}_m)\sqrt{\zeta}\sqrt{\kappa_1\kappa_3}\delta e^{i(\phi+\phi_3'-\phi_1)} \tag{60}$$

$$= \omega^2 - \left(\widetilde{\omega}_c + i\left[\kappa_1 + \sqrt{\zeta}\sqrt{\kappa_1\kappa_3}\delta e^{i(\phi+\phi_3'-\phi_1)}\right] + \widetilde{\omega}_m\right)\omega + \left(\widetilde{\omega}_c + i\left[\kappa_1 + \sqrt{\zeta}\sqrt{\kappa_1\kappa_3}\delta e^{i(\phi+\phi_3'-\phi_1)}\right]\right)\widetilde{\omega}_m \tag{61}$$

$$- \widetilde{g}\widetilde{g}' - i\widetilde{g}'\sqrt{\kappa_1\kappa_3}\delta e^{i(\phi+\phi_3-\phi_1)}$$

$$= \omega^2 - (\widetilde{\omega}_c'' + \widetilde{\omega}_m)\omega + \widetilde{\omega}_c''\widetilde{\omega}_m - \widetilde{G}^2 \tag{62}$$

where $\omega_c'' = \omega_c + i\left[\kappa_1 + \sqrt{\zeta}\sqrt{\kappa_1\kappa_3}\delta e^{i(\phi+\phi_3'-\phi_1)}\right]$ and, recalling that $g = |g|e^{i\varphi}$,

$$\widetilde{G} = \sqrt{\widetilde{g}\widetilde{g}' + i\widetilde{g}'\sqrt{\kappa_1\kappa_3}\delta e^{i(\phi+\phi_3-\phi_1)}} \tag{63}$$

$$= \sqrt{\left(g - i\sqrt{\zeta}e^{i(\phi_3-\phi_3')}\frac{\kappa_3}{2}\right)\left(g^* - i\sqrt{\zeta}e^{-i(\phi_3-\phi_3')}\frac{\kappa_3}{2}\right) + i\left(g^* - i\sqrt{\zeta}e^{-i(\phi_3-\phi_3')}\frac{\kappa_3}{2}\right)\sqrt{\kappa_1\kappa_3}\delta e^{i(\phi+\phi_3-\phi_1)}} \tag{64}$$

$$= |g|\sqrt{1 + \frac{\sqrt{\kappa_1\kappa_3}}{|g|}\delta e^{i(\phi+\phi_3-\phi_1+\frac{\pi}{2}-\varphi)} - \frac{\sqrt{\zeta}\kappa_3}{|g|}\left(\frac{\sqrt{\zeta}}{4}\frac{\kappa_3}{|g|} + i\cos(\varphi+\phi_3'-\phi_3) - \frac{\sqrt{\kappa_1\kappa_3}}{2|g|}\delta e^{i(\phi+\phi_3'-\phi_1)}\right)}. \tag{65}$$

The first two terms under the square root correspond to the formula given in the main text, which corresponds to $\zeta = 0$. In fig. 1 we plot the reflection coefficient with parameters identical to those used in the main text, where $\kappa_3/g = 1/2$.

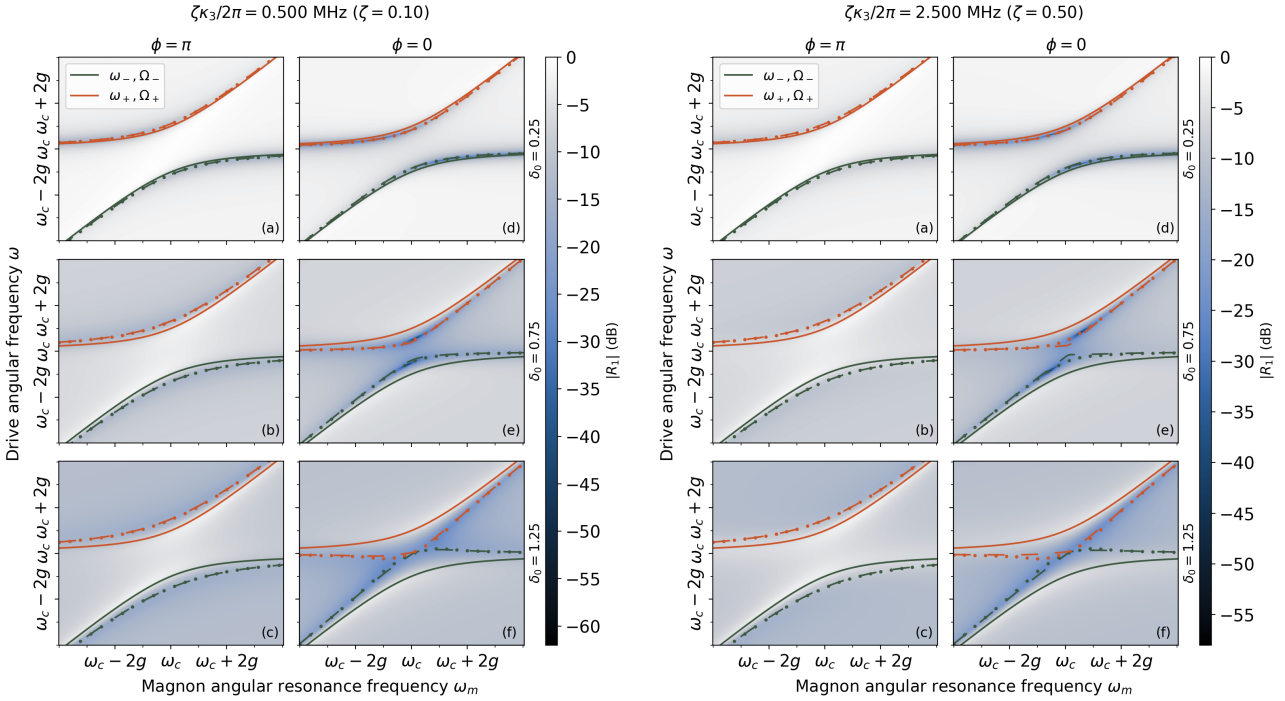


FIG. 1. Plot of the reflection amplitude $|R_1|$ for $\zeta = 0.1$ (left) and $\zeta = 0.5$ (right), with other parameters as in figure 2 of the main text. The dashed lines corresponds to $\zeta \neq 0$ (they are exactly the same as in figure 2 of the main text) while the dots corresponds to $\zeta = 0$.

Simplification of the effective Hamiltonian

The effective Hamiltonian in the main text reads

$$H_{\text{eff}} = \hbar\widetilde{\omega}_c c^\dagger c + \hbar\widetilde{\omega}_m m^\dagger m + \hbar g\big(cm^\dagger + c^\dagger m\big) + i\hbar\big(\mathcal{E}_1 c e^{i\omega t} - \text{h.c}\big) + i\hbar\big(\mathcal{E}_3 m e^{i\omega t} - \text{h.c}\big). \tag{66}$$

To simplify the calculations, we define $\epsilon_c = i\mathcal{E}_1$ and $\epsilon_m = i\mathcal{E}_3$, and we obtain

$$H_{\text{eff}} = \hbar\widetilde{\omega}_c c^\dagger c + \hbar\widetilde{\omega}_m m^\dagger m + \hbar g\big(cm^\dagger + c^\dagger m\big) + \hbar\big(\epsilon_c c e^{i\omega t} + \epsilon_c^* c^\dagger e^{-i\omega t}\big) + \hbar\big(\epsilon_m m e^{i\omega t} + \epsilon_m^* m^\dagger e^{-i\omega t}\big). \tag{67}$$

In a frame rotating with the drive, which corresponds to the unitary transformation $U = \exp\big[i\omega_d t\big(c^\dagger c + m^\dagger m\big)\big]$, we obtain

$$H_{\text{eff}} = \hbar\widetilde{\Delta}_c c^\dagger c + \hbar\widetilde{\Delta}_m m^\dagger m + \hbar g\big(cm^\dagger + c^\dagger m\big) + \hbar\big(\epsilon_c^* c + \epsilon_c^* c^\dagger\big) + \hbar\big(\epsilon_m^* m + \epsilon_m^* m^\dagger\big), \tag{68}$$

with the detunings $\widetilde{\Delta}_c = \widetilde{\omega}_c - \omega_d$, $\widetilde{\Delta}_m = \widetilde{\omega}_m - \omega_d$.

Let us consider the driving terms as a perturbation V, and split the Hamiltonian of eq. (68) into $H = H_0 + V$ where

$$H_0 = \hbar\Delta_c c^\dagger c + \Delta_m m^\dagger m + \hbar g\big(cm^\dagger + c^\dagger m\big), \tag{69}$$

$$V = \hbar\big(\epsilon_c c + \epsilon_c^* c^\dagger\big) + \hbar\big(\epsilon_m m + \epsilon_m^* m^\dagger\big). \tag{70}$$

We try to find a Schrieffer-Wolf transformation [7] $U = e^\Lambda$ with $\Lambda = (\lambda_c c - \lambda_c^* c^\dagger) + (\lambda_m m - \lambda_m^* m^\dagger)$, and λ_c, λ_m

constants to determine such that $V + [\Lambda, H_0] = 0$. Note that $\Lambda^\dagger = -\Lambda$, such that e^Λ is unitary. We have

$$\begin{aligned} V + [\Lambda, H_0] &= \epsilon_c c + \epsilon_c^* c^\dagger + \epsilon_m m + \epsilon_m^* m^\dagger \\ &\quad + \big[\lambda_c c - \lambda_c^* c^\dagger, \hbar\Delta_c c^\dagger c\big] + \big[\lambda_c c - \lambda_c^* c^\dagger, \hbar g\big(c m^\dagger + c^\dagger m\big)\big] \\ &\quad + \big[\lambda_m m - \lambda_m^* m^\dagger, \hbar\Delta_m m^\dagger m\big] + \big[\lambda_m m - \lambda_m^* m^\dagger, \hbar g\big(c m^\dagger + c^\dagger m\big)\big] \qquad (71) \\ &= \epsilon_c c + \epsilon_c^* c^\dagger + \epsilon_m m + \epsilon_m^* m^\dagger \\ &\quad + \hbar\Delta_c\big(\lambda_c c + \lambda_c^* c^\dagger\big) + \hbar g\big(\lambda_c m + \lambda_c^* m^\dagger\big) \\ &\quad + \hbar\Delta_m\big(\lambda_m m + \lambda_m^* m^\dagger\big) + \hbar g\big(\lambda_m c + \lambda_m^* c^\dagger\big) \qquad (72) \\ &= \hbar\big[(\epsilon_c + \Delta_c\lambda_c + g\lambda_m)c + (\epsilon_c^* + \Delta_c\lambda_c^* + g\lambda_m^*)c^\dagger\big] \qquad (73) \\ &\quad + \hbar\big[(\epsilon_m + g\lambda_c + \Delta_m\lambda_m)m + (\epsilon_m^* + g\lambda_c^* + \Delta_m\lambda_m^*)m^\dagger\big]. \end{aligned}$$

Imposing $V + [\Lambda, H_0] = 0$ (Schrieffer-Wolff condition) leads to

$$\begin{cases} \epsilon_c + \Delta_c\lambda_c + g\lambda_m = 0 \\ \epsilon_c^* + \Delta_c\lambda_c^* + g\lambda_m^* = 0 \\ \epsilon_m + g\lambda_c + \Delta_m\lambda_m = 0 \\ \epsilon_m^* + g\lambda_c^* + \Delta_m\lambda_m^* = 0 \end{cases}, \qquad (74)$$

where we recognise that we get twice the same constraints by hermiticity. We can reduce the system to

$$\begin{cases} \epsilon_c + \Delta_c\lambda_c + g\lambda_m = 0 \\ \epsilon_m + g\lambda_c + \Delta_m\lambda_m = 0 \end{cases}, \quad \begin{cases} g\epsilon_c + g\Delta_c\lambda_c + g^2\lambda_m = 0 \\ \Delta_c\epsilon_m + g\Delta_c\lambda_c + \Delta_c\Delta_m\lambda_m = 0 \end{cases}, \qquad (75)$$

$$\begin{cases} \Delta_c\epsilon_m - g\epsilon_c + \big(\Delta_c\Delta_m - g^2\big)\lambda_m = 0 \\ g\lambda_c = -\epsilon_m - \Delta_m\lambda_m \end{cases}, \quad \begin{cases} \lambda_m = \frac{\Delta_c\epsilon_m - g\epsilon_c}{\Delta_c\Delta_m - g^2} \\ \lambda_c = -\frac{\epsilon_m}{g} - \frac{\Delta_m}{g}\frac{\Delta_c\epsilon_m - g\epsilon_c}{\Delta_c\Delta_m - g^2} \end{cases}. \qquad (76)$$

The resulting Hamiltonian is

$$\begin{aligned} H' &= H_0 + \frac{1}{2}[\Lambda, V] + \frac{1}{2}[\Lambda, [\Lambda, V]] + \mathcal{O}(\Lambda^3) \qquad (77) \\ &= \hbar\Delta_c c^\dagger c + \hbar\Delta_m m^\dagger m + \hbar g\big(c m^\dagger + c^\dagger m\big) \qquad (78) \\ &\quad + \frac{1}{2}\big[\lambda_c c - \lambda_c^* c^\dagger, \hbar\big(\epsilon_c c + \epsilon_c^* c^\dagger\big)\big] + \frac{1}{2}\big[\lambda_m m - \lambda_m^* m^\dagger, \hbar\big(\epsilon_m m + \epsilon_m^* m^\dagger\big)\big] \\ &= \hbar\Delta_c c^\dagger c + \hbar\Delta_m m^\dagger m + \hbar g\big(c m^\dagger + c^\dagger m\big) + \frac{\hbar}{2}(\lambda_c\epsilon_c^* + \lambda_c^*\epsilon_c + \lambda_m\epsilon_m^* + \lambda_m^*\epsilon_m). \end{aligned}$$

Note that the transformation is exact, since higher order commutators vanish (indeed, this is simply a displacement transformation). Furthermore, the last term is simply a constant energy offset with not physical effect, so it can be discarded.

The transformed Hamiltonian H' tells us that under coherent driving of both photons and magnons, the spectrum is equivalent to that of the undriven Hamiltonian H after the replacements $(\omega_c, \omega_m \mapsto (\widetilde{\omega}_c - \omega_d, \widetilde{\omega}_m - \omega_d)$, with $\omega_d/2\pi$ the frequency of the drive. Hence, the standard level repulsion is obtained, and no level attraction can occur.

Finite element modelling results

Cavity design. In this note, we detail the numerical results obtained using the RF module COMSOL Multiphysics® to simulate the two-tone driving experiment described by figure 1 in the main text. In the main text, p_1^{in} and p_3^{in} are defined as the signals output by the vector network analyser. Due to differing cable lengths or the geometry of the microwave probes, these signals can be dephased modelled using the phases ϕ_1 and ϕ_3. To limit these effects as much as possible, we chose to use identical probes for Port 1 and Port 3. To that effect,the probe for Port 3 is inserted from the bottom of the cavity instead of on the side, as pictured in fig. 2.

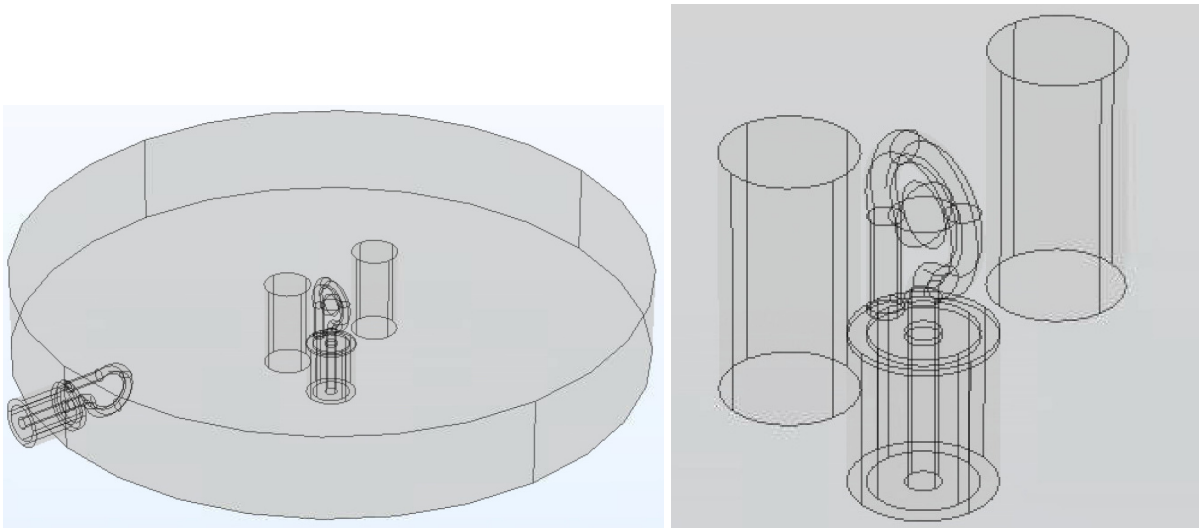


FIG. 2. Model of the two-post cavity we used in the COMSOL Multiphysics® simulations. The probes for Port 1 and Port 3 are an exact copy (dimensions and materials) limiting the effects of potential dephasings ϕ_1 and ϕ_3.

S parameters. We first performed a frequency domain simulation to obtain the S-parameters of the cavity, shown in fig. 3. As expected, we observe energy level repulsion due to the coherent coupling of the photon and magnon in both reflection and transmission. Therefore, these simulations show that the physics of this system match with that predicted by the Hamiltonian model of equation (1) of the main text. We also note the presence of higher-order magnon modes corresponding to diagonal lines offset from the ferromagnetic frequency $\omega_m/2\pi$. This is especially the case for S_{33}, potentially due to the non-uniform magnetic field generated by the loop antenna.

Estimation of δ and ϕ_0. Next, we used the numerical values of S_{11} and S_{13} to compute and plot $R_1 = S_{11}+\delta e^{i\phi} S_{13}$ for a range of δ and ϕ. The results, plotted in fig. 4, allow us to estimate very simply numerically which value of δ and ϕ are required to obtain level repulsion or attraction. We see that level repulsion and attraction are clearly visible for $\delta = 12$ and $\phi \in \{\pi, 0\}$ as predicted by the theory. This implies that the phase offset $\phi_0 = \phi_1 - \phi_3 + \arg g - \frac{\pi}{2}$ in this system is $\phi_0 = \pi$ since level repulsion is obtained when $\phi - \phi_0 = \pi - \phi_0 = 0$. Alternatively, one can extract the linewidths $\kappa_1/2\pi, \kappa_3/2\pi$ and the coherent coupling $|g|/2\pi$ from the S-parameters of fig. 3, and then use $\delta_0 = \frac{\sqrt{\kappa_1\kappa_3}}{|g|}\delta$ to estimate δ. Then, one needs to sweep the dephasing ϕ between the two drives to determine the phase offset ϕ_0.

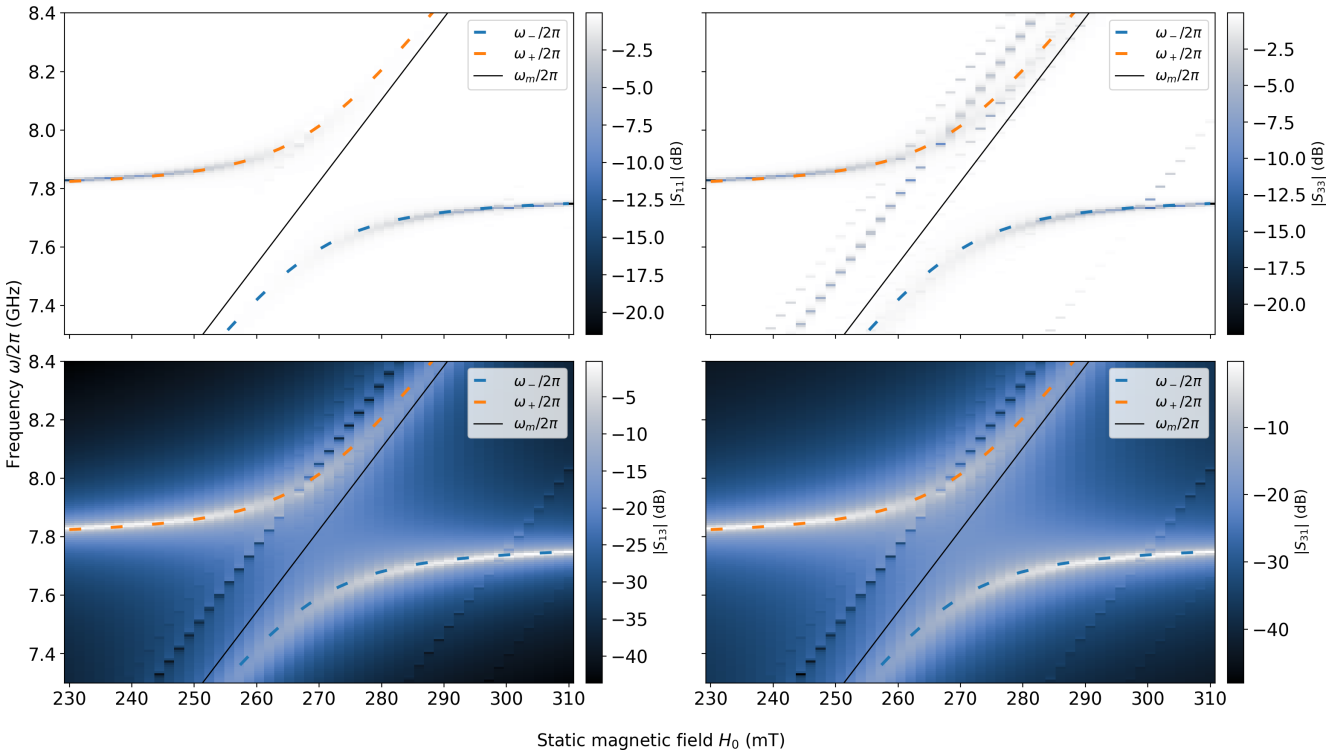


FIG. 3. Numerical calculations of the amplitude of the S parameters of the cavity. The polaritonic frequencies $\omega_\pm/2\pi$ are given by equation (8) of the main text, and describe level repulsion, the signature of coherent coupling physics. The fit parameters are a coupling strength of $g/2\pi = 210$ MHz and a cavity resonance at $\omega_c/2\pi = 7.853$ GHz.

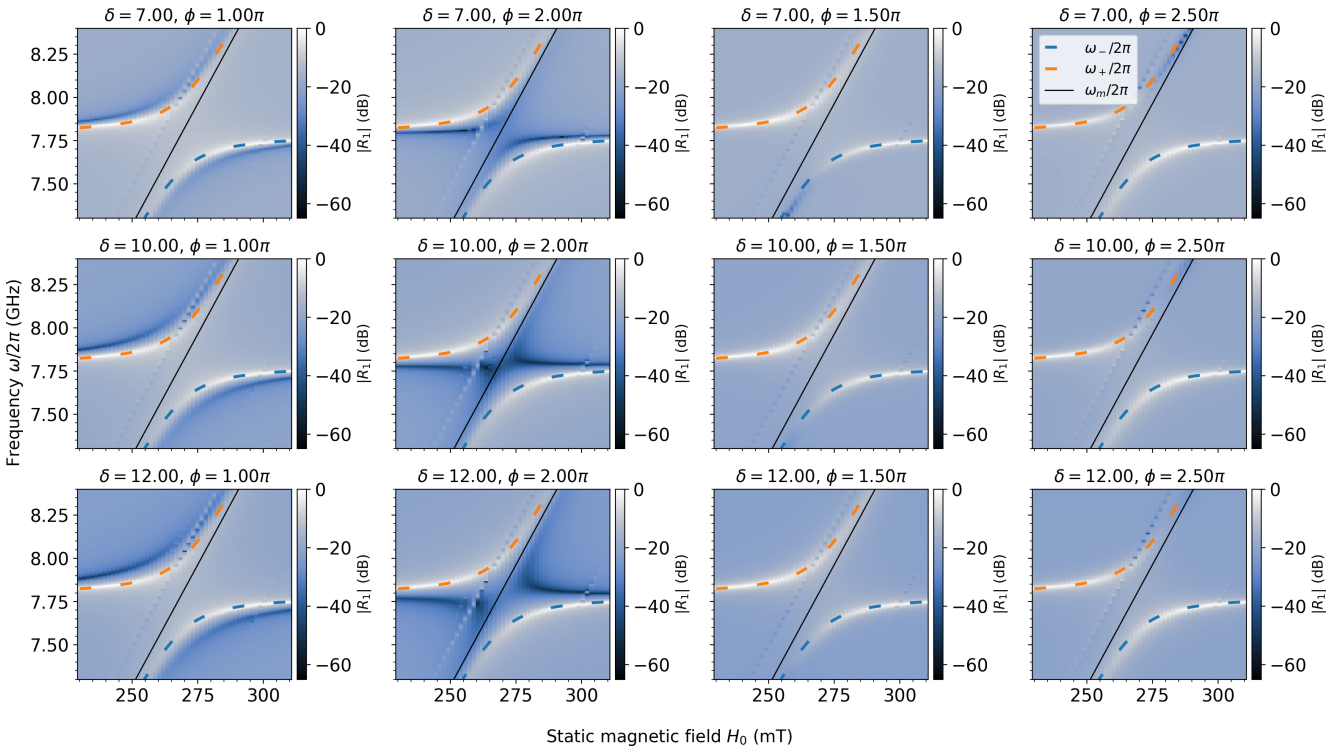


FIG. 4. Numerical calculations of the reflection R_1 using the S parameters obtained using COMSOL Multiphysics®. The legend is common to all figures The fit parameters are identical to this in fig. 3.

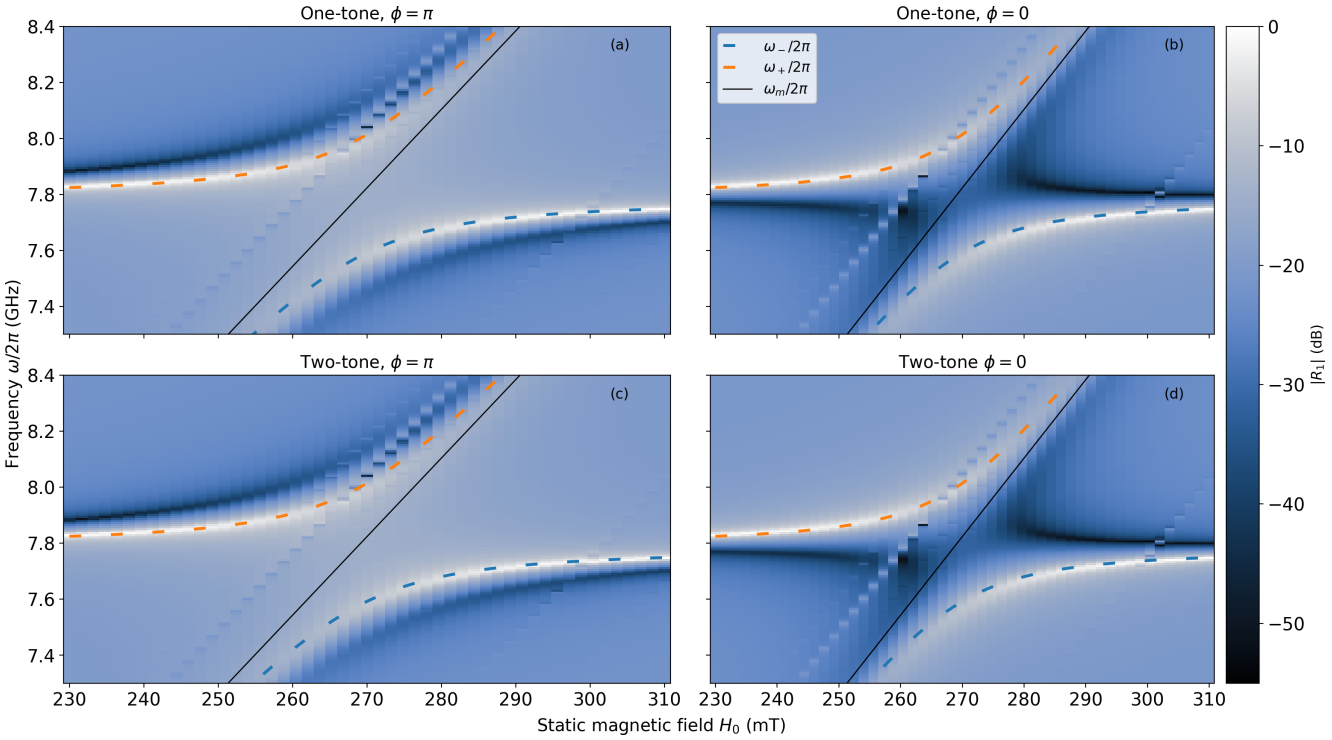


FIG. 5. Numerical calculations of the reflection at Port 1 with Port 3 active (R_1) using COMSOL Multiphysics® for $\delta = 12$. (a-b) Evaluation of R_1 from the S parameters using $R_1 = S_{11} + \delta e^{i\phi} S_{13}$. By definition of the S parameters, these are essentially a combination of one-tone simulations. (c-d) Fully two-tone simulation where both Port 1 and Port 3 are simultaneously active.

Having determined a suitable δ, we can now perform a true two-tone driving experiment by enabling both Port 1 and Port 3 in COMSOL Multiphysics®. The results for $\delta = 12$ (figs. 5(c) and 5(d)) are compared with the manual evaluation of R_1 using the S parameters (figs. 5(a) and 5(b)). We observe a perfect agreement between the two.

[1] A. Frisk Kockum, A. Miranowicz, S. De Liberato, S. Savasta, and F. Nori, Ultrastrong coupling between light and matter, Nature Reviews Physics **1**, 19–40 (2019).
[2] A. Le Boité, Theoretical methods for ultrastrong light–matter interactions, Advanced Quantum Technologies **3**, 1900140 (2020), https://onlinelibrary.wiley.com/doi/pdf/10.1002/qute.201900140.
[3] G. Flower, M. Goryachev, J. Bourhill, and M. E. Tobar, Experimental implementations of cavity-magnon systems: from ultra strong coupling to applications in precision measurement, New Journal of Physics **21**, 095004 (2019).
[4] A. Gardin, J. Bourhill, V. Vlaminck, C. Person, C. Fumeaux, V. Castel, and G. C. Tettamanzi, Manifestation of the coupling phase in microwave cavity magnonics, Physical Review Applied **19**, 054069 (2023), arXiv:2212.05389 [quant-ph].
[5] G. Bourcin, A. Gardin, J. Bourhill, V. Vlaminck, and V. Castel, Level attraction in a quasi-closed cavity, (2024), type: article, arxiv:2402.06258 [quant-ph].
[6] M. Fox, *Quantum Optics: An Introduction*, Oxford Master Series in Physics (OUP Oxford, 2006).
[7] J. R. Schrieffer and P. A. Wolff, Relation between the anderson and kondo hamiltonians, Physical Review **149**, 491 (1966).

C.6) Engineering non-reciprocal behaviour in a ring of four bosonic modes

Statement of Authorship

Title of Paper	Engineering non-reciprocal behaviour in a ring of four bosonic modes
Publication Status	☐ Published ☐ Accepted for Publication ☐ Submitted for Publication ☑ Unpublished and Unsubmitted w ork w ritten in manuscript style
Publication Details	

Principal Author

Name of Principal Author (Candidate)	Alan Gardin		
Contribution to the Paper	Performed theoretical calculations and wrote the manuscript.		
Overall percentage (%)	80		
Certification:	This paper reports on original research I conducted during the period of my Higher Degree by Research candidature and is not subject to any obligations or contractual agreements with a th its inclusion in this thesis. I am the primary author of this paper.		
Signature		Date	22/01/2024

Co-Author Contributions

By signing the Statement of Authorship, each author certifies that:

i. the candidate's stated contribution to the publication is accurate (as detailed above);

ii. permission is granted for the candidate in include the publication in the thesis; and

iii. the sum of all co-author contributions is equal to 100% less the candidate's stated contribution.

Name of Co-Author	Christian Person		
Contribution to the Paper	Read and provided comments on the manuscript.		
Signature		Date	18/03/2024

Name of Co-Author	Christophe Fumeaux		
Contribution to the Paper	Read and provided comments on the manuscript.		
Signature		Date	13/03/2024

Name of Co-Author	Giuseppe Tettamanzi		
Contribution to the Paper	Read and provided comments on the manuscript.		
Signature		Date	18-03-2024

Name of Co-Author	Vincent Castel		
Contribution to the Paper	Read and provided comments on the manuscript.		
Signature		Date	18/03/2024

Engineering non-reciprocal behaviour in a ring of four bosonic modes

Alan Gardin,[1,2,3,*] Christian Person,[2,3] Christophe Fumeaux,[4,3] Giuseppe C. Tettamanzi,[5] and Vincent Castel[2]

[1] *School of Physics, The University of Adelaide, Adelaide SA 5005, Australia*
[2] *IMT Atlantique, Technopole Brest-Iroise, CS 83818, 29238 Brest Cedex 3, France*
[3] *Lab-STICC (UMR 6285), CNRS, Technopole Brest-Iroise, CS 83818, 29238 Brest Cedex 3, France*
[4] *School of Electrical and Electronic Engineering, The University of Adelaide, Adelaide SA 5005, Australia*
[5] *School of Chemical Engineering and Advanced Materials, The University of Adelaide, Adelaide SA 5005, Australia*

We consider a ring of four bosonic modes, in which a discrete gauge-invariant parametrises the physics. We investigate the possibility of creating non-reciprocal behaviour in such a system.

a. Introduction In this short note, we investigate the potential non-reciprocal interactions that can arise in a ring of four bosonic modes. We begin by examining the usual methods to create non-reciprocal interactions, and we see that they are not directly applicable in such a system. To be more precise, while non-reciprocal interactions can be achieved, they do not correspond to non-reciprocal transmission.

b. Model We consider a ring made up of four bosonic modes a_k with Hamiltonian

$$H = \sum_{k=0}^{3} \hbar\omega_k a_k^\dagger a_k + \hbar\Big(g_0 a_0 a_1^\dagger + g_1 a_1 a_2^\dagger + g_2 a_2 a_3^\dagger + g_3 e^{i\theta} a_3 a_0^\dagger + \text{h.c}\Big), \tag{1}$$

and pictured in fig. 1. Because the system is loop-coupled, there exists a gauge-invariant phase θ parametrising the model. Such a phase can occur naturally due to coupling phases [1], or occur due to the time-modulation of either one of the mode's frequency, or the coupling strength [2].

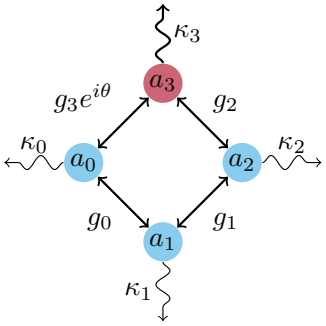


FIG. 1. Ring of four bosonic modes a_k coupled together with strength $g_k/2\pi$, and with intrinsic dissipation rate $\kappa_k/2\pi$. Since the system is loop-coupled, a gauge-invariant phase θ parametrises the model.

* alan.gardin@adelaide.edu.au

c. Adiabatic elimination of a_3 We begin by assuming that a_3 is strongly dissipative, and we adiabatically eliminate this mode from the ring. Following [2], we write the QLE for a_3, which reads

$$\dot{a}_3 = \Big(-i\omega_3 - \frac{\kappa_3}{2}\Big)a_3 - i(g_2 a_2 + g_3 e^{-i\theta} a_0) - \sqrt{\kappa_3}a_{\text{in},3}. \tag{2}$$

In frequency space,

$$-i\omega\widetilde{a}_3 = \Big(-i\omega_3 - \frac{\kappa_3}{2}\Big)\widetilde{c}_3 - i(g_2\widetilde{a}_2 + g_3 e^{-i\theta}\widetilde{a}_0) - \sqrt{\kappa_3}\widetilde{a}_{\text{in},3}, \tag{3}$$

$$\Big(i(\omega-\omega_3) - \frac{\kappa_3}{2}\Big)\widetilde{a}_3 = i(g_2\widetilde{a}_2 + g_3 e^{-i\theta}\widetilde{a}_0) + \sqrt{\kappa_3}\widetilde{a}_{\text{in},3}, \tag{4}$$

$$\widetilde{a}_3 = \frac{i(g_2\widetilde{a}_2 + g_3 e^{-i\theta}\widetilde{a}_0) + \sqrt{\kappa_3}\widetilde{a}_{\text{in},3}}{i(\omega-\omega_3) - \frac{\kappa_3}{2}}. \tag{5}$$

We now assume that $|\omega - \omega_3| \ll \frac{\kappa_{a,3}}{2}$, which corresponds to an adiabatic approximation. Indeed, returning to the time domain we have

$$a_3(t) \simeq -\frac{2i(g_2 a_2 + g_3 e^{-i\theta} a_0)}{\kappa_3} - \frac{2}{\sqrt{\kappa_3}}a_{\text{in},3}, \tag{6}$$

and we see that a_3 responds to the instantaneous values of a_0 and a_2.

Considering the QLEs for the remaining modes,

$$\dot{a}_0 = \Big(-i\omega_0 - \frac{\kappa_0}{2}\Big)a_0 - i(g_0 a_1 + g_3 e^{i\theta} a_3) - \sqrt{\kappa_0}a_{\text{in},0}, \tag{7}$$

$$\dot{a}_1 = \Big(-i\omega_1 - \frac{\kappa_1}{2}\Big)a_1 - i(g_0 a_0 + g_1 a_2) - \sqrt{\kappa_1}a_{\text{in},1}, \tag{8}$$

$$\dot{a}_2 = \Big(-i\omega_2 - \frac{\kappa_2}{2}\Big)a_2 - i(g_1 a_1 + g_2 a_3) - \sqrt{\kappa_2}a_{\text{in},2}, \tag{9}$$

we insert the solution for a_3 into the QLEs for a_0 and a_1,

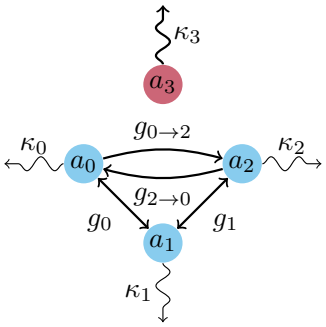


FIG. 2. System of fig. 1 after the adiabatic elimination of a_3, where a non-reciprocal interaction exists between a_0 and a_2 ($g_{02} \neq g_{20}$, see main text).

and we obtain

$$\dot{a}_0 = \left(-i\omega_0 - \frac{\kappa_0}{2} - \frac{2g_3^2}{\kappa_3}\right)a_0 - ig_0 a_1 - \frac{2g_2 g_3}{\kappa_3}e^{i\theta}a_2 + \frac{2ig_3 e^{i\theta}}{\sqrt{\kappa_3}}a_{\text{in},3} - \sqrt{\kappa_0}a_{\text{in},0}, \tag{10}$$

$$\dot{a}_2 = \left(-i\omega_2 - \frac{\kappa_2}{2} - \frac{2g_2^2}{\kappa_3}\right)a_2 - ig_1 a_1 - \frac{2g_2 g_3 e^{-i\theta}}{\kappa_3}a_0 + \frac{2ig_2}{\sqrt{\kappa_3}}a_{\text{in},3} - \sqrt{\kappa_2}a_{\text{in},2}. \tag{11}$$

Finally, the QLEs for the remaining modes are

$$\dot{a}_0 = \left(-i\omega_0 - \frac{\widetilde{\kappa}_0}{2}\right)a_0 - ig_0 a_1 - \frac{2g_2 g_3}{\kappa_3}e^{i\theta}a_2 + \frac{2ig_3 e^{i\theta}}{\sqrt{\kappa_3}}a_{\text{in},3} - \sqrt{\kappa_0}a_{\text{in},0}, \tag{12}$$

$$\dot{a}_1 = \left(-i\omega_1 - \frac{\kappa_1}{2}\right)a_1 - ig_0 a_0 - ig_1 a_2 - \sqrt{\kappa_1}a_{\text{in},1}, \tag{13}$$

$$\dot{a}_2 = \left(-i\omega_2 - \frac{\widetilde{\kappa}_2}{2}\right)a_2 - ig_1 a_1 - \frac{2g_2 g_3 e^{-i\theta}}{\kappa_3}a_0 + \frac{2ig_{23}^*}{\sqrt{\kappa_3}}a_{\text{in},3} - \sqrt{\kappa_2}a_{\text{in},2}, \tag{14}$$

with where $\widetilde{\kappa}_0 = \kappa_0 + \frac{4|g_{30}|^2}{\kappa_3}$ and $\widetilde{\kappa}_2 = \kappa_2 + \frac{4|g_{23}|^2}{\kappa_3}$.

We now assume that the input noise has zero mean, so that $\langle a_{\text{in},i}\rangle = 0$ for all operators. By considering the averages, we can write

$$\frac{\mathrm{d}}{\mathrm{d}t}\begin{pmatrix}\langle a_0\rangle\\ \langle a_1\rangle\\ \langle a_2\rangle\end{pmatrix} = -iH_{\text{eff}}\begin{pmatrix}\langle a_0\rangle\\ \langle a_1\rangle\\ \langle a_2\rangle\end{pmatrix} \tag{15}$$

with the effective Hamiltonian

$$H_{\text{eff}}/\hbar = \begin{pmatrix}\omega_0 - i\frac{\widetilde{\kappa}_0}{2} & g_0 & -i\Gamma e^{i\theta}\\ g_0 & \omega_1 - i\frac{\kappa_1}{2} & g_1\\ -i\Gamma e^{-i\theta} & g_1 & \omega_2 - i\frac{\widetilde{\kappa}_2}{2}\end{pmatrix}, \tag{16}$$

where $\Gamma = \frac{2g_2 g_3}{\kappa_3}$. This system is pictured in fig. 2.

Interestingly, we see that H_{eff} leads to an asymmetric coupling between a_0 and a_2. Formally, we have a coupling term $g_{0\to2}a_2^\dagger a_0 + g_{2\to0}a_0^\dagger a_2$ with $g_{2\to0} = -i\Gamma e^{i\theta}$ and $g_{0\to2} = -i\Gamma e^{-i\theta}$. Critically, we have $g_{0\to2} \neq g_{2\to0}^*$, which does not lead to a purely coherent coupling. In fact, due to the gauge-invariant phase θ, the couplings $g_{0\to2}, g_{2\to0}$ lead to a balance of coherent and dissipative couplings, which are described by the real and imaginary parts. Formally,

$$g_{2\to0} = \Gamma(\sin\theta - i\cos\theta), \tag{17}$$

$$g_{0\to2} = \Gamma(-\sin\theta - i\cos\theta). \tag{18}$$

In these equations, the real part contributes to coherent coupling (level repulsion), while the imaginary part contributes to dissipative coupling (level attraction). Thus, we can steer the system between purely coherent coupling (by tuning the gauge-invariant phase to $\theta = \pm\frac{\pi}{2}$ so that the imaginary parts vanish) and purely dissipative coupling (using $\theta = 0$) by mere control of the phase θ. Additionally, we see that we cannot achieve non-reciprocal transmission. Indeed, this would require either $g_{0\to2} = 0$ or $g_{2\to0} = 0$, which from eqs. (17) and (18) do not have a solution (except for the trivial case $\Gamma = 0$, but then we do not have any transmission at all).

d. Superposition of asymmetric couplings Equations (17) and (18) describe an effective coupling between a_0 and a_2 due to the adiabatic elimination of a_3. We may legitimately hope that by adiabatic elimination of a_1, we obtain a second asymmetric coupling, which could interfere to produce non-reciprocal transmission. Using a similar calculation, we show in appendix A that such a system is described by

$$\frac{\mathrm{d}}{\mathrm{d}t}\begin{pmatrix}\langle a_0\rangle\\ \langle a_2\rangle\end{pmatrix} = -iH_{\text{eff}}\begin{pmatrix}\langle a_0\rangle\\ \langle a_2\rangle\end{pmatrix} \tag{19}$$

with the effective Hamiltonian

$$H_{\text{eff}}/\hbar = \begin{pmatrix}\omega_0 - i\frac{\widetilde{\kappa}_0}{2} & -i\Gamma\\ -i\Gamma^* & \omega_2 - i\frac{\widetilde{\kappa}_2}{2}\end{pmatrix}, \tag{20}$$

with dissipation rates

$$\widetilde{\kappa}_0 = \kappa_0 + \frac{4g_0^2}{\kappa_1} + \frac{4g_3^2}{\kappa_3}, \tag{21}$$

$$\widetilde{\kappa}_2 = \kappa_2 + \frac{4g_1^2}{\kappa_1} + \frac{4g_2^2}{\kappa_3}, \tag{22}$$

and effective coupling strength

$$\Gamma = 2\frac{g_0 g_1 \kappa_3 + g_2 g_3 \kappa_1 e^{i\theta}}{\kappa_1 \kappa_3}. \tag{23}$$

The system is pictued in fig. 3, and this time we have $g_{2\to0} = -i\Gamma^*$ and $g_{0\to2} = -i\Gamma$. In terms of real and

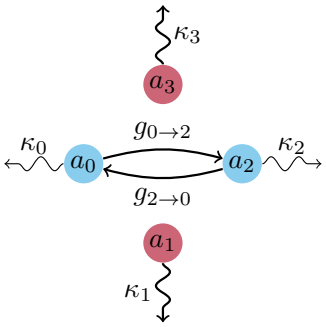


FIG. 3. Equivalent system after the adiabatic elimination of two strong dissipative modes a_1 and a_3.

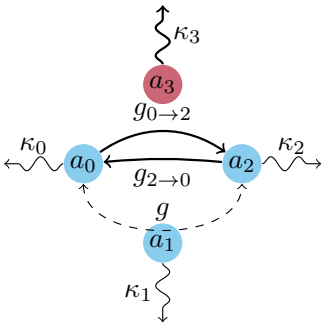


FIG. 4. The adiabatic elimination of a_3 mediates asymmetrical dissipative couplings $g_{0\to2}, g_{2\to0}$ while a_1 mediates a coherent coupling between a_0 and a_2.

imaginary parts,

$$g_{2\to0} = -2i\left[\left(\frac{g_0 g_1}{\kappa_1} + \frac{g_2 g_3}{\kappa_3}\cos\theta\right) + i\frac{g_2 g_3}{\kappa_3}\sin\theta\right] \quad (24)$$

$$= 2\left[\frac{g_2 g_3}{\kappa_3}\sin\theta - i\left(\frac{g_0 g_1}{\kappa_1} + \frac{g_2 g_3}{\kappa_3}\cos\theta\right)\right], \quad (25)$$

$$g_{0\to2} = 2\left[-\frac{g_2 g_3}{\kappa_3}\sin\theta - i\left(\frac{g_0 g_1}{\kappa_1} + \frac{g_2 g_3}{\kappa_3}\cos\theta\right)\right]. \quad (26)$$

This time, we have different weights for the coherent and dissipative couplings, since the real and imaginary parts have different prefactors, but we still cannot achieve non-reciprocal transmission. To see this, let us rewrite

$$g_{2\to0} = \Gamma_3\sin\theta - i(\Gamma_1 + \Gamma_3\cos\theta), \quad (27)$$

$$g_{0\to2} = -\Gamma_3\sin\theta - i(\Gamma_1 + \Gamma_3\cos\theta), \quad (28)$$

where $\Gamma_1 = \frac{g_0 g_1}{\kappa_1}$ and $\Gamma_3 = \frac{g_2 g_3}{\kappa_3}$. To make the couplings vanish, must have both the real and imaginary part vanishing. For $\Gamma_3 \neq 0$, we thus see that necessarily $\theta = \pi$ to eliminate the real part, and we obtain

$$g_{2\to0} = -i(\Gamma_1 - \Gamma_3), \quad (29)$$

$$g_{0\to2} = -i(\Gamma_1 - \Gamma_3). \quad (30)$$

We see that the condition $\Gamma_1 = \Gamma_3$ to make the imaginary part vanish applied to both $g_{2\to0}$ and $g_{0\to2}$, which corresponds to having no transmission at all.

e. Competition with coherent coupling To obtain a non-reciprocal interaction, it is sufficient to have a competition between a coherent coupling g and a dissipative coupling Γ, parametrised by a synthetic gauge field. For instance, in a ring of three bosonic modes, the adiabatic elimination of one mode mediates a dissipative coupling that interference with an already existing coherent coupling, as shown for instance by [2].

Returning to the ring of four bosonic modes of fig. 1, we see that after the adiabatic elimination of a_3 mediating an asymmetric dissipative coupling $g_{0\to2}, g_{2\to0}$, the mode a_1 still mediates a coherent coupling between a_0 and a_2. Hence, eliminating this mode, for instance using a Schrieffer-Wolff transformation, could lead to a non-reciprocal interaction. This situation is illustrated in fig. 4

However, as shown in appendix B, using the standard Schrieffer-Wolff transformations fails in this situation, because of the dissipative coupling.

f. Conclusion Through the adiabatic elimination of a_3, we showed that we can induce a hybrid coherent/dissipative coupling between modes a_0 and a_2 (see eqs. (17) and (18)). This allows to steer the system from level repulsion to level attraction by controlling θ. Such a scheme could be implemented in cavity magnonics using a three-post re-entrant cavity, which achieves a ring of four bosonic modes as studied here (two cavity modes, each simultaneously coupling to two magnon modes). In such a system, one could use a YIG sphere badly polished to increase dissipation, and play the role of the dissipative mode. Thus this would create an effective coupling between two cavity modes. However, the gauge-invariant phase would be fixed by the cavity geometry. Instead, we could engineer the cavity such that one of the cavity modes is strongly dissipative (for instance by varying the length of an loop antenna to excite cavity modes, as done in [3]). Then, by driving a magnon mode parallel to the static magnetic field, we could create a controllable phase offset, and this achieve coherent and dissipative coupling between two magnon modes. Note that in cavity magnonics, a two-tone driving scheme was proposed in [4] (and later realised by [5, 6]) to control the magnon/photon hybridisation by driving the magnon mode. However, there is no true dissipative coupling in this scheme, since here level attraction is produced due to interferences in the measurement setup.

To create non-reciprocal transmission, we attempted the adiabatic elimination of two modes, but we understood that non-reciprocal transmission was impossible. Instead, a potential solution consists of exhibit some indirect coherent coupling, to balance against the dissipative coupling induced by adiabatic elimination. While this is usually done using Schrieffer-Wolff transformations, the direct application of the method fails here. Going into momentum space may be a good idea. Alternatively, one may be tempted to consider a non-loop

coupled system, but then we lose the synthetic gauge field. Additionally, we can consider performing the adiabatic elimination after performing the Schrieffer-Wolff transformation. However, it is unclear how to perform an adiabatic elimination after perturbation theory, since by then the system is decoupled. Thus, in a sense we need to perform simultaneously an adiabatic elimination and a Schrieffer-Wolff transformation. [7] may be useful to that effect, and alternatively note that [8] performed a Schrieffer-Wolff transformation and then introduced dissipation, from which an adiabatic elimination could be possible.

[1] A. Gardin, J. Bourhill, V. Vlaminck, C. Person, C. Fumeaux, V. Castel, and G. C. Tettamanzi, Manifestation of the coupling phase in microwave cavity magnonics, Physical Review Applied **19**, 054069 (2023), arXiv:2212.05389 [quant-ph].

[2] A. Clerk, Introduction to quantum non-reciprocal interactions: from non-hermitian hamiltonians to quantum master equations and quantum feedforward schemes, SciPost Physics Lecture Notes 10.21468/scipostphyslectnotes.44 (2022).

[3] J. Zhao, Y. Liu, L. Wu, C.-K. Duan, Y.-x. Liu, and J. Du, Observation of anti-pt-symmetry phase transition in the magnon-cavity-magnon coupled system, Physical Review Applied **13**, 014053 (2020).

[4] V. L. Grigoryan, K. Shen, and K. Xia, Synchronized spin-photon coupling in a microwave cavity, Physical Review B **98**, 024406 (2018).

[5] I. Boventer, M. Kläui, R. Macêdo, and M. Weides, Steering between level repulsion and attraction: broad tunability of two-port driven cavity magnon-polaritons, New Journal of Physics **21**, 125001 (2019).

[6] I. Boventer, C. Dörflinger, T. Wolz, R. Macêdo, R. Lebrun, M. Kläui, and M. Weides, Control of the coupling strength and linewidth of a cavity magnon-polariton, Physical Review Research **2**, 013154 (2020).

[7] K. Ullah, M. T. Naseem, and O. E. Mustecaplioglu, Macroscopic distant magnon modes entanglement via a squeezed drive 10.48550/ARXIV.2308.13586 (2023), arXiv:2308.13586 [physics.optics].

[8] W. Yu, J. Wang, H. Yuan, and J. Xiao, Prediction of attractive level crossing via a dissipative mode, Physical Review Letters **123**, 227201 (2019).

Appendix A: Adiabatic elimination of modes a_1 and a_3

a. Derivation of the effective coupling We write the QLEs for a_1 and a_3 as

$$\dot{a}_1 = \Big(-i\omega_1 - \frac{\kappa_1}{2}\Big)a_1 - i(g_0 a_0 + g_1 a_2) - \sqrt{\kappa_1}a_{\mathrm{in},1}, \tag{A1}$$

$$\dot{a}_3 = \Big(-i\omega_3 - \frac{\kappa_3}{2}\Big)a_3 - i(g_3 e^{-i\theta} a_0 + g_2 a_2) - \sqrt{\kappa_3}a_{\mathrm{in},3}. \tag{A2}$$

In frequency space, we find

$$\widetilde{a}_1 = \frac{i(g_0\widetilde{a}_0 + g_1\widetilde{a}_2) + \sqrt{\kappa_1}\widetilde{a}_{\mathrm{in},1}}{i(\omega-\omega_1) - \frac{\kappa_1}{2}}, \tag{A3}$$

$$\widetilde{a}_3 = \frac{i(g_2\widetilde{a}_2 + g_3 e^{-i\theta}\widetilde{a}_0) + \sqrt{\kappa_3}\widetilde{a}_{\mathrm{in},3}}{i(\omega-\omega_3) - \frac{\kappa_3}{2}}. \tag{A4}$$

Assuming $|\omega-\omega_k| \ll \frac{\kappa_k}{2}$ for $k\in\{1,3\}$ (adiabatic approximation), we find the time-domain expressions

$$a_1(t) \simeq -\frac{2i(g_0 a_0 + g_1 a_2)}{\kappa_1} - \frac{2}{\sqrt{\kappa_1}}a_{\mathrm{in},1}, \tag{A5}$$

$$a_3(t) \simeq -\frac{2i(g_2 a_2 + g_3 e^{-i\theta} a_0)}{\kappa_3} - \frac{2}{\sqrt{\kappa_3}}a_{\mathrm{in},3}, \tag{A6}$$

We now consider the QLEs for the other modes, and we insert the adiabatic approximations of a_1 and a_3 to obtain

$$\dot{a}_0 = \Big(-i\omega_0 - \frac{\kappa_0}{2}\Big)a_0 - i(g_0 a_1 + g_3 e^{i\theta} a_3) - \sqrt{\kappa_0}a_{\mathrm{in},0} \tag{A7}$$

$$= \Big(-i\omega_0 - \frac{\kappa_0}{2}\Big)a_0 - \frac{2g_0^2}{\kappa_1}a_0 - \frac{2g_0 g_1}{\kappa_1}a_2 + 2i\frac{g_0}{\sqrt{\kappa_1}}a_{\mathrm{in},1} - \frac{2g_3^2}{\kappa_3}a_0 - \frac{2g_2 g_3 e^{i\theta}}{\kappa_3}a_2 + 2i\frac{g_3 e^{i\theta}}{\sqrt{\kappa_3}}a_{\mathrm{in},3} - \sqrt{\kappa_0}a_{\mathrm{in},0} \tag{A8}$$

$$= \left(-i\omega_0 - \frac{\kappa_0 + \frac{4g_0^2}{\kappa_1} + \frac{4g_3^2}{\kappa_3}}{2}\right)a_0 - \left(\frac{2g_0 g_1}{\kappa_1} + \frac{2g_2 g_3 e^{i\theta}}{\kappa_3}\right)a_2 + 2i\frac{g_0}{\sqrt{\kappa_1}}a_{\mathrm{in},1} + 2i\frac{g_3 e^{i\theta}}{\sqrt{\kappa_3}}a_{\mathrm{in},3} - \sqrt{\kappa_0}a_{\mathrm{in},0} \tag{A9}$$

$$\dot{a}_2 = \Big(-i\omega_2 - \frac{\kappa_2}{2}\Big)a_2 - i(g_1 a_1 + g_2 a_3) - \sqrt{\kappa_2}a_{\mathrm{in},2} \tag{A10}$$

$$= \left(-i\omega_2 - \frac{\kappa_2 + \frac{4g_1^2}{\kappa_1} + \frac{4g_2^2}{\kappa_3}}{2}\right)a_0 - \left(\frac{2g_0 g_1}{\kappa_1} + \frac{2g_2 g_3 e^{-i\theta}}{\kappa_3}\right)a_0 + 2i\frac{g_1}{\sqrt{\kappa_1}}a_{\mathrm{in},1} + 2i\frac{g_2}{\sqrt{\kappa_3}}a_{\mathrm{in},3} - \sqrt{\kappa_0}a_{\mathrm{in},0} \tag{A11}$$

Defining $\widetilde{\kappa}_0 = \kappa_0 + \frac{4g_0^2}{\kappa_1} + \frac{4g_3^2}{\kappa_3}$, $\widetilde{\kappa}_2 = \kappa_2 + \frac{4g_1^2}{\kappa_1} + \frac{4g_2^2}{\kappa_3}$, $\Gamma = \frac{2g_0 g_1}{\kappa_1} + \frac{2g_2 g_3}{\kappa_3}e^{i\theta}$, and assuming the noise have zero mean, we obtain

Appendix B: Details of the Schrieffer-Wolff calculations

Here we assume that a_1 is far detuned from a_0 and a_2, so that a_1 mediates an effective coherent coupling between a_0 and a_2. We hence place ourselves in the dispersive regime where $|\omega_1-\omega_2| \gg g_2$ and $|\omega_1-\omega_0| \gg g_0$. We use perturbation theory on the couplings involving a_1. Formally, we write the effective Hamiltonian above as $H_0 + V$ where

$$H_0 = \sum_{k=0}^{2}\hbar\omega_k a_k^\dagger a_k - i\Gamma\Big(e^{-i\theta}a_0 a_2^\dagger + e^{i\theta}a_0^\dagger a_2\Big), \tag{B1}$$

$$V = \hbar g_0(a_0 a_1^\dagger + a_0^\dagger a_1) + \hbar g_1(a_2 a_1^\dagger + a_2^\dagger a_1). \tag{B2}$$

We consider the Schrieffer-Wolff transformation e^{Λ} where

$$\Lambda = \lambda_0\Big(a_0 a_1^\dagger - a_0^\dagger a_1\Big) + \lambda_2\Big(a_2 a_1^\dagger - a_2^\dagger a_1\Big) \tag{B3}$$

with λ_0, λ_2 to determine. The Schrieffer-Wolff condition $V + [\Lambda, H_0]$ reads

$$\begin{aligned} V + [\Lambda, H_0] &= g_0\Big(a_0 a_1^\dagger + a_0^\dagger a_1\Big) + g_1\Big(a_2 a_1^\dagger + a_2^\dagger a_1\Big) \qquad \text{(B4)} \\ &\quad + \widetilde{\omega}_0\Big(\lambda_0 a_0 a_1^\dagger + \lambda_0^* a_0^\dagger a_1\Big) - \widetilde{\omega}_1\Big(\lambda_0 a_0 a_1^\dagger + \lambda_0^* a_0^\dagger a_1\Big) \\ &\quad - \widetilde{\omega}_1\Big(\lambda_2 a_2 a_1^\dagger + \lambda_2^* a_2^\dagger a_1\Big) + \widetilde{\omega}_2\Big(\lambda_2 a_2 a_1^\dagger + \lambda_2^* a_2^\dagger a_1\Big) \\ &\quad + (-i\Gamma)\Big[\lambda_0 a_0 a_1^\dagger - \lambda_0^* a_0^\dagger a_1, e^{-i\theta} a_0 a_2^\dagger + e^{i\theta} a_0^\dagger a_2\Big] \\ &\quad + (-i\Gamma)\Big[\lambda_2 a_2 a_1^\dagger - \lambda_2^* a_2^\dagger a_1, e^{-i\theta} a_0 a_2^\dagger + e^{i\theta} a_0^\dagger a_2\Big] \\ &= g_0\Big(a_0 a_1^\dagger + a_0^\dagger a_1\Big) + g_1\Big(a_2 a_1^\dagger + a_2^\dagger a_1\Big) \qquad \text{(B5)} \\ &\quad + (\widetilde{\omega}_0 - \widetilde{\omega}_1)\Big(\lambda_0 a_0 a_1^\dagger + \lambda_0^* a_0^\dagger a_1\Big) + (\widetilde{\omega}_2 - \widetilde{\omega}_1)\Big(\lambda_2 a_2 a_1^\dagger + \lambda_2^* a_2^\dagger a_1\Big) \\ &\quad - i\Gamma\Big(\lambda_0 e^{i\theta} a_1^\dagger a_2 + \lambda_0^* e^{-i\theta} a_1 a_2^\dagger\Big) - i\Gamma\Big(\lambda_2 e^{-i\theta} a_0 a_1^\dagger + \lambda_2^* e^{i\theta} a_1 a_0^\dagger\Big) \\ &= \big(g_0 + \lambda_0(\widetilde{\omega}_0 - \widetilde{\omega}_1) - i\Gamma\lambda_2 e^{-i\theta}\big) a_0 a_1^\dagger + \big(g_0 + \lambda_0^*(\widetilde{\omega}_0 - \widetilde{\omega}_1) - i\Gamma\lambda_2^* e^{i\theta}\big) a_0^\dagger a_1 \\ &\quad + \big(g_1 + \lambda_2(\widetilde{\omega}_2 - \widetilde{\omega}_1) - i\Gamma\lambda_0 e^{i\theta}\big) a_2 a_1^\dagger + \big(g_1 + \lambda_2^*(\widetilde{\omega}_2 - \widetilde{\omega}_1) - i\Gamma\lambda_0^* e^{-i\theta}\big) a_2 a_1^\dagger \qquad \text{(B6)} \end{aligned}$$

which does not have a solution. We see that the culprit is the $i\Gamma$ term, which once removed allows to go on with the calculation.

C.7) Effective Hamiltonian for the ultrastrong magnon-photon Zeeman coupling

Statement of Authorship

Title of Paper	Effective Hamiltonian for the ultrastrong magnon-photon Zeeman coupling
Publication Status	☐ Published ☐ Accepted for Publication ☐ Submitted for Publication ☑ Unpublished and Unsubmitted w ork w ritten in manuscript style
Publication Details	

Principal Author

Name of Principal Author (Candidate)	Alan Gardin		
Contribution to the Paper	Analysed experimental data and performed theoretical calculations. Proposed and investigated several ideas and wrote the manuscript.		
Overall percentage (%)	70		
Certification:	This paper reports on original research I conducted during the period of my Higher Degree by Research candidature and is not subject to any obligations or contractual agreements with a thir strain its inclusion in this thesis. I am the primary author of this paper.		
Signature		Date	22/01/2024

Co-Author Contributions

By signing the Statement of Authorship, each author certifies that:

i. the candidate's stated contribution to the publication is accurate (as detailed above);

ii. permission is granted for the candidate in include the publication in the thesis; and

iii. the sum of all co-author contributions is equal to 100% less the candidate's stated contribution.

Name of Co-Author	Guillaume Bourcin		
Contribution to the Paper	Carried out experiment, performed theoretical and numerical calculations.		
Signature		Date	03/12/2024

Name of Co-Author	Christian Person		
Contribution to the Paper	Read and provided comments on the manuscript.		
Signature		Date	18/03/2024

Name of Co-Author	Christophe Fumeaux		
Contribution to the Paper	Read and provided comments on the manuscript.		
Signature		Date	13/03/2024

Name of Co-Author	Giuseppe Tettamanzi		
Contribution to the Paper	Read and provided comments on the manuscript.		
Signature		Date	18-03-2024

Name of Co-Author	Vincent Castel		
Contribution to the Paper	Carried out experiments and numerical calculations using COMSOL. Read and provided comments on the manuscript.		
Signature		Date	12/03/2024

Effective Hamiltonian for the ultrastrong magnon-photon Zeeman coupling

Alan Gardin,[1,*] Guillaume Bourcin,[1,2] Christian Person,[1,2] Christophe Fumeaux,[1,2] Giuseppe C. Tettamanzi,[1,2] and Vincent Castel

[1] *School of Physics, The University of Adelaide, Adelaide SA 5005, Australia*
[2] *School of Chemical Engineering and Advanced Materials, The University of Adelaide, Adelaide SA 5005, Australia*

Several experiments in the ultrastrong coupling of a magnon and a photon have shown a frequency shift in the magnon's resonance frequency. In this work, we investigate the possible reasons for such a shift. We find that a diamagnetic term for the magnon gives the appropriate scaling of the frequency shift that has been observed in experiments.

I. INTRODUCTION

In the last decade several experiments have reached the magnon-photon ultrastrong coupling regime [1–9]. It is known that in the ultrastrong coupling regime, the rotating wave approximation fails [10, 11] and the diamagnetic term cannot be neglected, at it drastically changes the physics [12]. However, [9] showed (using a combination of experimental data and finite element modelling numerical solvers) that the standard model used in cavity magnonics did not successfully reproduce the trends of the polaritonic frequencies. Thus, an appropriate Hamiltonian model for ultrastrong magnon-photon coupling remains elusive. In this work, we review possible first steps towards this goal. We find that the presence of a diamagnetic term for the magnon is the most promising explanation.

II. MAGNON-PHOTON MODEL AND ITS APPROXIMATIONS

In this section, we review the main steps in the derivation of the usual magnon-photon interaction [13, 14], while paying special attention to all the approximations.

a. Quantised electromagnetic field with a relative permeability The first approximation concerns the expression for the quantised electromagnetic field. Indeed, the expressions used in [13, 14] use expressions valid when the relative permeability μ_r is a scalar equal to unity [15]. However, in the presence of a weak time-dependent magnetic field, one can linearise the Landau-Lifshitz-Gilbert equation and we obtain an anistropic relative permeability [16, 17]. Instead, one should quantise the electromagnetic field in the presence of the magnon degrees of freedom, accounted for by an anisotropic permeability. We note that the quantisation of the electromagnetic in dispersive and lossy media has been tackled before in the literature, see [18, 19]. In the following, we assume that the expressions used for the quantised electromagnetic field are valid.

b. Heisenberg exchange Hamiltonian The starting point for the derivation of the magnon Hamiltonian is the Heisenberg exchange Hamiltonian

$$H = -\frac{1}{2} J \sum_{\langle i,j \rangle} \mathbf{S}_i \cdot \mathbf{S}_j. \tag{1}$$

with J the exchange energy, $\mathbf{S}_i$ spin operators at lattice site i, and $\langle i, j \rangle$ restricts the sum to nearest neighbours. This Hamiltonian thus models nearest-neighbour spin-spin interactions, which can be justified by Coulomb interactions of electric charges [16].

Then, one usually considers a static applied magnetic field $\mathbf{H}_0 = H_0 \hat{\mathbf{z}}$, which induces a Zeeman coupling term

$$-\frac{g \mu_B B_0}{\hbar} \sum_i^N S_i^z. \tag{2}$$

where g_L is the Langé g-factor and μ_B is the Bohr magneton. Note that since $B = \nabla \times \mathbf{A}$, a change of gauge $\mathbf{A} \mapsto \mathbf{A} + \nabla \chi$ leaves the static magnetic field invariant.

c. Holstein-Primakoff transformations Assuming that the Heisenberg exchange Hamiltonian is valid, an approximation used to diagonalise it the Holstein-Primakoff (HP) transformation. The HP transformation is used to obtain a bosonic description of the magnonic modes, which is valid provided the number of magnon excitation is weak compared to the total number of spins [16]. For Yttrium-Iron-Garnet used in all the experiments above, this approximation is valid even at room temperature [20]. Thus, after considering collective excitations by going into recriprocal space, the magnon Hamiltonian is found to be [16]

$$H_m = \sum_{\mathbf{k}} \hbar \omega_{\mathbf{k}} m_{\mathbf{k}}^\dagger m_{\mathbf{k}}, \tag{3}$$

where $\mathbf{k}$ are the wave vectors.

d. Long wavelength approximation The next step in the derivation is the long wavelength approximation, which corresponds to $ak \ll 1$, with a the lattice constant and k the norm of $\mathbf{k}$. The energies $\hbar \omega_{\mathbf{k}}$ increase with k, therefore it is legitimate to only keep the lowest order terms in eq. (3).

* alan.gardin@adelaide.edu.au

e. Higher magnetostatic mode with $\mathbf{k} \neq 0$ Nevertheless, the long wavelength approximation does not tell us when should the sum in eq. (3) be truncated. The Kittel mode $\mathbf{k} = 0$ corresponds to a uniform precession of the spins, and is excited by an homogeneous time-dependent magnetic field. Higher-order modes correspond to non-inhomogeneous excitation of the spins. Therefore, if the the cavity mode is uniform over the sample, one can simply keep the Kittel mode $\mathbf{k} = 0$ in eq. (3). If this is not the case, we should observe higher-frequency anti-crossings if the higher-order modes $\mathbf{k} \neq 0$ couple with the cavity mode.

Assuming a single cavity mode and a single magnon mode, the Hamiltonian is [13]

$$H = \hbar\omega_c c^\dagger c + \hbar\omega_m m^\dagger m + \hbar g\big(c + c^\dagger\big)\big(m + m^\dagger\big) \qquad (4)$$

where $g/2\pi$ is the coupling strength, c (m) is the cavity (magnon) annihilation operator, and we have neglected the coupling phases for simplicity [14]. This Hamiltonian corresponds to the Dicke model, and including a diamagnetic term $D(c + c^\dagger)^2$, we obtain the Hopfield model

$$H = \hbar\omega_c c^\dagger c + \hbar\omega_m m^\dagger m + \hbar g\big(c + c^\dagger\big)\big(m + m^\dagger\big) + D(c + c^\dagger)^2. \qquad (5)$$

The diamagnetic term originates for the vector potential A, which when quantised leads to $A^2 \propto (c + c^\dagger)^2$.

f. Dipole approximation The dipole approximation is commonly made in the derivation of light/matter interaction models, for instance for the Jaynes-Cummings model in cavity quantum electrodynamics (QED). In the dipole approximation, the size of the matter sample should be smaller than the typical wavelengths $\lambda = \frac{c}{f}$. For frequencies between 1 Ghz and 20 GHz, the corresponding wavelengths are between 300 mm to 15 mm. Thus, as long as we consider YIG samples of size smaller than these values, the dipole approximation should hold, and we note that the experiment of [9] was close to this limit. However, the dipole approximation is not used in the derivation of the magnon-photon interaction Hamiltonian. Indeed, contrary to an electric dipole interaction (where the typical distances are atomic), the spatial dependence of the magnetic field is taken into account by the filling factor η which intervenes in the expression of the coupling strength [13, 21].

g. Finite element simulation method COMSOL Multiphysics®is a finite-element modelling (FEM) software that has been used successfully to model various cavity magnonics system, see for instance [9, 21–24]. In this approach, the first step is to find the response of an equilibrium magnetisation to small RF magnetic fields. This response is given by the Polder susceptibility tensor χ, and can be obtained by linearising the Landau-Lifschitz-Gilbert equation [16]. From χ, we find the expression of the magnetic permeability of YIG and insert this variable into COMSOL Multiphysics®. The FEM software can then compute the electromagnetic field in the cavity in the presence of the magnetic sample. Critically, the response of the magnetic sample is dependent on the static applied magnetic field $\mathbf{H}_0$ used to tune the ferromagnetic resonance frequency of the Kittel magnon mode. We note that COMSOL Multiphysics® works directly with the electric and magnetic fields, not the vector and scalar potentials, and therefore this method is gauge-invariant.

III. ATTEMPTS AT EXPLAINING THE MAGNON FREQUENCY SHIFT

In [9], the authors demonstrated an ultrastrong coupling between magnon and photons by using an optimised two-post re-entrant cavity. They placed a YIG slab in the cavity, and modelled the system using COMSOL Multiphysics®. They obtained remarkable agreement between their experiments and the simulations.

An important result of [9] is the observed scaling of the magnon resonance frequency $\omega_m/2\pi$ with g^2/ω_c. Indeed, the authors first attempted to fit their experiments and simulations using the Dicke and Hopfield models, where the diamagnetic term was left as a fit constant. What they found is that neither the Dicke not the Hopfield models could fit, but using the Dicke model with a shift of the magnon resonance frequency $\omega_m/2\pi$, they obtained good agreement. Thanks to their simulations, they managed to prove that the frequency shift scaled as g^2/ω_c.

Note that in [9], the relative permeability entered neglected both exchange and anisotropy fields. Therefore, since the simulation results matched with experimental data, it is unlikely that the frequency shift can be explained due to these effects. More generally, the fact that a FEM software accurately reproduced the experimental trends tells us that the origin of the frequency shift can, in principle, be explained solely based on coupling the Landau-Lifschitz-Gilbert equation and Maxwell's equations.

In this section, we examine several possibilities that can explain such a frequency shift.

A. Diamagnetic term

a. Presence of a photonic diamagnetic term In the ultrastrong coupling regime, the diamagnetic term can have important consequences. For instance, it allows or blocks the phase transition of the Dicke model [10, 11], and is responsible for light-matter decoupling far in the ultrastrong coupling regime [12]. The diamagnetic term is expected to be non-negligible for strong electromagnetic fields, which is not the situation in cavity magnonics experiments. Indeed, the cavity's RF field, originating from the vector network analyser used in the experiment of [9], is usually weak (typically a power of a few dBm). Furthermore, the FEM modelling based on linearising the Landau-Lifschitz-Gilbert equation also assumed a weak

cavity magnetic field, and thus it is a valid approximation.

Usually, the prefactor D of the diamagnetic term can be estimated by the Thomas-Reiche-Kuhn sum rule, which gives $D = g^2/\omega_m$. Clearly, this is inapplicable for cavity magnonics, since for small values of the static magnetic fields, i.e vanishing $\omega_m/2\pi$, the diamagnetic term $D = g^2/\omega_m$ diverges. Thus, the presence of a photonic diamagnetic term is unlikely. While a diamagnetic term naturally appears in the derivation of light-matter models based on electronic degrees of freedom, this is not the case for magnons.

b. Magnonic diamagnetic term In the presence of multiple matter modes it is possible that a diamagnetic term appears for the matter degrees of freedom [25, 26]. In this context, it was shown in different physical systems that a shift of the matter frequency that scales as g^2 [25, 26]. In cavity magnonics, this could be due to the presence of higher magnon modes with $\mathbf{k} \neq 0$. Therefore, in the following we assume the presence of a diamagnetic term for the magnons, and investigate its effect on the spectrum.

The spectrum of the usual Hopfield model

$$H = \hbar\omega_c c^\dagger c + \hbar\omega_m m^\dagger m + \hbar g\left(c + c^\dagger\right)\left(m + m^\dagger\right) + D\left(c + c^\dagger\right)^2 \tag{6}$$

is [5]:

$$\omega_\pm^2 = \frac{\omega_c^2 + \omega_m^2 + 4\omega_c D}{2} \pm \frac{1}{2}\sqrt{\left(\omega_c^2 - \omega_m^2 + 4\omega_c D\right)^2 + 16\omega_c\omega_m g^2} \tag{7}$$

If there is a diamagnetic term on the matter degree of freedom only, the Hamiltonian is

$$H = \hbar\omega_c c^\dagger c + \hbar\omega_m m^\dagger m + \hbar g\left(c + c^\dagger\right)\left(m + m^\dagger\right) + d(m + m^\dagger)^2. \tag{8}$$

By analogy with the spectrum of the Hopfield Hamiltonian given in eq. (7), we have

$$\omega_\pm^2 = \frac{\omega_c^2 + \omega_m^2 + 4\omega_m D}{2} \pm \frac{1}{2}\sqrt{\left(\omega_m^2 - \omega_c^2 + 4\omega_m D\right)^2 + 16\omega_c\omega_m g^2} \tag{9}$$

In the case where the diamagnetic term is on the cavity mode, the Thomas-Reiche-Kuhn rule gives $D = g^2/\omega_m$. By analogy, let us assume that $D = \frac{g^2}{\omega_c}$ instead. We obtain

$$\omega_\pm^2 = \frac{\omega_c^2 + \omega_m^2 + \omega_m\frac{4g^2}{\omega_c}}{2} \pm \frac{1}{2}\sqrt{\left(\omega_m^2 + 4\omega_m\frac{g^2}{\omega_c} - \omega_c^2\right)^2 + 16\omega_c\omega_m g^2} \tag{10}$$

Then, by defining $\Omega_m^2 = \omega_m^2 + \omega_m\frac{4g^2}{\omega_c}$, we find

$$\omega_\pm^2 = \frac{\omega_c^2 + \Omega_m^2}{2} \pm \frac{1}{2}\sqrt{\left(\Omega_m^2 - \omega_c^2\right)^2 + 16\omega_c\omega_m g^2}. \tag{11}$$

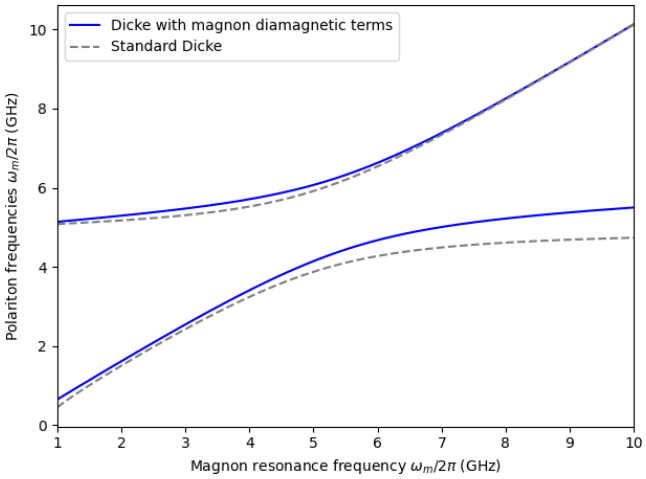


FIG. 1. Comparison of the polaritonic frequencies of the standard Dicke model (dashed lines) with the case where a mangon diamagnetic term is included (solid lines). I9n this figure, $\omega_c/2\pi = 5$ GHz and $g/\omega_c = 0.2$.

We can rewrite the term $16\omega_c\omega_m g^2$ as

$$16\omega_c\omega_m g^2 = 16\omega_c\omega_m\sqrt{1 + \frac{1}{\omega_m}\frac{4g^2}{\omega_c}}\frac{g^2}{\sqrt{1 + \frac{1}{\omega_m}\frac{4g^2}{\omega_c}}} \tag{12}$$

$$= 16\omega_c\Omega_m\frac{g^2}{\sqrt{1 + \frac{1}{\omega_m}\frac{4g^2}{\omega_c}}} = 16\omega_c\Omega_m G^2 \tag{13}$$

with a renormalised coupling strength $G^2 = \frac{g^2}{\sqrt{1+\frac{1}{\omega_m}\frac{4g^2}{\omega_c}}}$. In particular, for $g^2/\omega_c \ll 1$, we can expand the square root of $\Omega_m = \omega_m\sqrt{1 + \frac{1}{\omega_m}\frac{4g^2}{\omega_c}}$ to find to first order

$$\Omega_m \simeq \omega_m\left(1 + \frac{1}{2}\frac{1}{\omega_m}\frac{4g^2}{\omega_c}\right) = \omega_m + \frac{2g^2}{\omega_c} \tag{14}$$

which mirrors the scaling $\frac{g^2}{\omega_c}$ observed in [9]. This leads to a small albeit noticeable shift of the polaritonic frequencies, as illustrated in fig. 1. However, a first-principle justification of such a diamagnetic term remains an open question.

c. Particle in a potential The presence of a diamagnetic term in cavity magnonics remains an open question. The standard way one gets a diamagnetic term A^2 where A is the vector potential, is by performing a minimal coupling replacement $p \mapsto p + qA$ on the Hamiltonian

$$H_{\text{particle}} = \frac{p^2}{2m} + V(q), \tag{15}$$

describing a particle of mass m, momentum p, in a potential V depending on the particle's position q. Note that p and q satisfy the canonical commutation relations $[q, p] = i\hbar$.

In YIG for instance, the spins do come from electrons, i.e. charged particles, so that a Hamiltonian description at the particle level should exist, but it is unclear how to properly do this. Instead, we note that the Hamiltonian for the magnons could be expressed in terms of its quadrature operators, akin to the position and momentum of a particle. The idea we propose is to attempt to rewrite the magnon/photon coupling Hamiltonian as that of an effective particle in a potential. We hope that this alternative description would enlightens the effective minimal-coupling mechanism associated to magnons, bypassing the fundamental entities at the origin of these quasiparticles.

We define the magnon's quadratures x and p as

$$x = \frac{m + m^\dagger}{\sqrt{2}}, \quad p = \frac{m^\dagger - m}{i\sqrt{2}}. \tag{16}$$

We note that

$$\begin{aligned} x^2 + p^2 &= \frac{1}{2}\Big(m^2 + {m^\dagger}^2 + mm^\dagger + m^\dagger m\Big) && (17)\\ &\quad - \frac{1}{2}\Big(m^2 + {m^\dagger}^2 - mm^\dagger - m^\dagger m\Big) \\ &= m^\dagger m + \big(1 + m^\dagger m\big) = 2m^\dagger m + 1, && (18) \end{aligned}$$

where we used $\big[m, m^\dagger\big] = 1$. The Hamiltonian for magnon/photon coupling can then be written

$$\begin{aligned} H &= \hbar\omega_c c^\dagger c + \hbar\omega_m m^\dagger m + \hbar g(c + c^\dagger)\big(m + m^\dagger\big) && (19)\\ &= \hbar\omega_c c^\dagger c + \hbar\frac{\omega_m}{2}\big(p^2 + x^2\big) + \hbar g\sqrt{2}(c + c^\dagger)x && (20)\\ &= \hbar\omega_c c^\dagger c + \frac{p^2}{2m} + V(x) + \hbar\frac{g\sqrt{2}}{A_0}xA, && (21) \end{aligned}$$

where we defined $m = (\hbar\omega_m)^{-1}$, $V(x) = \frac{1}{2}\hbar\omega_m x^2$ the potential, and $A = A_0(c + c^\dagger)$ the vector potential with A_0 its amplitude. If we compare with the minimal coupling replacement,

$$\frac{(p + qA)^2}{2m} = \frac{p^2}{2m} + \frac{q}{m}pA + \frac{q^2}{2m}A^2, \tag{22}$$

we see that a very different mechanism is at play here. In the minimal coupling replacement, the momentum of the particle is coupled to A, whereas for our magnon, the position is coupled to A.

B. Gauge invariance

In the USC regime, it was shown that gauge invariance can become an issue [10, 11]. More specifically, it should be possible to perform a gauge transformation on light-matter models to obtain equivalent physical predictions. However, it was shown, notably In the Dicke model, that a breakdown of gauge invariance occurs due to the two-level system approximation made for the matter degrees of freedom. Since in cavity magnonics we are concerned with spins, which are true two-level systems, we expect we will not suffer from gauge-invariance problems for cavity magnonics.

Still, keeping track of the gauge dependence in the derivation leading up to the Dicke model is a good sanity check. In principle, the quantisation of the electromagnetic field is performed in the Coulomb gauge, so that the Dicke model is only valid in the Coulomb gauge. For the matter degrees of freedom, we note that all the steps leading up to eq. (3) seem gauge-invariant, because they are due to a Zeeman coupling which involves the magnetic field $\mathbf{B}$, a gauge-independent observables. Similarly, the coupling of the magnons to the cavity mode is due to a Zeeman coupling, but this time the expression used for the magnetic field is only valid in the Couloumb gauge. To summarise, the free magnon Hamiltonian should be gauge-independent, while the free photon and magnon-photon interaction Hamiltonians are only valid in the Coulomb gauge.

C. Classical modelling

The fact that a FEM software successfully reproduced the data of [9] suggests that a fully electromagnetic field approach could allow to explain the origin of the magnon frequency shift. Indeed, it is possible derive scattering parameters using a classical approach based on coupling the LLG equation with Maxwell's equations [23, 27–30]. Hence, we could expect that this method would capture the observed FMR shift.

However, in [28–30], the authors consider magnetic spheres in spherical cavities. The spherical symmetry allows to express the magnetisation and the microwave fields in spherical harmonics, which can then be used to derive the scattering parameter. Such an expansion is not adapted to the setup of Bourcin *et al.* (2022) [31]. Thus, such a perturbation theory is unlikely to be valid.

As for [23], they rely consider the magnetic sample only weakly perturbs the electromagnetic eigenmodes of COMSOL Multiphysics®cavity. However, an eigenmode analysis using COMSOL shows that the cavity without the YIG slab, and with the YIG slab, significantly affect the resulting eigenmodes [32].

D. Coupling to other cavity modes

If one considers the full data of [9], we can observe the presence of other couplings, that manifest as additional anti-crossings. This suggest the presence of couplings at higher frequency. Could the coupling of the Kittel mode to another cavity mode induce the observed shift of the Kittel mode's resonance frequency?

We tested this hypothesis numerically, by considering

the Hamiltonian

$$H = \hbar\omega_c c^\dagger c + \hbar\omega_m m^\dagger m + \hbar g\big(c + c^\dagger\big)\big(m + m^\dagger\big) + \sum_n \hbar\omega_n c_n^\dagger c_n + \hbar g_n (c_n m^\dagger + h.c), \tag{23}$$

where the c_n are additional cavity modes with frequency ω_n and couplings g_n to the magnon. One can rapidly understand that couplings to higher frequency modes push the spectral lines lower in frequency, due the additional anti-crossings. Similarly, coupling to lower cavity modes push the anti-crossing of interest downward.

Since we observed a positive shift of ω_m, only coupling to lower frequency cavity modes could produce this shift. Numerical experiments showed that such lower cavity modes coupling should happen far in the deep strong coupling regime. However, in the cavity design proposed in [9] no such lower frequency cavity modes exists. Hence, we concluded that coupling other cavity modes could not account for the observed shift.

E. Magnetisation self-energy

We consider the Hamiltonian of the electromagnetic energy,

$$H = \int \mathrm{d}^3 r \left(\frac{1}{2}\epsilon_0^2 \mathbf{E}^2 + \frac{1}{2}\frac{\mathbf{B}^2}{\mu_0}\right) = \int \mathrm{d}^3 r\, \mathcal{H}, \tag{24}$$

where $\mathcal{H}$ is the Hamiltonian density. Writing $\mathbf{B} = \mu_0\mathbf{H} + \mathbf{M}$,

$$\mathcal{H} = \frac{1}{2}\epsilon_0^2\mathbf{E}^2 + \frac{1}{2}\mu_0\mathbf{H}^2 + \frac{1}{2\mu_0}(\mu_0\mathbf{H}\cdot\mathbf{M} + \mu_0\mathbf{M}\cdot\mathbf{H}) + \frac{1}{2}\frac{\mathbf{M}^2}{\mu_0} \tag{25}$$

$$= \frac{1}{2}\epsilon_0^2\mathbf{E}^2 + \frac{1}{2}\mu_0\mathbf{H}^2 + \mu_0\mathbf{H}\cdot\mathbf{M} + \frac{1}{2}\frac{\mathbf{M}^2}{\mu_0}, \tag{26}$$

where for the last line we used the fact that $\mathbf{H}$ and $\mathbf{M}$ commute [33]. Often, one neglects the magnetisation self-energy term, proportional to $\mathbf{M}^2$. This last term leads to a Kerr interaction term. Indeed, using $\mathbf{M} = \frac{\gamma}{V_m}\mathbf{S}$,

$$\frac{1}{2}\frac{\mathbf{M}^2}{\mu_0} = \frac{\gamma^2}{2\mu_0 V_m^2}\mathbf{S}^2 = \frac{\gamma^2}{2\mu_0 V_m^2}\big(S_x^2 + S_y^2 + S_z^2\big) \tag{27}$$

$$= \frac{\gamma^2}{2\mu_0 V_m^2}\left(\frac{1}{4}\big[S^+ + S^-\big]\big[S^+ + S^-\big] + \frac{1}{(2i)^2}\big[S^+ - S^-\big]\big[S^+ - S^-\big] + S_z^2\right) \tag{28}$$

$$= \frac{\gamma^2}{2\mu_0 V_m^2}\left(\frac{\hbar^2 2S}{4}\big[m + m^\dagger\big]\big[m + m^\dagger\big] - \frac{\hbar^2 2S}{4}\big[m - m^\dagger\big]\big[m - m^\dagger\big] + \hbar^2\big[S - m^\dagger m\big]\big[S - m^\dagger m\big]\right) \tag{29}$$

$$= \frac{\hbar^2\gamma^2}{2\mu_0 V_m^2}\left(\frac{S}{2}\big[m^\dagger m + m m^\dagger\big] - \frac{S}{2}\big[-m^\dagger m - m m^\dagger\big] + \Big[-2S m^\dagger m + \big(m^\dagger m\big)^2\Big]\right) \tag{30}$$

$$= \frac{\hbar^2\gamma^2}{2\mu_0 V_m^2}\big(m^\dagger m\big)^2. \tag{31}$$

Hence, we can rewrite the Hamiltonian density as

$$\mathcal{H} = \frac{1}{2}\epsilon_0^2\mathbf{E}^2 + \frac{1}{2}\mu_0\mathbf{H}^2 + \mu_0\mathbf{H}\cdot\mathbf{M} + \frac{1}{2}\frac{\mathbf{M}^2}{\mu_0} \tag{32}$$

$$= \hbar\omega_c c^\dagger c + \hbar(c + c^\dagger)\big(gm + g^* m^\dagger\big) + \hbar K\big(m^\dagger m\big)^2, \tag{33}$$

where $K = \frac{\hbar\gamma^2}{2\mu_0 V_m^2}$. For the slab dimensions used in [9], $V_m = 1.42 \times 10^{-8}$ m^3, and we find $K = 6.4$ GHz.

F. Manipulating the counter-rotating terms with parametric driving

For the quantum Rabi model, it was shown that [34, 35] allows to manipulate the coupling strengths to reach the ultrastrong coupling regime. Alternatively, [36] considered the effect of a parametric driving of a cavity mode, and its effect on the photon-magnon interaction. In all of these works, the parametric drive leads to additional nonlinear terms which could potentially be made to interfere with the magnon-photon coupling counter-rotating terms. Therefore, it may be possible by appropriately choosing the parameters of the parametric drive to enhance either the co-rotating or counter-rotating terms. For instance, in a regime where the co-rotating terms can be neglected, while the counter-rotating terms remain, we would obtain an interaction of the form

$$H_{\mathrm{int}} = -\hbar g(cm + c^\dagger m^\dagger), \tag{34}$$

similar to that obtain in cavity optomechanics in the blue-detuned regime [37]. Notably, the spectrum displays level attraction [37]. The presence of a diamagnetic term would affect this spectral signature, and thus it can be used as a test to verify the appropriate magnon-photon Hamiltonian.

In the same spirit, it would be interesting to see if, using the counterdiabatic formalism, one can remove some of the terms in the interaction Hamiltonian (see [38]). Then, we could propose another test to figure out what is the proper model of USC cavity magnonics

IV. CONCLUSION AND OUTLOOK

a. Magnonic diamagnetic term The presence of a diamagnetic term seems promising to explain the frequency shift. As shown in [25, 26], a diamagnetic term on the matter degrees of freedom can arise due to the presence of multiple magnon modes. This could indeed be the case in the system studied by [9], since higher-order modes do not correspond to an homogeneous excitation of the magnon modes. Notably, the length of the YIG sample questions the dipole approximation, and thus it may be possible that the magnetic field felt by the sample is non-uniform, hence exciting higher order modes. Furthermore, the Landau-Lifschitz-Gilbert equation is valid for arbitrary magnon modes. Thus, the relative permeability entered in the FEM software does include higher-order magnon modes.

To clarify this, one possibility is the examination of the transmission spectrum of [9] for signatures of higher-order magnon modes. Furthermore, these modes could be computed numerically, in particular their frequency, which would help recognising their experimental signature. If these modes are well characterised, the next step is to go back to the magnon Hamiltonian and see how there higher order modes could bring about a diamagnetic term.

b. Further investigations on gauge-invariance The two-level approximation for the matter degrees of freedom was shown to break gauge-invariance. Thus, we can legitimately wonder whether truncating the sum in the magnon Hamiltonian (see eq. (3)) to only the Kittel mode could affect gauge-invariance. One possible way to check this would be to perform a gauge-transformation on the Dicke model, and examine whether the physical predictions (notably the spectrum), are identical. However, the other gauge used in the literature is the *dipole gauge*, which originates from the electric dipole moments of atomic degrees of freedom. Thus, such a gauge seems meaningless for magnons. A potential solution consists of finding an analogous gauge transformation for the magnetic dipole interaction (the Zeeman coupling).

c. Generalised minimal-coupling replacement applied to the Dirac equation We need to see if there is an additional term that appear due to the generalised minimal coupling replacement in the Dirac equation. This is required to make sure that the Zeeman coupling due to spin is unaffected.

d. Other possible routes In [9], the cavity mode frequency was taken as a shift parameter, because the macroscopic YIG slab significantly affected the resonance frequencies of the cavity modes. Therefore, it would be interesting to perform an eigenmode analysis on the cavity design of [9] by using the magnetic susceptibility of the YIG. Indeed, observing the evolution of the cavity modes depending on the applied static magnetic field would provide valuable information.

Furthermore, in this work we have ignored the long-range magneto-dipolar interaction and the Dzyaloshinskii-Moriya interaction [39]. Additionally, it may be possible for the higher-order Walker modes to be degenerate with the Kittel mode [40].

Finally, we note that the presence of spins is due to the presence of electrons, but their orbital degrees of freedom do not appear in the Heisenberg exchange Hamiltonian. Notably, the diamagnetic term appears in the Dicke and Hopfield model due to the presence of the electrons, which are always left out by solely using the Heisenberg exchange Hamiltonian. Instead, we could take the opposite first-principles approach (e.g. starting from the Pauli equation or the Hubbard model), and determine how the electronic degrees of freedom lead to a Heisenberg Hamiltonian, or at least an effective description of ferrimagnets. This approach would allow to understand how the electronic degrees of freedom, which we recall are at the origin of the Heisenberg exchange Hamiltonian, become irrelevant for the physics of magnons. Moreover, this would allow to keep track of the gauge-dependence as the vector potential would naturally appear due to the consideration of electronic degrees of freedom. A possible direction towards that route is the microscopic theory of magnetic susceptibility in insualtors proposed by [41], or a gauge-invariant formulation of cavity quantum electrodynamics in the presence of arbitrary electric and magnetic moments [42].

ACKNOWLEDGMENTS

We acknowledge financial support from Thales Australia and Thales Research and Technology. The scientific colour map *oslo* [43] is used in this study to prevent visual distortion of the data and exclusion of readers with colourvision deficiencies [44].

[1] M. Goryachev, W. G. Farr, D. L. Creedon, Y. Fan, M. Kostylev, and M. E. Tobar, High-cooperativity cavity qed with magnons at microwave frequencies, Phys. Rev. Applied **2**, 054002 (2014).

[2] X. Zhang, C.-L. Zou, L. Jiang, and H. X. Tang, Strongly coupled magnons and cavity microwave photons, Physical Review Letters **113**, 156401 (2014).

[3] J. Bourhill, N. Kostylev, M. Goryachev, D. L. Creedon, and M. E. Tobar, Ultrahigh cooperativity interactions between magnons and resonant photons in a YIG sphere,

Physical Review B **93**, 144420 (2016).
[4] N. Kostylev, M. Goryachev, and M. E. Tobar, Superstrong coupling of a microwave cavity to yttrium iron garnet magnons, Applied Physics Letters **108**, 062402 (2016).
[5] I. Golovchanskiy, N. Abramov, V. Stolyarov, A. Golubov, M. Y. Kupriyanov, V. Ryazanov, and A. Ustinov, Approaching deep-strong on-chip photon-to-magnon coupling, Phys. Rev. Applied **16**, 034029 (2021).
[6] I. A. Golovchanskiy, N. N. Abramov, V. S. Stolyarov, M. Weides, V. V. Ryazanov, A. A. Golubov, A. V. Ustinov, and M. Y. Kupriyanov, Ultrastrong photon-to-magnon coupling in multilayered heterostructures involving superconducting coherence via ferromagnetic layers, Science Advances **7**, 10.1126/sciadv.abe8638 (2021).
[7] M. Silaev, Ultrastrong magnon-photon coupling, squeezed vacuum, and entanglement in superconductor/ferromagnet nanostructures, Physical Review B **107**, L180503 (2023), arXiv:2211.00462 [cond-mat.mes-hall].
[8] A. Ghirri, C. Bonizzoni, M. Maksutoglu, A. Mercurio, O. Di Stefano, S. Savasta, and M. Affronte, Ultrastrong magnon-photon coupling achieved by magnetic films in contact with superconducting resonators, Physical Review Applied **20**, 024039 (2023), arXiv:2302.00804 [cond-mat.mes-hall].
[9] G. Bourcin, J. Bourhill, V. Vlaminck, and V. Castel, Strong to ultrastrong coherent coupling measurements in a YIG/cavity system at room temperature, Physical Review B **107**, 214423 (2023).
[10] P. Forn-Díaz, L. Lamata, E. Rico, J. Kono, and E. Solano, Ultrastrong coupling regimes of light-matter interaction, Reviews of Modern Physics **91**, 025005 (2019).
[11] A. Frisk Kockum, A. Miranowicz, S. De Liberato, S. Savasta, and F. Nori, Ultrastrong coupling between light and matter, Nature Reviews Physics **1**, 19–40 (2019).
[12] S. De Liberato, Light-matter decoupling in the deep strong coupling regime: The breakdown of the purcell effect, Phys. Rev. Lett. **112**, 016401 (2014).
[13] G. Flower, M. Goryachev, J. Bourhill, and M. E. Tobar, Experimental implementations of cavity-magnon systems: from ultra strong coupling to applications in precision measurement, New Journal of Physics **21**, 095004.
[14] A. Gardin, J. Bourhill, V. Vlaminck, C. Person, C. Fumeaux, V. Castel, and G. C. Tettamanzi, Manifestation of the coupling phase in microwave cavity magnonics, Physical Review Applied **19**, 054069 (2023), arXiv:2212.05389 [quant-ph].
[15] F. Rana, Chapter 5: Quantization of radiation in cavities and free space (2017).
[16] D. D. Stancil and A. Prabhakar, *Spin Waves* (Springer US, 2009).
[17] M. Harder and C.-M. Hu, Cavity spintronics: An early review of recent progress in the study of magnon–photon level repulsion, Solid State Physics , 47–121 (2018).
[18] B. Huttner and S. M. Barnett, Quantization of the electromagnetic field in dielectrics, Physical Review A **46**, 4306 (1992).
[19] N. Rivera and I. Kaminer, Light–matter interactions with photonic quasiparticles, Nature Reviews Physics **2**, 538 (2020).
[20] I. R. Boventer, *Cavity Magnon-Polariton Spectroscopy*, Ph.D. thesis (2019).
[21] J. Bourhill, V. Castel, A. Manchec, and G. Cochet, Universal characterization of cavity–magnon polariton coupling strength verified in modifiable microwave cavity, Journal of Applied Physics **128**, 073904.
[22] W. Yu, J. Wang, H. Yuan, and J. Xiao, Prediction of attractive level crossing via a dissipative mode, Physical Review Letters **123**, 227201 (2019).
[23] R. Macêdo, R. C. Holland, P. G. Baity, L. J. McLellan, K. L. Livesey, R. L. Stamps, M. P. Weides, and D. A. Bozhko, Electromagnetic approach to cavity spintronics, Physical Review Applied **15**, 024065 (2021).
[24] M.-W. Hu, W. Yu, and Y.-P. Wang, Auxiliary mode mediated coherent and complex couplings in a cavity magnonic system, Annalen der Physik **534**, 2100534 (2022).
[25] E. Cortese and S. D. Liberato, Exact solution of polaritonic systems with arbitrary light and matter frequency-dependent losses, The Journal of Chemical Physics **156**, 10.1063/5.0077950 (2022).
[26] S. Hughes, C. Gustin, and F. Nori, Reconciling quantum and classical spectral theories of ultrastrong coupling: Role of cavity bath coupling and gauge corrections 10.48550/ARXIV.2309.15788 (2023), arXiv:2309.15788 [quant-ph].
[27] Y. Cao, P. Yan, H. Huebl, S. T. B. Goennenwein, and G. E. W. Bauer, Exchange magnon-polaritons in microwave cavities, Physical Review B **91**, 094423 (2015).
[28] B. Z. Rameshti, Y. Cao, and G. E. W. Bauer, Magnetic spheres in microwave cavities, Physical Review B **91**, 214430 (2015).
[29] B. Z. Rameshti and G. E. W. Bauer, Indirect coupling of magnons by cavity photons, Physical Review B **97**, 014419 (2018).
[30] T. Neuman, D. S. Wang, and P. Narang, Nanomagnonic cavities for strong spin-magnon coupling and magnon-mediated spin-spin interactions, Physical Review Letters **125**, 247702 (2020).
[31] G. Bourcin, J. Bourhill, V. Vlaminck, and V. Castel, Strong to ultra-strong coherent coupling measurements in a yig/cavity system at room temperature, (2022), arXiv:2209.14643 [quant-ph].
[32] However, it was noticed that the eigenmode analysis did not match the resonances obtained using a full frequency domain simulation. Hence, the eigenmode simulation of COMSOL Multiphysics®may be erroneous.
[33] To convince yourself, simply expand these quantities in terms of creation annihilation operators.
[34] W. Qin, A. Miranowicz, P.-B. Li, X.-Y. Lü, J. You, and F. Nori, Exponentially enhanced light-matter interaction, cooperativities, and steady-state entanglement using parametric amplification, Physical Review Letters **120**, 093601 (2018).
[35] C. Leroux, L. Govia, and A. Clerk, Enhancing cavity quantum electrodynamics via antisqueezing: Synthetic ultrastrong coupling, Physical Review Letters **120**, 093602 (2018).
[36] H. Y. Yuan, S. Zheng, Q. Y. He, J. Xiao, and R. A. Duine, Unconventional magnon excitation by off-resonant microwaves, Physical Review B **103**, 134409 (2021).
[37] N. R. Bernier, L. D. Tóth, A. K. Feofanov, and T. J. Kippenberg, Level attraction in a microwave optomechanical circuit, Physical Review A **98**, 023841 (2018).
[38] R. R. Ancheyta, Vacuum radiation versus shortcuts to adiabaticity, Physical Review A **108**, 022217 (2023).

[39] T. Yu, Z. Luo, and G. E. Bauer, Chirality as generalized spin–orbit interaction in spintronics, Physics Reports **1009**, 1 (2023).
[40] B. Z. Rameshti, S. V. Kusminskiy, J. A. Haigh, K. Usami, D. Lachance-Quirion, Y. Nakamura, C.-M. Hu, H. X. Tang, G. E. Bauer, and Y. M. Blanter, Cavity magnonics (2021), arXiv:2106.09312 [cond-mat.mes-hall].
[41] A. H. Duff, A. Lau, and J. E. Sipe, Microscopic theory of the magnetic susceptibility of insulators 10.48550/ARXIV.2306.03820 (2023), arXiv:2306.03820 [cond-mat.mes-hall].
[42] D. M. Rouse, B. W. Lovett, E. M. Gauger, and N. Westerberg, Avoiding gauge ambiguities in cavity quantum electrodynamics, Scientific Reports **11**, 10.1038/s41598-021-83214-z (2021).
[43] F. Crameri, Scientific colour maps (2021).
[44] F. Crameri, G. E. Shephard, and P. J. Heron, The misuse of colour in science communication, Nature Communications **11**, 10.1038/s41467-020-19160-7 (2020).

C.8) Cavity-mediated ultrastrong magnon-magnon coupling

Statement of Authorship

Title of Paper	Cavity-mediated ultrastrong magnon-magnon coupling
Publication Status	☐ Published ☐ Accepted for Publication ☐ Submitted for Publication ☑ Unpublished and Unsubmitted w ork w ritten in manuscript style
Publication Details	

Principal Author

Name of Principal Author (Candidate)	Alan Gardin		
Contribution to the Paper	Proposed the original cavity design and wrote the manuscript.		
Overall percentage (%)	70		
Certification:	This paper reports on original research I conducted during the period of my Higher Degree by Research candidature and is not subject to any obligations or contractual agreements with a third party that would constrain its inclusion in this thesis. I am the primary author of this paper.		
Signature		Date	22/01/2024

Co-Author Contributions

By signing the Statement of Authorship, each author certifies that:

i. the candidate's stated contribution to the publication is accurate (as detailed above);

ii. permission is granted for the candidate in include the publication in the thesis; and

iii. the sum of all co-author contributions is equal to 100% less the candidate's stated contribution.

Name of Co-Author	Guillaume Bourcin		
Contribution to the Paper	Read and provided comments on the manuscript.		
Signature		Date	03/12/2024

Name of Co-Author	Christian Person		
Contribution to the Paper	Read and provided comments on the manuscript.		
Signature		Date	18/03/2024

Name of Co-Author	Christophe Fumeaux		
Contribution to the Paper	Read and provided comments on the manuscript.		
Signature		Date	13/03/2024

Name of Co-Author	Giuseppe Tettamanzi		
Contribution to the Paper	Read and provided comments on the manuscript.		
Signature		Date	18-03-2024

Name of Co-Author	Vincent Castel		
Contribution to the Paper	Read and provided comments on the manuscript.		
Signature		Date	12/03/2024

Cavity-mediated ultrastrong magnon/magnon coupling

Alan Gardin,[1, 2, 3, *] Guillaume Bourcin,[2, 3] and Vincent Castel[2, 3]

[1] *School of Physics, The University of Adelaide, Adelaide SA 5005, Australia*
[2] *IMT Atlantique, Technopole Brest-Iroise, CS 83818, 29238 Brest Cedex 3, France*
[3] *Lab-STICC (UMR 6285), CNRS, Technopole Brest-Iroise, CS 83818, 29238 Brest Cedex 3, France*

In cavity magnonics, coherent coupling has been extensively studied, from the ultrastrong coupling regime to the cavity-mediated coupling. However, the combination of the ultrastrong coupling regime and cavity-mediated coupling has not been explored, neither theoretically nor experimentally. In this paper, we propose a platform to ultrastrongly couple the Kittel modes of two distant Yttrium-Iron-Garnet slabs to two common cavity modes. The two cavity modes mediate an indirect coupling between the two magnon modes, which is shown to also reach the ultrastrong coupling regime. Furthermore, the resulting system is loop-coupled, so that the coupling phases influence the physics. We study the resulting synthetic gauge field, and comment on the impact of the ultrastrong coupling regime.

I. INTRODUCTION

Coherent coupling describes the continuous exchange of quanta of energy between two systems, at the so-called vacuum Rabi frequency. In the case of the coupling of a bosonic mode with a two-level system, the Hamiltonian is the well-known Jaynes-Cummings model. This model is actually the result of applying the rotating wave approximation to the Rabi model, which neglects the counter-rotating terms. These terms are non-resonant for $g/\omega < 0.1$ with $g/2\pi$ the coupling strength and $\omega/2\pi$ the light or matter frequency. However, in the ultrastrong coupling regime [1] which starts for $0.1 < g/\omega$, the terms affect the physics and thus the rotating wave approximation cannot be used.

The field of cavity magnonics has attracted interest thanks to its potential for information transductions. Cavity-mediated coupling of magnons have been extensively studied. On the other hand, the coherent ultrastrong coupling regime has been reached in cavity magnonics user planar superconducting structures, and three-dimensional cavities, even at room temperature [2]. However, there has been no theoretical studies, nor experiments, of the effect of the ultrastrong coupling on the cavity-mediated coupling. We aim to bridge this gap in this work.

We consider an architecture in which two magnons are ultrastrongly coupled with the same cavity mode, and we study the resulting physics, using a second-quantisation formalism. To support our analysis, we propose a 3-post re-entrant cavity design, similar to that used in [2] to ultrastrongly couple a YIG slab with a cavity mode.

II. THEORETICAL MODELLING

We consider two cavity eigenmodes of frequencies $\omega_1/2\pi$ and $\omega_2/2\pi$, described by annihilation operators c_1 and c_2. The two magnons are also represented by two bosonic annihilation operators m_1 and m_2 (with frequency $\omega_m/2\pi$ tuned by a static applied magnetic field $\mathbf{H}_0 = H_0\hat{\mathbf{z}}$) after performing the Holstein-Primakoff transformation [3, 4]. Hence, without interactions, the Hamiltonian reads

$$H_{\text{free}} = \sum_{k=1}^{2} \hbar\omega_k c_k^\dagger c_k + \hbar\omega_m m_k^\dagger m_k. \tag{1}$$

The coupling between the cavity mode k and the magnon mode l, due to the Zeeman interaction, is characterised by a coupling strength $g_{kl}/2\pi$ and a coupling phase φ_{kl} defined as [4, 5]

$$g_{kl}/2\pi = \eta_{kl}\sqrt{\omega_k}\frac{\gamma}{4\pi}\sqrt{\frac{\mu}{g_L\mu_B}\hbar\mu_0 n_s}, \tag{2}$$

$$\varphi_{kl} = \arg\left\{\int_{V_m} \mathrm{d}^3r\, \mathbf{h}_k(\mathbf{r})\cdot\hat{\mathbf{x}} + i\int_{V_m} \mathrm{d}^3r\, \mathbf{h}_k(\mathbf{r})\cdot\hat{\mathbf{x}}\right\}, \tag{3}$$

where $\gamma/2\pi = 28$ GHz/T is the gyromagnetic ratio, $\mu = 5\mu_B$ is the magnetic moment of YIG, μ_B is the Bohr magneton, μ_0 is the magnetic permeability of vacuum, $g_L = 2$ is the Landé g-factor, $n_s = 4.22\times10^{23}$ m^{-3} is the spin density of YIG, $\mathbf{h}_k$ is the magnetic field of the cavity mode $k \in \{1, 2\}$, V_m is the volume of the YIG spheres, and

$$\eta_{kl} = \sqrt{\frac{\left(\int_{V_m} \mathrm{d}^3r\, \mathbf{h}_k(\mathbf{r})\cdot\hat{\mathbf{x}}\right)^2 + \left(\int_{V_m} \mathrm{d}^3r\, \mathbf{h}_k(\mathbf{r})\cdot\hat{\mathbf{y}}\right)^2}{V_m\int_{V_c} \mathrm{d}^3r\, |\mathbf{h}_k(\mathbf{r})|^2}} \tag{4}$$

is the filling-factor, with V_c the volume of the cavity. The resulting interaction Hamiltonian is

$$H_I = \sum_{k,l=1}^{2} \hbar g_{kl}\left(c_k + c_k^\dagger\right)e^{-i\varphi_{kl}}m_l + \text{h.c}, \tag{5}$$

where h.c corresponds to the hermitian conjugate terms.

* alan.gardin@adelaide.edu.au

To simplify the discussion, from now on we set $g_1 = g_{11} = g_{12}$ and $g_2 = g_{21} = g_{22}$. Additionally, we consider an equivalent system, by successively applying the unitary transformations

$$U_k = \exp\left\{i\varphi_{1k} m_k^\dagger m_k\right\}, \quad k \in \{1,2\}, \tag{6}$$

which takes $m_k \mapsto e^{i\varphi_{1k}} m_k$. The interaction Hamiltonian transforms to

$$\begin{aligned} H_I = {} & \hbar g_1 (c_1 + c_1^\dagger)(m_1 + m_2) \\ & + \hbar g_2 (c_2 + c_2^\dagger)\left(e^{-i\varphi_1} m_1 + e^{-i\varphi_2} m_2\right) + \text{h.c}, \end{aligned} \tag{7}$$

where $\varphi_k = \varphi_{k2} - \varphi_{k1}$. We now introduce the operator

$$M_\theta = \frac{e^{-i\varphi_1} m_1 + e^{-i\varphi_2} m_2}{\sqrt{2}} = e^{-i\varphi_1} \frac{m_1 + e^{-i\theta} m_2}{\sqrt{2}} \tag{8}$$

where $\theta = \varphi_2 - \varphi_1$. We observe that

$$M_\theta + M_{\theta+\pi} = \sqrt{2} e^{-i\varphi_1} m_1 \tag{9}$$

$$M_\theta - M_{\theta+\pi} = \sqrt{2} e^{-i\varphi_1} e^{-i\theta} m_2, \tag{10}$$

and hence

$$\frac{m_1 + m_2}{\sqrt{2}} = e^{i\varphi_1}(M_\theta + M_{\theta+\pi}) + e^{i\varphi_1} e^{i\theta}(M_\theta - M_{\theta+\pi}) \tag{11}$$

$$= e^{i\varphi_1}\left(\left[1 + e^{i\theta}\right] M_\theta + \left[1 - e^{i\theta}\right] M_{\theta+\pi}\right). \tag{12}$$

We have

$$1 + e^{i\theta} = e^{i\frac{\theta}{2}}\left[e^{i\frac{\theta}{2}} + e^{-i\frac{\theta}{2}}\right] \tag{13}$$

$$= 2e^{i\frac{\theta}{2}} \cos\left(\frac{\theta}{2}\right), \tag{14}$$

$$1 - e^{i\theta} = -2ie^{i\frac{\theta}{2}} \sin\left(\frac{\theta}{2}\right). \tag{15}$$

We can then rewrite the interaction Hamiltonian of eq. (7) as

$$\begin{aligned} H_I/\hbar = {} & 2e^{i\frac{\varphi_1+\theta}{2}} \widetilde{g}_1 \cos\left(\frac{\theta}{2}\right)\left(c_1 + c_1^\dagger\right) M_\theta \\ & - 2ie^{i\frac{\varphi_1+\theta}{2}} \widetilde{g}_1 \sin\left(\frac{\theta}{2}\right)\left(c_1 + c_1^\dagger\right) M_{\theta+\pi} \\ & + \widetilde{g}_2\left(c_2 + c_2^\dagger\right) M_\theta + \text{h.c}, \end{aligned} \tag{16}$$

where $\widetilde{g}_k = \sqrt{2} g_k$.

Note $\{M_\theta, M_{\theta+\pi}\}$ is a good basis, since we have $\left[M_\theta, M_\theta^\dagger\right] = \left[M_{\theta+\pi}, M_{\theta+\pi}^\dagger\right] = 1$ and $\left[M_\theta, M_{\theta+\pi}^\dagger\right] = 0$. Moreover, we have

$$M_\theta^\dagger M_\theta = \frac{1}{2}\sum_{k=1}^{2} m_k^\dagger m_k + \frac{1}{2}\left(e^{i\theta} m_1 m_2^\dagger + \text{h.c}\right), \tag{17}$$

$$M_{\theta+\pi}^\dagger M_{\theta+\pi} = \frac{1}{2}\sum_{k=1}^{2} m_k^\dagger m_k - \frac{1}{2}\left(e^{i\theta} m_1 m_2^\dagger + \text{h.c}\right), \tag{18}$$

so that $\sum_{k=1}^{2} \hbar\omega_m m_k^\dagger m_k = \hbar\omega_m\left(M_\theta^\dagger M_\theta + M_{\theta+\pi}^\dagger M_{\theta+\pi}\right)$ and eq. (1) can be rewritten in terms of the $\{M_\theta, M_{\theta+\pi}\}$ basis.

A. Spectrum

Similar to [5], we now examine the spectrum. We see that the basis $\{M_\theta, M_{\theta+\pi}\}$ is solely characterised by $\theta = \varphi_2 - \varphi_1$. However, the interaction Hamiltonian depends on both φ_1 and θ, so a priori the physics depends on both quantities. Still, numerical investigation shows that the spectrum depends only on θ. If it is indeed the case, then, there should be a unitary transformation which removes φ_1 from the interaction Hamiltonian. *This is an unresolved question.* In the following, I set $\varphi_1 = 0$.

B. Cavity-mediated coupling

We study the system when $\omega_m = \omega_c = \frac{\omega_1+\omega_2}{2}$. The goal is to perform perturbation theory using Schrieffer-Wolff transformations. The difference with [5] is that they considered teh system under the rotating wave approximation, which we do not make here.

III. EXPERIMENTAL PROPOSAL

We propose a three-post re-etrant cavity based on [2], but with three equally spaced posts instead of two (see fig. 1). As a results, we obtain two cavity eigenmodes with frequencies $\omega_1/2\pi = 8$GHz and $\omega_2/2\pi = 8.8$ GHz, where the magnetic field is focused between the posts, as shown in fig. 2. Two YIG slabs are placed between the posts. Note that the frequency gap δ_c between the two cavity eigenmodes can be increased by increasing the radius of the cavity.

The numerical calculation of the coupling strengths and phases using the eigenmode analysis of COMSOL Multiphysics® is shown in table I. In light of the results, we can safely assume $g_1/2\pi = g_{11}/2\pi = g_{12}/2\pi = 1.895$

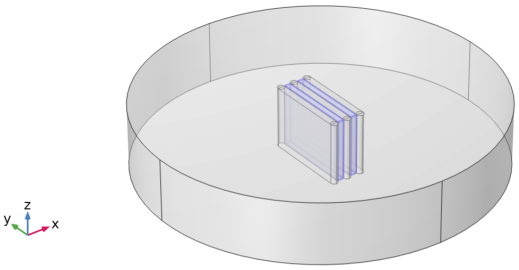


FIG. 1. Design of the three-posts re-entrant cavity, with the rectangular YIG slabs (in blue) placed between the posts.

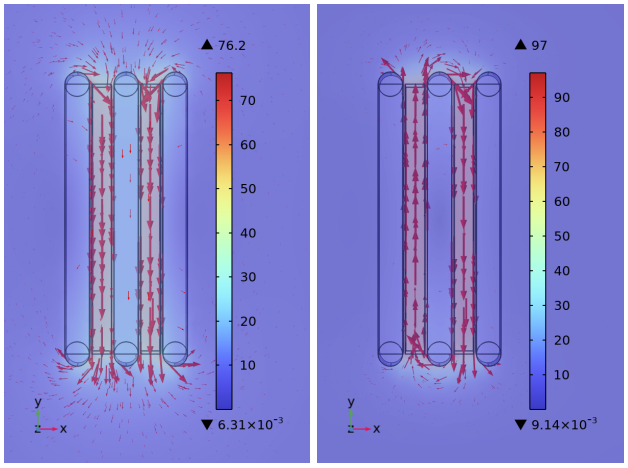


FIG. 2. Magnetic field distribution of the three cavity eigenmodes of interest. For each cavity mode, the magnetic field is focused between the posts, where the YIG slabs are placed.

TABLE I. Numerical calculation of the coupling strengths g_{kl} and coupling phases φ_{kl} using COMSOL Multiphysics®.

Coupling strength (GHz)		Phase (radians)	
$g_{11}/2\pi$	1.898	φ_{10}	$-\frac{\pi}{2}$
$g_{12}/2\pi$	1.889	φ_{11}	$-\frac{\pi}{2}$
$g_{21}/2\pi$	2.094	φ_{21}	$+\frac{\pi}{2}$
$g_{22}/2\pi$	2.101	φ_{21}	$-\frac{\pi}{2}$

GHz and $g_2/2\pi = g_{21}/2\pi = g_{22}/2\pi = 2095$ GHz, which gives $g_1/\omega_1 = 23.9\%$ and $g_2/\omega_2 = 23.7\%$. As a consequence, we are in the ultrastrong coupling regime for both cavity eigenmodes.

Now we apply the results obtained in section II B to evaluate the indirect magnon-magnon coupling mediated by the two cavity modes.

IV. CONCLUSION

ACKNOWLEDGMENTS

We acknowledge financial support from Thales Australia and Thales Research and Technology. The scientific colour map *oslo* [6] is used in this study to prevent visual distortion of the data and exclusion of readers with colourvision deficiencies [7].

[1] A. Frisk Kockum, A. Miranowicz, S. De Liberato, S. Savasta, and F. Nori, Ultrastrong coupling between light and matter, Nature Reviews Physics **1**, 19–40 (2019).
[2] G. Bourcin, J. Bourhill, V. Vlaminck, and V. Castel, Strong to ultra-strong coherent coupling measurements in a yig/cavity system at room temperature, (2022), arXiv:2209.14643 [quant-ph].
[3] T. Holstein and H. Primakoff, Field dependence of the intrinsic domain magnetization of a ferromagnet, Phys. Rev. **58**, 1098 (1940).
[4] G. Flower, M. Goryachev, J. Bourhill, and M. E. Tobar, Experimental implementations of cavity-magnon systems: from ultra strong coupling to applications in precision measurement, New Journal of Physics **21**, 095004.
[5] A. Gardin, J. Bourhill, V. Vlaminck, C. Person, C. Fumeaux, V. Castel, and G. C. Tettamanzi, Manifestation of the coupling phase in microwave cavity magnonics, Physical Review Applied **19**, 054069 (2023), arXiv:2212.05389 [quant-ph].
[6] F. Crameri, Scientific colour maps (2021).
[7] F. Crameri, G. E. Shephard, and P. J. Heron, The misuse of colour in science communication, Nature Communications **11**, 10.1038/s41467-020-19160-7 (2020).

C.9) Study of the optomechanical coupling between a cavity photon and a magnon

Statement of Authorship

Title of Paper	Study of the optomechanical coupling between a cavity photon and a magnon
Publication Status	☐ Published ☐ Accepted for Publication ☐ Submitted for Publication ☑ Unpublished and Unsubmitted w ork w ritten in manuscript style
Publication Details	

Principal Author

Name of Principal Author (Candidate)	Alan Gardin
Contribution to the Paper	Identification of the relevance of the work, writing of the manuscript, carried out theoretical and numerical calculations.
Overall percentage (%)	80
Certification:	This paper reports on original research I conducted during the period of my Higher Degree by Research candidature and is not subject to any obligations or contractual agreements with a third party that would constrain its inclusion in this thesis. I am the primary author of this paper.
Signature	Date 29/01/2024

Co-Author Contributions

By signing the Statement of Authorship, each author certifies that:

i. the candidate's stated contribution to the publication is accurate (as detailed above);

ii. permission is granted for the candidate in include the publication in the thesis; and

iii. the sum of all co-author contributions is equal to 100% less the candidate's stated contribution.

Name of Co-Author	Vincent Castel
Contribution to the Paper	Read the manuscript and provided comments, helped understand how to optimise the cavity design.
Signature	Date 18/03/2024

Name of Co-Author	Christian Person
Contribution to the Paper	Read the manuscript and provided comments
Signature	Date 18/03/2024

Name of Co-Author	Christophe Fumeaux		
Contribution to the Paper	Read the manuscript and provided comments		
Signature		Date	13/03/2024

Name of Co-Author	Giuseppe Tettamanzi		
Contribution to the Paper	Read the manuscript and provided comments		
Signature		Date	18-03-2024

Study of the optomechanical coupling between a cavity photon and a magnon

Alan Gardin,[1,2,*] Vincent Castel,[2] Christian Person,[2] Christophe Fumeaux,[3] and Giuseppe C. Tettamanzi[4]

[1] *School of Physics, The University of Adelaide, Adelaide SA 5005, Australia*
[2] *IMT Atlantique, Lab-STICC, UMR CNRS 6285, F-29238 Brest, France*
[3] *School of Electrical Engineering and Computer Science, The University of Queensland, Brisbane QLD 4072, Australia*
[4] *School of Chemical Engineering and Advanced Materials, The University of Adelaide, Adelaide SA 5005, Australia*

In cavity magnonics, light confined to a cavity interacts with magnons, the quanta of spin waves, through a Zeeman coupling. A static magnetic field is usually applied to tune the magnon resonance frequency, which enables strong coupling between magnons and cavity photons on resonance. There exists a coupling between magnons and cavity photons in the direction parallel to the static magnetic field. The resulting interaction takes the form of an interaction reminiscent of cavity optomechanics. In this work, we evaluate the strength of this interaction, and whether it can be used to create entanglement.

a. Introduction Cavity magnonics aims at studying the interaction between photons confined to a cavity, and magnons, the quanta of spin-wave excitation in magnetically ordered materials [1–3]. At microwave frequencies, these two quasi-particles interact through the magnetic dipole interaction, i.e. the Zeeman coupling. Over the last decade, this coherent coupling has reach the strong and ultrastrong coupling regime [4–13], with applications in quantum information transduction between light and magnetic excitations.

In recent years, there has been growing interest in the creation of non-classical states of photons and magnons for quantum information processing [14]. An important resource is the presence of a non-linearity in the system, which is usually the source of non-classical correlations between the different subsystems. Magnonics possesses many such intrinsic non-linearities [15], but so far the non-linear self-Kerr [16–20], magnetostrictive [21–27], and optical interactions [28–32] have been the most used. An alternative to intrinsic non-linearities are extrinsic ones, for instance coupling to a superconducting qubit [33–37], or driving the system with either a parametric or squeezed vacuum drive [38–44].

Among the different non-linear interactions, the magnetostrictive interaction between magnons and phonons [45] is especially interesting because of its resemblance with cavity optomechanics [46, 47]. Similar to cavity optomechanics, the phonon has a frequency $\omega_p/2\pi \simeq 10$ MHz which is much lower than that of the magnon mode, and the coupling strength is typically small, between 0.1 and 0.3 Hz [21–23, 45]. However, a strong drive allows to overcome this, linearise the equation of motion, and create entanglement in the steady state [21–27].

Formally, an interaction similar to the magnetostrictive interaction exists between cavity photons and magnons, as a result of the Zeeman coupling between them. This non-linear interaction arise when the cavity photons couple to the magnons in the same direction as the static magnetic applied used to tune the magnon resonance frequency. This coupling is expected to be very small, due to it not being dependent on the spin number [48]. Nevertheless, the examples of cavity optomechanics and the magnetostrictive interaction show that it may still be possible to leverage this non-linear interaction to create entanglement [49]. In this work, we carry out such an analysis.

b. Zeeman photon-magnon coupling The interaction between a cavity mode and the Kittel mode, corresponding to the lowest-order magnon mode, has been derived in [48]. If the cavity mode of frequency $\omega_c/2\pi$ is described by an annihilation operator c, and the magnon mode of frequency $\omega_m/2\pi$ is described by an annihilation operator m, then the magnon-photon Hamilotnian reads

$$\begin{aligned} H = {} & \hbar\omega_c c^\dagger c + \hbar\omega_m m^\dagger m + \hbar g\big(c + c^\dagger\big)m^\dagger m \\ & + \hbar g_{x,y}(c + c^\dagger)(m + m^\dagger), \end{aligned} \tag{1}$$

where $g_{x,y}$ is the coherent coupling due to the $\hat{\mathbf{x}}$ and $\hat{\mathbf{y}}$ components of the cavity mode and $g/2\pi$ is the coupling to the $\hat{\mathbf{z}}$ component of the cavity mode, provided the static magnetic field $H_0\hat{\mathbf{z}}$ is applied along $\hat{\mathbf{z}}$. In the last interaction term, the coupling strength $g_{x,y}/2\pi$ is complex-valued and scales as $\sqrt{S}$, with $S \gg 1$ the total spin. On the other hand, $g/2\pi$ does not have such a scaling, and is therefore much smaller. In the rest of this work, we drop the last term in the Hamiltonian to focus on the optomechanical-like interaction given by the third term.

The coupling strength for the remaining non-linear interaction is given by [48, 50]

$$g = \frac{\gamma}{V_m}\sqrt{\frac{\hbar\omega_c}{2}\mu_0}\frac{\int_{V_m}\mathbf{h}_c\cdot\hat{\mathbf{z}}\,\mathrm{d}^3r}{\int_{V_c}|\mathbf{h}_c|^2\,\mathrm{d}^3r}, \tag{2}$$

where $\mathbf{h}_c$ is the magnetic field of the cavity mode, γ the gyromagnetic ratio, ϵ_0 the electric permittivity of vacuum, μ_0 the magnetic permeability of vacuum, V_m the volume of the magnetic sample, and V_c the volume of the cavity.

* alan.gardin@adelaide.edu.au

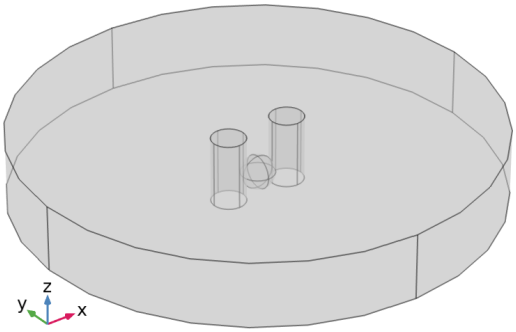


FIG. 1. Two-post re-entrant cavity based on [4, 50], with the YIG sphere placed between the two posts. The radius is 14mm, with a height of 4 mm. The posts and the YIG sphere have a radius of 1mm.

c. Cavity design To evaluate the coupling strength $g/2\pi$, we consider a two-post re-entrant cavity [4] which has been extensively studied using COMSOL Multiphysics® for cavity magnonics applications [50]. The cavity we consider is pictured in fig. 1, where a YIG sphere is placed between the two posts. We use COMSOL Multiphysics® to numerically evaluate eq. (2), and we find $g/2\pi = 35$ Hz. Note that the cavity geometry was optimised to maximise this value. Notably, the corresponding value of $g_{x,y}/2\pi$ by taking advantage of the spin density gives $g_{x,y}/\omega_c = 0.18$, putting this cavity design in the ultrastrong coupling regime.

The relatively high value of the coupling strength was obtained using a YIG sample of macroscopic dimensions. This allows us to neglect the self-Kerr interaction due to anisotropy, which scales inversely to the volume of the sphere [51].

d. Calculation of the bipartite entanglement The system Hamtiltonian is

$$H = \hbar\omega_c c^\dagger c + \hbar\omega_m m^\dagger m + \hbar g\big(c + c^\dagger\big)m^\dagger m, \tag{3}$$

and we additionally consider a coherent drive of the magnon mode, through a loop antenna. Following the standard method of cavity optomechanics [46, 47], we consider the quantum fluctuations of the cavity and magnon modes around their steady-state values $\langle c\rangle, \langle m\rangle$. The quantum fluctuations are described by the annihilation operators $\delta c, \delta m$, from which we can define their quadratures

$$x = \frac{\delta c + \delta c^\dagger}{\sqrt{2}}, \quad y = i\frac{\delta c^\dagger - \delta c}{\sqrt{2}} \tag{4}$$

$$X = \frac{\delta m + \delta m^\dagger}{\sqrt{2}}, \quad Y = i\frac{\delta m^\dagger - \delta m}{\sqrt{2}}. \tag{5}$$

The quantum Langevin equations for the fluctuations can be put in matrix form (see supplemental material) as $\dot{u}(t) = Au(t) + n(t)$, where A is the drift matrix, $u = (\delta x, \delta y, \delta X, \delta Y)^t$ is the column vector of quadratures, $n = \big(\sqrt{2\kappa_c}x_{\rm in}, \sqrt{2\kappa_c}y_{\rm in}, \sqrt{2\kappa_m}X_{\rm in}, \sqrt{2\kappa_m}Y_{\rm in}\big)$ the column vector of input noise operators, where $\kappa_c/2\pi$ ($\kappa_m/2\pi$) dissipation rate of the cavity (magnon) mode, and $x_{\rm in}, y^{\rm in}$ ($X_{\rm in}, Y^{\rm in}$) the quadratures of the input noise operator $c^{\rm in}$ ($m^{\rm in}$). The input noise operators account for thermal fluctuations with correlation functions

$$\left\langle c_{\rm in}^\dagger(t)c_{\rm in}(t')\right\rangle = N(\omega_c)\delta(t-t'), \tag{6}$$

$$\left\langle c_{\rm in}(t)c_{\rm in}(t')^\dagger\right\rangle = (N(\omega_c)+1)\delta(t-t'), \tag{7}$$

and similarly for $m^{\rm in}$, where

$$N(\omega) = \frac{1}{e^{\frac{\hbar\omega}{k_b T}} - 1} \tag{8}$$

is the Bose-Einstein distribution, T the temperature, and $k_B = 86.17\times10^{-3}$ meV/K the Boltzmann constant. The correlation functions allow us to find the expression of the diffusion matrix

$$\delta(t-t')D_{ij} = \frac{1}{2}\left\langle n_i(t)n_j(t') + n_j(t')n_i(t)\right\rangle. \tag{9}$$

Using the drift matrix A and the diffusion matrix D, we can solve the Lyapunov equation

$$AV + VA^t = -D, \tag{10}$$

to obtain the steady-state covariance matrix $V(t) = (\frac{1}{2}\langle u_i(t)u_j(t') + u_j(t')u_i(t)\rangle)_{1\leqslant i,j\leqslant 2}$. Finally, the logarithmic negativity [52] is used to compute the bipartite entanglement between the magnon and the photon.

e. Results We set $\kappa_c/2\pi = \kappa_m/2\pi = 1$ MHz, which are typical values of cavity magnonical setups. We further assume that the cavity resonance frequency is $\omega_c/2\pi = 10$ GHz, while that of the magnon is $\omega_m/2\pi = \omega_c/2\pi$. We also assume that the coupling of the magnon

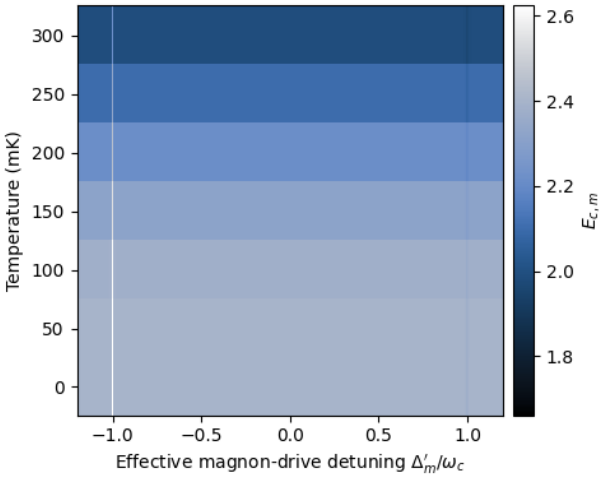


FIG. 2. Magnon-photon entanglement as a function of the detuning between the magnon frequency $\omega_m/2\pi$ and the drive frequency, and temperature.

of the drive is $\kappa_d/2\pi = 10$ MHz. We assume that the drive power is adjusted to lead to an effective magnon-photon coupling strength $G/2\pi = 3$ MHz. The resulting magnon-photon entanglement is plotted in fig. 2.

The magnitude of the generated entanglement is much higher than that observed in other schemes, and is non-vanishing even away from the red-detuned and blue-detuned sidebands $\Delta'_m = \pm\omega_c$. Usually, only the red-detuned sideband $\Delta'_m = -\omega_c$ leads to entanglement [21, 49]. Moreover, the entanglement is quite robust against temperature.

f. Conclusion The preliminary results seem too promising to be correct: the entanglement is much better than in other schemes, and much more robust against temperature. This suggests an error in either the theoretical or numerical calculations.

Furthermore, we have neglected the magnetostrictive interaction, which leads to a magnon-phonon interaction due to the precessing magnetisation of the Kittel mode. While this effect is usually weak, it increases in the presence of a strong drive of the magnon mode. Therefore, the magnon-photon interaction is expected to compete with the magnetostrictive interaction, an effect which have not explored in this work.

[1] M. Harder and C.-M. Hu, Cavity spintronics: An early review of recent progress in the study of magnon–photon level repulsion, Solid State Physics , 47–121 (2018).

[2] M. Harder, B. M. Yao, Y. S. Gui, and C.-M. Hu, Coherent and dissipative cavity magnonics, Journal of Applied Physics **129**, 201101 (2021).

[3] B. Z. Rameshti, S. V. Kusminskiy, J. A. Haigh, K. Usami, D. Lachance-Quirion, Y. Nakamura, C.-M. Hu, H. X. Tang, G. E. Bauer, and Y. M. Blanter, Cavity magnonics (2021), arXiv:2106.09312 [cond-mat.mes-hall].

[4] M. Goryachev, W. G. Farr, D. L. Creedon, Y. Fan, M. Kostylev, and M. E. Tobar, High-cooperativity cavity qed with magnons at microwave frequencies, Phys. Rev. Applied **2**, 054002 (2014).

[5] X. Zhang, C.-L. Zou, L. Jiang, and H. X. Tang, Strongly coupled magnons and cavity microwave photons, Physical Review Letters **113**, 156401 (2014).

[6] J. Bourhill, N. Kostylev, M. Goryachev, D. L. Creedon, and M. E. Tobar, Ultrahigh cooperativity interactions between magnons and resonant photons in a YIG sphere, Physical Review B **93**, 144420 (2016).

[7] N. Kostylev, M. Goryachev, and M. E. Tobar, Superstrong coupling of a microwave cavity to yttrium iron garnet magnons, Applied Physics Letters **108**, 062402 (2016).

[8] J. R. Everts, G. G. G. King, N. J. Lambert, S. Kocsis, S. Rogge, and J. J. Longell, Ultrastrong coupling between a microwave resonator and antiferromagnetic resonances of rare-earth ion spins, Physical Review B **101**, 214414 (2020).

[9] I. Golovchanskiy, N. Abramov, V. Stolyarov, A. Golubov, M. Y. Kupriyanov, V. Ryazanov, and A. Ustinov, Approaching deep-strong on-chip photon-to-magnon coupling, Phys. Rev. Applied **16**, 034029 (2021).

[10] I. A. Golovchanskiy, N. N. Abramov, V. S. Stolyarov, M. Weides, V. V. Ryazanov, A. A. Golubov, A. V. Ustinov, and M. Y. Kupriyanov, Ultrastrong photon-to-magnon coupling in multilayered heterostructures involving superconducting coherence via ferromagnetic layers, Science Advances **7**, 10.1126/sciadv.abe8638 (2021).

[11] A. Ghirri, C. Bonizzoni, M. Maksutoglu, A. Mercurio, O. Di Stefano, S. Savasta, and M. Affronte, Ultrastrong magnon-photon coupling achieved by magnetic films in contact with superconducting resonators, Physical Review Applied **20**, 024039 (2023), arXiv:2302.00804 [cond-mat.mes-hall].

[12] M. Silaev, Ultrastrong magnon-photon coupling, squeezed vacuum, and entanglement in superconductor/ferromagnet nanostructures, Physical Review B **107**, L180503 (2023), arXiv:2211.00462 [cond-mat.mes-hall].

[13] G. Bourcin, J. Bourhill, V. Vlaminck, and V. Castel, Strong to ultrastrong coherent coupling measurements in a YIG/cavity system at room temperature, Physical Review B **107**, 214423 (2023).

[14] H. Yuan, Y. Cao, A. Kamra, R. A. Duine, and P. Yan, Quantum magnonics: When magnon spintronics meets quantum information science, Physics Reports **965**, 1 (2022).

[15] S. Zheng, Z. Wang, Y. Wang, F. Sun, Q. He, P. Yan, and H. Y. Yuan, Tutorial: Nonlinear magnonics, Journal of Applied Physics **134**, 10.1063/5.0152543 (2023), arXiv:2303.16313 [cond-mat.mes-hall].

[16] Z. Zhang, M. O. Scully, and G. S. Agarwal, Quantum entanglement between two magnon modes via kerr nonlinearity driven far from equilibrium, Physical Review Research **1**, 023021 (2019).

[17] Z. Haghshenasfard and M. G. Cottam, Sub-poissonian statistics and squeezing of magnons due to the kerr effect in a hybrid coupled cavity–magnon system, Journal of Applied Physics **128**, 033901 (2020).

[18] Z.-B. Yang, H. Jin, J.-W. Jin, J.-Y. Liu, H.-Y. Liu, and R.-C. Yang, Bistability of squeezing and entanglement in cavity magnonics, Physical Review Research **3**, 023126 (2021).

[19] X. Jiang, S. Tang, and S. Li, Kerr-nonlinearity-triggered nonclassicality of magnons in a photon-magnon coupling system, Photonics **9**, 681 (2022).

[20] Z.-B. Yang, W.-J. Wu, J. Li, Y.-P. Wang, and J. Q. You, Steady-entangled-state generation via the cross-kerr effect in a ferrimagnetic crystal, Physical Review A **106**, 012419 (2022).

[21] J. Li, S.-Y. Zhu, and G. Agarwal, Magnon-photon-phonon entanglement in cavity magnomechanics, Physical Review Letters **121**, 203601 (2018).

[22] J. Li, S.-Y. Zhu, and G. S. Agarwal, Squeezed states of magnons and phonons in cavity magnomechanics, Physical Review A **99**, 021801 (2019).

[23] J. Li and S.-Y. Zhu, Entangling two magnon modes via magnetostrictive interaction, New Journal of Physics **21**, 085001 (2019).

[24] M. Yu, H. Shen, and J. Li, Magnetostrictively induced stationary entanglement between two microwave fields, Physical Review Letters **124**, 213604 (2020).
[25] H. Tan and J. Li, Einstein-podolsky-rosen entanglement and asymmetric steering between distant macroscopic mechanical and magnonic systems, Physical Review Research **3**, 013192 (2021).
[26] W. Zhang, D.-Y. Wang, C.-H. Bai, T. Wang, S. Zhang, and H.-F. Wang, Generation and transfer of squeezed states in a cavity magnomechanical system by two-tone microwave fields, Optics Express **29**, 11773 (2021).
[27] J. Li, Y.-P. Wang, J.-Q. You, and S.-Y. Zhu, Squeezing microwaves by magnetostriction, National Science Review **10**, 10.1093/nsr/nwac247 (2022), arXiv:2101.02796 [quant-ph].
[28] Q. Cai, J. Liao, and Q. Zhou, Stationary entanglement between light and microwave via ferromagnetic magnons, Annalen der Physik **532**, 2000250 (2020).
[29] J. Li, Y.-P. Wang, W.-J. Wu, S.-Y. Zhu, and J. You, Quantum network with magnonic and mechanical nodes, PRX Quantum **2**, 040344 (2021).
[30] F.-X. Sun, S.-S. Zheng, Y. Xiao, Q. Gong, Q. He, and K. Xia, Remote generation of magnon schrödinger cat state via magnon-photon entanglement, Physical Review Letters **127**, 087203 (2021).
[31] W.-J. Wu, Y.-P. Wang, J.-Z. Wu, J. Li, and J. Q. You, Remote magnon entanglement between two massive ferrimagnetic spheres via cavity optomagnonics, Physical Review A **104**, 023711 (2021).
[32] Y. long Ren, J. kun Xie, X. ke Li, S. li Ma, and F. li Li, Long-range generation of a magnon-magnon entangled state, Physical Review B **105**, 094422 (2022).
[33] Y. Tabuchi, S. Ishino, A. Noguchi, T. Ishikawa, R. Yamazaki, K. Usami, and Y. Nakamura, Coherent coupling between a ferromagnetic magnon and a superconducting qubit, Science **349**, 405 (2015).
[34] Y. Tabuchi, S. Ishino, A. Noguchi, T. Ishikawa, R. Yamazaki, K. Usami, and Y. Nakamura, Quantum magnonics: The magnon meets the superconducting qubit, Comptes Rendus Physique **17**, 729 (2016), quantum microwaves / Micro-ondes quantiques.
[35] D. Lachance-Quirion, Y. Tabuchi, S. Ishino, A. Noguchi, T. Ishikawa, R. Yamazaki, and Y. Nakamura, Resolving quanta of collective spin excitations in a millimeter-sized ferromagnet, Science Advances **3**, 10.1126/sciadv.1603150 (2017).
[36] D. Lachance-Quirion, S. P. Wolski, Y. Tabuchi, S. Kono, K. Usami, and Y. Nakamura, Entanglement-based single-shot detection of a single magnon with a superconducting qubit, Science **367**, 425 (2020).
[37] S. Wolski, D. Lachance-Quirion, Y. Tabuchi, S. Kono, A. Noguchi, K. Usami, and Y. Nakamura, Dissipation-based quantum sensing of magnons with a superconducting qubit, Physical Review Letters **125**, 117701 (2020).
[38] J. M. P. Nair and G. S. Agarwal, Deterministic quantum entanglement between macroscopic ferrite samples, Applied Physics Letters **117**, 084001 (2020).
[39] M. Yu, S.-Y. Zhu, and J. Li, Macroscopic entanglement of two magnon modes via quantum correlated microwave fields, Journal of Physics B: Atomic, Molecular and Optical Physics **53**, 065402 (2020).
[40] J. Li and S. Gröblacher, Entangling the vibrational modes of two massive ferromagnetic spheres using cavity magnomechanics, Quantum Science and Technology **6**, 024005 (2021).
[41] H. Y. Yuan, S. Zheng, Q. Y. He, J. Xiao, and R. A. Duine, Unconventional magnon excitation by off-resonant microwaves, Physical Review B **103**, 134409 (2021).
[42] B. Hussain, S. Qamar, and M. Irfan, Entanglement enhancement in cavity magnomechanics by an optical parametric amplifier, Physical Review A **105**, 063704 (2022).
[43] Y. Zhou, J. Xu, S. Xie, and Y. Yang, Squeezed driving induced entanglement and squeezing among cavity modes and magnon mode in a magnon-cavity qed system, (2022), arXiv:2201.09154 [quant-ph].
[44] W. Zhang, T. Wang, X. Han, S. Zhang, and H.-F. Wang, Quantum entanglement and one-way steering in a cavity magnomechanical system via a squeezed vacuum field, Optics Express **30**, 10969 (2022).
[45] X. Zhang, C.-L. Zou, L. Jiang, and H. X. Tang, Cavity magnomechanics, Science Advances **2**, 10.1126/sciadv.1501286 (2016).
[46] M. Aspelmeyer, T. J. Kippenberg, and F. Marquardt, Cavity optomechanics, Reviews of Modern Physics **86**, 1391 (2014).
[47] S. Barzanjeh, A. Xuereb, S. Gröblacher, M. Paternostro, C. A. Regal, and E. M. Weig, Optomechanics for quantum technologies, Nature Physics **18**, 15 (2021).
[48] G. Flower, M. Goryachev, J. Bourhill, and M. E. Tobar, Experimental implementations of cavity-magnon systems: from ultra strong coupling to applications in precision measurement, New Journal of Physics **21**, 095004 (2019).
[49] D. Vitali, S. Gigan, A. Ferreira, H. R. Böhm, P. Tombesi, A. Guerreiro, V. Vedral, A. Zeilinger, and M. Aspelmeyer, Optomechanical entanglement between a movable mirror and a cavity field, Physical Review Letters **98**, 030405 (2007).
[50] J. Bourhill, V. Castel, A. Manchec, and G. Cochet, Universal characterization of cavity–magnon polariton coupling strength verified in modifiable microwave cavity, Journal of Applied Physics **128**, 073904 (2020).
[51] G. Zhang, Y. Wang, and J. You, Theory of the magnon kerr effect in cavity magnonics, Science China Physics, Mechanics & Astronomy **62**, 10.1007/s11433-018-9344-8 (2019).
[52] G. Vidal and R. F. Werner, Computable measure of entanglement, Physical Review A **65**, 032314 (2002).
[53] Note that the expression is similar to that of [**?**], except for the factor 2 because we used $c + c^\dagger$ instead of the position quadrature, which differ exactly by a factor 2.
[54] Writing $\langle m\rangle = |\langle m\rangle| e^{i\theta}$, we simply need to rotate δm using $U = \exp\left(i\theta\delta m^\dagger \delta m\right)$, which maps $\langle m\rangle^* \delta m + \langle m\rangle \delta m^\dagger = |\langle m\rangle|\left(e^{i\theta} m + e^{-i\theta} m^\dagger\right)$ to $|\langle m\rangle|\left(m + m^\dagger\right)$.

Appendix A: Derivation of the quantum Langevin equations

a. Standard quantum Langevin equations The system Hamiltonian is

$$H = \hbar\omega_c c^\dagger c + \hbar\omega_m m^\dagger m + \hbar g\big(c + c^\dagger\big)m^\dagger m. \tag{A1}$$

The magnon mode is coupled to two bosonic bath, representing intrinsic dissipation and a coherent drive, while the cavity mode is coupled to a unique heat bath. The QLEs read

$$\dot{c} = -i\omega_c c - \kappa_c c - igm^\dagger m + \sqrt{2\kappa_c}c_{\rm in}, \tag{A2}$$

$$\dot{m} = -i\omega_m m - (\kappa_m + \kappa_d)m - ig\big(c + c^\dagger\big)m + \sqrt{2\kappa_d}p_{\rm in} + \sqrt{2\kappa_m}m_{\rm in}, \tag{A3}$$

where $\kappa_c/2\pi$ ($\kappa_m/2\pi$) is the dissipation rate of the cavity (magnon) modes, and $\kappa_d/2\pi$ the coupling of the magnon mode to the drive. We assume $p_{\rm in}$ is a coherent drive such that $\langle p_{\rm in}\rangle = \sqrt{\frac{P}{\hbar\omega_d}}e^{-i\omega_d t}$, where P is the power of the drive.

In the rotating frame of the drive, the QLEs become

$$\dot{c} = -i\omega_c c - \kappa_c c - igm^\dagger m + \sqrt{2\kappa_c}c_{\rm in}, \tag{A4}$$

$$\dot{m} = -i\Delta_m m - (\kappa_m + \kappa_d)m - ig\big(c + c^\dagger\big)m + \Omega + \sqrt{2\kappa_m}m_{\rm in}. \tag{A5}$$

with $\Delta_m = \omega_m - \omega_d$ and $\Omega = \sqrt{2\kappa_d}\sqrt{\frac{P}{\hbar\omega_d}}$.

The input noise operators have the correlations of thermal noise, i.e.

$$\Big\langle c_{\rm in}^\dagger(t)c_{\rm in}(t')\Big\rangle = N(\omega_c)\delta(t-t'), \quad \big\langle c_{\rm in}(t)c_{\rm in}(t')^\dagger\big\rangle = (N(\omega_c)+1)\delta(t-t'), \tag{A6}$$

$$\Big\langle m_{\rm in}^\dagger(t)m_{\rm in}(t')\Big\rangle = N(\omega_m)\delta(t-t'), \quad \big\langle m_{\rm in}(t)m_{\rm in}(t')^\dagger\big\rangle = (N(\omega_m)+1)\delta(t-t'), \tag{A7}$$

with the Bose-Einstein distribution

$$N(\omega) = \frac{1}{e^{\frac{\hbar\omega}{k_b T}} - 1} \tag{A8}$$

where T is the temperature, and $k_B = 86.17 \times 10^{-3}$ meV/K the Boltzmann constant.

b. Linearisation Under a sufficiently strong drive, $m = \langle m\rangle + \delta m$, with $|\langle m\rangle| \gg 1$ the steady-state magnon amplitude and δm the annihilation operator for quantum fluctuations. We also write $c = \langle c\rangle + \delta c$, and we can derive the QLEs for the steady states

$$0 = -i(\omega_c - i\kappa_c)\langle c\rangle - ig|\langle m\rangle|^2, \tag{A9}$$

$$0 = -i(\Delta_m - i(\kappa_m + \kappa_d))\langle m\rangle - 2ig\,\mathrm{Re}\{\langle c\rangle\}\langle m\rangle + \Omega, \tag{A10}$$

and that for the fluctuations

$$\dot{\delta c} = -i\omega_c\delta c - \kappa_c\delta c - ig\big(\langle m\rangle\,\delta m^\dagger + \langle m\rangle^*\,\delta m\big) + \sqrt{2\kappa_c}c_{\rm in}, \tag{A11}$$

$$\dot{\delta m} = -i\Delta_m\delta m - (\kappa_m + \kappa_d)\delta m - 2ig\,\mathrm{Re}\{\langle c\rangle\}\delta m - ig\big(\delta c + \delta c^\dagger\big)\langle m\rangle + \sqrt{2\kappa_m}m_{\rm in}, \tag{A12}$$

where we neglected second-order terms in the fluctuations, i.e. products of fluctuations.

Focusing on the steady-state values, we have $\langle c\rangle = -\frac{g}{\omega_c - i\kappa_c}|\langle m\rangle|^2$ and we deduce

$$(\Delta_m + 2g\,\mathrm{Re}\{\langle c\rangle\} - i(\kappa_m + \kappa_d))\langle m\rangle = \Omega \tag{A13}$$

$$\langle m\rangle = \frac{\Omega}{\Delta'_m - i(\kappa_m + \kappa_d)}, \tag{A14}$$

where $\Delta'_m = \Delta_m + 2g\,\mathrm{Re}\{\langle c\rangle\}$ is the effective detuning[53].

Returning to the QLEs for the fluctuations, we deduce that they result from the effective Hamiltonian

$$H = \hbar\omega_c\delta c^\dagger\delta c + \hbar(\Delta'_m - i(\kappa_m + \kappa_d))\delta m^\dagger\delta m + \hbar g\big(\delta c + \delta c^\dagger\big)\big(\langle m\rangle^*\,\delta m + \langle m\rangle\,\delta m^\dagger\big) \tag{A15}$$

describing the fluctuations. Up to a unitary transformation, we can choose $\langle m\rangle$ to be real [54], and we obtain

$$H = \hbar\omega_c\delta c^\dagger\delta c + \hbar(\Delta'_m - i(\kappa_m + \kappa_d))\delta m^\dagger\delta m + \hbar g|\langle m\rangle|\big(\delta c + \delta c^\dagger\big)\big(\delta m + \delta m^\dagger\big), \tag{A16}$$

where we see that the coupling strength is enhanced by the magnon drive through $\langle m\rangle$. From now on, we define $G = g|\langle m\rangle|$.

c. Equations for the quantum fluctuations We now derive the QLEs for the quadrature fluctuations, defined as $\delta x = \frac{\delta c + \delta c^\dagger}{\sqrt{2}}, \delta y = i\frac{\delta c^\dagger - \delta c}{\sqrt{2}}, \delta X = \frac{\delta m + \delta m^\dagger}{\sqrt{2}}, \delta Y = i\frac{\delta m^\dagger - \delta m}{\sqrt{2}}$. The quadratures for the input noise operators $x_{\rm in}, y_{\rm in}, X_{\rm in}, Y_{\rm in}$ are similarly defined. The QLEs for the creation/annihilation operators of the effective Hamiltonian are

$$\dot{\delta c} = -\kappa_c \delta c - i\omega_c \delta c - iG\big(\delta m + \delta m^\dagger\big) + \sqrt{2\kappa_c} c_{\rm in}, \tag{A17}$$

$$\dot{\delta m} = -(\kappa_m + \kappa_d)\delta m - i\Delta'_m \delta m - iG\big(\delta c + \delta c^\dagger\big) + \sqrt{2\kappa_m} m_{\rm in}, \tag{A18}$$

and by linear combination we obtain

$$\dot{\delta x} = -\kappa_c \delta x + \omega_c \delta y + \sqrt{2\kappa_c} x_{\rm in}, \tag{A19}$$

$$\dot{\delta y} = -\kappa_c \delta y - \omega_c \delta x - 2G\delta X + \sqrt{2\kappa_c} y_{\rm in}, \tag{A20}$$

$$\dot{\delta X} = -(\kappa_m + \kappa_d)\delta X + \Delta'_m \delta Y + \sqrt{2\kappa_m} X_{\rm in}, \tag{A21}$$

$$\dot{\delta Y} = -(\kappa_m + \kappa_d)\delta Y - \Delta'_m \delta X - 2G\delta x + \sqrt{2\kappa_m} Y_{\rm in}. \tag{A22}$$

We can write these QLEs in matrix form as $\dot{u}(t) = Au(t) + n(t)$, where $u = (\delta x, \delta y, \delta X, \delta Y)^t$ is the column vector of quadratures, $n = \big(\sqrt{2\kappa_c} x_{\rm in}, \sqrt{2\kappa_c} y_{\rm in}, \sqrt{2\kappa_m} X_{\rm in}, \sqrt{2\kappa_m} Y_{\rm in}\big)$ the column vector of input noise operators, and

$$A = \begin{pmatrix} -\kappa_c & \omega_c & 0 & 0 \\ -\omega_c & -\kappa_c & -2G & 0 \\ 0 & 0 & -(\kappa_m + \kappa_d) & \Delta'_m \\ -2G & 0 & -\Delta'_m & -(\kappa_m + \kappa_d) \end{pmatrix} \tag{A23}$$

is the drift matrix, similar to [49].

The fluctuations of the cavity and magnon modes constitute a two-mode Gaussian state, characterised by the covariance matrix $V(t) = (\frac{1}{2}\langle u_i(t)u_j(t') + u_j(t')u_i(t)\rangle)_{1\leqslant i,j\leqslant 2}$. In the steady-state, the covariance matrix V can be obtained by solving the Lyapunov equation

$$AV + VA^t = -D, \tag{A24}$$

with the diffusion matrix

$$D = \mathrm{diag}[\kappa_c(2N(\omega_c)+1), \kappa_c(2N(\omega_c)+1), \kappa_m(2N(\omega_m)+1), \kappa_m(2N(\omega_m)+1)]. \tag{A25}$$

The form of the diffusion matrix is deduced from the thermal correlation functions of eqs. (A6) and (A7).

d. Bipartite entanglement From the covariance matrix, which encodes the quantum correlations between the quadratures of the cavity and magnon modes, we can extract a measure of bipartite entanglement using the logarithmic negativity [52] defined as

$$E = \max\big\{0, -\ln\big(2\eta^-\big)\big\} \tag{A26}$$

where η^- is the smallest symplectic eigenvalue of the steady-state covariance matrix V.

e. Steady-state magnon population The effective coupling strength $G/2\pi$ must be sufficient (of the order of MHz [21]) to create entanglement. For instance, imposing $G = g|\langle m\rangle| \simeq 3$ MHz, since $g/2\pi \simeq 30$ Hz, we need $|\langle m\rangle| = 10^5$.

We saw above that

$$\langle m\rangle = \frac{\Omega}{\Delta'_m - i(\kappa_m + \kappa_d)}, \tag{A27}$$

which in the limit of small dissipation and $|\Delta'_m| \simeq \omega_c$, where the latter is expected to obtain entanglement [49], becomes have $|\langle m\rangle| \simeq \frac{\Omega}{\omega_c}$. Hence we need $\Omega \simeq \omega_c|\langle m\rangle| = 10^{14}$ for $\omega_c/2\pi$ in the GHz range.

Following [21], we have $\Omega = \frac{\sqrt{5}}{4}\gamma\sqrt{\rho V}B_0$ with $\gamma/2\pi = 28$ GHz/T the gyromagnetic ratio, $\rho = 4.22 \times 10^{27}$ m^{-3} the spin density of YIG, V the volume of the sphere, and B_0 the amplitude of the magnetic field generated by the loop driving the YIG sphere. Therefore, $B_0 = \frac{4\Omega}{\gamma\sqrt{5\rho V}} \simeq 4.8 \times 10^{-11}$ T for a YIG of radius 1mm.

Finally, still following [21], we find that the drive power is $P = \pi c B_0^2 r^2/2\mu_0 \simeq 0.9$ μW, which is much weaker than the typical values used in cavity magnonics experiments.

C.10) Nonadiabatic quantum control of valley states in silicon

Statement of Authorship

Title of Paper	Nonadiabatic quantum control of valley states in silicon
Publication Status	☑ Published ☐ Accepted for Publication ☐ Submitted for Publication ☐ Unpublished and Unsubmitted work written in manuscript style
Publication Details	Physical Review B , Vol. 105, No. 7, 2022-02

Principal Author

Name of Principal Author (Candidate)	Alan Gardin		
Contribution to the Paper	Performed numerical and theoretical calculations, proposed the miscut model, wrote the manuscript.		
Overall percentage (%)	60		
Certification:	This paper reports on original research I conducted during the period of my Higher Degree by Research candidature and is not subject to any obligations or contractual agreements with a third party that would constrain its inclusion in this thesis. I am the primary author of this paper.		
Signature		Date	22/01/2024

Co-Author Contributions

By signing the Statement of Authorship, each author certifies that:

i. the candidate's stated contribution to the publication is accurate (as detailed above);
ii. permission is granted for the candidate in include the publication in the thesis; and
iii. the sum of all co-author contributions is equal to 100% less the candidate's stated contribution.

Name of Co-Author	Ross Monaghan		
Contribution to the Paper	Carried out the Landau-Zener calculations, helped propose the miscut model, checked the numerical calculations, read and corrected the manuscript.		
Signature		Date	30/01/2024

Name of Co-Author	Tyler Whittaker		
Contribution to the Paper	Performed NEMO calculations, read and corrected the manuscript.		
Signature		Date	30/01/2024

Name of Co-Author	Rajib Rahman		
Contribution to the Paper	Managed the project, gave directions on the theoretical and numerical methods to use, read and corrected the manuscript.		
Signature		Date	01/02/2024

Name of Co-Author	Giuseppe Tettamanzi		
Contribution to the Paper	Proposed and Managed the project and gave directions, help propose the miscut model, read and corrected the manuscript.		
Signature		Date	30/01/2024

PHYSICAL REVIEW B **105**, 075406 (2022)

Nonadiabatic quantum control of valley states in silicon

Alan Gardin [1,*] Ross D. Monaghan [1] Tyler Whittaker [1] Rajib Rahman [2] and Giuseppe C. Tettamanzi [1,†]
[1]*School of Physics & Institute of Photonics and Advanced Sensing, The University of Adelaide, Adelaide SA 5005, Australia*
[2]*School of Physics, The University of New South Wales, Sydney NSW 2052, Australia*

(Received 28 May 2021; revised 17 November 2021; accepted 25 January 2022; published 7 February 2022)

Nonadiabatic quantum effects, often experimentally observed in semiconductor nanodevices such as single-electron pumps operating at high frequencies, can result in undesirable and uncontrollable behavior. However, when combined with the valley degree of freedom inherent to silicon, these unfavourable effects may be leveraged for quantum information processing schemes. By using an explicit time evolution of the Schrödinger equation, we study numerically nonadiabatic transitions between the two lowest valley states of an electron in a quantum dot formed in a SiGe/Si heterostructure. The presence of a single-atomic layer step at the top SiGe/Si interface opens an anticrossing in the electronic spectrum as the center of the quantum dot is varied. We show that an electric field applied perpendicularly to the interface allows tuning of the anticrossing energy gap. As a result, by moving the electron through this anticrossing, and by electrically varying the energy gap, it is possible to electrically control the probabilities of the two lowest valley states.

DOI: 10.1103/PhysRevB.105.075406

I. INTRODUCTION

Adiabatic theorem and manifestations in single-electron pumps. According to the adiabatic theorem, a system initially in its ground state, and whose Hamiltonian evolves slowly in time, is expected to remain in the ground state of the instantaneous Hamiltonian, provided the ground state is nondegenerate. However, if the Hamiltonian varies quickly, then this approximation is no longer valid and the state is best described by a superposition of eigenstates of the instantaneous Hamiltonian. This superposition of states induces spatial oscillations of the wave function, which are an observable manifestation of the violation of the adiabatic theorem. This is encountered in single-electron pumps operating at fast pumping frequencies, where being in the nonadiabatic regime leads to a decrease in the accuracy and precision of the pump [1]. For instance, in the work of Yamahata *et al.* [2] nonadiabatic oscillations were experimentally measured in single-electron pumps formed by a silicon nanowire field effect transistor. They also presented a one-dimensional simulation of nonadiabatic oscillations between electron orbitals for a moving quantum dot and demonstrated the resulting spatial oscillations of the wave function.

Valleys in silicon and SiGe structures. In a [001] grown Si_xGe_{1-x} heterostructure, the tensile strain between the Si and SiGe layers breaks the sixfold valley degeneracy of bulk silicon, leading to a fourfold degeneracy (k_x and k_y valleys) raised in energy and a twofold degeneracy (k_z valleys) lowered in energy. The latter can be further broken by interface roughness, impurities, or electric fields [3,4]. It is sufficient to focus on the two lowest k_z valley states because of the high energy gap (typically around 200 meV [3]) between them and the other k_x and k_y valley states.

Nonadiabatic transitions with valleys is unexplored. Whilst Yamahata *et al.* considered electron orbitals, they do not take into account the valley degrees of freedom inherent to silicon, which are expected to couple with the orbital states in any realistic device [3,5,6]. Hence it may be possible, due to valley-orbit coupling, to observe nonadiabatic transitions between valley states. Note that coherent oscillations between valley states has been previously studied in pure valley qubit schemes based on double quantum dots [7,8], while we instead focus on a single quantum dot. Similarly, Boross *et al.* [9] considered coherent oscillations between valley states in a single dot, but their driving scheme is limited to a weak electric field, contrary to our scheme.

Model and contribution of the paper. In this paper, we study the dynamics of a single electron trapped in a quantum dot formed by a [001] grown $Si_{0.8}Ge_{0.2}$/Si heterostructure. The appearance of valley physics stems from our modeling of the SiGe/Si heterostructure by use of a two-band model. Nonadiabatic effects are then introduced by quickly varying the center of the quantum dot potential. We then successively consider two two-dimensional models of a simplified SiGe/Si heterostructure, both introduced in Sec. II.

In the first model, we present an ideally grown heterostructure, where the orbital degrees of freedom originating from the quantum dot are decoupled from the valley degrees of freedom, and thusly observe only nonadiabatic transitions between orbital states. An analytic study of such transitions is tackled in Sec. III.

In the second model, we model a miscut SiGe/Si heterostructure by introducing a single-atomic step at the interface, akin to that of Boross *et al*. In Sec. IV, we explain why the introduction of this step alters the spectrum of the system as the quantum dot position is varied. The key physics

*alan.gardin@adelaide.edu.au
†giuseppe.tettamanzi@adelaide.edu.au

 ©2022 American Physical Society

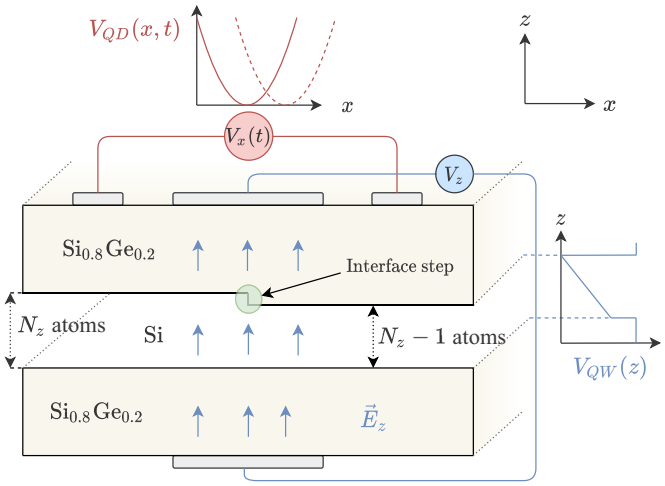


FIG. 1. Geometry of the two-dimensional SiGe heterostructure model with the y axis neglected. We apply a time-dependent harmonic quantum dot potential V_{QD} in x, and an electric field in z. The quantum well in the z axis, originating from the SiGe/Si interfaces, is composed of N_z atoms and decreases by one atomic layer at the step (green circle). The dashed parabola represents the potential profile at $t' > t$, reflecting the spatial movement of the harmonic potential.

is that an anticrossing between the two lowest valley states opens, with an energy gap tuneable by an electric field applied along the z direction. This behavior is verified by a realistic tight-binding calculation using NEMO 3D's 20 band $sp^3d^5s^*$ model [10]. We detail this in Appendix A. As a result of the anticrossing, the nonadiabatic pulsing of the electron through this step allows one to induce transitions from one valley state to another. Section V discusses the main result of the paper, namely that the final state can be electrically controlled by varying the anticrossing energy gap. Due to the appearance of the avoided crossing in the spectrum, we model the transition using the Landau-Zener approximation [11] and achieve good concordance. From studying the results there exists a range of driving parameters in which the final state forms a good two-level system, opening the door for qubit applications. We discuss the viability of such nonadiabatic valley qubit in Sec. VI.

II. MODELS

A. Ideal model

Quantum dot potential. We now present the two-dimensional model, in the (x, z) plane, used throughout this paper. We assume the growth axis z of our heterostructure to be orthogonal to the x axis, as shown in Fig. 1. In the x direction, the electron has a transverse effective mass $m_x = 0.19\, m_e$. The quantum dot potential V_{QD} is a harmonic potential of angular frequency ω whose minimum follows a trajectory ξ, hence $V_{QD}(x,t) = \frac{1}{2}m_x\omega^2(x - \xi(t))^2$. We choose ω such that we obtain an orbital level spacing $\Delta\epsilon = \hbar\omega = 2$ meV for the orbital states. This value is chosen to isolate the higher orbital states from the two lowest valley states. Note that the y axis is neglected in our paper since it does not affect the physics discussed.

Quantum dot trajectory. The evolution in time of the quantum dot position is the only source of time-dependence in Hamiltonian. The quantum dot is initially at position $x_0 = 0$ nm at $t_0 = 0$ ps, and moves with constant velocity v_{QD} until it reaches x_1 at time t_1. The parameters x_1 and t_1 are varied to obtain different values for v_{QD}. The trajectory ξ of the quantum dot can be written:

$$\xi(t) = \begin{cases} x_0 & \text{for } t \leqslant t_0 \\ x_0 + v_{QD}(t - t_0) & \text{for } t_0 \leqslant t \leqslant t_1 \\ x_1 & \text{for } t_1 \leqslant t \end{cases} \quad (1)$$

The Hamiltonian describing the dynamics along the x axis corresponds to an effective mass method, given by

$$H_x(x,t) = \frac{p_x^2}{2m_x} + V_{QD}(x,t) \quad (2)$$

and is identical for all z in the ideal model.

Description of the z confinement. The z confinement and the valley effects are modelled using the tight-binding model for strained silicon quantum wells of Boykin *et al.* [12,13]. The resulting Hamiltonian for the z slices depends on three parameters: the on-site energy η, the nearest-neighbor hopping v and the second-neighbor hopping u giving the Hamiltonian in Eq. (3):

$$H_z(\eta,u,v) = \begin{pmatrix} \eta & v & u & 0 & \dots & \dots & 0 \\ v & \eta & v & u & 0 & \ddots & \vdots \\ u & v & \eta & v & u & \ddots & \vdots \\ 0 & \ddots & \ddots & \ddots & \ddots & \ddots & 0 \\ \vdots & \ddots & u & v & \eta & v & u \\ \vdots & \ddots & 0 & u & v & \eta & v \\ 0 & \dots & \dots & 0 & u & v & \eta \end{pmatrix}. \quad (3)$$

In this Hamiltonian, each site represents an atom of the quantum well in the z axis.

We will define $N_z = 40$ to be the total number of atoms in the z axis, where each atom is separated by 1.366 Å. We will also refer to N_z as the quantum well width, expressed in number of atoms. A monolayer corresponds to two atoms, so that our choice of quantum well width corresponds to 20 monolayers. Note that varying the width of the Si/SiGe quantum well, as we could do in the simulations, is experimentally feasible. For clarity, we should mention that this Hamiltonian corresponds to a single chain of N_z atoms, and one can model a chain of $N_z - 1$ atoms by setting the last row and column to zero.

Expected eigenstates and spectrum. In our model, the quantum well width is $L_z = N_z \times 0.1366 = 5.464$ nm. The energies of this infinite quantum well barrier are given by $E_m = m^2 \frac{\hbar^2\pi^2}{2m_l L_z^2}$ with $m_l = 0.92m_e$ the electron's longitudinal effective mass and $m \in \mathbb{N}^*$ the orbital number. The energy gap between the first and second quantum well eigenstates is then $3\frac{\hbar^2\pi^2}{2m_l L_z^2} = 13$ meV. Because of this high energy gap, it is reasonable to only consider the first eigenstate of the quantum well. The eigenstates of H_x, which are eigenstates of the harmonic oscillator, are denoted by φ_n with $n \in \mathbb{N}$ describing the orbital number.

The Hamiltonian describing the z confinement gives a valley splitting less than the orbital spacing $\Delta\epsilon = \hbar\omega$ induced by the harmonic oscillator. As a consequence, we expect to observe two well defined valley states for each orbital. We will denote the corresponding eigenstates $\psi_{n,v}$ and energies $\epsilon_{n,v}$, with (n, v) where $n \in \mathbb{N}$ is the orbital index and $v \in \{-, +\}$ the valley index. It will be convenient later on to index the states and the energies with a single index for readability. Since the $v = -$ valley states always have lower energies than the $v = +$ states for a given n, we will use the natural mapping $(0, -) \to 0$, $(0, +) \to 1$, $(1, -) \to 2$ and so on to label the energies and eigenstates by increasing energies. The meaning of the indices will be understood from context depending on whether there is one or two indices.

As a final note, the full Hamiltonian for this idealised model is $H = H_x \otimes H_z$ and corresponds to a hybrid tight-binding/effective mass model. This ideal model is separable in x and z, and hence the valley degrees of freedom do not couple to the orbital degree of freedom. The eigenstates are the product of the eigenstates of the Hamiltonians H_x and H_z, and indeed the indices (n, v) are good quantum numbers.

B. Single-step model

Description of the interface step, and experimental justification. As in the work of Boross *et al.*, we introduce an interface step consisting of a single-atomic layer at $x_s = 30$ nm, modelled by decreasing the width of the quantum well for all z slices where $x \geqslant x_s$ (see Fig. 1). This interface step is motivated by the single-atomic layer steps observed in SiGe/Si heterostructures grown on slightly vicinal [0 0 1] Si substrates [14–17]. In particular, these steps occur at polar miscut angles $\theta \leqslant 2^\circ$, with terrace width on the order of 10 nm [15–17]. Given θ can be controlled by manufacturers to within 0.1° [14] and uniform terrace width can be achieved as in [15], one could manufacture a structure with an interface step similar to that modelled in this paper.

Differences with Boross et al. Unlike Boross *et al.*, we do not allow the wave function to penetrate inside the SiGe layer, instead enforcing hard-wall boundary conditions, however, the physics observed is expected to be similar. And indeed as shown in Fig. 5, the evolution of the spectrum is similar to that obtained in Boross *et al*. Another difference in our paper is that we do not limit ourselves to weak perturbations along the x axis: we study the opposite limit of strong nonadiabatic perturbations. Furthermore, our modeling has been validated with NEMO 3D's 20 band $sp^3d^5s^*$ model, see Appendix A.

Implementation. Due to the presence of the interface step, the Hamiltonian is not separable in x and z anymore, since the Hamiltonian H_z of Eq. (3) gains a x dependence. For the simulations, we simply set the last row and last column of H_z to zero for all $x > x_s$. This amounts to diminishing the length of the quantum well by one atom for all $x > x_s$, hence implementing the step. In line with Fig. 1, we also add an electric field E_z, which is implemented by varying the on-site parameters η of H_z. Hence, H_z also gains a z dependence.

C. Methods

We numerically solve the ground state of the total Hamiltonian H at the initial time $t_0 = 0$ ps and use this result as the initial wave function for solving the time-dependent Schrödinger equation. The time-dependent Schrödinger equation is solved using the Crank-Nicolson scheme [18]. The on-site energy parameter η of H_z [Eq. (3)] is set to 1.395 eV such that the spectrum has negative values close to zero, allowing for easier differentiation between "real" eigenvectors and "artificial" eigenvectors (eigenvalues of 0). Indeed, this is necessitated by the setting the column and row of the relevant lattice sites to zero in the Hamiltonian to produce the step in the interface, described above, as this introduces null eigenvalues. The difference between our chosen value of η and the choice made in Boykin *et al.* is then restored after diagonalisation. The values used for the off-diagonal elements can be found in Fig. 2 of Boykin *et al.* [12].

In all simulations, we fix $x_0 = 0$ nm and $t_0 = 0$ ps. For the simulations involving the ideal model, we fix $t_1 - t_0$ to 5 ps and vary x_1 to change v_{QD}. This choice ensures that the perturbation is applied for the same amount of time in all simulations. For the step model however, we fix $x_1 = 55$ nm and vary t_1 to change v_{QD}. As discussed later, the spatial evolution of the dot relative to the step is critical for analysis of the simulations, such that fixing the initial and final positions and changing the time is the more appropriate choice of altering the velocity.

III. NONADIABATIC EFFECTS IN THE IDEAL MODEL

A. Preliminary remarks

Introduction. In this section, we comment on the numerical results obtained with the ideal model (Fig. 2) of Sec. II A, i.e., when no interface step is present. As explained in the previous section, the Hamiltonian is separable in the x and z coordinates. Since the time-dependence only originates from the x axis, the dynamics of the system reduce to that of a driven quantum harmonic oscillator described by the Hamiltonian H_x of Eq. (2). As a consequence, the only parameter we vary in our simulations is the quantum dot speed v_{QD} (in particular, the applied electric field E_z does not influence the numerical results). This model is essentially the same as the one from Yamahata *et al.* [2], with the difference being the trajectory ξ of the quantum dot. Our choice for the trajectory ξ [see Eq. (1)] will simplify the interpretation of the numerical results.

Oscillatory features of the probabilities amplitude and period. As a preliminary remark, one can notice that the states of energy $\epsilon_{n,+}$ have a zero probability of occupation for all time. Indeed, since the dynamics only originate from the orbital degree of freedom, and no valley orbit coupling exist in this ideal model, no transition to a state of valley index $v = +$ can happen because we started in a state with $v = -$.

A second striking feature is the oscillatory behavior of the probabilities. Noticeably, the period of the oscillations is constant (it depends only on the potential of the quantum dot), but the amplitude can be increased through v_{QD}. An analytical derivation of this fact is performed in the next subsection under the adiabatic approximation. Note, however, that higher

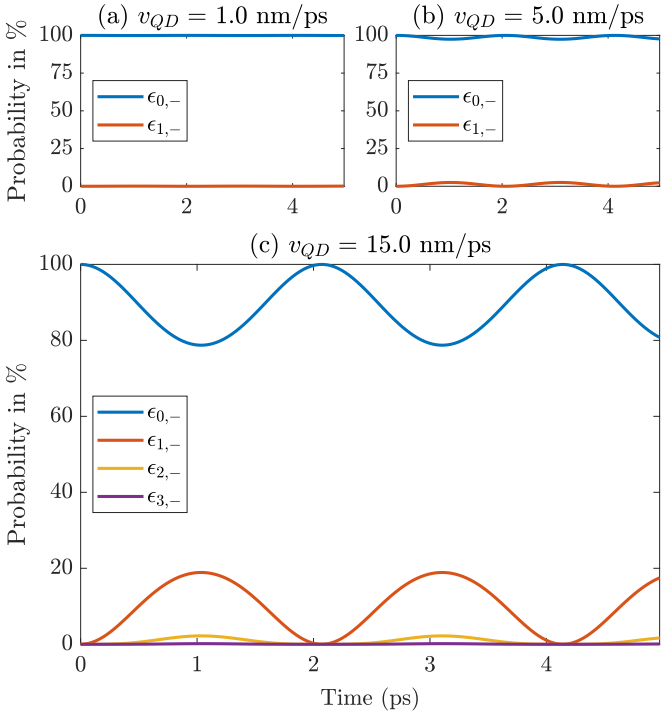


FIG. 2. Time evolution of the probabilities for the ideal model (no step and hence no valley physics). For small speeds, the system mostly occupies the two lowest energy orbitals, forming a two-dimensional Hilbert space, as needed for a qubit. However, a higher speed introduces higher excited states and does not behave as a two-level system anymore. Note that the period of oscillations is constant and the higher the speed the bigger the amplitudes of the probability oscillations.

values of v_{QD} slowly increase the probabilities of higher orbital states (i.e states with $n \geqslant 1$), as can be seen in the last row. For low values of v_{QD}, the coherent oscillations between the two states are effectively Rabi oscillations encountered in qubits, but this does not hold at higher quantum dot speeds.

Classical analogy and spatial oscillations of the probability density. A consequence of the presence of states other than the ground state manifests itself in the spatial oscillations of the probability density. The spatial oscillations of the electron can easily be understood classically as follows. Applying the Heisenberg equation of motion to the operators $\hat{x}$ and $\hat{p}_x$, we obtain:

$$\begin{aligned}\frac{d\langle\hat{p}_x\rangle}{dt} &= \left\langle \frac{1}{i\hbar}\left[\hat{p}_x, \hat{H}_x\right]\right\rangle \\ &= m\omega^2(\xi(t) - \langle\hat{x}\rangle(t)), \\ \frac{d\langle\hat{x}\rangle}{dt} &= \frac{\langle\hat{p}_x\rangle}{m}.\end{aligned}$$

From which we can derive the following equation of motion for $\langle\hat{x}\rangle$:

$$\frac{d^2\langle\hat{x}\rangle}{dt^2} + \omega^2\langle\hat{x}\rangle = \omega^2\xi(t). \tag{4}$$

This is exactly the equation of motion of a classical harmonic oscillator driven by some force ξ. Hence we see that the average position behaves exactly as in the classical case

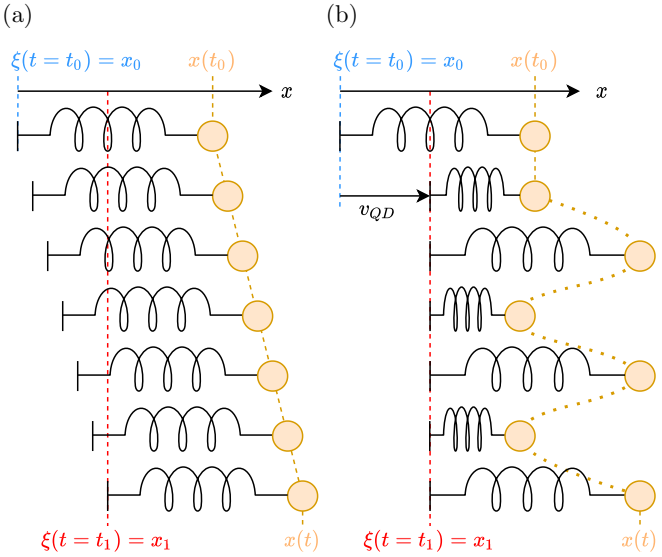


FIG. 3. Adiabatic and nonadiabatic driving of a classical harmonic oscillator. (a) In the adiabatic case, the mass follows the position of the spring. (b) In the nonadiabatic case, the spring is moved so quickly that the mass initially stays at the initial position—it does not have enough time to react to the external perturbation.

of a driven harmonic oscillator. The period of the spatial oscillations depends only on ω and not on the initial conditions, whilst the amplitude increases with an increase in the driving force.

Classically, the movement of the quantum dot can be understood by pushing a spring to which a mass is attached, as shown in Fig. 3. Pushing the spring adiabatically, the mass is expected to follow the movement of the spring, i.e., adapt to the perturbation at each time. However, pushing the spring over the same distance during a shorter period of time, one expects the mass to oscillate, as it does not have time to adjust to the perturbation.

Spatial oscillations from a quantum superposition Returning to the quantum case, one can assume that the effect of a nonadiabatic perturbation is to put the wave function into a superposition of states. For instance, assuming that at the end of the quantum dot's trajectory, i.e., for $t = t_1$, and for relatively low values of v_{QD}, the state is of the form:

$$|\psi(t = t_1)\rangle = \sqrt{1-p}|\varphi_0\rangle + \sqrt{p}|\varphi_1\rangle$$

where φ_0 and φ_1 are respectively the ground and first excited state of the harmonic oscillator at t_1, and p if the state probability. Since for $t > t_1$ the Hamiltonian becomes time independent [it corresponds to a harmonic oscillator centered at $\xi(t_1) = x_1$], the time evolution of the state is of the form:

$$|\psi(t)\rangle = \sqrt{1-p}|\varphi_0\rangle + e^{-i2\pi\frac{t}{\tau}}\sqrt{p}|\varphi_1\rangle$$

with $\tau = \frac{2\pi\hbar}{\Delta\epsilon}$ and period corresponding to a pulsation $\omega = \frac{\Delta\epsilon}{\hbar}$. Note that here the superposition is time dependent but the state probability is time independent, since the probability p does not depend on time.

The average position for $t > t_1$ can then be expressed as:

$$\langle x\rangle(t) = \langle\psi(t)|\hat{x}|\psi(t)\rangle$$

$$
\begin{aligned}
&= (1-p)\langle\varphi_0|\hat{x}|\varphi_0\rangle + p\langle\varphi_1|\hat{x}|\varphi_1\rangle \\
&\quad + 2\sqrt{p(1-p)}\cos\left(2\pi\frac{t}{\tau}\right)\Re\langle\varphi_0|\hat{x}|\varphi_1\rangle \\
&= x_1 + \sqrt{\frac{2\hbar p(1-p)}{m\omega}}\cos\left(2\pi\frac{t}{\tau}\right)
\end{aligned}
$$

where we have used Eq. (4.174) of Ref. [19] to write $\langle\varphi_0|\hat{x}|\varphi_1\rangle = \sqrt{\frac{\hbar}{2m\omega}}$. Hence, we recover the fact that the probability density oscillates in space, due to a quantum superposition of states. These spatial oscillations of the probability density are at the root of the oscillations experimentally observed by Yamahata *et al.*

B. Transition probabilities in the weak nonadiabatic regime

In this section, we follow a method by B. H. Bransden [19] to derive an analytical expression for the probability of the first orbital excited state, i.e., the state $\psi_{1,-}$. To simplify notations, we will drop the time dependence of ξ and denote by $m = m_x$ the electron's transverse effective mass and $\hat{H}(t) = H_x$ the Hamiltonian. We will also make use of the single index notation defined in Sec. II, such that we study the transition $\psi_{0,-} \equiv \psi_0 \to \psi_2 \equiv \psi_{1,-}$. One can expand the Hamiltonian of the 1D model as follows:

$$
\hat{H}(t) = \frac{\hat{p_x}^2}{2m} + \frac{1}{2}m\omega^2\hat{x}^2 + \frac{1}{2}m\omega^2\xi^2 - m\omega^2\xi\hat{x}.
$$

The derivative with respect to time comes out as:

$$
\frac{\partial\hat{H}}{\partial t} = m\omega^2\dot{\xi}(\xi - \hat{x}) = -m\omega^2\dot{\xi}(\hat{x} - \xi) \tag{5}
$$

Following B. H. Bransden, the probability amplitude of the first orbital excited state ψ_2 under the adiabatic approximation is (Eq. 9.100):

$$
c_2(t) = \hbar^{-1}\int_{t_0}^{t} dt' \frac{\langle\varphi_1(t')|\frac{\partial\hat{H}}{\partial t'}|\varphi_0(t')\rangle}{\omega}\exp\left(i\int_{t_0}^{t'}\omega du\right) \tag{6}
$$

with $\{\varphi_n(t)\}_{n\in\mathbb{N}}$ denoting the eigenstates of the harmonic oscillator centered at $\xi(t)$. We can simplify the numerator using Eq. (5):

$$
\begin{aligned}
\langle\varphi_1(t')|\frac{\partial\hat{H}}{\partial t'}|\varphi_0(t')\rangle &= -m\omega^2\dot{\xi}\langle\varphi_1(t')|\hat{x} - \xi(t')|\varphi_0(t')\rangle \\
&= -m\omega^2\dot{\xi}\langle\varphi_1(0)|\hat{x} - \xi(0)|\varphi_0(0)\rangle.
\end{aligned}
$$

Using the generating function for the Hermite polynomials (see equation 4.174 of Ref. [19]), one has the following identity:

$$
\langle\varphi_n|\hat{x}|\varphi_m\rangle = \begin{cases} \sqrt{\frac{\hbar}{m\omega}}\sqrt{\frac{n}{2}} & \text{if } m = n-1 \\ \sqrt{\frac{\hbar}{m\omega}}\sqrt{\frac{n+1}{2}} & \text{if } m = n+1 \\ 0 & \text{else} \end{cases}. \tag{7}
$$

Hence

$$
\langle\varphi_1(t')|\frac{\partial\hat{H}}{\partial t'}|\varphi_0(t')\rangle = -m\omega^2\dot{\xi}\sqrt{\frac{\hbar}{2m\omega}}.
$$

We can then obtain a more explicit expression for the probability amplitude of the first orbital excited state:

$$
\begin{aligned}
c_2(t) &= \frac{-m\omega^2}{\hbar\omega}\sqrt{\frac{\hbar}{2m\omega}}\int_{t_0}^{t} dt'\,\dot{\xi}(t')\exp\left(i\omega(t'-t_0)\right) \\
&= -\omega\sqrt{\frac{m}{2\hbar\omega}}\int_{t_0}^{t} dt'\,\dot{\xi}(t')\exp\left(i\omega(t'-t_0)\right).
\end{aligned}
$$

At this stage, it is useful to introduce the maximum speed of a quantum harmonic oscillator in the ground state. Assuming that the total energy corresponds to kinetic energy, we have $\epsilon_0 = \frac{\hbar\omega}{2} = \frac{1}{2}mv_{max}^2$, where $v_{\max} \equiv \sqrt{\frac{\hbar\omega}{m}} = \sqrt{\frac{\Delta\epsilon}{m}}$ the maximal speed. We can then rewrite the expression for $c_2(t)$ as

$$
c_2(t) = \frac{-\omega}{\sqrt{2}}\int_{t_0}^{t} dt'\frac{\dot{\xi}(t')}{v_{\max}}\exp\left(i\omega(t'-t_0)\right). \tag{8}
$$

For $t_0 \leqslant t \leqslant t_1$, $\dot{\xi}(t) = v_{QD}$ we can obtain the transition probability from the modulus squared of $c_2(t)$:

$$
P_2(t) = 2\left(\frac{v_{QD}}{v_{\max}}\right)^2\left|\sin\left(\frac{\omega}{2}(t-t_0)\right)\right|^2. \tag{9}
$$

Hence, the state probabilities oscillate with an amplitude proportional to v_{QD}^2 as observed in Fig. 2. The period of oscillations can be made more apparent by rearranging the equation above:

$$
\begin{aligned}
P_2(t) &= 2\left(\frac{v_{QD}}{v_{\max}}\right)^2\left|\sin\left(\frac{\omega}{2}(t-t_0)\right)^2\right| \\
&= \left(\frac{v_{QD}}{v_{\max}}\right)^2\left|1 - \cos\left(2\pi\frac{(t-t_0)}{\frac{2\pi}{\omega}}\right)\right| \\
&= \left(\frac{v_{QD}}{v_{\max}}\right)^2\left|1 - \cos\left(2\pi\frac{(t-t_0)}{\tau}\right)\right|
\end{aligned}
$$

with $\tau = \frac{2\pi\hbar}{\Delta\epsilon}$ as previously defined. In the context of our simulations, the orbital spacing $\Delta\epsilon = 2\,\text{meV}$ gives $\tau = 2.1$ ps, which matches the period observed in Fig. 2.

In Appendix B, a similar calculation is performed to estimate the probability of the second excited orbital state $\psi_{2,-} = \psi_4$.

C. Criterion for the transition to the nonadiabatic regime

Strictly speaking, an adiabatic evolution implies that the probability of being in eigenstate remains the same throughout the infinitely slow perturbation. For instance, if the initial probability of the state ψ_2 is initially zero, then it should continue being zero at all future times. In practice, it is convenient to adopt a less restrictive definition by comparing how well an adiabatic approximation matches with the actual results.

Using Eq. (9) we can find an upper bound for the probability of the first orbital in the adiabatic approximation, namely the maximum value of $P_{0\to2}$ is given by

$$
\max_t P_{0\to2}(t) = 2m\frac{v_{QD}^2}{\Delta\epsilon} \quad . \tag{10}
$$

As the bound is directly proportional to the square of v_{QD} (the orbital spacing $\Delta\epsilon$ is fixed to 2 meV), one can appreciate that

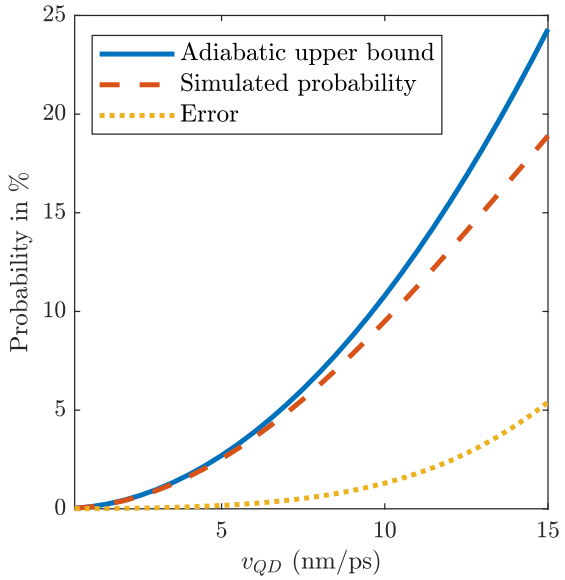


FIG. 4. Maximum value of the probability of the first excited orbital state ψ_2 for different values of v_{QD}. The blue-solid line is the upper bound of Eq. (10) derived in the adiabatic approximation. The red-dashed line correspond to the maximum over time of the probability of observing the state ψ_2 in our numerical simulations. The dotted-yellow line gives an indication of how well the adiabatic approximation agrees with the numerical results. For small values of v_{QD}, the upper bound is a very good approximation, but the error widens at v_{QD} increases, reflecting the smooth transition to the nonadiabatic regime.

the physics is particularly sensitive to the quantum dot speed. This upper bound is plotted in Fig. 4 (blue-solid line).

As discussed in the previous subsection, and considering the results of Fig. 2, the value of the final probabilities depend on the time at which we look for a fixed value of v_{QD}. As a consequence, we plot in Fig. 4 the the maximum value of the probability of $P_{0\to 2}$ depending on v_{QD}, as obtained from the simulations (red-dashed line).

We remark that the numerical data matches the adiabatic approximation for low v_{QD}, i.e., when the adiabatic approximation is valid. However, as v_{QD} increases, the adiabatic approximation, utilised to derive the analytic expression, becomes invalid and the difference between the upper bound and the numerical results widens as expected. Indeed, this can easily be interpreted by looking at the results of Fig. 2 where we see higher orbital states appearing as v_{QD} increases. As a consequence, some of the probability leaks to these higher orbital states, explaining why the results diverge. The yellow-dotted line gives an estimation of how "nonadiabatic" the system is. Low values testify to an adiabatic system for the orbitals, while values above a certain threshold (arbitrarily chosen) indicate a nonadiabatic regime.

To conclude this section, we would like to emphasise that the plot of Fig. 4 only considers the orbital degrees of freedom, as the valley degrees of freedom do not play a role in the ideal model. Still, Fig. 4 will prove useful for analyzing the results involving the valley degrees of freedom of the step model, discussed in Sec. V.

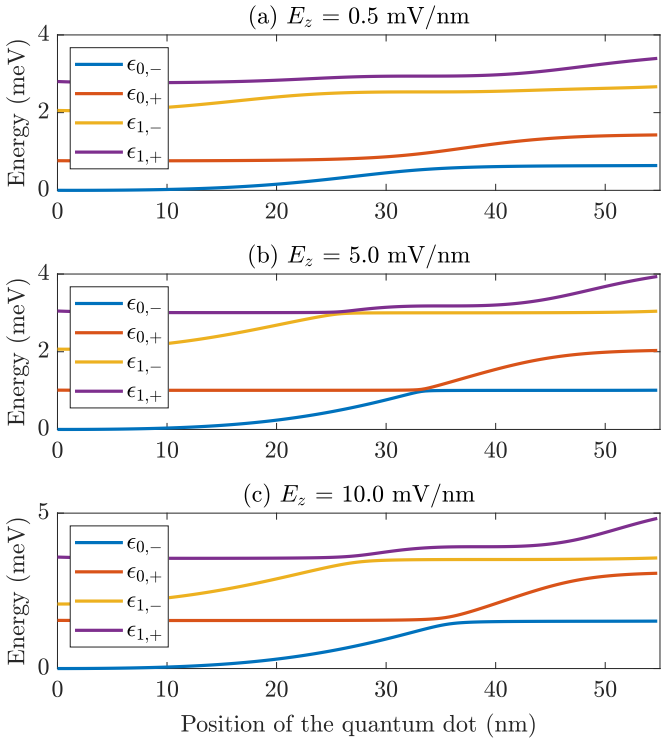


FIG. 5. Spatial evolution of the spectra of the single-step model for different electric fields E_z. In this figure, the reference energy has been set to 0 meV to increase readability. An anticrossing opens after the step located at $x_s = 30$ nm, and can be understood by the probability densities of the two lowest states. The numerical results show that the energy gap at the anticrossing can be tuned by the electric field E_z applied perpendicular to the SiGe interfaces (see Fig. 1). Note also the global increase of the energies as the electron is confined to a tighter region, as we would expect.

IV. SPECTRUM IN THE STEP MODEL

We now perform the same analysis but with the step model. Critically, the perturbation now couples the orbitals with the valley states of the electron.

General remarks on the spectrum. We now discuss the salient features of the spectrum of the step model as the minimum of the quantum dot potential is varied. The results are plotted in Fig. 5 for different electric fields E_z. To simplify notations, we continue to label the energies with the indices $(n, v) \in \mathbb{N} \times \{-, +\}$, but one should be reminded that near the step, the strong valley-orbit coupling prevents (n, v) from being good quantum numbers. Note that far away from the steps, the wave functions are well defined valley states, and the indices (n, v) are still good quantum numbers.

Origin of the anticrossing. A critical observation is the existence of an anticrossing near the step location (at $x_s =$ 30 nm). As mentioned in the previous paragraph, the step causes the coupling of the valley and orbital degrees of freedom. In the absence of disorder at the well interface there exists globally defined valley states, where the valley states are translationally invariant, however, the step potential explicitly breaks this symmetry resulting in the observed anticrossing.

The physics behind this avoided crossing can be understood by examining the probability density of the two lowest

energetic states, and is well described in Boross *et al*. Indeed, as shown in both atomistic simulations [12,13] and effective mass theories [5,20], the wave functions exhibit modulations on the atomic scale of the envelope function. The two lowest k_z valley states are symmetric and antisymmetric superpositions of $\pm k_0$ with $k_0 \simeq 0.82\frac{2\pi}{a}$, where $a = 5.41$ Å is the lattice spacing of the silicon crystal. The atomic scale oscillations of the two valley states are similar except for a spatial dephasing. A consequence of this spatial dephasing is that one of the state will have a maxima at the step location, while the other will have a minima. Hence, as the quantum dot goes through the step, the lowest energetic state will feel the step, increasing its energy, while the other will not.

Control of the anticrossing gap with electric field. As shown in Fig. 5, the energy gap at the anticrossing of the two lowest valley states can be electrically controlled through the applied electric field E_z. The dependence of the gap with the electric field is nontrivial and also depends on the quantum well width, which we have fixed to $N_z = 40$ atoms in this paper. As discussed in later sections, the values of E_z for which the energy gap of the anticrossing is small will prove particularly useful for electrical control of the final state. One could question whether this behavior is expected in real devices, or if it is an artifact of the two-band model we are using to model the valleys. In Appendix A, NEMO 3D calculations using a 20 band $sp^3d^5s^*$ model show that the gap at the anticrossing is indeed controllable with the electric field E_z. Akin to the results of the two-band model, the anticrossing gap varies in the same nontrivial way, but it seems the trend can be reproduced only for certain quantum well widths. As a result, we expect the control of the anticrossing gap to be feasible in real devices.

Higher orbital anticrossing. We notice that a similar anticrossing happens between valley states of higher orbitals too (states of energies $\epsilon_{1,-}$ and $\epsilon_{1,+}$). However, this anticrossing happens before that of the ground-state orbital. This makes sense since the higher orbital states of the harmonic oscillators have a wider spatial extent over the x position as the orbital number n increases. In turn, the step is felt earlier, explaining the earlier appearance of the anticrossing.

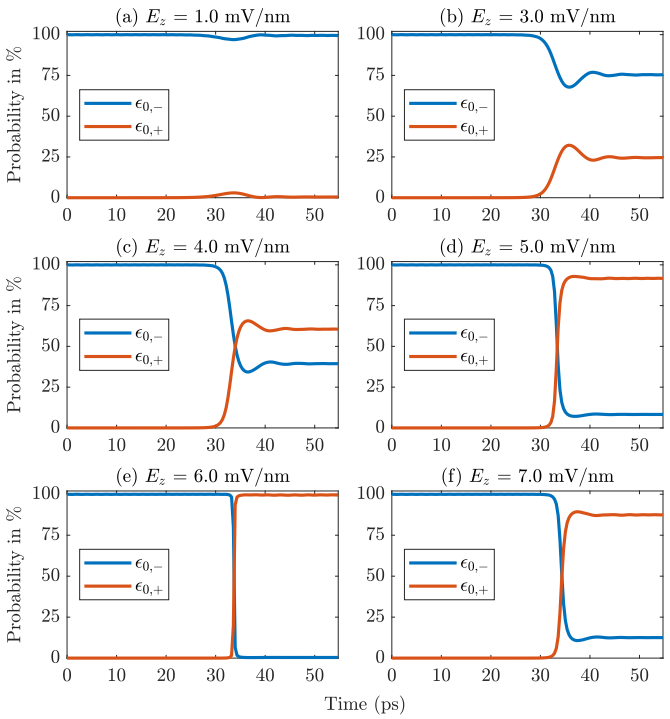


FIG. 6. Evolution of the probabilities at $v_{QD} = 1$ nm/ps for different electric fields E_z. The probabilities of higher energy states were at most 0.25%, so they have been omitted here for readability. To a good approximation $v_{QD} = 1$ nm/ps results in a two-level system (see Fig. 4) and can form the basis states of a qubit. Through the applied electric field E_z, the energy gap of the anticrossing can be tuned, which results in the control of the valley states.

V. NONADIABATIC EFFECTS IN THE STEP MODEL

A. General comments

Results at a fixed low quantum dot speed. The movement of the quantum dot potential has the effect of bringing energy into the system. This additional energy allows the ground state to overcome the anticrossing gap observed in the spectrum. As intuitively expected, the smaller the gap between the two lowest eigenstates, for the same perturbation the stronger the probability of transitioning to other valley states. This is illustrated well in Fig. 6 for $v_{QD} = 1$ nm/ps where the value of v_{QD} is small enough that the system is mostly confined to the two valleys of the first orbital state (this can be verified by examining the yellow dashed line of Fig. 4, showing that the perturbation is adiabatic for the orbitals). For this fixed quantum dot speed, the variation of the applied electric field is the only parameter used to tune the final probabilities of the valley states. Comparing the gaps in the spectra of Fig. 5 and the final probabilities of Fig. 6, one can relate the final probabilities to the tuning of the anticrossing gap.

Results for different combinations of quantum dot speeds and electric fields. In the ideal model, the final probabilities were tuned through v_{QD} (see Fig. 4). In the step model too, the quantum dot speed v_{QD} can be used to tune the final probabilities. In Fig. 7, we plot the probability of the state $\psi_{0,+}$ for a combination of electric fields E_z and quantum dot speeds v_{QD}. As expected from the spectra of Fig. 5, the "sweet spot" for transitioning to the state $\psi_{0,+}$ corresponds to small anticrossing gaps, which happens in a range of electric fields $E_z \in [4, 6]$ mV/nm. One can also remark that increasing the quantum dot speed increases the transition probability for relatively small values of v_{QD}. For higher values of v_{QD} however, the transition probability actually decreases with increasing v_{QD}, since transition to higher orbital states starts to take place instead. This is easily interpreted from Fig. 4, which testifies to the presence of higher orbital states.

Higher orbital valley flipping. The spectra of Fig. 5 show that an anticrossing exists between the states of the first excited orbital. Since the transition between valley states is due to the anticrossing, it is legitimate to expect valley flipping behavior for the first excited orbital. Still, according to the spectrum, this valley exchange should happen before that of the ground orbital states, as the anticrossing happens at an earlier position as explained in Sec. IV. This behavior is indeed verified at higher quantum dot speeds as shown in Fig. 8.

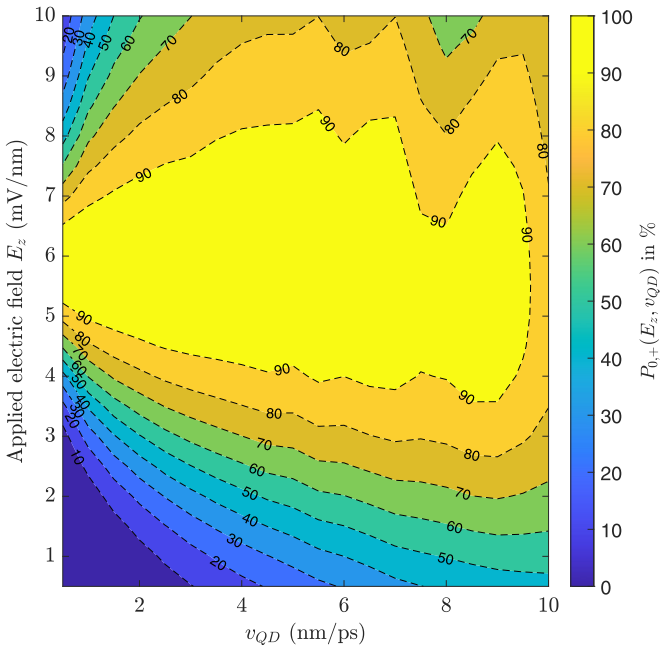


FIG. 7. Probability of the state $\psi_{0,+}$. This allows to find the combination of parameters (v_{QD}, E_z) to reach a specific final probability for $\psi_{0,+}$. For the quantum well width we chose, the anticrossing gap is the smallest at values of $E_z \simeq 6$ mV/nm. This explains the high transition probabilities observed for this range of electric fields. For high values of v_{QD}, transition to higher orbital states take place, which explains the reduction of the probability occurring around $v_{QD} = 9$ nm/ps.

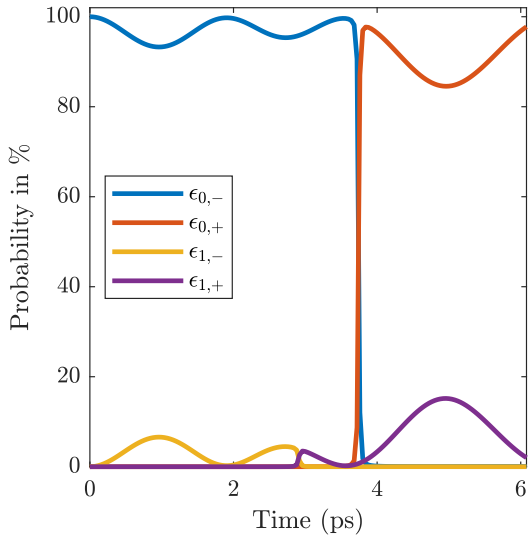


FIG. 8. In this figure, $v_{QD} = 9$ nm/ps and $E_z = 6$ mV/nm. We can observe an exchange of valley states for the orbital $(n = 1)$, due to an anticrossing in the spectrum happening earlier than that of the ground orbital $(n = 0)$. Another interesting feature is the change in both the amplitude and the period of the oscillations after the valley flipping occurs.

B. Landau-Zener approximation

Standard Landau-Zener formula and anticrossings. The probability of nonadiabatic transitions in a two-level system with an avoided crossing has been heavily studied, see Ref. [11] for instance. In particular, the Landau-Zener formula can be used to estimate the transition probabilities due to nonadiabatic effects. The benefit of such an analysis is that one can simply compute the final state probabilities without solving the full time-dependent Schrödinger equation.

Under the Landau-Zener approximation, the energy separation between the uncoupled states is a linear function of time with gradient α, which is assumed to extend over all time. Furthermore, due to the presence of the avoided crossing in the spectrum of the step model, and its absence in the ideal model, then the step couples the valley states. We can introduce an off-diagonal fitting parameter W to mix the two valley states and account for this induced coupling. As per the Landau-Zener approximation, we also assume it is constant in time. Knowing this, we can define the quantity

$$\Gamma = \frac{W^2}{\hbar|\alpha|} \tag{11}$$

where the probability of transitioning to the excited state is given by the formula

$$P_{LZ} = e^{-2\pi\Gamma}. \tag{12}$$

Fit to Landau-Zener. In a realistic model the perturbation is only linear over a finite range of time, as our numerical results for the spectra show in Fig. 5. An analytical modeling of our spectra is complicated, as the expression of the wave functions is not analytical in a quantum well with an applied electric field. As a consequence, we take the approach of fitting our numerical results to a simpler model. Luckily, such a simpler model is provided by Rubbmark *et al.* [11]. Hence we fit the energy level separation between the two lowest energy states $(\epsilon_{0,+} - \epsilon_{0,-})$ to Eq. (18) of Ref. [11] reproduced below (α and τ are the fitting parameters). The resulting transition probabilities are plotted in Fig. 9(b) for different values of v_{QD} and E_z:

$$\epsilon_{0,+}(t) - \epsilon_{0,-}(t) = \alpha\tau\left(\frac{1}{1+\exp(-4t/\tau)} - \frac{1}{2}\right). \tag{13}$$

A surprising result is that the evolution of the transition probabilities is well captured by the Landau-Zener fit for almost all electric field values and the quantum dot speeds. In Fig. 9(a), the simulated transition probabilities $1 - P_{0,-}$ are plotted. The Landau-Zener approximation in Fig. 9(b) shows the same evolution as that of our numerical results. In Fig. 10, we plot the difference between the simulated transition probabilities and the ones obtained from the Landau-Zener approximation P_{LZ}. This illustrates that the Landau-Zener approximation deviates only slightly from our numerical results. However, one should note that for large v_{QD} one would certainly observe transitions to higher orbitals and valley states whilst Landau-Zener only considers the transition to the other state in the two-level system. Regardless, the maximum value of the relative error across all values of electric field and quantum dot speed was only 1.0% (not shown in Fig. 10), and hence it provides a good measure of whether the electron is in the ground state or not—with perhaps no qualification on which state is has transitioned to.

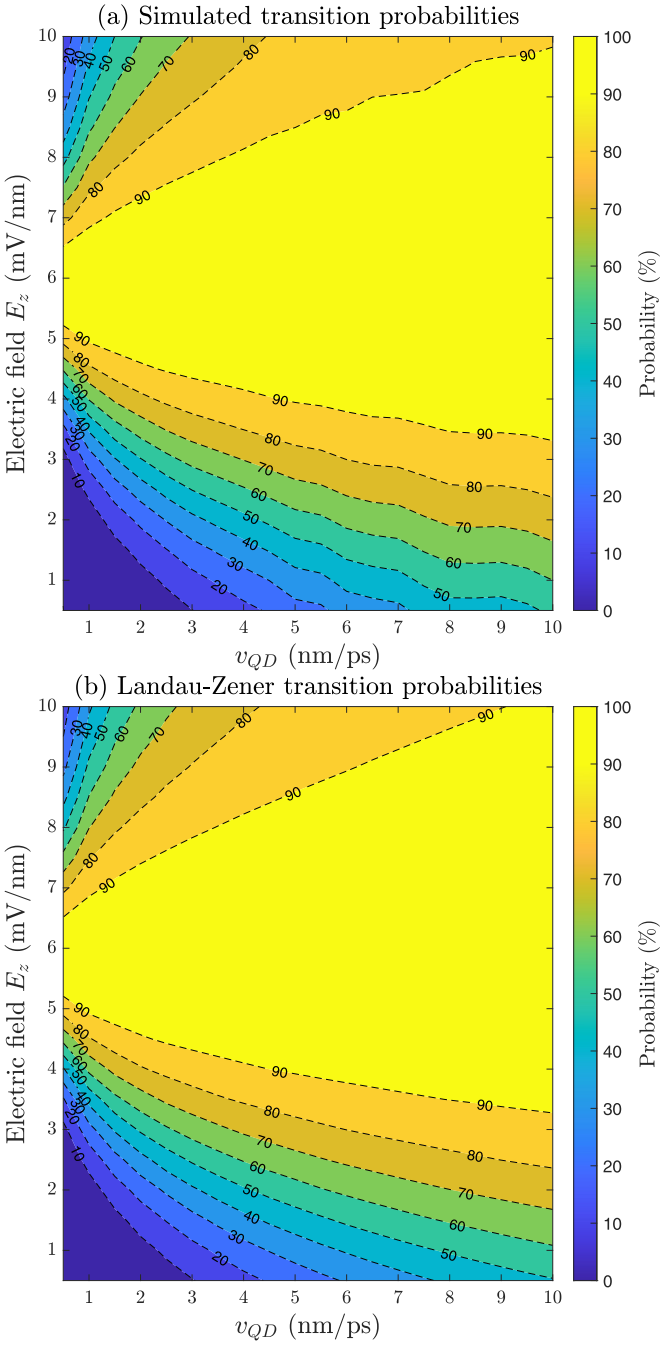


FIG. 9. Result of the Landau-Zener approximation. (a) The simulated transition probabilities ($1 - P_{0,-}$, see main text) in the step model. (b) Transition probabilities under the Landau-Zener approximation in the step model. We can observe a remarkable agreement between our numerical results and those obtained from the Landau-Zener approximation.

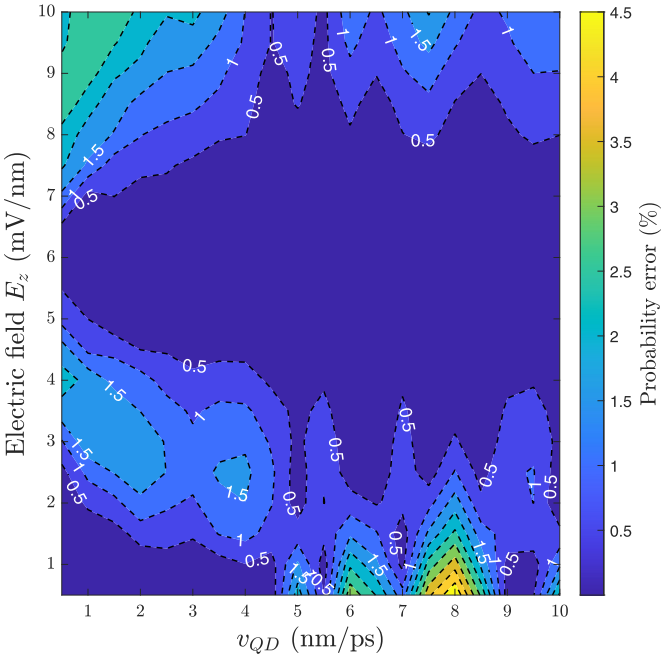


FIG. 10. Difference between the simulated transition probabilities and those obtained under the Landau-Zener approximation. We can see that the Landau-Zener approximation gives good agreement with our numerical results. The maximum value of the relative error was 1.0%, not shown in this figure.

VI. QUBIT APPLICATION

Validity of the two-level system and qubit application. The choice of the wide energy level spacing $\Delta\epsilon = \hbar\omega = 2\,\text{meV}$ for the orbital states allows one to prevent transitions to higher orbital states, thus allowing for a two-level valley system to form. However large values of v_{QD} can still lead to leakage to higher orbitals, and the electric field E_z also plays a complex role. Regardless, there does exist a range of parameters for which the probability of higher orbital states is negligible and a set of qubit basis states is realized. We can estimate the range of parameters for which the final state is a two-level system numerically by summing the probabilities of the two states $\psi_{0,-}$ and $\psi_{0,+}$ forming our preferred two-level system, as shown in Fig. 11. Using the two lowest energy states as a computational basis, our model effectively describes the time-evolution of a pure valley qubit with all-electrical control.

Coherence time and protection from charge noise. The use of the valley degrees of freedom to encode the quantum information is interesting in that it provides certain immunity to charge noise [21]. Charge noise is one of the leading sources of decoherence of silicon qubits [21–24]. The resistance to charge noise has been experimentally verified through Laudau-Zener interferometry in a Si/SiGe double quantum dot by Mi *et al.* [25]. Previous implementations of qubits leveraging valley states in double quantum dots have shown a coherence time on the scale of nanoseconds [7,8,26,27]. Although those qubits were implemented in double quantum dots, whilst our system is a single quantum dot, we expect the coherence time of our architecture to have a similar order of magnitude.

Experimental advantage. The all-electrical control of the final state probabilities is critical for scalability, as one would not need magnetic fields for qubit manipulation as in most spin qubit implementations [23,24]. The absence of applied magnetic field, and hence large microwave antennas, makes the integration of such a system significantly more simple. A second advantage is that we are not constrained by any adiabatic condition, as a consequence, provided the

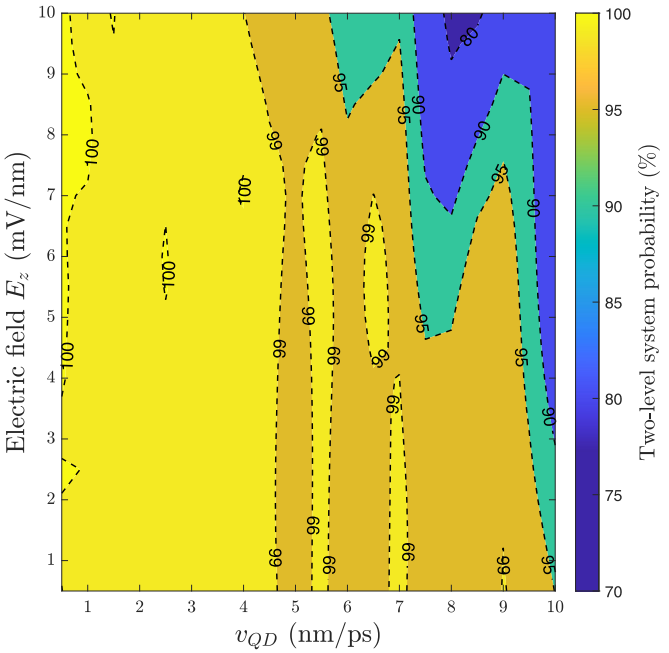


FIG. 11. Evolution of the probability of being in a two-level system based on the two lowest valley states $\psi_{0,-}$ and $\psi_{0,+}$ at the final simulation time. The two-level system probability is defined to be the sum of the probabilities of the states $\psi_{0,-}$ and $\psi_{0,+}$. The bright yellow/orange regions give a range of parameters for which the final state is a good two-level system suitable for qubit applications.

decoherence times are similar to that of other hybrid valley qubits, we can perform orders of magnitude more gate operations.

Coupling, readout, and other issues. Serious difficulties are to be overcome for this scheme to be usable in practice. First, the engineering of the control pulses may pose significant experimental hurdles. As argued by Boross *et al.*, it may be somewhat achievable using a double quantum dot architecture and varying the barrier and detuning to move the electron through the step [28]. However, this procedure will inevitably be complicated by the additional gates needed to apply the electric field E_z, due to the existence of cross couplings. Another issue may be raised concerning the picosecond scales of the pulses, but one should remember that the control is determined by the spatial movement of the center of the quantum dot. As an example, Yamahata *et al.* demonstrated a movement of the electron on similar time scales in a single-electron pump based on a silicon nanowire [2]. Furthermore, we have been limiting ourselves to constant speeds for ξ, and hence more complicated trajectories are unexplored and may partly solve some of these issues.

We should also mention that finite barrier heights and diffused interfaces present in realistic devices significantly suppress the valley splitting [6,29]. Critically, if the avoided crossing in the spectrum remains, the physics observed will be similar. The reduced magnitude of the valley splitting will facilitate transitions to higher excited states because of the smaller energy gap. A possible solution could be decreasing the strength of the perturbations, i.e., the quantum dot speed. This will also have the advantage of potentially reducing the complexity of engineering fast control pulses, at the expense of the speed of operation.

Finally, both readout and coupling to other such qubits has not been explored and may pose a significant technical challenge for the scalability of the proposed scheme. A potential avenue towards readout could be implemented with a form of charge sensing, as is done in most silicon qubits [24]. This would require the incorporation of another dot after the step, and adjusting the energy levels so that only the highest energy valley states tunnels to the second dot.

VII. CONCLUSION

To summarize our paper, we have shown that displacing a quantum dot potential through an interface step leads to an anticrossing in the spectrum of the two lowest energetic states. A critical observation, which was verified with tight-binding calculations of NEMO 3D, is that the energy gap at the anticrossing can be controlled by applying an electric field perpendicular to the interface. Since the transition probabilities depend on the energy gap, and the latter is electrically controlled, we can achieve all-electrical control of the final state probabilities. There is a range of parameters for which the final state behaves as a charge qubit encoded on valley states, though readout and coupling have not been explored.

There are two main limitations of our results. The first is the qualitative nature due to our highly idealized modeling. Indeed, we enforced hard-wall boundary conditions for the z confinement, so that the wave function does not penetrate through the SiGe layers, while a more realistic choice would be adding a finite height barrier of around 150 meV. We also neglected both the strain and alloy disorder of the Ge atoms. We also note that our work is only valid in the low-density limit hence ignoring both Coulomb and exchange effects. Despite these remarks, the results obtained from NEMO 3D indicate that the physics discussed should still be applicable to real devices, with only qualitative modifications. Finally, the precise engineering of both the device geometry and the applied voltages for adequate control poses additional experimental challenges.

The second limitation is due to the experimental feasibility, namely, the precise control of the fast electrical pulses to move the quantum dot and the existence of a single-atomic step. Indeed, we expect multiple steps to form over the spatial range chosen for our simulations. We have also neglected relaxation mechanism, as these are supposed to occur on a timescale greater than the operation times.

Nevertheless, nonadiabatic control of valley states may open quantum information processing schemes. In this paper, we have limited ourselves to the study of a single quantum dot, but we suspect that the results could be adaptable to more complicated double-dot systems making the possible implementation of these ideas more realistic. Additionally, in some emerging 2D and topological materials, spin and valleys are strongly momentum locked, thus fast manipulation of valleys could lead to nonadiabatic control of spins.

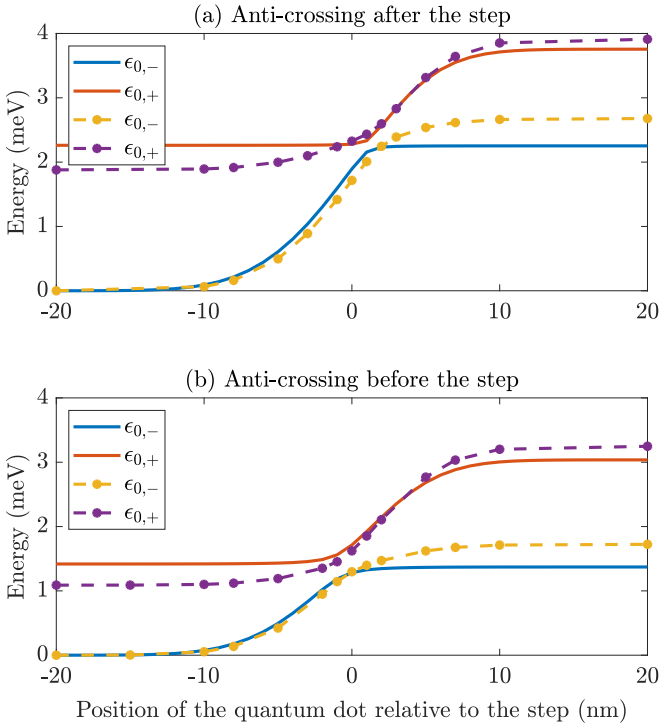


FIG. 12. Evolution of the spectrum with the location of the quantum dot relative to the step at 0 nm. The anticrossing can happen either before (a) or after (b) the step, a fact captured in both our step model (solid lines) and NEMO 3D's 20 band $sp^3d^5s^*$ model (dotted lines). In (a), the quantum well width is 16.5 monolayers for the solid lines and 18 monolayers for NEMO 3D. In (b), the quantum well width is 21 monolayers for the solid lines, and 20 monolayers for NEMO 3D. The applied electric field is $E_z = 10$ mV/nm for all the curves in this figure.

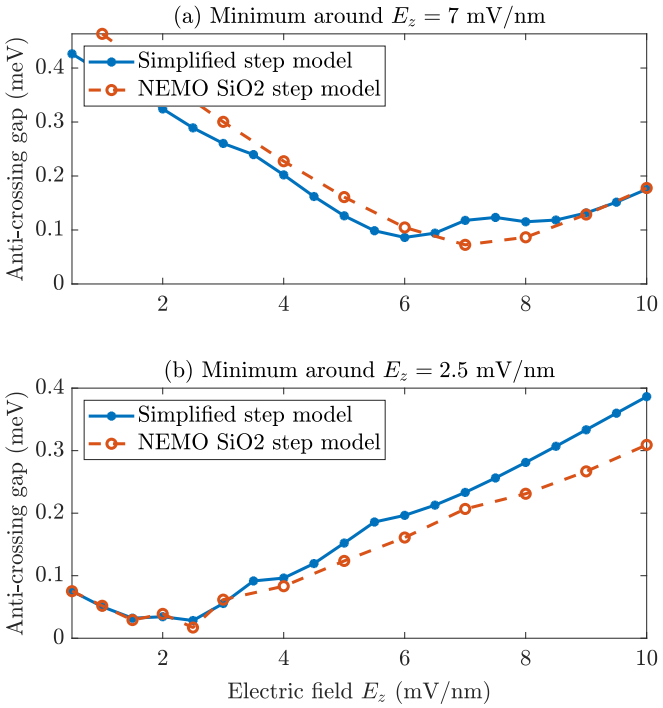


FIG. 13. Evolution of the anticrossing energy gap with the electric field in the step model (solid-dotted blue) and NEMO simulations (dashed-circled red). Depending on the quantum well width, the magnitude and location of the minimum of the gap can change. (a) In the step model, we used 16.5 monolayers, while 19 monolayers were used for NEMO 3D. (b) In the step model, we used 19 monolayers, while 20 monolayers were used for NEMO 3D.

ACKNOWLEDGMENTS

We acknowledge useful discussions with Edyta Osika concerning alternative simulation methods, and Vyacheslavs Kashcheyevs concerning the anticrossing. This work was partly funded under the Nicolas Baudin initiative and Thales Australia. R.R. acknowledges support from the US Army Research Office under Grant No. W911NF-17-1-0202. The research was undertaken with the assistance of re-sources and services from the National Computational Infrastructure (NCI) under NCMAS 2020 and 2021 allocation, supported by the Australian Government. This work was also supported with supercomputing resources provided by the Phoenix HPC service at the University of Adelaide.

APPENDIX A: VALIDATION OF THE MODEL

Objective. Most results discussed in the main text depend on two critical facts: the existence of an anticrossing between the two lowest valley states, and the relative control of the anticrossing gap with the electric field E_z. While hybrid tight-binding/effective mass models have been used to model interface steps, in this Appendix we propose to verify that the main results are supported by more sophisticated calculations, using NEMO 3D's 20 band $sp^3d^5s^*$ model [10].

NEMO model. In our step model of Sec. II B, we used hard-wall boundary conditions, which corresponds to an infinite barrier height. To model this in NEMO 3D, we utilised a SiO2 interface, which has a large barrier height of 3 eV. To reduce simulation time, we also adopted a tighter confinement for the quantum dot. In all results presented in this Appendix, the curvature of the quantum dot was set to $k = 10^{-1}$ meV/nm^2, which amounts to an energy level spacing $\Delta\epsilon = \hbar\omega \approx 9$ meV.

Limitations. In their paper, Boykin *et al.* showed that the two-band model they proposed correctly reproduced the trends expected for the valley splitting evolution with the width of the quantum well. In particular, the valley splittings have the correct order of magnitude but differ from NEMO 3D calculations. As such, their model is qualitative and not quantitative, and we expect to observe the same differences with our model. Similarly, we shall focus on only verifying that the critical trends necessary for our conclusions, namely the anticrossing and the control of the energy gap, are mirrored by NEMO 3D.

Results. In Fig. 12, we compare spectra obtained using our step model (solid lines) and those obtained from NEMO 3D calculations (dotted lines). The reference energy was set to 0 to facilitate the comparison of both spectra. We remark that in both simulations, the location of the anticrossing can happen before or after the step depending on the quantum well width. In both cases, the existence of the anticrossing is verified by NEMO 3D.

Similarly, the tuning of the anticrossing gap with the electric field is observed in both simulations, as shown in Fig. 13. As mentioned in the main text, the tuning of the gap with the electric field depends on the quantum well width. Some key features are exhibited by both our step model and the NEMO 3D calculations. Namely, the range of the tuning of the gap, the existence of a minimum, and the location of this minimum all depend on the quantum well width.

APPENDIX B: ESTIMATION OF THE PROBABILITY OF THE SECOND EXCITED ORBITAL STATE IN THE IDEAL MODEL

In this Appendix we estimate the form of the probability P_4 of the state $\psi_4 = \psi_{2,-}$ in the ideal model. We adopt the notations of Sec. III B. From Eqs. (4.174) and (9.97) of Ref. [19], we can estimate that the probability amplitude of the second excited state $c_4(t)$ is related to the amplitude of the first excited state $c_2(t)$ by:

$$\dot{c_4}(t) = \frac{c_2(t)}{\hbar\omega}\langle\varphi_2(t)|\frac{\partial\hat{H}}{\partial t}|\varphi_1(t)\rangle e^{i\omega(t-t_0)}.$$

Following Eq. (7), we find that $\langle\varphi_2(t)|\frac{\partial\hat{H}}{\partial t}|\varphi_1(t)\rangle = -m\omega^2\dot{\xi}\sqrt{\frac{\hbar}{m\omega}}$. Using Eq. (8) we find

$$\dot{c_2}(t) = -i\omega\left(\frac{v_{QD}}{v_{\max}}\right)^2\left(e^{2i\omega(t-t_0)} - e^{i\omega(t-t_0)}\right).$$

The integration is straightforward and gives

$$c_2(t) = 2\left(\frac{v_{QD}}{v_{\max}}\right)^2 \sin\left(\frac{\omega}{2}(t-t_0)\right)^2 e^{i\omega(t-t_0)}.$$

Finally, the transition probability to the second excited state can be computed as

$$\begin{aligned} P_{0\to4}(t) &= 4\left(\frac{v_{QD}}{v_{\max}}\right)^4 \left|\sin\left(\frac{\omega}{2}(t-t_0)\right)\right|^4 \\ &= P_{0\to2}(t)^2. \end{aligned} \tag{B1}$$

Comparing Eq. (9) and Eq. (B1) we see that the probability of the electron being in the state ψ_4 at time t is the square of it being in the state ψ_2.

[1] B. Kaestner and V. Kashcheyevs, Non-adiabatic quantized charge pumping with tunable-barrier quantum dots: A review of current progress, Rep. Prog. Phys. **78**, 103901 (2015).

[2] G. Yamahata, S. Ryu, N. Johnson, H.-S. Sim, A. Fujiwara, and M. Kataoka, Picosecond coherent electron motion in a silicon single-electron source, Nat. Nanotechnol. **14**, 1019 (2019).

[3] F. A. Zwanenburg, A. S. Dzurak, A. Morello, M. Y. Simmons, L. C. L. Hollenberg, G. Klimeck, S. Rogge, S. N. Coppersmith, and M. A. Eriksson, Silicon quantum electronics, Rev. Mod. Phys. **85**, 961 (2013).

[4] R. Rahman, J. Verduijn, N. Kharche, G. P. Lansbergen, G. Klimeck, L. C. L. Hollenberg, and S. Rogge, Engineered valley-orbit splittings in quantum-confined nanostructures in silicon, Phys. Rev. B **83**, 195323 (2011).

[5] M. Friesen and S. N. Coppersmith, Theory of valley-orbit coupling in a Si/SiGe quantum dot, Phys. Rev. B **81**, 115324 (2010).

[6] B. Tariq and X. Hu, Effects of interface steps on the valley-orbit coupling in a Si/SiGe quantum dot, Phys. Rev. B **100**, 125309 (2019).

[7] J. Schoenfield, B. Freeman, and H. Jiang, Coherent manipulation of valley states at multiple charge configurations of a silicon quantum dot device, Nat. Commun. **8**, 64 (2017).

[8] N. Penthorn, J. Schoenfield, J. D. Rooney, L. F. Edge, and H. W. Jiang, Two-axis quantum control of a fast valley qubit in silicon, npj Quantum Inf. **5**, 94 (2019).

[9] P. Boross, G. Széchenyi, D. Culcer, and A. Pályi, Control of valley dynamics in silicon quantum dots in the presence of an interface step, Phys. Rev. B **94**, 035438 (2016).

[10] F. Oyafuso, G. Klimeck, R. Bowen, and T. Boykin, Nano-electronic 3-D (nemo 3-D) simulation of multimillion atom quantum dot systems, in *International Conference on Simulation of Semiconductor Processes and Devices* (IEEE, 2002), pp. 163–166.

[11] J. R. Rubbmark, M. M. Kash, M. G. Littman, and D. Kleppner, Dynamical effects at avoided level crossings: A study of the Landau-Zener effect using Rydberg atoms, Phys. Rev. A **23**, 3107 (1981).

[12] T. B. Boykin, G. Klimeck, M. Friesen, S. N. Coppersmith, P. von Allmen, F. Oyafuso, and S. Lee, Valley splitting in low-density quantum-confined heterostructures studied using tight-binding models, Phys. Rev. B **70**, 165325 (2004).

[13] T. B. Boykin, G. Klimeck, M. A. Eriksson, M. Friesen, S. N. Coppersmith, P. von Allmen, F. Oyafuso, and S. Lee, Valley splitting in strained silicon quantum wells, Appl. Phys. Lett. **84**, 115 (2004).

[14] C. Teichert, Self-organization of nanostructures in semiconductor heteroepitaxy, Phys. Rep. **365**, 335 (2002).

[15] J. Mysliveek, C. Schelling, F. Schffler, G. Springholz, P. milauer, J. Krug, and B. Voigtlnder, On the microscopic origin of the kinetic step bunching instability on vicinal Si(001), Surf. Sci. **520**, 193 (2002).

[16] P. G. Evans, D. E. Savage, J. R. Prance, C. B. Simmons, M. G. Lagally, S. N. Coppersmith, M. A. Eriksson, and T. U. Schlli, Nanoscale distortions of Si quantum wells in Si/SiGe quantum-electronic heterostructures, Adv. Mater. **24**, 5217 (2012).

[17] Y. H. Phang, C. Teichert, M. G. Lagally, L. J. Peticolos, J. C. Bean, and E. Kasper, Correlated-interfacial-roughness anisotropy in $Si_{1-x}Ge_x$/Si superlattices, Phys. Rev. B **50**, 14435 (1994).

[18] J. Crank and P. Nicolson, A practical method for numerical evaluation of solutions of partial differential equations of the heat-conduction type, Math. Proc. Cambridge Philos. Soc. **43**, 50 (1947).

[19] B. H. Bransden and C. J. Joachain, *Quantum Mechanics, 2nd Edition* (Pearson, London, 2000).

[20] M. Friesen, S. Chutia, C. Tahan, and S. N. Coppersmith, Valley splitting theory of SiGe/Si/SiGe quantum wells, Phys. Rev. B **75**, 115318 (2007).

[21] D. Culcer, A. L. Saraiva, B. Koiller, X. Hu, and S. Das Sarma, Valley-Based Noise-Resistant Quantum Computation

using Si Quantum Dots, Phys. Rev. Lett. **108**, 126804 (2012).

[22] D. Culcer, X. Hu, and S. Das Sarma, Dephasing of Si spin qubits due to charge noise, Appl. Phys. Lett. **95**, 073102 (2009).

[23] T. D. Ladd and M. S. Carroll, Silicon qubits, in *Encyclopedia of Modern Optics*, 2nd ed. (Elsevier, Amsterdam, 2018).

[24] A. Chatterjee, P. Stevenson, S. De Franceschi, A. Morello, N. P. de Leon, and F. Kuemmeth, Semiconductor qubits in practice, Nat. Rev. Phys. **3**, 157 (2021).

[25] X. Mi, S. Kohler, and J. R. Petta, Landau-Zener interferometry of valley-orbit states in Si/SiGe double quantum dots, Phys. Rev. B **98**, 161404(R) (2018).

[26] C. H. Yang, A. Rossi, R. Ruskov, N. S. Lai, F. A. Mohiyaddin, S. Lee, C. Tahan, G. Klimeck, A. Morello, and A. S. Dzurak, Spin-valley lifetimes in a silicon quantum dot with tunable valley splitting, Nat. Commun. **4**, 2069 (2013).

[27] D. Kim, D. R. Ward, C. B. Simmons, D. E. Savage, M. G. Lagally, M. Friesen, S. N. Coppersmith, and M. A. Eriksson, High-fidelity resonant gating of a silicon-based quantum dot hybrid qubit, npj Quantum Inf. **1**, 15004 (2015).

[28] D. M. Zajac, T. M. Hazard, X. Mi, K. Wang, and J. R. Petta, A reconfigurable gate architecture for Si/SiGe quantum dots, Appl. Phys. Lett. **106**, 223507 (2015).

[29] T. B. Boykin, N. Kharche, and G. Klimeck, Valley splitting in finite barrier quantum wells, Phys. Rev. B **77**, 245320 (2008).

Bibliography

[1] Alan Gardin et al. “Manifestation of the Coupling Phase in Microwave Cavity Magnonics”. In: *Physical Review Applied* 19.5 (May 2023), p. 054069. DOI: 10.1103/physrevapplied.19.054069. arXiv: 2212.05389 [quant-ph].

[2] Alan Gardin et al. “Engineering synthetic gauge fields through the coupling phases in cavity magnonics”. In: *Physical Review Applied* 21.6 (June 13, 2024), p. 064033. DOI: 10.1103/PhysRevApplied.21.064033. arXiv: 2312.04915 [quant-ph]. URL: https://link.aps.org/doi/10.1103/PhysRevApplied.21.064033 (visited on 06/18/2024).

[3] Alan Gardin et al. *Level attraction from interference in two-tone driving*. arXiv:2404.17108. type: article. arXiv, Apr. 25, 2024. arXiv: 2404.17108. URL: http://arxiv.org/abs/2404.17108 (visited on 04/29/2024).

[4] Alan Gardin et al. “Nonadiabatic quantum control of valley states in silicon”. In: *Physical Review B* 105.7 (Feb. 2022), p. 075406. DOI: 10.1103/physrevb.105.075406.

[5] Michael A. Nielsen and Isaac L. Chuang. *Quantum Computation and Quantum Information: 10th Anniversary Edition*. 10th. USA: Cambridge University Press, 2011. ISBN: 1107002176.

[6] Smite-Meister. *Bloch sphere.svg*. URL: https://en.wikipedia.org/wiki/File:Bloch_sphere.svg.

[7] Creative Commons. “Creative Commons Attribution-Share Alike 3.0 Unported”. In: (). URL: https://creativecommons.org/licenses/by-sa/3.0/deed.en.

[8] J.R. Johansson, P.D. Nation, and Franco Nori. “QuTiP: An open-source Python framework for the dynamics of open quantum systems”. In: *Computer Physics Communications* 183.8 (Aug. 2012), pp. 1760–1772. ISSN: 0010-4655. DOI: 10.1016/j.cpc.2012.02.021.

[9] J.R. Johansson, P.D. Nation, and Franco Nori. “QuTiP 2: A Python framework for the dynamics of open quantum systems”. In: *Computer Physics Communications* 184.4 (Apr. 2013), pp. 1234–1240. ISSN: 0010-4655. DOI: 10.1016/j.cpc.2012.11.019.

[10] C. Cohen-Tannoudji, B. Diu, and F. Laloë. *Mécanique quantique: Tome I*. Savoirs actuels. Série Physique. EDP sciences, 2018. ISBN: 9782271124982. URL: https://books.google.com.au/books?id=thq5vAEACAAJ.

[11] Tom Lancaster and Stephen J Blundell. *Quantum field theory for the gifted amateur*. Oxford: Oxford University Press, 2014. DOI: 0199699321. URL: https://cds.cern.ch/record/1629337.

[12] H. P. Robertson. “The Uncertainty Principle”. In: *Physical Review* 34.1 (July 1, 1929), pp. 163–164. DOI: 10.1103/PhysRev.34.163. URL: https://link.aps.org/doi/10.1103/PhysRev.34.163 (visited on 11/21/2023).

[13] P. T. Cochrane, G. J. Milburn, and W. J. Munro. “Macroscopically distinct quantum-superposition states as a bosonic code for amplitude damping”. In: *Physical Review A* 59.4 (Apr. 1999), pp. 2631–2634. DOI: 10.1103/physreva.59.2631.

[14] Atharv Joshi, Kyungjoo Noh, and Yvonne Y Gao. “Quantum information processing with bosonic qubits in circuit QED”. In: *Quantum Science and Technology* 6.3 (Apr. 2021), p. 033001. DOI: 10.1088/2058-9565/abe989.

[15] Wojciech Hubert Zurek. "Decoherence, einselection, and the quantum origins of the classical". In: *Reviews of Modern Physics* 75.3 (May 2003), pp. 715–775. DOI: 10.1103/revmodphys.75.715.

[16] Shasha Zheng et al. "Tutorial: Nonlinear magnonics". In: *Journal of Applied Physics* 134.15 (Oct. 2023). DOI: 10.1063/5.0152543. arXiv: 2303.16313 [cond-mat.mes-hall].

[17] H.Y. Yuan et al. "Quantum magnonics: When magnon spintronics meets quantum information science". In: *Physics Reports* 965 (June 2022), pp. 1–74. DOI: 10.1016/j.physrep.2022.03.002.

[18] H. M. Wiseman, S. J. Jones, and A. C. Doherty. "Steering, Entanglement, Nonlocality, and the Einstein-Podolsky-Rosen Paradox". In: *Physical Review Letters* 98.14 (Apr. 6, 2007), p. 140402. DOI: 10.1103/PhysRevLett.98.140402. URL: https://link.aps.org/doi/10.1103/PhysRevLett.98.140402 (visited on 11/23/2023).

[19] S. J. Jones, H. M. Wiseman, and A. C. Doherty. "Entanglement, Einstein-Podolsky-Rosen correlations, Bell nonlocality, and steering". In: *Physical Review A* 76.5 (Nov. 28, 2007), p. 052116. DOI: 10.1103/PhysRevA.76.052116. URL: https://link.aps.org/doi/10.1103/PhysRevA.76.052116 (visited on 11/23/2023).

[20] E. G. Cavalcanti et al. "Experimental criteria for steering and the Einstein-Podolsky-Rosen paradox". In: *Physical Review A* 80.3 (Sept. 18, 2009), p. 032112. DOI: 10.1103/PhysRevA.80.032112. URL: https://link.aps.org/doi/10.1103/PhysRevA.80.032112 (visited on 11/23/2023).

[21] Marco Túlio Quintino et al. "Inequivalence of entanglement, steering, and Bell nonlocality for general measurements". In: *Physical Review A* 92.3 (Sept. 2015), p. 032107. DOI: 10.1103/physreva.92.032107.

[22] A. Einstein, B. Podolsky, and N. Rosen. "Can Quantum-Mechanical Description of Physical Reality Be Considered Complete?" In: *Physical Review* 47.10 (May 1935), pp. 777–780. DOI: 10.1103/physrev.47.777.

[23] M. D. Reid et al. "Colloquium: The Einstein-Podolsky-Rosen paradox: From concepts to applications". In: *Reviews of Modern Physics* 81.4 (Dec. 2009), pp. 1727–1751. DOI: 10.1103/revmodphys.81.1727.

[24] Roope Uola et al. "Quantum steering". In: *Reviews of Modern Physics* 92.1 (Mar. 2020), p. 015001. DOI: 10.1103/revmodphys.92.015001.

[25] Nicolas Brunner et al. "Bell nonlocality". In: *Reviews of Modern Physics* 86.2 (Apr. 2014), pp. 419–478. DOI: 10.1103/revmodphys.86.419.

[26] Ingemar Bengtsson and Karol Zyczkowski. "A brief introduction to multipartite entanglement". In: (Dec. 2016). DOI: 10.48550/ARXIV.1612.07747. arXiv: 1612.07747 [quant-ph].

[27] Gerardo Adesso and Fabrizio Illuminati. "Entanglement in continuous-variable systems: recent advances and current perspectives". In: *Journal of Physics A: Mathematical and Theoretical* 40.28 (June 2007), p. 7821. ISSN: 1751-8121. DOI: 10.1088/1751-8113/40/28/S01. URL: https://dx.doi.org/10.1088/1751-8113/40/28/S01 (visited on 11/23/2023).

[28] G. Vidal and R. F. Werner. "Computable measure of entanglement". In: *Physical Review A* 65.3 (Feb. 2002), p. 032314. DOI: 10.1103/physreva.65.032314.

[29] Ioannis Kogias et al. "Quantification of Gaussian Quantum Steering". In: *Physical Review Letters* 114.6 (Feb. 12, 2015), p. 060403. DOI: 10.1103/PhysRevLett.114.060403. URL: https://link.aps.org/doi/10.1103/PhysRevLett.114.060403 (visited on 11/23/2023).

[30] Gerardo Adesso and Fabrizio Illuminati. "Continuous variable tangle, monogamy inequality, and entanglement sharing in Gaussian states of continuous variable systems". In: *New Journal of Physics* 8.1 (Jan. 2006), p. 15. ISSN: 1367-2630. DOI: 10.1088/1367-2630/8/1/015. URL: https://dx.doi.org/10.1088/1367-2630/8/1/015 (visited on 11/23/2023).

[31] Q. Y. He and M. D. Reid. "Genuine Multipartite Einstein-Podolsky-Rosen Steering". In: *Physical Review Letters* 111.25 (Dec. 18, 2013), p. 250403. DOI: 10.1103/PhysRevLett.111.250403. URL: https://link.aps.org/doi/10.1103/PhysRevLett.111.250403 (visited on 11/23/2023).

[32] Yu Xiang et al. "Multipartite Gaussian steering: Monogamy constraints and quantum cryptography applications". In: *Physical Review A* 95.1 (Jan. 12, 2017), p. 010101. DOI: 10.1103/PhysRevA.95.010101. URL: https://link.aps.org/doi/10.1103/PhysRevA.95.010101 (visited on 11/23/2023).

[33] M. Fox. *Quantum Optics: An Introduction*. Oxford Master Series in Physics. OUP Oxford, 2006. ISBN: 9780198566731. URL: https://books.google.com.au/books?id=2%5C_ZP-LDF9jkC.

[34] D.F. Walls and Gerard J. Milburn. *Quantum Optics*. 2nd ed. Springer-Verlag Berlin Heidelberg, 2008. DOI: 10.1007/978-3-540-28574-8.

[35] Ajbura. "Photon bunching.svg". In: (Oct. 1, 2018). URL: https://commons.wikimedia.org/wiki/File:Photon_bunching.svg.

[36] Creative Commons. "Creative Commons Attribution-Share Alike 4.0 International license". In: (). URL: https://creativecommons.org/licenses/by-sa/4.0/deed.en.

[37] Daniel. *What is the difference between quantum sensing and quantum metrology?* Physics Stack Exchange. June 2, 2021. URL: https://physics.stackexchange.com/q/497009 (visited on 12/06/2023).

[38] C. L. Degen, F. Reinhard, and P. Cappellaro. "Quantum sensing". In: *Reviews of Modern Physics* 89.3 (July 25, 2017), p. 035002. DOI: 10.1103/RevModPhys.89.035002. URL: https://link.aps.org/doi/10.1103/RevModPhys.89.035002 (visited on 12/31/2023).

[39] Michael A. Taylor and Warwick P. Bowen. "Quantum metrology and its application in biology". In: *Physics Reports*. Quantum metrology and its application in biology 615 (Feb. 23, 2016), pp. 1–59. ISSN: 0370-1573. DOI: 10.1016/j.physrep.2015.12.002. URL: https://www.sciencedirect.com/science/article/pii/S0370157315005001 (visited on 12/06/2023).

[40] Ben Stray et al. "Quantum sensing for gravity cartography". In: *Nature* 602.7898 (Feb. 2022), pp. 590–594. ISSN: 1476-4687. DOI: 10.1038/s41586-021-04315-3. URL: https://www.nature.com/articles/s41586-021-04315-3 (visited on 12/14/2023).

[41] J. Aasi et al. "Enhanced sensitivity of the LIGO gravitational wave detector by using squeezed states of light". In: *Nature Photonics* 7.8 (Aug. 2013), pp. 613–619. ISSN: 1749-4893. DOI: 10.1038/nphoton.2013.177. URL: https://www.nature.com/articles/nphoton.2013.177 (visited on 12/31/2023).

[42] Johannes Franke et al. "Quantum-enhanced sensing on optical transitions through finite-range interactions". In: *Nature* 621.7980 (Sept. 2023), pp. 740–745. ISSN: 1476-4687. DOI: 10.1038/s41586-023-06472-z. URL: https://www.nature.com/articles/s41586-023-06472-z (visited on 12/14/2023).

[43] M. Auzinsh et al. "Can a Quantum Nondemolition Measurement Improve the Sensitivity of an Atomic Magnetometer?" In: *Physical Review Letters* 93.17 (Oct. 19, 2004), p. 173002. DOI: 10.1103/PhysRevLett.93.173002. URL: https://link.aps.org/doi/10.1103/PhysRevLett.93.173002 (visited on 12/14/2023).

[44] Géza Tóth and Iagoba Apellaniz. "Quantum metrology from a quantum information science perspective". In: *Journal of Physics A: Mathematical and Theoretical* 47.42 (Oct. 2014), p. 424006. ISSN: 1751-8121. DOI: 10.1088/1751-8113/47/42/424006. URL: https://dx.doi.org/10.1088/1751-8113/47/42/424006 (visited on 12/06/2023).

[45] Dong Li et al. "Phase sensitivity at the Heisenberg limit in an SU(1,1) interferometer via parity detection". In: *Physical Review A* 94.6 (Dec. 19, 2016), p. 063840. DOI: 10.1103/PhysRevA.94.063840. URL: https://link.aps.org/doi/10.1103/PhysRevA.94.063840 (visited on 12/07/2023).

[46] Jeffrey H. Shapiro. "The Quantum Illumination Story". In: *IEEE Aerospace and Electronic Systems Magazine* 35.4 (Apr. 2020), pp. 8–20. DOI: 10.1109/maes.2019.2957870.

[47] Seth Lloyd. "Enhanced Sensitivity of Photodetection via Quantum Illumination". In: *Science* 321.5895 (Sept. 12, 2008), pp. 1463–1465. DOI: 10.1126/science.1160627. URL: https://www.science.org/doi/10.1126/science.1160627 (visited on 12/30/2023).

[48] Si-Hui Tan et al. "Quantum Illumination with Gaussian States". In: *Physical Review Letters* 101.25 (Dec. 18, 2008), p. 253601. DOI: 10.1103/PhysRevLett.101.253601. URL: https://link.aps.org/doi/10.1103/PhysRevLett.101.253601 (visited on 12/30/2023).

[49] Shabir Barzanjeh et al. "Microwave Quantum Illumination". In: *Physical Review Letters* 114.8 (Feb. 27, 2015), p. 080503. DOI: 10.1103/PhysRevLett.114.080503. URL: https://link.aps.org/doi/10.1103/PhysRevLett.114.080503 (visited on 12/30/2023).

[50] Ricardo Gallego Torromé, Nadya Ben Bekhti-Winkel, and Peter Knott. "Introduction to quantum radar". In: (June 2020). DOI: 10.48550/ARXIV.2006.14238. arXiv: 2006.14238 [quant-ph].

[51] Giacomo Sorelli et al. "Detecting a Target With Quantum Entanglement". In: *IEEE Aerospace and Electronic Systems Magazine* 37.5 (May 2022), pp. 68–90. DOI: 10.1109/maes.2021.3116323.

[52] H. J. Kimble. "The quantum internet". In: *Nature* 453.7198 (June 2008), pp. 1023–1030. ISSN: 1476-4687. DOI: 10.1038/nature07127. URL: https://www.nature.com/articles/nature07127 (visited on 01/01/2024).

[53] D. Dieks. "Communication by EPR devices". In: *Physics Letters A* 92.6 (Nov. 1982), pp. 271–272. ISSN: 0375-9601. DOI: 10.1016/0375-9601(82)90084-6.

[54] W. K. Wootters and W. H. Zurek. "A single quantum cannot be cloned". In: *Nature* 299.5886 (Oct. 1982), pp. 802–803. ISSN: 1476-4687. DOI: 10.1038/299802a0. URL: https://www.nature.com/articles/299802a0 (visited on 01/03/2024).

[55] Charles H. Bennett et al. "Teleporting an unknown quantum state via dual classical and Einstein-Podolsky-Rosen channels". In: *Physical Review Letters* 70.13 (Mar. 1993), pp. 1895–1899. ISSN: 0031-9007. DOI: 10.1103/physrevlett.70.1895.

[56] Xiao-Min Hu et al. "Progress in quantum teleportation". In: *Nature Reviews Physics* 5.6 (June 2023), pp. 339–353. ISSN: 2522-5820. DOI: 10.1038/s42254-023-00588-x. URL: https://www.nature.com/articles/s42254-023-00588-x (visited on 11/21/2023).

[57] Stephanie Wehner, David Elkouss, and Ronald Hanson. "Quantum internet: A vision for the road ahead". In: *Science* 362.6412 (Oct. 19, 2018), eaam9288. DOI: 10.1126/science.aam9288. URL: https://www.science.org/doi/10.1126/science.aam9288 (visited on 01/01/2024).

[58] Nicolas Gisin and Rob Thew. "Quantum communication". In: *Nature Photonics* 1.3 (Mar. 2007), pp. 165–171. ISSN: 1749-4893. DOI: 10.1038/nphoton.2007.22. URL: https://www.nature.com/articles/nphoton.2007.22 (visited on 12/29/2023).

[59] Nikolai Lauk et al. "Perspectives on quantum transduction". In: *Quantum Science and Technology* 5.2 (Mar. 2020), p. 020501. DOI: 10.1088/2058-9565/ab788a.

[60] Zhonghui Li et al. “Entanglement-Assisted Quantum Networks: Mechanics, Enabling Technologies, Challenges, and Research Directions”. In: *IEEE Communications Surveys & Tutorials* (2023), pp. 1–1. ISSN: 1553-877X. DOI: 10.1109/COMST.2023.3294240. URL: https://ieeexplore.ieee.org/document/10177948 (visited on 11/02/2023).

[61] Nicolas Gisin et al. “Quantum cryptography”. In: *Reviews of Modern Physics* 74.1 (Mar. 8, 2002), pp. 145–195. DOI: 10.1103/RevModPhys.74.145. URL: https://link.aps.org/doi/10.1103/RevModPhys.74.145 (visited on 01/07/2024).

[62] Xiaoyun Wang, Guangwu Xu, and Yang Yu. “Lattice-Based Cryptography: A Survey”. In: *Chinese Annals of Mathematics, Series B* 44.6 (Nov. 1, 2023), pp. 945–960. ISSN: 1860-6261. DOI: 10.1007/s11401-023-0053-6. URL: https://doi.org/10.1007/s11401-023-0053-6 (visited on 12/24/2023).

[63] Julius Hekkala et al. “Implementing Post-quantum Cryptography for Developers”. In: *SN Computer Science* 4.4 (Apr. 29, 2023), p. 365. ISSN: 2661-8907. DOI: 10.1007/s42979-023-01724-1. URL: https://doi.org/10.1007/s42979-023-01724-1 (visited on 12/24/2023).

[64] Anne Broadbent and Christian Schaffner. “Quantum cryptography beyond quantum key distribution”. In: *Designs, Codes and Cryptography* 78.1 (Jan. 1, 2016), pp. 351–382. ISSN: 1573-7586. DOI: 10.1007/s10623-015-0157-4. URL: https://doi.org/10.1007/s10623-015-0157-4 (visited on 12/23/2023).

[65] Akshata Shenoy-Hejamadi, Anirban Pathak, and Srikanth Radhakrishna. “Quantum Cryptography: Key Distribution and Beyond”. In: *Quanta* 6.1 (June 2017), p. 1. DOI: 10.12743/quanta.v6i1.57.

[66] Mohsen Razavi et al. “Quantum key distribution and beyond: introduction”. In: *Journal of the Optical Society of America B* 36.3 (Mar. 2019), QKD1. DOI: 10.1364/josab.36.00qkd1.

[67] Charles H. Bennett and Gilles Brassard. “Quantum cryptography: Public key distribution and coin tossing”. In: *Theoretical Computer Science* 560 (Dec. 2014), pp. 7–11. ISSN: 0304-3975. DOI: 10.1016/j.tcs.2014.05.025.

[68] Vadim Makarov. “Controlling passively quenched single photon detectors by bright light”. In: *New Journal of Physics* 11.6 (June 2009), p. 065003. DOI: 10.1088/1367-2630/11/6/065003.

[69] Lars Lydersen et al. “Hacking commercial quantum cryptography systems by tailored bright illumination”. In: *Nature Photonics* 4.10 (Aug. 2010), pp. 686–689. DOI: 10.1038/nphoton.2010.214.

[70] Z. L. Yuan, J. F. Dynes, and A. J. Shields. “Avoiding the blinding attack in QKD”. In: *Nature Photonics* 4.12 (Dec. 2010), pp. 800–801. DOI: 10.1038/nphoton.2010.269.

[71] Zhihao Wu et al. “Hacking single-photon avalanche detectors in quantum key distribution via pulse illumination”. In: *Optics Express* 28.17 (Aug. 2020), p. 25574. DOI: 10.1364/oe.397962.

[72] N. Gisin et al. “Trojan-horse attacks on quantum-key-distribution systems”. In: *Physical Review A* 73.2 (Feb. 2006), p. 022320. DOI: 10.1103/physreva.73.022320.

[73] Audun Nystad Bugge et al. “Laser Damage Helps the Eavesdropper in Quantum Cryptography”. In: *Physical Review Letters* 112.7 (Feb. 2014), p. 070503. DOI: 10.1103/physrevlett.112.070503.

[74] Vadim Makarov et al. “Creation of backdoors in quantum communications via laser damage”. In: *Physical Review A* 94.3 (Sept. 2016), p. 030302. DOI: 10.1103/physreva.94.030302.

[75] Anqi Huang et al. “Laser-Damage Attack Against Optical Attenuators in Quantum Key Distribution”. In: *Physical Review Applied* 13.3 (Mar. 2020), p. 034017. DOI: 10.1103/physrevapplied.13.034017.

[76] Richard P. Feynman. “Simulating physics with computers”. In: *International Journal of Theoretical Physics* 21.6-7 (June 1982), pp. 467–488. DOI: 10.1007/bf02650179.

[77] Iulia Buluta and Franco Nori. “Quantum Simulators”. In: *Science* 326.5949 (Oct. 2, 2009), pp. 108–111. DOI: 10.1126/science.1177838. URL: https://www.science.org/doi/10.1126/science.1177838 (visited on 01/05/2024).

[78] I. M. Georgescu, S. Ashhab, and Franco Nori. “Quantum simulation”. In: *Reviews of Modern Physics* 86.1 (Mar. 10, 2014), pp. 153–185. DOI: 10.1103/RevModPhys.86.153. URL: https://link.aps.org/doi/10.1103/RevModPhys.86.153 (visited on 01/05/2024).

[79] Christian W. Bauer et al. “Quantum simulation of fundamental particles and forces”. In: *Nature Reviews Physics* 5.7 (July 2023), pp. 420–432. ISSN: 2522-5820. DOI: 10.1038/s42254-023-00599-8. URL: https://www.nature.com/articles/s42254-023-00599-8 (visited on 11/21/2023).

[80] Alexander M. Dalzell et al. “Quantum algorithms: A survey of applications and end-to-end complexities”. In: (Oct. 2023). DOI: 10.48550/ARXIV.2310.03011. arXiv: 2310.03011 [quant-ph].

[81] Sauro Succi et al. “Quantum computing for fluids: where do we stand?” In: (July 2023). DOI: 10.48550/ARXIV.2307.05157. arXiv: 2307.05157 [physics.comp-ph].

[82] D. Aharonov et al. “Adiabatic quantum computation is equivalent to standard quantum computation”. In: *45th Annual IEEE Symposium on Foundations of Computer Science*. 45th Annual IEEE Symposium on Foundations of Computer Science. ISSN: 0272-5428. Oct. 2004, pp. 42–51. DOI: 10.1109/FOCS.2004.8. URL: https://ieeexplore.ieee.org/document/1366223 (visited on 01/05/2024).

[83] Tameem Albash and Daniel A. Lidar. “Adiabatic quantum computation”. In: *Reviews of Modern Physics* 90.1 (Jan. 29, 2018), p. 015002. DOI: 10.1103/RevModPhys.90.015002. URL: https://link.aps.org/doi/10.1103/RevModPhys.90.015002 (visited on 01/05/2024).

[84] Robert Raussendorf and Hans J. Briegel. “A One-Way Quantum Computer”. In: *Physical Review Letters* 86.22 (May 2001), pp. 5188–5191. DOI: 10.1103/physrevlett.86.5188.

[85] Michael A. Nielsen. “Cluster-state quantum computation”. In: *Reports on Mathematical Physics* 57.1 (Feb. 2006), pp. 147–161. DOI: 10.1016/s0034-4877(06)80014-5.

[86] Kishor Bharti et al. “Noisy intermediate-scale quantum algorithms”. In: *Reviews of Modern Physics* 94.1 (Feb. 15, 2022), p. 015004. DOI: 10.1103/RevModPhys.94.015004. URL: https://link.aps.org/doi/10.1103/RevModPhys.94.015004 (visited on 01/05/2024).

[87] R. Jozsa. “Quantum factoring, discrete logarithms, and the hidden subgroup problem”. In: *Computing in Science & Engineering* 3.2 (Mar. 2001), pp. 34–43. ISSN: 1558-366X. DOI: 10.1109/5992.909000. URL: https://ieeexplore.ieee.org/document/909000 (visited on 01/05/2024).

[88] Andrew M. Childs and Wim van Dam. “Quantum algorithms for algebraic problems”. In: *Reviews of Modern Physics* 82.1 (Jan. 15, 2010), pp. 1–52. DOI: 10.1103/RevModPhys.82.1. URL: https://link.aps.org/doi/10.1103/RevModPhys.82.1 (visited on 01/05/2024).

[89] Dylan Herman et al. “Quantum computing for finance”. In: *Nature Reviews Physics* 5.8 (Aug. 2023), pp. 450–465. ISSN: 2522-5820. DOI: 10.1038/s42254-023-00603-1. URL: https://www.nature.com/articles/s42254-023-00603-1 (visited on 11/02/2023).

[90] Kamila Zaman et al. “A Survey on Quantum Machine Learning: Current Trends, Challenges, Opportunities, and the Road Ahead”. In: (Oct. 2023). DOI: 10.48550/ARXIV.2310.10315. arXiv: 2310.10315 [quant-ph].

[91] David P. DiVincenzo. "The Physical Implementation of Quantum Computation". In: *Fortschritte der Physik* 48.9 (2000), pp. 771–783. ISSN: 1521-3978. DOI: 10.1002/1521-3978(200009)48:9/11<771::AID-PROP771>3.0.CO;2-E. URL: https://onlinelibrary.wiley.com/doi/abs/10.1002/1521-3978%28200009%2948%3A9/11%3C771%3A%3AAID-PROP771%3E3.0.CO%3B2-E (visited on 12/11/2023).

[92] Anton Frisk Kockum and Franco Nori. "Quantum Bits with Josephson Junctions". In: *Fundamentals and Frontiers of the Josephson Effect*. Springer International Publishing, 2019, pp. 703–741. DOI: 10.1007/978-3-030-20726-7_17.

[93] Anasua Chatterjee et al. "Semiconductor qubits in practice". In: *Nature Reviews Physics* 3.3 (Feb. 2021), pp. 157–177. ISSN: 2522-5820. DOI: 10.1038/s42254-021-00283-9. URL: http://dx.doi.org/10.1038/s42254-021-00283-9.

[94] Babak Zare Rameshti et al. *Cavity magnonics*. Sept. 2022. DOI: 10.1016/j.physrep.2022.06.001. arXiv: 2106.09312 [cond-mat.mes-hall].

[95] E.G. Rieffel and W.H. Polak. *Quantum Computing: A Gentle Introduction*. MIT Press, 2011. ISBN: 9780262015066.

[96] Jonas Larson, Erik Sjöqvist, and Patrik Öhberg. *Conical Intersections in Physics*. Springer International Publishing, 2020. DOI: 10.1007/978-3-030-34882-3.

[97] Avimita Chatterjee, Koustubh Phalak, and Swaroop Ghosh. "Quantum Error Correction For Dummies". In: (Apr. 2023). DOI: 10.48550/ARXIV.2304.08678. arXiv: 2304.08678 [quant-ph].

[98] Peter W. Shor. "Scheme for reducing decoherence in quantum computer memory". In: *Physical Review A* 52.4 (Oct. 1, 1995), R2493–R2496. DOI: 10.1103/PhysRevA.52.R2493. URL: https://link.aps.org/doi/10.1103/PhysRevA.52.R2493 (visited on 01/06/2024).

[99] Andrew M. Steane. *A Tutorial on Quantum Error Correction*. URL: https://www2.physics.ox.ac.uk/sites/default/files/ErrorCorrectionSteane06.pdf.

[100] Isaac L. Chuang, Debbie W. Leung, and Yoshihisa Yamamoto. "Bosonic quantum codes for amplitude damping". In: *Physical Review A* 56.2 (Aug. 1, 1997), pp. 1114–1125. DOI: 10.1103/PhysRevA.56.1114. URL: https://link.aps.org/doi/10.1103/PhysRevA.56.1114 (visited on 01/06/2024).

[101] Weizhou Cai et al. "Bosonic quantum error correction codes in superconducting quantum circuits". In: *Fundamental Research* 1.1 (Jan. 2021), pp. 50–67. DOI: 10.1016/j.fmre.2020.12.006.

[102] Jérémie Guillaud, Joachim Cohen, and Mazyar Mirrahimi. "Quantum computation with cat qubits". In: *SciPost Physics Lecture Notes* (June 2023). ISSN: 2590-1990. DOI: 10.21468/scipostphyslectnotes.72.

[103] Daniel Gottesman, Alexei Kitaev, and John Preskill. "Encoding a qubit in an oscillator". In: *Physical Review A* 64.1 (June 11, 2001), p. 012310. DOI: 10.1103/PhysRevA.64.012310. URL: https://link.aps.org/doi/10.1103/PhysRevA.64.012310 (visited on 01/06/2024).

[104] Marios H. Michael et al. "New Class of Quantum Error-Correcting Codes for a Bosonic Mode". In: *Physical Review X* 6.3 (July 2016), p. 031006. DOI: 10.1103/physrevx.6.031006.

[105] Sisi Zhou et al. "Achieving the Heisenberg limit in quantum metrology using quantum error correction". In: *Nature Communications* 9.1 (Jan. 8, 2018), p. 78. ISSN: 2041-1723. DOI: 10.1038/s41467-017-02510-3. URL: https://www.nature.com/articles/s41467-017-02510-3 (visited on 12/07/2023).

[106] Jeremy C. Adcock et al. "Advances in Silicon Quantum Photonics". In: *IEEE Journal of Selected Topics in Quantum Electronics* 27.2 (Mar. 2021), pp. 1–24. DOI: 10.1109/jstqe.2020.3025737.

[107] Rohit K. Ramakrishnan et al. “Integrated photonic platforms for quantum technology: a review”. In: *ISSS Journal of Micro and Smart Systems* 12.2 (Nov. 1, 2023), pp. 83–104. ISSN: 2509-7997. DOI: 10.1007/s41683-023-00115-1. arXiv: 2206.15383 [quant-ph]. URL: https://doi.org/10.1007/s41683-023-00115-1 (visited on 01/07/2024).

[108] Joseph A. Dolphin et al. “A hybrid integrated quantum key distribution transceiver chip”. In: *npj Quantum Information* 9.1 (Sept. 6, 2023), pp. 1–8. ISSN: 2056-6387. DOI: 10.1038/s41534-023-00751-3. URL: https://www.nature.com/articles/s41534-023-00751-3 (visited on 11/02/2023).

[109] Dongning Liu et al. “Controllable Entanglement Distribution Network Based on Silicon Quantum Photonics”. In: (July 22, 2022). arXiv: 2207.10935 [quant-ph].

[110] Emanuele Pelucchi et al. “The potential and global outlook of integrated photonics for quantum technologies”. In: *Nature Reviews Physics* 4.3 (Mar. 2022), pp. 194–208. ISSN: 2522-5820. DOI: 10.1038/s42254-021-00398-z. URL: https://www.nature.com/articles/s42254-021-00398-z (visited on 11/17/2023).

[111] Terry Rudolph. “Why I am optimistic about the silicon-photonic route to quantum computing”. In: *APL Photonics* 2.3 (Mar. 2017), p. 030901. DOI: 10.1063/1.4976737.

[112] Chao-Yang Lu and Jian-Wei Pan. “Quantum-dot single-photon sources for the quantum internet”. In: *Nature Nanotechnology* 16.12 (Dec. 2021), pp. 1294–1296. DOI: 10.1038/s41565-021-01033-9.

[113] Christophe Couteau et al. “Applications of single photons to quantum communication and computing”. In: *Nature Reviews Physics* 5.6 (June 2023), pp. 326–338. ISSN: 2522-5820. DOI: 10.1038/s42254-023-00583-2. URL: https://www.nature.com/articles/s42254-023-00583-2 (visited on 11/21/2023).

[114] Shigeki Takeuchi. “Recent progress in single-photon and entangled-photon generation and applications”. In: *Japanese Journal of Applied Physics* 53.3 (Feb. 12, 2014), p. 030101. DOI: 10.7567/jjap.53.030101.

[115] Christophe Couteau et al. “Applications of single photons in quantum metrology, biology and the foundations of quantum physics”. In: *Nature Reviews Physics* 5.6 (June 2023), pp. 354–363. ISSN: 2522-5820. DOI: 10.1038/s42254-023-00589-w. URL: https://www.nature.com/articles/s42254-023-00589-w (visited on 12/31/2023).

[116] Adeline Orieux et al. “Semiconductor devices for entangled photon pair generation: a review”. In: *Reports on Progress in Physics* 80.7 (May 2017), p. 076001. DOI: 10.1088/1361-6633/aa6955.

[117] Pascale Senellart, Glenn Solomon, and Andrew White. “High-performance semiconductor quantum-dot single-photon sources”. In: *Nature Nanotechnology* 12.11 (Nov. 2017), pp. 1026–1039. DOI: 10.1038/nnano.2017.218.

[118] Daniel Huber et al. “Semiconductor quantum dots as an ideal source of polarization-entangled photon pairs on-demand: a review”. In: *Journal of Optics* 20.7 (June 2018), p. 073002. DOI: 10.1088/2040-8986/aac4c4.

[119] Yasuhiko Arakawa and Mark J. Holmes. “Progress in quantum-dot single photon sources for quantum information technologies: A broad spectrum overview”. In: *Applied Physics Reviews* 7.2 (June 2020), p. 021309. DOI: 10.1063/5.0010193.

[120] Christian Schimpf et al. “Quantum dots as potential sources of strongly entangled photons: Perspectives and challenges for applications in quantum networks”. In: *Applied Physics Letters* 118.10 (Mar. 2021), p. 100502. DOI: 10.1063/5.0038729.

[121] Tobias Heindel et al. “Quantum dots for photonic quantum information technology”. In: *Advances in Optics and Photonics* 15.3 (Aug. 2023), p. 613. DOI: 10.1364/aop.490091.

[122] Nicolas Maring et al. “A general-purpose single-photon-based quantum computing platform”. In: (June 2023). DOI: 10.48550/ARXIV.2306.00874. arXiv: 2306.00874 [quant-ph].

[123] Robert H. Hadfield. "Single-photon detectors for optical quantum information applications". In: *Nature Photonics* 3.12 (Dec. 2009), pp. 696–705. ISSN: 1749-4893. DOI: 10.1038/nphoton.2009.230. URL: https://www.nature.com/articles/nphoton.2009.230 (visited on 01/07/2024).

[124] Chandra M. Natarajan, Michael G. Tanner, and Robert H. Hadfield. "Superconducting nanowire single-photon detectors: physics and applications". In: *Superconductor Science and Technology* 25.6 (Apr. 2012), p. 063001. ISSN: 0953-2048. DOI: 10.1088/0953-2048/25/6/063001. URL: https://dx.doi.org/10.1088/0953-2048/25/6/063001 (visited on 01/07/2024).

[125] Eric A. Dauler et al. "Review of superconducting nanowire single-photon detector system design options and demonstrated performance". In: *Optical Engineering* 53.8 (June 2014), p. 081907. ISSN: 0091-3286, 1560-2303. DOI: 10.1117/1.OE.53.8.081907. URL: https://www.spiedigitallibrary.org/journals/optical-engineering/volume-53/issue-8/081907/Review-of-superconducting-nanowire-single-photon-detector-system-design-options/10.1117/1.OE.53.8.081907.full (visited on 01/07/2024).

[126] A. Engel et al. "Detection mechanism of superconducting nanowire single-photon detectors". In: *Superconductor Science and Technology* 28.11 (Sept. 2015), p. 114003. ISSN: 0953-2048. DOI: 10.1088/0953-2048/28/11/114003. URL: https://dx.doi.org/10.1088/0953-2048/28/11/114003 (visited on 01/07/2024).

[127] Taro Yamashita, Shigehito Miki, and Hirotaka Terai. "Recent Progress and Application of Superconducting Nanowire Single-Photon Detectors". In: *IEICE TRANSACTIONS on Electronics* E100-C.3 (Mar. 1, 2017), pp. 274–282. ISSN: 1745-1353, 0916-8516. URL: https://search.ieice.org/bin/summary.php?id=e100-c_3_274&category=C&year=2017&lang=E&abst= (visited on 01/07/2024).

[128] Itamar Holzman and Yachin Ivry. "Superconducting Nanowires for Single-Photon Detection: Progress, Challenges, and Opportunities". In: *Advanced Quantum Technologies* 2.3 (2019), p. 1800058. ISSN: 2511-9044. DOI: 10.1002/qute.201800058. URL: https://onlinelibrary.wiley.com/doi/abs/10.1002/qute.201800058 (visited on 01/07/2024).

[129] Lixing You. "Superconducting nanowire single-photon detectors for quantum information". In: *Nanophotonics* 9.9 (Sept. 1, 2020), pp. 2673–2692. ISSN: 2192-8614. DOI: 10.1515/nanoph-2020-0186. URL: https://www.degruyter.com/document/doi/10.1515/nanoph-2020-0186/html (visited on 01/07/2024).

[130] Iman Esmaeil Zadeh et al. "Superconducting nanowire single-photon detectors: A perspective on evolution, state-of-the-art, future developments, and applications". In: *Applied Physics Letters* 118.19 (May 13, 2021), p. 190502. ISSN: 0003-6951. DOI: 10.1063/5.0045990. URL: https://doi.org/10.1063/5.0045990 (visited on 01/07/2024).

[131] Stephan Steinhauer, Samuel Gyger, and Val Zwiller. "Progress on large-scale superconducting nanowire single-photon detectors". In: *Applied Physics Letters* 118.10 (Mar. 9, 2021), p. 100501. ISSN: 0003-6951. DOI: 10.1063/5.0044057. URL: https://doi.org/10.1063/5.0044057 (visited on 01/07/2024).

[132] Sankar Raman Sathyamoorthy, Thomas M. Stace, and Göran Johansson. "Detecting itinerant single microwave photons". In: *Comptes Rendus Physique* 17.7 (Aug. 2016), pp. 756–765. DOI: 10.1016/j.crhy.2016.07.010.

[133] Ming-Xing Luo et al. "Quantum Computation Based on Photons with Three Degrees of Freedom". In: *Scientific Reports* 6.1 (May 13, 2016), p. 25977. ISSN: 2045-2322. DOI: 10.1038/srep25977. URL: https://www.nature.com/articles/srep25977 (visited on 01/07/2024).

[134] Mingxuan Li et al. "Design of a Broadband and Low Loss TM Magneto-Optical Waveguide Isolator Based on Lithium Niobate on Insulator". In: *IEEE Photonics Journal* 13.2 (Apr. 2021), pp. 1–11. DOI: 10.1109/jphot.2021.3058686.

[135] Shuyuan Liu, Yuya Shoji, and Tetsuya Mizumoto. "Mode-evolution-based TE mode magneto-optical isolator using asymmetric adiabatic tapered waveguides". In: *Optics Express* 29.15 (July 2021), p. 22838. DOI: 10.1364/oe.427914.

[136] Shuyuan Liu, Yuya Shoji, and Tetsuya Mizumoto. "TE-mode magneto-optical isolator based on an asymmetric microring resonator under a unidirectional magnetic field". In: *Optics Express* 30.6 (Mar. 2022), p. 9934. DOI: 10.1364/oe.454751.

[137] S. Haroche, M. Brune, and J. M. Raimond. "From cavity to circuit quantum electrodynamics". In: *Nature Physics* 16.3 (Mar. 2020), pp. 243–246. ISSN: 1745-2481. DOI: 10.1038/s41567-020-0812-1. URL: https://www.nature.com/articles/s41567-020-0812-1 (visited on 01/08/2024).

[138] Isaac Chuang. *Lecture 19: How to Build Your Own Quantum Computer*. Nov. 13, 2003. URL: https://ocw.mit.edu/courses/18-435j-quantum-computation-fall-2003/c95a265dc90e89f2323d84be985fd322_qc_lec19.pdf.

[139] Jay M. Gambetta, Jerry M. Chow, and Matthias Steffen. "Building logical qubits in a superconducting quantum computing system". In: *npj Quantum Information* 3.1 (Jan. 2017). ISSN: 2056-6387. DOI: 10.1038/s41534-016-0004-0. URL: http://dx.doi.org/10.1038/s41534-016-0004-0.

[140] Creative Commons. *Creative Commons Attribution 4.0 International License*. URL: http://creativecommons.org/licenses/by/4.0/.

[141] T. P. Orlando et al. "Superconducting persistent-current qubit". In: *Physical Review B* 60.22 (Dec. 1999), pp. 15398–15413. ISSN: 1095-3795. DOI: 10.1103/physrevb.60.15398. URL: http://dx.doi.org/10.1103/PhysRevB.60.15398.

[142] A. A. Houck et al. "Life after charge noise: recent results with transmon qubits". In: *Quantum Information Processing* 8.2-3 (Feb. 2009), pp. 105–115. ISSN: 1573-1332. DOI: 10.1007/s11128-009-0100-6. URL: http://dx.doi.org/10.1007/s11128-009-0100-6.

[143] P. Krantz et al. "A quantum engineer's guide to superconducting qubits". In: *Applied Physics Reviews* 6.2 (June 17, 2019), p. 021318. DOI: 10.1063/1.5089550.

[144] He-Liang Huang et al. "Superconducting quantum computing: a review". In: *Science China Information Sciences* 63.8 (July 2020). DOI: 10.1007/s11432-020-2881-9.

[145] Alexandre Blais et al. "Cavity quantum electrodynamics for superconducting electrical circuits: An architecture for quantum computation". In: *Physical Review A* 69.6 (June 2004), p. 062320. DOI: 10.1103/physreva.69.062320.

[146] Alex Krasnok et al. "Advancements in Superconducting Microwave Cavities and Qubits for Quantum Information Systems". In: (Apr. 2023). DOI: 10.48550/ARXIV.2304.09345. arXiv: 2304.09345 [quant-ph].

[147] Frank Arute et al. "Quantum supremacy using a programmable superconducting processor". In: *Nature* 574.7779 (Oct. 2019), pp. 505–510. DOI: 10.1038/s41586-019-1666-5.

[148] Yulin Wu et al. "Strong Quantum Computational Advantage Using a Superconducting Quantum Processor". In: *Physical Review Letters* 127.18 (Oct. 2021), p. 180501. DOI: 10.1103/physrevlett.127.180501.

[149] Qingling Zhu et al. "Quantum computational advantage via 60-qubit 24-cycle random circuit sampling". In: *Science Bulletin* 67.3 (Feb. 2022), pp. 240–245. DOI: 10.1016/j.scib.2021.10.017.

[150] G. Wendin. "Quantum information processing with superconducting circuits: a perspective". In: (Feb. 9, 2023). DOI: 10.48550/ARXIV.2302.04558. arXiv: 2302.04558 [quant-ph].

[151] Archana Kamal, John Clarke, and M. H. Devoret. "Noiseless non-reciprocity in a parametric active device". In: *Nature Physics* 7.4 (Apr. 2011), pp. 311–315. ISSN: 1745-2481. DOI: 10.1038/nphys1893. URL: https://www.nature.com/articles/nphys1893 (visited on 11/16/2023).

[152] Baleegh Abdo et al. "Directional Amplification with a Josephson Circuit". In: *Physical Review X* 3.3 (July 1, 2013), p. 031001. DOI: 10.1103/PhysRevX.3.031001. URL: https://link.aps.org/doi/10.1103/PhysRevX.3.031001 (visited on 11/16/2023).

[153] K. M. Sliwa et al. "Reconfigurable Josephson Circulator/Directional Amplifier". In: *Physical Review X* 5.4 (Nov. 5, 2015), p. 041020. DOI: 10.1103/PhysRevX.5.041020. URL: https://link.aps.org/doi/10.1103/PhysRevX.5.041020 (visited on 11/16/2023).

[154] H HAFFNER, C ROOS, and R BLATT. "Quantum computing with trapped ions". In: *Physics Reports* 469.4 (Dec. 2008), pp. 155–203. DOI: 10.1016/j.physrep.2008.09.003.

[155] Colin D. Bruzewicz et al. "Trapped-ion quantum computing: Progress and challenges". In: *Applied Physics Reviews* 6.2 (June 2019), p. 021314. ISSN: 1931-9401. DOI: 10.1063/1.5088164. URL: http://dx.doi.org/10.1063/1.5088164.

[156] Francesco Bernardini, Abhijit Chakraborty, and Carlos Ordóñez. "Quantum computing with trapped ions: a beginner's guide". In: (Mar. 2023). DOI: 10.48550/ARXIV.2303.16358. arXiv: 2303.16358 [quant-ph].

[157] L.-M. Duan and C. Monroe. "Colloquium: Quantum networks with trapped ions". In: *Reviews of Modern Physics* 82.2 (Apr. 2010), pp. 1209–1224. DOI: 10.1103/revmodphys.82.1209.

[158] S. Debnath et al. "Demonstration of a small programmable quantum computer with atomic qubits". In: *Nature* 536.7614 (Aug. 2016), pp. 63–66. DOI: 10.1038/nature18648.

[159] S. A. Moses et al. "A Race Track Trapped-Ion Quantum Processor". In: (May 2023). DOI: 10.48550/ARXIV.2305.03828. arXiv: 2305.03828 [quant-ph].

[160] Lukas Postler et al. "Demonstration of fault-tolerant Steane quantum error correction". In: (Dec. 15, 2023). DOI: 10.48550/ARXIV.2312.09745. arXiv: 2312.09745 [quant-ph].

[161] M. Malinowski, D.T.C. Allcock, and C.J. Ballance. "How to Wire a 1000-Qubit Trapped-Ion Quantum Computer". In: *PRX Quantum* 4.4 (Oct. 19, 2023), p. 040313. DOI: 10.1103/PRXQuantum.4.040313. arXiv: 2305.12773 [quant-ph]. URL: https://link.aps.org/doi/10.1103/PRXQuantum.4.040313 (visited on 01/06/2024).

[162] Shabir Barzanjeh et al. "Optomechanics for quantum technologies". In: *Nature Physics* 18.1 (Dec. 2021), pp. 15–24. DOI: 10.1038/s41567-021-01402-0.

[163] Amarendra K. Sarma and Sampreet Kalita. "Tutorial: Cavity Quantum Optomechanics". In: (Nov. 4, 2022). arXiv: 2211.02596 [quant-ph].

[164] Markus Aspelmeyer, Tobias J. Kippenberg, and Florian Marquardt. "Cavity optomechanics". In: *Reviews of Modern Physics* 86.4 (Dec. 2014), pp. 1391–1452. DOI: 10.1103/revmodphys.86.1391.

[165] Markus Aspelmeyer, Tobias J. Kippenberg, and Florian Marquardt, eds. *Cavity Optomechanics*. Springer Berlin Heidelberg, 2014. DOI: 10.1007/978-3-642-55312-7.

[166] Srujan Meesala et al. "Non-classical microwave-optical photon pair generation with a chip-scale transducer". In: (Mar. 2023). DOI: 10.48550/ARXIV.2303.17684. arXiv: 2303.17684 [quant-ph].

[167] Zhen Shen et al. "Nonreciprocal Frequency Conversion and Mode Routing in a Microresonator". In: *Physical Review Letters* 130.1 (Jan. 2023), p. 013601. DOI: 10.1103/physrevlett.130.013601.

[168] Freek Ruesink et al. “Nonreciprocity and magnetic-free isolation based on optomechanical interactions”. In: *Nature Communications* 7.1 (Nov. 2016). DOI: 10.1038/ncomms13662.

[169] Zhen Shen et al. “Experimental realization of optomechanically induced non-reciprocity”. In: *Nature Photonics* 10.10 (Aug. 2016), pp. 657–661. DOI: 10.1038/nphoton.2016.161.

[170] N. R. Bernier et al. “Nonreciprocal reconfigurable microwave optomechanical circuit”. In: *Nature Communications* 8.1 (Sept. 2017). DOI: 10.1038/s41467-017-00447-1.

[171] Kejie Fang et al. “Generalized non-reciprocity in an optomechanical circuit via synthetic magnetism and reservoir engineering”. In: *Nature Physics* 13.5 (Jan. 2017), pp. 465–471. DOI: 10.1038/nphys4009.

[172] Freek Ruesink et al. “Optical circulation in a multimode optomechanical resonator”. In: *Nature Communications* 9.1 (May 2018). DOI: 10.1038/s41467-018-04202-y.

[173] Zhen Shen et al. “Reconfigurable optomechanical circulator and directional amplifier”. In: *Nature Communications* 9.1 (May 2018). DOI: 10.1038/s41467-018-04187-8.

[174] H. Xu et al. “Topological energy transfer in an optomechanical system with exceptional points”. In: *Nature* 537.7618 (July 2016), pp. 80–83. DOI: 10.1038/nature18604.

[175] B. D. Hauer, J. Combes, and J. D. Teufel. “Nonlinear Sideband Cooling to a Cat State of Motion”. In: *Physical Review Letters* 130.21 (May 25, 2023), p. 213604. DOI: 10.1103/PhysRevLett.130.213604. URL: https://link.aps.org/doi/10.1103/PhysRevLett.130.213604 (visited on 01/08/2024).

[176] M. J. Woolley et al. “Nanomechanical squeezing with detection via a microwave cavity”. In: *Physical Review A* 78.6 (Dec. 2008), p. 062303. DOI: 10.1103/physreva.78.062303.

[177] M. J. Woolley and A. A. Clerk. “Two-mode squeezed states in cavity optomechanics via engineering of a single reservoir”. In: *Physical Review A* 89.6 (June 2014), p. 063805. DOI: 10.1103/physreva.89.063805.

[178] Jian Huang, Deng-Gao Lai, and Jie-Qiao Liao. “Controllable generation of mechanical quadrature squeezing via dark-mode engineering in cavity optomechanics”. In: *Physical Review A* 108.1 (July 2023), p. 013516. DOI: 10.1103/physreva.108.013516. arXiv: 2304.00963 [quant-ph].

[179] D. Vitali et al. “Optomechanical Entanglement between a Movable Mirror and a Cavity Field”. In: *Physical Review Letters* 98.3 (Jan. 2007), p. 030405. DOI: 10.1103/physrevlett.98.030405.

[180] T. A. Palomaki et al. “Entangling Mechanical Motion with Microwave Fields”. In: *Science* 342.6159 (Nov. 2013), pp. 710–713. DOI: 10.1126/science.1244563.

[181] Kevin Araya-Sossa and Miguel Orszag. “Generation of entanglement via squeezing on a tripartite-optomechanical system”. In: *Physical Review A* 108.1 (July 25, 2023), p. 012432. DOI: 10.1103/PhysRevA.108.012432. URL: https://link.aps.org/doi/10.1103/PhysRevA.108.012432 (visited on 11/02/2023).

[182] Sebastian G. Hofer et al. “Quantum entanglement and teleportation in pulsed cavity optomechanics”. In: *Physical Review A* 84.5 (Nov. 2011), p. 052327. DOI: 10.1103/physreva.84.052327.

[183] Shao-Xiong Wu et al. “Enhancing the quantum entanglement and EPR steering of a coupled optomechanical system with a squeezed vacuum field”. In: *Journal of the Optical Society of America B* 40.11 (Oct. 2023), p. 2885. DOI: 10.1364/josab.495520.

[184] Pierre Meystre and Murray Sargent. *Elements of Quantum Optics*. Springer Berlin Heidelberg, 2007. DOI: 10.1007/978-3-540-74211-1.

[185] Marlan O. Scully and M. Suhail Zubairy. *Quantum Optics*. Cambridge University Press, Sept. 1997. DOI: 10.1017/cbo9780511813993.

[186] Christopher Gerry and Peter Knight. *Introductory Quantum Optics*. Cambridge University Press, Oct. 2004. DOI: 10.1017/cbo9780511791239.

[187] Farhan Rana. *Chapter 5: Quantization of Radiation in Cavities and Free Space*. 2017. URL: https://bpb-us-w2.wpmucdn.com/sites.coecis.cornell.edu/dist/4/81/files/2017/03/ece5310_handout5-2062ta5.pdf.

[188] M. Maggiore. *A Modern Introduction to Quantum Field Theory*. EBSCO ebook academic collection. Oxford University Press, 2005. ISBN: 9780198520733. URL: https://books.google.com.au/books?id=yykTDAAAQBAJ.

[189] Jonathan Keeling. *Light-Matter Interactions and Quantum Optics*. URL: https://www.st-andrews.ac.uk/~jmjk/keeling/teaching/quantum-optics.pdf.

[190] Claudiu Genes. *Quantum Physics of Light-Matter Interactions*. 2019. URL: https://mpl.mpg.de/fileadmin/user_upload/LectureNotes.pdf.

[191] Carlos Navarrete-Benlloch. "Introduction to Quantum Optics". In: (Mar. 20, 2022). arXiv: 2203.13206 [quant-ph].

[192] Bruno Huttner and Stephen M. Barnett. "Quantization of the electromagnetic field in dielectrics". In: *Physical Review A* 46.7 (Oct. 1992), pp. 4306–4322. DOI: 10.1103/physreva.46.4306.

[193] Salvatore Savasta, Omar Di Stefano, and Raffaello Girlanda. "Three-dimensional quantum-optical input–output relations for arbitrary planar dielectrics". In: *Journal of the Optical Society of America B* 19.2 (Feb. 2002), p. 304. DOI: 10.1364/josab.19.000304.

[194] Daniel D. Stancil and Anil Prabhakar. *Spin Waves*. Springer US, 2009. DOI: 10.1007/978-0-387-77865-5.

[195] "IEEE Standard Definitions of Terms for Radio Wave Propagation". In: *IEEE Std 211-1997* (Nov. 1997), pp. 1–44. DOI: 10.1109/IEEESTD.1997.8638365. URL: https://ieeexplore.ieee.org/document/8638365 (visited on 11/19/2023).

[196] "IEEE Standard Definitions of Terms for Radio Wave Propagation". In: *IEEE Std 211-2018 (Revision of IEEE Std 211-1997)* (Feb. 2019), pp. 1–57. DOI: 10.1109/IEEESTD.2019.8657413. URL: https://ieeexplore.ieee.org/document/8657413 (visited on 11/19/2023).

[197] Farhan Rana. *Chapter 11: Matter-Photon Interactions and Cavity Quantum Electrodynamics*. 2017. URL: https://bpb-us-w2.wpmucdn.com/sites.coecis.cornell.edu/dist/4/81/files/2017/03/ece5310_handout11-27cw9iy.pdf.

[198] Jared Lolli. "Quantum Measurement and Feedback Control of highly nonclassical Photonic States". Theses. Université Sorbonne Paris Cité, Nov. 2017. URL: https://theses.hal.science/tel-02127613.

[199] Mor M. Roses and Emanuele G. Dalla Torre. "Dicke model". In: *PLOS ONE* 15.9 (Sept. 2020), pp. 1–8. DOI: 10.1371/journal.pone.0235197. URL: https://doi.org/10.1371/journal.pone.0235197.

[200] Peter Kirton et al. "Introduction to the Dicke Model: From Equilibrium to Nonequilibrium, and Vice Versa". In: *Advanced Quantum Technologies* 2.1-2 (2019), p. 1800043. DOI: https://doi.org/10.1002/qute.201800043. eprint: https://onlinelibrary.wiley.com/doi/pdf/10.1002/qute.201800043. URL: https://onlinelibrary.wiley.com/doi/abs/10.1002/qute.201800043.

[201] Diego Barberena, Lucas Lamata, and Enrique Solano. "Dispersive Regimes of the Dicke Model". In: *Scientific Reports* 7.1 (Aug. 2017). ISSN: 2045-2322. DOI: 10.1038/s41598-017-09110-7. URL: http://dx.doi.org/10.1038/s41598-017-09110-7.

[202] Clive Emary and Tobias Brandes. "Chaos and the quantum phase transition in the Dicke model". In: *Physical Review E* 67.6 (June 2003), p. 066203. DOI: 10.1103/physreve.67.066203.

[203] Clive Emary and Tobias Brandes. "Quantum Chaos Triggered by Precursors of a Quantum Phase Transition: The Dicke Model". In: *Physical Review Letters* 90.4 (Jan. 2003), p. 044101. DOI: 10.1103/physrevlett.90.044101.

[204] T. Holstein and H. Primakoff. "Field Dependence of the Intrinsic Domain Magnetization of a Ferromagnet". In: *Phys. Rev.* 58 (12 Dec. 1940), pp. 1098–1113. DOI: 10.1103/PhysRev.58.1098. URL: https://link.aps.org/doi/10.1103/PhysRev.58.1098.

[205] Jonas Larson and Th. K. Mavrogordatos. "The Jaynes-Cummings model and its descendants". In: *IOP ebooks, 2021* (Feb. 1, 2022). DOI: 10.1088/978-0-7503-3447-1. arXiv: 2202.00330 [quant-ph].

[206] J. J. Hopfield. "Theory of the Contribution of Excitons to the Complex Dielectric Constant of Crystals". In: *Phys. Rev.* 112 (5 Dec. 1958), pp. 1555–1567. DOI: 10.1103/PhysRev.112.1555. URL: https://link.aps.org/doi/10.1103/PhysRev.112.1555.

[207] Félix Beaudoin, Jay M. Gambetta, and A. Blais. "Dissipation and ultrastrong coupling in circuit QED". In: *Phys. Rev. A* 84 (4 Oct. 2011), p. 043832. DOI: 10.1103/PhysRevA.84.043832. URL: https://link.aps.org/doi/10.1103/PhysRevA.84.043832.

[208] David Zueco and Juanjo García-Ripoll. "Ultrastrongly dissipative quantum Rabi model". In: *Physical Review A* 99.1 (Jan. 2019). ISSN: 2469-9934. DOI: 10.1103/physreva.99.013807. URL: http://dx.doi.org/10.1103/PhysRevA.99.013807.

[209] L. Giannelli et al. "Detecting virtual phothons in ultrastrongly coupled superconducting quantum circuits". In: (Feb. 2023). DOI: 10.48550/ARXIV.2302.10973. arXiv: 2302.10973 [quant-ph].

[210] Zheng-Yuan Xue et al. "Non-adiabatic holonomic manipulation of the polariton qubit in circuit QED". In: *The European Physical Journal D* 69.2 (Feb. 2015). ISSN: 1434-6079. DOI: 10.1140/epjd/e2015-50886-0. URL: http://dx.doi.org/10.1140/epjd/e2015-50886-0.

[211] Xuan Zuo et al. "Entangling Two Bosonic Polaritons via Dispersive Coupling with a Third Mode". In: (Mar. 2023). DOI: 10.48550/ARXIV.2303.15217. arXiv: 2303.15217 [quant-ph].

[212] J. R. Schrieffer and P. A. Wolff. "Relation between the Anderson and Kondo Hamiltonians". In: *Physical Review* 149.2 (Sept. 1966), pp. 491–492. DOI: 10.1103/physrev.149.491.

[213] Yutaka Tabuchi et al. "Coherent coupling between a ferromagnetic magnon and a superconducting qubit". In: *Science* 349.6246 (July 2015), pp. 405–408. DOI: 10.1126/science.aaa3693.

[214] Yutaka Tabuchi et al. "Quantum magnonics: The magnon meets the superconducting qubit". In: *Comptes Rendus Physique* 17.7 (2016). Quantum microwaves / Micro-ondes quantiques, pp. 729–739. ISSN: 1631-0705. DOI: https://doi.org/10.1016/j.crhy.2016.07.009. URL: https://www.sciencedirect.com/science/article/pii/S1631070516300603.

[215] N. J. Lambert et al. "Cavity-mediated coherent coupling of magnetic moments". In: *Physical Review A* 93.2 (Feb. 2016), p. 021803. DOI: 10.1103/physreva.93.021803.

[216] Sergey Bravyi, David P. DiVincenzo, and Daniel Loss. "Schrieffer–Wolff transformation for quantum many-body systems". In: *Annals of Physics* 326.10 (Oct. 2011), pp. 2793–2826. DOI: 10.1016/j.aop.2011.06.004.

[217] Takashi Mori. "Floquet States in Open Quantum Systems". In: *Annual Review of Condensed Matter Physics* 14.1 (Mar. 30, 2022), pp. 35–56. DOI: 10.1146/annurev-conmatphys-040721-015537. arXiv: 2203.16358 [cond-mat.stat-mech].

[218] C. W. Gardiner and M. J. Collett. "Input and output in damped quantum systems: Quantum stochastic differential equations and the master equation". In: *Physical Review A* 31.6 (June 1985), pp. 3761–3774. DOI: 10.1103/physreva.31.3761.

[219] *Lindblad and Input-Output Formalism in Quantum Optics*. URL: https://physics.stackexchange.com/q/461054.

[220] Shanhui Fan, Şükrü Ekin Kocabaş, and Jung-Tsung Shen. "Input-output formalism for few-photon transport in one-dimensional nanophotonic waveguides coupled to a qubit". In: *Physical Review A* 82.6 (Dec. 2010), p. 063821. DOI: 10.1103/physreva.82.063821.

[221] Michael Harder et al. "Study of the cavity-magnon-polariton transmission line shape". In: *Science China Physics, Mechanics & Astronomy* 59.11 (Sept. 2016). ISSN: 1869-1927. DOI: 10.1007/s11433-016-0228-6. URL: http://dx.doi.org/10.1007/s11433-016-0228-6.

[222] Antti-Pekka Jauho, Ned S. Wingreen, and Yigal Meir. "Time-dependent transport in interacting and noninteracting resonant-tunneling systems". In: *Physical Review B* 50.8 (Aug. 1994), pp. 5528–5544. ISSN: 1095-3795. DOI: 10.1103/physrevb.50.5528.

[223] A. A. Clerk et al. "Introduction to quantum noise, measurement, and amplification". In: *Reviews of Modern Physics* 82.2 (Apr. 2010), pp. 1155–1208. ISSN: 1539-0756. DOI: 10.1103/revmodphys.82.1155. URL: http://dx.doi.org/10.1103/RevModPhys.82.1155.

[224] Dominik Lentrodt and Jörg Evers. "Ab Initio Few-Mode Theory for Quantum Potential Scattering Problems". In: *Physical Review X* 10.1 (Jan. 2020), p. 011008. DOI: 10.1103/physrevx.10.011008.

[225] Cristiano Ciuti and Iacopo Carusotto. "Input-output theory of cavities in the ultrastrong coupling regime: The case of time-independent cavity parameters". In: *Phys. Rev. A* 74 (3 Sept. 2006), p. 033811. DOI: 10.1103/PhysRevA.74.033811. URL: https://link.aps.org/doi/10.1103/PhysRevA.74.033811.

[226] Michael Harder and Can-Ming Hu. "Cavity Spintronics: An Early Review of Recent Progress in the Study of Magnon–Photon Level Repulsion". In: *Solid State Physics* (2018), pp. 47–121. ISSN: 0081-1947. DOI: 10.1016/bs.ssp.2018.08.001. URL: http://dx.doi.org/10.1016/bs.ssp.2018.08.001.

[227] Xufeng Zhang et al. "Magnon dark modes and gradient memory". In: *Nature Communications* 6.1 (Nov. 2015). DOI: 10.1038/ncomms9914.

[228] S. A. Wolf et al. "Spintronics: A Spin-Based Electronics Vision for the Future". In: *Science* 294.5546 (Nov. 2001), pp. 1488–1495. DOI: 10.1126/science.1065389.

[229] A. V. Chumak et al. "Magnon spintronics". In: *Nature Physics* 11.6 (June 2015), pp. 453–461. DOI: 10.1038/nphys3347.

[230] György Csaba, Ádám Papp, and Wolfgang Porod. "Perspectives of using spin waves for computing and signal processing". In: *Physics Letters A* 381.17 (May 2017), pp. 1471–1476. DOI: 10.1016/j.physleta.2017.02.042.

[231] A V Chumak, A A Serga, and B Hillebrands. "Magnonic crystals for data processing". In: *Journal of Physics D: Applied Physics* 50.24 (May 2017), p. 244001. DOI: 10.1088/1361-6463/aa6a65.

[232] A. V. Chumak. "Fundamentals of magnon-based computing". In: (Jan. 2019). DOI: 10.48550/ARXIV.1901.08934. arXiv: 1901.08934 [cond-mat.mes-hall].

[233] Anjan Barman et al. "The 2021 Magnonics Roadmap". In: *Journal of Physics: Condensed Matter* 33.41 (Aug. 2021), p. 413001. DOI: 10.1088/1361-648x/abec1a.

[234] Abdulqader Mahmoud et al. "Introduction to spin wave computing". In: *Journal of Applied Physics* 128.16 (Oct. 2020). DOI: 10.1063/5.0019328.

[235] Pieter M. Gunnink, Tim Ludwig, and Rembert A. Duine. "Magnon spin capacitor". In: (Oct. 2023). DOI: 10.48550/ARXIV.2310.09064. arXiv: 2310.09064 [cond-mat.mes-hall].

[236] Giovanni Finocchio et al. “The promise of spintronics for unconventional computing”. In: *Journal of Magnetism and Magnetic Materials* 521 (Mar. 1, 2021), p. 167506. ISSN: 0304-8853. DOI: 10.1016/j.jmmm.2020.167506. URL: https://www.sciencedirect.com/science/article/pii/S0304885320324732 (visited on 11/02/2023).

[237] G. Finocchio et al. “Perspectives on spintronic diodes”. In: *Applied Physics Letters* 118.16 (Apr. 22, 2021), p. 160502. ISSN: 0003-6951. DOI: 10.1063/5.0048947. URL: https://doi.org/10.1063/5.0048947 (visited on 11/02/2023).

[238] Shuvro Chowdhury and Kerem Y. Camsari. “Machine Learning Quantum Systems with Magnetic p-bits”. In: *2023 IEEE International Magnetic Conference - Short Papers (INTERMAG Short Papers)*. IEEE, May 2023. DOI: 10.1109/intermagshortpapers58606.2023.10228205.

[239] Giacomo Talmelli et al. “Reconfigurable submicrometer spin-wave majority gate with electrical transducers”. In: *Science Advances* 6.51 (Dec. 2020). DOI: 10.1126/sciadv.abb4042.

[240] Michael Harder, Yongsheng Gui, and Can-Ming Hu. “Electrical detection of magnetization dynamics via spin rectification effects”. In: *Physics Reports* 661 (Nov. 2016), pp. 1–59. DOI: 10.1016/j.physrep.2016.10.002.

[241] Sabpreet Bhatti et al. “Spintronics based random access memory: a review”. In: *Materials Today* 20.9 (Nov. 2017), pp. 530–548. DOI: 10.1016/j.mattod.2017.07.007.

[242] A V Chumak et al. “Roadmap on spin-wave computing concepts”. In: (Feb. 2022). working paper or preprint. URL: https://hal.archives-ouvertes.fr/hal-03381543.

[243] J. Grollier et al. “Neuromorphic spintronics”. In: *Nature Electronics* 3.7 (Mar. 2020), pp. 360–370. DOI: 10.1038/s41928-019-0360-9.

[244] Kaito Kobayashi and Yukitoshi Motome. “Video recognition by physical reservoir computing in magnetic materials”. In: (Oct. 2023). DOI: 10.48550/ARXIV.2310.06497. arXiv: 2310.06497 [cond-mat.mes-hall].

[245] T. Jungwirth et al. “Antiferromagnetic spintronics”. In: *Nature Nanotechnology* 11.3 (Mar. 2016), pp. 231–241. DOI: 10.1038/nnano.2016.18.

[246] O. Gomonay, T. Jungwirth, and J. Sinova. “Concepts of antiferromagnetic spintronics”. In: *physica status solidi (RRL) – Rapid Research Letters* 11.4 (Feb. 2017). DOI: 10.1002/pssr.201700022.

[247] Hongyu Chen et al. “Noncollinear Antiferromagnetic Spintronics”. In: *Materials Lab* 1 (July 22, 2022). DOI: 10.54227/mlab.20220032. arXiv: 2207.10875 [cond-mat.mes-hall].

[248] Fengjun Zhuo et al. “Topological Phases in Magnonics: A Review”. In: (May 2023). DOI: 10.48550/ARXIV.2305.14861. arXiv: 2305.14861 [cond-mat.mes-hall].

[249] Tao Yu et al. “Non-Hermitian Topological Magnonics”. In: (June 2023). DOI: 10.48550/ARXIV.2306.04348. arXiv: 2306.04348 [cond-mat.mes-hall].

[250] Kouki Nakata and Kei Suzuki. “Magnonic Casimir Effect in Ferrimagnets”. In: *Physical Review Letters* 130.9 (May 27, 2022), p. 096702. DOI: 10.1103/physrevlett.130.096702. arXiv: 2205.13802 [quant-ph].

[251] J. S. Harms, H. Y. Yuan, and Rembert A. Duine. “Antimagnonics”. In: (Oct. 29, 2022). arXiv: 2210.16698 [cond-mat.mes-hall].

[252] Libor Šmejkal, Jairo Sinova, and Tomas Jungwirth. “Emerging research landscape of altermagnetism”. In: (Apr. 22, 2022). arXiv: 2204.10844 [cond-mat.mes-hall].

[253] G. A. Knyazev et al. “Direct observation of magnon BEC in an out-of-plane magnetized yttrium iron garnet film”. In: (Jan. 24, 2023). DOI: 10.48550/ARXIV.2301.10725. arXiv: 2301.10725 [cond-mat.mes-hall].

[254] Yi-Pu Wang et al. “Bistability of Cavity Magnon Polaritons”. In: *Physical Review Letters* 120.5 (Jan. 2018), p. 057202. DOI: 10.1103/physrevlett.120.057202.

[255] Zeng-Xing Liu et al. “Absorption of magnons in dispersively coupled hybrid quantum systems”. In: *Physical Review A* 103.6 (June 2021), p. 063702. DOI: 10.1103/physreva.103.063702.

[256] M. X. Bi et al. “Bistability of cavity magnon polaritons beyond the Holstein–Primakoff transformation”. In: *Journal of Applied Physics* 130.24 (Dec. 2021), p. 243902. DOI: 10.1063/5.0073446.

[257] Dany Lachance-Quirion et al. “Hybrid quantum systems based on magnonics”. In: *Applied Physics Express* 12.7 (June 2019), p. 070101. ISSN: 1882-0786. DOI: 10.7567/1882-0786/ab248d. URL: http://dx.doi.org/10.7567/1882-0786/ab248d.

[258] Graeme Flower et al. “Broadening frequency range of a ferromagnetic axion haloscope with strongly coupled cavity–magnon polaritons”. In: *Physics of the Dark Universe* 25 (Sept. 2019), p. 100306. DOI: 10.1016/j.dark.2019.100306.

[259] C. A. Potts and J. P. Davis. “Strong magnon–photon coupling within a tunable cryogenic microwave cavity”. In: *Applied Physics Letters* 116.26 (June 2020), p. 263503. DOI: 10.1063/5.0015660.

[260] Bimu Yao et al. “Cooperative polariton dynamics in feedback-coupled cavities”. In: *Nature Communications* 8.1 (Nov. 2017). DOI: 10.1038/s41467-017-01796-7.

[261] M. Harder et al. “Coherent and dissipative cavity magnonics”. In: *Journal of Applied Physics* 129.20 (May 2021), p. 201101. ISSN: 1089-7550. DOI: 10.1063/5.0046202. URL: http://dx.doi.org/10.1063/5.0046202.

[262] S.H. Simon. *The Oxford Solid State Basics*. OUP Oxford, 2013. ISBN: 9780199680764. URL: https://books.google.com.au/books?id=QI8jLeTOBAsC.

[263] Andrew J. Princep et al. “The full magnon spectrum of yttrium iron garnet”. In: *npj Quantum Materials* 2.1 (Nov. 14, 2017), pp. 1–5. ISSN: 2397-4648. DOI: 10.1038/s41535-017-0067-y. URL: https://www.nature.com/articles/s41535-017-0067-y (visited on 11/07/2023).

[264] C. Cohen-Tannoudji, B. Diu, and F. Laloë. *Mécanique quantique: Tome II*. Savoirs actuels. Série Physique. EDP sciences, 2018. ISBN: 9782271125026. URL: https://books.google.com.au/books?id=ezkGvgEACAAJ.

[265] Charles Kittel. “On the Theory of Ferromagnetic Resonance Absorption”. In: *Physical Review* 73.2 (Jan. 15, 1948), pp. 155–161. DOI: 10.1103/PhysRev.73.155. URL: https://link.aps.org/doi/10.1103/PhysRev.73.155 (visited on 01/21/2024).

[266] Isabella Rahel Boventer. “Cavity Magnon-Polariton Spectroscopy”. en. PhD thesis. 2019. DOI: 10.25358/OPENSCIENCE-2335.

[267] Graeme Flower et al. “Experimental implementations of cavity-magnon systems: from ultra strong coupling to applications in precision measurement”. In: *New Journal of Physics* 21.9 (Sept. 2019), p. 095004. DOI: 10.1088/1367-2630/ab3e1c. URL: https://doi.org/10.1088/1367-2630/ab3e1c.

[268] Yi-Pu Wang et al. “Magnon Kerr effect in a strongly coupled cavity-magnon system”. In: *Phys. Rev. B* 94 (22 Dec. 2016), p. 224410. DOI: 10.1103/PhysRevB.94.224410. URL: https://link.aps.org/doi/10.1103/PhysRevB.94.224410.

[269] GuoQiang Zhang, YiPu Wang, and JianQiang You. “Theory of the magnon Kerr effect in cavity magnonics”. In: *Science China Physics, Mechanics & Astronomy* 62.8 (Mar. 2019). ISSN: 1869-1927. DOI: 10.1007/s11433-018-9344-8. URL: http://dx.doi.org/10.1007/s11433-018-9344-8.

[270] Ö. O. Soykal and M. E. Flatté. “Strong Field Interactions between a Nanomagnet and a Photonic Cavity”. In: *Phys. Rev. Lett.* 104 (7 Feb. 2010), p. 077202. DOI: 10.1103/PhysRevLett.104.077202. URL: https://link.aps.org/doi/10.1103/PhysRevLett.104.077202.

[271] Ö. O. Soykal and M. E. Flatté. "Size dependence of strong coupling between nanomagnets and photonic cavities". In: *Phys. Rev. B* 82 (10 Sept. 2010), p. 104413. DOI: 10.1103/PhysRevB.82.104413. URL: https://link.aps.org/doi/10.1103/PhysRevB.82.104413.

[272] Zhedong Zhang, Marlan O. Scully, and Girish S. Agarwal. "Quantum entanglement between two magnon modes via Kerr nonlinearity driven far from equilibrium". In: *Physical Review Research* 1.2 (Sept. 2019), p. 023021. DOI: 10.1103/physrevresearch.1.023021.

[273] Mei Yu, Shi-Yao Zhu, and Jie Li. "Macroscopic entanglement of two magnon modes via quantum correlated microwave fields". In: *Journal of Physics B: Atomic, Molecular and Optical Physics* 53.6 (Feb. 2020), p. 065402. DOI: 10.1088/1361-6455/ab68b5.

[274] Jeremy Bourhill et al. "Universal characterization of cavity–magnon polariton coupling strength verified in modifiable microwave cavity". In: *Journal of Applied Physics* 128.7 (Aug. 2020), p. 073904. ISSN: 1089-7550. DOI: 10.1063/5.0006753. URL: http://dx.doi.org/10.1063/5.0006753.

[275] Rair Macêdo et al. "Electromagnetic Approach to Cavity Spintronics". In: *Physical Review Applied* 15.2 (Feb. 2021), p. 024065. DOI: 10.1103/physrevapplied.15.024065.

[276] V. Veerakumar and R. E. Camley. "Magnon focusing in thin ferromagnetic films". In: *Physical Review B* 74.21 (Dec. 1, 2006), p. 214401. DOI: 10.1103/PhysRevB.74.214401. URL: https://link.aps.org/doi/10.1103/PhysRevB.74.214401 (visited on 02/22/2024).

[277] Babak Zare Rameshti, Yunshan Cao, and Gerrit E. W. Bauer. "Magnetic spheres in microwave cavities". In: *Physical Review B* 91.21 (June 2015), p. 214430. DOI: 10.1103/physrevb.91.214430.

[278] Sweden COMSOL AB Stockholm. *COMSOL Multiphysics®*. Version 5.6. 2020. URL: www.comsol.com.

[279] Guillaume Bourcin et al. "Level attraction in a quasi-closed cavity". In: arXiv:2402.06258 (Feb. 9, 2024). type: article. arXiv: 2402.06258[quant-ph]. URL: http://arxiv.org/abs/2402.06258 (visited on 02/12/2024).

[280] *RF Module User's Guide, COMSOL 6.1*. URL: https://doc.comsol.com/6.1/doc/com.comsol.help.rf/RFModuleUsersGuide.pdf.

[281] Michael V. Berry. "Quantal phase factors accompanying adiabatic changes". In: *Proc. Roy. Soc. Lond. A* 392 (1984), pp. 45–57. DOI: 10.1098/rspa.1984.0023.

[282] Y. Aharonov and D. Bohm. "Significance of Electromagnetic Potentials in the Quantum Theory". In: *Physical Review* 115.3 (Aug. 1959), pp. 485–491. DOI: 10.1103/physrev.115.485.

[283] Wikipedia. *Adiabatic process: Divergent usages of the word adiabatic*. URL: https://en.wikipedia.org/wiki/Adiabatic_process#Divergent_usages_of_the_word_adiabatic.

[284] Wikipedia. *Adiabatic theorem: Diabatic vs. adiabatic processes*. URL: https://en.wikipedia.org/wiki/Adiabatic_theorem#Diabatic_vs._adiabatic_processes.

[285] Gento Yamahata et al. "Picosecond coherent electron motion in a silicon single-electron source". In: *Nature Nanotechnology* 14.11 (Nov. 2019), pp. 1019–1023. ISSN: 1748-3395. DOI: 10.1038/s41565-019-0563-2. URL: http://dx.doi.org/10.1038/s41565-019-0563-2.

[286] K. Husimi. "Miscellanea in Elementary Quantum Mechanics, II". In: *Progress of Theoretical Physics* 9.4 (Apr. 1953), pp. 381–402. DOI: 10.1143/ptp/9.4.381.

[287] S.N. Shevchenko, S. Ashhab, and Franco Nori. "Landau–Zener–Stückelberg interferometry". In: *Physics Reports* 492.1 (July 2010), pp. 1–30. DOI: 10.1016/j.physrep.2010.03.002.

[288] Oleh V. Ivakhnenko, Sergey N. Shevchenko, and Franco Nori. "Nonadiabatic Landau–Zener–Stückelberg–Majorana transitions, dynamics, and interference". In: *Phys. Rep. 995 (2023) 1-89* 995 (Mar. 30, 2022), pp. 1–89. DOI: 10.1016/j.physrep.2022.10.002. arXiv: 2203.16348 [quant-ph].

[289] K Saito et al. "Quantum state preparation in circuit QED via Landau-Zener tunneling". In: *Europhysics Letters (EPL)* 76.1 (Oct. 2006), pp. 22–28. DOI: 10.1209/epl/i2006-10232-4.

[290] Martijn Wubs, Sigmund Kohler, and Peter Hänggi. "Entanglement creation in circuit QED via Landau–Zener sweeps". In: *Physica E: Low-dimensional Systems and Nanostructures* 40.1 (Oct. 2007), pp. 187–197. DOI: 10.1016/j.physe.2007.05.014.

[291] Shinichi Deguchi and Kazuo Fujikawa. "Second-quantized formulation of geometric phases". In: *Physical Review A* 72.1 (July 2005), p. 012111. DOI: 10.1103/physreva.72.012111.

[292] Raffaele Resta. "Manifestations of Berry's phase in molecules and condensed matter". In: *Journal of Physics: Condensed Matter* 12.9 (Feb. 2000), R107–R143. DOI: 10.1088/0953-8984/12/9/201.

[293] Angelo C.M. Carollo and Vlatko Vedral. "Holonomic quantum computation". In: (2005). URL: https://arxiv.org/abs/quant-ph/0504205.

[294] Barry Simon. "Holonomy, the Quantum Adiabatic Theorem, and Berry's Phase". In: *Physical Review Letters* 51.24 (Dec. 1983), pp. 2167–2170. DOI: 10.1103/physrevlett.51.2167.

[295] D. Bleecker. *Gauge Theory and Variational Principles*. Dover Books on Mathematics. Dover Publications, 1981. ISBN: 9780486151878.

[296] Eliahu Cohen et al. "Geometric phase from Aharonov–Bohm to Pancharatnam–Berry and beyond". In: *Nature Reviews Physics* 1.7 (June 2019), pp. 437–449. DOI: 10.1038/s42254-019-0071-1.

[297] C. Cisowski, J. B. Götte, and S. Franke-Arnold. "Colloquium : Geometric phases of light: Insights from fiber bundle theory". In: *Reviews of Modern Physics* 94.3 (July 2022), p. 031001. DOI: 10.1103/revmodphys.94.031001.

[298] Frank Wilczek and A. Zee. "Appearance of Gauge Structure in Simple Dynamical Systems". In: *Physical Review Letters* 52.24 (June 1984), pp. 2111–2114. DOI: 10.1103/physrevlett.52.2111.

[299] Paolo Zanardi and Mario Rasetti. "Holonomic quantum computation". In: *Physics Letters A* 264.2 (1999), pp. 94–99. ISSN: 0375-9601. DOI: https://doi.org/10.1016/S0375-9601(99)00803-8. URL: https://www.sciencedirect.com/science/article/pii/S0375960199008038.

[300] Jiannis Pachos and Paolo Zanardi. "Quantum Holonomies For Quantum Computing". In: 2001.

[301] Y. Aharonov and J. Anandan. "Phase change during a cyclic quantum evolution". In: *Physical Review Letters* 58.16 (Apr. 1987), pp. 1593–1596. DOI: 10.1103/physrevlett.58.1593.

[302] J. Anandan. "Non-adiabatic non-abelian geometric phase". In: *Physics Letters A* 133.4-5 (Nov. 1988), pp. 171–175. DOI: 10.1016/0375-9601(88)91010-9.

[303] Jiang Zhang et al. "Geometric and holonomic quantum computation". In: *Physics Reports* 1027 (July 2023), pp. 1–53. DOI: 10.1016/j.physrep.2023.07.004.

[304] Tatsuki Tojo and Kyozaburo Takeda. "Non-adiabatic Berry phase for semiconductor heavy holes under the coexistence of Rashba and Dresselhaus spin-orbit interactions". In: (Feb. 2023). DOI: 10.48550/ARXIV.2302.07436. arXiv: 2302.07436 [cond-mat.mes-hall].

[305] Xiao-Dong Yu and D. M. Tong. "Evolution Operator Can Always Be Separated into the Product of Holonomy and Dynamic Operators". In: *Physical Review Letters* 131.20 (Nov. 15, 2023), p. 200202. DOI: 10.1103/PhysRevLett.131.200202. URL: https://link.aps.org/doi/10.1103/PhysRevLett.131.200202 (visited on 11/17/2023).

[306] Artur Ekert et al. "Geometric quantum computation". In: *Journal of Modern Optics* 47.14-15 (July 3, 2009), pp. 2501–2513. ISSN: 1362-3044. DOI: 10.1080/09500340008232177. URL: http://dx.doi.org/10.1080/09500340008232177.

[307] Jonathan A. Jones et al. "Geometric quantum computation using nuclear magnetic resonance". In: *Nature* 403.6772 (Feb. 2000), pp. 869–871. DOI: 10.1038/35002528.

[308] Y.-Y. Huang et al. "Experimental Realization of Robust Geometric Quantum Gates with Solid-State Spins". In: *Physical Review Letters* 122.1 (Jan. 2019), p. 010503. DOI: 10.1103/physrevlett.122.010503.

[309] Niklas Hörnedal and Ole Sönnerborn. "Tight lower bounds on the time it takes to generate a geometric phase". In: *Physica Scripta* 98.10 (Sept. 2023), p. 105108. DOI: 10.1088/1402-4896/acf8a2. arXiv: 2305.12156 [quant-ph].

[310] Wang Xiang-Bin and Matsumoto Keiji. "Nonadiabatic Conditional Geometric Phase Shift with NMR". In: *Physical Review Letters* 87.9 (Aug. 2001), p. 097901. DOI: 10.1103/physrevlett.87.097901.

[311] Hiromitsu Imai and Atsuo Morinaga. "Demonstration of pure geometric universal single-qubit operation on two-level atoms". In: *Physical Review A* 78.1 (July 2008), p. 010302. DOI: 10.1103/physreva.78.010302.

[312] Li Wang et al. "Experimental realization of non-adiabatic universal quantum gates using geometric Landau-Zener-Stückelberg interferometry". In: *Scientific Reports* 6.1 (Jan. 2016). DOI: 10.1038/srep19048.

[313] Felix Kleißler, Andrii Lazariev, and Silvia Arroyo-Camejo. "Universal, high-fidelity quantum gates based on superadiabatic, geometric phases on a solid-state spin-qubit at room temperature". In: *npj Quantum Information* 4.1 (Oct. 2018). DOI: 10.1038/s41534-018-0098-7.

[314] Chao Song et al. "Continuous-variable geometric phase and its manipulation for quantum computation in a superconducting circuit". In: *Nature Communications* 8.1 (Oct. 2017). DOI: 10.1038/s41467-017-01156-5.

[315] Y. Xu et al. "Experimental Implementation of Universal Nonadiabatic Geometric Quantum Gates in a Superconducting Circuit". In: *Physical Review Letters* 124.23 (June 2020), p. 230503. DOI: 10.1103/physrevlett.124.230503.

[316] PeiZi Zhao et al. "Experimental realization of nonadiabatic geometric gates with a superconducting Xmon qubit". In: *Science China Physics, Mechanics & Astronomy* 64.5 (Feb. 2021). DOI: 10.1007/s11433-020-1641-1.

[317] D. Leibfried et al. "Experimental demonstration of a robust, high-fidelity geometric two ion-qubit phase gate". In: *Nature* 422.6930 (Mar. 2003), pp. 412–415. DOI: 10.1038/nature01492.

[318] Shi-Liang Zhu and Z. D. Wang. "Unconventional Geometric Quantum Computation". In: *Phys. Rev. Lett.* 91 (18 Oct. 2003), p. 187902. DOI: 10.1103/PhysRevLett.91.187902. URL: https://link.aps.org/doi/10.1103/PhysRevLett.91.187902.

[319] Jiangfeng Du, Ping Zou, and Z. D. Wang. "Experimental implementation of high-fidelity unconventional geometric quantum gates using an NMR interferometer". In: *Physical Review A* 74.2 (Aug. 2006), p. 020302. DOI: 10.1103/physreva.74.020302.

[320] Shi-Biao Zheng. "Unconventional geometric quantum phase gates with a cavity QED system". In: *Phys. Rev. A* 70 (5 Nov. 2004), p. 052320. DOI: 10.1103/PhysRevA.70.052320. URL: https://link.aps.org/doi/10.1103/PhysRevA.70.052320.

[321] Xun-Li Feng et al. “Scheme for unconventional geometric quantum computation in cavity QED”. In: *Physical Review A* 75.5 (May 2007), p. 052312. DOI: 10.1103/physreva.75.052312.

[322] Chunfeng Wu et al. “Unconventional geometric quantum computation in a two-mode cavity”. In: *Phys. Rev. A* 76 (2 Aug. 2007), p. 024302. DOI: 10.1103/PhysRevA.76.024302. URL: https://link.aps.org/doi/10.1103/PhysRevA.76.024302.

[323] L.-M. Duan, J. I. Cirac, and P. Zoller. “Geometric Manipulation of Trapped Ions for Quantum Computation”. In: *Science* 292.5522 (June 2001), pp. 1695–1697. DOI: 10.1126/science.1058835.

[324] Jiannis Pachos. “Topological features in ion-trap holonomic computation”. In: *Physical Review A* 66.4 (Oct. 2002), p. 042318. DOI: 10.1103/physreva.66.042318.

[325] A. Recati et al. “Holonomic quantum computation with neutral atoms”. In: *Physical Review A* 66.3 (Sept. 2002), p. 032309. DOI: 10.1103/physreva.66.032309.

[326] Paolo Solinas et al. “Holonomic quantum gates: A semiconductor-based implementation”. In: *Physical Review A* 67.6 (June 27, 2003), p. 062315. DOI: 10.1103/physreva.67.062315.

[327] Paolo Solinas et al. “Semiconductor-based geometrical quantum gates”. In: *Physical Review B* 67.12 (Mar. 2003), p. 121307. DOI: 10.1103/physrevb.67.121307.

[328] Yi-Cong Zheng and Todd A. Brun. “Geometric manipulation of ensembles of atoms on an atom chip for quantum computation”. In: *Physical Review A* 86.3 (Sept. 2012), p. 032323. DOI: 10.1103/physreva.86.032323.

[329] B. A. Bernevig and Shou-Cheng Zhang. “Holonomic quantum computing based on the Stark effect”. In: *Physical Review B* 71.3 (Jan. 2005), p. 035303. DOI: 10.1103/physrevb.71.035303.

[330] Vitaly N. Golovach, Massoud Borhani, and Daniel Loss. “Holonomic quantum computation with electron spins in quantum dots”. In: *Physical Review A* 81.2 (Feb. 2010), p. 022315. DOI: 10.1103/physreva.81.022315.

[331] J. C. Budich et al. “All-electric qubit control in heavy hole quantum dots via non-Abelian geometric phases”. In: *Physical Review B* 85.20 (May 2012), p. 205425. DOI: 10.1103/physrevb.85.205425.

[332] Yan Liang et al. “Nonadiabatic holonomic quantum computation and its optimal control”. In: *Science China Information Sciences* 66.8 (July 2023). DOI: 10.1007/s11432-023-3824-0.

[333] A. A. Abdumalikov Jr et al. “Experimental realization of non-Abelian non-adiabatic geometric gates”. In: *Nature* 496.7446 (Apr. 2013), pp. 482–485. DOI: 10.1038/nature12010.

[334] Zhenxing Zhang et al. “Single-shot realization of nonadiabatic holonomic gates with a superconducting Xmon qutrit”. In: *New Journal of Physics* 21.7 (July 2019), p. 073024. DOI: 10.1088/1367-2630/ab2e26.

[335] Zheng-Yuan Xue et al. “Nonadiabatic Holonomic Quantum Computation with Dressed-State Qubits”. In: *Physical Review Applied* 7.5 (May 2017), p. 054022. DOI: 10.1103/physrevapplied.7.054022.

[336] Zhuo-Ping Hong et al. “Implementing universal nonadiabatic holonomic quantum gates with transmons”. In: *Physical Review A* 97.2 (Feb. 2018), p. 022332. DOI: 10.1103/physreva.97.022332.

[337] Silvia Arroyo-Camejo et al. “Room temperature high-fidelity holonomic single-qubit gate on a solid-state spin”. In: *Nature Communications* 5.1 (Sept. 2014). DOI: 10.1038/ncomms5870.

[338] C. Zu et al. “Experimental realization of universal geometric quantum gates with solid-state spins”. In: *Nature* 514.7520 (Oct. 2014), pp. 72–75. DOI: 10.1038/nature13729.

[339] Guanru Feng, Guofu Xu, and Guilu Long. "Experimental Realization of Nonadiabatic Holonomic Quantum Computation". In: *Physical Review Letters* 110.19 (May 2013), p. 190501. DOI: 10.1103/physrevlett.110.190501.

[340] K. Toyoda et al. "Realization of holonomic single-qubit operations". In: *Physical Review A* 87.5 (May 2013), p. 052307. DOI: 10.1103/physreva.87.052307.

[341] Vahid Azimi Mousolou. "Universal non-adiabatic geometric manipulation of pseudo-spin charge qubits". In: *EPL (Europhysics Letters)* 117.1 (Jan. 2017), p. 10006. DOI: 10.1209/0295-5075/117/10006.

[342] Erik Sjoqvist et al. "Non-adiabatic holonomic quantum computation". In: *New Journal of Physics* 14.10 (Oct. 2012), p. 103035. ISSN: 1367-2630. DOI: 10.1088/1367-2630/14/10/103035. URL: http://dx.doi.org/10.1088/1367-2630/14/10/103035.

[343] Jian Zhou et al. "Fast holonomic quantum computation based on solid-state spins with all-optical control". In: *Science China Physics, Mechanics & Astronomy* 61.1 (Oct. 2017). ISSN: 1869-1927. DOI: 10.1007/s11433-017-9119-8. URL: http://dx.doi.org/10.1007/s11433-017-9119-8.

[344] P. Z. Zhao et al. "Nonadiabatic holonomic quantum computation with Rydberg superatoms". In: *Physical Review A* 98.3 (Sept. 2018), p. 032313. DOI: 10.1103/physreva.98.032313.

[345] J. Majer et al. "Coupling superconducting qubits via a cavity bus". In: *Nature* 449.7161 (Sept. 2007), pp. 443–447. DOI: 10.1038/nature06184.

[346] A. Imamoglu et al. "Quantum Information Processing Using Quantum Dot Spins and Cavity QED". In: *Physical Review Letters* 83.20 (Nov. 1999), pp. 4204–4207. DOI: 10.1103/physrevlett.83.4204.

[347] Dima Mozyrsky, Vladimir Privman, and M. Lawrence Glasser. "Indirect Interaction of Solid-State Qubits via Two-Dimensional Electron Gas". In: *Physical Review Letters* 86.22 (May 2001), pp. 5112–5115. DOI: 10.1103/physrevlett.86.5112.

[348] Yimin Wang et al. "Dephasing-Protected Scalable Holonomic Quantum Computation on a Rabi Lattice". In: *Physical Review Applied* 14.4 (Oct. 2020), p. 044043. DOI: 10.1103/physrevapplied.14.044043.

[349] Takuya Hatomura. "Shortcuts to adiabaticity: theoretical framework, relations between different methods, and versatile approximations". In: (Nov. 16, 2023). DOI: 10.48550/ARXIV.2311.09720. arXiv: 2311.09720 [quant-ph].

[350] Erik Torrontegui et al. "Shortcuts to Adiabaticity". In: *Advances in Atomic, Molecular, and Optical Physics* (2013), pp. 117–169. ISSN: 1049-250X. DOI: 10.1016/b978-0-12-408090-4.00002-5. URL: http://dx.doi.org/10.1016/B978-0-12-408090-4.00002-5.

[351] D. Guéry-Odelin et al. "Shortcuts to adiabaticity: Concepts, methods, and applications". In: *Reviews of Modern Physics* 91.4 (Oct. 2019). ISSN: 1539-0756. DOI: 10.1103/revmodphys.91.045001. URL: http://dx.doi.org/10.1103/RevModPhys.91.045001.

[352] Zhen-Tao Liang et al. "Proposal for implementing universal superadiabatic geometric quantum gates in nitrogen-vacancy centers". In: *Physical Review A* 93.4 (Apr. 2016), p. 040305. DOI: 10.1103/physreva.93.040305.

[353] Tongxing Yan et al. "Experimental Realization of Nonadiabatic Shortcut to Non-Abelian Geometric Gates". In: *Physical Review Letters* 122.8 (Feb. 2019), p. 080501. DOI: 10.1103/physrevlett.122.080501.

[354] H. Georgi. *Weak Interactions and Modern Particle Theory*. Dover Books on Physics Series. Dover Publications, 2009. ISBN: 9780486469041. URL: https://books.google.com.au/books?id=aN9PPQAACAAJ.

[355] M V Berry. "Transitionless quantum driving". In: *Journal of Physics A: Mathematical and Theoretical* 42.36 (Aug. 2009), p. 365303. DOI: 10.1088/1751-8113/42/36/365303. URL: https://doi.org/10.1088/1751-8113/42/36/365303.

[356] Jin-Fu Chen. "Speeding up quantum adiabatic processes with a dynamical quantum geometric tensor". In: *Physical Review Research* 4.2 (Mar. 7, 2022), p. 023252. DOI: 10.1103/physrevresearch.4.023252. arXiv: 2203.03164 [quant-ph].

[357] Mikio Nakahara. "Counterdiabatic formalism of shortcuts to adiabaticity". In: *Philosophical Transactions of the Royal Society A: Mathematical, Physical and Engineering Sciences* 380.2239 (Aug. 15, 2022). DOI: 10.1098/rsta.2021.0272. arXiv: 2208.07346 [quant-ph].

[358] Kazutaka Takahashi. "Counterdiabatic driving for periodically driven open quantum systems". In: *Philosophical Transactions of the Royal Society A: Mathematical, Physical and Engineering Sciences* 380.2239 (Mar. 17, 2022). DOI: 10.1098/rsta.2021.0276. arXiv: 2203.09408 [quant-ph].

[359] Kazutaka Takahashi. "Dynamical invariant formalism of shortcuts to adiabaticity". In: *Philosophical Transactions of the Royal Society A: Mathematical, Physical and Engineering Sciences* 380.2239 (Sept. 9, 2022). DOI: 10.1098/rsta.2022.0301. arXiv: 2209.04367 [quant-ph].

[360] Michael Kolodrubetz et al. "Geometry and non-adiabatic response in quantum and classical systems". In: *Physics Reports* 697 (June 2017), pp. 1–87. DOI: 10.1016/j.physrep.2017.07.001.

[361] Jonas F. G. Santos. "Shortcut-to-adiabaticity for coupled harmonic oscillators". In: (Oct. 2023). DOI: 10.48550/ARXIV.2310.09576. arXiv: 2310.09576 [quant-ph].

[362] Kazutaka Takahashi and Adolfo del Campo. "Shortcuts to Adiabaticity in Krylov Space". In: (Feb. 10, 2023). DOI: 10.48550/ARXIV.2302.05460. arXiv: 2302.05460 [quant-ph].

[363] Gabriel Cardoso. "A Landau-Zener formula for the Adiabatic Gauge Potential". In: (Mar. 2023). DOI: 10.48550/ARXIV.2303.12066. arXiv: 2303.12066 [quant-ph].

[364] Monika Aidelsburger, Sylvain Nascimbene, and Nathan Goldman. "Artificial gauge fields in materials and engineered systems". In: *Comptes Rendus Physique* 19.6 (Sept. 2018), pp. 394–432. DOI: 10.1016/j.crhy.2018.03.002.

[365] Yi Yang et al. "Non-Abelian physics in light and sound". In: (May 2023). DOI: 10.48550/ARXIV.2305.12206. arXiv: 2305.12206 [physics.optics].

[366] Jürg Fröhlich. "Gauge invariance and anomalies in condensed matter physics". In: *Journal of Mathematical Physics* 64.3 (Mar. 2023). DOI: 10.1063/5.0135142.

[367] T. Fujita et al. "Gauge fields in spintronics". In: *Journal of Applied Physics* 110.12 (Dec. 2011). DOI: 10.1063/1.3665219.

[368] Jean Dalibard et al. "Colloquium: Artificial gauge potentials for neutral atoms". In: *Reviews of Modern Physics* 83.4 (Nov. 2011), pp. 1523–1543. DOI: 10.1103/revmodphys.83.1523.

[369] O. Băzăvan et al. "Synthetic $\mathbb{Z}_2$ gauge theories based on parametric excitations of trapped ions". In: (May 2023). DOI: 10.48550/ARXIV.2305.08700. arXiv: 2305.08700 [quant-ph].

[370] Jonas Larson and Sergey Levin. "Effective Abelian and Non-Abelian Gauge Potentials in Cavity QED". In: *Physical Review Letters* 103.1 (July 2009), p. 013602. DOI: 10.1103/physrevlett.103.013602.

[371] Farokh Mivehvar. *Cavity-Induced Synthetic Gauge Potentials*. 2016. DOI: 10.11575/PRISM/25231.

[372] Seiji Sugawa et al. "Wilson loop and Wilczek-Zee phase from a non-Abelian gauge field". In: *npj Quantum Information* 7.1 (Sept. 2021). DOI: 10.1038/s41534-021-00483-2.

[373] Dali Cheng, Kai Wang, and Shanhui Fan. "Artificial Non-Abelian Lattice Gauge Fields for Photons in the Synthetic Frequency Dimension". In: *Physical Review Letters* 130.8 (Aug. 31, 2022), p. 083601. DOI: 10.1103/physrevlett.130.083601. arXiv: 2208.14967 [physics.optics].

[374] W. B. Rui, Y. X. Zhao, and Z. D. Wang. "Making topologically trivial non-Hermitian systems non-trivial via gauge fields". In: (Sept. 2023). DOI: 10.48550/ARXIV.2309.14042. arXiv: 2309.14042 [cond-mat.mes-hall].

[375] Gabriel Wong, Robert Raussendorf, and Bartlomiej Czech. "The Gauge Theory of Measurement-Based Quantum Computation". In: (July 20, 2022). arXiv: 2207.10098 [hep-th].

[376] Pablo Arnault et al. "Quantum walks and non-Abelian discrete gauge theory". In: *Physical Review A* 94.1 (July 2016), p. 012335. DOI: 10.1103/physreva.94.012335.

[377] Iván Márquez-Martin et al. "Electromagnetic lattice gauge invariance in two-dimensional discrete-time quantum walks". In: *Physical Review A* 98.3 (Sept. 2018), p. 032333. DOI: 10.1103/physreva.98.032333.

[378] Pablo Arrighi, Giuseppe Di Molfetta, and Nathanaël Eon. "A Gauge-Invariant Reversible Cellular Automaton". In: *Cellular Automata and Discrete Complex Systems*. Springer International Publishing, 2018, pp. 1–12. DOI: 10.1007/978-3-319-92675-9_1.

[379] Pablo Arrighi, Giuseppe Di Molfetta, and Nathanaël Eon. "Non-abelian Gauge-Invariant Cellular Automata". In: *Theory and Practice of Natural Computing*. Springer International Publishing, 2019, pp. 211–221. DOI: 10.1007/978-3-030-34500-6_15.

[380] Pablo Arrighi, Giuseppe Di Molfetta, and Nathanaël Eon. "Gauge-invariance in cellular automata". In: *Natural Computing* 22.3 (Jan. 2022), pp. 587–599. DOI: 10.1007/s11047-022-09879-1.

[381] Kevissen Sellapillay, Pablo Arrighi, and Giuseppe Di Molfetta. "A discrete relativistic spacetime formalism for 1+1-QED with continuum limits". In: *Scientific Reports* 12.1 (Feb. 2022). DOI: 10.1038/s41598-022-06241-4.

[382] Nathanaël Eon et al. "A relativistic discrete spacetime formulation of 3+1 QED". In: (May 6, 2022). DOI: 10.48550/ARXIV.2205.03148. arXiv: 2205.03148 [quant-ph].

[383] Charles Kittel. *Introduction to Solid State Physics*. 8th ed. Wiley, 2004. ISBN: 9780471415268. URL: http://www.amazon.com/Introduction-Solid-Physics-Charles-Kittel/dp/047141526X/ref=dp_ob_title_bk.

[384] Aashish Clerk. "Introduction to quantum non-reciprocal interactions: from non-Hermitian Hamiltonians to quantum master equations and quantum feedforward schemes". In: *SciPost Physics Lecture Notes* (Mar. 2022). DOI: 10.21468/scipostphyslectnotes.44.

[385] Y. Li et al. "Non-Abelian geometric quantum memory with an atomic ensemble". In: *Physical Review A* 70.3 (Sept. 2004), p. 032330. DOI: 10.1103/physreva.70.032330.

[386] Valentina Brosco et al. "Non-Abelian Superconducting Pumps". In: *Physical Review Letters* 100.2 (Jan. 2008), p. 027002. DOI: 10.1103/physrevlett.100.027002.

[387] J.-M. Pirkkalainen et al. "Non-Abelian geometric phases in ground-state Josephson devices". In: *Physical Review B* 81.17 (May 2010), p. 174506. DOI: 10.1103/physrevb.81.174506.

[388] Longwen Zhou and Da-Jian Zhang. "Non-Hermitian Floquet Topological Matter—A Review". In: *Entropy* 25.10 (Sept. 2023), p. 1401. DOI: 10.3390/e25101401. arXiv: 2305.16153 [quant-ph].

[389] Hilary M. Hurst and Benedetta Flebus. "Non-Hermitian physics in magnetic systems". In: *Journal of Applied Physics* 132.22 (Sept. 8, 2022). DOI: 10.1063/5.0124841. arXiv: 2209.03946 [cond-mat.mes-hall].

[390] Qiang Wang and Y. D. Chong. "Non-Hermitian photonic lattices: tutorial". In: *Journal of the Optical Society of America B* 40.6 (Dec. 1, 2022), p. 1443. DOI: 10.1364/josab.481963. arXiv: 2212.00307 [physics.optics].

[391] Yunshan Cao and Peng Yan. "Exceptional magnetic sensitivity of PT-symmetric cavity magnon polaritons". In: *Physical Review B* 99.21 (June 2019), p. 214415. DOI: 10.1103/physrevb.99.214415.

[392] Chia Wei Hsu et al. “Bound states in the continuum”. In: *Nature Reviews Materials* 1.9 (July 2016). DOI: 10.1038/natrevmats.2016.48.

[393] Longwen Zhou. “Entanglement phase transitions in non-Hermitian Floquet systems”. In: (Oct. 2023). DOI: 10.48550/ARXIV.2310.11351. arXiv: 2310.11351 [quant-ph].

[394] Xi-guang Wang et al. “Floquet-engineering the exceptional points in parity-time-symmetric magnonics”. In: (Oct. 2023). DOI: 10.48550/ARXIV.2310.09300. arXiv: 2310.09300 [cond-mat.mes-hall].

[395] Xi-guang Wang, Guang-hua Guo, and Jamal Berakdar. “PT-Symmetry Enabled Spintronic Thermal Diodes and Logic Gates”. In: *Advanced Electronic Materials* (Oct. 2023). DOI: 10.1002/aelm.202300325.

[396] A A Zyablovsky et al. “PT-symmetry in optics”. In: *Physics-Uspekhi* 57.11 (Nov. 2014), pp. 1063–1082. DOI: 10.3367/ufne.0184.201411b.1177.

[397] Jianming Wen et al. “Parity-time symmetry in optical microcavity systems”. In: *Journal of Physics B: Atomic, Molecular and Optical Physics* 51.22 (Oct. 2018), p. 222001. DOI: 10.1088/1361-6455/aae42f.

[398] Han Zhao and Liang Feng. “Parity–time symmetric photonics”. In: *National Science Review* 5.2 (Jan. 2018), pp. 183–199. DOI: 10.1093/nsr/nwy011.

[399] Ş. K. Özdemir et al. “Parity–time symmetry and exceptional points in photonics”. In: *Nature Materials* 18.8 (Apr. 2019), pp. 783–798. DOI: 10.1038/s41563-019-0304-9.

[400] Ramy El-Ganainy et al. “Non-Hermitian physics and PT symmetry”. In: *Nature Physics* 14.1 (Jan. 2018), pp. 11–19. DOI: 10.1038/nphys4323.

[401] Shishir Khandelwal et al. “Chiral Bell-state transfer via dissipative Liouvillian dynamics”. In: (Oct. 2023). DOI: 10.48550/ARXIV.2310.11381. arXiv: 2310.11381 [quant-ph].

[402] Zeng-Zhao Li et al. “Speeding Up Entanglement Generation by Proximity to Higher-Order Exceptional Points”. In: *Physical Review Letters* 131.10 (Sept. 8, 2023), p. 100202. DOI: 10.1103/PhysRevLett.131.100202. arXiv: 2210.05048 [quant-ph]. URL: https://link.aps.org/doi/10.1103/PhysRevLett.131.100202 (visited on 11/16/2023).

[403] A. Metelmann and A. A. Clerk. “Nonreciprocal Photon Transmission and Amplification via Reservoir Engineering”. In: *Physical Review X* 5.2 (June 2015), p. 021025. DOI: 10.1103/physrevx.5.021025.

[404] Weichao Yu et al. “Prediction of Attractive Level Crossing via a Dissipative Mode”. In: *Physical Review Letters* 123.22 (Nov. 2019), p. 227201. DOI: 10.1103/physrevlett.123.227201.

[405] Kevin Lalumière et al. “Input-output theory for waveguide QED with an ensemble of inhomogeneous atoms”. In: *Physical Review A* 88.4 (Oct. 7, 2013), p. 043806. DOI: 10.1103/physreva.88.043806. URL: https://link.aps.org/doi/10.1103/PhysRevA.88.043806 (visited on 11/03/2023).

[406] Bimu Yao et al. “The microscopic origin of magnon-photon level attraction by traveling waves: Theory and experiment”. In: *Physical Review B* 100.21 (Dec. 2019), p. 214426. DOI: 10.1103/physrevb.100.214426.

[407] Bimu Yao et al. “Coherent control of magnon radiative damping with local photon states”. In: *Communications Physics* 2.1 (Dec. 2019). DOI: 10.1038/s42005-019-0264-z.

[408] Jie Zhao et al. “Observation of Anti-PT-Symmetry Phase Transition in the Magnon-Cavity-Magnon Coupled System”. In: *Physical Review Applied* 13.1 (Jan. 28, 2020), p. 014053. DOI: 10.1103/PhysRevApplied.13.014053. URL: https://link.aps.org/doi/10.1103/PhysRevApplied.13.014053 (visited on 11/07/2023).

[409] M. Harder et al. “Level Attraction Due to Dissipative Magnon-Photon Coupling”. In: *Physical Review Letters* 121.13 (Sept. 2018), p. 137203. DOI: 10.1103/physrevlett.121.137203.

[410] Biswanath Bhoi et al. “Abnormal anticrossing effect in photon-magnon coupling”. In: *Physical Review B* 99.13 (Apr. 17, 2019), p. 134426. DOI: 10.1103/PhysRevB.99.134426. URL: https://link.aps.org/doi/10.1103/PhysRevB.99.134426 (visited on 11/05/2023).

[411] Y. Yang et al. “Control of the Magnon-Photon Level Attraction in a Planar Cavity”. In: *Physical Review Applied* 11.5 (May 8, 2019), p. 054023. DOI: 10.1103/PhysRevApplied.11.054023. URL: https://link.aps.org/doi/10.1103/PhysRevApplied.11.054023 (visited on 11/05/2023).

[412] J. W. Rao et al. “Interactions between a magnon mode and a cavity photon mode mediated by traveling photons”. In: *Physical Review B* 101.6 (Feb. 5, 2020), p. 064404. DOI: 10.1103/PhysRevB.101.064404. URL: https://link.aps.org/doi/10.1103/PhysRevB.101.064404 (visited on 11/05/2023).

[413] Yi-Pu Wang et al. “Nonreciprocity and Unidirectional Invisibility in Cavity Magnonics”. In: *Physical Review Letters* 123.12 (Sept. 2019), p. 127202. DOI: 10.1103/physrevlett.123.127202.

[414] N. R. Bernier et al. “Level attraction in a microwave optomechanical circuit”. In: *Physical Review A* 98.2 (Aug. 2018), p. 023841. DOI: 10.1103/physreva.98.023841.

[415] M. Khanbekyan et al. “Unconventional collective normal-mode coupling in quantum-dot-based bimodal microlasers”. In: *Physical Review A* 91.4 (Apr. 28, 2015), p. 043840. DOI: 10.1103/PhysRevA.91.043840. URL: https://link.aps.org/doi/10.1103/PhysRevA.91.043840 (visited on 11/07/2023).

[416] Igor Proskurin, Rair Macêdo, and Robert L Stamps. “Microscopic origin of level attraction for a coupled magnon-photon system in a microwave cavity”. In: *New Journal of Physics* 21.9 (Sept. 2019), p. 095003. DOI: 10.1088/1367-2630/ab3cb7.

[417] Nathan R. Bernier, Emanuele G. Dalla Torre, and Eugene Demler. “Unstable Avoided Crossing in Coupled Spinor Condensates”. In: *Physical Review Letters* 113.6 (Aug. 5, 2014), p. 065303. DOI: 10.1103/PhysRevLett.113.065303. URL: https://link.aps.org/doi/10.1103/PhysRevLett.113.065303 (visited on 11/07/2023).

[418] J W Rao et al. “Level attraction and level repulsion of magnon coupled with a cavity anti-resonance”. In: *New Journal of Physics* 21.6 (June 2019), p. 065001. DOI: 10.1088/1367-2630/ab2482.

[419] John Jeffers et al. “Bound mode of an atom laser”. In: *Physical Review A* 62.4 (Sept. 11, 2000), p. 043602. DOI: 10.1103/PhysRevA.62.043602. URL: https://link.aps.org/doi/10.1103/PhysRevA.62.043602 (visited on 11/14/2023).

[420] Vahram L. Grigoryan, Ka Shen, and Ke Xia. “Synchronized spin-photon coupling in a microwave cavity”. In: *Physical Review B* 98.2 (July 2018), p. 024406. DOI: 10.1103/physrevb.98.024406.

[421] Isabella Boventer et al. “Steering between level repulsion and attraction: broad tunability of two-port driven cavity magnon-polaritons”. In: *New Journal of Physics* 21.12 (Dec. 2019), p. 125001. DOI: 10.1088/1367-2630/ab5c12.

[422] Isabella Boventer et al. “Control of the coupling strength and linewidth of a cavity magnon-polariton”. In: *Physical Review Research* 2.1 (Feb. 2020), p. 013154. DOI: 10.1103/physrevresearch.2.013154.

[423] Ying-Ying Wang et al. “Dispersive Non-reciprocity between a Qubit and a Cavity”. In: (July 2023). DOI: 10.48550/ARXIV.2307.05298. arXiv: 2307.05298 [quant-ph].

[424] Jens Koch et al. “Time-reversal-symmetry breaking in circuit-QED-based photon lattices”. In: *Physical Review A* 82.4 (Oct. 2010), p. 043811. DOI: 10.1103/physreva.82.043811.

[425] Jin-Feng Huang, Jie-Qiao Liao, and Le-Man Kuang. "Ultrastrong Jaynes-Cummings model". In: *Physical Review A* 101.4 (Apr. 2020). ISSN: 2469-9934. DOI: 10.1103/physreva.101.043835. URL: http://dx.doi.org/10.1103/PhysRevA.101.043835.

[426] J. Casanova et al. "Deep Strong Coupling Regime of the Jaynes-Cummings Model". In: *Physical Review Letters* 105.26 (Dec. 2010). ISSN: 1079-7114. DOI: 10.1103/physrevlett.105.263603. URL: http://dx.doi.org/10.1103/PhysRevLett.105.263603.

[427] Qiongtao Xie et al. "The quantum Rabi model: solution and dynamics". In: *Journal of Physics A: Mathematical and Theoretical* 50.11 (Feb. 2017), p. 113001. ISSN: 1751-8121. DOI: 10.1088/1751-8121/aa5a65. URL: http://dx.doi.org/10.1088/1751-8121/aa5a65.

[428] Anton Frisk Kockum et al. "Ultrastrong coupling between light and matter". In: *Nature Reviews Physics* 1.1 (Jan. 2019), pp. 19–40. ISSN: 2522-5820. DOI: 10.1038/s42254-018-0006-2. URL: http://dx.doi.org/10.1038/s42254-018-0006-2.

[429] P. Forn-Diaz et al. "Ultrastrong coupling regimes of light-matter interaction". In: *Reviews of Modern Physics* 91.2 (June 2019), p. 025005. DOI: 10.1103/revmodphys.91.025005.

[430] Aji A. Anappara et al. "Signatures of the ultrastrong light-matter coupling regime". In: *Physical Review B* 79.20 (May 11, 2009), p. 201303. DOI: 10.1103/PhysRevB.79.201303. URL: https://link.aps.org/doi/10.1103/PhysRevB.79.201303 (visited on 01/11/2024).

[431] Fuyang Tay et al. "Ultrastrong photon-photon coupling". In: (Aug. 2023). DOI: 10.48550/ARXIV.2308.12427. arXiv: 2308.12427 [quant-ph].

[432] Soumya Ranjan Das et al. "Instabilities near Ultrastrong Coupling in a Microwave Optomechanical Cavity". In: *Physical Review Letters* 131.6 (Aug. 2023), p. 067001. DOI: 10.1103/physrevlett.131.067001.

[433] Xinwei Li et al. "Vacuum Bloch–Siegert shift in Landau polaritons with ultra-high cooperativity". In: *Nature Photonics* 12.6 (June 2018), pp. 324–329. ISSN: 1749-4893. DOI: 10.1038/s41566-018-0153-0. URL: https://doi.org/10.1038/s41566-018-0153-0.

[434] T. Niemczyk et al. "Circuit quantum electrodynamics in the ultrastrong-coupling regime". In: *Nature Physics* 6.10 (Oct. 2010), pp. 772–776. ISSN: 1745-2481. DOI: 10.1038/nphys1730. URL: https://www.nature.com/articles/nphys1730 (visited on 01/11/2024).

[435] Alexandre Le Boité. "Theoretical Methods for Ultrastrong Light–Matter Interactions". In: *Advanced Quantum Technologies* 3.7 (2020), p. 1900140. DOI: https://doi.org/10.1002/qute.201900140. eprint: https://onlinelibrary.wiley.com/doi/pdf/10.1002/qute.201900140. URL: https://onlinelibrary.wiley.com/doi/abs/10.1002/qute.201900140.

[436] Salvatore Savasta, Omar Di Stefano, and Franco Nori. "Thomas–Reiche–Kuhn (TRK) sum rule for interacting photons". In: *Nanophotonics* 10.1 (Nov. 2020), pp. 465–476. DOI: 10.1515/nanoph-2020-0433.

[437] Simone De Liberato. "Light-Matter Decoupling in the Deep Strong Coupling Regime: The Breakdown of the Purcell Effect". In: *Phys. Rev. Lett.* 112 (1 Jan. 2014), p. 016401. DOI: 10.1103/PhysRevLett.112.016401. URL: https://link.aps.org/doi/10.1103/PhysRevLett.112.016401.

[438] Omar Di Stefano et al. "Feynman-diagrams approach to the quantum Rabi model for ultrastrong cavity QED: stimulated emission and reabsorption of virtual particles dressing a physical excitation". In: *New Journal of Physics* 19.5 (May 2017), p. 053010. DOI: 10.1088/1367-2630/aa6cd7. URL: https://doi.org/10.1088/1367-2630/aa6cd7.

[439] L. Garziano et al. "Vacuum-induced symmetry breaking in a superconducting quantum circuit". In: *Phys. Rev. A* 90 (4 Oct. 2014), p. 043817. DOI: 10.1103/PhysRevA.90.043817. URL: https://link.aps.org/doi/10.1103/PhysRevA.90.043817.

[440] Shuai-Peng Wang et al. “Detecting the symmetry breaking of the quantum vacuum in a light–matter coupled system”. In: (Sept. 2022). DOI: 10.48550/ARXIV.2209.05747. arXiv: 2209.05747 [quant-ph].

[441] C. M. Wilson et al. “Observation of the dynamical Casimir effect in a superconducting circuit”. In: *Nature* 479.7373 (Nov. 2011), pp. 376–379. DOI: 10.1038/nature10561.

[442] Joshua Mornhinweg et al. “Extremely Non-Adiabatic Switching of Deep-Strong Light-Matter Coupling”. In: *The 22nd International Conference on Ultrafast Phenomena 2020*. OSA, 2020. DOI: 10.1364/up.2020.w3b.2.

[443] Michael Stone. *Bose Bogoliubov transformations*. 2017. URL: http://people.physics.illinois.edu/stone/bose_bogoliubov.pdf.

[444] Peter Woit. *Quantum Theory, Groups and Representations*. Springer International Publishing, 2017. ISBN: 9783319646121. DOI: 10.1007/978-3-319-64612-1.

[445] Cristiano Ciuti, Gérald Bastard, and Iacopo Carusotto. “Quantum vacuum properties of the intersubband cavity polariton field”. In: *Physical Review B* 72.11 (Sept. 2005), p. 115303. DOI: 10.1103/physrevb.72.115303.

[446] Qingtian Miao and G. S. Agarwal. “Polaritonic Ultrastrong Coupling: Quantum Entanglement in Ground State”. In: (Apr. 2023). DOI: 10.48550/ARXIV.2304.00680. arXiv: 2304.00680 [quant-ph].

[447] Roy J. Glauber. “The Quantum Theory of Optical Coherence”. In: *Phys. Rev.* 130 (6 June 1963), pp. 2529–2539. DOI: 10.1103/PhysRev.130.2529. URL: https://link.aps.org/doi/10.1103/PhysRev.130.2529.

[448] Omar Di Stefano et al. “Photodetection probability in quantum systems with arbitrarily strong light-matter interaction”. In: *Scientific Reports* 8.1 (Dec. 2018). ISSN: 2045-2322. DOI: 10.1038/s41598-018-36056-1. URL: http://dx.doi.org/10.1038/s41598-018-36056-1.

[449] Sanwu Wang. “Generalization of the Thomas-Reiche-Kuhn and the Bethe sum rules”. In: *Physical Review A* 60.1 (July 1, 1999), pp. 262–266. DOI: 10.1103/PhysRevA.60.262. URL: https://link.aps.org/doi/10.1103/PhysRevA.60.262 (visited on 01/15/2024).

[450] Omar Di Stefano et al. “Resolution of gauge ambiguities in ultrastrong-coupling cavity quantum electrodynamics”. In: *Nature Physics* 15.8 (June 2019), pp. 803–808. ISSN: 1745-2481. DOI: 10.1038/s41567-019-0534-4. URL: http://dx.doi.org/10.1038/s41567-019-0534-4.

[451] S. Ashhab. “Superradiance transition in a system with a single qubit and a single oscillator”. In: *Physical Review A* 87.1 (Jan. 23, 2013), p. 013826. DOI: 10.1103/PhysRevA.87.013826. URL: https://link.aps.org/doi/10.1103/PhysRevA.87.013826 (visited on 03/18/2024).

[452] J. J. Garcia-Ripoll, B. Peropadre, and S. De Liberato. “Light-matter decoupling and A2 term detection in superconducting circuits”. In: *Scientific Reports* 5.1 (Nov. 2015). DOI: 10.1038/srep16055.

[453] Daniele De Bernardis et al. “Breakdown of gauge invariance in ultrastrong-coupling cavity QED”. In: *Phys. Rev. A* 98 (5 Nov. 2018), p. 053819. DOI: 10.1103/PhysRevA.98.053819. URL: https://link.aps.org/doi/10.1103/PhysRevA.98.053819.

[454] Adam Stokes and Ahsan Nazir. “Gauge ambiguities imply Jaynes-Cummings physics remains valid in ultrastrong coupling QED”. In: *Nature Communications* 10.1 (Jan. 2019). DOI: 10.1038/s41467-018-08101-0.

[455] Luigi Garziano et al. “Gauge invariance of the Dicke and Hopfield models”. In: *Phys. Rev. A* 102 (2 Aug. 2020), p. 023718. DOI: 10.1103/PhysRevA.102.023718. URL: https://link.aps.org/doi/10.1103/PhysRevA.102.023718.

[456] Alessio Settineri et al. “Gauge freedom, quantum measurements, and time-dependent interactions in cavity QED”. In: *Phys. Rev. Research* 3 (2 Apr. 2021), p. 023079. DOI: 10.1103/PhysRevResearch.3.023079. URL: https://link.aps.org/doi/10.1103/PhysRevResearch.3.023079.

[457] Adam Stokes and Ahsan Nazir. “Ultrastrong time-dependent light-matter interactions are gauge relative”. In: *Phys. Rev. Research* 3 (1 Feb. 2021), p. 013116. DOI: 10.1103/PhysRevResearch.3.013116. URL: https://link.aps.org/doi/10.1103/PhysRevResearch.3.013116.

[458] Maxim Goryachev et al. “High-Cooperativity Cavity QED with Magnons at Microwave Frequencies”. In: *Phys. Rev. Applied* 2 (5 Nov. 2014), p. 054002. DOI: 10.1103/PhysRevApplied.2.054002. URL: https://link.aps.org/doi/10.1103/PhysRevApplied.2.054002.

[459] Xufeng Zhang et al. “Strongly Coupled Magnons and Cavity Microwave Photons”. In: *Physical Review Letters* 113.15 (Oct. 2014), p. 156401. DOI: 10.1103/physrevlett.113.156401.

[460] Nikita Kostylev, Maxim Goryachev, and Michael E. Tobar. “Superstrong coupling of a microwave cavity to yttrium iron garnet magnons”. In: *Applied Physics Letters* 108.6 (Feb. 2016), p. 062402. DOI: 10.1063/1.4941730.

[461] J. Bourhill et al. “Ultrahigh cooperativity interactions between magnons and resonant photons in a YIG sphere”. In: *Physical Review B* 93.14 (Apr. 2016), p. 144420. DOI: 10.1103/physrevb.93.144420.

[462] Igor A. Golovchanskiy et al. “Ultrastrong photon-to-magnon coupling in multilayered heterostructures involving superconducting coherence via ferromagnetic layers”. In: *Science Advances* 7.25 (June 2021). DOI: 10.1126/sciadv.abe8638.

[463] Mikhail Silaev. “Ultrastrong magnon-photon coupling, squeezed vacuum, and entanglement in superconductor/ferromagnet nanostructures”. In: *Physical Review B* 107.18 (May 26, 2023), p. L180503. DOI: 10.1103/PhysRevB.107.L180503. arXiv: 2211.00462 [cond-mat.mes-hall]. URL: https://link.aps.org/doi/10.1103/PhysRevB.107.L180503 (visited on 01/12/2024).

[464] I.A. Golovchanskiy et al. “Approaching Deep-Strong On-Chip Photon-To-Magnon Coupling”. In: *Phys. Rev. Applied* 16 (3 Sept. 2021), p. 034029. DOI: 10.1103/PhysRevApplied.16.034029. URL: https://link.aps.org/doi/10.1103/PhysRevApplied.16.034029.

[465] Guillaume Bourcin et al. “Strong to ultrastrong coherent coupling measurements in a YIG/cavity system at room temperature”. In: *Physical Review B* 107.21 (June 2023), p. 214423. DOI: 10.1103/physrevb.107.214423.

[466] Xufeng Zhang et al. “Cavity magnomechanics”. In: *Science Advances* 2.3 (Mar. 2016). DOI: 10.1126/sciadv.1501286.

[467] Jie Li, Shi-Yao Zhu, and G. S. Agarwal. “Magnon-Photon-Phonon Entanglement in Cavity Magnomechanics”. In: *Physical Review Letters* 121.20 (Nov. 2018), p. 203601. DOI: 10.1103/physrevlett.121.203601.

[468] Jie Li, Shi-Yao Zhu, and G. S. Agarwal. “Squeezed states of magnons and phonons in cavity magnomechanics”. In: *Physical Review A* 99.2 (Feb. 2019), p. 021801. DOI: 10.1103/physreva.99.021801.

[469] Silvia Viola Kusminskiy, Hong X. Tang, and Florian Marquardt. “Coupled spin-light dynamics in cavity optomagnonics”. In: *Physical Review A* 94.3 (Sept. 12, 2016), p. 033821. DOI: 10.1103/PhysRevA.94.033821. URL: https://link.aps.org/doi/10.1103/PhysRevA.94.033821 (visited on 01/18/2024).

[470] Feng-Xiao Sun et al. “Remote Generation of Magnon Schrödinger Cat State via Magnon-Photon Entanglement”. In: *Physical Review Letters* 127.8 (Aug. 2021), p. 087203. DOI: 10.1103/physrevlett.127.087203.

[471] Zahra Haghshenasfard and Michael G. Cottam. "Sub-Poissonian statistics and squeezing of magnons due to the Kerr effect in a hybrid coupled cavity–magnon system". In: *Journal of Applied Physics* 128.3 (July 15, 2020), p. 033901. DOI: 10.1063/5.0012072.

[472] Xi Jiang, Shiqing Tang, and Songsong Li. "Kerr-Nonlinearity-Triggered Nonclassicality of Magnons in a Photon-Magnon Coupling System". In: *Photonics* 9.10 (Sept. 21, 2022), p. 681. DOI: 10.3390/photonics9100681.

[473] V. A. S. V. Bittencourt et al. "Magnomechanical backaction corrections due to coupling to higher-order Walker modes and Kerr nonlinearities". In: *Physical Review B* 107.14 (Apr. 10, 2023), p. 144411. DOI: 10.1103/PhysRevB.107.144411. arXiv: 2301.11920 [cond-mat.mes-hall]. URL: https://link.aps.org/doi/10.1103/PhysRevB.107.144411 (visited on 01/21/2024).

[474] Zhi-Bo Yang et al. "Steady-entangled-state generation via the cross-Kerr effect in a ferrimagnetic crystal". In: *Physical Review A* 106.1 (July 2022), p. 012419. DOI: 10.1103/physreva.106.012419.

[475] M. Kounalakis et al. "Tuneable hopping and nonlinear cross-Kerr interactions in a high-coherence superconducting circuit". In: *npj Quantum Information* 4.1 (Aug. 6, 2018), pp. 1–7. ISSN: 2056-6387. DOI: 10.1038/s41534-018-0088-9. URL: https://www.nature.com/articles/s41534-018-0088-9 (visited on 01/21/2024).

[476] Andrei Vrajitoarea et al. "Quantum control of an oscillator using a stimulated Josephson nonlinearity". In: *Nature Physics* 16.2 (Feb. 2020), pp. 211–217. ISSN: 1745-2481. DOI: 10.1038/s41567-019-0703-5. URL: https://www.nature.com/articles/s41567-019-0703-5 (visited on 01/21/2024).

[477] Matthew Elliott, Jaewoo Joo, and Eran Ginossar. "Designing Kerr interactions using multiple superconducting qubit types in a single circuit". In: *New Journal of Physics* 20.2 (Feb. 2018), p. 023037. ISSN: 1367-2630. DOI: 10.1088/1367-2630/aa9243. URL: https://dx.doi.org/10.1088/1367-2630/aa9243 (visited on 01/21/2024).

[478] Io-Chun Hoi et al. "Giant Cross–Kerr Effect for Propagating Microwaves Induced by an Artificial Atom". In: *Physical Review Letters* 111.5 (Aug. 2, 2013), p. 053601. DOI: 10.1103/PhysRevLett.111.053601. URL: https://link.aps.org/doi/10.1103/PhysRevLett.111.053601 (visited on 01/21/2024).

[479] Pieter Kok. "Photonic quantum information processing". In: *Contemporary Physics* 57.4 (May 2016), pp. 526–544. DOI: 10.1080/00107514.2016.1178472.

[480] Stefanie Barz. "Quantum computing with photons: introduction to the circuit model, the one-way quantum computer, and the fundamental principles of photonic experiments". In: *Journal of Physics B: Atomic, Molecular and Optical Physics* 48.8 (Mar. 2015), p. 083001. DOI: 10.1088/0953-4075/48/8/083001. URL: https://doi.org/10.1088/0953-4075/48/8/083001.

[481] Zhan Zheng et al. "Entanglement in a four-wave mixing process". In: *Optics Letters* 42.14 (July 2017), p. 2754. ISSN: 1539-4794. DOI: 10.1364/ol.42.002754.

[482] Qizhi Cai, Jinkun Liao, and Qiang Zhou. "Stationary Entanglement between Light and Microwave via Ferromagnetic Magnons". In: *Annalen der Physik* 532.12 (Oct. 2020), p. 2000250. DOI: 10.1002/andp.202000250.

[483] Ali Anwar et al. "Entangled photon-pair sources based on three-wave mixing in bulk crystals". In: *Review of Scientific Instruments* 92.4 (Apr. 7, 2021), p. 041101. ISSN: 0034-6748. DOI: 10.1063/5.0023103. URL: https://doi.org/10.1063/5.0023103 (visited on 01/20/2024).

[484] G. S. Agarwal and Sumei Huang. "Strong mechanical squeezing and its detection". In: *Physical Review A* 93.4 (Apr. 25, 2016), p. 043844. DOI: 10.1103/PhysRevA.93.043844. URL: https://link.aps.org/doi/10.1103/PhysRevA.93.043844 (visited on 01/21/2024).

[485] Jayakrishnan M. P. Nair and G. S. Agarwal. "Deterministic quantum entanglement between macroscopic ferrite samples". In: *Applied Physics Letters* 117.8 (Aug. 2020), p. 084001. DOI: 10.1063/5.0015195.

[486] Jie Li and Simon Gröblacher. "Entangling the vibrational modes of two massive ferromagnetic spheres using cavity magnomechanics". In: *Quantum Science and Technology* 6.2 (Feb. 2021), p. 024005. DOI: 10.1088/2058-9565/abd982.

[487] Mei Yu, Heng Shen, and Jie Li. "Magnetostrictively Induced Stationary Entanglement between Two Microwave Fields". In: *Physical Review Letters* 124.21 (May 2020), p. 213604. DOI: 10.1103/physrevlett.124.213604.

[488] Jie Li and Shi-Yao Zhu. "Entangling two magnon modes via magnetostrictive interaction". In: *New Journal of Physics* 21.8 (Aug. 2019), p. 085001. DOI: 10.1088/1367-2630/ab3508.

[489] Ming-Song Ding et al. "Magnon squeezing enhanced entanglement in a cavity magnomechanical system". In: *Journal of the Optical Society of America B* 39.10 (Sept. 2022), p. 2665. DOI: 10.1364/josab.465554. arXiv: 2205.14569 [quant-ph].

[490] Jiaojiao Chen et al. "Nonreciprocal entanglement in cavity-magnon optomechanics". In: *Physical Review B* 108.2 (July 25, 2023), p. 024105. DOI: 10.1103/PhysRevB.108.024105. arXiv: 2305.03325 [quant-ph]. URL: https://link.aps.org/doi/10.1103/PhysRevB.108.024105 (visited on 01/23/2024).

[491] Bakht Hussain, Shahid Qamar, and Muhammad Irfan. "Entanglement enhancement in cavity magnomechanics by an optical parametric amplifier". In: *Physical Review A* 105.6 (June 2022), p. 063704. DOI: 10.1103/physreva.105.063704.

[492] Wei Zhang et al. "Quantum entanglement and one-way steering in a cavity magnomechanical system via a squeezed vacuum field". In: *Optics Express* 30.7 (Mar. 2022), p. 10969. DOI: 10.1364/oe.453787.

[493] Mohamed Amazioug, Berihu Teklu, and Muhammad Asjad. "Enhancement of magnon–photon–phonon entanglement in a cavity magnomechanics with coherent feedback loop". In: *Scientific Reports* 13.1 (Mar. 7, 2023), p. 3833. ISSN: 2045-2322. DOI: 10.1038/s41598-023-30693-x. arXiv: 2211.17052 [quant-ph]. URL: https://www.nature.com/articles/s41598-023-30693-x (visited on 12/01/2023).

[494] M. Amazioug et al. "Coherent feedback control of quantum correlations in cavity magnomechanical system with magnon squeezing". In: (Feb. 2023). DOI: 10.48550/ARXIV.2302.08567. arXiv: 2302.08567 [quant-ph].

[495] Ming-Song Ding et al. "Enhanced entanglement and steering in PT-symmetric cavity magnomechanics". In: *Optics Communications* 490 (July 2021), p. 126903. DOI: 10.1016/j.optcom.2021.126903.

[496] H. Y. Yuan et al. "Steady Bell State Generation via Magnon-Photon Coupling". In: *Physical Review Letters* 124.5 (Feb. 2020), p. 053602. DOI: 10.1103/physrevlett.124.053602.

[497] Ting-Ting Dong et al. "Enhanced Entanglement and Quantum Steering Induced by a Common Reservoir in Cavity Magnomechanics". In: *Advanced Quantum Technologies* (Oct. 2023). DOI: 10.1002/qute.202300212.

[498] M. Dakna et al. "Generating Schr\"odinger-cat-like states by means of conditional measurements on a beam splitter". In: *Physical Review A* 55.4 (Apr. 1, 1997), pp. 3184–3194. DOI: 10.1103/PhysRevA.55.3184. URL: https://link.aps.org/doi/10.1103/PhysRevA.55.3184 (visited on 01/24/2024).

[499] J. Bourassa et al. "Josephson-junction-embedded transmission-line resonators: From Kerr medium to in-line transmon". In: *Physical Review A* 86.1 (July 11, 2012), p. 013814. DOI: 10.1103/PhysRevA.86.013814. URL: https://link.aps.org/doi/10.1103/PhysRevA.86.013814 (visited on 01/24/2024).

[500] Mark J. Everitt et al. “Engineering Dissipative Channels for Realizing Schrödinger Cats in SQUIDs”. In: *Frontiers in ICT* 1 (2014). ISSN: 2297-198X. URL: https://www.frontiersin.org/articles/10.3389/fict.2014.00001 (visited on 01/24/2024).

[501] Jie-Qiao Liao, Jin-Feng Huang, and Lin Tian. “Generation of macroscopic Schr\”odinger-cat states in qubit-oscillator systems”. In: *Physical Review A* 93.3 (Mar. 28, 2016), p. 033853. DOI: 10.1103/PhysRevA.93.033853. URL: https://link.aps.org/doi/10.1103/PhysRevA.93.033853 (visited on 01/24/2024).

[502] Z. Xiao et al. “Fast amplification and rephasing of entangled cat states in a qubit-oscillator system”. In: *Physical Review A* 99.1 (Jan. 16, 2019), p. 013827. DOI: 10.1103/PhysRevA.99.013827. URL: https://link.aps.org/doi/10.1103/PhysRevA.99.013827 (visited on 01/24/2024).

[503] Angelo Bassi et al. “Models of wave-function collapse, underlying theories, and experimental tests”. In: *Reviews of Modern Physics* 85.2 (Apr. 2, 2013), pp. 471–527. DOI: 10.1103/RevModPhys.85.471. URL: https://link.aps.org/doi/10.1103/RevModPhys.85.471 (visited on 01/24/2024).

[504] Markus Arndt and Klaus Hornberger. “Testing the limits of quantum mechanical superpositions”. In: *Nature Physics* 10.4 (Apr. 2014), pp. 271–277. ISSN: 1745-2481. DOI: 10.1038/nphys2863. URL: https://www.nature.com/articles/nphys2863 (visited on 01/24/2024).

[505] Florian Fröwis et al. “Macroscopic quantum states: Measures, fragility, and implementations”. In: *Reviews of Modern Physics* 90.2 (May 31, 2018), p. 025004. DOI: 10.1103/RevModPhys.90.025004. URL: https://link.aps.org/doi/10.1103/RevModPhys.90.025004 (visited on 01/24/2024).

[506] Dany Lachance-Quirion et al. “Resolving quanta of collective spin excitations in a millimeter-sized ferromagnet”. In: *Science Advances* 3.7 (July 2017). DOI: 10.1126/sciadv.1603150.

[507] Dany Lachance-Quirion et al. “Entanglement-based single-shot detection of a single magnon with a superconducting qubit”. In: *Science* 367.6476 (Jan. 2020), pp. 425–428. DOI: 10.1126/science.aaz9236.

[508] S.P. Wolski et al. “Dissipation-Based Quantum Sensing of Magnons with a Superconducting Qubit”. In: *Physical Review Letters* 125.11 (Sept. 2020), p. 117701. DOI: 10.1103/physrevlett.125.117701.

[509] Da Xu et al. “Quantum Control of a Single Magnon in a Macroscopic Spin System”. In: *Physical Review Letters* 130.19 (May 12, 2023), p. 193603. DOI: 10.1103/PhysRevLett.130.193603. arXiv: 2211.06644 [quant-ph]. URL: https://link.aps.org/doi/10.1103/PhysRevLett.130.193603 (visited on 01/17/2024).

[510] Jochen Kaupp et al. “Purcell-Enhanced Single-Photon Emission in the Telecom C-Band”. In: *Advanced Quantum Technologies* 6.12 (Oct. 2023). ISSN: 2511-9044. DOI: 10.1002/qute.202300242.

[511] Akira Fujiwara, Katsuhiko Nishiguchi, and Yukinori Ono. “Nanoampere charge pump by single-electron ratchet using silicon nanowire metal-oxide-semiconductor field-effect transistor”. In: *Applied Physics Letters* 92.4 (Jan. 28, 2008), p. 042102. ISSN: 0003-6951. DOI: 10.1063/1.2837544. URL: https://doi.org/10.1063/1.2837544 (visited on 02/21/2024).

[512] B. Roche et al. “A two-atom electron pump”. In: *Nature Communications* 4.1 (Mar. 12, 2013), p. 1581. ISSN: 2041-1723. DOI: 10.1038/ncomms2544. URL: https://www.nature.com/articles/ncomms2544 (visited on 02/23/2024).

[513] Alessandro Rossi et al. “An Accurate Single-Electron Pump Based on a Highly Tunable Silicon Quantum Dot”. In: *Nano Letters* 14.6 (June 11, 2014), pp. 3405–3411. ISSN: 1530-6984. DOI: 10.1021/nl500927q. URL: https://doi.org/10.1021/nl500927q (visited on 02/21/2024).

[514] Bernd Kaestner and Vyacheslavs Kashcheyevs. "Non-adiabatic quantized charge pumping with tunable-barrier quantum dots: a review of current progress". In: *Reports on Progress in Physics* 78.10 (Sept. 2015), p. 103901. ISSN: 1361-6633. DOI: 10.1088/0034-4885/78/10/103901. URL: http://dx.doi.org/10.1088/0034-4885/78/10/103901.

[515] J. van der Heijden, G. C. Tettamanzi, and S. Rogge. "Dynamics of a single-atom electron pump". In: *Scientific Reports* 7.1 (Mar. 15, 2017), p. 44371. ISSN: 2045-2322. DOI: 10.1038/srep44371. URL: https://www.nature.com/articles/srep44371 (visited on 02/21/2024).

[516] Alessandro Rossi et al. "Gigahertz Single-Electron Pumping Mediated by Parasitic States". In: *Nano Letters* 18.7 (July 11, 2018), pp. 4141–4147. ISSN: 1530-6984. DOI: 10.1021/acs.nanolett.8b00874. URL: https://doi.org/10.1021/acs.nanolett.8b00874 (visited on 02/21/2024).

[517] Kazunari Hashimoto and Chikako Uchiyama. "Nonadiabaticity in Quantum Pumping Phenomena under Relaxation". In: *Entropy* 21.9 (Sept. 2019), p. 842. ISSN: 1099-4300. DOI: 10.3390/e21090842. URL: https://www.mdpi.com/1099-4300/21/9/842 (visited on 02/21/2024).

[518] Shuji Nakamura et al. "Universality and Multiplication of Gigahertz-Operated Silicon Pumps with Parts Per Million-Level Uncertainty". In: *Nano Letters* 24.1 (Jan. 10, 2024), pp. 9–15. ISSN: 1530-6984. DOI: 10.1021/acs.nanolett.3c02858. URL: https://doi.org/10.1021/acs.nanolett.3c02858 (visited on 02/16/2024).

[519] R. Pillarisetty et al. "Qubit Device Integration Using Advanced Semiconductor Manufacturing Process Technology". In: *2018 IEEE International Electron Devices Meeting (IEDM)*. IEEE, Dec. 2018. DOI: 10.1109/iedm.2018.8614624.

[520] Ruoyu Li et al. "A crossbar network for silicon quantum dot qubits". In: *Science Advances* 4.7 (July 2018). DOI: 10.1126/sciadv.aar3960.

[521] Elena Ferraro and Enrico Prati. "Is all-electrical silicon quantum computing feasible in the long term?" In: *Physics Letters A* 384.17 (2020), p. 126352. ISSN: 0375-9601. DOI: https://doi.org/10.1016/j.physleta.2020.126352. URL: https://www.sciencedirect.com/science/article/pii/S0375960120301626.

[522] Michael A. Fogarty. "Silicon edge-dot architecture for quantum computing with global control and integrated trimming". In: (Aug. 19, 2022). arXiv: 2208.09172 [quant-ph].

[523] Zeheng Wang et al. "Jellybean Quantum Dots in Silicon for Qubit Coupling and On-Chip Quantum Chemistry". In: *Advanced Materials* 35.19 (2023), p. 2208557. ISSN: 1521-4095. DOI: 10.1002/adma.202208557. arXiv: 2208.04724 [cond-mat.mes-hall]. URL: https://onlinelibrary.wiley.com/doi/abs/10.1002/adma.202208557 (visited on 02/05/2024).

[524] Andrea Corna et al. "Electrically driven electron spin resonance mediated by spin–valley–orbit coupling in a silicon quantum dot". In: *npj Quantum Information* 4.1 (Feb. 2, 2018), pp. 1–7. ISSN: 2056-6387. DOI: 10.1038/s41534-018-0059-1. URL: https://www.nature.com/articles/s41534-018-0059-1 (visited on 02/05/2024).

[525] N.E. Penthorn, J.S. Schoenfield, and J.D. et al. Rooney. "Two-axis quantum control of a fast valley qubit in silicon". In: *npj Quantum Information* 5.94 (Nov. 2019). DOI: 10.1038/s41534-019-0212-5. URL: https://doi.org/10.1038/s41534-019-0212-5.

[526] Stephan G. J. Philips et al. "Universal control of a six-qubit quantum processor in silicon". In: *Nature* 609.7929 (Sept. 2022), pp. 919–924. ISSN: 1476-4687. DOI: 10.1038/s41586-022-05117-x. URL: https://www.nature.com/articles/s41586-022-05117-x (visited on 01/28/2024).

[527] Floris A. Zwanenburg et al. "Silicon quantum electronics". In: *Reviews of Modern Physics* 85.3 (2013), pp. 961–1019. ISSN: 1539-0756. DOI: 10.1103/revmodphys.85.961. URL: http://dx.doi.org/10.1103/RevModPhys.85.961.

[528] Malcolm S. Carroll and Thaddeus D. Ladd. "Silicon Qubits". In: *Library Journal* 1.SAND-2017-5868J (Feb. 28, 2018). ISSN: 0363-0277. DOI: 10.1016/b978-0-12-803581-8.09736-8. URL: https://www.osti.gov/biblio/1478329 (visited on 01/28/2024).

[529] Ben Mills. *Silicon-unit-cell-3D-balls.png*. URL: https://commons.wikimedia.org/wiki/File:Silicon-unit-cell-3D-balls.png.

[530] Inductiveload. *Brillouin Zone (1st, FCC).svg*. URL: https://commons.wikimedia.org/wiki/File:Brillouin_Zone_(1st,_FCC).svg.

[531] Cepheiden. *Band structure Si schematic.svg*. URL: https://fr.m.wikipedia.org/wiki/Fichier:Band_structure_Si_schematic.svg.

[532] Creative Commons. *Creative Commons Attribution Attribution-ShareAlike 2.5 Generic*. URL: https://creativecommons.org/licenses/by-sa/2.5/.

[533] Roger Lake et al. "Single and multiband modeling of quantum electron transport through layered semiconductor devices". In: *Journal of Applied Physics* 81.12 (June 15, 1997), pp. 7845–7869. ISSN: 0021-8979. DOI: 10.1063/1.365394. URL: https://doi.org/10.1063/1.365394 (visited on 02/02/2024).

[534] Timothy B. Boykin et al. "Valley splitting in strained silicon quantum wells". In: *Applied Physics Letters* 84.1 (Jan. 2004), pp. 115–117. ISSN: 1077-3118. DOI: 10.1063/1.1637718. URL: http://dx.doi.org/10.1063/1.1637718.

[535] Timothy B. Boykin et al. "Valley splitting in low-density quantum-confined heterostructures studied using tight-binding models". In: *Phys. Rev. B* 70 (16 Oct. 2004), p. 165325. DOI: 10.1103/PhysRevB.70.165325. URL: https://link.aps.org/doi/10.1103/PhysRevB.70.165325.

[536] Mark Friesen. "Theory of the Stark Effect for P Donors in Si". In: *Physical Review Letters* 94.18 (May 2005), p. 186403. DOI: 10.1103/physrevlett.94.186403.

[537] Mark Friesen et al. "Valley splitting theory of SiGe/Si/SiGe quantum wells". In: *Phys. Rev. B* 75 (11 Mar. 2007), p. 115318. DOI: 10.1103/PhysRevB.75.115318. URL: https://link.aps.org/doi/10.1103/PhysRevB.75.115318.

[538] Mark Friesen and S. N. Coppersmith. "Theory of valley-orbit coupling in a Si/SiGe quantum dot". In: *Phys. Rev. B* 81 (11 Mar. 2010), p. 115324. DOI: 10.1103/PhysRevB.81.115324. URL: https://link.aps.org/doi/10.1103/PhysRevB.81.115324.

[539] Xin Zhang et al. "Semiconductor quantum computation". In: *National Science Review* 6.1 (Dec. 2018), pp. 32–54. ISSN: 2053-714X. DOI: 10.1093/nsr/nwy153. URL: http://dx.doi.org/10.1093/nsr/nwy153.

[540] Dohun Kim et al. "Microwave-driven coherent operation of a semiconductor quantum dot charge qubit". In: *Nature Nanotechnology* 10.3 (Feb. 2015), pp. 243–247. DOI: 10.1038/nnano.2014.336.

[541] Aleksander Lasek et al. "Pulse-controlled qubit in semiconductor double quantum dots". In: (Mar. 2023). DOI: 10.48550/ARXIV.2303.04823. arXiv: 2303.04823 [quant-ph].

[542] J.S. Schoenfield, B.M. Freeman, and H Jiang. "Coherent manipulation of valley states at multiple charge configurations of a silicon quantum dot device". In: *Nat Commun* 8.64 (2017). DOI: 10.1038/s41467-017-00073-x. URL: https://doi.org/10.1038/s41467-017-00073-x.

[543] Y. H. Phang et al. "Correlated-interfacial-roughness anisotropy in ${\mathrm{Si}}_{1\mathrm{\ensuremath{-}}\mathit{x}}$${\mathrm{Ge}}_{\mathit{x}}$/Si superlattices". In: *Physical Review B* 50.19 (Nov. 15, 1994), pp. 14435–14445. DOI: 10.1103/PhysRevB.50.14435. URL: https://link.aps.org/doi/10.1103/PhysRevB.50.14435 (visited on 02/04/2024).

[544] Christian Teichert. "Self-organization of nanostructures in semiconductor heteroepitaxy". In: *Physics Reports* 365.5 (Aug. 1, 2002), pp. 335–432. ISSN: 0370-1573. DOI: 10.1016/S0370-1573(02)00009-1. URL: https://www.sciencedirect.com/science/article/pii/S0370157302000091 (visited on 02/04/2024).

[545] J Myslivečeк et al. "On the microscopic origin of the kinetic step bunching instability on vicinal Si(001)". In: *Surface Science* 520.3 (Dec. 1, 2002), pp. 193–206. ISSN: 0039-6028. DOI: 10.1016/S0039-6028(02)02273-2. URL: https://www.sciencedirect.com/science/article/pii/S0039602802022732 (visited on 02/04/2024).

[546] P. G. Evans et al. "Nanoscale Distortions of Si Quantum Wells in Si/SiGe Quantum-Electronic Heterostructures". In: *Advanced Materials* 24.38 (2012), pp. 5217–5221. ISSN: 1521-4095. DOI: 10.1002/adma.201201833. URL: https://onlinelibrary.wiley.com/doi/abs/10.1002/adma.201201833 (visited on 02/04/2024).

[547] Charles Tahan and Robert Joynt. "Relaxation of excited spin, orbital, and valley qubit states in ideal silicon quantum dots". In: *Physical Review B* 89.7 (Feb. 5, 2014), p. 075302. DOI: 10.1103/PhysRevB.89.075302. URL: https://link.aps.org/doi/10.1103/PhysRevB.89.075302 (visited on 02/05/2024).

[548] Guido Burkard et al. "Semiconductor spin qubits". In: *Reviews of Modern Physics* 95.2 (June 2023), p. 025003. DOI: 10.1103/revmodphys.95.025003.

[549] Zeng-Xing Liu, Hao Xiong, and Ying Wu. "Magnon blockade in a hybrid ferromagnet-superconductor quantum system". In: *Physical Review B* 100.13 (Oct. 2019), p. 134421. DOI: 10.1103/physrevb.100.134421.

[550] Ji-kun Xie, Sheng-li Ma, and Fu-li Li. "Quantum-interference-enhanced magnon blockade in an yttrium-iron-garnet sphere coupled to superconducting circuits". In: *Physical Review A* 101.4 (Apr. 2020), p. 042331. DOI: 10.1103/physreva.101.042331.

[551] Kun Wu et al. "Phase-controlled multimagnon blockade and magnon-induced tunneling in a hybrid superconducting system". In: *Physical Review A* 103.5 (May 2021), p. 052411. DOI: 10.1103/physreva.103.052411.

[552] Zhu-yao Jin and Jun Jing. "Magnon blockade in magnon-qubit systems". In: *Physical Review A* 108.5 (Nov. 1, 2023), p. 053702. DOI: 10.1103/PhysRevA.108.053702. arXiv: 2303.13823 [quant-ph]. URL: https://link.aps.org/doi/10.1103/PhysRevA.108.053702 (visited on 01/17/2024).

[553] Marios Kounalakis, Gerrit E. W. Bauer, and Yaroslav M. Blanter. "Analog Quantum Control of Magnonic Cat States on a Chip by a Superconducting Qubit". In: *Physical Review Letters* 129.3 (July 13, 2022), p. 037205. DOI: 10.1103/PhysRevLett.129.037205. URL: https://link.aps.org/doi/10.1103/PhysRevLett.129.037205 (visited on 11/02/2023).

[554] Shiwen He et al. "Generation of a Schrödinger cat state in a hybrid ferromagnet-superconductor system". In: *Physical Review A* 107.2 (Feb. 2023), p. 023709. DOI: 10.1103/physreva.107.023709.

[555] S. De Liberato et al. "Extracavity quantum vacuum radiation from a single qubit". In: *Phys. Rev. A* 80 (5 Nov. 2009), p. 053810. DOI: 10.1103/PhysRevA.80.053810. URL: https://link.aps.org/doi/10.1103/PhysRevA.80.053810.

[556] A. Ridolfo et al. "Photon Blockade in the Ultrastrong Coupling Regime". In: *Phys. Rev. Lett.* 109 (19 Nov. 2012), p. 193602. DOI: 10.1103/PhysRevLett.109.193602. URL: https://link.aps.org/doi/10.1103/PhysRevLett.109.193602.

[557] L. Garziano et al. "Switching on and off of ultrastrong light-matter interaction: Photon statistics of quantum vacuum radiation". In: *Physical Review A* 88.6 (Dec. 2013), p. 063829. DOI: 10.1103/physreva.88.063829.

[558] M. Schmidt et al. "Optomechanical creation of magnetic fields for photons on a lattice". In: *Optica* 2.7 (July 2015), p. 635. DOI: 10.1364/optica.2.000635.

[559] Weichao Yu, Tao Yu, and Gerrit E. W. Bauer. "Circulating cavity magnon polaritons". In: *Physical Review B* 102.6 (Aug. 2020), p. 064416. DOI: 10.1103/physrevb.102.064416.

[560] Jeremy Bourhill et al. "Generation of Circulating Cavity Magnon Polaritons". In: *Physical Review Applied* 19.1 (Jan. 2023), p. 014030. DOI: 10.1103/physrevapplied.19.014030.

[561] Simone De Liberato, Cristiano Ciuti, and Iacopo Carusotto. "Quantum Vacuum Radiation Spectra from a Semiconductor Microcavity with a Time-Modulated Vacuum Rabi Frequency". In: *Physical Review Letters* 98.10 (Mar. 2007), p. 103602. DOI: 10.1103/physrevlett.98.103602.

[562] J. R. Johansson et al. "Nonclassical microwave radiation from the dynamical Casimir effect". In: *Physical Review A* 87.4 (Apr. 2013), p. 043804. DOI: 10.1103/physreva.87.043804.

[563] Pasi Lähteenmäki et al. "Dynamical Casimir effect in a Josephson metamaterial". In: *Proceedings of the National Academy of Sciences* 110.11 (Feb. 2013), pp. 4234–4238. DOI: 10.1073/pnas.1212705110.

[564] R. Stassi et al. "Spontaneous Conversion from Virtual to Real Photons in the Ultrastrong-Coupling Regime". In: *Physical Review Letters* 110.24 (June 2013), p. 243601. DOI: 10.1103/physrevlett.110.243601.

[565] Viktor Dodonov. "Fifty Years of the Dynamical Casimir Effect". In: *Physics* 2.1 (Feb. 2020), pp. 67–104. DOI: 10.3390/physics2010007.

[566] Gheorghe Sorin Paraoanu and Göran Johansson. "Listening to the quantum vacuum: a perspective on the dynamical Casimir effect". In: *Europhysics News* 51.4 (July 2020), pp. 18–20. DOI: 10.1051/epn/2020402.

[567] M. Amooshahi and F. Kheirandish. "Electromagnetic field quantization in a magnetodielectric medium with external charges". In: *Physical Review A* 76.6 (Dec. 5, 2007), p. 062103. DOI: 10.1103/PhysRevA.76.062103. URL: https://link.aps.org/doi/10.1103/PhysRevA.76.062103 (visited on 02/07/2024).

[568] Stefan Scheel and Stefan Yoshi Buhmann. *Macroscopic QED - concepts and applications*. arXiv:0902.3586. type: article. arXiv, Feb. 20, 2009. DOI: 10.48550/arXiv.0902.3586. arXiv: 0902.3586[quant-ph]. URL: http://arxiv.org/abs/0902.3586 (visited on 02/07/2024).

[569] Kaushik P. Seshadreesan, Jonathan P. Dowling, and Girish S. Agarwal. "Non-Gaussian entangled states and quantum teleportation of Schrödinger-cat states*". In: *Physica Scripta* 90.7 (June 2015), p. 074029. ISSN: 1402-4896. DOI: 10.1088/0031-8949/90/7/074029. URL: https://dx.doi.org/10.1088/0031-8949/90/7/074029 (visited on 02/16/2024).

[570] Akira Kitagawa et al. "Entanglement evaluation of non-Gaussian states generated by photon subtraction from squeezed states". In: *Physical Review A* 73.4 (Apr. 10, 2006), p. 042310. DOI: 10.1103/PhysRevA.73.042310. URL: https://link.aps.org/doi/10.1103/PhysRevA.73.042310 (visited on 02/16/2024).

[571] G. S. Agarwal. "Engineering non-Gaussian entangled states with vortices by photon subtraction". In: *New Journal of Physics* 13.7 (July 2011), p. 073008. ISSN: 1367-2630. DOI: 10.1088/1367-2630/13/7/073008. URL: https://dx.doi.org/10.1088/1367-2630/13/7/073008 (visited on 02/16/2024).

[572] Franz Utermohlen. *Spin-Wave Theory Using the Holstein–Primakoff Transformation*. URL: https://cpb-us-w2.wpmucdn.com/u.osu.edu/dist/3/67057/files/2020/02/spin-wave_theory_using_the_Holstein-Primakoff_transformation.pdf. (accessed: 30.06.2021).

[573] D.M. Pozar. *Microwave Engineering, 4th Edition*. Wiley, 2011. ISBN: 9781118213636.

[574] Yunshan Cao et al. “Exchange magnon-polaritons in microwave cavities”. In: *Physical Review B* 91.9 (Mar. 2015), p. 094423. DOI: 10.1103/physrevb.91.094423.

[575] Babak Zare Rameshti and Gerrit E. W. Bauer. “Indirect coupling of magnons by cavity photons”. In: *Physical Review B* 97.1 (Jan. 2018), p. 014419. DOI: 10.1103/physrevb.97.014419.

[576] Tomáš Neuman, Derek S. Wang, and Prineha Narang. “Nanomagnonic Cavities for Strong Spin-Magnon Coupling and Magnon-Mediated Spin-Spin Interactions”. In: *Physical Review Letters* 125.24 (Dec. 2020), p. 247702. DOI: 10.1103/physrevlett.125.247702.

[577] Ming-Wen Hu, Weichao Yu, and Yi-Pu Wang. “Auxiliary Mode Mediated Coherent and Complex Couplings in a Cavity Magnonic System”. In: *Annalen der Physik* 534.4 (Jan. 2022), p. 2100534. DOI: 10.1002/andp.202100534.

[578] Rodolfo Gambini and Jorge Pullin. *A First Course in Loop Quantum Gravity*. Oxford University Press, Sept. 2011. DOI: 10.1093/acprof:oso/9780199590759.001.0001.